Design, Construction, and Conformational Analysis of γ- Peptide Double Helices

विद्या वाचस्पति की
उपाधि की अपेक्षाओं की आंशिक पूर्ति में प्रस्तुत शोध प्रबंध

A thesis submitted in partial fulfillment of the requirements of the degree of Doctor of Philosophy

द्वारा / by

सैकत पहन/ Saikat Pahan

पंजीकरण सं./ Registration No.: 20162023

शोध प्रबंध पर्यवेक्षक/Thesis Supervisor:

प्रो. एच. एन. गोपी/ Prof. H. N. Gopi



भारतीय विज्ञान शिक्षा एवं अनुसंधान संस्थान पुणे

INDIAN INSTITUTE OF SCIENCE EDUCATION AND RESEARCH PUNE

2023

Dedicated to

Teachers, Family, and Friends

CERTIFICATE

This is to certify that the work incorporated in the thesis entitled "**Design, Construction, and Conformational Analysis of γ-Peptide Double Helices**" submitted by **Saikat Pahan (ID No. 20162023)** carried out by the candidate at the Indian Institute of Science Education and Research (IISER), Pune, under my supervision. The work presented here or any part of it has not been included in any other thesis submitted previously for the award of any degree or diploma from any other University or Institution.

Date: 08-12-2023

Prof. Hosahudya N. Gopi
(Research Supervisor)
Professor, Department of Chemistry,
IISER-Pune
Pune-411008, India

Declaration

I hereby declare that the thesis entitled "**Design, Construction, and Conformational Analysis of γ-Peptide Double Helices**" submitted for the degree of Doctor of Philosophy in Chemistry at Indian Institute of Science Education and Research (IISER), Pune has not been submitted by me to any other University or Institution. This work was carried out at Indian Institute of Science Education and Research (IISER), Pune, India under the supervision of Prof. Hosahudya N. Gopi.

Date: 08-12-2023



Saikat Pahan

ID: 20162023

Research Fellow

Department of Chemistry, IISER-Pune.

Pune-411008

Acknowledgements

I would like to express my heartfelt gratitude to my supervisor, Prof. Hosahudya N. Gopi, whose unwavering support and guidance have been instrumental throughout my five-year research journey. His brilliance as a chemist, tireless work ethic, and commitment to both research and mentoring have been a constant source of inspiration. I am fortunate to work with him.

I extend my sincere thanks to our present Director, Prof. Sunil Bhagwat, and former Directors Prof. Jayant B. Udgaonkar and Prof. K. N. Ganesh for providing excellent facilities and financial support at the Indian Institute of Science Education and Research (IISER)-Pune. I am grateful for the four years of a research fellowship for my Ph.D. and the two years during my M.S. My appreciation also goes to Prof. Ramanathan Vaidhyanathan and Dr. Rajesh G. Gonnade for their invaluable contributions as members of my RAC committee. I am very much thankful to all chemistry faculties, technicians, and admin staff of IISER-Pune for their generous support.

I am fortunate to have had exceptional labmates, including Dr. Rajkumar, Dr. Sushil, Dr. Rahi, Dr. Veeresh, Dr. Anindita, and Dr. Puneeth. I also appreciate the guidance and knowledge gained from Dr. Rajkumar Misra during my M.S. I am grateful to my current labmates, Manjeet, Panda, Souvik, and Sandip, Sachin for their continuous support and camaraderie. They are cheerful and full of energy and highly motivated for science. We have got highly motivated undergraduate and summer project students Nithun, Manish, Devandanan, Avanthika, Utthara, and Prathibha to work in our lab as part of their summer internship or fifth-year project, they keep a joyful atmosphere in the lab.

For the last five years, I have been fortunate to have many good friends from IISER apart from my labmates. I am fortunate to have all our Int-PhD-2016 batchmates Debanjan, Pulak, Indra, Joy, Prakash, Mousakhi, Ateek, Suman, Abhishek, Markosh, and Gaurav. I also thank my juniors Panda, Pratim, Sumit, and Abhijit for being there always with me and we together have many good memories. Also, I would like to thank Rishu for his selfless help in Crystallography whenever I needed it.

I express my deepest gratitude to my family for their unwavering encouragement and belief in me. Lastly, I acknowledge the divine strength and courage granted by God, enabling me to pursue my aspirations.

Saikat Pahan

Contents

Abbreviations……i

Abstract……..…….……....iv

Publications……..……v

Chapter 1: A Comprehensive Introduction of Peptide Foldamers Composed of Unnatural Amino Acids

1.1. Introduction…….……..2

1.2. Protein Structure……...….2

1.3. Mimicking of Protein Secondary Structures ……..……...6

1.4. Peptide Foldamers of β-Amino Acids …….…….....6

1.5. Peptide Foldamers of γ-Amino Acids ……..9

1.6. Heterogeneous Foldamers Containing β- and γ-Amino Acids ……....11

1.7. α, β-Unsaturated γ-Amino Acids Based Peptide Foldamers……...14

1.8. Double Helical Foldamers……..….18

1.9. References…….....30

Chapter 2: Design of Chiral β-Double Helices from γ-Peptide Foldamers

2.1. Introduction……..…39

2.2. Objective of the Present Work ……..…….……..……40

2.3. Results and Discussion ……..……..40

2.3.1. Crystal Structure Analysis of **P1**……...……..…….41

2.3.2. Crystal Structure Analysis of **P3** and **P4**……...…43

2.3.3. Circular Dichroism Analysis of the Peptides **P1**-**P4**……...….47

2.3.4. Temperature-Dependent ^{1}H Experiments of **P1**-**P4**……..…...51

2.3.5. DMSO-d_6 Titration of Peptides **P1**, **P2**, **P3** & **P4**…….…….....54

2.3.6. 2D-NMR Analysis of Peptide **P4**……..……55

2.3.7. Structural Analogy with Other Synthetic and Natural Peptide β-Double Helices…….……57

2.3.8. Transmembrane Ion Channel Activity……...…59

2.4. Conclusion……...….60

2.5. Experimental Section……..60

2.5.1. Materials and Methods ……....60

2.5.2. Synthesis of Peptide **P1**…….……...…61

2.5.3. Synthesis of Peptides **P2**, **P3** and **P4**……..……...…63

2.6. Ion Transport Experiments ……....….65

2.7. Calcein Leakage Assay……....……..…..68

2.8. Characterization of Monomers and Peptides…… …….…….70

2.9. Appendix ……...…….....75

2.9.1. ORTEP Diagrams of **P1**, **P3** and **P4**…...……...……...…75

2.9.1.1. ORTEP Diagram of peptide **P1**…….....75

2.9.1.2. ORTEP Diagram of peptide **P3**……..…76

2.9.1.3. ORTEP Diagram of Peptide **P4**…….……..…..77

2.10. Crystal Structure Information…….…..78

2.11. References…….……...79

2.12. ^{1}H, ^{13}C NMR and Mass spectra of Peptides **P1**-**P4**…….……82

Chapter 3: Modulating β-Sheet Mimetics: Influence of Substituents on the Transformation of (*E*)-Vinylogous γ-Amino Acid Oligomers into β-Double Helix and C_{14}-Helix

3.1. Introduction……...……....…101

3.2. Object of the Present Work……...…….102

3.3. Results and Discussion……..…...103

3.3.1 Crystal Structure Analysis of **P4**…….…....103

3.3.2. Conformational Analysis of Peptides **P4** and **P5** in Solution State…….…...107

3.3.3. DMSO-d_6 Titration Experiment for **P4** and **P5**…….…..……107

3.3.4. Temperature-Dependent ^{1}H Experiments of **P4** and **P5**…….…108

3.3.5 Circular Dichroism Analysis…….…..110

3.3.6. Crystal Structure Analysis of **P6**…….....…115

3.3.7. Conformational Analysis of Peptides **P6** in Solution State…….……117

3.3.7.1. DMSO-d6 Titration Experiment for **P6**…….…..…118

3.3.7.2. Temperature-dependent experiments of **P6**……...……..……118

3.3.8. Circular Dichroism Analysis of **P6**……...……..…119

3.3.9. Crystal Structure Analysis of **P7**……..…...121

3.4. Conclusion……..…...123

3.5. Experimental Section……..……...123

3.5.1 Materials and Methods…….……..…..123

3.5.2 Synthetic Procedures for Peptides…….…..….124

3.5.3. Synthesis of Peptide P1, P2 and P3…….124

3.5.3.1. Synthesis of Peptide **P1**…….……..124

3.5.3.2. Synthesis of Peptide **P2**……..…….125

3.5.3.3. Synthesis of Peptide **P3**…….……..125

3.5.4. Synthesis of Peptide **P4**…….…….126

3.5.5. Synthesis of Peptide **P5**…….…….128

3.5.6. Synthesis of Peptide **P6**……...…129

3.5.7. Synthesis of Peptide **P7**…….….131

3.6. Characterization of Monomer and Peptides……...……131

3.7. Appendix……...…139

3.7.1. ORTEP Diagrams……..…….139

3.7.1.1. ORTEP Diagram of Peptide **P4**…….……..139

3.7.1.2. ORTEP Diagram of Peptide **P6**……..…….140

3.7.1.3. ORTEP Diagram of Peptide **P7**……...…141

3.8. Crystal Structure Information of the Peptides……..…..…142

3.9. References…….....…143

3.10. ^{1}H, ^{13}C NMR and Mass Spectra of Peptides **P1**-**P7**……..147

Chapter 4: Porous Frameworks of Double Helical Peptide Foldamers

4.1. Introduction……169

4.2. Object of the Present Work……169

4.3. Results and Discussions……170

4.3.1. Crystal Structure Analysis of Peptide **P1**……171

4.3.2. Crystal Structure Analysis of **P3**……173

4.3.3. Self-Assembly of Peptides **P1** and **P3**……175

4.3.4. Crystal Structure of Peptide **P4**……182

4.3.5. Crystal Structure of Peptide **P5**……184

4.3.6. Thermal Properties of Peptide **P1** and **P3**……188

4.3.7. Optical Properties of **P1**……188

4.3.8. Chiroptical Properties of Peptides **P1** and **P2**……191

4.4. Conclusion……192

4.5. Experimental Section……193

4.5.1 Materials and Methods……193

4.5.2 Synthesis Procedures for the Peptides……193

4.5.2.1 Synthesis of the Peptide **P1**……193

4.5.2.2. Synthesis of the Peptide **P2**……194

4.5.2.3. Synthesis of the Peptide **P3**……196

4.5.2.4. Synthesis of the Peptide **P4**……198

4.5.2.5. Synthesis of the Peptide **P5**……199

4.6. Characterization of Peptides **P1**-**P5**……..…….202

4.7. Appendix…….……..……207

4.7.1. ORTEP Diagrams……..….207

4.7.1.1 ORTEP Diagram of Peptide **P1**…….…...207

4.7.1.2. ORTEP Diagram of Peptide **P3**……..….208

4.7.1.3. ORTEP Diagram of peptide **P4**……..……..209

4.7.1.4 ORTEP Diagram of Peptide **P5**……..……..210

4.8. Crystal Structure Information……..……..211

4.9. References……..……...215

4.10. ^{1}H, ^{13}C NMR and Mass spectra of Peptides **P1**-**P5**……...……...219

Chapter 5: Supramolecular Assemblies and Optoelectronic Properties of β-Double Helices Appended with Donor-Acceptor Groups

5.1. Introduction…….…..…….235

5.2. Objective of the Present Work……..……236

5.3. Results and Discussions…….…….……...236

5.3.1. Crystal Structure Analysis of **P1**……..……...237

5.3.2 Self-Assembly of **P1**……..……..239

5.3.3. Crystal Structure Analysis of **P2**……..……..….243

5.3.4. Self-Assembly of **P2**……..……..…245

5.3.5. Crystal Structure Analysis of **P3**……..…...…248

5.3.6. Self-Assembly of **P3**……..……..…250

5.3.7. Photophysical Properties of the Peptides……..……..…254

5.3.8. Circular Dichroism Analysis of Peptides……..……..257

5.3.9. Current-Voltage Study of the Peptides…….…..…….258

5.3.10. Photo-switching Property……...……..……259

5.4. Conclusion……..……...260

5.5. Experimental Section…….……...260

5.5.1 Materials and Methods…….…...260

5.5.2. Synthesis Procedures for the Peptides…….……...261

5.5.2.1. Synthesis of the Peptide **P1**……..……261

5.5.2.2. Synthesis of Peptide **P2**……...……..……..263

5.5.2.3. Synthesis of Peptide **P3**…….……..265

5.6 Characterization of Peptides **P1**, **P2** and **P3**…….……...266

5.7. Appendix…….……..……270

5.7.1. ORTEP Diagrams…….……..……270

5.7.1.1. ORTEP Diagram of Peptide **P1**…….…..……..…270

5.7.1.2. ORTEP Diagram of peptide **P2**…….……..271

5.7.1.3. ORTEP Diagram of peptide **P3**…….…..…272

5.8 Crystal Structure Information…….…..……...273

5.9. References…….…….……...276

5.10. ^{1}H, ^{13}C NMR and Mass Spectra of Peptides **P1**-**P3**……...……...…281

Permission for Reuse of Figures from Journals……..…….....292

Abbreviations

Ac_2O = Acetic anhydride

ACN = Acetonitrile

AcOH = Acetic acid

Aib = α-Amino isobutyric acid

aq. = Aqueous

Bn = Benzyl

Boc = tert-Butoxycarbonyl

$(Boc)_2O$ = Boc anhydride

^tBu = tertiary Butyl

Calcd. = Calculated

CCDC no. = Cambridge Crystallographic Data Centre number

CD = Circular Dichroism

CPL = Circularly Polarized Luminescence

CIF = Crystallographic Information File

dγ = dehydro gamma

DCM = Dichloromethane

DIPEA = Diisopropylethyl Amine

DMF = Dimethylformamide

DMSO = Dimethylsulfoxide

EtOH = Ethanol

Et = Ethyl

EtOAc = Ethyl acetate

g = gram

h = hours

H-bond = Hydrogen bond

HOBt = Hydroxybenzotriazole

HCl = Hydrochloric acid

HEPES = 4-(2-hydroxyethyl)-1-piperazineethanesulfonic acid,

HPTS = 8-Hydroxypyrene-1,3,6-Trisulfonic Acid

LUV = Large Unimolecular Vesicles

M = Molar

MALDI-TOF/TOF = Matrix-Assisted Laser Desorption/Ionization-Time of Flight

Me = Methyl

MeOH = Methanol

mg = Milligram

min = Minutes

µL = Micro liter

mL = Milliliter

mM = Millimolar

mmol = millimoles

m.p = Melting Point

MPFs = Metal Peptide Frameworks

MS = Mass Spectroscopy

N = Normal

NDI = 1,8-Naphthaline diimide

NMI = 1,8-Naphthaline monoamide

NMR = Nuclear Magnetic Resonance

NOE = Nuclear Overhauser Effect

NOESY = **N**uclear **O**verhauser **E**ffect **S**pectroscopy

ODCB = 1,2-Dichlorobenzene

ORTEP = Oak Ridge Thermal-Ellipsoid Plot Program

PG = Protecting Group

ppm = Parts per million

R_f = Retention factor

R_t = Retention time

ROESY = **R**otating-frame nuclear **O**verhauser **E**ffect correlation **S**pectroscop**Y**

RP- HPLC = Reversed Phase-High Performance Liquid Chromatography

RT = Room Temperature

TFA = Trifluoroacetic acid

THF = Tetrahydrofuran

UV = Ultraviolet–Visible Spectroscopy

TOCSY = **TO**tal **C**orrelation **S**pectroscop**Y**

*Z*dγ = Z-dehydro gamma

Abstract

The double helix is the most common and very important structural motif in nucleic acids. In comparison, double helix motifs are rare in proteins and other biomolecules. Nevertheless, gramicidins A-D and feglymicin, linear natural polypeptides with alternating amino acid configuration, produced by Bacillus brevis have been shown to adopt double helix conformation. In addition, synthetic peptides with alternating α_L and α_D amino acids have also been shown to adopt double helix structures. These double helical structures of α_L, α_D -peptides are of particular interest because of their ability to form transmembrane channels. Extensive efforts have been made over the decades to design β-double helix structures from different building blocks. Besides the alternating α_L and α_D peptides, aromatic oligoamides and the aromatic building blocks capable of metal coordination have been used to construct double helices. Recently, we demonstrated the double helical structures from the homooligomers of achiral (*E*)-α,β-unsaturated 4, 4-dialkyl substituted γ-amino acids. In continuation, we sought to investigate the design of chiral double helices, the ability of the double helices to accommodate other than the (*E*)-α,β-unsaturated 4, 4-dialkyl substituted γ-amino acids, their supramolecular assemblies, and their transmembrane channel properties. In this work, we are demonstrating the construction of chiral double helices with opposite handedness from the oligomers of alternating (*E*)-α,β-unsaturated 4, 4-dialkyl substituted γ-amino acids (*E*)-α,β-unsaturated γ^4-amino acids and the utilization of chiral double helices as transmembrane channels. Further, we investigated the conformational flexibility of the double helix to accommodate saturated γ-amino acids and the transformation of β-double helices into C_{14}-helices by varying γ-amino acid content. Using fluorescent reporter groups, we demonstrated the formation of double helices from the linear peptides in solution. Additionally, these double helices are self-assembled into a remarkable porous framework through H-bond networks in the solid state. In continuation, we further designed double helices appended with electron-donating and electron-deficient systems and studied their conformations and their molecular assembly. Overall, we designed and studied new double helices from gamma-peptide foldamers. The new beta-double helices described here may serve as transmembrane channel-forming candidates, light harvesting, and conducting materials.

Publications

1. Design of Chiral β-Double Helices from γ-Peptide Foldamers. **Pahan**, **S.**; Dey, S.; George, G.; Panda Mahapatra, S.; Puneeth Kumar, Drgk.; Gopi, H. N. *Angew. Chemie Int. Ed.* **2023**, e202316309.

2. Tuning β-Sheet Mimetics: Crafting β-Double Helix and C14-Helix via Substituent-Driven Transformation in (E)-Vinylogous γ-Amino Acid Oligomers. **Pahan**, **S.**; Gopi, H. N. *Manuscript under review.*

3. Porous Frameworks of Double Helical Peptide Foldamers. **Pahan**, **S.**; Gopi, H. N. *Manuscript under submission.*

4. Supramolecular Assemblies and Optoelectronic Properties of β-Double Helices Appended with Donor-Acceptor Groups. **Pahan**, **S.**; Gopi, H. N. *Manuscript under preparation.*

5. Metal-Coordinated Supramolecular Polymers from the Minimalistic Hybrid Peptide Foldamers. Dey, S.; Misra, R.; Saseendran, A.; **Pahan**, **S**.; Gopi, H. N. *Angew. Chemie Int. Ed.* **2021**, *60*, 9863.

6. Proteolytically Stable Aαγ-Hybrid Peptides Inhibit the Aggregation and Cytotoxicity of Aβ 42. Puneeth Kumar, Drgk. R.; Nalawade, S. A.; **Pahan, S**.; Singh, M.; Senapati, D. K.; Roy, S.; Dey, S.; Toraskar, S. U.; Raghothama, S.; Gopi, H. N. *ACS Chem. Neurosci.* **2023**, *14*, 3398.

7. Foldamer Nanotubes Mediated Label-Free Detection of Protein-Small Molecule Interactions. Puneeth Kumar, Drgk. R.; Manzoor Bhat, Z.; Dey, S.; Roy, S.; Panda Mahapatra, **S.; Pahan**, S.; Thotiyl, M. O.; Gopi, H. N. *Chem.Eur. J.* **2023**,*29*, e2023004.

8. HBTU Mediated Synthesis of α,β-Unsaturated γ-Lactams from *E* -α,B-Unsaturated γ-Amino Acids. Singh, M.; Nalawade, S. A.; Kumar, Drgk. R. P.; Veeresh, K.; **Pahan, S**.; Dey, S.; Gopi, H. N. *Eur.J. Org.Chem*. **2023**,*26*, e2023006.

9. Anion Tuned Structural Modulation and Nonlinear Optical Effects of Metal-Ion Directed 3_{10}-Helix Networks. Roy, S.; Chaturvedi, A.; Dey, S.; Puneeth Kumar, Drgk. R.; **Pahan, S**.; Panda Mahapatra, S.; Mandal, P.; Gopi, H. N. *Chem.Eur.J*. **2023**, e202303135.

10. Designing β-Double-Helix Structures from α, γ-Hybrid Foldamers. Puneeth Kumar, Drgk. R, George, G.; **Pahan, S**.; Dey, S.; Gopi, H. N. *Manuscript under review.*

Chapter 1

A Brief Introduction of Peptide Foldamers Composed of Unnatural Amino Acids

1.1. Introduction

The exploration of proteins has long been a cornerstone in the field of biology, holding unparalleled significance in the intricate tapestry of life.[1] These remarkable macromolecules stand as the fundamental building blocks of living organisms, orchestrating a myriad of cellular processes crucial for life, growth, and development.[2] The intricate and precisely arranged folds enable proteins to interact with other molecules, facilitating their specific functions within the cellular environment. Precise protein folding is essential for ensuring the integrity and functionality of these molecular machines. Conversely, protein misfolding or denaturation can lead to a loss of function and, in certain instances, has been implicated in various pathological conditions. Diseases such as Alzheimer's, cystic fibrosis, Parkinson's, and diabetes have been linked to aberrant protein folding. Understanding the intricate relationship between protein structure and function is crucial for unraveling the molecular basis of diseases and developing potential therapies. This dynamic field of research contributes significantly to our understanding of the molecular foundations of life, providing opportunities for advancements in medicine and biotechnology.

1.2. Protein Structures

The 20 ribosomal amino acids are the building blocks from which nature has created a wide variety of proteins with distinct 3D structures and functions. According to Figure 1, there are four main levels at which protein architectures are described.

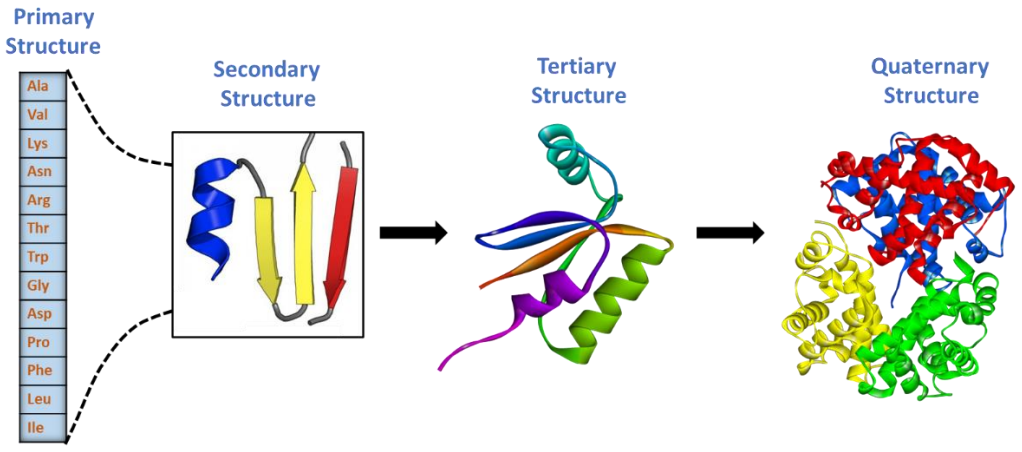


Figure 1: Schematic representation of protein structures (tertiary structure PDB code 1H75 and quaternary structure represents hemoglobin quaternary structure PDB code 1MKO).

Primary structure: The primary structure of a protein is determined by the linear arrangement of amino acids connected by peptide bonds. This sequence serves as the fundamental building block of a protein and is intricately linked to the genetic material of an organism, typically encoded in DNA. The precise order of amino acids in the primary structure holds paramount importance as it defines the overall identity of the protein. The functionality, stability, and interactions of a protein with other molecules are profoundly influenced by its specific amino acid sequence. Each amino acid brings unique properties to the protein chain, including its size, charge, and chemical characteristics. These attributes, in turn, dictate the protein's three-dimensional structure and its ability to perform specific biological functions.

Secondary structures: The secondary structure of a protein pertains to the local folding patterns occurring within specific segments of the polypeptide chain. The -helix and β-sheet structures were first described by Linus Pauling and colleagues in their groundbreaking work.[2] The distinct pattern of hydrogen bond pseudo cycles between the main chain NH and CO groups characterizes these secondary structures. Reverse turns are the loop regions that connect two neighboring anti-parallel β-strands. In their seminal work, G. N. Ramachandran and colleagues[3] used the two degrees of torsional freedom ϕ and ψ to characterize the sterically permitted stable conformations of polypeptide secondary structures (Figure 2C).

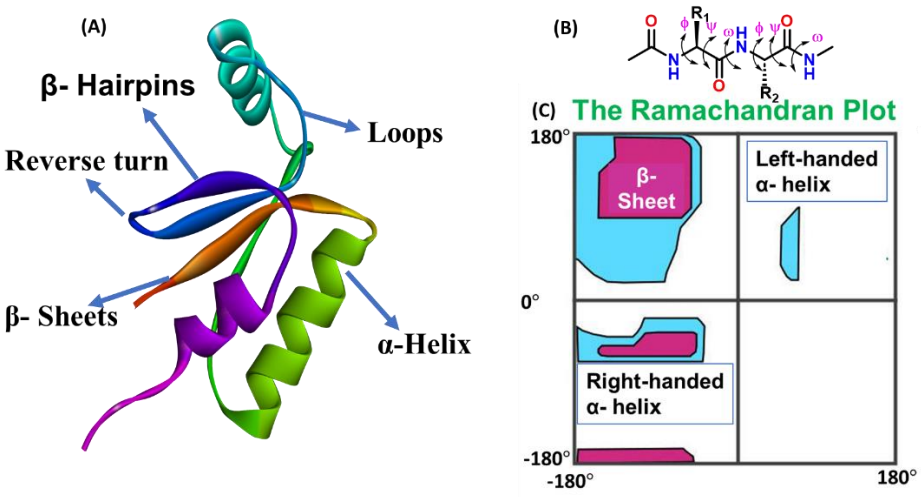


Figure 2: (A) The ribbon model of a protein visually represents various secondary structural elements, showcasing distinctive folds and patterns within the protein structure. (PDB code: 1H75) (B) Torsional angles variables ϕ and ψ on peptide backbone of α-amino acids (C) Classical Ramachandran plot and the allowed region for the torsional angles of different secondary structures.

Helices: Helices, a fundamental element of protein structures, are classified into four distinct categories based on the involvement of hydrogen-bond pseudocycles and the number of residues per turn: 2.2_7 (γ-helix), 3.0_{10}, 3.6_{13} (α-helix), and 4.4_{16} (π-helix). Among these, the α-helix is the most prevalent in proteins. In 1951, Linus Pauling introduced the α-helix structure, characterized by 3.6 residues per turn and a hydrogen-bond pseudocycle involving 13 atoms. The general nomenclature for the α-helix is 3.6_{13}-*P*-helix, with average torsion angles ϕ at -60° and ψ at -45°. In contrast, the 3.0_{10}-helix is less commonly found in proteins and typically occurs at the terminus of the α-helix in protein structures. The average torsion angles for the 3.0_{10}-*P*-helix are ϕ at -49° and ψ at -26°, with three residues per turn and 10-atom hydrogen-bond pseudo cycles. The π-helix is denoted as 4.4_{16}-*P*-helix (ϕ = -55°, ψ = -70°), while the γ-helix is described as the 2.2_7 helix (ϕ = -70°, ψ = 70°). Each of these helical structures contributes to the structural diversity of proteins, with the α-helix being the most prevalent and historically significant. Various helical configurations with different forms of H-bonding are depicted schematically in Figure 3**.**

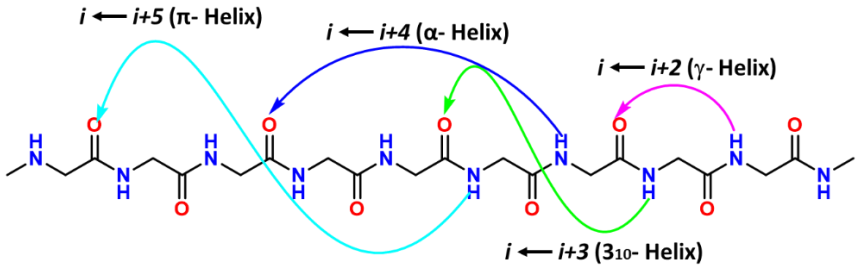


Figure 3: Representation of H-bonding pattern in different helices.

β-Sheets: β-sheets, also known as beta strands or beta pleated sheets, are the second major secondary structure motif in proteins. William Astbury[4] proposed the first -sheet structure in 1930. But Linus Pauling and Robert Corey[5] modified the β -sheet structure in 1951. β- sheets consist of multiple beta strands, which are extended segments of the polypeptide chain that run side by side and form hydrogen bonds between neighboring strands. The upper left quadrant of the Ramachandran Map (Figure 2C) shows that the torsion angles of the ϕ and ψ values are within the large structurally permissible region. Based upon the β-strands arranging directionality in β-pleated sheets, they are classified into (i) parallel β-sheets and (ii) anti-parallel β-sheets (Figure 4). In general, β-sheets commonly display a right-handed twist, primarily driven by intrastrand non-bonded interactions and interstrand geometric constraints. However, in the tertiary structure of

proteins, these β-sheets are positioned at approximately 30° angles relative to each other within their β-sheet configuration.

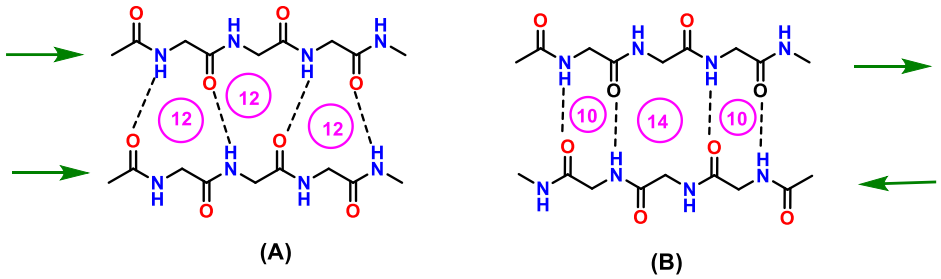


Figure 4: Depiction of the hydrogen bonding pattern and the directional arrangement of polypeptide chains within β-sheet structures. (a) Parallel β-sheets (b) Anti-parallel β-sheets.

Reverse-turns: Reverse turns, a crucial aspect of protein secondary structures, play a significant role in shaping the three-dimensional conformation of proteins. The categorization of reverse turns is primarily based on the number of amino acid residues responsible for inducing a change in the directionality of the polypeptide chain. These turns are distinguished as follows: π-turn (involving 6 amino acids), α-turn (involving 5 amino acids), β-turn (involving 4 amino acids), γ-turn (involving 3 amino acids), and δ-turn (involving 2 amino acids). Notably, β-turns are prevalent in protein structures. The classification of β-turns goes further, considering the dihedral angles ϕ and ψ of residues *i*+1 and *i*+2. This leads to subcategories such as type I, II, and III, along with their mirror image counterparts, known as type I', II', and III' turns. β-turns, particularly type I, II, and III, contribute significantly to the structural diversity observed in proteins.[6]

Tertiary structures: The overall 3D configuration of the complete polypeptide chain is represented by a protein's tertiary structure. The interactions between the R groups on the side chains of the amino acids that extend from the backbone control it. Hydrogen bonds, hydrophobic contacts, ionic bonds, and disulfide bridges are a few of these interactions. The protein's particular form and function are dictated by the tertiary structure.

Quaternary structure: A functional protein complex is made up of a variety of polypeptide chains, or subunits, that make up some proteins. The quaternary structure is made up of how these subunits are arranged and how they interact. The quaternary arrangement is crucial for proteins that have numerous subunits to function properly, such as hemoglobin (which transports oxygen in the blood) and DNA polymerase (which replicates DNA), to function effectively.

1.3. Mimicking of Protein Secondary Structures

The exploration of proteins' structural and functional properties has motivated chemists to devise protein structure mimetics using non-natural amino acid building blocks. In the past few decades, substantial efforts have been invested in creating folded architectures from α-amino acid units.[7] The de novo design and emulation of protein secondary structures have proven valuable in the development of diverse functional biomaterials and biologically impactful peptide-based drug molecules. However, owing to the limitations inherent in naturally occurring amino acid-based peptides or proteins, including issues such as proteolysis, protein-protein interactions, and activity, researchers have turned to a range of non-natural amino acid building blocks and organic templates. These unconventional elements have been employed to construct various protein secondary structures, with a focus on studying their functions. Additionally, beyond non-natural amino acids and organic templates, oligomers of β- and γ-amino acids have been extensively investigated for designing protein secondary structure mimetics, and their structural properties have been thoroughly examined.[8] These non-natural β- and γ-amino acid-based foldamers offer a unique avenue for designing and constructing protein structure mimetics with mixed sequences, such as α,β-, α,γ-, and β,γ-sequences. This expands the possibilities for creating diverse protein-like structures tailored for specific functions.

1.4. Peptide Foldamers of β-Amino Acids

The term "Foldamers" was introduced by Prof. Samuel H. Gellman, defined as "any oligomer capable of adopting a rigid conformation in solution."[8a] Various foldameric building blocks have been employed in the design of protein secondary structure mimetics, with a particular emphasis on the extensive use of β-amino acids. Figure 4 illustrates some of the β-amino acids employed in constructing protein secondary structures. Seminal work by Seebach[9] and Gellman[10] involved the utilization of acyclic chiral and cyclic β-amino acids, such as cyclic trans-2-amino cyclopentane carboxylic acid (ACPC) and trans-2-amino cyclohexane carboxylic acid (ACHC), which prompted the formation of 12- and 14-helical conformations, respectively. Continuing this line of research, Sharma[11] and colleagues reported mixed 10/12 or 12/10 helical structures from carbo-β-amino acid oligomers, while Atkins[12] and Fulop[13] groups utilized various cyclic amino acids to construct β-peptide foldamers.

The established folded structures originating from β-peptides indicate that the process of folding is not exclusive to proteins. Exploring the folding patterns of β- and their higher homologue peptides not only aids in comprehending the intricate nature of protein folding but also positions them as promising candidates in the fields of medicinal chemistry and drug discovery. The classification of β-amino acids into β^2- and β^3-amino acids is based on substitutions in the backbone.

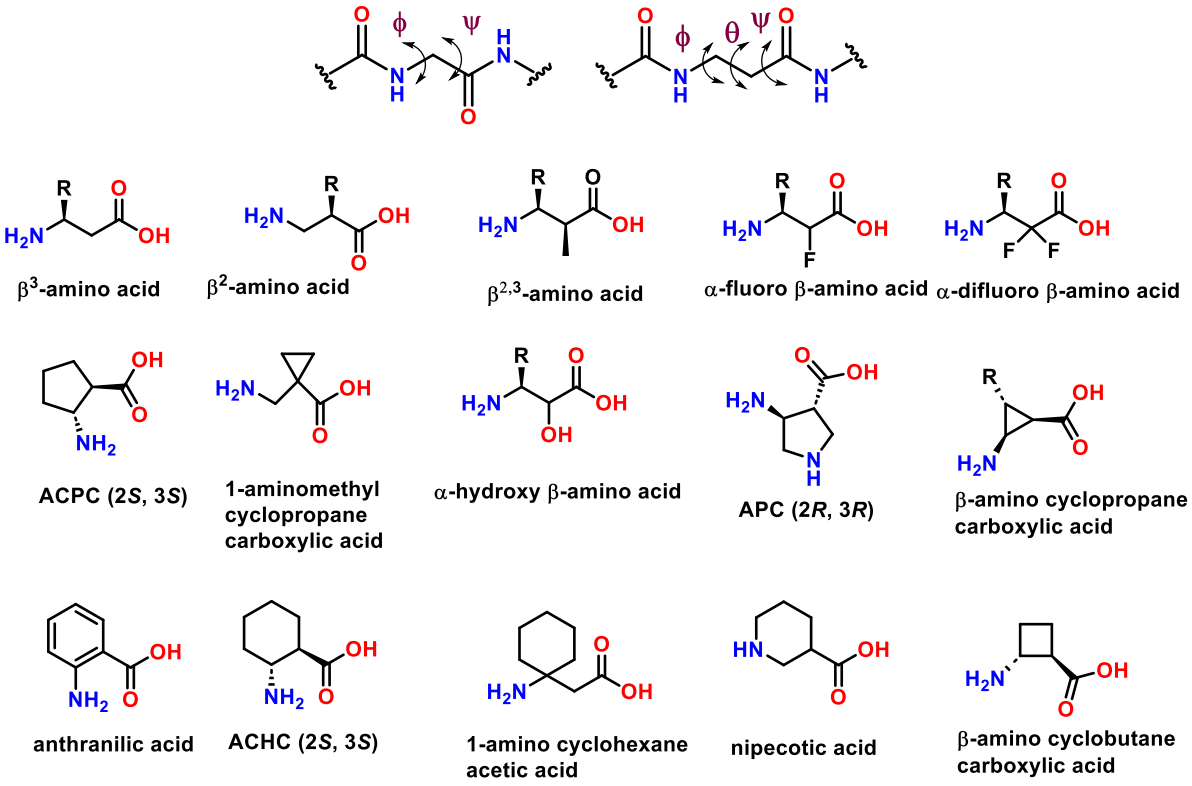


Figure 5: Various β-amino acids utilized for foldamers design.

An additional advantage of β-amino acids over their α counterparts is their resistance to proteolysis by various proteases, making them valuable for applications in intracellular drug delivery.[14] The secondary structures arising from both acyclic and cyclic β-amino acids primarily fall into categories such as helices, sheets, and turns. Unlike α-peptides, β-peptides exhibit helical structures with distinct hydrogen bonding pseudocycles. Figure 5 illustrates various types of helices observed in β-peptide foldamers. The β-peptide foldamers have been well-documented to exhibit distinct helical forms, including C_8, C_{10}, C_{12}, and C_{14} helices.[15] These helices demonstrate varying hydrogen-bonding polarities concerning the N and C-terminal ends. Specifically, both C_8

and C_{12} helices display a hydrogen bond direction (C ← N) akin to the α-helix, whereas C_{10} and C_{14} helices present the opposite hydrogen bonding direction (N ← C).

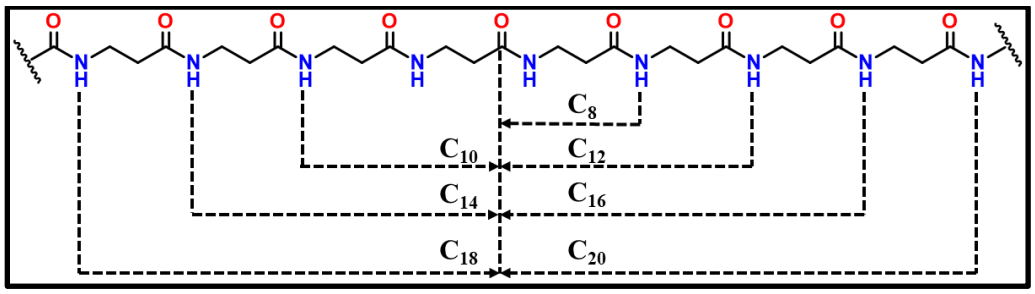


Figure 6: H-bonding patterns observed of β-peptide-based foldamer.

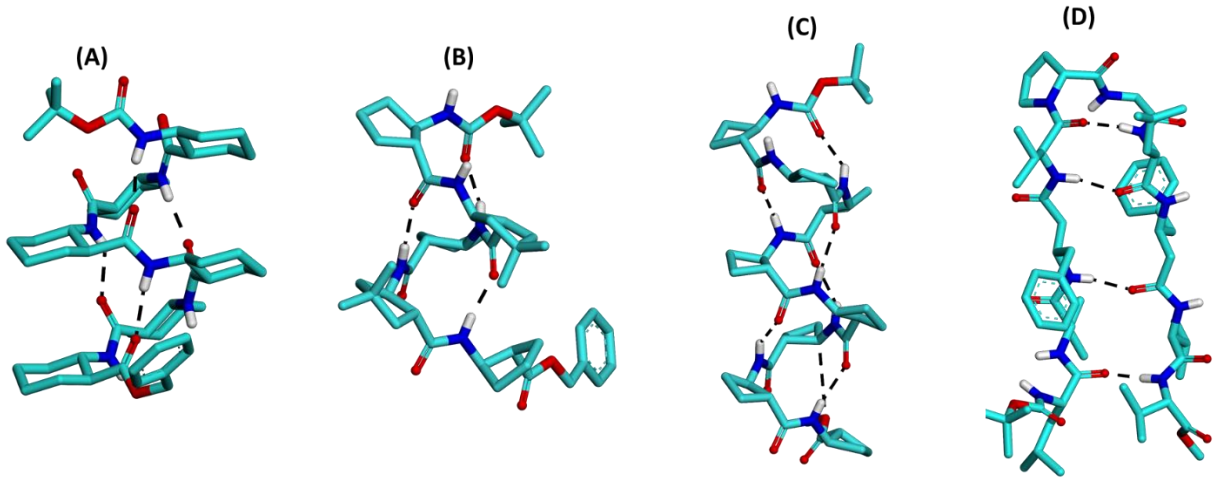


Figure 7: Crystal structure from (A) *trans*-ACHA (C_{14}-helix) (B12-helix formed derived from trans-ACPC β-amino acid (C) 12-helix constructed from cyclobutane β-amino acid. (D) Structure of a decapeptide β-hairpin with two facing β-phenylalanine residues.

Besides the helical structures, β-amino acid oligomers have also been documented to exhibit parallel and antiparallel sheets, as well as β-hairpin structures. In contrast to the 14-helical conformations observed in cyclic β-amino acids with a six-membered ring constraint, such as trans-2-amino cyclohexane carboxylic acid, and acyclic β-amino acids like β^3- and β^2-amino acids,[9b] homooligomers of cyclic β-amino acids with four (trans-2-aminocyclobutane carboxylic acid),[12] five (trans-2-aminocyclopentane carboxylic acid and its derivatives),[17] and bicycle [3.3.1] heptane skeleton[18] displayed stable 12-helical conformations. In continuation, Balaram and colleagues documented the use of synthetic β-amino acids in the creation of helices and β-hairpins[19a] and the three-stranded β-sheets.[19c] Three stranded β-sheets were investigated by

introducing β-Phe residues on opposite faces of anti-parallel β-strands, employing ^{D}Pro-Gly[19a,19b] at the turn. The primary distinction in β-sheets lies in the directional orientation of hydrogen bonds. In α-peptides, these bonds alternate in direction, resulting in an apolar β-sheet. Conversely, β-peptides form polar sheets where hydrogen bonds align in the same direction. The introduction of an additional methylene group in the backbone of β-amino acid residues introduces extra torsion angle freedom, encompassing θ (C^{β}-C^{α}), along with ϕ (N-C^{β}) and ψ (C^{α}-CO). It is noteworthy and somewhat surprising to observe the formation of stable higher-ordered structures from β-peptides despite the introduction of this additional freedom in backbone rotation.

1.5. Peptide Foldamers of γ-Amino Acids

Gamma (γ)-amino acids, as double-homologated α-amino acids, feature two -CH_2- groups positioned between the C^{α} carbon and the C=O carbon. The introduction of these two methylene groups gives rise to two additional torsional variables, θ_1 and θ_2, in addition to the standard ϕ and ψ angles. In contrast to β-amino acids, γ-amino acids have received limited exploration, likely attributed to challenges associated with synthesizing and isolating stereochemically pure forms of γ-amino acids. Nevertheless, in their preliminary investigations, Seebach[20]and coworkers, as well as Hanessian *et al.*,[21] recognized the emergence of 14-helical conformations in the oligomers of γ^4-amino acids and 2, 3, 4-substituted γ-amino acids.

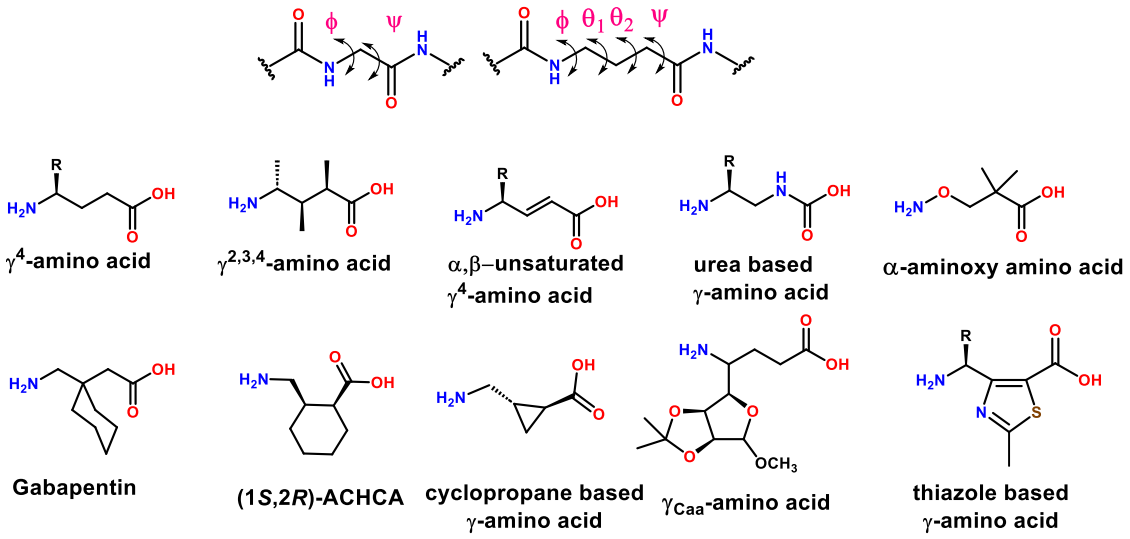


Figure 8: Chemical structure of γ-amino acids utilized for foldamers design

Furthermore, Hofmann and colleagues made predictions regarding a diverse array of helical arrangements arising from the oligomers of unsubstituted γ-amino acids and hybrid peptides that consisted of a 1:1 alternation of α- and γ-amino acids, utilizing ab initio theoretical calculations.[23] They indicated that among all conceivable helices, C_{14}- and C_9-helices stand out as the most stable structures. The forecasted C_9-helix structure was subsequently experimentally validated by Sharma and colleagues, who utilized alternating C-linked carbo-γ^4-amino acid and γ-aminobutyric acid (GABA).[24] In a groundbreaking study, Balaram and collaborators reported C_9 helical conformations from gabapentin (3,3-dialkyl-γ-amino acid) oligomers in single crystals. The stability of the C_9 helical structure is attributed to hydrogen bonds between the (*i*) and (*i* + 2) residues.[25] Beyond gabapentin, Balaram and colleagues also identified C_{14} helical conformations in the oligomers of γ^4-amino acids with proteinogenic side chains (γ^4-Val, γ^4-Leu, γ^4-Ile) in single crystals.[26] Gellman and co-workers documented the presence of stable C_{14} helices in cyclic γ-amino acids.[27,28]

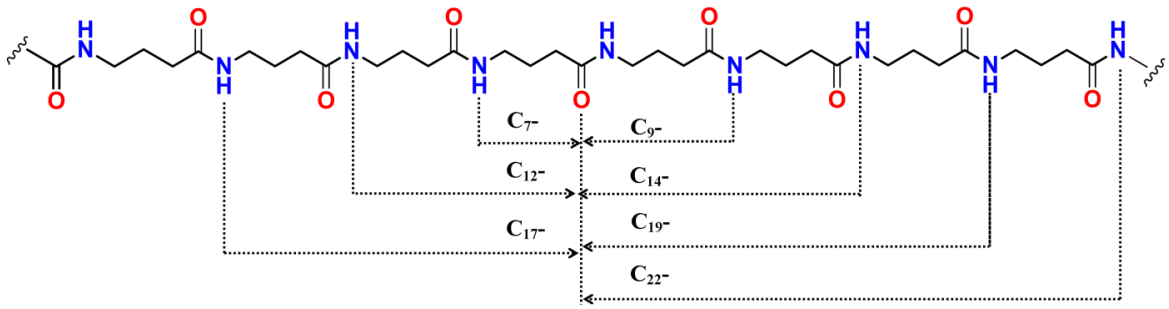


Figure 9: Possible H-bonding pattern in the oligomer of γ-peptide foldamer.

Additionally, Smith and colleagues reported the synthesis and conformational analysis of cyclopropane-based γ-amino acids.[29] They demonstrated that the oligomer of these γ-amino acids exhibited parallel-type β-sheet structures, and the stability of the structure was ensured by bifurcated hydrogen bonds involving the carbonyl oxygen with the amide NH group and one CH of the cyclopropane ring in the solid state. Furthermore, they employed these amino acids as non-peptidic reverse turns in the design of β-hairpins.[29] Additionally, homo-oligomers constrained by $\gamma^{2,3}$-trans-dioxolane have been investigated for the design of peptide foldamers.[30] In addition to cyclic γ-amino acids, backbones containing oxygen and nitrogen atoms have also been explored for the design of various functional foldamers.

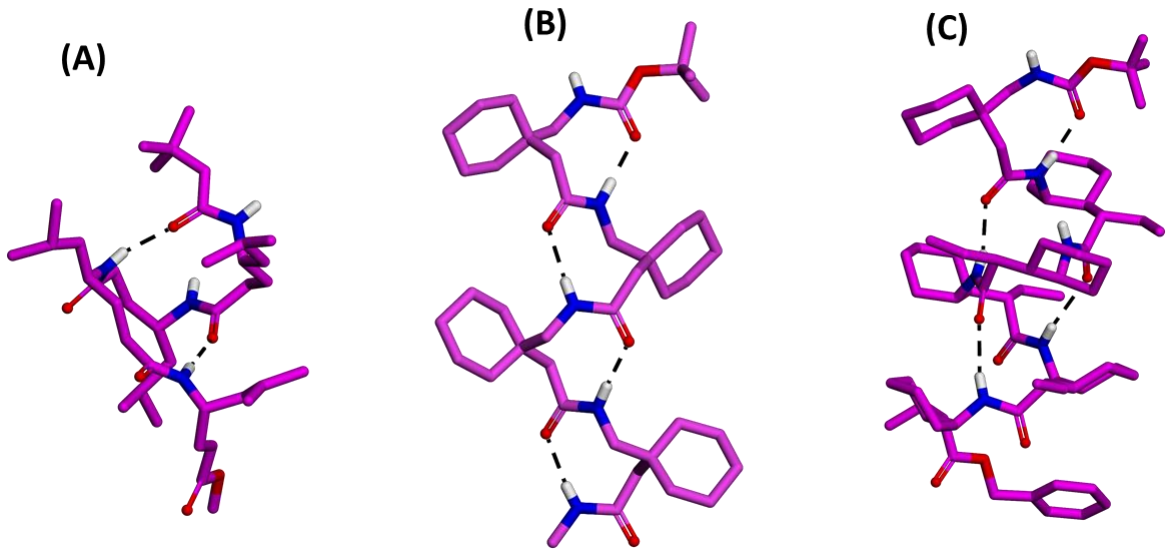


Figure 10: (a) C_{14}-helix of γ^4-peptide b) C_9 helix of gabapentin oligomer (c) C_{14} helix of the $\gamma^{2,3,4}$-oligomer peptide

Yang and co-authors documented the occurrence of C_8 helical conformations in α-aminoxy peptides.[31] Additionally, Guichard and collaborators employed oligourea-based peptide foldamers by substituting the γ^3-carbon in the γ-peptide backbone with NH.[32] In a recent investigation, Millard and colleagues reported the generation of C_9 helices from homo-oligomers of 4-amino-(methyl)-1,3-thiazole-5-carboxylic acids (ATCs).[33]

1.6. Heterogeneous Foldamers Containing β- and γ-Amino Acids

Recently, there has been a growing interest in peptide foldamers with heterogeneous backbones compared to their homogeneous counterparts. This is attributed to the fact that a diverse array of helices with distinct hydrogen-bonding patterns can be achieved through the strategic combination of different types of amino acids. In a pioneering study, Balaram and colleagues introduced hybrid peptides by incorporating β-amino acids into host α-peptides.[34] By employing quantum mechanical calculations, Hofmann and team postulated that α,β-hybrid peptides have the potential to generate helical structures, including 9-, 11/9-, 9/11-, 11-, 12/13-, 15/14-, 16/18-, and 18/16-helices.[35] Sharma and colleagues described an 11/9-helical conformation featuring alternating hydrogen bonding directions within an α,β-sequence composed of both α- and β^3-amino acids.[36,37] Gellman and co-workers documented peptide sequences of α, β-hybrid peptides incorporating constrained trans-ACPC amino acids and Aib residues, which demonstrate the capability to adopt both 11-

helical and 14/15-helical structures.[38] Along with this, Gellman and colleagues showcased the formation of $C_{11/11/12}$ and $C_{10/11/11}$-helices in ratios of 1:2 and 2:1, respectively, from α,β-hybrid peptides.[39] Fulop and collaborators investigated the impact of stereochemical patterns on the folding of α,β-hybrid peptides.[40] Furthermore, Gellman and co-workers documented the formation of quaternary structure helical bundles from oligomers featuring -β-β-α-β-β and α-α-α-β-α-α-β repeats.[41] The representative crystal structures are given below in Figure 11.

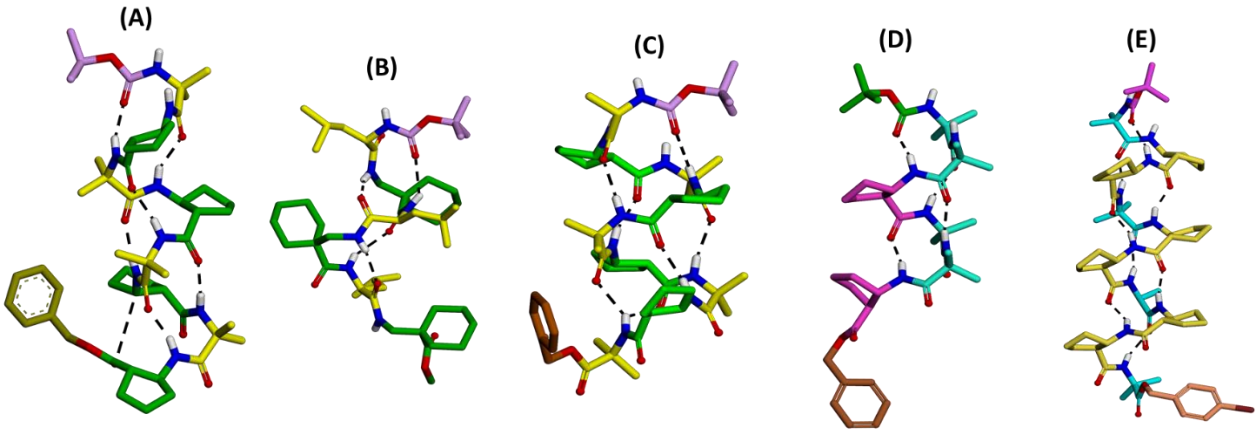


Figure 11: (A) C_{11} helix from α,β-hybrid peptide of Aib and ACPC residues (B) 11/9 helix from α,β-hybrid peptide of Leu and 1-(aminomethyl)cyclohexane-1-carboxylic acid (C) 14/15-helical structure from α,β-hybrid peptide of Ala, ACPC, and Aib residues (D) 10/11/11-helical structure of 2:1 α,β-hybrid peptide (E) 12/11/11-helical structure of 1:2 α,β-hybrid peptide.

In addition to mixed α, β-hybrid peptides, the structural characteristics of α, γ-hybrid peptides have also been explored in the literature. Hofmann and colleagues conducted predictions on the possible helical conformations of hybrid peptides composed of a 1:1 alternation of α- and γ-amino acids. They proposed that the 12-helix is the most stable, followed by 12/10- or 18/20-helices.[42] Furthermore, Balaram and co-workers reported the formation of a 12-helix from an α, γ-hybrid consisting of a 1:1 ratio of Aib and Gabapentin residues.[43a] A stable C_{12}-helix structure was also observed in a hybrid peptide with a 1:1 ratio of α- and γ^4-amino acids.[43b] This structure is stabilized by intramolecular hydrogen bonding between (*i*) and (*i*+3) residues. Various studies have explored the structural properties of α,γ-hybrid peptides. Sharma and colleagues investigated several 12/10-helices in α,γ-hybrid peptides composed of L-Ala and γ-Caa (C-linked carbo-γ-amino acid).[44] Gellman's group demonstrated the design, synthesis, and characterization of different α/γ-peptides containing sterically constrained cyclic γ-amino acids.[45]

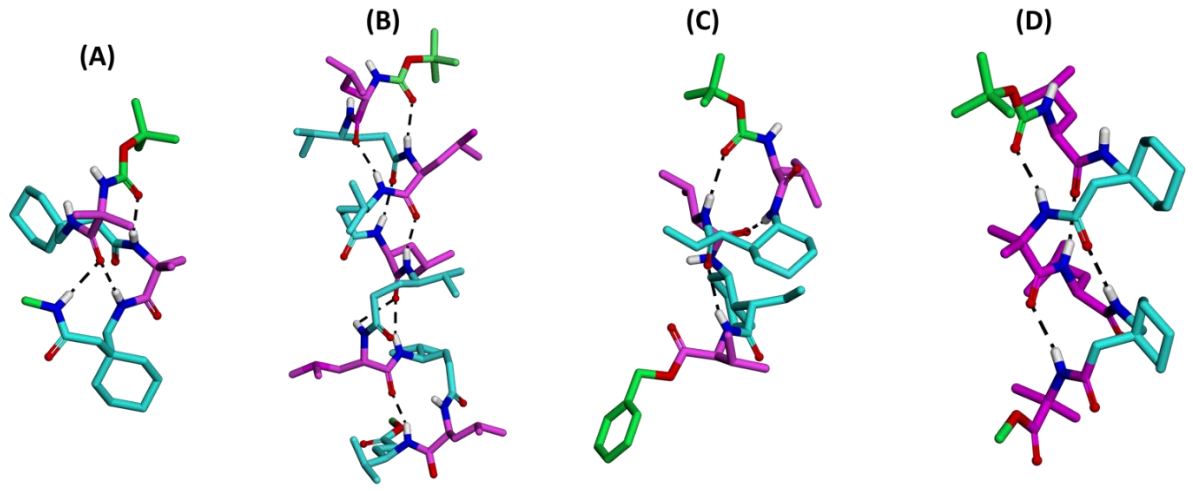


Figure 12: (A) 12-helix of α,γ-hybrid peptide foldamer composed of Boc-Aib-Gpn-Aib-Gpn-NHMe (B) 12-helix of α,γ-hybrid peptide foldamer composed of leu and γ-Val residues (C) 12/10-helix of α,γ-hybrid peptide foldamer composed of Val and EtACHA residues (d) 10/12-helix of αγα with Leu, Gpn, and Aib residues.

They characterized these structures through crystallographically and confirmed the stability of 12-helix structures in an aqueous buffer through NMR studies.[46] Balaram and colleagues utilized α/γ-peptides to create stable reverse turns in β-hairpin conformations.[47]A recent study by Misra *et al.* reported the co-existence of 12- and 15/17-helices in an achiral α/γ-hybrid peptide. However, when the Aib residue was replaced by α-amino acids, the 12-helix transformed into a 12/10-mixed helical structure.[48] Veeresh et al. showed the formation of a stable C_{12} helix in an α,γ-hybrid peptide from an initially unstructured peptide through base-mediated α,β → β,γ double-bond migration.[50]

In contrast to the extensive exploration of α,β- and α,γ-hybrid peptides, there are relatively fewer reports on the conformational properties of β/γ-peptides. The hydrogen bonding pattern in β/γ-peptides is depicted in Figure 11. Sharma and Kunwar reported a mixed 11/13 helical conformation in β/γ-peptides consisting of C-linked carbo-β- and γ-amino acids in solution.[51] Additionally, Balaram and colleagues reported the 13-helix structure from a short β,γ-hybrid peptide.[52] Gellman and colleagues demonstrated the 13-helix formation in β,γ-hybrid peptides.[53] The helical parameters in the 13-helix from β,γ-hybrid peptides resemble those of the α-helix, providing an opportunity to mimic the helical parameters of naturally occurring α-helices. Moreover, Aitken and colleagues studied a 9/8-ribbon structure in β,γ-hybrid peptides with stereochemically constrained β-amino acids, and a 13-helix in unconstrained γ^4-amino acids.[54]

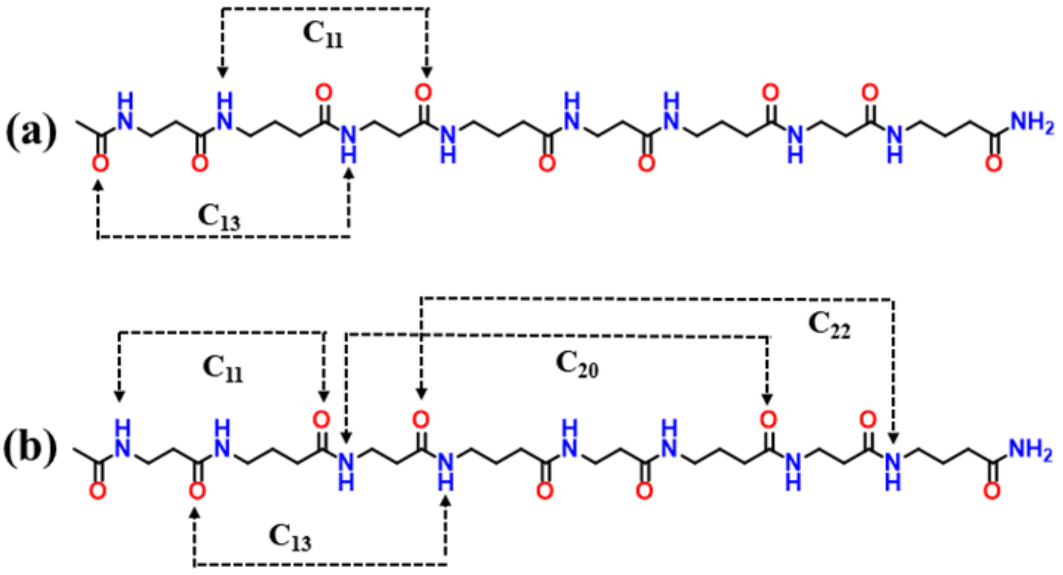


Figure 13: Instances of hybrid peptide helices that combine both β- and γ- amino acids. (a) Illustration of the hydrogen-bonding arrangement in 11 and 13 helices. b) Presentation of the hydrogen-bonding configuration observed in mixed helices, such as the 11/13 helix or the 20/22 helix.

1.7. α, β-Unsaturated γ-Amino Acids Based Peptide Foldamers

Vinylogous γ-amino acids, also known as α,β-unsaturated γ-amino acids, are amino acids characterized by the presence of a –CH=CH– group between the C^{α} and C=O in their chemical structure.

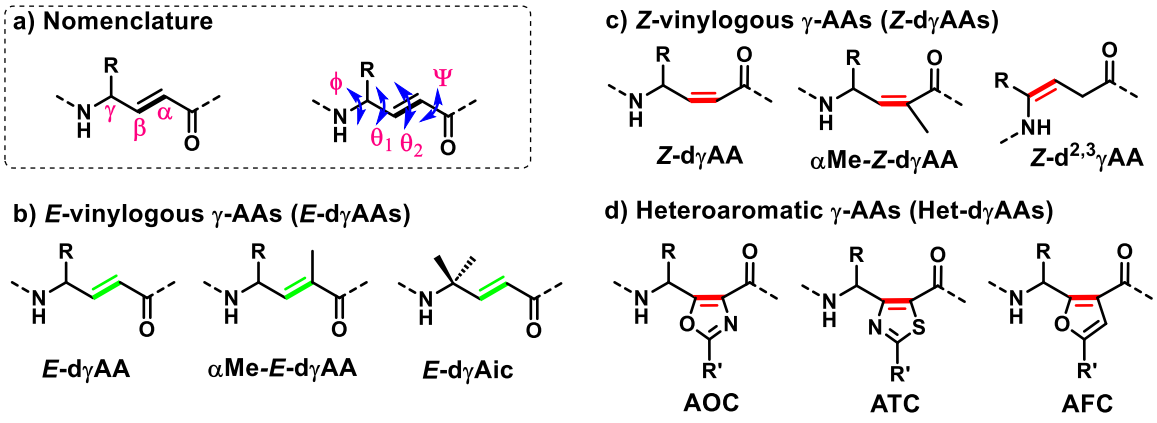


Figure 14. Different types of α,β-unsaturated γ-amino acids and their nomenclature

These α,β-unsaturated γ-amino acids have found utility as starting materials for the synthesis of γ-amino acids.[55] Additionally, they serve as substrates in various organic reactions, including 1,4-

conjugate addition,[56] epoxidation,[57] and the Diels-Alder reaction,[58] leading to the generation of diverse functional derivatives of γ-amino acids. The vinylogous γ-amino acids can be classified as *E*- and *Z*-isomers based on the configuration of the double bond. However, heteroaromatic γ-amino acids always have a default *Z*-configuration, as illustrated in Figure 14. Despite their potential, exploration of foldamers based on vinylogous γ-amino acids is limited due to the inherent challenges associated with obtaining stereochemically pure forms of these amino acids and their analogs.

(*E*)-α, β-unsaturated γ-amino acids are a type of non-ribosomal amino acid commonly present in diverse natural products like Gallinamide A, Cyclotheonamides (A, B, C, D, E), Luminmycin (A, B, C), and Miraziridine A (Figure 15).

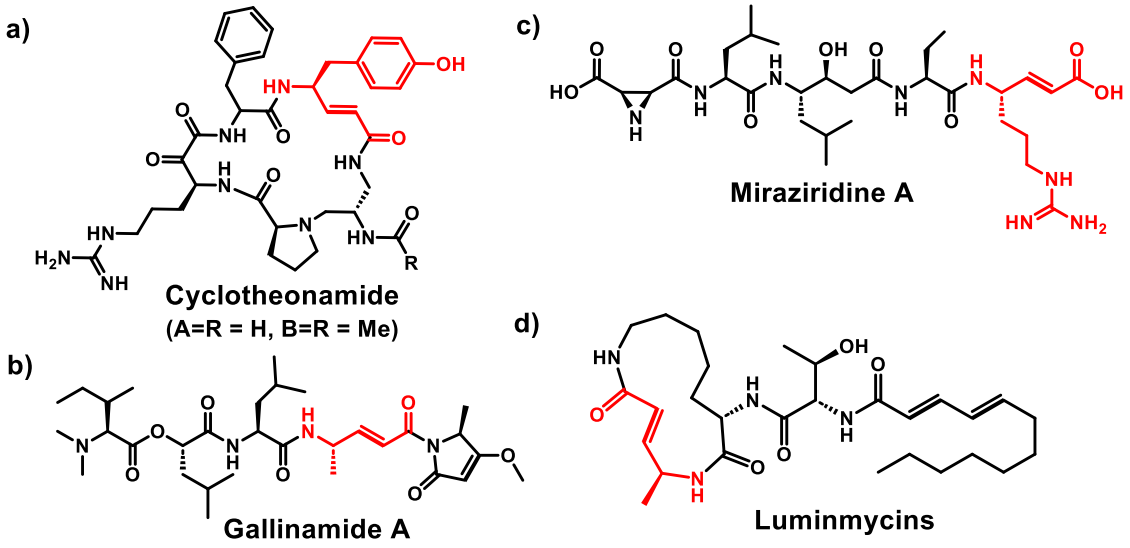


Figure 15: (A) Chemical configurations of cyclic and linear peptides containing naturally existing α,β-unsaturated γ-amino acids are depicted through molecular structures.

A comprehensive mechanistic investigation by Schreiber and colleagues unveiled the potent inhibitory role of Cyclotheonamides against serine protease and bovine β-trypsin.[59] These compounds exhibit noteworthy biological activities, with Gallinamide A demonstrating significant anti-malarial effects.[60] Miraziridine A, a natural cyclic peptide, serves as an inhibitor for various proteases, including trypsin-like protease, papain-like cysteine protease, and pepsin-like aspartyl protease.[61] The remarkable biological activities and natural presence of vinylogous amino acid

residues have spurred synthetic chemists to devise peptide inhibitors targeting serine and cysteine proteases.[62](Figure 16)

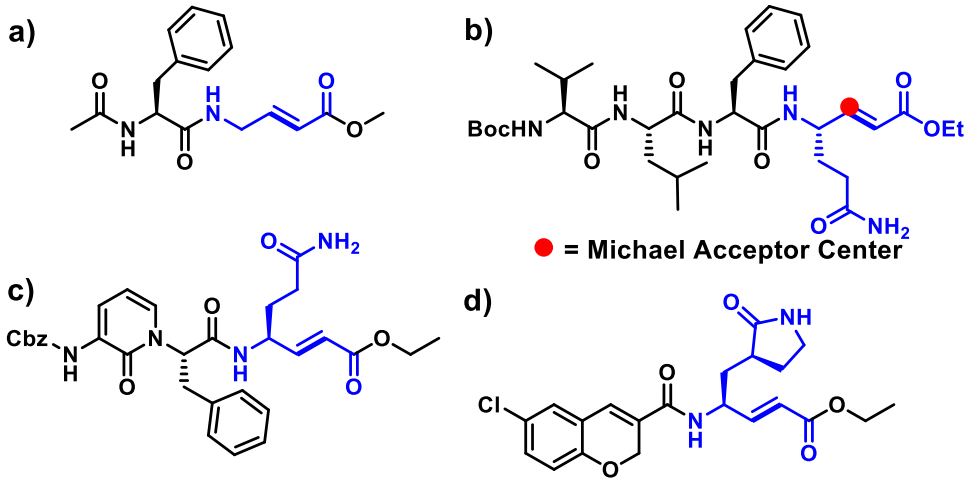


Figure 16: (A) Artificial peptides incorporating α, β-unsaturated γ-amino acids are employed as inhibitors for diverse proteases.

The combination of both biological and chemical properties inherent in (*E*)-vinylogous residues has sparked considerable interest among chemists. This interest is particularly evident in investigations into the conformational behavior of (*E*)-vinylogous amino acids, both as individual monomers and within the context of peptides. Understanding the conformational preferences of these amino acids is crucial for designing and optimizing the synthesis of peptides or small molecules with desired biological activities. The exploration of conformational behavior involves studying how (*E*)-vinylogous amino acids adopt specific shapes or spatial arrangements. Such studies contribute to the knowledge of how these amino acids interact with other molecules, whether in isolation or within larger peptide structures. The conformational analysis of (*E*)-vinylogous residues aids in elucidating the structural features that influence their biological activities and can guide the design of novel compounds with tailored properties.

Schreiber and collaborators illustrated the creation of β-sheet structures in dipeptides and unconventional helical formations in hybrid tetrapeptides.[63] Chakraborty and co-authors highlighted the application of (*E*)-vinylogous amino acids in prompting reverse turns within β-hairpins.[64] In a subsequent investigation, Hoffmann and colleagues documented diverse helical arrangements featuring larger H-bond pseudo cycles in homo-oligomers of both (*E*)- and (*Z*)-vinylogous amino acids, employing systematic theoretical calculations with ab initio MO theory

(Figure 17). Additionally, there is a proposal for constructing single-walled nanotubes from (*E*)-vinylogous amino acid homo-oligomers, which can serve as ion channels.[65] Furthermore, peptides composed of (*Z*)-vinylogous amino acid oligomers tend to adopt helices with smaller H-bonded pseudocycles, including 9 and 12-helices.

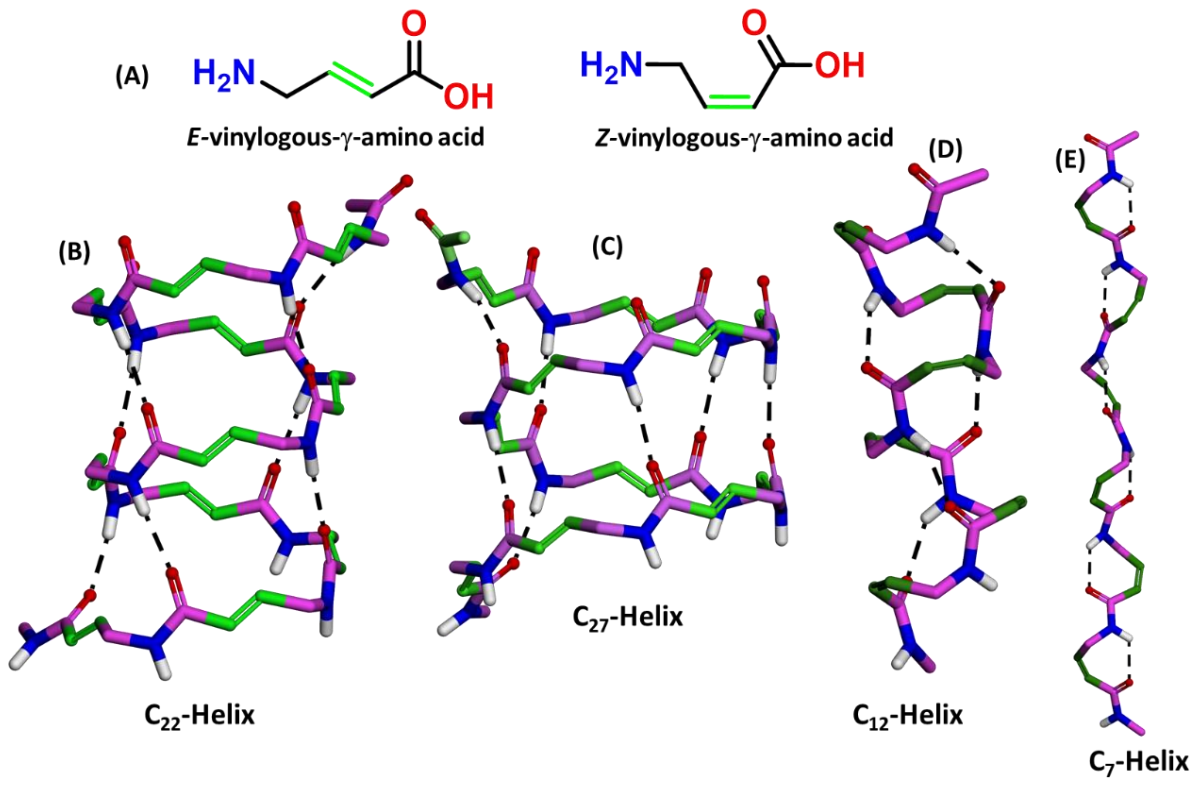


Figure 17: (A) vinylogous γ-amino acids (*E*)- and (*Z*). Molecular simulated structures of (B) C_{22}-helices (C) C_{27}-helices composed of homo-oligomers of (*E)*-vinylogous γ-amino acids (D) C_{12}-helices (E) C_7-helices composed of homo-oligomers of (*Z)*-vinylogous γ-amino acids.

Previously, our group demonstrated the use of (*E*)-vinylogous γ-amino acids in crafting stable β-hairpin structures,[66] miniature β-meanders,[67] and multiple β-sheet structures.[68] Additionally, our research group has engineered and explored the conformations of α,γ-hybrid peptide foldamers containing (*Z*)-vinylogous γ-amino acids.[69] Recently, we presented the conversion of an unstructured peptide containing (*E*)-vinylogous γ-amino acids into an α,γ-short hybrid tripeptide with a 12-helical structure through base-mediated double bond migration. This study highlights the conversion of (*E*)-vinylogous γ-amino acid units into (*Z*)-vinylogous γ-amino acids and the integration of carbon-carbon cis double bonds into the 12-helix.[70] We have also constructed a

parallel extended sheet structure from oligomers of (*E*)-vinylogous γ-amino Leu.[71] The structures are shown in Figure 18.

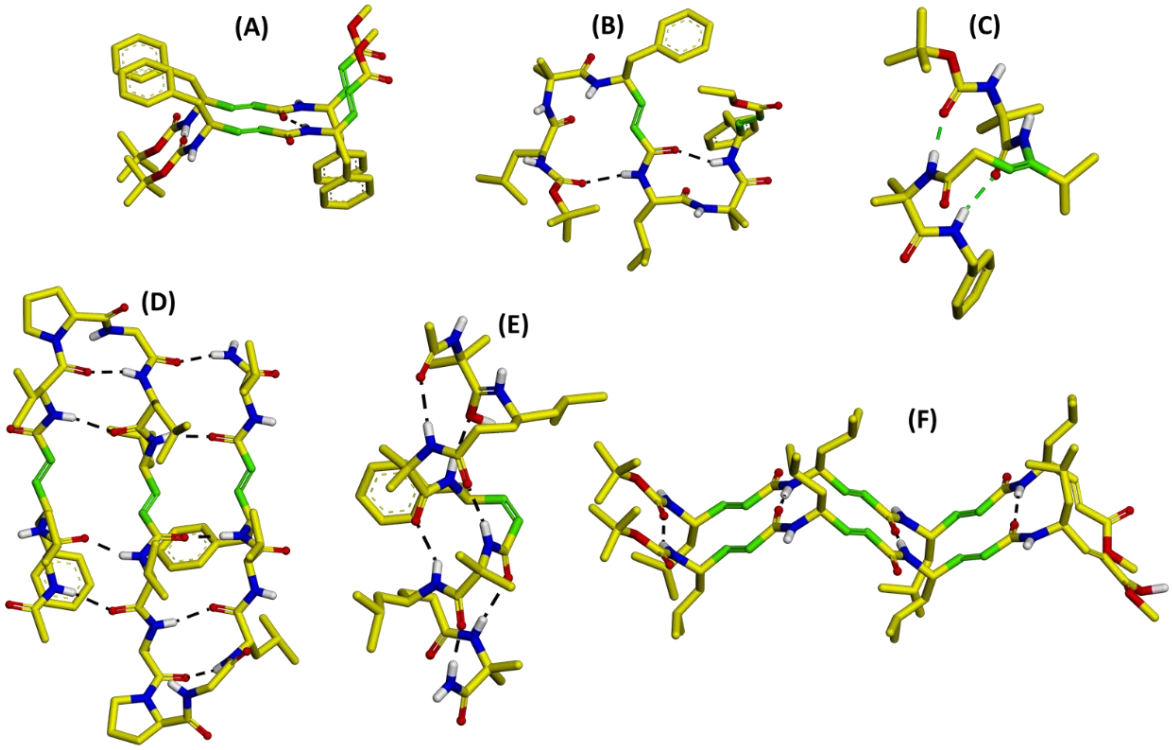


Figure 18: Peptide foldamers based on vinylogous γ-amino acids (A) Extended sheet structure of (*E*)-vinylogous γ-Phe dipeptide (B) β-meanders structures of ααγ-hybrid peptide of (*E*)-vinylogous γ-Phe, Aib and Leu (C) Conformational change (*E*)-vinylogous γ-amino acid unit into (*Z*)-vinylogous γ-amino acid unit in 12-helical α,γ-short hybrid tripeptide (D) Three stranded β-sheets constructed by incorporation of (E)-vinylogous amino acids (E) C_{12}-helical structure constructed from α,γ- hybrid peptides containing (Z)-vinylogous γ^4-amino acids (F) Extended sheet of (*E*)-vinylogous γ-Leu tripeptide.

1.8. Double Helical Foldamers

The design of peptide-based foldamers has evolved beyond reliance on α-amino acids; over time, foldamer chemists have incorporated β, γ, δ-amino acids, or various combinations thereof, creating a versatile library of structures. This expanded toolkit provides pathways to engineer novel peptide-based foldamers with applications spanning drug discovery to the design of biomaterials. While previous discussions on oligomer systems predominantly centered on folding reactions within a single chain, it's crucial to recognize that foldamers extend beyond this singular context. These entities extend beyond individual chains, forming multistrand assemblies where oligomer

chains unite and fold through noncovalent intermolecular interactions. In the intricate tapestry of biological systems, multi-stranded helical structures play indispensable roles. Unveiled by the groundbreaking work of James Watson and Francis Crick in 1953, the DNA double helix stands as one of the most iconic and fundamental structures in molecular biology. This helical structure is constituted by two complementary polynucleotide strands intricately linked through numerous hydrogen bonds. The stability of this helical arrangement is further fortified by π–π stacking interactions, which involve the noncovalent association of nucleobase pairs covalently attached to the strands.[72] The DNA double helix is not merely a structural marvel; its profound functional roles elevate its significance in the realm of molecular biology. One of its primary functions is to serve as a repository for genetic information. The sequence of nucleotides along the strands encodes the genetic instructions that govern the development, functioning, and regulation of living organisms.[73] Additionally, the DNA double helix facilitates the transfer of this genetic information during processes such as DNA replication and transcription. The construction of artificial double helices has emerged as a challenging and immensely intriguing area of scientific exploration. Researchers seek to replicate the structural and functional aspects of the natural DNA double helix, aiming to harness its unique properties for various applications. The challenges in constructing artificial double helices lie in achieving the precision and stability inherent in natural DNA. Researchers must carefully design molecules that can effectively form complementary pairs through hydrogen bonding and exhibit the stacking interactions crucial for stability. Furthermore, these artificial helices hold promise for applications in areas such as nanotechnology, materials science, and medicine. Double-helical structures are uncommon in many natural biopolymers; however, the peptide antibiotic gramicidin A, produced by Bacillus brevis, exhibits a double-helical conformation. A notable feature of gramicidin A is its composition of alternating L- and D-amino acids, all of which are fully hydrophobic.[74] Structural studies have revealed that the conformation of gramicidin A is environment-dependent. In organic solvents, it adopts both left-handed antiparallel β-double helix and right-handed parallel β-double helix conformations.[75a] In the presence of Cs^+ ions in a methanol-chloroform solvent mixture, it forms a right-handed anti-parallel double helix with ions bound.[75b] No definite structure was observed in 1:1 DMSO-acetone solvents.[75c] In ethanol, four different structures were identified, including parallel $\beta^{5.6}$ double helices with differing hydrogen bond registries, a right-handed parallel $\beta^{5.6}$ double helix, and a left-handed anti-parallel $\beta^{5.6}$ double helix. In benzene-ethanol solvent combinations and X-ray

diffracted single crystal structures, single anti-parallel double-helical structures were identified.[75d,e] Additionally, along with β-double helical conformations, gramicidin A adopts a single-stranded beta-helix structure in the lipid bilayer.[75f] Due to its alternating L- and D-amino acids, the peptide lacks a net dipole. The single-strand β-helix of gramicidin A is stabilized by intramolecular hydrogen bonds, and two single β-helices form head-to-head and tail-to-tail dimers in lipids.[75g] These dimer structures act as membrane channels for ion transport. Beyond experimental findings, theoretical studies have also indicated that gramicidin A possesses wide-bore helical structures wound around a helical axis.[75h] Apart from gramicidin A, another naturally occurring peptide antibiotic, feglymycin, derived from *Streptomyces sp*., comprises unnatural amino acids arranged in alternating L- and D-configurations, adopting a β-double helical conformation.[76a] This structure is akin to the beta-double helix seen in gramicidin A, with intermolecular hydrogen bonds intertwining the two strands. Unlike gramicidin A, however, feglymycin serves as an ion transporter rather than a membrane channel.[76b] Feglymycin demonstrates limited antibacterial activity against Gram-positive bacteria, but it exhibits robust inhibitory effects on HIV syncytia formation in vitro.[76c]

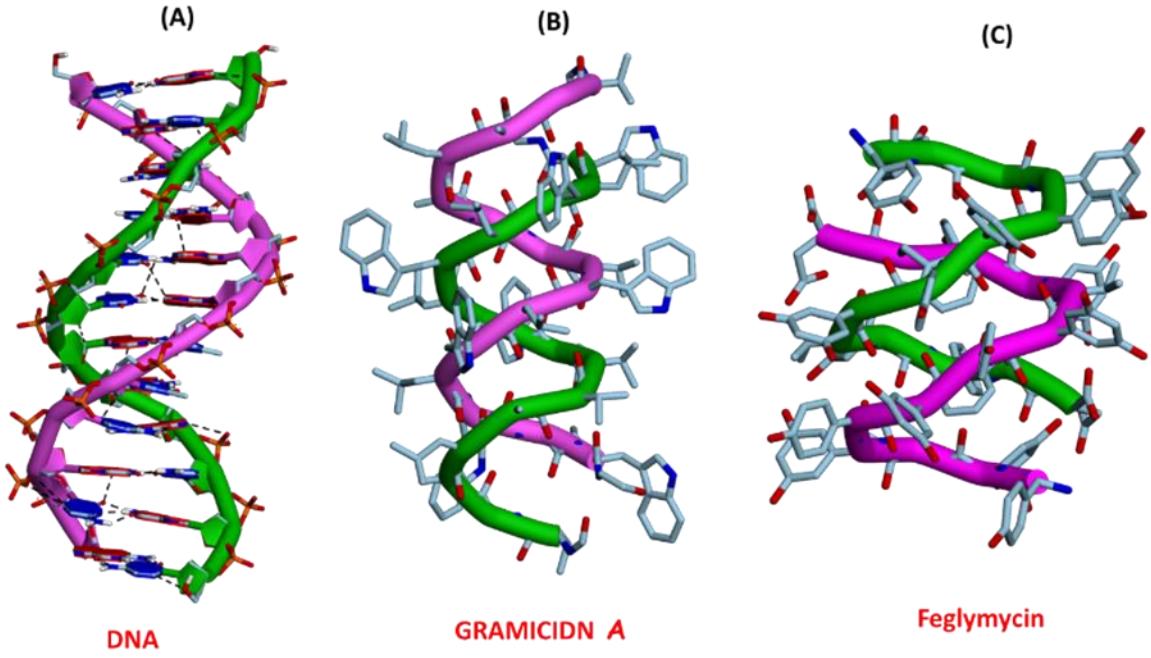


Figure 19: (A) Double helical structure of DNA. (B) Double helical structure of Gramicidin A (C) Double helical structure of Feglymycin.

Despite the notable achievements in creating artificial single helices, the realm of synthetic double helices are currently in its infancy, with the associated chemistry still in early developmental stages. The design of synthetic double helices has been explored to a limited extent, with only a few structural motifs documented in the existing literature. Drawing inspiration from structural insights gained from molecules like gramicidin A and feglymycin, researchers have embarked on endeavors to fashion double-helical structures using peptide sequences that incorporate alternating L- and D-amino acids. A noteworthy contribution in this domain comes from the work of Benedetti and colleagues, who presented a pioneering crystal structure of a β-double helix. This unique structure was derived from a synthetic peptide featuring a sequence of alternating L- and D-amino acids.[77] The alternating arrangement of these amino acids in the peptide sequence contributes to the formation of a stable double-helical structure. The successful design of a β-double helix from a peptide with alternating L- and D-amino acids represents a notable step forward, laying the foundation for further exploration and innovation in the evolving field of synthetic double helices.

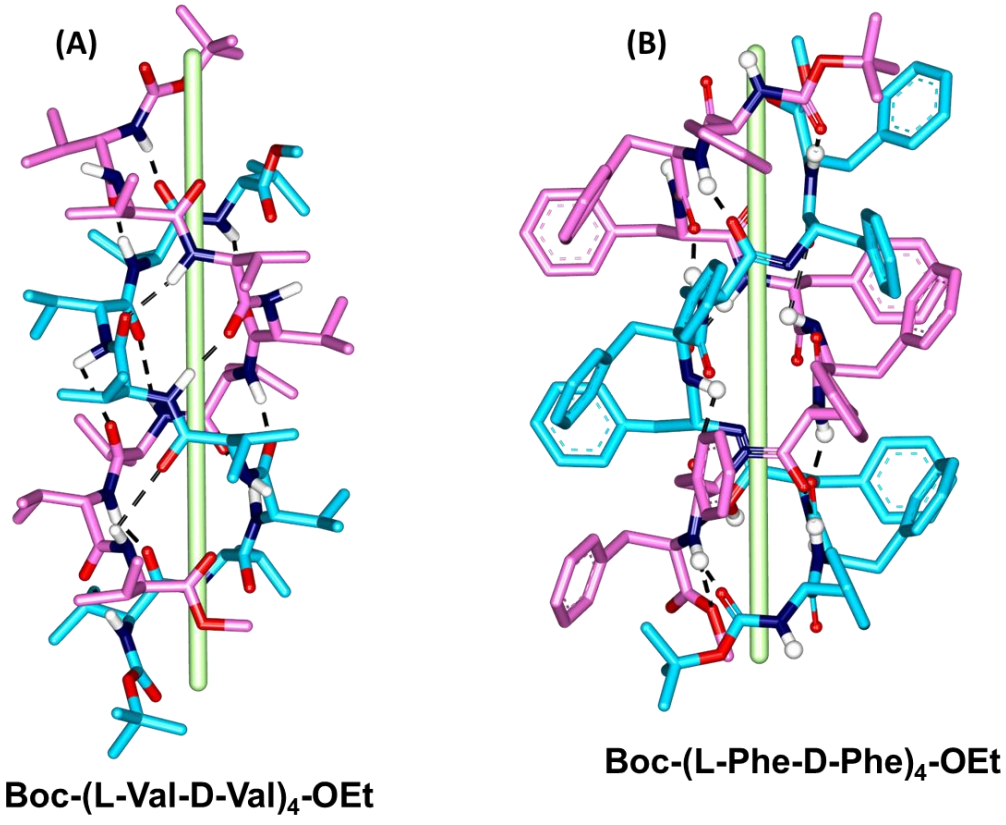


Figure 20: Alternating L-/D- valine based double helix

Constructing artificial double helices involves strategically utilizing noncovalent weak interactions such as metal coordination, aromatic interactions, hydrogen bonding, and solvophobic effect to intertwine molecular strands.[78] These noncovalent interactions play a pivotal role in stabilizing the structure and guiding the assembly of the helices. The effective combination of these noncovalent interactions allows for the design and construction of diverse artificial double helices with tailored properties and functions. The subsequent classification succinctly categorizes double helices according to diverse non-covalent interactions.

Metal Coordination

In 1987, a landmark paper by Lehn *et al*. marked the inception of intelligent self-assembly by introducing the term "helicate" to describe helical metal complexes with intertwining organic strands around metal centers.[79] This pioneering work focused on double-stranded helicates, where Lehn and colleagues observed the spontaneous self-assembly of ether-linked 6,6′-methyl-2,2′-bipyridine oligomers forming helical metal complexes with Cu(I) ions (Figure 21). Since this seminal discovery, the field of helicates has experienced significant advancements, primarily driven by the predictability of the helical structure during the molecular design phase.[80]

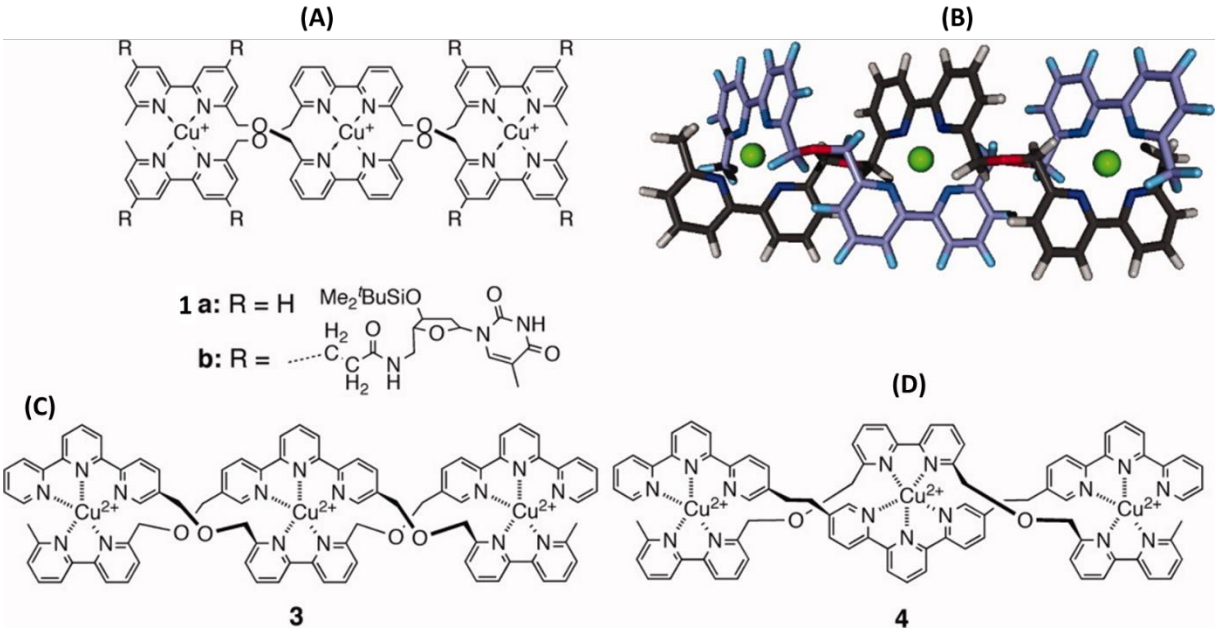


Figure 21: (A) Representation of Cu(I) helicates through structural formulae (B) The energy-minimized structure of **1a** (C) Illustration of heterotopic helicates **3** (D) **4**, formed by molecular strands with complementary sequences. (Reproduced with permission from ref 78; Copyright 2009 Wiley-VCH)

The geometric preferences exhibited by metal centers when coordinating with organic ligand strands are pivotal in influencing the helical structures of helicates. This understanding enables the intentional design of double helical configurations. In line with this concept, diverse functional groups have been integrated into helicates. The research team further expanded their investigation by developing ligands substituted with thymidine. Upon complexation with Cu(I) ions, these ligands led to the creation of deoxyribo-nucleohelicates (2b).[81] This configuration shares similarities with DNA, albeit with the unique characteristic of thymidine residues affixed to the external surface of the double helix.

To incorporate sequence information analogous to the genetic code of DNA into molecular strands of helicates, scientists utilized ligands featuring two distinct binding sites. This approach entailed employing two molecular strands with complementary sequences of bipyridine and terpyridine units. Upon interaction with Cu(II) ions, this strategy resulted in the selective and exclusive formation of the corresponding heteroleptic double-stranded helicates (3 and 4). The use of distinct binding sites on the ligands allows for the controlled assembly of these helicates, mimicking the sequence specificity observed in DNA. This selectivity arises from the Cu(II) ion's preference for a penta- or hexacoordinate geometry, unlike the Cu(I) ion's tendency toward tetracoordination.[82] The effective utilization of metal ion complexation played a pivotal role in enabling the reading and processing of sequence information within the molecular strands. Subsequently, researchers achieved sequence-specific sorting through the formation of complementary double helices for these molecular strands.[83] The success of this approach opens up avenues for the controlled manipulation of molecular information at the supramolecular level. It not only demonstrates the versatility of metal ion complexation in guiding the assembly of molecular structures but also mimics the sequence-specific interactions found in biological systems, providing a valuable tool for the design and engineering of functional supramolecular architectures.

Aromatic Interaction

In 2000, Lehn and Huc introduced a captivating category of metal-free double-stranded helices comprising aromatic oligoamides. These oligoamides are composed of alternating 2,6-aminopyridine and 2,6-pyridine dicarboxylic acids (Figure 22).[84] Interestingly, the oligoamide strands exhibit a unique helical configuration, facilitated by intramolecular hydrogen-bonding interactions involving the NH protons of amide groups and the nitrogen atoms of pyridine rings.

This specific conformation results in the creation of a robust double helix in solution, predominantly propelled by aromatic interactions among the pyridine rings, which are stacked one on top of the other. The evident dynamic exchange equilibrium between singular and double helices manifests in distinct signals within the ^{1}H NMR spectrum. This equilibrium exhibits a slow pace on the ^{1}H NMR timescale, and studies conducted at variable temperatures unveiled a temperature-dependent inclination towards double helices at lower temperatures, transitioning to the dissociation into single strands at elevated temperatures. Both single and double helical structures were thoroughly characterized through X-ray crystallography and NMR. Notably, the hybridization of aromatic oligoamide strands demonstrates a fascinating dependence on chain length. The fluctuation in the stability of double helices can be ascribed to the interaction of two opposing factors: the enthalpic gain from dimerization decreases as the strand length increases, concurrently with a reduction in entropic loss.

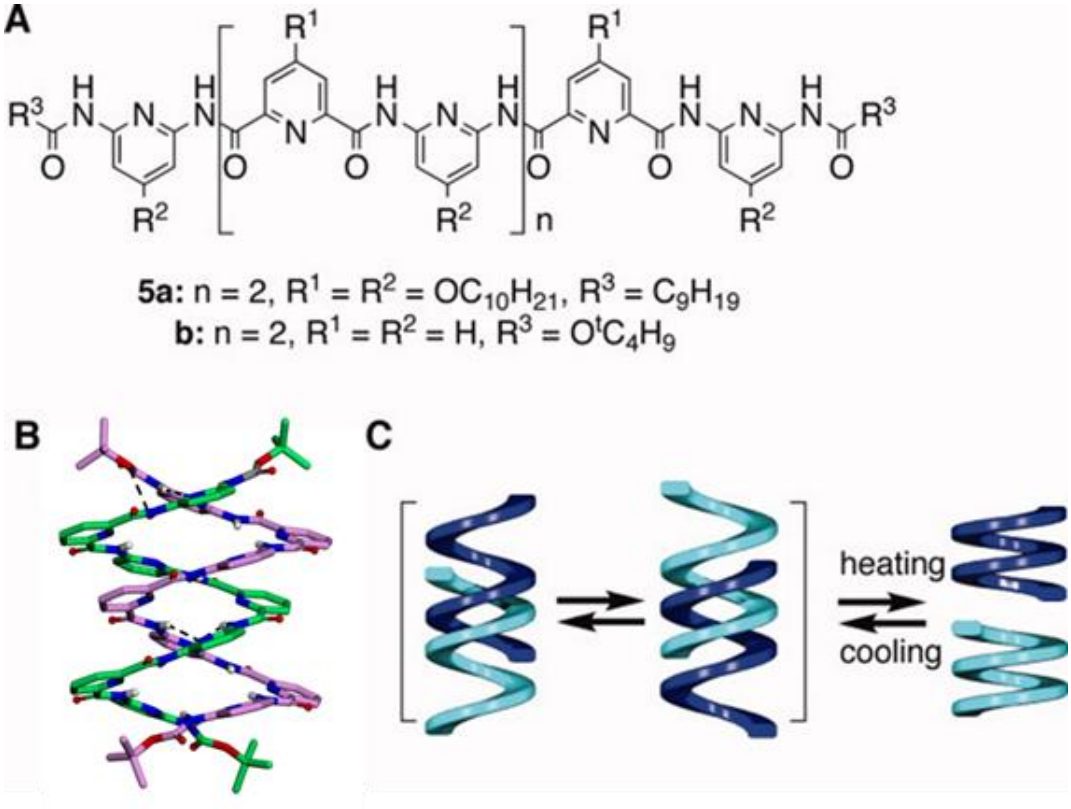


Figure 22: (A) Structural formulae depiction of the oligopyridine carboxamides. (B) The X-ray diffracted single crystal structure of 5b. (C) A diagram illustrating the transformation of dissymmetrical double helices through a sliding motion, succeeded by their separation into two individual single helices. (Reproduced with permission from ref 78; Copyright 2009 Wiley-VCH)

The stability of the double helices is markedly affected by interactions among the side chains of the strands. This finding was corroborated through a detailed analysis of the solid and solution structures of oligoamide double helices featuring various side chains.[85] Along with the above aromatic double helices, various other double helical structures have been developed by Huc and colleagues using different oligoamide residues.[86] Gabriel and Iverson strategically utilized aromatic interactions, employing alternating stacking of electron-rich and electron-poor aromatic systems to enhance double-stranded structure stability. The choice of oligomers, including the electron-poor 1,4,5,8-naphthalene-tetracarboxylic diimide (NDI) and the electron-rich 1,5-dialkoxy-naphthalene (DAN), facilitated intermolecular stacking. Remarkably, even in aqueous solutions, this interaction resulted in a stable double-stranded structure, showcasing the effectiveness of their approach in providing stability to such molecular arrangements.[87]

Hydrogen Bonding

The utilization of hydrogen bonding in supramolecular chemistry has garnered increasing interest, resulting in the creation of various supramolecular assemblies and molecular architectures. However, designing hydrogen bond-mediated double helices with predictable formation has remained a challenging task, primarily due to the tendency of most duplexes assembled by H-bonding interactions to adopt zipper or ladder structures.[88] A recent breakthrough in this regard involves the rational design and synthesis of complementary double helices by leveraging specific amidinium–carboxylate salt bridges (5·6) (Figure 23).[89]

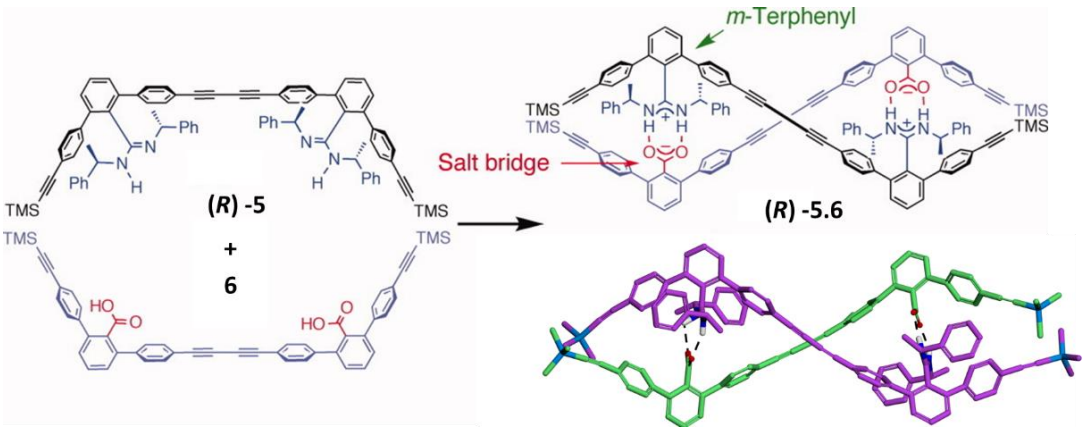


Figure 23: The (R)-5·6 complex creates a complementary double-stranded helix, with the crystal structure revealing specific molecular interactions between the amidinium and carboxylate components. (Reproduced with permission from ref 78; Copyright 2009 Wiley-VCH)

The amidinium–carboxylate salt bridge is identified by its dual hydrogen bonding and precise geometry, displaying a partially charged structure with notable association constants, even in polar environments. This unique property makes it a versatile component for constructing diverse supramolecular assemblies. Along with this, another crucial element contributing to the success of this approach is the utilization of rigid π-conjugated backbones constructed from *m*-terphenyl moieties. These backbones play a pivotal role in ensuring that the duplexes predominantly adopt the conformation of double helices, preventing the formation of other conformations. Experimental techniques, including ^{1}H NMR and ESI-MS, have demonstrated that the bisamidine and dicarboxylic acid strands (5·6) readily form a double helix (5·6) in chloroform. The application of X-ray crystallography has provided unambiguous evidence of the right-handed double helical structure of 5·6. This double helix signifies an innovative category of synthetic compounds, comprised of two complementary molecular strands intertwined through hydrogen-bonding interactions, resembling the structure of DNA. The use of the salt-bridge-type hydrogen bonding interactions has led to the discovery of various other duplex structures, as reported in the literature. This methodology, combining the specific characteristics of the amidinium–carboxylate salt bridge and rigid π-conjugated backbones, showcases a versatile and robust strategy for constructing synthetic double helices with well-defined structures, holding promise for applications in diverse areas of supramolecular chemistry.[90]

Solvophobic Effects

The fascination with water-soluble helical polymers and oligomers has surged, driven by the prevalence of crucial biological processes occurring in aqueous environments. Although numerous synthetic polymers and oligomers capable of folding into double helices in organic solvents have been developed, their water-soluble counterparts are comparatively limited. Despite notable advancements in supramolecular chemistry, achieving water-soluble double helical structures remains a synthetically intriguing and challenging goal. The development of water-soluble helical polymers and oligomers not only contributes to our understanding of molecular self-assembly in aqueous environments but also opens avenues for applications in drug delivery, biomimetic materials, and other biomedical fields.

Oligoresorcinols featuring oligo(m-phenylene) backbones, initially intended for a singular 5/1-helix with dynamic properties,[91] unexpectedly undergo self-assembly, forming well-defined

double-helical structures in water.[92] The establishment of these structures is substantiated by the hyperchromic effect evident in absorption spectroscopy, upfield shifts in ^{1}H NMR spectra, and assessments conducted through vapor pressure osmometry (VPO). In water, X-ray crystallography has disclosed the presence of both single and double helical structures in specific oligoresorcinols. The stabilization of double helices in water involves various interactions, including π–π and CH-π interactions. These helices coexist in equimolar mixtures of left- and right-handed conformations. The introduction of optically active groups at both ends induces a twist sense bias, resulting in a distinctive Cotton effect.

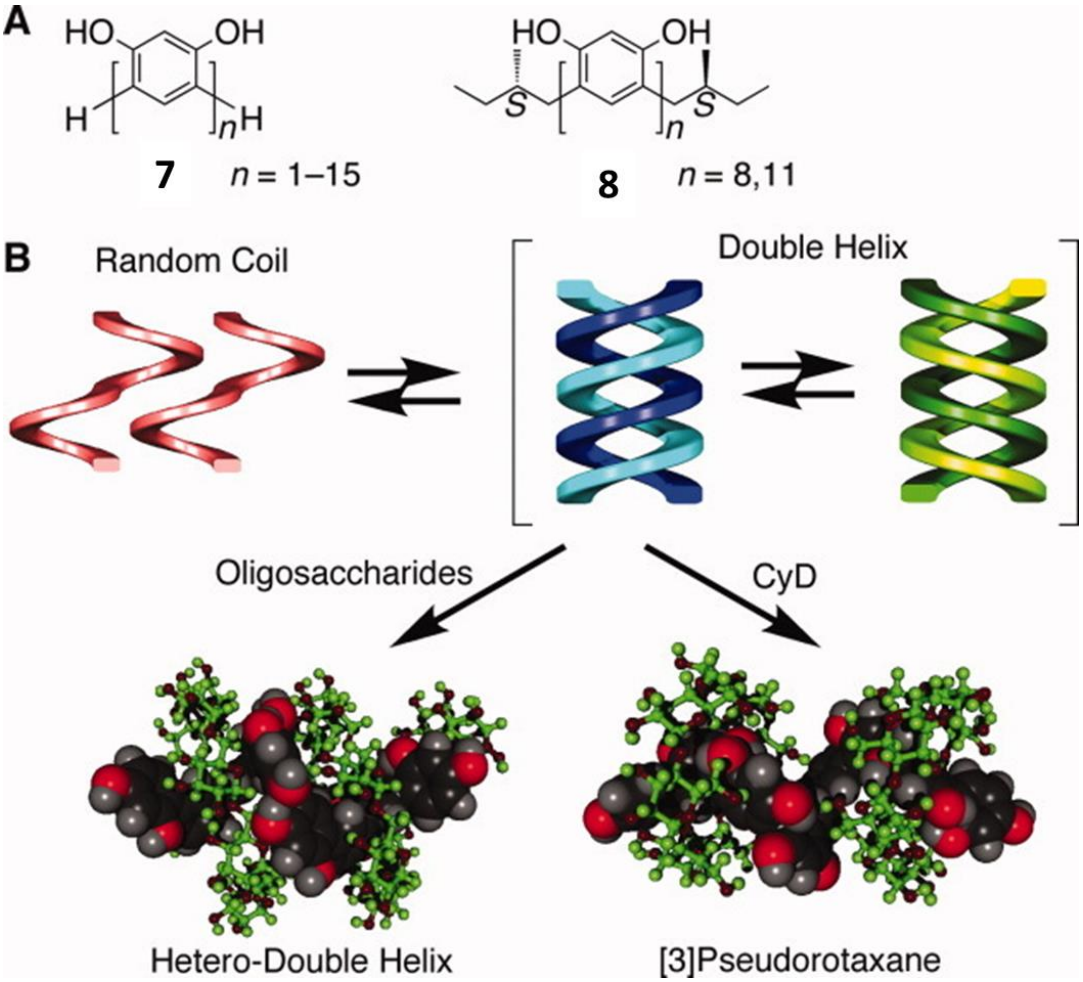


Figure 24: (A) Depictions of the structural arrangements of oligoresorcinols. (B) The creation of a double helix using oligoresorcinols, and the unwinding of this double helix led to the formation of [3]-pseudorotaxane with cyclodextrins, and the development of a heterodouble helix with linear oligosaccharides. Also provided are energy-minimized structures of the hetero double helix and the [3]-pseudorotaxane. (Reproduced with permission from ref 78; Copyright 2009 Wiley-VCH)

In contrast, in methanol, oligoresorcinols exhibit an anticipated random-coil conformation. The formation of double-stranded helices in oligoresorcinols is notably pH-dependent, attributed to the presence of two acidic hydroxyl groups on each benzene ring. Examinations utilizing 1H NMR, absorption, and CD spectroscopy demonstrate that in alkaline water, both optically active and inactive oligoresorcinols experience dissociation of their double helices into individual strands. This dissociation is prompted by electrostatic repulsion arising from the deprotonation of hydroxyl groups, leading to negatively charged strands. The resultant single strand subsequently adopts a single helix conformation with the aid of intramolecular hydrogen bonds in a water environment. Furthermore, when achiral oligo resorcinol (n = 9) is placed in alkaline water, it demonstrates a helix-sense bias in the presence of water-soluble chiral compounds like ammonium salts, amines, and alcohols. This characteristic makes oligoresorcinols highly promising candidates for water-soluble chirality sensors.[93] In the presence of β- or γ-cyclodextrin (CyD), the helical structure 18 forms [3]pseudorotaxanes with a twist-sense bias induced by the chirality of CyD. Reversion to the double helix occurs with β-CyD upon the addition of an adamantane derivative, forming an inclusion complex. In an aqueous environment, 18 and linear oligosaccharides undergo shuffling to create hetero double helices with a twist-sense bias, demonstrating high stereoselectivity dependent on chain lengths and glycosidic linkage patterns. This innovative approach unveils a novel method for saccharide recognition in water.[94]

In our lab, we are actively engaged in the exploration of various non-natural amino acid building blocks for the design and construction of diverse peptidic foldamers and peptidomimetic structures, with applications across different domains. As previously mentioned, the endeavor to design and engineer peptide-based double helices using unnatural amino acids represents an intriguing frontier in biomolecular chemistry. The introduction of chemical diversity has spurred efforts to create unique and well-defined secondary structures, with a specific emphasis on double helices. Such structures hold implications ranging from mimicking natural biomolecules to serving as platforms for applications in materials science and biotechnology.

Motivated by the structural intricacies observed in natural peptides such as gramicidin A and feglymycin, our laboratory has undertaken the challenge of designing artificial peptide double helices. In pursuit of this goal, we recently reported on the β-double-helical structures derived from the homo-oligomers of 4,4-gem-dimethyl α,β-unsaturated γ-amino acids[95a] and α,β-unsaturated γ-

amino Ac_6C-amino acids.[95b] These γ-peptides exhibit a parallel duplex structure in both solid and solution states, stabilized by interstrand hydrogen bonding. The depicted double helical structures are illustrated in Figure 25.

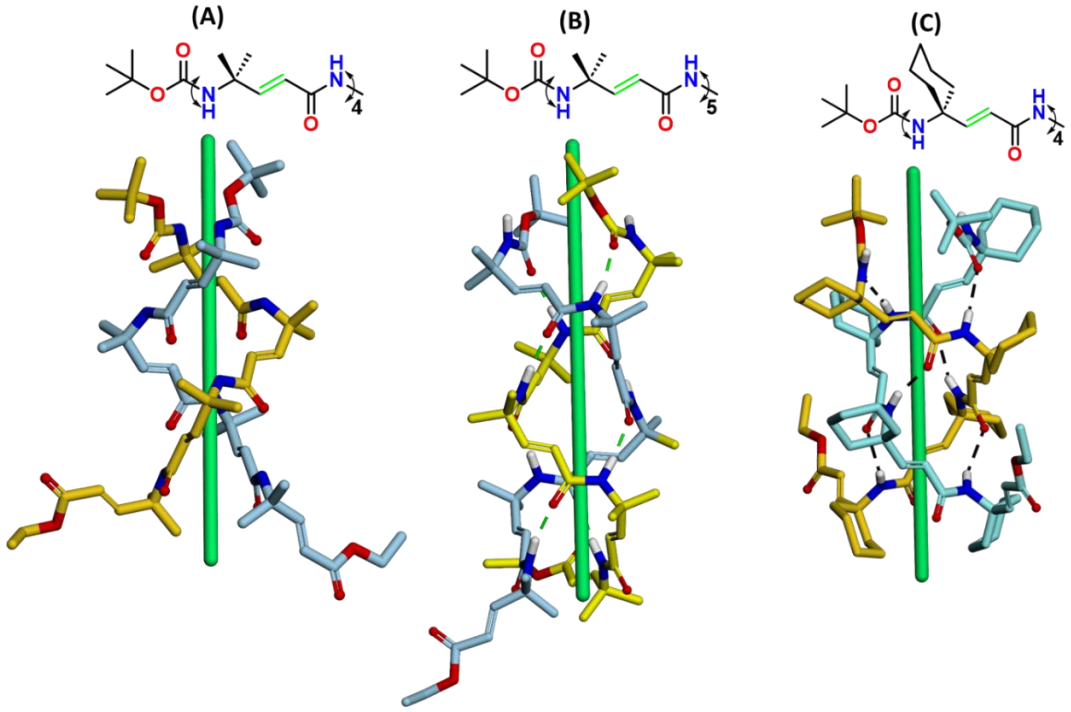


Figure 25: Crystal structure of α,β-unsaturated γ-Aic amino acids based double helices (A) tetrapeptide ester (B) pentapeptide ester (C) α,β-unsaturated γ-amino Ac_6C-amino acid based double helix.

Upon an in-depth examination of the existing literature, it is well-established that conventional double helices, formed through the alternation of L and D amino acids, inherently lack chirality. This characteristic holds true for the recently developed double helices in our research, where the monomers composing these sequences also lack inherent chirality. Given that chirality is a fundamental aspect with far-reaching implications across scientific disciplines—impacting molecular interactions, material properties, drug design, and sensory experiences—we are motivated to unravel and harness chirality in the context of peptide-based chiral double helices. In the current study, our focus revolves around exploring innovative strategies for designing and synthesizing peptide-based chiral double helices. We delve into the structural diversity achieved through a spectrum of synthetic methodologies, carefully dissecting the influence of stereochemistry and electronic properties on the resulting chiral structures. The insights gleaned from this investigation not only contribute to a foundational understanding of γ-peptide-based

chiral double helices and their assembly but also lay the groundwork for the development of pioneering materials and bioactive compounds characterized by distinct chiral signatures.

1.9. References

1. Linderstrom-Lang, K. U.; Schellman, J. A. (**1959**), *The Enzymes*, (P. D. Boyer, Ed.), *Vol. 1*, 2nd ed., pp. 443-510. Academic Press, New York.
2. Pauling, L.; Corey, R. B.; Branson, H. R. *Proc. Nat. Acad. Sci. USA*, **1951**, *37*, 205.
3. Ramachandran, G. N.; Sasisekaran, V. *Adv. Protein Chem.* **1968**, *23*, 283.
4. Astbury, W.; T.; Woods, H. J. *Nature* **1931**, *127*, 663.
5. Pauling, L.; Corey, R. B. *Proc. Nat. Acad. Sci. USA* **1951**, *37*, 729.
6. Venkatachalam, C. M. *Biopolymers* **1968**, *6*, 1425.
7. (a) Marshall, G. R.; Bosshard, H. E. *Circ. Res*. **1972**, *31*, 143. (b) Ramachandran, G. N.; Chandrasekaran, R. *Progress in Peptide Research.* Lande, S. Ed.; Gordon & Breach: New York, **1972**; Vol. II (*Proceedings of the Second American Peptide Symposium*, Cleveland, 1970), p 195. (c) Toniolo, C.; Benedetti, E. *ISI Atlas Sci. Biochem*. **1988**, *1*, 225. (d) Bosch, R.; Schmitt, H.; Jung, G.; Winter, W. *Biopolymers* **1985**, *24*, 961. (e) Toniolo, C.; Benedetti, E. *Trends Biochem. Sci.* **1991**, *16*, 350. (f) Karle, I. L.; Balaram, P. *Biochemistry* **1990**, *29*, 6747. (g) Marshall, G. R.; Hodgkin, E. E.; Langs, D. A.; Smith, G. D.; Zabrocki, J.; Leplawy, M. T. *Proc. Natl. Acad. Sci. U.S.A.* **1990**, *87*, 487. (h) Karle, I. L. *Acc. Chem. Res*. **1999**, *32*, 693. (i) Kaul, R.; Balaram, P. *Bioorg. Med. Chem*. **1999**, *7*, 105. (j) Balaram, P. *J. Pept. Res.* **1999**, *54*, 195. (k) Venkatraman, J.; Shankaramma, S. C.; Balaram, P. *Chem. Rev*. **2001**, *101*, 3131.
8. (a) Gellman, S. H. *Acc. Chem. Res.* **1998**, *31*, 173. (b) Frackenpohl , J.; Arvidsson , P. I.; Schreiber , J. V.; Seebach , D. *ChemBioChem* **2001**, *2*, 445. (c) Goodman, C. M.; Choi, S.; Shandler, S.; DeGrado, W.F. *Nat. Chem. Biol.* **2007**, *3*, 252.
9. (a) Hintermann, T.; Gademann, K.; Jaun, B.; Seebach, D. *Helv. Chim. Acta*, **1998**, *81*, 983. (b) Seebach, D.; Beck, A. K.; Bierbaum, D. J. *Chem. Biodiv*. **2004**, *1*, 1111.
10. (a) Appella, D. H.; Christianson, L. A.; Karle, I. L.; Powell, D. R.; Gellman, S. H. *J. Am. Chem. Soc*. **1996**, *118*, 13071. (b) Appella, D. H.; Christianson, L. A.; Karle, I. L.; Powell, D. R.; Gellman, S. H. *J. Am. Chem. Soc*. **1999**, *121*, 6206. (c) Appella, D. H.; Christianson, L. A.; Klein, D. A.; Richards, M. A.; Powell, D. R.; Gellman, S. H. *J. Am. Chem. Soc.*

1999, *121*, 7574. (d) Krauthauser, S.; Christianson, L. A.; Powell, D. R.; Gellman S. H. *J. Am. Chem. Soc*. **1997**, *119*, 11719.

11. (a) Sharma, G. V. M.; Reddy, R.; Krishna, P. R.; Ravi Sankar, A.; Narsimulu, K., Kumar, S. K.; Jayaprakash, P.; Jagannadh, B.; Kunwar, A. C. *J. Am. Chem. Soc*. **2003**, *125,* 13670. (b) Sharma, G. V. M.; Chandramouli, N.; Choudhary, M.; Nagendar, P.; Ramakrishna, K. V. S.; Kunwar, A. C.; Schramm, P.; Hofmann, H. -J. *J. Am. Chem. Soc*. **2009**, *131*, 17335.
12. Fernandes, C.; Faure, S.; Pereira, E.; Thery, V.; Declerck, V.; Guillot, R.; Aitken, D. J. *Org. Lett*. **2010**, *12*, 3606
13. (a) Fulop, F.; Forro, E.; Toth, G. K. *Org. Lett*. **2004**, 6, 4239. (b) Martinek, T. A.; Fulop, F. *Chem. Soc. Rev*. **2012**, *41*, 687
14. (a) Gopi, H. N.; Ravindra, G.; Pal, P. P.; Pattanaik, P.; Balaram, H.; Balaram, P. *FEBS Lett.* **2003**, *535*, 175. (b) Frackenpohl, J.; Arvidsson, P. I.; Schreiber, J. V.; Seebach, D. *ChemBioChem*, **2001**, *2*, 445. c) Hook, D. F.; Bindschädler, P.; Mahajan, Y. R.; Sebesta, R.; Kast, P.; Seebach, D. *Chem. Biodiv.* **2005**, *2*, 591.
15. Cheng, R.P.; Gellman, S. H.; DeGrado, W. F. *Chem. Rev.* **2001**, *101*, 3219.
16. Choi, S. H.; Guzei, I. A.; Spencer, L. C.; Gellman, S. H. *J. Am. Chem. Soc.* **2010**, *132*, 13879.
17. Mandity, I. M.; Fulop, L.; Vass, E.; Toth, G. K.; Martinek, T. A.; Fulop, F. *Org. Lett.* **2010**, *12*, 5584.
18. Kwon, S.; Jeon, A.; Yoo, S. H.; Chung, I. S.; Lee, H.-S. *Angew. Chem.Int. Ed*. **2010**, *49*, 8232.
19. a) Karle, I, L.; Gopi, H. N.; Balaram. P. *Proc. Nat. Acad. Sci. USA*, **2001**, *98*, 7. (b) Vasudev, P. G.; Chatterjee, S.; Shamala, N.; Balaram, P. *Chem. Rev.* **2011**, *111*, 657. (c) Sonti, R.; Gopi, H. N.; Muddegowda, U.; Ragothama, S.; Balaram, P. *Chem. Eur. J.* **2013**, *19*, 5955. (d) Aravinda, S.;Shamala, N.;Rajkishore, R.; Gopi, H. N.; Balaram, P. *Angew. Chem. Int. Ed.* **2002**, *20*, 3863.
20. Seebach, D.; Hook, D. F.; Glattli, A. *Biopolymers (Peptide Science)* **2006**, *84*, 23.
21. Hintermann, T.; Gademann, K.; Seebach, D. *Helv. Chim. Acta*. **1998**, *81*, 893.
22. Hanessian, S.; Luo, X.; Schaum, R.; Michnick, S. *J. Am. Chem. Soc*. **1998**, *120*, 8569.
23. Baldauf, C.; Gunther, R.; Hofmann, H. -J. *J. Org. Chem.* **2006**, *71*, 1200.

24. Sharma, G. V. M.; Jayaprakash, P.; Narsimulu, K.; Sankar, A. R.; Reddy, K. R.; Kunwar, A. C. *Angew. Chem.Int. Ed*. **2006**, *45*, 2944.
25. Vasudev, P. G.; Shamala, N.; Anandass, K.; Balaram, P. *Angew. Chem., Int. Ed.* **2005**, *44*, 4972.
26. Basuroy, K.; Dinesh, B.; Reddy, M. B. M.; Chandrappa, S.; Raghothama, S.; Shamala, N.; Balaram, P. *Org. Lett. 2013*, **15**, 4866.
27. Guo, L.; Zhang, W.; Reidenbach, A.G.; Giuliano, M.W.; Guzei, I.A.; Spencer, L.C.; Gellman, S. H. *Angew. Chem. Int. Ed*. **2011**, *50*, 5843.
28. Seebach, D.; Brenner, M.; Rueping, M.; Schweizer, B.; Jaun, B. *Chem. Commun*. **2001**, 207.
29. Khurram, M.; Qureshi, N.; Smith, M. D. *Chem. Commun.* **2006**, 5006
30. Kothari, A.; Khurram, M.; Qureshi, N.; Beck, E. M.; Smith, M. D. *Chem. Commun*. **2007**, 2814.
31. (a) Lee, X.; Yang, D. *Chem. Commun*. **2006**, 3367. (b) Chen, F.; Zhu, N.-Y.; Yang, D. *J. Am. Chem. Soc.* **2004**, *126*, 15980.
32. Pendem, N.; Nelli, Y. R.; Douat, C.; Fischer, L.; Laguerre, M.; Ennifar, E.; Kauffman, B.; Guichard, G. *Angew. Chem. Int. Ed*. **2013**, *52*, 4147.
33. Mathieu, L.; Legrand, B.; Deng, C.; Vezenkov, L.; Wenger, E.; Didierjean, C.; Amblard, M.; Averlant-Petit, M. C.; Masurier, N.; Lisowski, V.; Martinez, J.; Maillard, L. T. *Angew. Chem. Int. Ed.* **2013**, *52*, 6006.
34. (a) Karle, I. L.; Pramanik, A.; Banerjee, A.; Bhattacharjya, S.; Balaram, P. *J. Am. Chem. Soc*. **1997**, *119*, 9087. (b) Roy, R. S.; Karle, I. L.; Raghothama, S.; Balaram, *P. Proc. Natl. Acad. Sci. USA.* **2004**, *101*, 16478.
35. Baldauf, C.; Günther, R; Hofmann, H.-J. *Peptide Science*. **2006**, *84*, 408.
36. Srinivasulu, G.; Kumar, S. K.; Sharma, G. V. M.; Kunwar, A. C. *J. Org. Chem*. **2006**, *71*, 8395.
37. Jagadeesh, B.; Prabhakar, A.; Sarma, G. D.; Chandrasekhar, S.; Chandrashekar, G.; Reddy, M. S.; Jagannadh. B. *Chem. Commun*. **2007**, 371.
38. (a) Choi, S. H.; Guzei, I. A.; Gellman, S. H. *J. Am. Chem. Soc*. **2007**, *129*, 13780. (b) Schmitt, M. A.; Choi, S. H.; Guzei, I. A.; Gellman, S. H. *J. Am. Chem. Soc*. **2005**, *127*, 13130.

39. Schmitt, M. A.; Choi, S. H.; Guzei, I. A.; Gellman, S. H. *J. Am. Chem. Soc*. **2006**, 1*28*, 4538
40. Mándity, I. M.; Weber, E.; Martinek, T. A.; Olajos, G.; Tóth, G. K.; Vass, E.; Fülöp, F. *Angew*. *Chem., Int. Ed*. **2009**, *48*, 2171.
41. (a) Giuliano, M. W.; Horne, W. S.; Gellman, S. H. *J. Am. Chem. Soc*. **2009**, *131*, 9860. (b) Horne, W. S.; Price, J. L.; Keck, J. L.; Gellman, S. H. *J. Am. Chem. Soc*. **2007**, *129*, 4178.
42. Baldauf, C.; Gunther, R.; Hofmann, H.-J. *J. Org. Chem*. **2006**, *71*, 1200
43. (a) Ananda, K.; Vasudev, P.G.; Sengupta, A.; Raja, K.M.P.; Shamala N.; Balaram, P. *J. Am. Chem. Soc*. **2005**, *127*, 168. (b) Jadhav, S. V.; Bandyopadhyay, A.; Gopi, H. N. *Org. Biomol. Chem.* **2013**, *11*, 509.
44. Sharma, G. V. M.; Jadhav, V. B.; Ramakrishna, K. V. S.; Jayaprakash, P.; Narsimulu, K.; Subash, V.; Kunwar, A. C. *J. Am. Chem. Soc*. **2006**, *128*, 14657.
45. (a) Guo, L.; Chi, Y.; Almeida, A. M.; Guzei, I. A.; Parker, B. K.; Gellman, S. H. *J. Am. Chem. Soc.* **2009**, *131*, 16018. (b) Guo, L.; Zhang, W.; Guzei, I. A.; Spencer, L. C.; Samuel H. Gellman, S. H. *Org. Lett.* **2012**, *14*, 2582. (c) Giuliano, M. W.; Maynard, S. J.; Almeida, A. M.; Guo, L.; Guzei, I. A.; Spencer, L. C.; Gellman, S. H. *J. Am. Chem. Soc*. **2014**, *136*, 15046.
46. Fisher, B. F.; Gellman, S.H. *J. Am. Chem. Soc*. **2016**, *138*, 10766.
47. Chatterjee, S.; Vasudev, P. G.; Raghothama, S.; Ramakrishnan, C.; Shamala, N.; Balaram, P. *J. Am. Chem. Soc*. **2009**, *131*, 5956.
48. Misra, R.; Saseendran, A.; George, G.; Veeresh, K.; Raja, K. M. P.; Raghothama, S.; Hofmann, H.-J.; Gopi, H. N. *Chem. Eur. J.* **2017**, *23*, 3764
49. Misra, R.; Raja, K. M. P.; Hofmann, H. –J.; Gopi, H. N. *Chem. Eur. J.* **2017**, *23*, 16644.
50. Veeresh, K.; Gopi, H. N. *Org. Lett*. **2019**, *21*, 4500.
51. Sharma, G. V. M. Jadhav, V. B.; Ramakrishna, K. V. S.; Jayaprakash, P.; Narsimulu, K.; Subash, V.; Kunwar, A. C.; *J. Am. Chem. Soc.* **2006**, *128*, 14657.
52. Vasudev, P. G.; Ananda, K.; Chatterjee, S.; Aravinda, S.; Shamala, N.; Balaram, P. J. *Am. Chem. Soc*. **2007**, *129*, 4039.
53. Shin, Y.-H.; Mortenson, D. E.; Satyshur, K. A.; Forest, K. T.; Gellman, S. H. *J. Am. Chem. Soc.* **2013**, *135*, 8149.

54. (a) Grison, C. M.; Robin, S.; Aitken, D. J. *Chem. Commun*. **2016**, *52*, 7802. (b) Grison, C. M.; Robinab, S.; Aitken D. J. *Chem. Commun*. **2015**, *51*, 16233.
55. (a) Hintermann, T.; Gademann, K.; Jaun B.; Seebach, D. *Helv. Chim. Acta*. **1998**, *81*, 983; (b) Brenner, M.; Seebach, D. *Helv. Chim. Acta*. **2001**, *84*, 1181
56. (a) Santos, M. M. M.; Moreira, R. *Mini-Rev. Med. Chem*., **2007**, *7*, 1040. (b) J. S. Plummer, L. A. Emery, M. A. Stier and M. J. Suto, *Tetrahedron Lett*. **1993**, *34*, 7529.
57. Fu, Y.; Xu, B.; Zou, X.; Ma, C.; Yang, X.; Mou, K.; Fu, G.; Lu, Y.; Xu, P. *Bioorg. Med. Chem. Lett*. 2007, **17**, 1102.
58. Reetz, M. T. *Angew. Chem., Int. Ed. Engl*. **1991**, *30*, 1531.
59. Hagihara, M.; Schreiber, S. L. *J. Am. Chem. Soc.* **1992**, *114*, 6570.
60. Linington, R. G.; Clark, B. R.; Trimble, E. E.; Almanza, A.; Uren, L.-D.; Kyle, D. E.; Gerwick, W. H. J. *Nat. Prod.* **2009**, *72*, 14.
61. Nakao, Y.; Fujita, M.; Warabi, K.; Matsunaga, S.; Fusetani, N. *J. Am. Chem. Soc.* **2000**, *122*, 10462.
62. (a) Hanzlik, R. P.; Thompson, S. A. *J. Med. Chem*. **1984**, *27*, 711. (b) Bastiaans, H. M. M.; Van der Baan, J. L.; Ottenheijm, H. C. J. *J. Org. Chem*. **1997**, *62*, 3880. (c) Liu, S.; Hanzlik, R. P. *J. Med. Chem*. **1992**, *35*, 1067. (d) Kong, J-S.; Venkatraman, S.; Furness, K.; Nimkar, S.; Shepherd, T. A.; Wang, Q. M.; Aube, J.; Hanzlik, R. P. *J. Med. Chem*. **1998**, *41*, 2579. (e) Schaschke, N.; Sommerhoff, C. P. *ChemMedChem* **2010**, *5*, 367
63. Hagihara, M.; Anthony, N. J.; Stout, T. J.; Clardy, J.; Schreiber, S. L. *J. Am. Chem. Soc.* **1992**, *114*, 6568.
64. Chakraborty, T. K.; Ghosh, A.; Kumar, S. K.; Kunwar, A. C. *J. Org. Chem*. **2003**, *68*, 6459.
65. Baldauf, C.; Gunther, R.; Hofmann, H.-J. *J. Org. Chem.* **2005**, *70*, 5351.
66. Bandyopadhyay, A.; Mali, S. M.; Lunawat, P.; Raja, K. M. P.; Gopi, H. N. *Org. Lett*. **2011**, *13*, 4482.
67. Bandyopadhyay, A.; Gopi, H. N. *Org. Lett*. **2012**, *14*, 2770.
68. Bandyopadhyay, A.; Misra. R.; Gopi, H. N. *Chem. Commun.* **2016**, *52*, 4938.
69. Ganesh Kumar, M.; Thombare, V. J.; Katariya, M. M.; Veeresh, K.; Raja, K. M. P.; Gopi, H. N. *Angew. Chem. Int. Ed*. **2016**, *55*, 1.
70. Veeresh, K.; Gopi. H. N. *Org. Lett*. **2019**, *21*, 4500.
71. Veeresh, K.; Singh, M.; Gopi. H. N. *Org. Biomol. Chem*. **2019**, *17*, 9226.

72. (a) Watson, J. D.; Crick, F. C. H. *Nature*, **1953**, *171*, 737. (b) Alberts, B.; Johnson, A.; Lewis, J.; Morgan, D.; Raff, M.; Roberts, K.; Walter, P. *Mol. Biol. Cell*, 6th ed.; Garland Science: New York,
73. Saenger, W. *Principles of Nucleic Acid Structure*; Springer-Verlag: New York, **1984**.
74. (a) Langes, D. A. *Science* **1988**, *241*, 188. (b) Urry, D. W.; Glickson, J. D.; Mayers, D. F.; Haider, J. *Biochemistry* **1972**, *11*, 487. (c) Wallace, B. A.; Ravikumar, K. *Science* **1988**; *241*, 182. (d) Sychev, S. V.; Barsukov, L. I.; Ivanov, V. T. *J. Pept. Sci.* **2013**, *19*, 452. (e) Kelkar, D. A.; Chattopadhyay, A. *Biochim. Biophys. Acta.* **2007**, *1768*, 2011. (f) Sychev, S. V.; Barsukov, L. I.; Ivanov, V. T. *Eur. Biophys. J*. **1993**, *22*, 279.
75. (a) Zhang, Z.; Pascal, S. M.; Cross, T. A. *Biochemistry* **1992**, *31*, 8822. (b) Arsemev, A. S.; Barsukov, I. L.; Bystrov, V. F. *FEBS. Lett*. **1984**, *180*, 33. (c) Roux, B.; Bruschweiler, R.; Ernst, R. R. *Eur. J. Biochem.* **1990**, *194*, 57. (d) Pascal, S. M.; Cross, T. A. *J. Biomol. NMR* **1993**, *3*, 495. (e) Langs, D. A. *Biopolymers* **1989**, *28*, 259. (f) Woolley, G. A.; Wallace, B. A. *J. Membr. Biol*. **1992**, *129*, 109. (g) Ketchem, R. R.; Hu, W.; Cross, T. A. *Science*, **1993**, *261*, 1457. (h) Kovacs, F.; Quine, J.; Cross, T. A. *Proc. Natl. Acad. Sci. USA*. **1999**, *96*, 7910.
76. (a) Vertesy, L.; Aretz, W.; Knauf, M.; Markus, A.; Vogel, M.; Wink, J. *J. Antibiot.* **1999**, *52*, 374. (b) Férir, G.; Hänchen, A.; François, K. O.; Hoorelbeke, B.; Huskens, D.; Dettner, F.; Süssmuth, R. D.; Schols, D. *Virology*, **2012**, *433*, 308. (c) Dettner, F.; Hnchen, A.; Schols, D.; Toti, L.; Nusser, A.; Sussmuth, R. D. *Angew. Chem. Int. Ed.* **2009**, *48*, 1856.
77. (a) Benedetti, E.; Di Blasio, B.; Pedone, C.; Lorenzi, G. P.; Tomasic, L.; Gramlich, V. *Nature* **1979**, *282*, 630. (b) Di Blasio, B.; Benedetti, E.; Pavone, V.; Pedone, C.; Gerber, C.; Lorenzi, G. P. *Biopolymers* **1989**, *28*, 203. (c) Kulp, J. L.; Clark, T. D. *Chem. Eur. J.* **2009**, *15*, 11867. (d) Navarro, E.; Fenude, E.; Celda, B. *Biopolymers* **2004**, *73*, 229. (e) Sastry, M.; Brown, C.; Wagner, G.; Clark, T. D. *J. Am. Chem. Soc*. **2006**, *128*, 10650. (f) Schramm, P.; Hofmann, H. -J. *J. Pept. Sci.* **2010**, *16*, 276. (g) Jadhav, K. B.; Lichtenecker, R. J.; Bullach, A.; Mandal, B.; Arndt, H. -D. *Chem. Eur. J*. **2015**, *21*, 5898.
78. Furusho, Y.; Yashima, E. Development of Synthetic Double Helical Polymers and Oligomers. *J. Polym. Sci. Part A Polym. Chem.* **2009**, *47*, 5195.
79. Lehn, J. M.; Rigault, A.; Siegel, J.; Harrowfield, J.; Chevrier, B.; Moras, D. *Proc Natl Acad Sci USA* **1987**, *84*, 2565.

80. (a) Constable, E. C. *Tetrahedron* **1992**, *48*, 10013. (b) Piguet, C.; Bernardinelli, G.; Hopfgartner, G. *Chem. Rev.* **1997**, *97*, 2005. (c) Albrecht, M. *Chem Rev.* **2001**, *101*, 3457.
81. Koert, U.; Harding, M. M.; Lehn, J. M. *Nature* **1990**, *346*, 339
82. (a) Hasenknopf, B.; Lehn, J.-M.; Baum, G.; Fenske, D. *Proc. Natl. Acad. Sci. USA* **1996**, *93*, 1397. (b) Smith, V. C. M.; Lehn, J.-M. *Chem. Commun.* **1996**, *24*, 2733.
83. Marquis, A.; Smith, V.; Harrowfield, J.; Lehn, J.-M.; Herschbach, H.; Sanvito, R.; Leize-Wagner, E.; Van Dorsselaer, A. *Chem. Eu.r J.* **2006**, *12*, 5632.
84. (a) Berl, V.; Huc, I.; Khoury, R. G.; Krische, M. J.; Lehn, J.-M. *Nature* **2000**, *407*, 720. (b) Berl, V.; Huc, I.; Khoury, R. G.; Lehn, J.-M. *Chem. Eur. J.* **2001**, ***7***, 2810.
85. (a) Haldar, D.; Jiang, H.; Leger, J.-M.; Huc, I. *Angew. Chem. Int. Ed.* **2006**, *45*, 5483. (b) Haldar, D.; Jiang, H.; Leger, J.-M.; Huc, I. *Tetrahedron* **2007**, *63*, 6322.
86. (a) Gan, Q.; Wang, X.; Kauffmann, B.; Rosu, F.; Ferrand, Y.; Huc. I. *Nature Nanotech*. **2017**, *12*, 447. (b) Wang, X.; Wicher, B.; Ferrand, Y.; Huc, I. *J. Am. Chem. Soc.* **2017**, *139*, 9350. (c) Li, X.; Markandeya, N.; Jonusauskas, G.; McClenaghan, N. D.; Maurizot, V.; Denisov, S. A.; Huc, I. *J. Am. Chem. Soc.* **2016**, *138*, 13568. (d) Denisov, S. A.; Gan, Q.; Wang, X.; Scarpantonio, L.; Ferrand, Y.; Kauffmann, B.; Jonusauskas, G.; Huc, I.; McClenaghan, N. D. *Angew. Chem. Int. Ed*. **2016**, *55*, 1328. (e) Shang, J.; Gan, Q.; Dawson, S. J.; Rosu, F.; Jiang, H.; Ferrand, Y.; Huc I. *Org. Lett.* **2014,** *16*, 4992. (f) Denisov, S. A.; Gan, Q.; Wang, X.; Scarpantonio, L.; Ferrand, Y.; Kauffmann, B.; Jonusauskas, G.; Huc, I.; McClenaghan, N. D. *Angew. Chem. Int. Ed.* **2016**, 55, 1328. (g) Denisov, S. A.; Gan, Q.; Wang, X.; Scarpantonio, L.; Ferrand, Y.; Kauffmann, B.; Jonusauskas, G.; Huc, I.; McClenaghan, N. D. *Angew. Chem. Int. Ed.* **2016**, *55*, 1328. (h) Maurizot, V.; J. Léger, M.; Guionneau, P.; Huc, I. *Russ.Chem.Bull. Int.Ed*., **2004**, *53*, 1572. (i) Zhan, C.; Léger, J.-M.; Huc, I. *Angew. Chem. Int. Ed.* **2006**, *45*, 4625. (j) Haldar, D.; Jiang, H.; Léger, J.-M.; Huc, I. *Angew. Chem. Int. Ed.* **2006**, *45*, 5483.
87. Gabriel, G. J.; Iverson, B. L.; *J. Am. Chem. Soc.* **2002,** *124*, 15174. (b) Lokey, R.S.; Iverson, B.L. *Nature*, **1995**, *375*, 303. (c) Ikkanda, B. A.; Iverson, B. L. *Chem. Commun.* **2016**, *52*, 7752.
88. Sanford, A. R.; Yamato, K.; Yang, X.; Yuan, L.; Han, Y.; Gong, B. *Eur. J Biochem.* **2004**, *271*, 1416.

89. Tanaka, Y.; Katagiri, H.; Furusho, Y.; Yashima, E. *Angew. Chem. Int. Ed.* **2005**, *44*, 3867

90. (a) Ikeda, M.; Tanaka, Y.; Hasegawa, T.; Furusho, Y.; Yashima, E. *J. Am. Chem. Soc.* **2006**, *128*, 6806. (b) Kim, H.-J.; Lee, E.; Kim, M. G.; Kim, M.-C.; Lee, M.; Sim, E. *Chem. Eur. J.* **2008**, *14*, 3883. (c) Kim, H.-J.; Lim, Y.-B.; Lee, M. *J Polym Sci Part A: Polym. Chem.* **2008**, *46*, 1925. (d) Maeda, T.; Furusho, Y.; Sakurai, S.-I.; Kumaki, J.; Okoshi, K.; Yashima, E. *J. Am. Chem. Soc.* **2008**, *130*, 7938. (e) Nishiyama, H.; Sakaguchi, H.; Nakamura, T.; Horihata, M.; Kondo, M.; Itoh, K. *Organometallics* **1989**, *8*, 846. (f) Sugimoto, T.; Suzuki, T.; Shinkai, S.; Sada, K. *J. Am. Chem. Soc.* **2007**, *129*, 270. (g) Ito, H.; Furusho, Y.; Hasegawa, T.; Yashima, E. *J. Am. Chem. Soc.* **2008**, *130*, 14008

91. (a) Williams, D. J.; Colquhoun, H. M.; O'Mahoney, C. A. *J. Chem. Soc. Chem. Commun*. **1994**, 1643. (b) Kobayashi, N.; Sasaki, S.; Abe, M.; Watanabe, S.; Fukumoto, H.; Yamamoto, T. *Macromolecules* **2004**, *37*, 7986.

92. (a) Goto, H.; Katagiri, H.; Furusho, Y.; Yashima, E. *J. Am. Chem. Soc.* **2006,** *128*, 7176. (b) Goto, H.; Furusho, Y.; Miwa, K.; Yashima, E. *J. Am. Chem. Soc.* **2009**, *131*, 4710

93. Goto, H.; Furusho, Y.; Yashima, E. *Chem Commun* **2009,** *13*,1650

94. (a) Ben, T.; Goto, H.; Miwa, K.; Goto, H.; Morino, K.; Furusho, Y.; Yashima, E. *Macromolecules* **2008**, *41*, 4506. (b) Ben, T.; Furusho, Y.; Goto, H.; Miwa, K.; Yashima, E. *Org. Biomo.l Chem.* **2009**, *7*, 2509. (c) Sugiura, H.; Nigorikawa, Y.; Saiki, Y.; Nakamura, K.; Yamaguchi, M. *J Am Chem Soc* **2004**, *126*, 14858. (d) Amemiya, R.; Saito, N.; Yamaguchi, M. *J. Org. Chem.* **2008**, ***73***, 7137 (e) Sugiura, H.; Amemiya, R.; Yamaguchi, M. *Chem. Asian. J.* **2008**, *3*, 244.

95. (a) R. Misra, S. Dey, R. M. Reja, H. N. Gopi, *Angew. Chem. Int. Ed.* **2018**, *130*, 1069. (b) Veeresh, K.; Singh, M.; Gopi, H. N. *Org Biomol Chem* **2019**, *17*, 9226.

Chapter 2

Design of Chiral β-Double Helices from γ-Peptide Foldamers

2.1. Introduction

Chirality, the property of asymmetry in molecules, is widespread in nature, playing a crucial role in the structure and function of biomolecules. Homochirality, the prevalence of a single chirality in a given biological system, is a remarkable feature observed in many biomolecules. The concept of helicity, or the inherent property of a molecule to exhibit a helical structure, is widespread across various classes of biomolecules, with proteins, nucleic acids, and polysaccharides being prominent examples. The helical structures observed in these molecules play fundamental roles in their biological functions. In the context of nucleic acids, DNA, for instance, showcases the remarkable ability to adopt both right-handed (B-DNA) and left-handed (Z-DNA) double helix conformations.[1] The right-handed B-DNA is the more prevalent and biologically relevant form, with its specific pairing of nucleotide bases (adenine with thymine and guanine with cytosine) through hydrogen bonding. This complementary base pairing results in the formation of a stable right-handed double helix, known as B-DNA, which is essential for processes such as DNA replication and transcription. On the other hand, Z-DNA, the left-handed counterpart, is less common and typically induced by specific sequences, high salt concentrations, or binding proteins. This left-handed conformation is associated with dynamic processes, including gene expression regulation.[2] Similarly, in proteins, the right-handed α-helix is a prevalent structural motif. No double helix structures have been observed in proteins and peptides with the exception of a fifteen-residue natural peptide antibiotic gramicidin A[3] and a recently discovered thirteen residue peptide, feglymycin.[4] Both of these natural peptides adopted double helix conformations. The common feature between gramicidin A and feglymycin is that both peptides consist of alternating L- and D-amino acids. It has been established that gramicidin A adopts a β-double helix conformation in organic solvents and a β-helix conformation in lipids.[5] The structure and functions of gramicidin A and other natural peptides have attracted considerable attention from chemists aiming to design gramicidin mimetics. Drawing inspiration from natural sequences, synthetic double helices have been reported using sequences consisting of L- and D-amino acids.[6] No reports have emerged regarding β-double helix structures from peptides other than those composed of L- and D-amino acids. No peptide double helices with a single amino acid chirality have been reported. However, in their pioneering work, Lehn, Huc, and others have reported double helices formed from quinolone-based oligomers.[7] Additionally, a range of non-peptidic oligomers have been explored to design double-helical structures in both the absence and presence of metal ions.[8] Recently, we

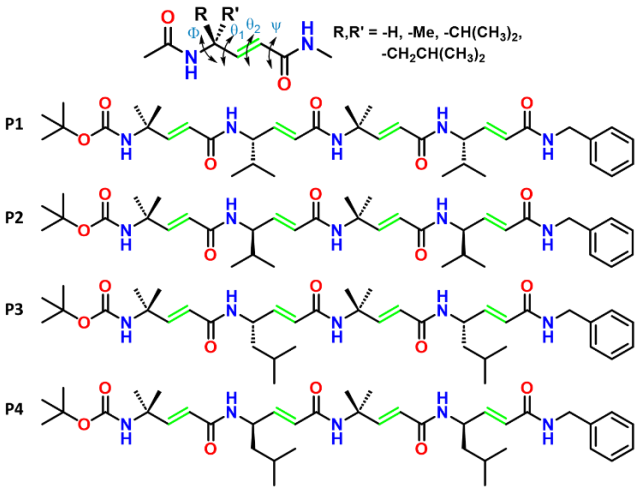
demonstrated double helical structures designed from the oligomers of achiral (*E*)-α, β-unsaturated 4, 4-dimethyl γ-amino acids (dγAic).[9]

2.2. Objective of the Present Work

In continuation of our efforts to comprehend the structure and functions of natural systems, we sought to investigate whether it is possible to design chiral β-double helices and study their structure and functions. In addition, we also sought to investigate whether the β-sheet promoting (*E*)-α, β-unsaturated γ-amino acids can be accommodated into the β-double helix structure. In this report, we detail the design, single crystal conformations, and solution structural analysis, structural analogy with other α-peptide β-double helices, their ion transport activity. This marks the first report demonstrating the design of chiral peptide double helices.

2.3. Results and Discussions

To investigate the potential formation of chiral-double helices, we designed four peptides, **P1** to **P4**. The sequences of these peptides are shown in Scheme 1.



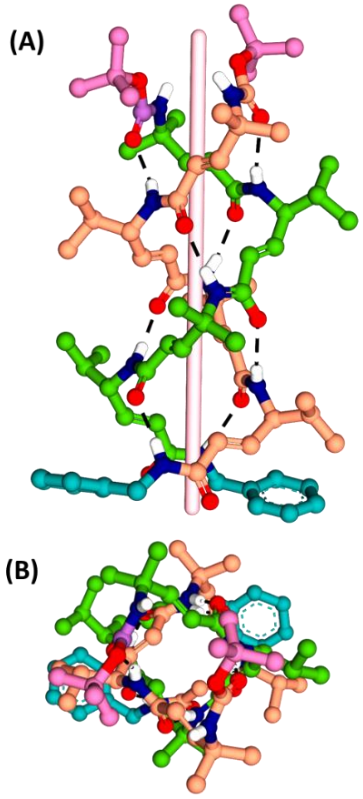
Scheme 1: Sequences of the chiral γ-peptides **P1**-**P4**

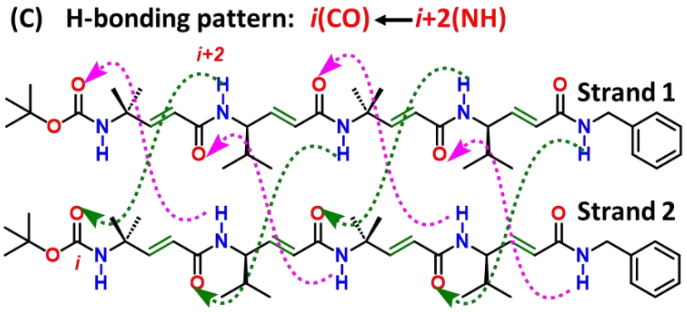
Chiral α,β-unsaturated γ-amino acids were incorporated with a 1:1 alternating arrangement alongside achiral 4,4-dimethyl α,β-unsaturated γ- amino acids. The oligomer of achiral 4,4-dialkyl α,β-unsaturated γ-amino acids are known to adopt β-double helix structure. Peptides **P1** and **P3** consist of chiral α,β-unsaturated γ-amino acids derived from L-amino acids, while peptides **P2** and **P4** consist of chiral α,β-unsaturated γ-amino acids derived from D-amino acids, respectively.

All peptides were synthesized utilizing solution-based methods and all α,β-unsaturated γ-amino acids were prepared in accordance with previously reported procedures.[10]

2.3.1. Crystal Structure Analysis of P1

To obtain unequivocal conformations of the designed peptides, we subjected them to crystallization using various solvent combinations. Single crystals of **P1** were successfully obtained from the peptide solution in chloroform and toluene, and the X-ray diffracted structure is depicted in Figure 1A.





(D) Torsion angles parameters:

	ϕ	θ_1	θ_2	ψ
Strand 1				
dγ Aib 1	-70.71	-6.91	-171.33	173.71
dγ Val(L) 1	-97.25	-5.36	179.31	-174.54
dγ Aib 2	-61.97	-21.34	-171.38	172.85
dγ Val(L) 2	-96.07	1.84	174.41	-176.36
Strand 2				
dγ Aib 1	-72.25	-12.69	-173.46	-177.44
dγ Val(L) 1	-82.40	-13.11	-179.68	164.28
dγ Aib 2	-76.84	-10.25	-172.88	177.90
dγ Val(L) 2	-86.53	-2.74	177.10	175.78

Figure 1: (A) The X-ray diffracted single crystal structure of **P1**. An imaginary rod is introduced along the central axis to facilitate the observation of the parallel β-double helices. Two strands are shown in two different colors. (B) Top view of **P1** double helix. (C) Interstrand H-bonding observed between amide carbonyl (CO) of residue (*i*) in strand 1 and amide NH residue (*i*+2) in strand 2. (D) Torsion angle parameters of strand 1 and strand 2 of **P1**.

The peptide adopted a β-double helix conformation in the single crystals, wherein two individual peptides intertwined through intermolecular hydrogen bonds. This double helix structure was

stabilized by eight intermolecular hydrogen bonds between the amide carbonyl (CO) of residue (*i*) in strand 1 and amide NH residue (*i*+2) in strand 2. The hydrogen bond parameters observed in the double helix are within standard limits and are tabulated in Table 1. The two strands in the double helix structure adopted right-handed helical conformation without any intramolecular hydrogen bonds. Overall, **P1** exhibited a remarkable right-handed (*P*)-β-double helix conformation in single crystals.

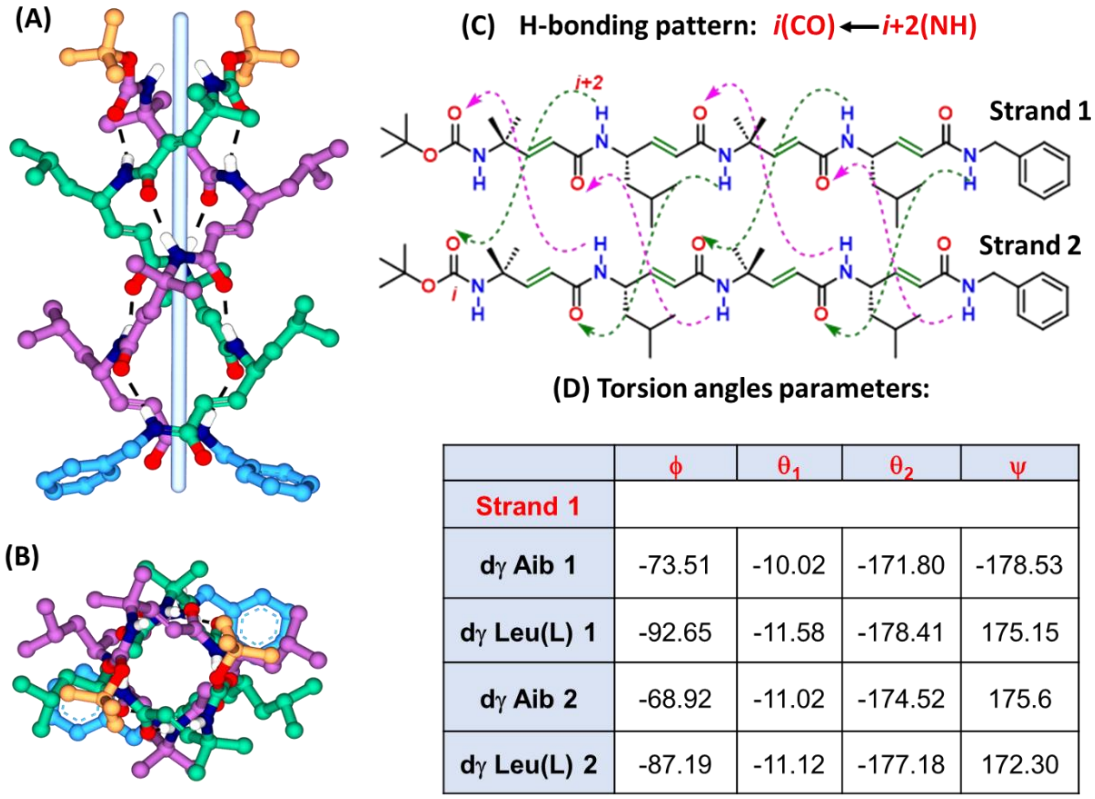
Table 1: Interstrand H-bond parameters of **P1**

Donor (D)	Acceptor (A)	D…..A (Å)	DH….A (Å)	∢NH….O (°)
N7	O2	2.964	2.172	153.19
N8	O3	2.843	1.996	171.31
N9	O4	2.826	1.969	174.12
N10	O5	2.820	1.990	161.69
N2	O8	2.843	2.036	155.85
N3	O9	2.846	2.000	167.25
N4	O10	3.007	2.185	159.87
N5	O11	2.792	1.942	168.93

Furthermore, we measured the torsion angles of α, β-unsaturated γ-amino acids using the torsion variables as depicted in Scheme 1. The torsion angle analysis revealed that achiral α,β-unsaturated 4,4-dimethyl γ-amino acids displayed average ϕ, θ_1, θ_2 and ψ angles of -70.51°±9°, -12.80°±9°, ±172°±2° and ±175.47°±5°, respectively. The torsion angle θ_1 displayed a value close to 0° whereas, θ_2 and ψ displayed values close to 180°. The first three torsion variables displayed negative signs, whereas ψ displayed a positive sign, with the exception of the terminal residue in one of the strands. The values displayed by the achiral residues are consistent with previously observed β-double helix structures. The average torsion angles of the chiral amino acids ϕ, θ_1, θ_2 and ψ were found to be -90.56°±8°, -5.76°±8°, ±176.94°±5° and ±172.74°, respectively. The sign is consistent in the torsion variables ϕ and θ_1, but not consistent in the fully extended θ_2 and ψ. In order to investigate whether D-amino acids can be used to design a β-double helix with opposite chirality, we synthesized peptide **P2**. However, we did not obtain good-quality crystals of **P2**.

2.3.2. Crystal Structures Analysis of P3 and P4

To explore whether other chiral α,β-unsaturated γ-amino acids can be employed in the design of chiral β-double helices, we synthesized peptides **P3** and **P4**. The chiral unsaturated amino acids in **P3** and **P4** were derived from L- and D-leucine, respectively. Both peptides were subjected to crystallization in various solvent combinations to understand their solid-state conformations. The single crystal of **P3** was obtained from its solution in chloroform and xylene and the structure is shown in Figure 2A.



	ϕ	θ_1	θ_2	ψ
Strand 1				
dγ Aib 1	-73.51	-10.02	-171.80	-178.53
dγ Leu(L) 1	-92.65	-11.58	-178.41	175.15
dγ Aib 2	-68.92	-11.02	-174.52	175.6
dγ Leu(L) 2	-87.19	-11.12	-177.18	172.30

Figure 2: (A) Single crystal structure of **P3.** An imaginary rod is inserted along the crystal axis for a better view of the double-helical structure. (B) Top view of the **P3.** (C) Hydrogen bonding pattern observed in **P3.** (D) Torsion angle parameters of **P3**.

One molecule of **P3** was found in the asymmetric unit along with three water molecules. The peptide adopted a right-handed helix-type conformation without any intramolecular hydrogen bonds. All amide NH and carbonyl groups were exposed for intermolecular hydrogen bonds. In sharp contrast to β-sheet structures, the peptide self-assembled with another molecule by involving all amide NH groups and CO groups for intermolecular hydrogen bonds, except Boc-NH and C-

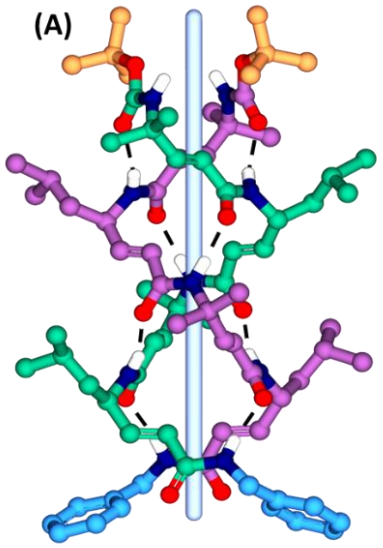
terminal CO groups. Two molecules of **P3** intertwined through hydrogen bonds between amide NH (i+2) groups in one strand and the CO (i) of the other strand, adopting a right-handed β-double helix structure. The double helix structure was stabilized by eight intermolecular hydrogen bonds. The N-terminal two Boc amide NH groups were involved in the intermolecular hydrogen bonds with the exposed C-terminal amide CO groups of the other double helix, leading to a continuous assembly of double helices. The hydrogen bonding parameters observed in **P3** are tabulated in Table 2.

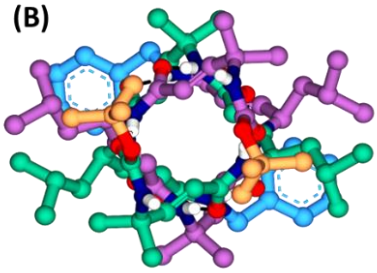
Table 2: Interstrand H-bond parameters of **P3**

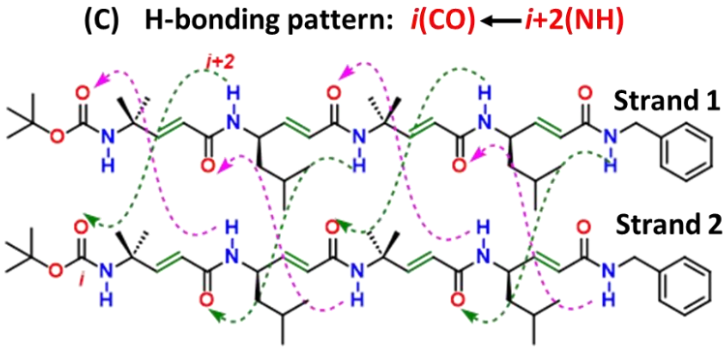
Donor (D)	Acceptor (A)	D.....A (Å)	DH....A (Å)	∡NH....O (deg)
N2 (strand 1)	O2 (strand 2)	2.840	2.053	148.43
N3 (strand 1)	O3 (strand 2)	2.810	1.943	168.42
N4 (strand 1)	O4 (strand 2)	2.838	1.998	159.55
N5 (strand 1)	O5 (strand 2)	2.884	2.032	163.12
N2 (strand 2)	O2 (strand 1)	2.840	2.053	148.43
N3 (strand 2)	O3 (strand 1)	2.810	1.943	168.42
N4 (strand 2)	O4 (strand 1)	2.838	1.998	159.55
N5 (strand 2)	O5 (strand 1)	2.884	2.032	163.12

The torsion angle analysis revealed that the peptide displayed similar torsion angles as observed in **P1**. The average torsion angles ϕ, θ_1, θ_2 and ψ of achiral residues were found to be -71.21°±3°, -10.5°±1°, -173.16°±2° and ±177.06°±1°, respectively. For the chiral amino acids, the average torsion angles were found to be -89.92°±3°, -11.35°±0.4°, -177.79°±1° and +173.72°±2°, respectively. **P3** adopted parallel double helix conformations in single crystals.

The single crystals of **P4** were obtained from its solution in DCM and xylene. The X-ray diffracted single crystal structure of the peptide is shown in Figure 3A. In the asymmetric unit, one molecule of **P4** and a water molecule were found. The peptide adopted a left-handed helical conformation without any intramolecular hydrogen bonds.







(D) Torsion angles parameters:

	ϕ	θ_1	θ_2	ψ
Strand 1				
dγ Aib 1	71.38	12.33	170.60	176.42
dγ Leu(D) 1	92.13	7.99	-179.40	-173.94
dγ Aib 2	71.01	11.89	174.77	-178.94
dγ Leu(D) 2	84.73	19.95	174.18	-170.51

Figure 3: (A) Single crystal structure of **P4.** An imaginary rod is inserted along the crystal axis for a better view of the double-helical structure. (B) Top view of the **P4.** (C) Hydrogen bonding pattern observed in **P4.** (D) Torsion angle parameters of **P4**.

All amide (NH) and carbonyl (CO) groups of **P4** were exposed for intermolecular hydrogen bonds. Two molecules of **P4** intertwined to form a left-handed parallel β-double helix structure. This entwined structure was stabilized by eight intermolecular hydrogen bonds between the CO (*i*) in one strand and NH of (*i*+2) residue in the other strand, except for the N-terminal Boc-NH and the C-terminal amide CO group. The two exposed Boc-NH groups in the double helix interacted with the C-terminal carbonyl groups of the other double helix structures, facilitating the self-assembly of β-double helical structures in single crystals. The hydrogen bonding parameters observed in **P4** are tabulated in Table 3. As a left-handed β-double helix, **P4** exhibited the opposite sign in ϕ and θ_1 torsion angles. The average torsion angles for achiral residues were found to be +71.2°±0.2°, +12.06°±0.17°, ±172.68°±2° and ±177.68°±1°. For the chiral amino acids, the average torsion

angles were found to be +88.43°±4°, +13.97°±6°, ±172.68°±1° and ±176.72°±2°, respectively, for ϕ, θ_1, θ_2 and ψ.

Table 3: Interstrand H-bond parameters of **P4**

Donor (D)	Acceptor (A)	D.....A (Å)	DH....A (Å)	∡NH....O (deg)
N1 (strand 1)	O2 (strand 2)	2.846	1.979	168.49
N2 (strand 1)	O3 (strand 2)	2.833	1.982	162.11
N3 (strand 1)	O4 (strand 2)	2.799	1.920	175.87
N4 (strand 1)	O5 (strand 2)	2.853	2.043	152.77
N1 (strand 2)	O2 (strand 1)	2.846	1.979	168.49
N2 (strand 2)	O3 (strand 1)	2.833	1.982	162.11
N3 (strand 2)	O4 (strand 1)	2.799	1.920	175.87
N4 (strand 2)	O5 (strand 1)	2.853	2.043	152.77

Both achiral amino acids also adopted left-handed conformations similar to unsaturated amino acids derived from D-Leu. The achiral amino acid can adopt a right-handed or left-handed conformation depending on the nature of the chiral amino acids.

An In Depth Comparison of the Crystal Structures of Chiral β-Double Helices

In the previous analysis, it was observed that peptides **P1**, **P3**, and **P4** adopt a β-double helical conformation in the solid state. In the asymmetric unit, two molecules of **P1** intertwine with each other, while **P3** and **P4** exhibit a single-strand arrangement. Overall, these peptides form a β-double helix stabilized by eight interstrand hydrogen bonds between the amide carbonyl (CO) of residue (*i*) in strand 1 and the amide NH residue (*i*+2) in strand 2. Notably, the Boc-amide NH and C-terminal CO groups do not participate in hydrogen bonding; instead, they form hydrogen bonds with other double helices, contributing to a continuous hydrogen-bonded assembly.

Torsion angle analysis revealed specific patterns for achiral α,β-unsaturated 4,4-dimethyl γ-amino acids and chiral amino acids in **P1**, **P3**, and **P4**. The torsion angle analysis revealed that achiral α,β-unsaturated 4,4-dimethyl γ-amino acids displayed average ϕ, θ_1, θ_2 and ψ angles of -70.51°±9°, -12.80°±9°, ±172°±2° and ±175.47°±5°, respectively for **P1**, -71.21°±3°, -10.5°±1°, -173.16°±2°

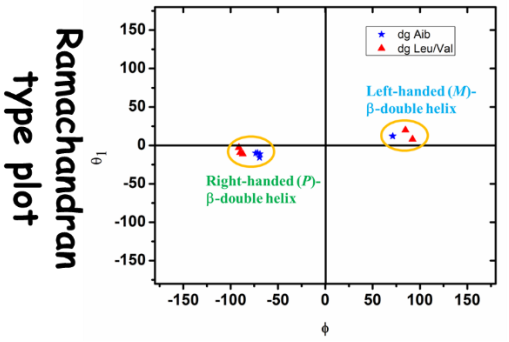
and ±177.06°±1°, respectively for **P3**, and +71.2°±0.2°, +12.06°±0.17°, ±172.68°±2° and ±177.68°±1° respectively for **P4**. . The average torsion angles of the chiral amino acids ϕ, θ1, θ2 and ψ were found to be -90.56°±8°, -5.76°±8°, ±176.94°±5° and ±172.74°, respectively for **P1**, -89.92°±3°, -11.35°±0.4°, -177.79°±1° and +173.72°±2°, respectively for **P3**, and +71.2°±0.2°, +12.06°±0.17°, ±172.68°±2° and ±177.68°±1° respectively for **P4**.

In our study, the torsion angles ϕ and θ_1 emerge as pivotal factors influencing double helix formation. We prioritize examining the sign and magnitude of these angles. Analysis of the average torsion angle data indicates that ϕ tends to be negative for L-isomers and positive for D-isomers. While achiral α,β-unsaturated 4,4-dimethyl γ-amino acids can exhibit both positive and negative torsional angles, the presence of chiral amino acids results in a specific torsion angle sign for these compounds. Across all cases, θ_1 values tend to hover near zero.

Peptide P1	ϕ	θ_1	θ_2	ψ
Strand 1				
dγ Aib 1	-70.71	-6.91	-171.33	173.71
dγ Val 1 (L)	-97.25	-5.36	179.31	-174.54
dγ Aib 2	-61.97	-21.34	-171.38	172.85
dγ Val 2 (L)	-96.07	1.84	174.41	-176.36
Strand 2				
dγ Aib 1	-72.25	-12.69	-173.49	-177.44
dγ Val 1 (L)	-82.40	-13.11	-179.68	164.28
dγ Aib 2	-76.84	-10.25	-172.88	177.90
dγ Val 2 (L)	-86.53	-2.74	177.10	175.78

Peptide P3	ϕ	θ_1	θ_2	ψ
Strand 1				
dγ Aib 1	-73.51	-10.02	-171.80	-178.53
dγ Leu1 (L)	-92.65	-11.58	-178.41	175.15
dγ Aib 2	-68.92	-11.02	-174.52	175.6
dγ Leu2 (L)	-87.19	-11.12	-177.18	172.30

Peptide P4	ϕ	θ_1	θ_2	ψ
Strand 1				
dγ Aib 1	71.38	12.23	170.60	176.42
dγ Leu1 (D)	92.13	7.99	-179.40	-173.94
dγ Aib 2	71.01	11.89	174.77	-178.94
dγ Leu2 (D)	84.73	19.95	174.18	-170.51



In summary, L-isomers adopt a right-handed (*P*)-β-double helix conformation in single crystals, while D-isomers form a left-handed (*M*)-β-double helix conformation. A Ramachandran plot was constructed using ϕ vs θ_1 values, where the right-handed (*P*)-β-double helix and left-handed (*M*)-β-double helix occupied mirror-image positions.

2.3.3. Circular Dichroism Analysis of the Peptides P1-P4

Circular dichroism (CD) is an indispensable tool for comprehending the conformation of polypeptides.[11] To understand the solution conformations of peptides, we subjected them to CD

analysis in chloroform, 1,1,2,2-tetrachloroethane, and methanol. Since circular dichroism employs both left- and right-circularly polarized light, we examined both left-handed and right-handed β-double helices to grasp their structural characteristics in chloroform. All four peptides exhibited distinct CD signatures. Peptide **P1** and **P3** displayed a small CD minimum at 226 nm and a large CD maximum at 242 nm, whereas **P2** and **P4** exhibited precisely the opposite spectrum, featuring a small CD maximum at 226 nm and a large CD minimum at 242 nm. Figure 4A illustrates the CD spectra of **P1** and **P2**. Similar spectra were observed for P3 and P4 in chloroform (Figure 4B).

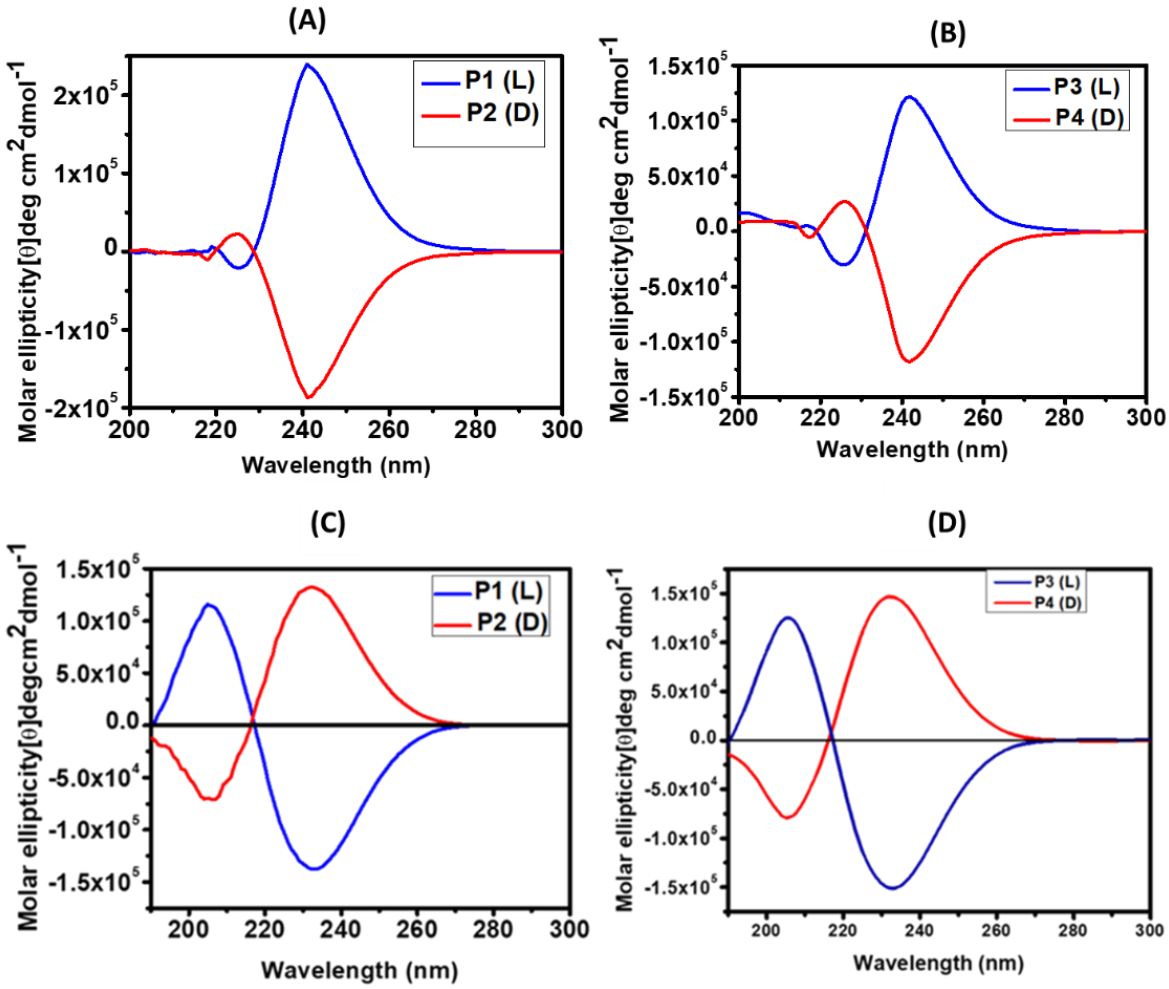


Figure 4: (A) CD spectra of **P1** and **P2** in chloroform. (B) CD spectra of **P3** and **P4** in chloroform. (C) CD spectra of **P1** and **P2** in methanol. (D) CD spectra of **P3** and **P4** in methanol

Interestingly, both **P1** and **P2** displayed different CD spectra in methanol compared to chloroform. The mirror-image spectra observed in methanol are shown in Figure 4C. **P1** exhibited a CD

maximum at 205 nm and a minimum at 238 nm, whereas **P2** displayed a CD minimum at 205 nm and a maximum at 238 nm. Similar spectra were observed for **P3** and **P4** in methanol (Figure 4D). Interestingly, we observed temperature-dependent changes in the intensities of CD maxima and minima for **P1** and **P2**, with no alterations observed in the CD spectra of **P1** and **P2** in methanol across different temperatures (see Figure 5).

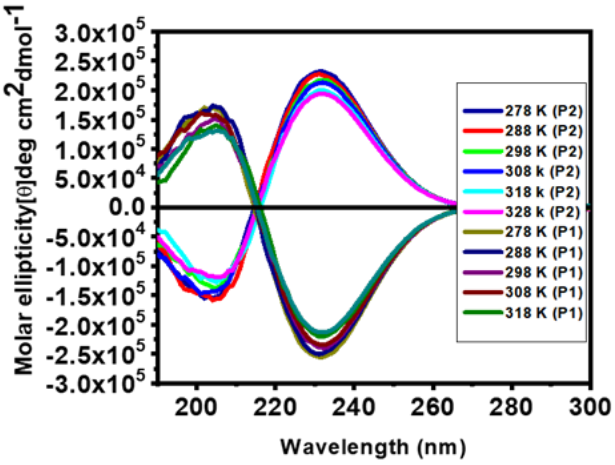


Figure 5: Temperature-dependent CD spectra for peptides **P1** and **P2** in methanol.

We further recorded the CD spectra of **P1**-**P4** in 1,1,2,2-tetrachloroethane to elucidate their structural properties. All peptides displayed similar spectra to those observed in chloroform. Additionally, all peptides exhibited temperature-dependent CD spectra. The temperature-dependent CD spectra of **P1** and **P2** are depicted in Figure 6A.

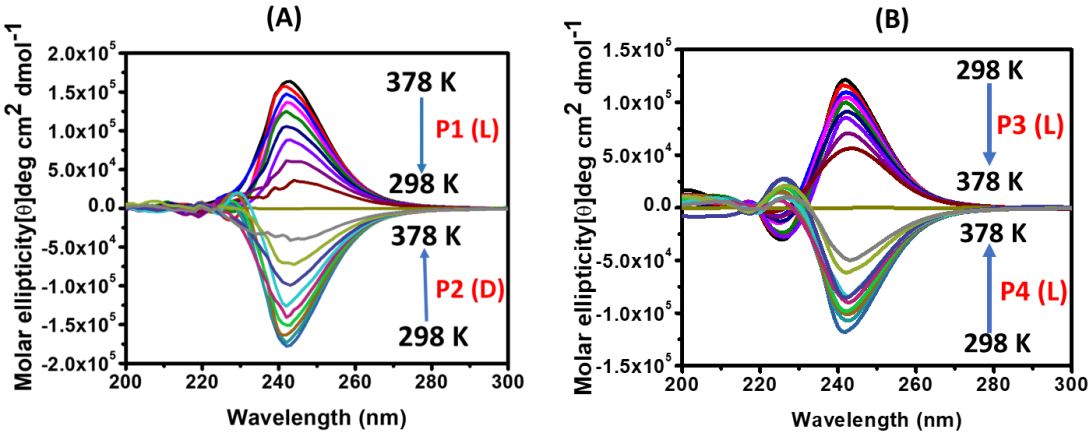


Figure 6: (A) Temperature-dependent CD spectra of **P1** and **P2** in 1,1,2,2-tetrachloroethane. (B) Temperature-dependent CD spectra of **P3** and **P4** in 1,1,2,2-tetrachloroethane.

The intensity of CD maxima for **P1** decreased with increasing temperature from 298 K to 378 K and similarly, the intensity of CD minima for **P2** decreased with higher temperatures. The temperature-dependent CD analysis suggested that peptides partly adopted double helix conformations even at 378 K. The temperature-dependent CD spectra of **P3** and **P4** also showed similar observations and are depicted in Figure 6B. The melting temperatures were found to be 73±1.6 °C, 71±1.47 °C, 70±1.98 °C, and 68±1.95 °C, respectively, for **P1**, **P2**, **P3**, and **P4**. All four peptides showed similar melting temperatures. The melting temperature plot is shown in Figures 7A, 7B, 7C and 7D for **P1**, **P2**, **P3** and **P4** respectively.

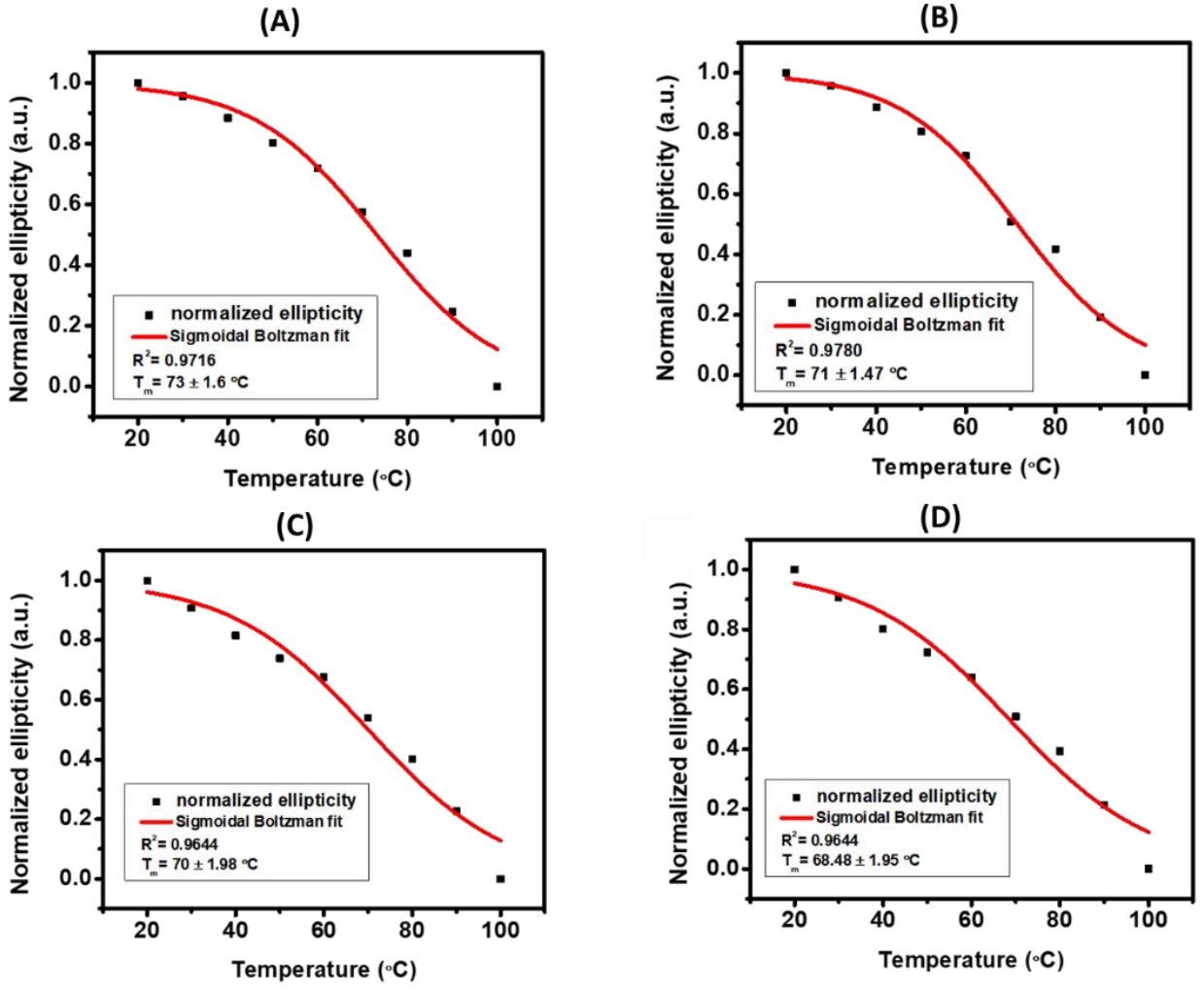


Figure 7: The melting temperature (T_m) plots for the peptides. (A) **P1**. (B) **P2**. (C) **P3**. (D) **P4**. The ellipticity values at 242 nm with different temperatures were normalized and plotted against the respective temperatures. The points are fitted using the sigmoidal-Boltzmann fit.

2.3.4. Temperature-Dependent ^{1}H Experiments of P1-P4

Motivated by the distinctive circular dichroism (CD) signatures observed in aprotic solvents for the peptides, we conducted NMR analysis to gain a more in-depth understanding of their solution conformations. Each of the four peptides displayed well-dispersed ^{1}H NMR spectra in solution. Temperature-dependent ^{1}H NMR analysis of **P1** in $C_2D_2Cl_4$ revealed a gradual upfield shift in chemical shifts for all amide NH groups with increasing temperature from 298 K to 378 K, except for the Boc amide NH, which showed minimal change in chemical shift values. Similar trends were observed for the other peptides, suggesting that all amide NH groups are involved in intermolecular, possibly inter-strand hydrogen bonds. The reverse trend was observed when decreasing the temperature from 378 K to 298 K, with a downfield shift of amide NH chemical shifts. The chemical shift values of each temperature vs temperature plot for both increasing and decreasing temperature are given in Figures 8A and 8B for **P1** and Figures 10A and 10B for **P3**. The plot shows that while increasing or decreasing the temperature the chemical shift values at a particular temperature attain almost similar values. This in way also describes the reversibility of our double-helices with respect to temperature. We observed similar phenomena in the case of Peptide **P2** and **P4**. Consistent with observations in single crystals, the Boc-NH was not involved in inter-strand intermolecular hydrogen bonds. All the Temperature-dependent NMR spectra for peptides **P1-P4** are given below.

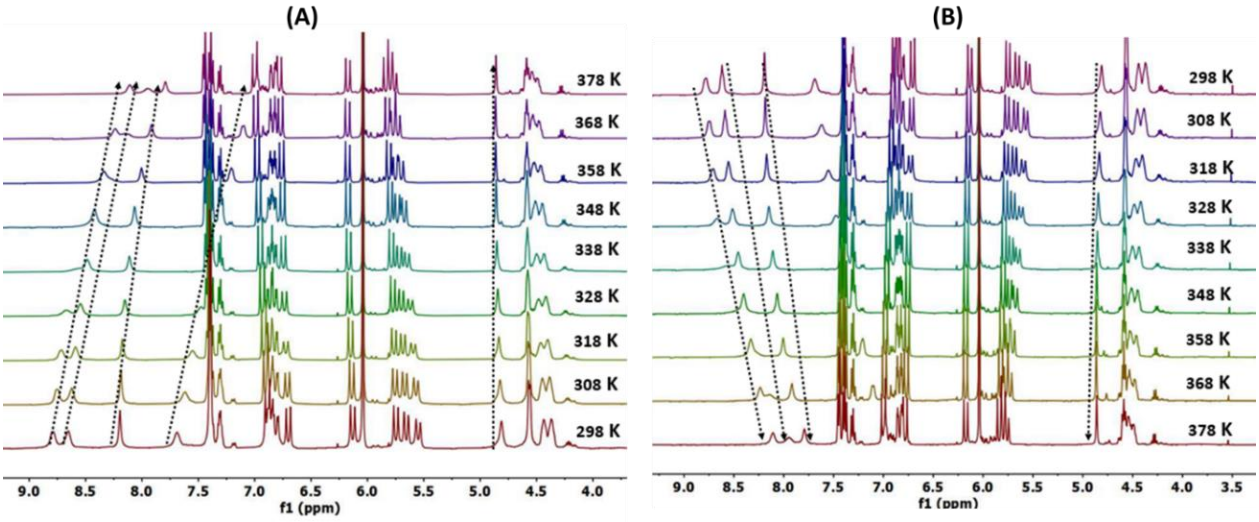


Figure 8: Partial ^{1}H NMR spectra of peptide **P1** in $C_2D_2Cl_4$ at different (A) increasing temperatures and (B) decreasing temperatures.

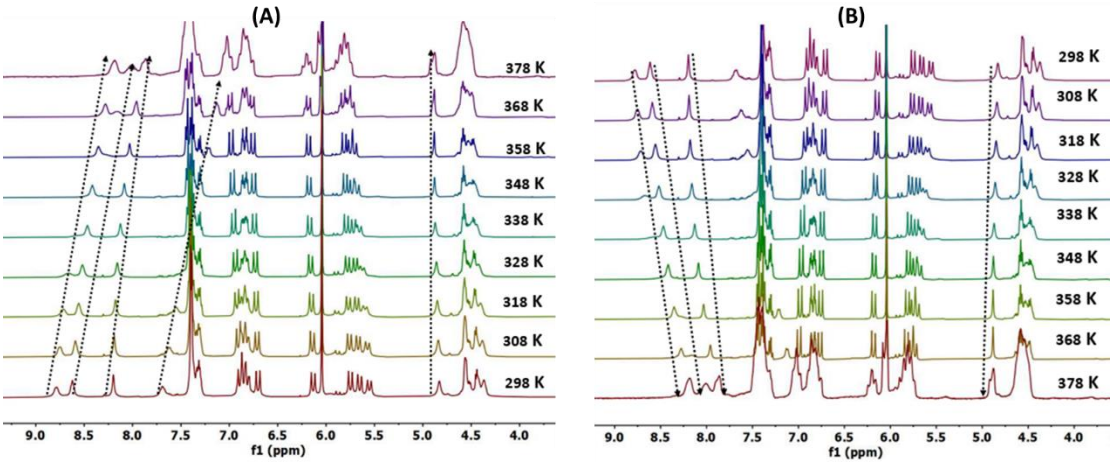


Figure 9: Partial ^{1}H NMR spectra of peptide **P2** in $C_2D_2Cl_4$ at different (A) increasing temperatures and (B) decreasing temperature

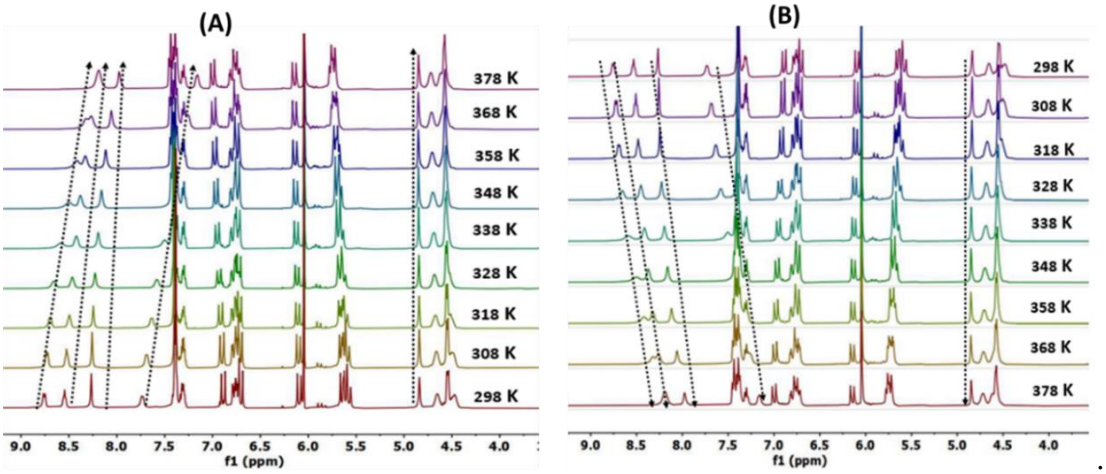


Figure 10: Partial ^{1}H NMR spectra of peptide **P3** in $C_2D_2Cl_4$ at different (A) increasing temperatures and (B) decreasing temperature

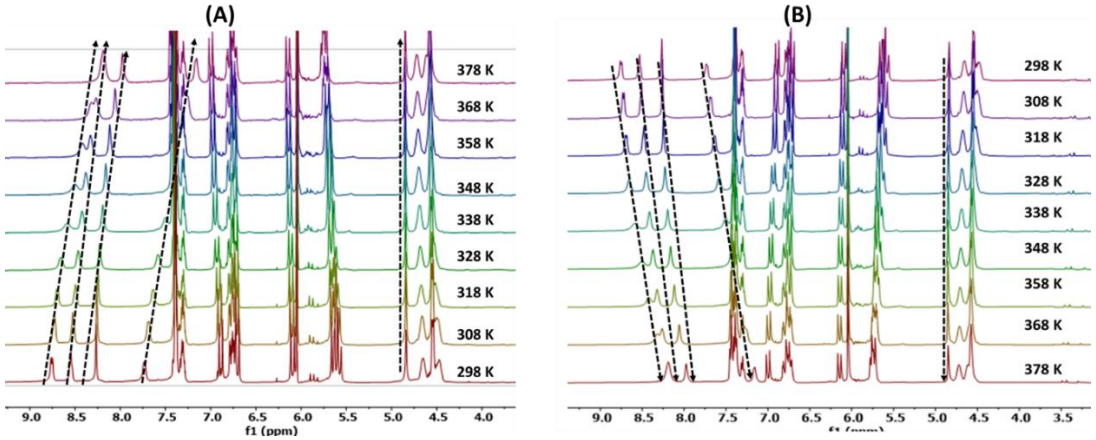


Figure 11: Partial ^{1}H NMR spectra of peptide **P4** in $C_2D_2Cl_4$ at different (A) increasing temperatures and (B) decreasing temperature

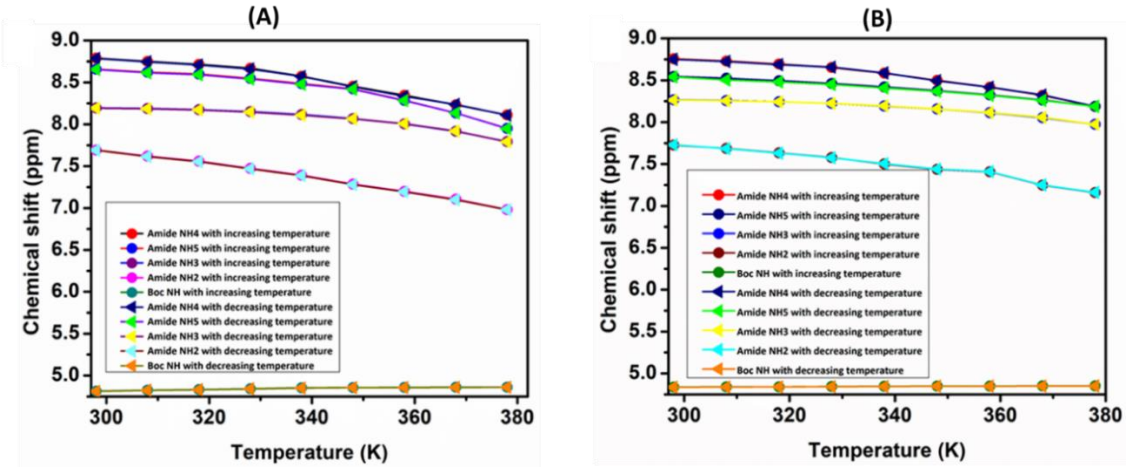


Figure 12: chemical shifts of NHs vs temperature with increasing and decreasing temperature plotted together for (A) **P1** and (B) **P3.**

Table 4: Chemical shifts (in ppm) of amide NHs of peptide **P1**

Temp. (K)	NH 4	NH 5	NH 3	NH2	Boc-NH
298	8.713	8.499	8.221	7.683	4.792
308	8.687	8.476	8.212	7.639	4.793
318	8.652	8.45	8.201	7.591	4.797
328	8.612	8.42	8.183	7.54	4.8
338	8.54	8.376	8.149	7.456	4.803
348	8.455	8.335	8.114	7.28	4.805
358	8.368	8.283	8.072	7.204	4.806
368	8.277	8.219	8.01	7.204	4.805
378	8.139	8.139	7.929	7.119	4.805
dδ/dT (ppb K^{-1})	**-7 (±0.6)**	**-6.1 (±0.46)**	**-4.51 (±0.09)**	**-7.2 (±0.04)**	**0.18 (±0.27)**

Table 5: Chemical shifts (in ppm) of amide NHs of peptide **P3**

Temp. (K)	NH 4	NH 5	NH 3	NH2	Boc-NH
298	8.79	8.658	8.196	7.691	4.814
308	8.749	8.621	8.189	7.618	4.826
318	8.716	8.598	8.174	7.559	4.833
328	8.668	8.548	8.151	7.472	4.842
338	8.574	8.485	8.115	7.391	4.853
348	8.452	8.422	8.068	7.285	4.857
358	8.346	8.285	8.005	7.199	4.859
368	8.233	8.134	7.916	7.106	4.86
378	8.111	7.952	7.793	6.981	4.861
dδ/dT (ppb K^{-1})	**-8.7 (±0.69)**	**-8.39 (±0.46)**	**-5.12 (±0.66)**	**-8.81 (±0.28)**	**0.59 (±0.07)**

2.3.5. DMSO-d_6 Titration of Peptides P1, P2, P3 & P4

To confirm whether all NH groups were involved in inter-strand hydrogen bonds, we conducted DMSO-d_6 titration experiments. The titration experiments indicated that, with the exception of the N-terminal Boc amide NH, negligible changes in the chemical shift positions were observed for the other amide NH protons in peptides **P1**-**P4** as the concentration of DMSO-d_6 increased. These findings strongly suggest the involvement of backbone amide NH and CO groups in intermolecular hydrogen bonding between peptide strands within the double helix. However, a notable downfield shift was observed for Boc-NH as the concentration of DMSO-d_6 increased, indicating the exposure of N-terminal NH protons in all peptides to the solvent for hydrogen bonding. The DMSO-d_6 titration results for all peptides are provided in below Figure 13 and Figure 14.

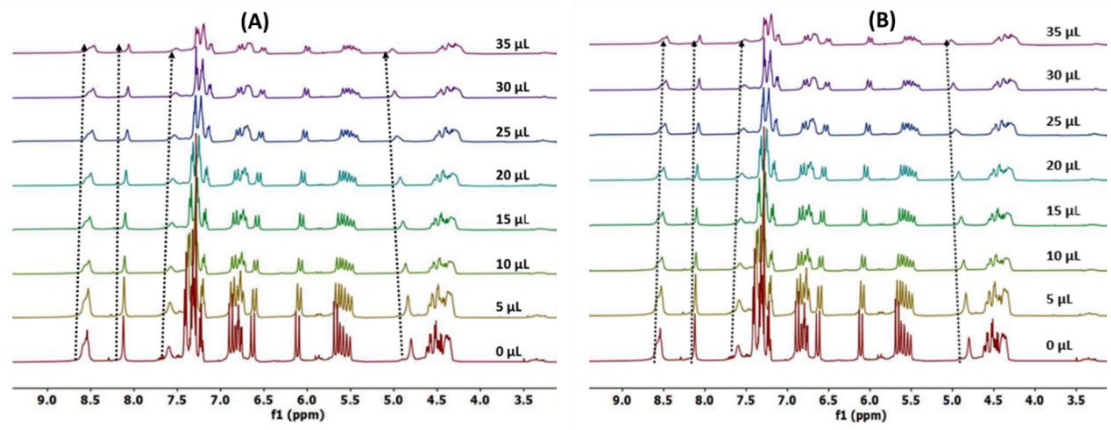


Figure 13: Solvent dependence of NH chemical shifts of the peptides (A) **P1** and (B) **P2** at varying concentrations of DMSO-d_6

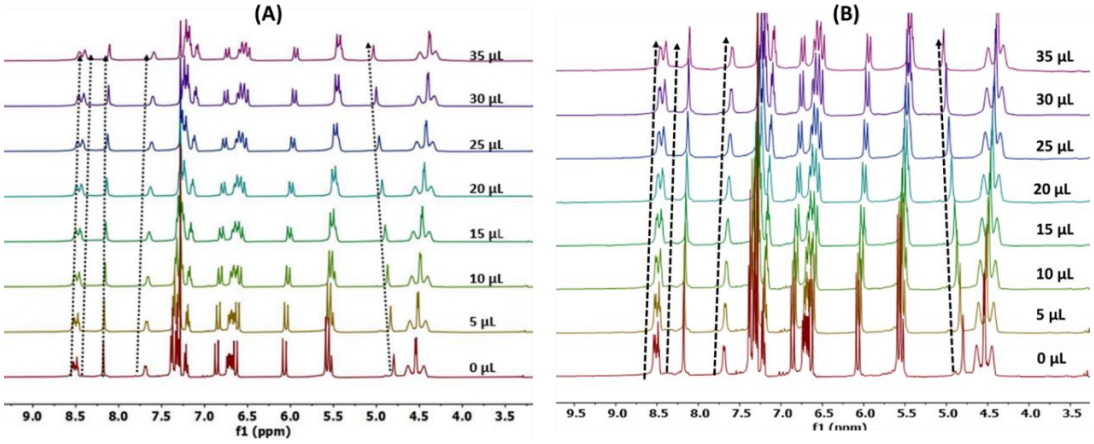
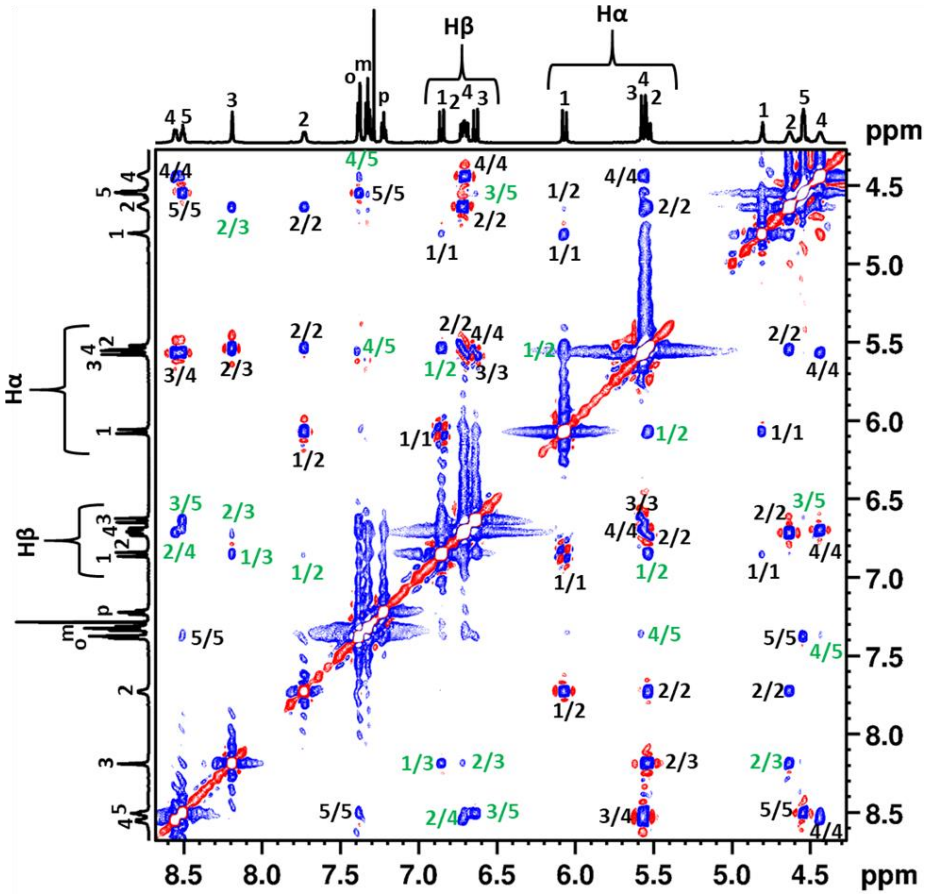


Figure 14: Solvent dependence of NH chemical shifts of the peptides (A) **P3** and (B) **P4** at varying concentrations of DMSO-d_6

2.3.6. 2D-NMR Analysis of Peptide P4

Given that all peptides yielded similar results in temperature-dependent NMR and DMSO-d_6 titration experiments, we selected peptide **P4** for 2D NMR analysis in $CDCl_3$ to delve deeper into its solution conformation. The positions of all amino acids in the sequence were confirmed by TOCSY and ROSEY spectroscopy. Figure 15 shows the partial ROSEY spectra of peptide **P4**. We observed very strong NOEs between Boc CH_3 and 1NH, medium NOEs between residues, 1C$^{\beta}$H and 2C$^{\alpha}$H, 2C$^{\gamma}$H and 3NH, 1C$^{\beta}$H and 3NH, 1C$^{\alpha}$H and 2C$^{\alpha}$H, 2C$^{\beta}$H and 4NH, and 3C$^{\beta}$H and NH benzylamine. Additionally, we noted weak NOEs between 1C$^{\beta}$H and 2NH, and 2C$^{\beta}$H and 3NH. In addition to these crucial NOEs, we observed various other intermolecular and intramolecular NOEs, all of which are tabulated in Tables 6 and 7.



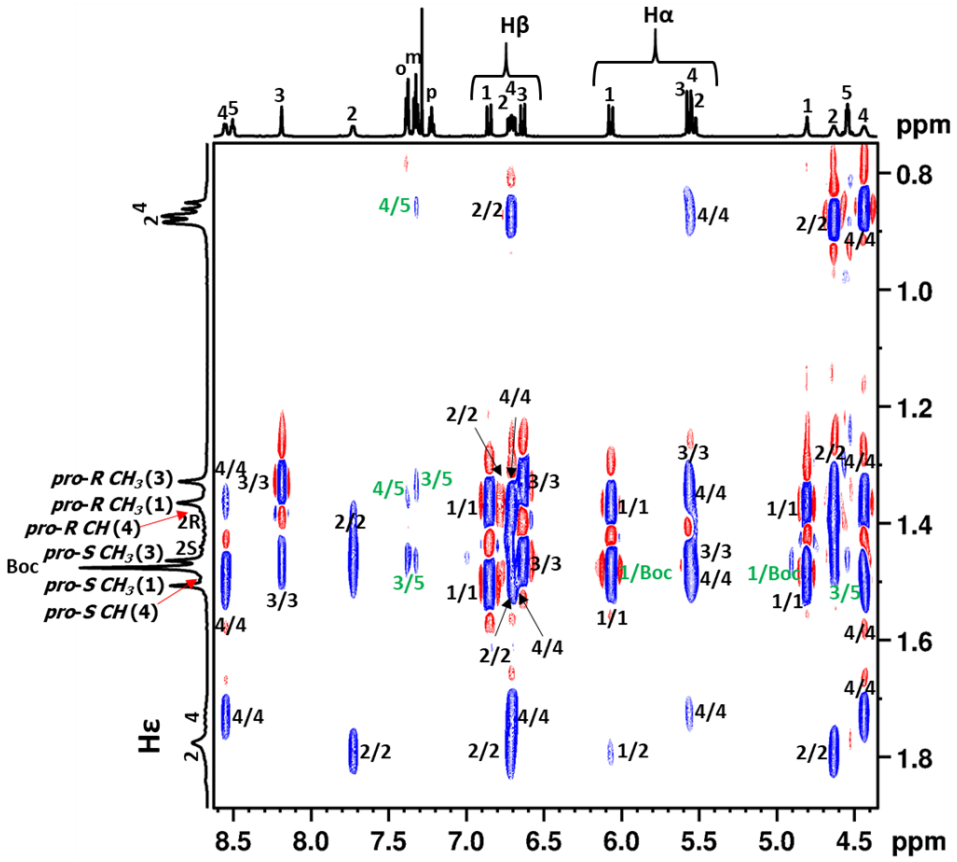


Figure 15: Partial ROSEY spectra of **P4**

Table 6: Intra-molecular NOEs used in structure calculation and their classification

H^{γ}/H^{β} (2/2), H^{α}/NH (2/3), H^{γ}/H^{β} (4/4), NH/CH_3(pro-R) (1/1), NH/CH_3 (pro-R) (3/3), H^{γ}/H^{δ}(pro-R) (4/4), H^{α}/NH (1/2), CH_3(pro-S)/H^{β} (1/1), H^{α}/NH (3/4)	Very Strong
H^{δ}(pro-R)/H^{β} (4/4), NH/H^{γ} (4/4), H^{δ}(pro-R)/H^{β} (2/2), CH_3 (pro-S)/H^{α} (3/3), NH/H^{δ}(pro-S) (2/2), NH/H^{α} (2/2), H^{γ}/H^{δ}(pro-S) (4/4), CH_3 (pro-R)/H^{β} (3/3), CH_3 (pro-S)/H^{β} (3/3), CH_3(pro-R)/H^{α} (1/1), NH/H^{δ}(pro-S) (4/4), $H^{\varepsilon}/H^{\beta}$ (4/4), CH_3(pro-R)/H^{β} (1/1)	Strong
CH_3 (pro-R)/H^{α} (3/3), NH/H^{γ} (2/2), $H^{\gamma}/H^{\varepsilon}$ (4/4), NH/H^{α} (1/1), NH/CH_3 (pro-S) (3/3), H^{δ}(pro-S)/H^{β} (2/2), H^{γ}/H^{α} (2/2), H^{δ}(pro-S)/H^{α} (4/4), $H^{\gamma}/H^{\varepsilon}$ (2/2), NH/H(o) (5/5), NH/H^{ε} (2/2), H^{δ}(pro-S)/H^{β} (4/4), H^{γ}/Hα (4/4), NH/H^{ε} (4/4)	Medium
$H^{\alpha}/H^{\varepsilon}$ (1/2), H^{δ}(pro-R)/H^{α} (4/4), $H^{\varepsilon}/H^{\alpha}$ (4/4), $H^{\varepsilon}/H^{\beta}$ (2/2), NH/H^{δ}(pro-R) (4/4), NH/H^{δ}(pro-R) (2/2), NH/H^{β} (1/1), CH_3(pro-S)/H^{α} (1/1), H^{α}/H^{γ} (1/2)	Weak

Table 7: Inter-molecular NOEs used in structure calculation and their classification

Boc/NH (0/1), Boc/H^{α} (0/1)	Very Strong
H^{β}/H^{α} (1/2), H^{β}/NH (2/4), H^{γ}/NH (2/3), H^{β}/NH (1/3), H^{α}/H^{α} (1/2), H^{β}/NH (3/5)	Medium
H^{γ}/H(o) (4/5), H^{β}/NH (1/2), H^{α}/H(o) (4/5), H^{β}/NH (2/3), H^{δ}(pro-R)/H(o) (4/5), CH_3 (pro-S)/H(m) (3/5), CH_3 (pro-R)/H(m) (3/5), CH_3 (pro-S)/H(o) (3/5)	Weak

We used all the NOEs to construct the solution conformation of peptide **P4** using the Desmond software, as reported earlier.[12] The twenty lowest energy conformations of **P4** are depicted in Figure 16A. The peptide adopted a β-double helix conformation in solution, similar to the structure observed in the single crystals. The overlay of the solution structure and the crystal structure is shown in Figure 16B. We did not observe any intermolecular NOEs in the CD_3OH solution, suggesting that the peptide did not adopt a β-double helix structure in protic solvents. These results are consistent with the achiral β-double helices reported earlier.

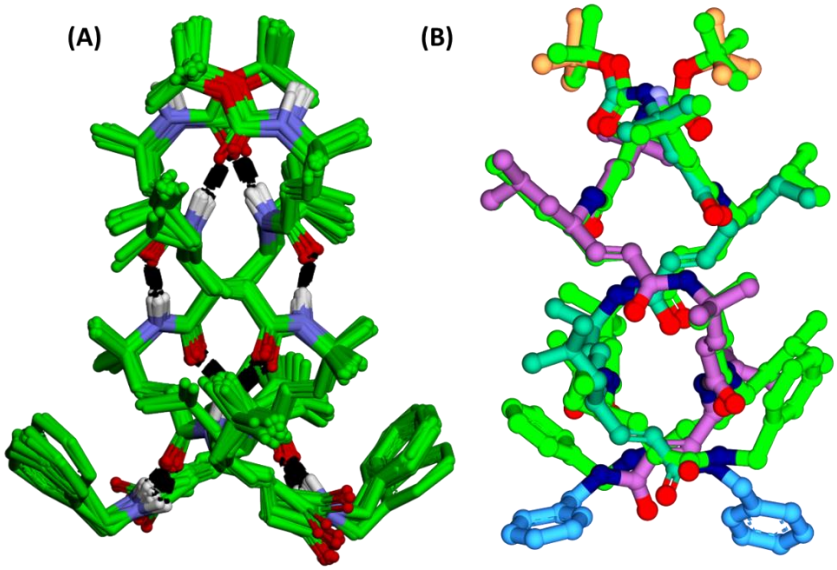


Figure 16: (A) Twenty low-energy structures of **P4** derived from 2D-NMR structure calculations. (B) Superposition of crystal structure and solution structure of **P4**.

2.3.7. Structural Analogy with Other Synthetic and Natural Peptide β-Double Helices

As peptides **P1**-**P4** displayed remarkable chiral β-double helical structures, we aimed to examine their structural similarities with other synthetic and naturally occurring peptide β-double helices.

Recently, we demonstrated that the presence of 4,4-dialkyl substitution in α,β-unsaturated γ-amino acids is crucial for adopting β-double helix conformations. Without this substitution, the oligomers tend to adopt a β-sheet conformation.[13] In the β-double helices derived from the α,β-unsaturated γ-amino acids, both the torsion variables θ_2 and ψ showed values close to ±180° due to the presence of the C=C bond and the *s-cis* conformation of the C-CO bond, respectively. The two torsion variables, ϕ and θ_1, play a crucial role in determining the β-double helix conformation. To understand the similarities between different types of peptide β-double helices, we examined their torsion variables using the reported crystal structures of synthetic double helices, gramicidin A, and feglymycin, along with the γ-peptide β-double helices. The ϕ and ψ/θ_1 values are depicted in Figure 17. Since θ_2 and ψ consistently adopted extended conformations for the γ-peptide β-double helices, we treated them as constants. A clear distinction was observed in the β-double helices derived from alternating L- and D-α-peptides and α,β-unsaturated γ-peptides. The ϕ and ψ angles in the α-peptide β-double helices fall within the left- and right-handed β-sheet regions, whereas ϕ and θ_1 for γ-peptide β-double helices fall within the left- and right-handed helical regions. The studies reported here, suggest that β-double helices derived from the γ-peptides are distinct from those derived from alternating L- and D-α-peptides.

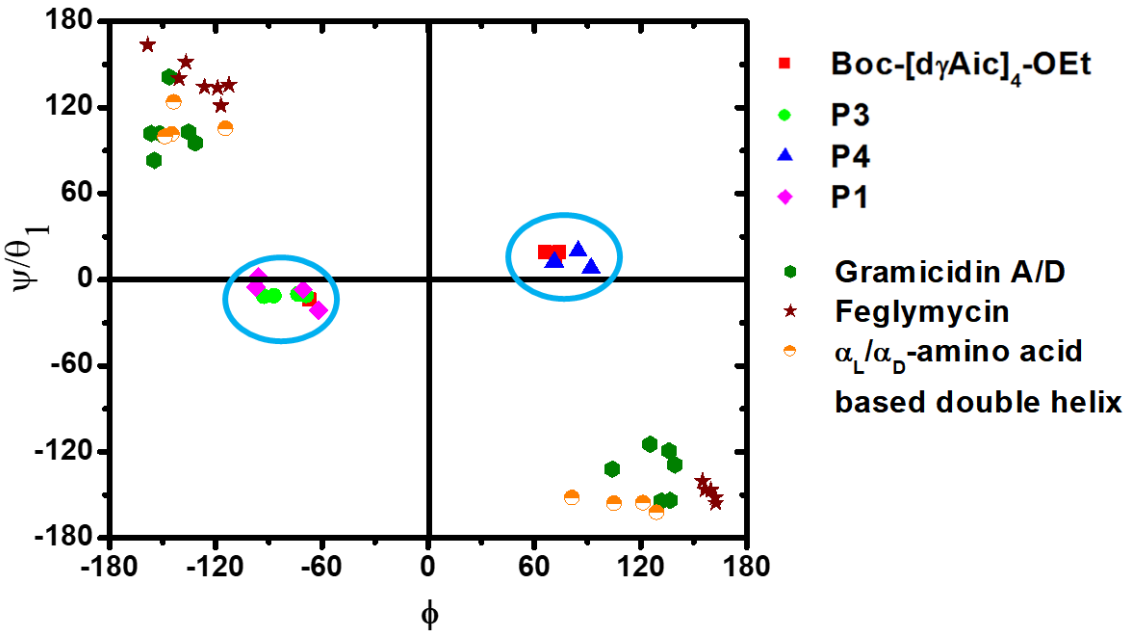


Figure 17: Two-dimensional ϕ and ψ/θ_1 plot of Gramicidin A/D, Feglymycin, L-/D-double helix, and γ-amino acid-based double helices. The plot shows two distinct regions of the double helices.

2.3.8. Transmembrane Ion Channel Activity

Gramicidin A has been extensively utilized as a transmembrane ion channel and its mechanism of ion transportation has been thoroughly investigated.[14] Although peptides **P1**-**P4** are relatively short, we aimed to determine whether they can facilitate ion transport across the membrane. To address this, we created liposomes encapsulating 8-hydroxypyrene-1,3,6-trisulfonic acid (HPTS), following previously established procedures,[15] in a HEPES buffer for the membrane transport assay. The pH gradient was maintained using 0.5 *N* NaOH, and increasing concentrations of individual peptides **P1** and **P3** were introduced to the solution, with fluorescence monitored over time. As peptide concentration increased, a corresponding rise in fluorescence emission was observed (Figure 18). Finally, liposomes were lysed using Triton X-100. Based on the concentration-dependent fluorescence emission, the EC_{50} values were calculated using the Hill equation, yielding values of 0.4 μM and 1.6 μM for **P1** and **P3**, respectively. To investigate whether these peptides act as membrane-disrupting agents instead of ion transporters, we conducted a calcein leakage assay (see in experimental section Figure 23). Interestingly, we observed no fluorescence emission even at high peptide concentrations, strongly suggesting that these peptides function as ion transporters. Given their concise length, it is plausible that these peptides operate primarily as ion transporters rather than membrane channels.

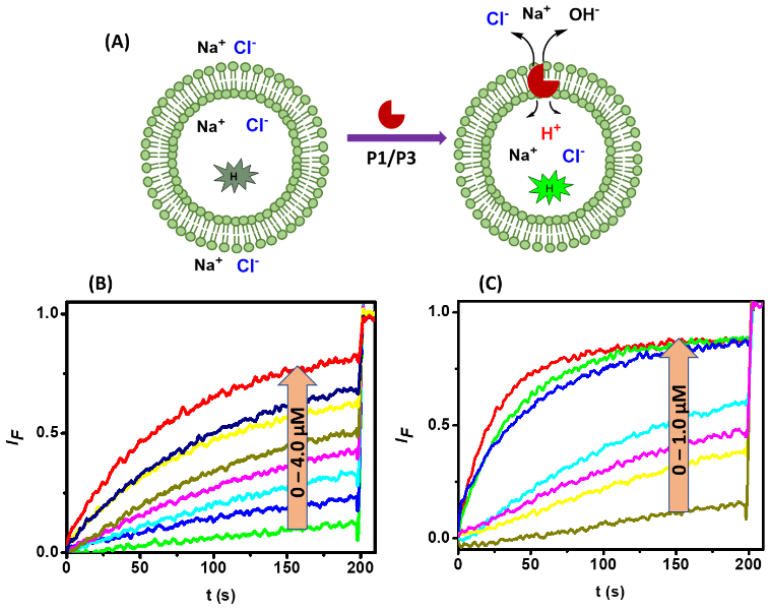


Figure 18. (A) Schematic representation of ion-transport activity of peptides **P1** and **P3**. The Concentration-dependent ion transport activity of (B) Peptide **P1** and (C) Peptide **P3**.

2.4. Conclusion

In summary, we have successfully engineered chiral-double helices, elucidating their conformations in both crystal and solution states. Our findings demonstrate the accommodation of amino acids with proteinogenic side chains alongside 4,4-dialkyl substituted γ-amino acids within the β-double helical structure. We have established the feasibility of designing both left-handed and right-handed double helices. Notably, achiral amino acids exhibited distinct torsion angles contingent upon the chiral nature of the β-double helix. A profound structural disparity was unveiled between β-double helices derived from α,β-unsaturated γ-amino acids and those composed of L- and D-peptides. The torsion angles exhibited by these peptides closely align with helical torsion angles rather than β-sheet structures. Circular dichroism analysis underscored that these short peptides retained their double helical conformations even at elevated temperatures in aprotic solvents. Intriguingly, these peptides, despite their brevity, also functioned as ion transporters within synthetic liposomes. The results presented in this study hold promise for the development of transmembrane ion channels and the creation of self-assembled biomaterials using chiral β-double helices.

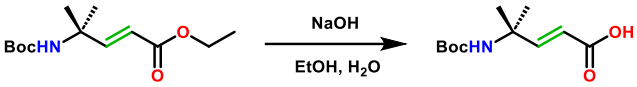
2.5. Experimental Section

2.5.1. Materials and Methods

All reagents and solvents were used without further purification. Column chromatography was performed over silica gel. Final peptides were purified through reverse phase HPLC (C_{18} column, MeOH/H_2O 95:5 as a gradient with flow rate 2.00 mL/min). All the reactions were monitored by analytical thin-layered chromatography. The TLC visualization was done through UV light, $KMNO_4$ stain, and ninhydrin stain. ^1H NMR and ^{13}C NMR were performed through deuterated solvent on 400 MHz and 101 MHz respectively. We used a Matrix Assisted LASER Desorption Ionization mass spectrometer (MALDI-TOF/TOF) to calculate the accurate mass of our peptides. Fluorescence data was measured through the Spectrofluorometer instrument. X-ray crystal structures were determined through APEX(III) DUO X-ray diffractometer using Mo-Kα (λ=0.71073 Å) graphite monochromatic radiation.

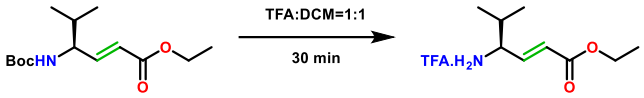
2.5.2. Synthesis of Peptide P1

Ethyl Ester Deprotection of Boc-dγAic-OEt



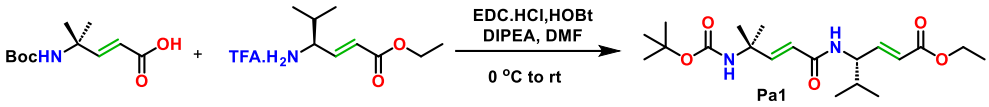
Boc-dγAic-OEt (6.5 mmol, 1.49 g) was dissolved in 50 ml ethanol and 20 mL 1N NaOH was added to the solution dropwise over 3 minutes. The reaction mixture was then allowed to stir for 30 minutes till the completion of hydrolysis. The reaction mixture is then acidified with 1N aqueous HCl solution and then extracted with ethyl acetate. The organic layer was washed with brine solution (3 x 100 mL) and dried over anhydrous Sodium sulfate (Na_2SO_4). The combined organic layer was concentrated under the vacuum and further utilized for coupling.

Boc deprotection of BocHN-(*S*, *E*) $d^{2,3}$γVal(L)-OEt



BocHN-(*S*, *E*) $d^{2,3}$γVal(L)-OEt was treated with a 1:1(v/v) mixture of TFA and DCM. The reaction mixture was then stirred for about 30 minutes at room temperature. After completion of the reaction (monitored by TLC) solution was evaporated under a vacuum and the excess TFA was removed by co-evaporation with DCM thrice under a vacuum. The gummy product H_2N-(*S*, *E*) $d^{2,3}$γVal(L)-OEt was further used for coupling.

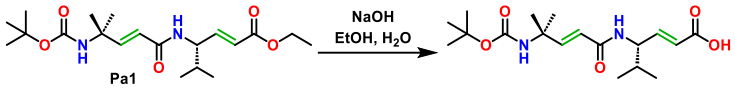
Synthesis of BocHN-dγAic-dγVal(L)-OEt (Pa1)



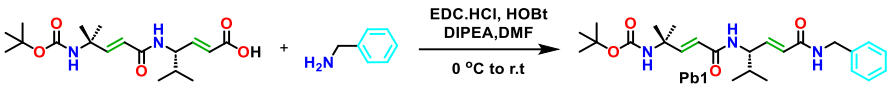
For coupling reaction typically, Boc-dγAic-OH (6.5 mmol, 1.49 g) and TFA·H_2N-(*S*, *E*) $d^{2,3}$γVal(L)-OEt (6.5 mmol, 1.11 g) were dissolved together in DMF (6 mL), followed by EDC.HCl (7.205 mmol, 1.38 g) and HOBt (6.5 mmol, 880 mg) were added. The reaction mixture was allowed to cool at 0 ℃ for 5 min. Then DIPEA (19.65 mmol, 3.52 ml) was added to the reaction mixture in stirring condition and the reaction mixture was allowed to come to room temperature. The progress of the reaction was monitored by TLC. After completion of the reaction (roughly 16 hrs), the reaction mixture was diluted with 250 mL of ethyl acetate and washed with

5% HCl (5 % by vol. in water, 3 × 100 mL), 10 % sodium carbonate solution in water (3 × 100 mL) and followed by brine (3 x 100 mL). The organic layer was dried over Na_2SO_4 and evaporated under reduced pressure. The crude product was purified on silica gel column chromatography using an EtOAc/Hexane solvent system. Overall yield 72% (4.68 mmol, 1.79 g).

Synthesis of BocHN-dγAic-dγVal(L)-NHBn (Pb1)

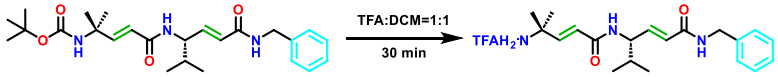


Hydrolysis of **Pa1** was carried out following the previously mentioned procedure above.



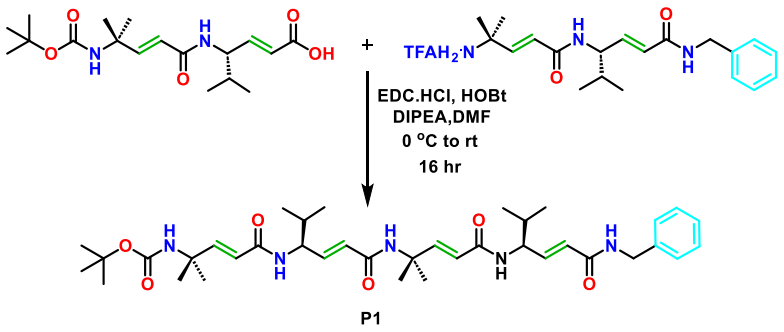
The peptide BocHN-dγAic-dγVal(L)-OH (4 mmol, 1.42 g), EDC.HCl (4.4mmol, 843 mg) and HOBt (4 mmol, 540 mg) were dissolved together in DMF (6 mL). To this solution (12 mmol, 1.5 ml) DIPEA was added. After stirring the reaction mixture for about 5 minutes at ice-cold conditions, benzylamine (9 mmol, 1.0 mL) was added. The reaction mixture was stirred overnight at room temperature. After completion of the reaction (monitored by TLC), the compound was extracted with ethyl acetate followed by successive washings with 10% HCl (3 × 40 mL), 10% (3× 40 mL) and brine solution (3 × 40 mL). The combined organic layer was dried over anhydrous Na_2SO_4 and concentrated under reduced pressure. The crude product was purified on silica gel column chromatography using an EtOAc/Hexane solvent system Overall yield was 68% (2.72 mmol, 1.21 g).

Boc deprotection of peptide Pb1



BocHN-dγAic-dγVal(L)-NHBn (**Pb1**) was treated with 1:1(v/v) mixture of Trifluroacetic acid DCM. The reaction mixture was then stirred for about 30 minutes at room temperature. After completion of the reaction (monitored by TLC) solution was evaporated under vacuum and the excess trifluoroacetic acid was removed by co-evaporation with DCM thrice under vacuum. The gummy product TFA.H_2N dγAic-dγVal(L)-NHBn was further used for coupling.

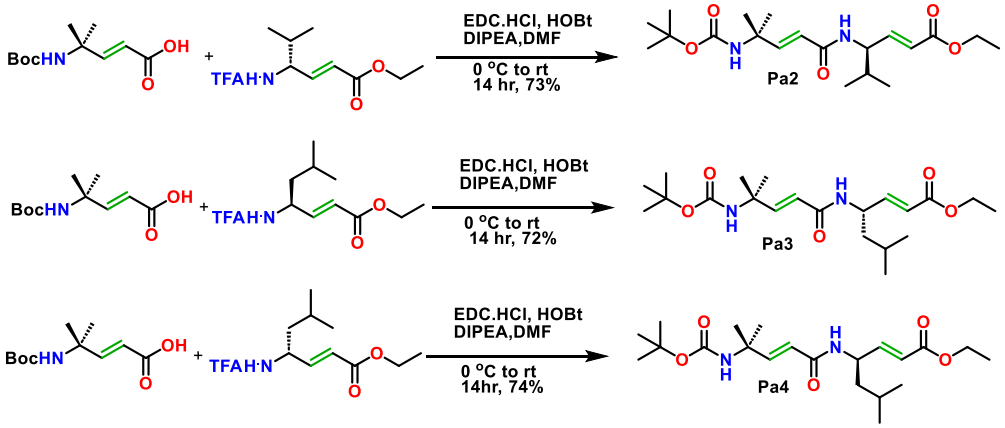
Synthesis of P1



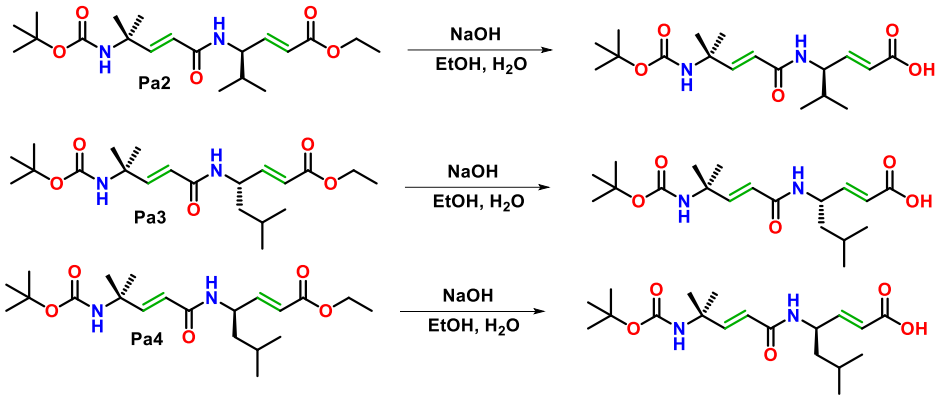
The peptide Boc-dγAic-dγVal(L)-dγAic-dγVal(L)-NHBn (**P1)** was prepared by [2+3] condensation involving *N*-terminal dipeptide acid Boc-dγAic-dγVal(L)-OH. For the coupling reaction, BocHN-dγAic-dγVal(L)-OH (1.0 mmol, 0.35 gm), EDC.HCl (1.1 mmol, 211 mg) and HOBt (1 mmol, 135 mg) were dissolved together in DMF (4 mL). To this solution (4 mmol, 0.7 ml) DIPEA was added. After stirring the reaction mixture for about 5 min at ice-cold conditions, TFA.H_2N dγAic-dγVal(L)-NHBn was added. The reaction mixture was stirred overnight at room temperature. After completion of the reaction (monitored by TLC), the compound was extracted with ethyl acetate followed by successive washings with 10% HCl (3 × 40mL), 10% Na_2CO_3 (3 × 40 mL) and brine solution (3 × 40 mL). The combined organic layer was dried over anhydrous Na_2SO_4 and concentrated under reduced pressure. Final peptide **P1** was purified through reverse phase HPLC (C_{18} column, MeOH/H_2O 95:5 as gradient with flow rate 2.00 mL/min).

2.5.3. Synthesis of Peptides P2, P3 and P4

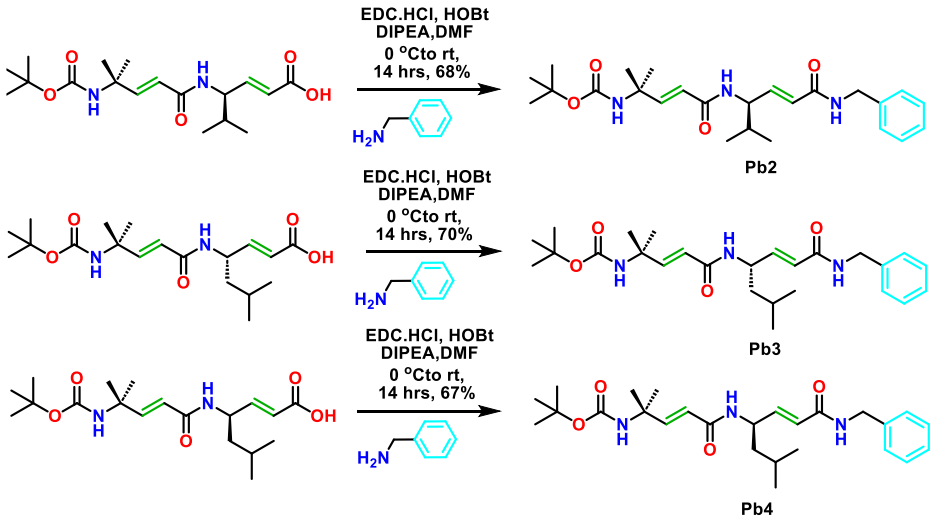
Following the same synthetic protocol for **P1**, we have synthesized **Pa2**, **Pa3,** and **Pa4**. The synthetic scheme is given below.



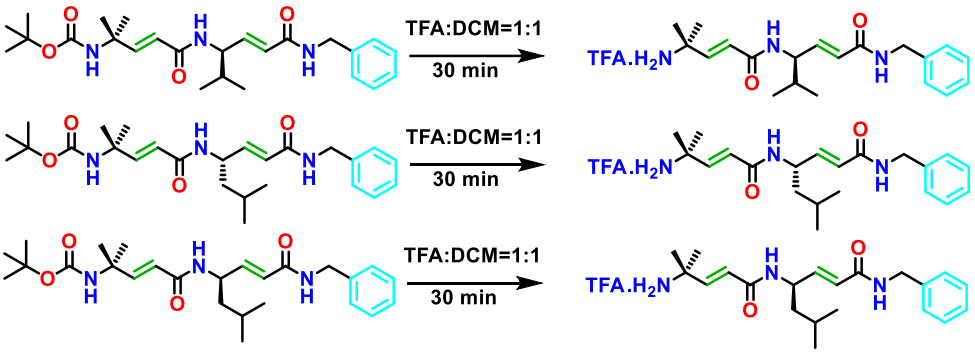
Dipeptide acids of **Pa2**, **Pa3,** and **Pa4** were prepared by following the method described in 5.1.1. The schematic representation is as follows.



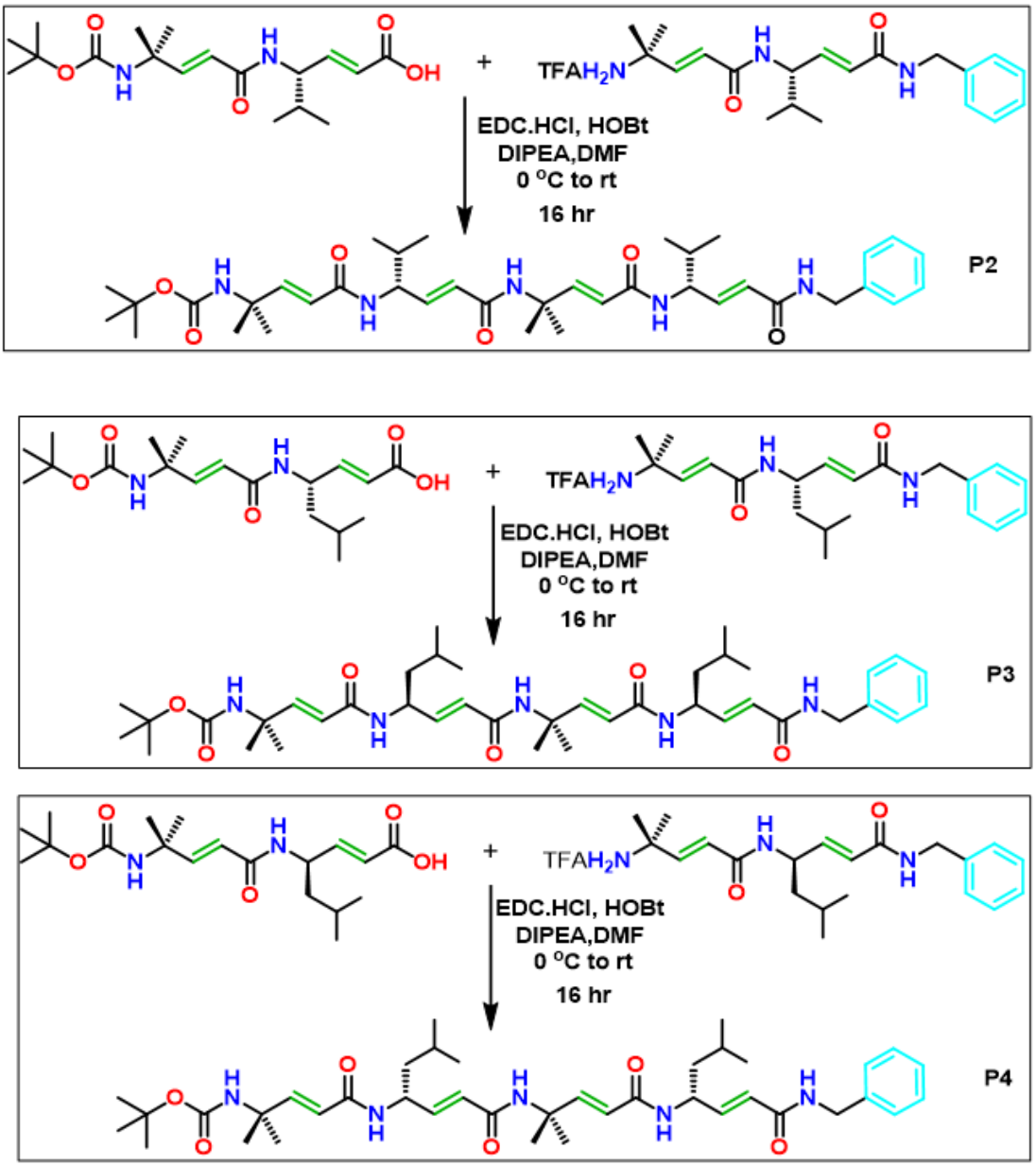
Synthesis of dipeptide benzyl amines **Pb2**, **Pb3,** and **Pb4 was** also achieved following the same strategy as described in 5.1.4. The schematic representation of the peptide is given below.



Boc deprotection of **Pb2**, **Pb3,** and **Pb4** was carried out by method using peptide **Pb1**. The schematic representation is given below.



Finally, peptides **P2**, **P3,** and **P4** were synthesized by following the method for synthesis of **P1**.



2.6. Ion Transport Experiments

Study of Ion Transport across EYPC-LUVs⊃HPTS: Preparation of HEPES buffer and stock solutions: The HEPES buffer (pH = 7.0) was prepared by dissolving solid HEPES (10 mM) and NaCl (100 mM) in autoclaved Milli-Q water, followed by adjustment of pH to 7.0 by addition of aliquots of 0.5 M NaOH solution. Stock solutions of all transporter molecules were prepared in HPLC grade DMSO.

Preparation of EYPC-LUVs⊃HPTS in NaCl: In a clean, dry 10 mL round-bottom flask, 1 mL of egg yolk phosphatidylcholine (EYPC, 25 mg/mL in $CHCl_3$) was evaporated to form a thin, transparent film by purging nitrogen gas while continuously rotating. The resulting transparent film underwent high vacuum treatment for 4-5 hours to eliminate all traces of $CHCl_3$. Subsequently, the film was hydrated with 1 mL of HEPES buffer (1 mM HPTS, 10 mM HEPES, 100 mM NaCl, pH = 7.0) through vortexing at 10-minute intervals over a total duration of 1 hour. This hydrated suspension was then subjected to at least 9 cycles of freeze-thaw (liquid N_2, 55 °C). Extrusions were carried out using a Mini-extruder through a polycarbonate membrane (Avanti) with a pore size of 100 nm, repeated 25 times (an odd number). Unentrapped HPTS dye was removed through size exclusion chromatography using Sephadex G-50 (Sigma-Aldrich) with HEPES buffer (10 mM HEPES, 100 mM NaCl, pH = 7.0). The collected vesicles were subsequently diluted to 6 mL to obtain EYPC-LUVs⊃HPTS. The final conditions comprised approximately 5 mM EYPC, with the internal environment containing 1 mM HPTS, 10 mM HEPES, 100 mM NaCl at pH = 7.0, and the external environment composed of 10 mM HEPES, 100 mM NaCl at pH = 7.0.

Ion transport Activity by HPTS Assay: In a clean and dry fluorescence cuvette, 1975 µL of HEPES buffer (10 mM HEPES, 100 mM NaCl, pH = 7.0) was introduced, followed by the addition of 25 µL of EYPC-LUVs⊃HPTS. The cuvette was then positioned in the fluorescence instrument with gentle stirring facilitated by a magnetic stirrer integrated into the instrument (t = 0 s). The fluorescence emission intensity of HPTS was continuously monitored at λ_{em} = 510 nm (λ_{ex} = 450 nm). To establish a pH gradient (ΔpH = 0.8) across the intra- and extra-vesicular system, 20 µL of 0.5 M NaOH was introduced at t = 20 s. At t = 100 s, the required concentrations of transporter molecules were added, and ultimately, the vesicles were disrupted by the addition of 25 µL of 10% Triton X-100 at t = 300 s to eliminate the pH gradient. The collected data was then normalized to the percentage change in fluorescence intensity with respect to time using the equation 1:

$$I_F = [(I_t - I_0)/(I_\infty - I_0)] \times 100 \qquad \text{Eq. 1}$$

Where I_0 is the initial intensity (just before transporter addition), I_t is the intensity at time t and I_∞ the final intensity after the addition of Triton X-100.

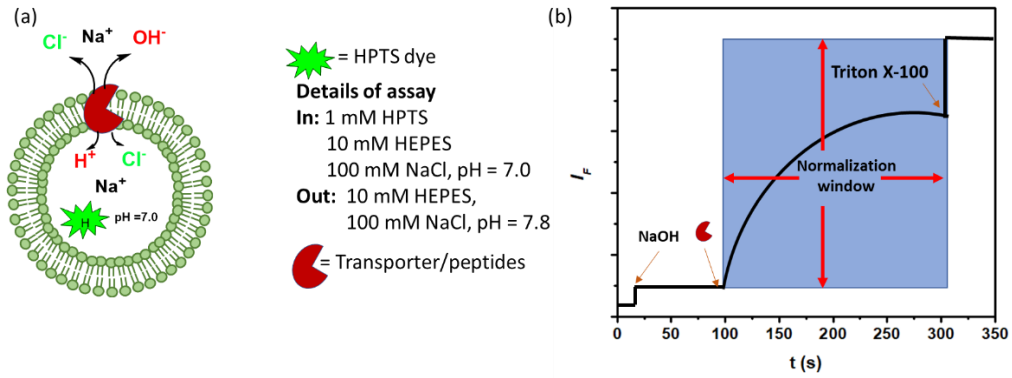


Figure 19: (a) Schematic of fluorescence-based assay of ion transport activity using EYPC-LUVs⊃HPTS, and (b) Diagram of ion transport kinetics depicting the normalization window.

Dose-Response Activity: The ion transport activities of all the peptides were assessed at various concentrations. The ion transport activity of **P1** and **P3** at different concentrations is presented below. The concentration profile data were analyzed at t = 290 s to determine the effective concentration, EC_{50} (i.e., the concentration of transporter required to achieve 50% ion efflux activity) by utilizing the Hill equation (Eq. 2).

$$Y = Y_\infty + (Y_0 - Y_\infty) / [1 + (c/EC_{50})^n] \qquad \text{Eq. S2}$$

where, Y_0 = Fluorescence intensity just before the addition of channel-forming molecule (at t = 0 s), Y_∞ = Fluorescence intensity with excess compound concentration, c = concentration of a channel-forming molecule, and n = Hill coefficient (*i.e.*, The number of molecules required for the transportation of a single ion).

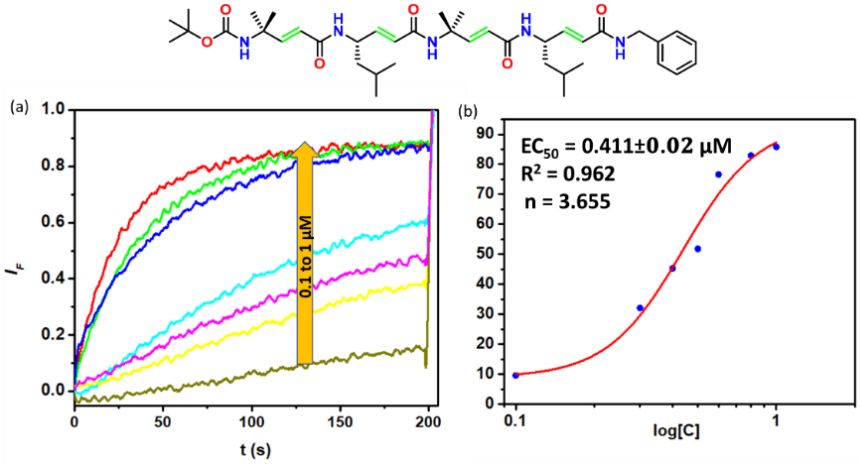


Figure 20: (a) Concentration-dependent ion transport activity of Peptide **P1** (0.1-1 μM) with NaCl salt across EYPC–LUVs⊃HPTS, and (b) corresponding Hill plot of **P1** at t = 290 s

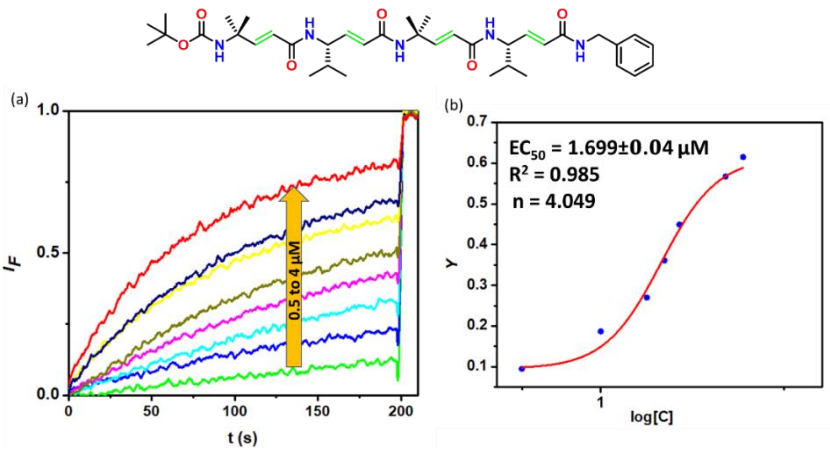


Figure 21: (a) Concentration-dependent ion transport activity of Peptide **P3** (0.5-4 µM) with NaCl salt across EYPC–LUVs⊃HPTS, and (b) corresponding Hill plot of **P3** at t = 290 s.

2.7. Calcein Leakage Assay

Preparation of Buffer Solutions: The Calcein-HEPES buffer was prepared by combining solid calcein at a concentration of 50 mM with a solution containing 10 mM NaCl and 10 mM HEPES. The mixture was dissolved by adding aliquots of concentrated NaOH, and the pH was subsequently adjusted to 7.0. For the extravesicular buffer, NaCl (100 mM) and HEPES (10 mM) were dissolved in MilliQ water, and the pH was set to 7.0 using 0.5 M NaOH.

Preparation of EYPC-LUVs⊃calcein: A thin lipid film was produced by evaporating a solution comprising 25 mg of EYPC in 1 ml of CHCl3 under vacuum conditions for 4 hours. Subsequently, the lipid film underwent hydration with 0.5 mL of a buffer solution (10 mM HEPES, 10 mM NaCl, 50 mM calcein, pH 7.0) for 1 hour, with intermittent vortexing (4-5 times), followed by a freeze-thaw cycle (≥ 20 times) using liquid nitrogen and a temperature of 55 °C. The resulting vesicle solution was then extruded through a polycarbonate membrane (Avanti) featuring 100 nm pores, repeated 19 times (must be an odd number), resulting in vesicles with an average diameter of approximately 100 nm. To eliminate the extracellular dye, size exclusion chromatography (Sephadex G-50) was employed with a 10 mM HEPES buffer (100 mM NaCl, pH 7.0). The collected vesicles were subsequently diluted to 3 mL, yielding EYPC-LUVs⊃calcein. The final composition included approximately 5.0 mM EYPC lipid, with an intravesicular solution containing 10 mM HEPES, 10 mM NaCl, 50 mM calcein at pH 7.0, and an extravesicular solution comprising 10 mM HEPES, 100 mM NaCl at pH 7.0.

Determination of Ion Leakage by Calcein Assay: In a clean and dry fluorescence cuvette, 1980 µL of HEPES buffer (containing 10 mM HEPES, 100 mM NaCl, and pH 7.0) was taken, followed by the addition of 20 µL of EYPC-LUVs⊃Calcein. The cuvette was placed in the fluorescence instrument equipped with a magnetic stirrer for gentle agitation starting at t = 0 s. The fluorescence emission intensity of calcein was continuously measured at λem = 515 nm (λex = 495 nm). At t = 50 s, the required concentrations of peptides were introduced, and at t = 300 s, 25 µL of 10% Triton X-100 was added to disrupt the pH gradient and lyse the vesicles.Subsequently, the acquired data was normalized to express the percentage change in fluorescence intensity over time using Eq. S1.

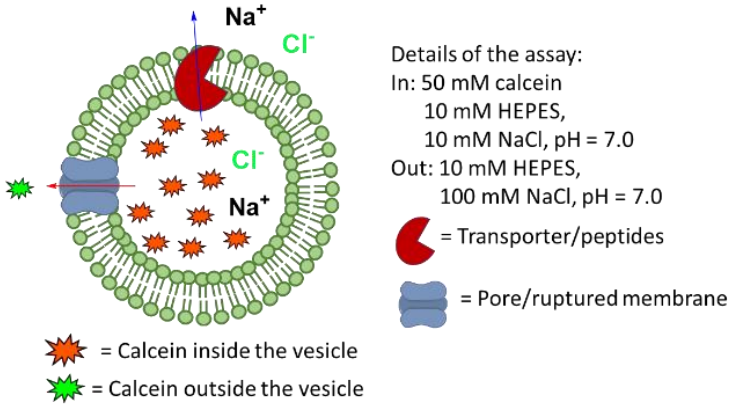


Figure 22: Schematic of calcein leakage in EYPC-LUVs⊃calcein in the presence of ion transporter vs pore or membrane disrupting agent.

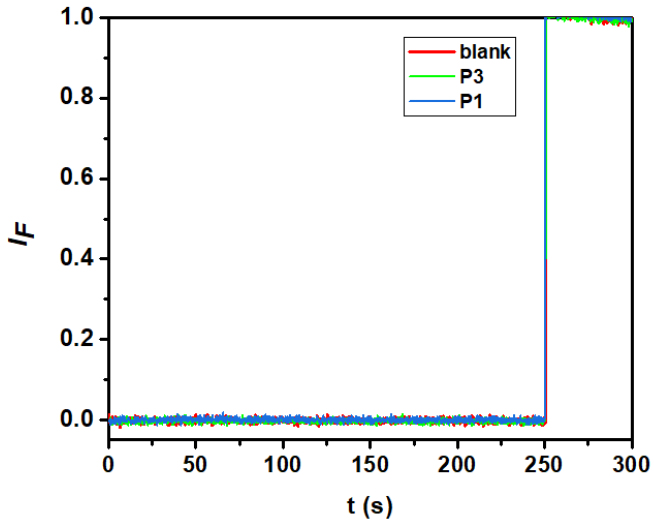
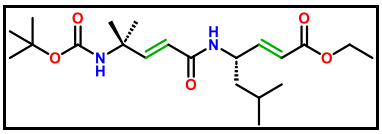


Figure 23: Activity of **P1** and **P3** across EYPC-LUVs⊃calcein. No increase in fluorescence signal was observed even for compound treatment at 5 µM, corresponding to negligible calcein leakage, indicating **P1** and **P3** do not compromise membrane integrity even at high concentrations.

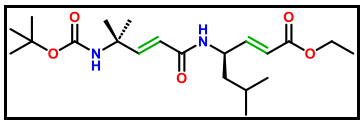
2.8. Characterization of Monomers and Peptides

Characterization of BocNH-dγAic-dγLeu(L)-OEt (Pa3)



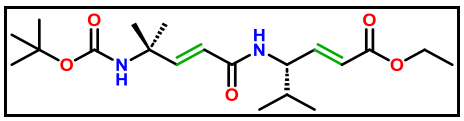
^{1}H NMR (400 MHz, $CDCl_3$) δ 6.88 – 6.84 (m, 1H), 6.84 – 6.80 (m, 1H), 5.92 (dd, *J* = 15.7, 1.6 Hz, 1H), 5.83 (d, *J* = 15.5 Hz, 1H), 5.72 (d, *J* = 7.8 Hz, 1H), 4.81 – 4.73 (m, 1H), 4.71 (s, 1H), 4.18 (q, *J* = 7.1 Hz, 2H), 1.66 (dq, *J* = 13.4, 6.7 Hz, 1H), 1.46 (d, *J* = 7.3 Hz, 2H), 1.43 (s, 9H), 1.41 (d, *J* = 2.0 Hz, 6H), 1.28 (t, *J* = 7.1 Hz, 3H), 0.94 (s, 3H), 0.93 (s, 3H). **^{13}C NMR** (101 MHz, CDCl3) δ 166.18, 165.02, 147.84, 120.68, 120.22, 79.26, 60.26, 52.62, 48.20, 43.29, 28.20, 27.21, 24.56, 22.51, 21.99, 14.02. **MALDI TOF/TOF** m/z calculated value for $C_{21}H_{36}N_2O_5$ $[M+K]^+$ = 435.26 and observed $[M+K]^+$ = 435.38

Characterization of BocNH-dγAic-dγLeu(L)-OEt (Pa4)



^{1}H NMR (400 MHz, $CDCl_3$) δ 6.87 – 6.82 (m, 1H), 6.82 – 6.77 (m, 1H), 5.89 (dd, *J* = 15.7, 1.6 Hz, 1H), 5.82 (d, *J* = 15.5 Hz, 1H), 5.72 (s, 1H), 4.74 (dt, *J* = 15.2, 7.1 Hz, 2H), 4.16 (q, *J* = 7.1 Hz, 2H), 1.65 (dp, *J* = 13.5, 6.8 Hz, 1H), 1.43 (s, 2H), 1.40 (d, *J* = 1.2 Hz, 9H), 1.39 (s, 6H), 1.26 (t, *J* = 7.1 Hz, 3H), 0.91 (dt, *J* = 6.6, 1.3 Hz, 6H). **^{13}C NMR** (101 MHz, CDCl3) δ 166.51, 165.37, 148.20, 120.95, 120.56, 79.55, 60.56, 52.92, 48.50, 43.56, 28.50, 27.50, 24.86, 22.82, 22.28, 14.32. **MALDI TOF/TOF** m/z calculated value for $C_{21}H_{36}N_2O_5$ $[M+K]^+$ = 435.26 and observed $[M+K]^+$ = 435.58

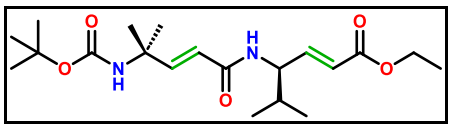
Characterization of BocNH-dγAic-dγVal(L)-OEt (Pa1)



^{1}H NMR (400 MHz, $CDCl_3$) δ 6.89 – 6.86 (m, 1H), 6.85 – 6.82 (m, 1H), 5.91 (dd, *J* = 15.6, 1.7 Hz, 1H), 5.84 (d, *J* = 15.6 Hz, 1H), 5.55 (s, 1H), 4.63 (d, *J* = 7.7 Hz, 1H), 4.59 (ddd, *J* = 8.9, 5.5, 1.7 Hz, 1H), 4.18 (q, *J* = 7.1 Hz, 2H), 1.97 – 1.87 (m, 1H), 1.42 (s, 9H), 1.42 (s, 6H), 1.28 (t, *J* =

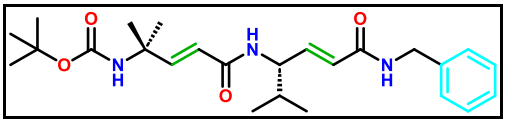
7.1 Hz, 3H), 0.95 (d, *J* = 2.7 Hz, 3H), 0.94 (d, *J* = 2.8 Hz, 3H). **^{13}C NMR** (101 MHz, CDCl3) δ 166.33, 165.53, 146.48, 122.20, 120.62, 105.45, 83.60, 60.63, 55.42, 52.97, 32.21, 28.54, 27.55, 19.01, 18.41, 14.37. **MALDI TOF/TOF** m/z calculated value for $C_{20}H_{34}N_2O_5$ $[M+Na]^+$ = 405.25 and observed $[M+Na]^+$ = 405.63

Characterization of BocNH-dγAic-dγVal(D)-OEt (Pa2)



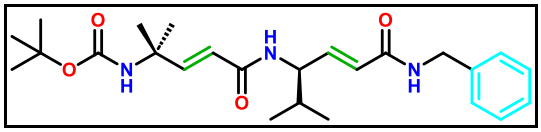
^{1}H NMR (400 MHz, $CDCl_3$) δ 6.89 – 6.86 (m, 1H), 6.85 – 6.82 (m, 1H), 5.91 (dd, *J* = 15.7, 1.6 Hz, 1H), 5.84 (d, *J* = 15.5 Hz, 1H), 5.56 (d, *J* = 9.0 Hz, 1H), 4.64 (s, 1H), 4.63 – 4.56 (m, 1H), 4.18 (q, *J* = 7.1 Hz, 2H), 1.97 – 1.87 (m, 1H), 1.42 (s, 9H), 1.41 (s, 6H), 1.28 (t, *J* = 7.1 Hz, 4H), 0.95 (dd, *J* = 6.8, 2.7 Hz, 7H).). **^{13}C NMR** (101 MHz, CDCl3) δ 166.33, 165.53, 146.48, 122.20, 120.62, 60.63, 55.42, 52.97, 32.21, 28.54, 27.55, 19.01, 18.41, 14.37 **MALDI TOF/TOF** m/z calculated value for $C_{20}H_{34}N_2O_5$ $[M+Na]^+$ = 405.25 and observed $[M+Na]^+$ = 405.62

Characterization of BocNH-dγAic-dγVal(L)-CH$_2$-Ph (Pb1)



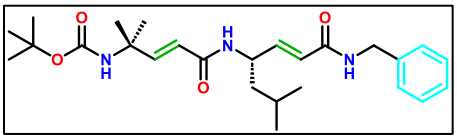
^{1}H NMR (400 MHz, $CDCl_3$) δ 7.37 – 7.33 (m, 1H), 7.33 – 7.27 (m, 4H), 7.26 – 7.21 (m, 1H), 6.84 – 6.67 (m, 2H), 6.18 (d, *J* = 9.3 Hz, 1H), 5.84 (d, *J* = 15.4 Hz, 1H), 5.77 (d, *J* = 14.9 Hz, 1H), 4.92 (d, *J* = 25.6 Hz, 1H), 4.59 – 4.47 (m, 2H), 4.43 (dd, *J* = 14.6, 5.7 Hz, 1H), 1.87 – 1.76 (m, 1H), 1.40 (d, *J* = 6.0 Hz, 3H), 1.39 (s, 9H), 1.34 (d, *J* = 8.2 Hz, 3H), 0.90 (td, *J* = 6.9, 3.2 Hz, 6H). **^{13}C NMR** (101 MHz, CDCl3) δ 165.56, 150.02, 142.60, 138.85, 128.79, 128.72, 128.28, 127.97, 127.47, 124.24, 120.60, 55.27, 53.02, 43.68, 32.53, 28.56, 27.90, 19.13, 18.48. **MALDI TOF/TOF** m/z calculated value for $C_{25}H_{37}N_3O_4$ $[M+Na]^+$ = 466.28 and observed $[M+Na]^+$ = 466.46

Characterization of BocNH-dγAic-dγVal(L)-NHBn (Pb2)



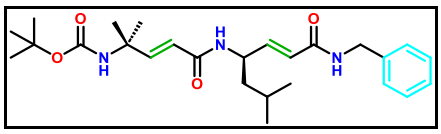
^{1}H NMR (400 MHz, $CDCl_3$) δ 7.34 (d, *J* = 2.0 Hz, 1H), 7.33 – 7.27 (m, 4H), 7.26 – 7.21 (m, 1H), 6.83 – 6.70 (m, 2H), 6.18 (d, *J* = 9.3 Hz, 1H), 5.84 (d, *J* = 15.4 Hz, 1H), 5.77 (d, *J* = 14.9 Hz, 1H), 4.92 (d, *J* = 25.6 Hz, 1H), 4.59 – 4.48 (m, 2H), 4.43 (dd, *J* = 14.6, 5.7 Hz, 1H), 1.87 – 1.77 (m, 1H), 1.40 (d, *J* = 6.0 Hz, 3H), 1.39 (s, 9H), 1.34 (d, *J* = 8.2 Hz, 3H), 0.91 (dd, *J* = 7.0, 3.1 Hz, 3H), 0.88 (d, *J* = 3.4 Hz, 3H). **^{13}C NMR** (101 MHz, CDCl3) δ 165.72, 165.55, 150.04, 142.59, 128.78, 128.72, 128.29, 128.25, 127.47, 124.28, 120.60, 55.29, 53.01, 43.68, 32.51, 28.56, 27.91, 19.13, 18.50. **MALDI TOF/TOF** m/z calculated value for $C_{25}H_{37}N_3O_4$ $[M+Na]^+$ = 466.28 and observed $[M+Na]^+$ = 466.51

Characterization of BocNH-dγAic-dγLeu(L)-NHBn (Pb3)



^{1}H NMR (400 MHz, $CDCl_3$) δ 7.56 (s, 1H), 7.34 – 7.27 (m, 5H), 7.25 – 7.19 (m, 1H), 6.72 (d, *J* = 13.4 Hz, 1H), 6.70 – 6.64 (m, 1H), 6.49 (s, 1H), 5.83 (d, *J* = 15.4 Hz, 1H), 5.71 (d, *J* = 15.3 Hz, 1H), 4.82 (s, 1H), 4.63 (s, 1H), 4.50 (qd, *J* = 14.6, 6.0 Hz, 2H), 1.40 (s, 9H), 1.39 – 1.35 (m, 2H), 1.34 (s, 3H), 1.32 (s, 3H), 0.88 (d, *J* = 3.4 Hz, 3H), 0.87 (d, *J* = 3.2 Hz, 3H). **^{13}C NMR** (101 MHz, CDCl3) δ 165.69, 165.60, 149.75, 143.95, 139.08, 128.94, 128.62, 128.22, 127.96, 127.26, 122.56, 120.27, 79.94, 53.32, 48.58, 43.78, 43.57, 28.58, 27.94, 27.30, 24.88, 23.00, 22.09. **MALDI TOF/TOF** m/z calculated value for $C_{26}H_{39}N_3O_4$ $[M+Na]^+$ = 496.29 and observed $[M+Na]^+$ = 496.64

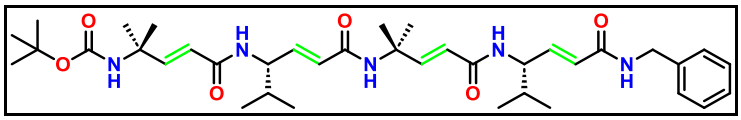
Characterization of BocNH-dγAic-dγLeu(D)-NHBn (Pb4)



^{1}H NMR (400 MHz, $CDCl_3$) δ 7.45 (s, 1H), 7.31 (d, *J* = 6.1 Hz, 4H), 7.25 – 7.20 (m, 1H), 6.73 (d, *J* = 12.8 Hz, 1H), 6.70 – 6.66 (m, 1H), 6.40 (s, 1H), 5.82 (d, *J* = 15.4 Hz, 1H), 5.73 (d, *J* = 15.3 Hz, 1H), 4.80 (s, 1H), 4.64 (s, 1H), 4.50 (qd, *J* = 14.7, 5.9 Hz, 2H), 1.40 (s, 9H), 1.37 (dd, *J* = 4.0, 1.9 Hz, 2H), 1.35 (s, 3H), 1.33 (s, 3H), 0.89 (d, *J* = 3.2 Hz, 3H), 0.87 (d, *J* = 3.1 Hz, 3H). **^{13}C NMR** (101 MHz, CDCl3) δ 165.65, 143.95, 128.96, 128.66, 128.22, 127.33, 122.72, 120.33,

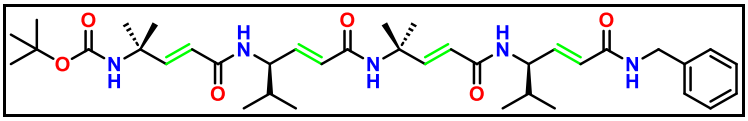
79.76, 53.28, 48.60, 43.80, 43.63, 28.59, 27.86, 24.88, 22.98, 22.30, 22.15. **MALDI TOF/TOF** m/z calculated value for $C_{26}H_{39}N_3O_4$ $[M+Na]^+$ = 496.29 and observed $[M+Na]^+$ = 496.54

Characterization of BocNH-dγAic-dγVal(L)- dγAic-dγVal(L)-NHBn (P1)



^{1}H NMR (400 MHz, $CDCl_3$) δ 8.53 (d, *J* = 14.0 Hz, 2H), 8.09 (s, 1H), 7.57 (s, 1H), 7.39 (d, *J* = 7.0 Hz, 2H), 7.34 – 7.27 (m, 2H), 7.23 – 7.18 (m, 1H), 6.86 (d, *J* = 15.2 Hz, 1H), 6.82 – 6.73 (m, 2H), 6.61 (d, *J* = 15.3 Hz, 1H), 6.09 (d, *J* = 15.3 Hz, 1H), 5.65 (d, *J* = 15.2 Hz, 1H), 5.58 (dd, *J* = 15.4, 2.1 Hz, 1H), 5.50 (d, *J* = 15.3 Hz, 1H), 4.76 (s, 1H), 4.58 (dd, *J* = 14.6, 5.8 Hz, 1H), 4.48 (dd, *J* = 14.6, 6.0 Hz, 1H), 4.42 – 4.30 (m, 2H), 1.86 – 1.74 (m, 2H), 1.47 (s, 3H), 1.45 (s, 9H), 1.36 (s, 3H), 1.34 (s, 3H), 1.29 (s, 3H), 0.98 (d, *J* = 6.7 Hz, 3H), 0.96 (d, *J* = 6.7 Hz, 3H), 0.93 (d, *J* = 2.7 Hz, 3H), 0.91 (d, *J* = 2.6 Hz, 3H). **^{13}C NMR** (101 MHz, CDCl3) δ 167.08, 166.62, 165.88, 164.23, 155.30, 150.32, 148.97, 143.24, 143.03, 139.68, 128.42, 128.34, 126.84, 122.65, 122.46, 119.57, 119.12, 80.39, 57.32, 55.59, 54.53, 53.98, 43.31, 32.68, 32.59, 30.42, 30.18, 28.72, 28.50, 26.77, 25.64, 19.75, 19.66, 19.46, 18.70. **MALDI TOF/TOF** m/z calculated value for $C_{38}H_{57}N_5O_6$ $[M+Na]^+$ = 702.43 and observed $[M+Na]^+$ = 703.00

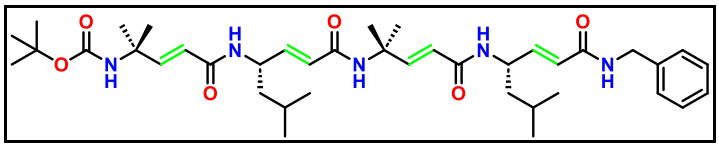
Characterization of BocNH-dγAic-dγVal(D)- dγAic-dγVal(D)-NHBn (P2)



^{1}H NMR (400 MHz, $CDCl_3$) δ 8.52 (t, *J* = 5.9 Hz, 2H), 8.10 (s, 1H), 7.57 (s, 1H), 7.38 (d, *J* = 6.9 Hz, 2H), 7.32 – 7.27 (m, 3H), 7.23 – 7.18 (m, 1H), 6.86 (d, *J* = 15.2 Hz, 1H), 6.77 (ddd, *J* = 15.7, 12.6, 3.7 Hz, 2H), 6.61 (d, *J* = 15.3 Hz, 1H), 6.09 (d, *J* = 15.2 Hz, 1H), 5.65 (d, *J* = 15.3 Hz, 1H), 5.58 (dd, *J* = 15.4, 2.1 Hz, 1H), 5.50 (d, *J* = 15.3 Hz, 1H), 4.78 (s, 1H), 4.57 (dd, *J* = 14.7, 5.8 Hz, 1H), 4.50 (d, *J* = 6.0 Hz, 1H), 4.41 – 4.29 (m, 2H), 1.83 – 1.77 (m, 2H), 1.47 (s, 3H), 1.45 (s, 9H), 1.36 (s, 3H), 1.34 (s, 3H), 1.29 (s, 4H), 0.98 (d, *J* = 6.6 Hz, 3H), 0.96 (d, *J* = 6.7 Hz, 3H), 0.93 (d, *J* = 2.9 Hz, 3H), 0.91 (d, *J* = 2.8 Hz, 3H). **^{13}C NMR** (101 MHz, CDCl3) δ 166.48, 166.33, 165.94, 164.50, 155.17, 150.28, 149.00, 144.80, 144.15, 139.67, 128.42, 128.24, 126.76, 121.54, 121.27, 119.50, 119.29, 80.39, 54.60, 54.00, 49.49, 48.78, 43.74, 43.47, 43.36, 30.54, 30.13, 28.72, 26.67,

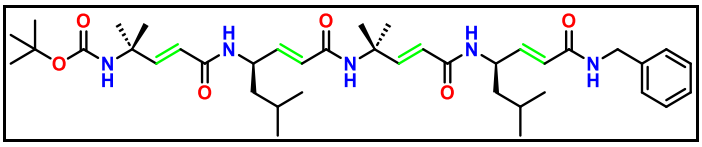
25.69, 25.16, 25.00, 23.01, 22.83, 22.42, 21.83.**MALDI TOF/TOF** m/z calculated value for $C_{38}H_{57}N_5O_6$ $[M+Na]^+$ = 702.43 and observed $[M+Na]^+$ = 702.64

Characterization of BocNH-dγAic-dγLeu(L)- dγAic-dγLeu(L)-NHBn (P3)



^{1}H NMR (400 MHz, $CDCl_3$) δ 8.51 (d, *J* = 7.8 Hz, 1H), 8.45 (s, 1H), 8.16 (s, 1H), 7.67 (d, *J* = 7.1 Hz, 1H), 7.37 – 7.27 (m, 4H), 7.19 (t, *J* = 7.3 Hz, 1H), 6.84 (d, *J* = 15.2 Hz, 1H), 6.68 (ddd, *J* = 15.3, 10.0, 3.9 Hz, 2H), 6.62 (d, *J* = 15.1 Hz, 1H), 6.05 (d, *J* = 15.2 Hz, 1H), 5.53 (ddd, *J* = 15.2, 10.2, 2.2 Hz, 3H), 4.78 (s, 1H), 4.66 – 4.37 (m, 4H), 1.48 (s, 3H), 1.45 (s, 9H), 1.44 (s, 3H), 1.42 – 1.37 (m, 2H), 1.34 (s, 3H), 1.31 (s, 3H), 0.88 – 0.82 (m, 12H). **^{13}C NMR** (101 MHz, CDCl3) δ 166.47, 166.33, 165.94, 164.50, 155.17, 150.28, 149.00, 144.79, 144.15, 139.68, 128.43, 128.25, 126.77, 121.55, 121.28, 119.51, 119.30, 80.39, 54.61, 54.01, 49.50, 48.78, 43.75, 43.48, 43.37, 30.54, 30.13, 28.72, 26.67, 25.70, 25.16, 25.00, 23.01, 22.83, 22.42, 21.83. **MALDI TOF/TOF** m/z calculated value for $C_{40}H_{61}N_5O_6$ $[M+Na]^+$ = 730.46 and observed $[M+Na]^+$ = 730.97

Characterization of BocNH-dγAic-dγLeu(D)- dγAic-dγLeu(D)-NHBn (P4)



^{1}H NMR (400 MHz, $CDCl_3$) δ 8.51 (d, *J* = 7.9 Hz, 1H), 8.46 (t, *J* = 5.9 Hz, 1H), 8.16 (s, 1H), 7.66 (d, *J* = 7.1 Hz, 1H), 7.38 – 7.34 (m, 2H), 7.31 (d, *J* = 7.4 Hz, 2H), 7.22 – 7.17 (m, 1H), 6.84 (d, *J* = 15.2 Hz, 1H), 6.68 (ddd, *J* = 15.3, 8.2, 3.8 Hz, 2H), 6.62 (d, *J* = 15.2 Hz, 1H), 6.05 (d, *J* = 15.2 Hz, 1H), 5.57 (d, *J* = 1.6 Hz, 1H), 5.55 – 5.49 (m, 2H), 4.77 (s, 1H), 4.61 (s, 1H), 4.55 – 4.50 (m, 2H), 4.43 (s, 1H), 1.75 (d, *J* = 12.9 Hz, 2H), 1.72 – 1.68 (m, 2H), 1.48 (s, 3H), 1.45 (s, 9H), 1.44 (s, 3H), 1.42 (s, 1H), 1.39 (s, 1H), 1.35 (s, 3H), 1.31 (s, 3H), 0.87 (d, *J* = 1.8 Hz, 6H), 0.85 – 0.82 (m, 6H). **^{13}C NMR** (101 MHz, CDCl3) δ 166.47, 166.33, 165.94, 164.50, 155.17, 150.28, 149.00, 144.79, 144.15, 139.68, 128.43, 128.25, 126.77, 121.55, 121.28, 119.51, 119.30, 80.39, 54.61, 54.01, 49.50, 48.78, 43.75, 43.48, 43.37, 30.54, 30.13, 28.72, 26.67, 25.70, 25.16, 25.00, 23.01, 22.83, 22.42, 21.83.**MALDI TOF/TOF** m/z calculated value for $C_{40}H_{61}N_5O_6$$[M+Na]^+$ = 730.46 and observed $[M+Na]^+$ = 730.98

2.9. Appendix

2.9.1. ORTEP Diagrams of P1, P3 and P4

2.9.1.1. ORTEP diagram of peptide P1

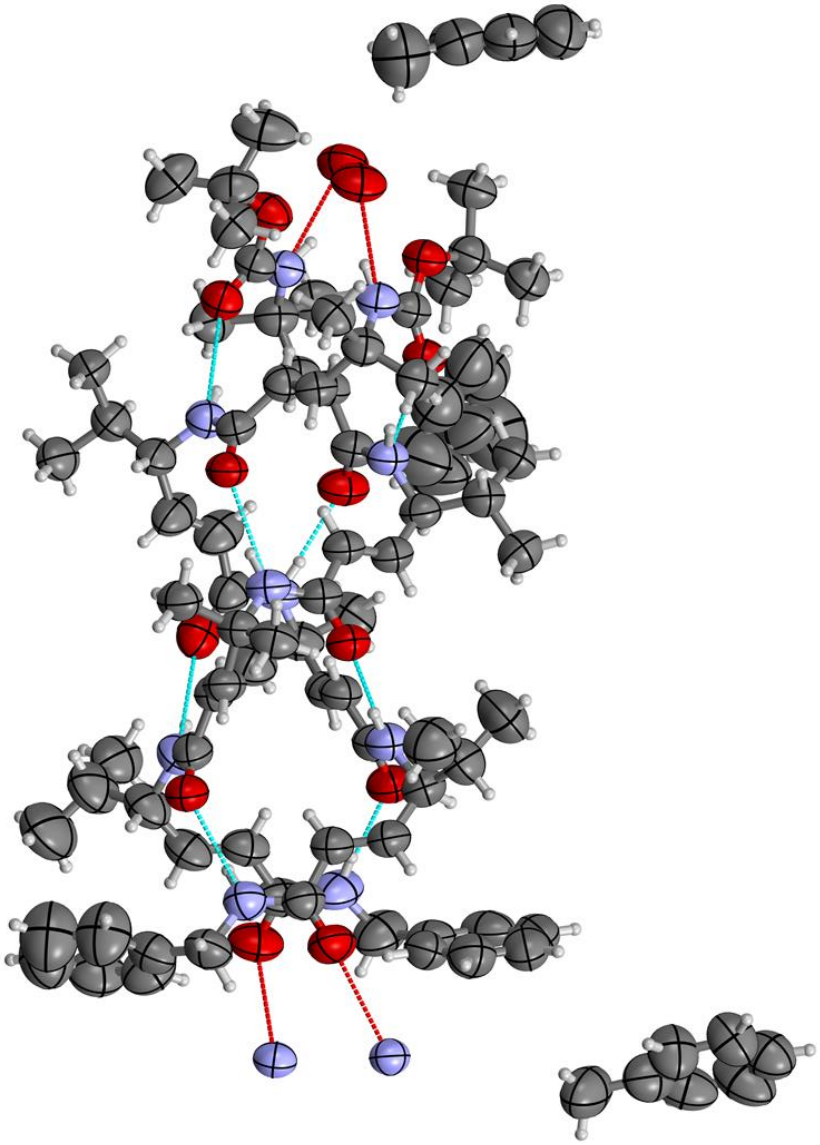


Figure 24: ORTEP diagram of peptide **P1**. H-bonds are shown in dotted lines. Ellipsoids are drawn at 50% probability. CCDC no. 2284152

2.9.1.2. ORTEP Diagram of Peptide P3

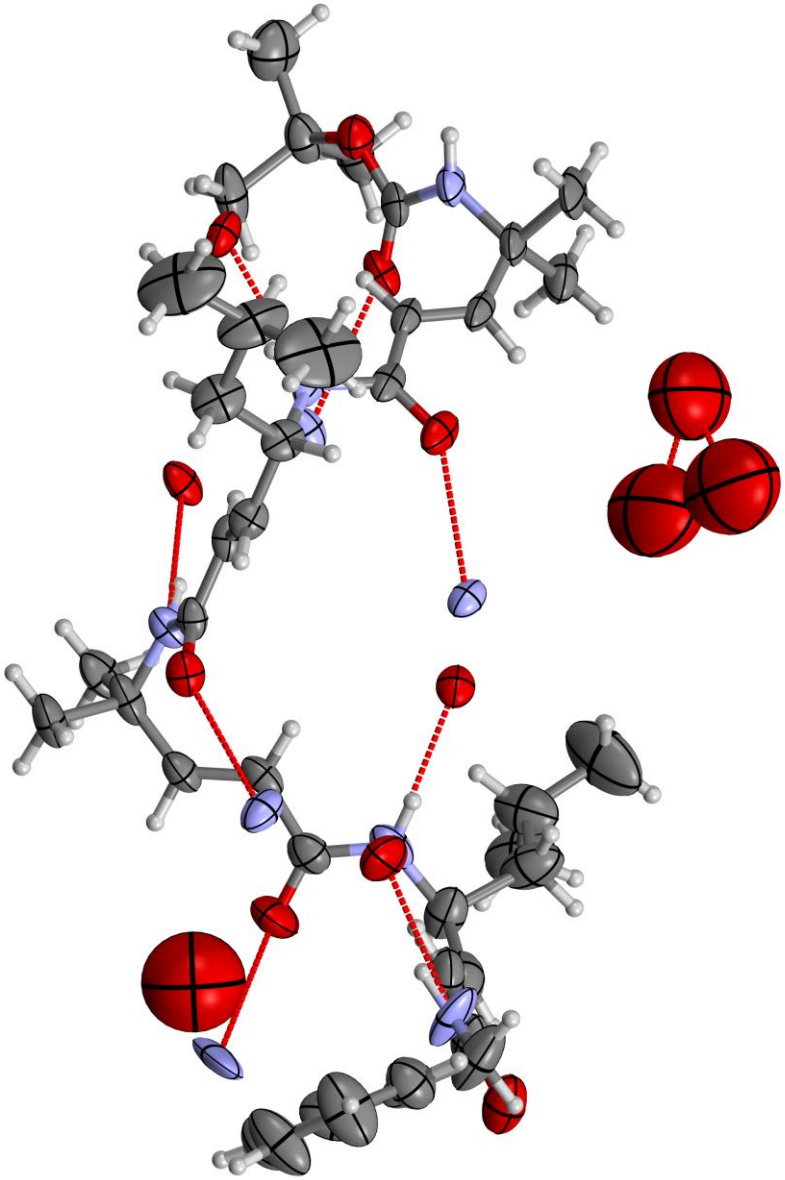


Figure 25: ORTEP diagram of peptide **P3.** H-bonds are shown in dotted lines. Ellipsoids are drawn at 50% probability. CCDC no 2289536

2.9.1.3. ORTEP Diagram of Peptide P4

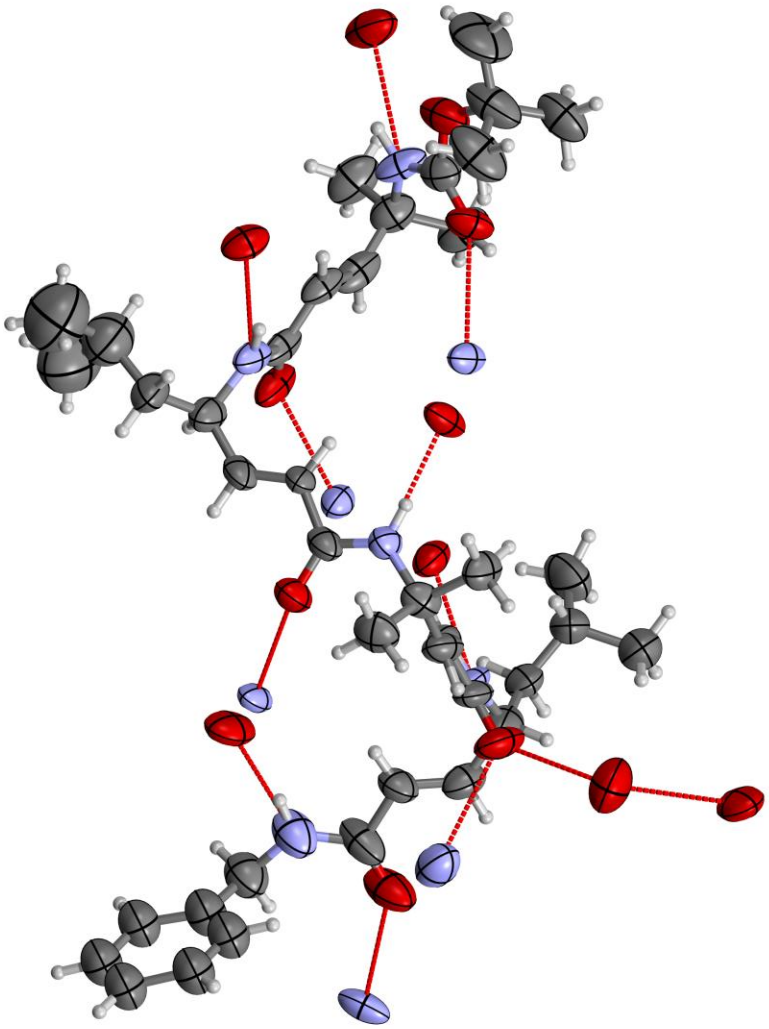


Figure 26: ORTEP diagram of peptide **P4.** H-bonds are shown in dotted lines. Ellipsoids are drawn at 50% probability. CCDC no 22895

2.10. Crystal Structure Information:

Crystal structure analysis of P1: Crystals were grown from chloroform/toluene solution by slow evaporation. A single crystal (0.4 × 0.28 × 0.12 mm) was mounted on a loop with a small amount of the paraffin oil. The X-ray data were collected at 296 K temperature using Cu K_α radiation (λ = 1.54178Å), ω-scans (2θ = 68.625), for a total of 17289 independent reflections. Space group P 21/c, a = 18.5058(8), b = 21.8417(9), c = 24.6835(11), α = 90, β = 108.127, γ = 90 V = 9481.9(7) Å^3, triclinic, Z = 4 for chemical formula C97 H138 N10 O12, with two molecules in asymmetric unit; ρcalcd = 1.146 gcm^{-3}, μ = 0.599 mm^{-1}, F (000) = 3544.0, The structure was obtained by direct methods using SHELXS- 97.[1] The final R value was 0.1137 (wR2 = 0.4248) 5536 observed reflections ($F_0 \geq 4\sigma$ (|F_0|))and 1087 variables, S = 0.728.The largest difference in peak and hole were 0.99 and -0.53eÅ^3 respectively.

Crystal structure analysis of P3: Crystals were grown from chloroform/toluene solution by slow evaporation. A single crystal (0.28 × 0.09 × 0.15 mm) was mounted on a loop with a small amount of the paraffin oil. The X-ray data were collected at 100 K temperature using Mo K_α radiation (λ = 0.71073Å), and ω-scans (2θ = 50.038), for a total of 8271 independent reflections. Space group 'C 2 2 21', a = 12.386(3), b = 36.126(3), c = 20.992(3), α = 90, β = 90, γ = 90 V = 9393(4)Å^3, orthorhombic, Z = 8 for chemical formula C_{40} H_{61} N_5 O_6, 2O with one molecule in asymmetric unit; ρcalcd = 1.046 gcm^{-3}, μ = 0.073mm^{-1}, F (000) = 3200, The structure was obtained by direct methods using SHELXS- 97.[1] The final R value was 0.1112 (wR2 = 0.3399) 5954 observed reflections ($F_0 \geq 4\sigma$ (|F_0|))and 491 variables, S = 1.056. The largest difference in peak and hole were 1.03 and -0.61eÅ^3 respectively.

Crystal structure analysis of P4: Crystals were grown from dichloromethane/xylene solution by slow evaporation. A single crystal (0.3 × 0.02 × 0.09 mm) was mounted on a loop with a small amount of the paraffin oil. The X-ray data were collected at 150 K temperature using Mo K_α radiation (λ = 0.71073Å), ω-scans (2θ = 52.072), for a total of 116575 independent reflections. Space group 'C 2 2 21', a = 12.638(19), b = 35.27(6), c = 21.44(3), α = 90, β = 90, γ = 90 V = 9557(25)Å^3, orthorhombic, Z = 4 for chemical formula 2(C40 H60 N5 O6), O with one molecule in asymmetric unit; ρcalcd = 0.994 gcm^{-3}, μ = 0.068 mm^{-1}, F (000) = 3096, The structure was obtained by direct methods using SHELXS- 97.[1] The final R value was 0.1215 (wR2 = 0.3715) 3431 observed reflections ($F_0 \geq 4\sigma$ (|F_0|))and 446 variables, S = 1.014. The largest difference in peak and hole were 0.48 and -0.31 eÅ^3 respectively.

2.11. References

1. (a) Watson, J. D.; Crick, F. C. H. *Nature* **1953**, *171*, 737. (b) Alberts, B.; Johnson, A.; Lewis, J.; Raff, M.; Roberts, K.; Walter, P. *Molecular Biology of the Cell*, W.W. Norton & Company, **2007**. (c) Saenger, W. Principles of Nucleic Acid Structure; *Springer-Verlag:* New York, **1984**.
2. (a) Rich, A.; Zhang, S. *Nat Rev Genet* **2003,** *4*, 566. (b) Ravichandran S, Subramani VK, Kim KK. *Biophys Rev*. **2019,** *11*, 383.
3. (a) Langes, D. A. *Science* **1988**, *241*, 188. (b) Urry, D. W.; Glickson, J. D.; Mayers, D. F.; Haider, J. *Biochemistry* **1972**, *11*, 487. (c) Wallace, B. A.; Ravikumar, K. *Science* **1988**; *241*, 182. (d) Sychev, S. V.; Barsukov, L. I.; Ivanov, V. T. *J. Pept. Sci.* **2013**, *19*, 452. (e) Kelkar, D. A.; Chattopadhyay, A. *Biochim. Biophys. Acta.* **2007**, *1768*, 2011. (f) Sychev, S. V.; Barsukov, L. I.; Ivanov, V. T. *Eur. Biophys. J*. **1993**, *22*, 279.
4. (a) Vertesy, L.; Aretz, W.; Knauf, M.; Markus, A.; Vogel, M.; Wink, J. J. *Antibiot.* **1999**, *52*, 374. (b) Bunkóczi, G.; Vértesy, L.; Sheldrick, G. M.; *Angew. Chem. Int. Ed.* **2005**; *44*, 1340. (c) F. Dettner, A. Hänchen, D. Schols, L. Toti, A. Nußer, R. D. Süssmuth, *Angew. Chem. Int. Ed.* **2009**, *48*, 1856. (d) Férir, G.; Hänchen, A.; François, K. O.; Hoorelbeke, B.; Huskens, D.; Dettner, F.; Süssmuth, R. D.; Schols, D. *Virology* **2012**, *433*, 308. (e) Rausch, S.; Hänchen, A.; Denisiuk, A.; Löhken, M.; Schneider, T.; Süssmuth, R. D. *ChemBioChem* **2011**, *12*, 1171. (f) Fuse, S.; Mifune, Y.; Nakamura, H.; Tanaka, H. *Nat. Commun.* **2016**, *7*, 13491.
5. (a) Zhang, Z.; Pascal, S. M.; Cross, T. A. *Biochemistry* **1992**, *31*, 8822. (b) Arsemev, A. S.; Barsukov, I. L.; Bystrov, V. F. *FEBS. Lett.* **1984,** 1*80*, 33. (c) Roux, B.; Bruschweiler, R.; Ernst, R. R. *Eur. J. Biochem*. **1990**, *194*, 57. (d) Pascal, S. M.; Cross, T. A. *J. Biomol. NMR* **1993**, *3*, 495. (e) Langs D. A. *Biopolymers* **1989**, *28*, 259. (f) Woolley, G. A.; Wallace, B. A. *J. Membr. Biol*. **1992**, *129*, 109. (g) Ketchem, R. R.; Hu, W.; Cross, T. A. *Science* **1993**, *261*, 1457. (h) Kovacs, F.; Quine, J.; Cross, T. A. *Proc. Natl. Acad. Sci. USA.* **1999**, *96*, 7910. (i) Sychev, S. V.; Barsukov, L. I.; Ivanov V. T.; *J. Pept. Sci.* **2013**, *19*, 452. (j) Sychev, S.V.; Barsukov, L. I.; Ivanov, V. T. *Eur. Biophys. J.* **1993**, *22*, 279.
6. (a) Benedetti, E.; Di Blasio, B.; Pedone, C.; Lorenzi, G. P.; Tomasic, L.; Gramlich, V. *Nature* **1979**, *282*, 630. (b) Di Blasio, B.; Benedetti, E.; Pavone, V.; Pedone, C.; Gerber, C.; Lorenzi, G. P. *Biopolymers* **1989**, *28*, 203. (c) Kulp, J. L.; Clark, T. D. *Chem. Eur. J.*

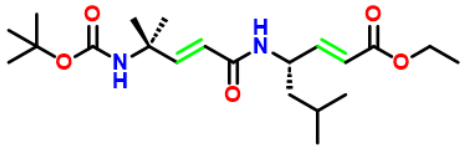
2009, *15*, 11867. (d) Navarro, E.; Fenude, E.; Celda, B. *Biopolymers* **2004**, *73*, 229. (e) Sastry, M.; Brown, C.; Wagner, G.; Clark, T. D. *J. Am. Chem. Soc*. **2006**, *128*, 10650. (f) Schramm, P.; Hofmann, H. -J. *J. Pept. Sci.* **2010**, *16*, 276. (g) Jadhav, K. B.; Lichtenecker, R. J.; Bullach, A.; Mandal, B.; Arndt, H. -D. *Chem. Eur. J*. **2015**, *21*, 5898.

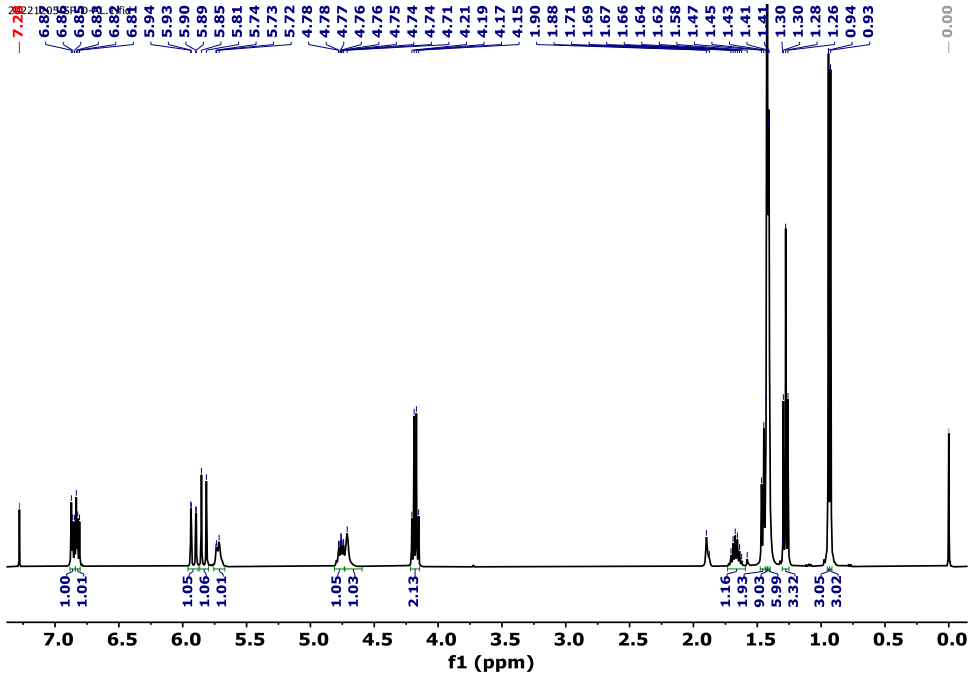
7. (a) Berl, V.; Huc, I.; Khoury, R. G.; Krische, M. J.; Lehn, J.-M. *Nature* **2000**, *407*, 720. (b) Ferrand, Y.; Gan, Q.; Kauffmann, B.; Jiang, H.; Huc, I. *Angew. Chemie Int. Ed.* **2011**, *50*, 7572. (C) Shang, J.; Gan, Q.; Dawson, S. J.; Rosu, F.; Jiang, H.; Ferrand, Y.; Huc, I. *Org. Lett.* **2014**, *16* , 4992. (d) Gan, Q.; Wang, X.; Kauffmann, B.; Rosu, F.; Ferrand, Y.; Huc, I. *Nat. Nanotechnol.* **2017**, *12*, 447. (e) Gan, Q.; Ferrand, Y.; Chandramouli, N.; Kauffmann, B.; Aube, C.; Dubreuil, D.; Huc, I. *J. Am. Chem. Soc.* **2012**, *134*, 15656.
8. (a) Yashima, E.; Maeda, K.; Furusho, Y. *Acc. Chem. Res.* **2008**, *41*, 1166. (b) Koert, U.; Harding, M. M.; Lehn, J.-M.; *Nature* **1990**, *346*, 339. (c) Gabriel, G. J.; Iverson, B. L. *J. Am. Chem. Soc*., **2002**, *124*, 15174. (d) Lokey, R. S.; Iverson, B. L. *Nature* **1995**, *375*, 303. (e) Ikkanda, B. A.; Iverson, B. L. *Chem. Commun.* **2016**, *52*, 7752. (f) Yashima, E.; Ousaka, N.; Taura, D.; Shimomura, K.; Ikai,T.; Maeda, K. *Chem. Rev.* **2016**, *116*, 13752. (g) Wang, J.; Meersman, F.; Esnouf, R.; Froeyen, M.; Busson, R.; Heremans, K.; Herdewijn, P. *Helv. Chim. Acta*. **2001**, *84*, 2398. (i) Wang, Y.; He, Y.; Yu, Z.; Gao, J.; Brinck, S. Ten.; Slebodnick, C.; Fahs, G. B.; Zanelotti, C. J.; Hegde, M.; Moore, R. B.; Ensing, B.; Dingemans, T. J.; Qiao, R.; Madsen, L. A.; *Nat. Commun.* **2019**, *10*, 801. (j) Hu, Y.; Teat, S.J.; Gong, W.; Zhou, Z.; Jin, Y.; Chen, H.; Wu, J.; Cui, Y.; Jiang, T.; Cheng, X.; Zhang, W. *Nat. Chem.* **2021**, *13*, 660. (k) Liu, C.; Koppireddi, S.; Wang, H.; Zhang, D.; Li, Z. *Angew. Chem. Int. Ed.* **2019**, *58*, 226.
9. Misra, R.; Dey, S.; Reja, R. M.; Gopi, H. N. *Angew. Chem., Int. Ed.* **2018**, *57*, 1057.
10. Mali, S. M.; Bandyopadhyay, A.; Jadhav, S. V.; Ganesh Kumar, M.; Gopi, H. N. *Org. Biomol. Chem.* **2011**, *9*, 6566.
11. (a) Sreerama, N.; Yu, S.; Venyaminov, S. Y.; Woody, R.W. *Anal. Biochem.* **2001**, *299*, 271. (b) Adler, A. J.; Greenfield, N. J.; Fasman, G. D. *Methods Enzymol.* **1973**, *27*, 675; c) Beychok, S. *Science* **1966**, *154*, 1288. (d) Lees, J. G.; Miles, A. J.; Wien, F.; Wallace, B. A. *Bioinformatics* **2006**, *22*, 1955. (e) Chothia, C. *J. Mol. Biol.* **1973**, *75*, 295. (f) Whitmore, L.; Woollett, B.; Miles, A. J.; Klose, D. P.; Janes, Wallace, R. W.; B. A. *Nucleic Acids Res.* **2011**, *39*, 480. (g) Woollett, B.; Whitmore, L.; Janes, R. W.; Wallace, B. A. *Nucleic Acids*

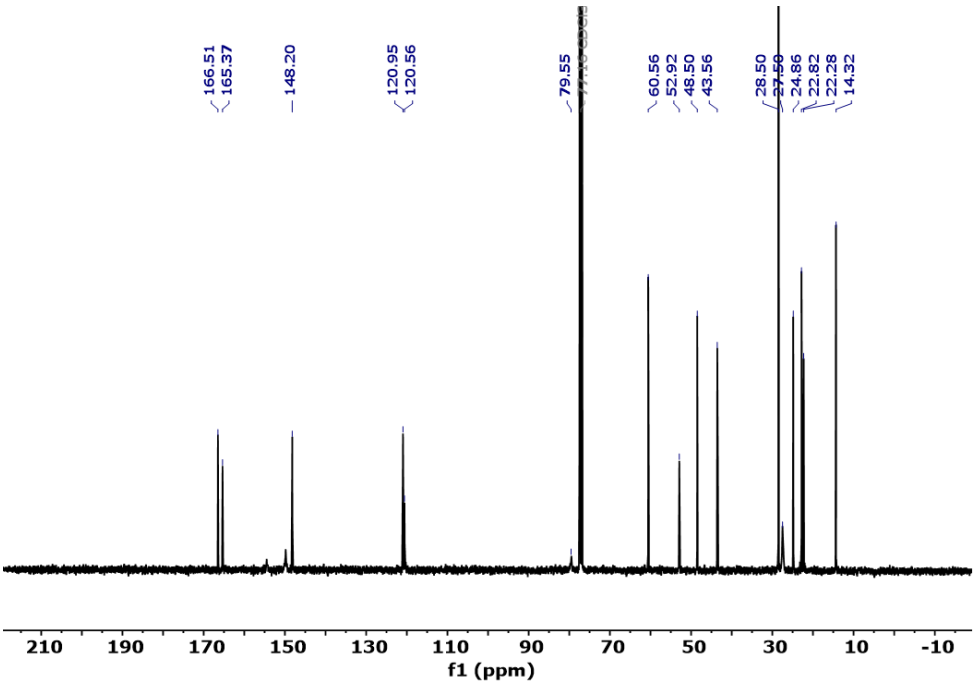
Res. **2013**, *41*, 417. (h) Greenfield, N. J. *Nat. Protoc.* **2007**, *1*, 2876. (i) Holzwarth, G.; Doty, P. *J. Am. Chem. Soc.* **1965**, *87*, 218.

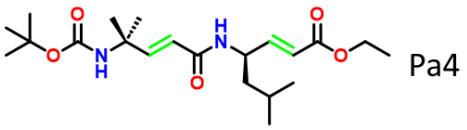
12. Misra, R.; Saseendran, A.; George, G.; Veeresh, K.; Raja, K. M. P.; Raghothama, S.; Hofmann, H.-J.; Gopi, H. N. *Chem. Eur. J.* **2017**, *23*, 3764.
13. Veeresh, K.; Singh, M.; Gopi, H. N. *Org Biomol Chem* **2019**, *17*, 9226.
14. (a) Allen, T. W.; Andersen, O. S.; Roux, B. *Proc. Natl. Acad. Sci. U. S. A.* **2004**, *101*, 117. (b) Diamanti, E.; Gutiérrez-Pineda, E.; Politakos, N.; Andreozzi, P.; Rodriguez-Presa, M. J.; Knoll, W.; Azzaroni, O.; C. A. Gervasi, C. A.; Moya, S. E. *Soft Matter* **2017**, *13*, 8922. (c) Chattopadhyay, S.; Rawat, S.; Greathouse, D. V.; Kelkar, D. A.; Koeppe, R. E. *Biophys. J.* **2008**, *95*, 166. (d) Sun, D.; He, S.; Bennett, W. F. D.; Bilodeau, C. L.; Andersen, O. S.; Lightstone, F. C.; Ingólfsson, H, I. *J. Chem. Theory Comput.* **2021**, *17*, 7. (e) Kelkar, D. A.; Chattopadhyay A. *Biochim. Biophys. Acta - Biomembr.* **2007**, *1768*, 2011. (f) Beaven, A. H.; Sodt, A. J.; Pastor, R. W.; Koeppe, R. E.; Andersen, O. S.; Im, W. *J. Chem. Theory Comput.* **2017**, *13*, 5054. (g) Beaven, A. H.; Maer, A. M.; Sodt, A. J.; Rui, H.; Pastor, R. W.; Andersen, O. S.; Im, W. *Biophys. J.* **2017**, *112*, 1185. (h) Miloshevsky, G. V.; Jordan, P. C. *Biophys. J.* **2004**, *86*, 92. (i) Stevenson, P.; Tokmakoff, A. *Proc. Natl. Acad. Sci. U. S. A.* **2017**, *114*, 10840. (j) Lundbaek, J. A.; Andersen, O.S. *Biophys. J.* **1999**, *76*, 889.
15. (a) Qi, S.; Zhang, C.; Yu, H.; Zhang, J.; Yan, T.; Lin, Z.; Yang, B.; Dong, Z. *J. Am. Chem. Soc.* **2021**, *143*, 328. (b) Lang, C.; Li, W.; Dong, Z.; Zhang, X.; Yang, F.; Yang, B.; Deng, X.; Zhang, C.; Xu, J.; Liu, J. *Angew. Chem. Int. Ed.* **2016**, *55*, 9723. (c) Zheng, S.; Huang, L.; Sun, Z.; Barboiu, M. *Angew. Chem. Int. Ed.* **2021**, *60*, 566. (d) Xin, P.; Kong, H.; Sun, Y.; Zhao, L.; Fang, H.; Zhu, H.; Jiang, T.; Guo, J.; Zhang, Q.; Dong, W.; Chen, C. *Angew. Chem. Int. Ed.* **2019**, *58*, 2779. (e) Bai, D.; Yan, T.; Wang, S.; Wang, Y.; Fu, J.; Fang, X.; Zhu, J.; Liu, J. *Angew. Chem. Int. Ed.* **2020**, *59*, 13602.
16. (a) Dutta, S.; Watson, B.; Mattoo, S.; Rochet, J.-C. *Bio-Protoc.*, **2020**, *10*, e3690. (b) Biron, E.; Otis, F.; Meillon, J.-C.; Robitaille, M.; Lamothe, J.; Van Hove, P.; Cormier, M.-E.; Voyer, N. *Bioorg. Med. Chem.* **2004**, *12*, 1279. (c) Otis, F.; Auger, M.; Voyer, N. *Acc. Chem. Res.* **2013**, *46*, 2934.

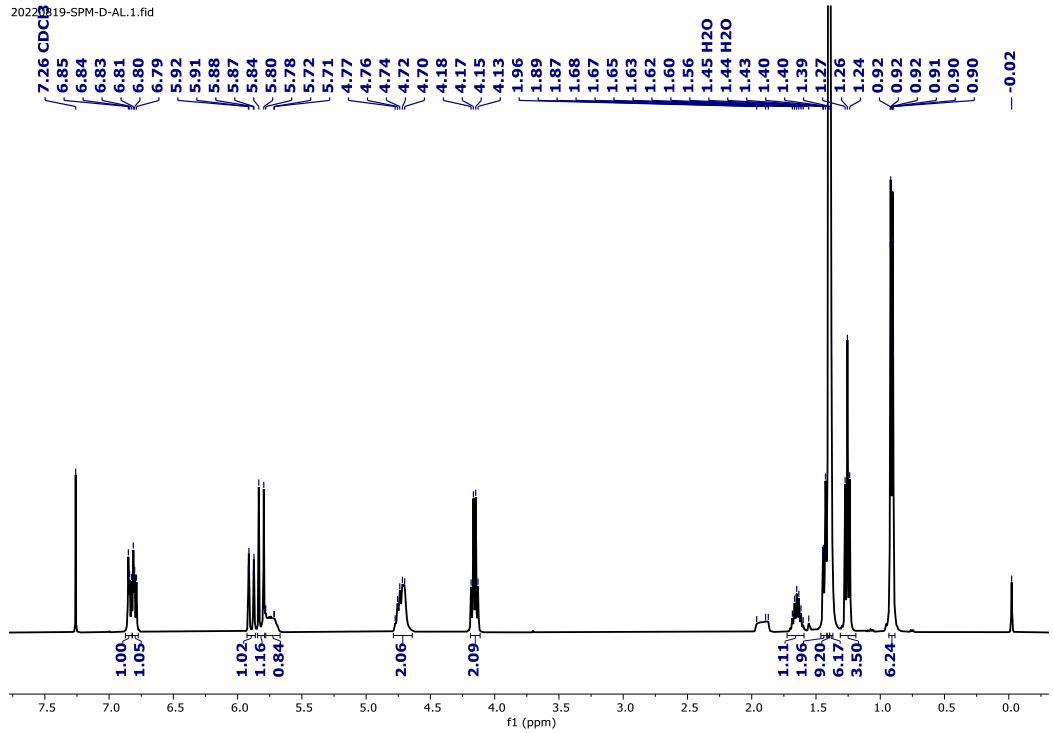
2.12. ^{1}H, ^{13}C NMR, and Mass spectra of Peptides P1-P4

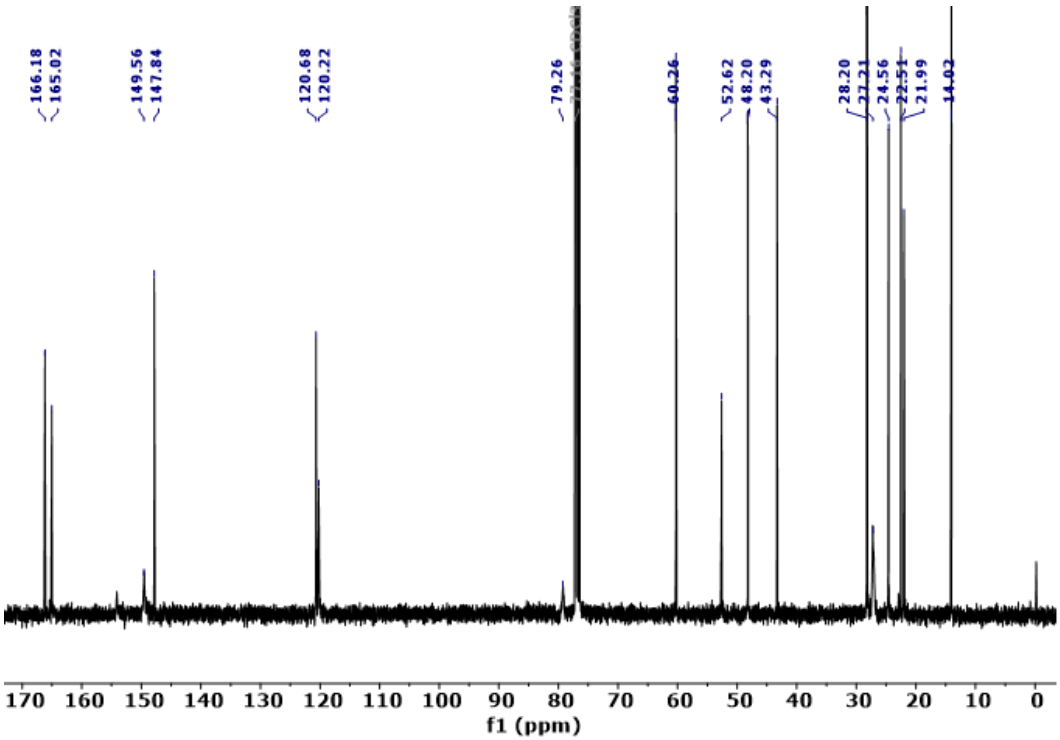


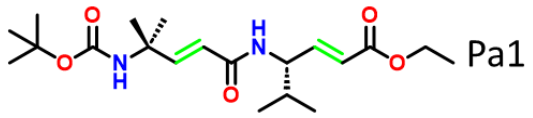


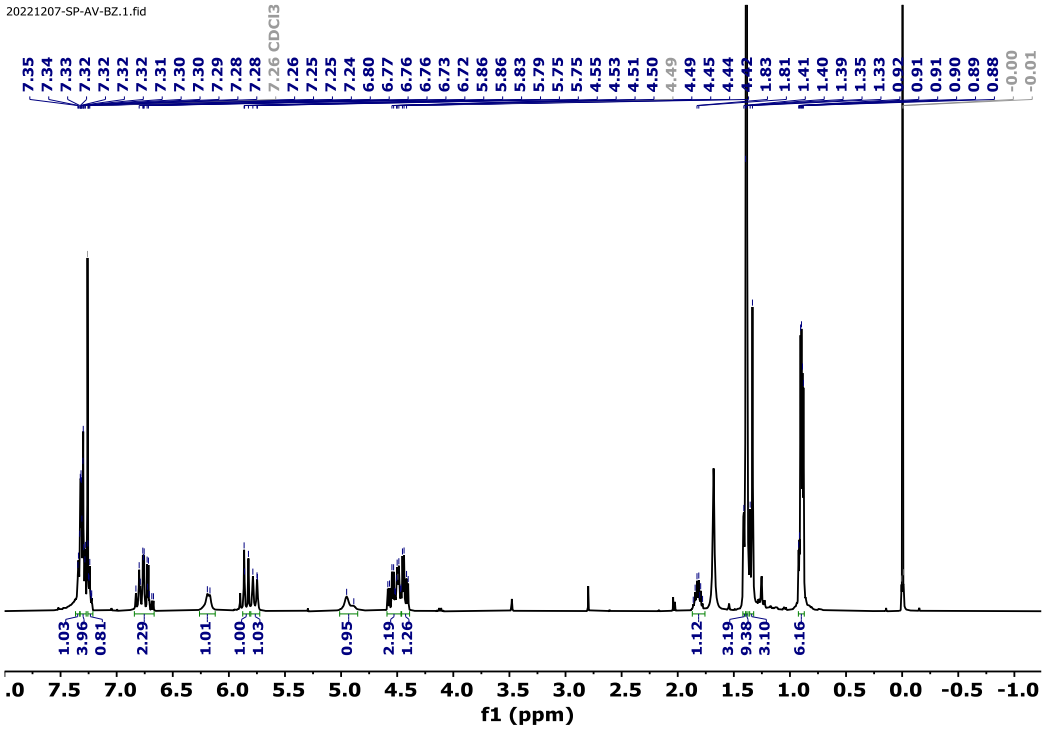


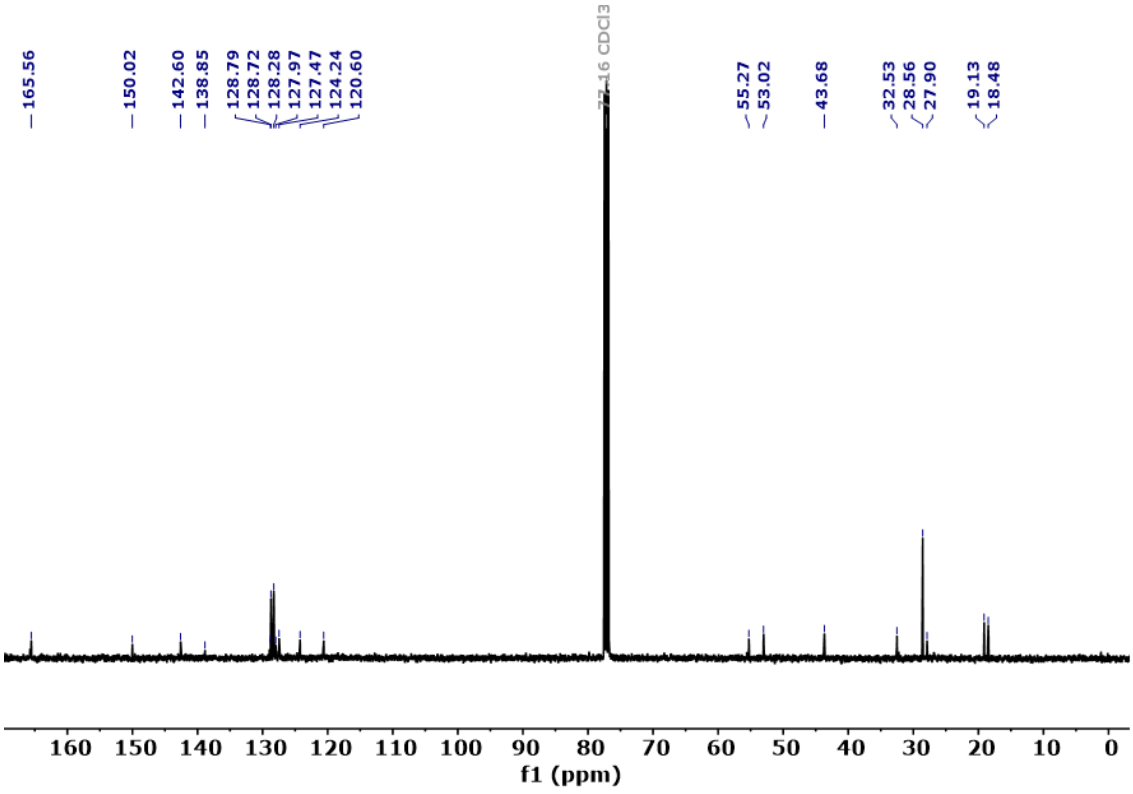

Pa4


20220819-SPM-D-AL.1.fid
7.26 CDCl3
6.85 6.84 6.83 6.81 6.80 6.79 5.92 5.91 5.88 5.87 5.84 5.80 5.78 5.72 5.71 4.77 4.76 4.74 4.72 4.70 4.18 4.17 4.15 4.13 1.96 1.89 1.87 1.68 1.67 1.65 1.63 1.62 1.60 1.56 1.45 H2O 1.44 H2O 1.43 1.40 1.40 1.39 1.27 1.26 1.24 0.92 0.92 0.92 0.91 0.90 0.90 -0.02
1.00 1.05 1.02 1.16 0.84 2.06 2.09 1.11 1.96 9.20 6.17 3.50 6.24
7.5 7.0 6.5 6.0 5.5 5.0 4.5 4.0 3.5 3.0 2.5 2.0 1.5 1.0 0.5 0.0
f1 (ppm)

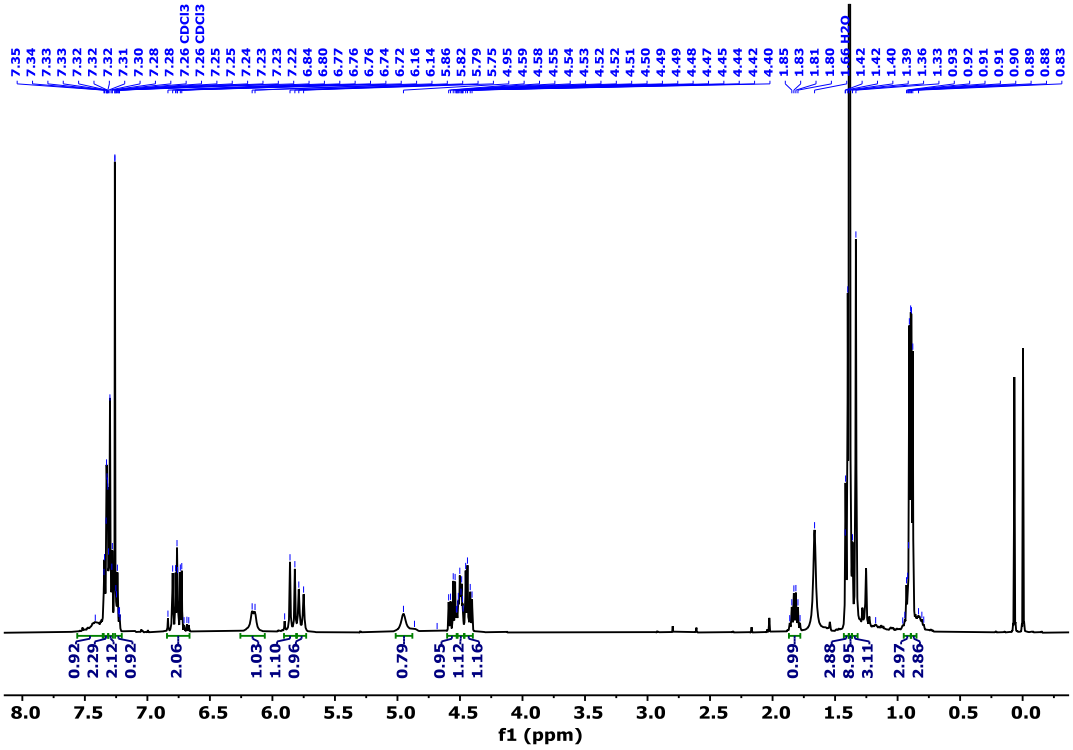

166.18 165.02 149.56 147.84 120.68 120.22 79.26 60.26 52.62 48.20 43.29 28.20 27.21 24.56 22.51 21.99 14.02
170 160 150 140 130 120 110 100 90 80 70 60 50 40 30 20 10 0
f1 (ppm)

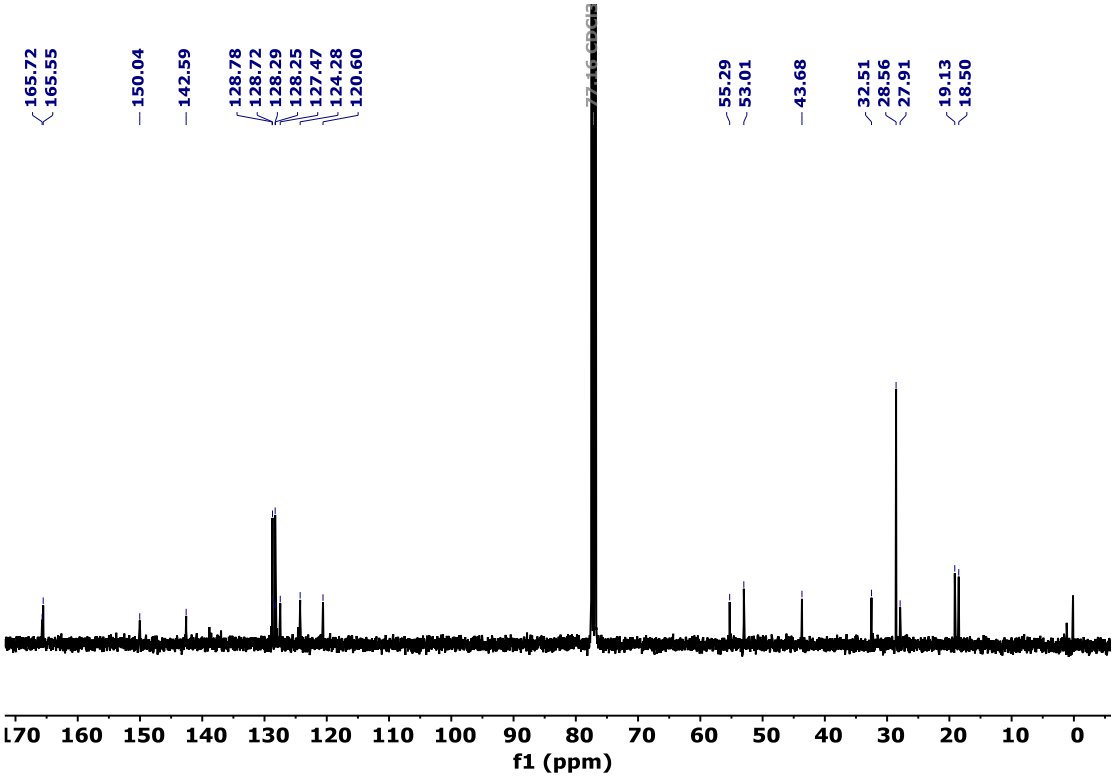

Pa1

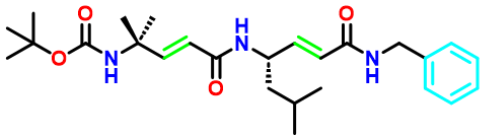

20221207-SP-AV-BZ.1.fid
f1 (ppm)


f1 (ppm)

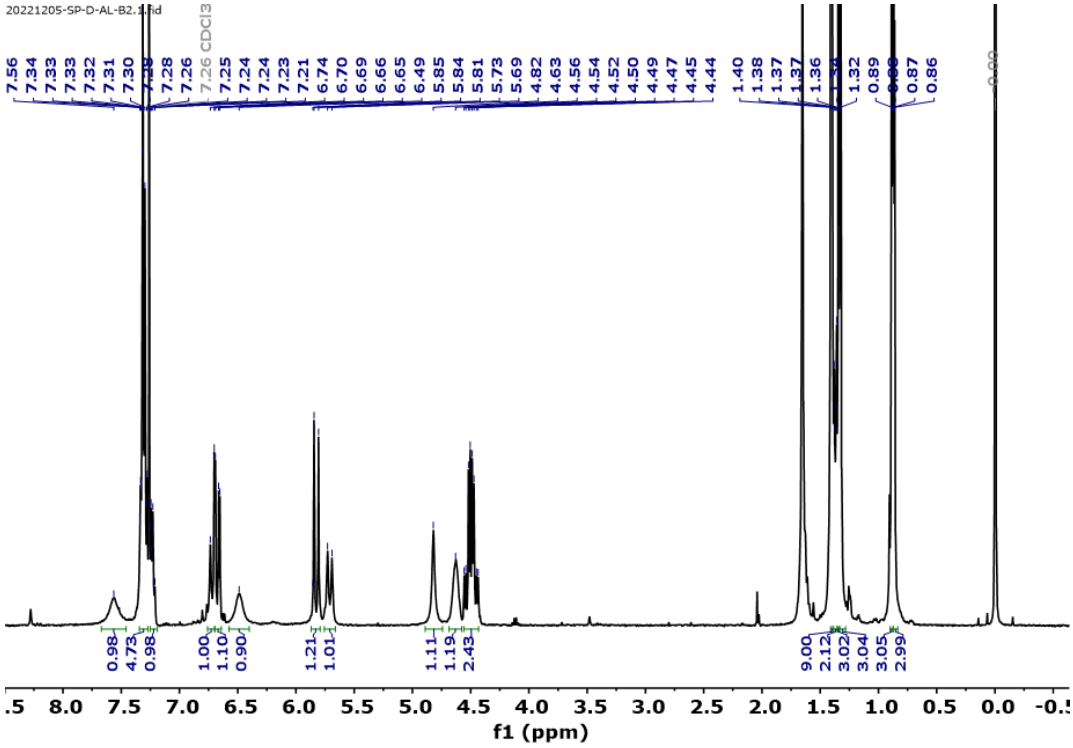

Pa2

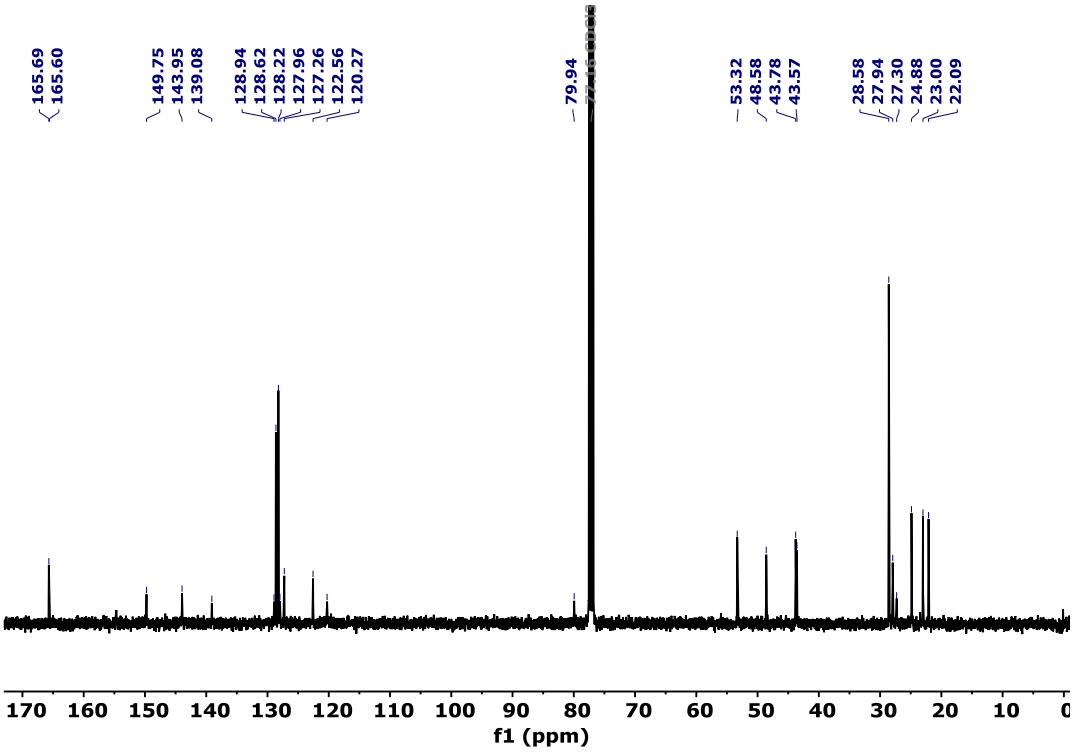

f1 (ppm)

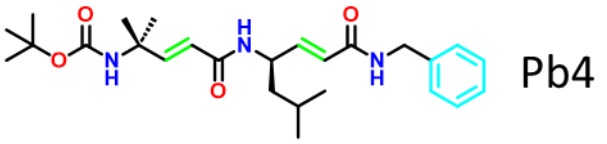

f1 (ppm)



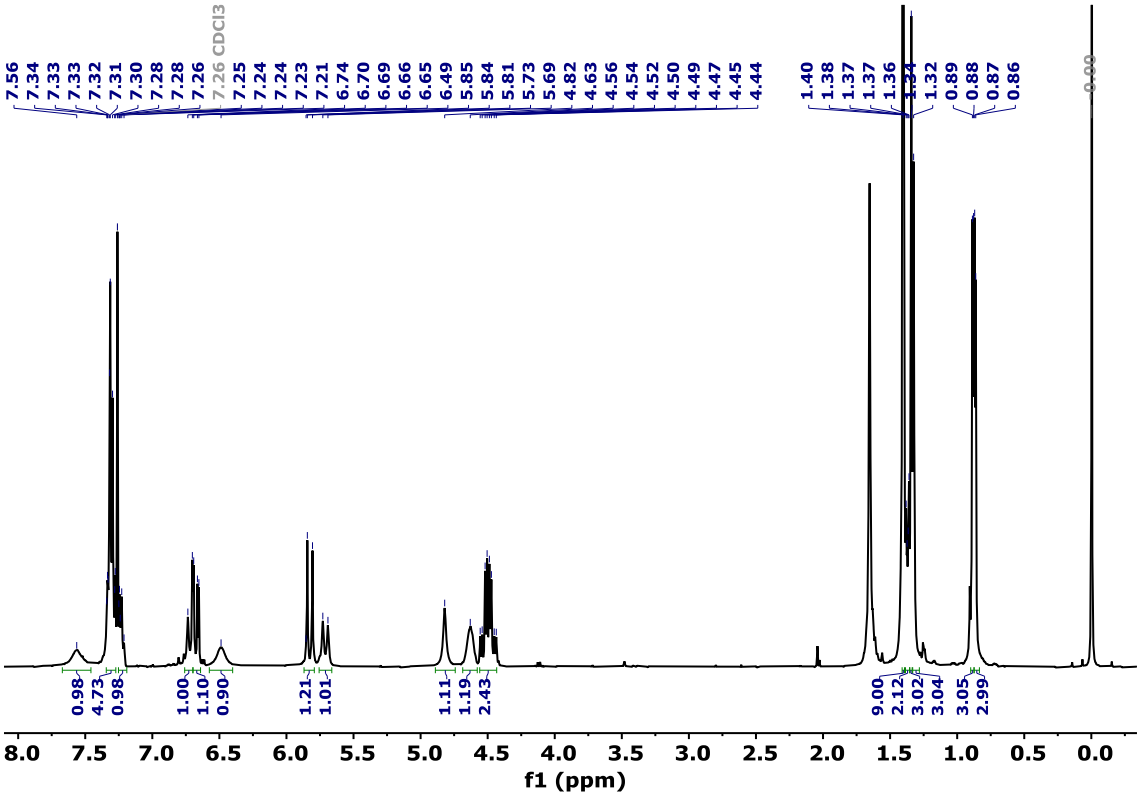
Pb3

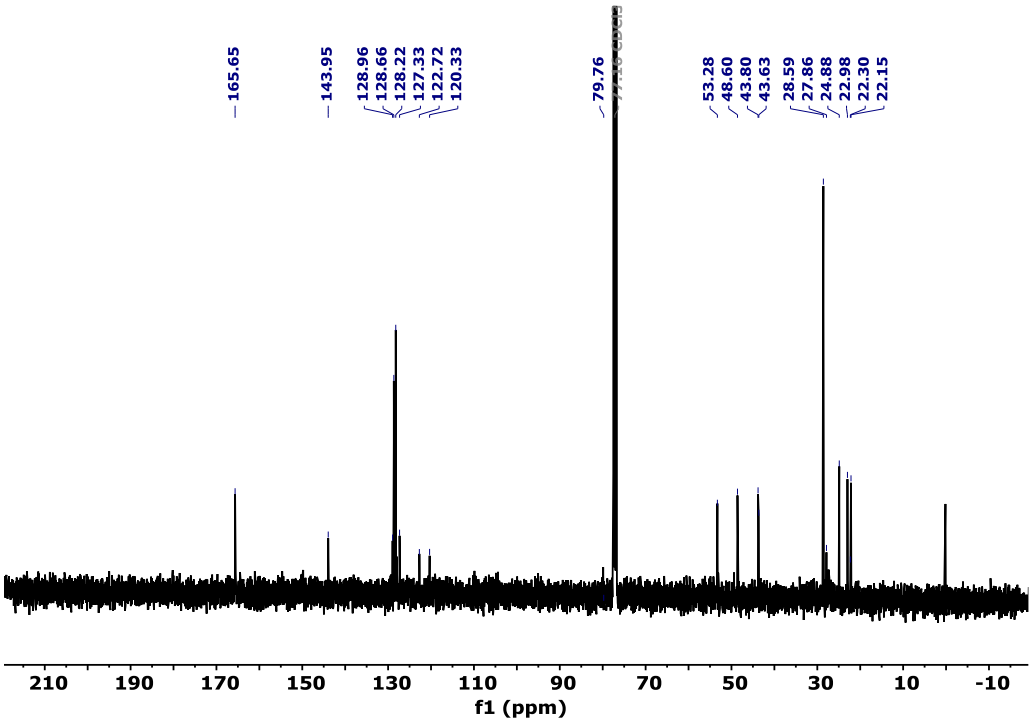

20221205-SP-D-AL-B2.1.fid
7.56 7.34 7.33 7.33 7.32 7.31 7.30 7.28 7.28 7.26 7.26 CDCl3 7.25 7.24 7.24 7.23 7.21 6.74 6.70 6.69 6.66 6.65 6.49 5.85 5.84 5.81 5.73 5.69 4.82 4.63 4.56 4.54 4.52 4.50 4.49 4.47 4.45 4.44 1.40 1.38 1.37 1.37 1.36 1.32 0.89 0.88 0.87 0.86 0.00
0.98 4.73 0.98 1.00 1.10 0.90 1.21 1.01 1.11 1.19 2.43 9.00 2.12 3.02 3.04 3.05 2.99
f1 (ppm)

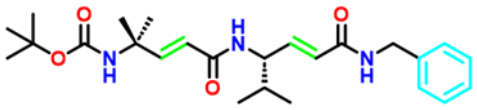

165.69 165.60 149.75 143.95 139.08 128.94 128.62 128.22 127.96 127.26 122.56 120.27 79.94 53.32 48.58 43.78 43.57 28.58 27.94 27.30 24.88 23.00 22.09
f1 (ppm)



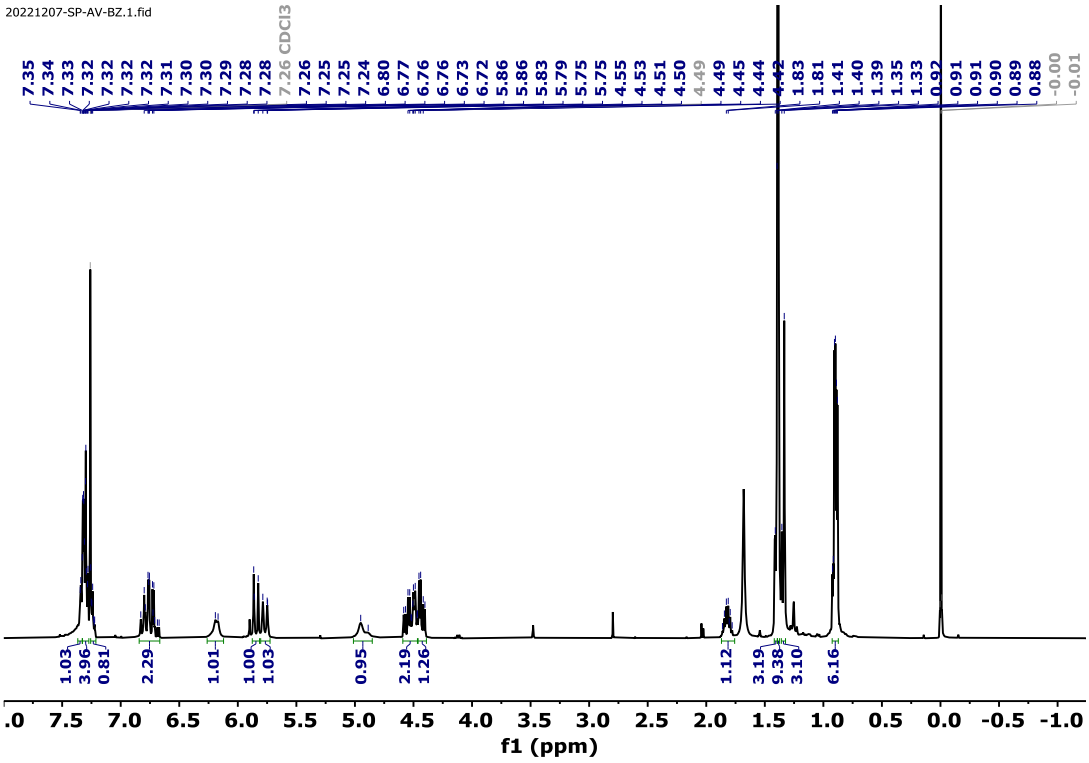
Pb4

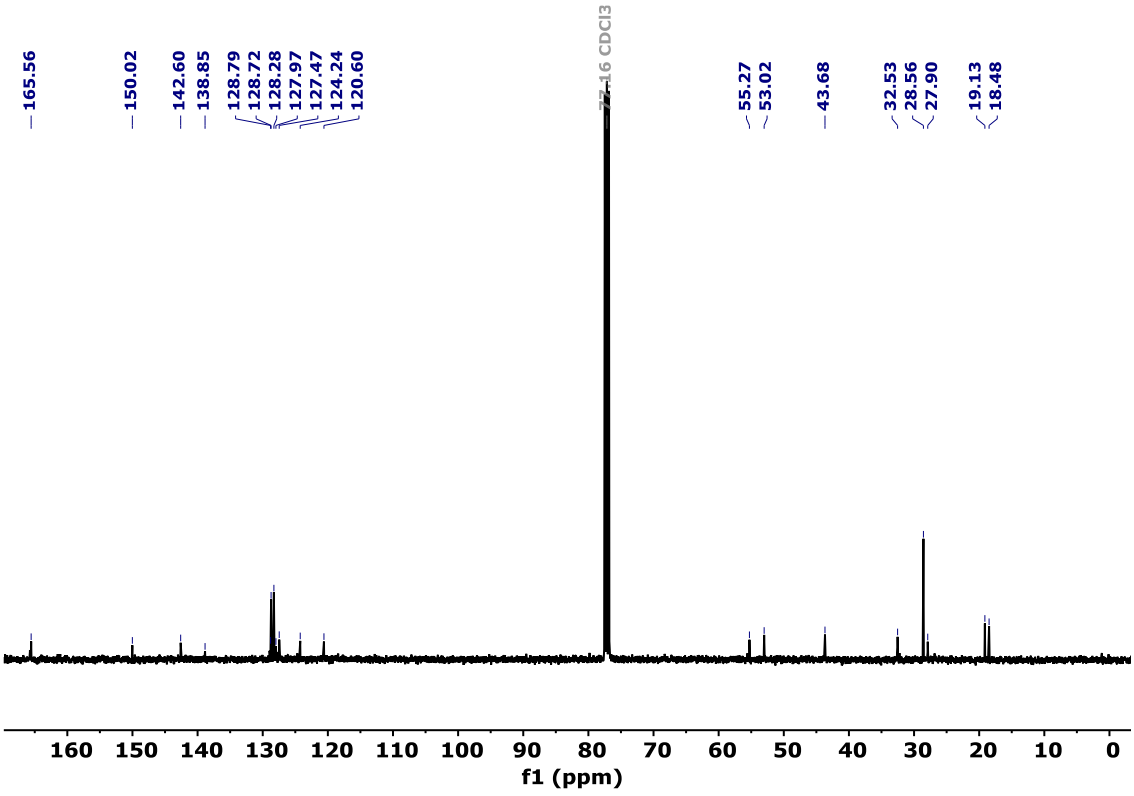

7.56
7.34
7.33
7.33
7.32
7.31
7.30
7.28
7.28
7.26
7.26 CDCl3
7.25
7.24
7.24
7.23
7.21
6.74
6.70
6.69
6.66
6.65
6.49
5.85
5.84
5.81
5.73
5.69
4.82
4.63
4.56
4.54
4.52
4.50
4.49
4.47
4.45
4.44
1.40
1.38
1.37
1.37
1.36
1.34
1.32
0.89
0.88
0.87
0.86
0.98
4.73
0.98
1.00
1.10
0.90
1.21
1.01
1.11
1.19
2.43
9.00
2.12
3.02
3.04
3.05
2.99
8.0 7.5 7.0 6.5 6.0 5.5 5.0 4.5 4.0 3.5 3.0 2.5 2.0 1.5 1.0 0.5 0.0
f1 (ppm)

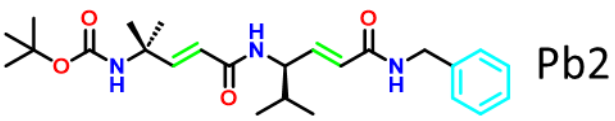

165.65
143.95
128.96
128.66
128.22
127.33
122.72
120.33
79.76
53.28
48.60
43.80
43.63
28.59
27.86
24.88
22.98
22.30
22.15
210 190 170 150 130 110 90 70 50 30 10 -10
f1 (ppm)

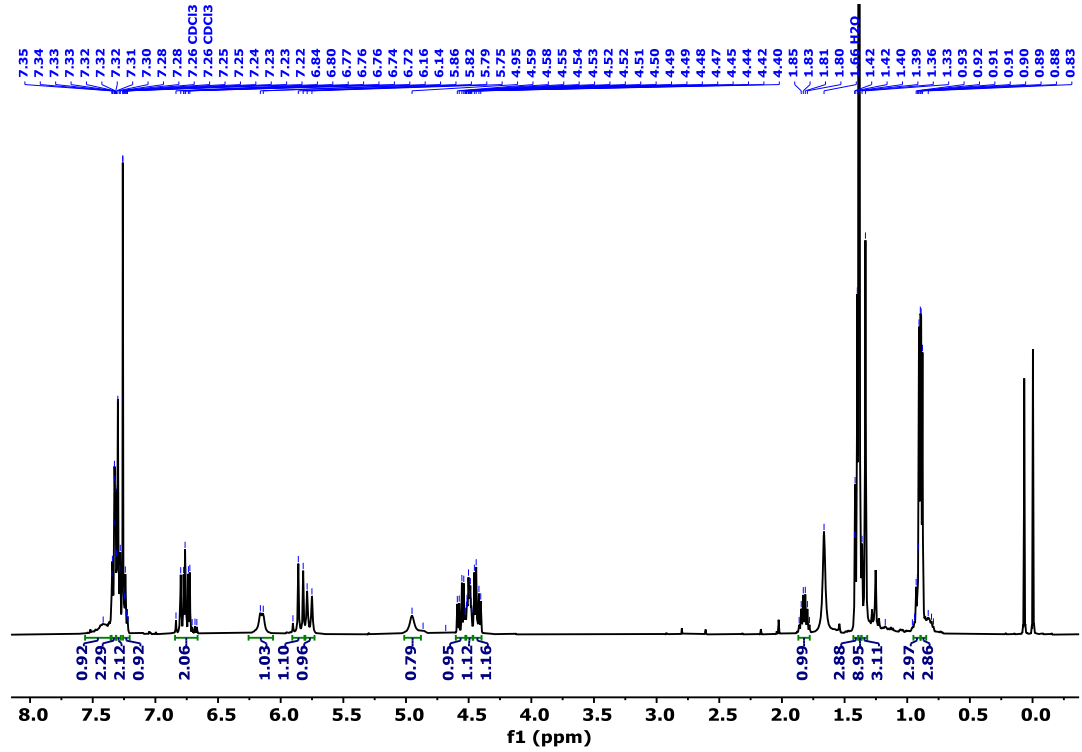


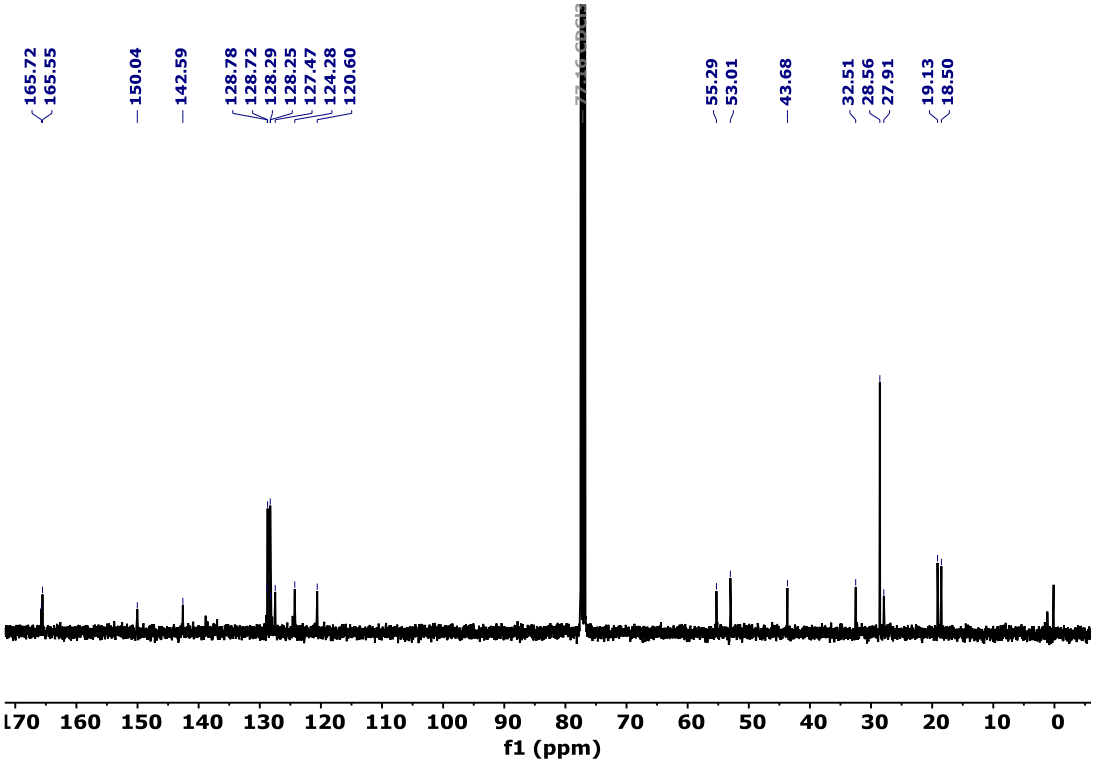
Pb1

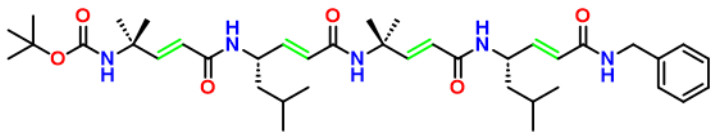




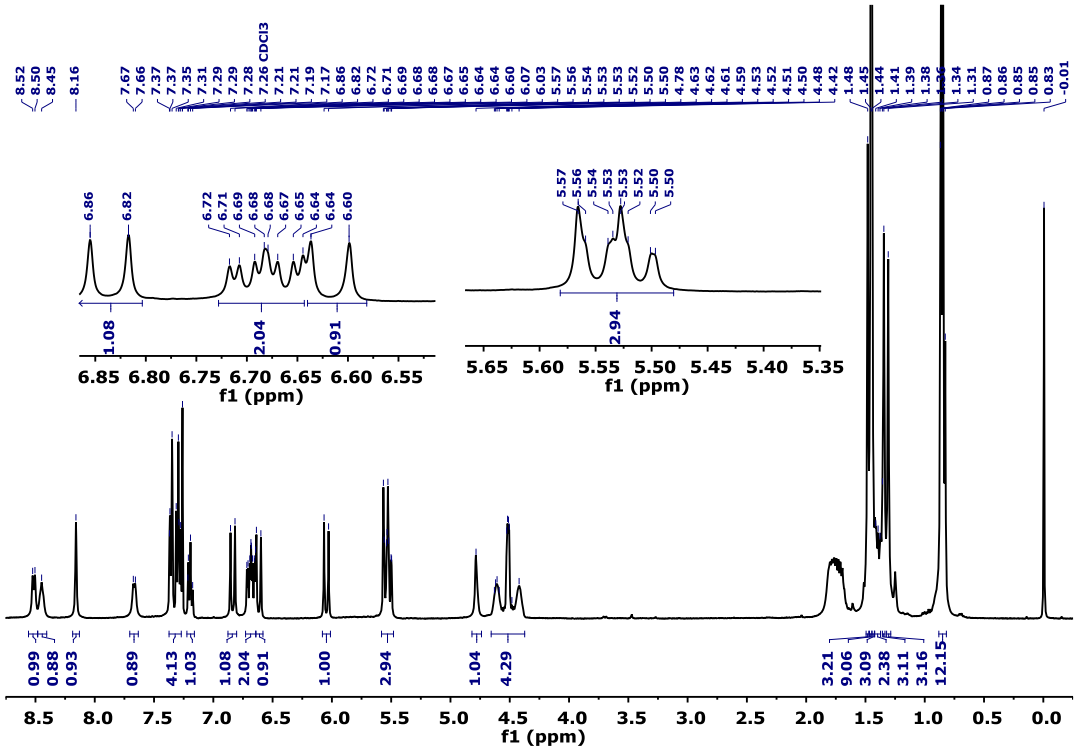

Pb2

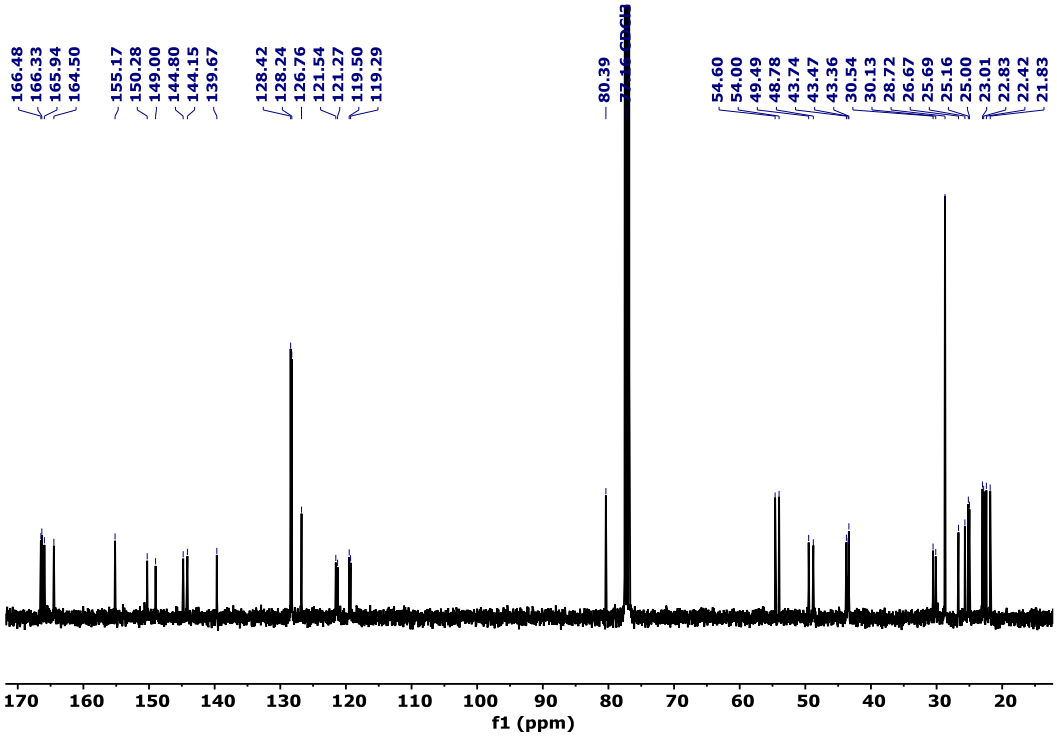

7.35 7.34 7.33 7.33 7.32 7.32 7.32 7.31 7.30 7.28 7.28 7.26 CDCl3 7.26 CDCl3 7.25 7.25 7.24 7.23 7.23 7.22 6.84 6.80 6.77 6.76 6.76 6.74 6.72 6.16 6.14 5.86 5.82 5.79 5.75 4.95 4.59 4.58 4.55 4.54 4.53 4.52 4.52 4.51 4.50 4.49 4.49 4.48 4.47 4.45 4.44 4.42 4.40 1.85 1.83 1.81 1.80 1.66 H2O 1.42 1.42 1.40 1.39 1.36 1.33 0.93 0.92 0.91 0.91 0.90 0.89 0.88 0.83
0.92 2.29 2.12 0.97 2.06 1.03 1.10 0.96 0.79 0.95 1.12 1.16 0.99 2.88 8.95 3.11 2.97 2.86
8.0 7.5 7.0 6.5 6.0 5.5 5.0 4.5 4.0 3.5 3.0 2.5 2.0 1.5 1.0 0.5 0.0
f1 (ppm)

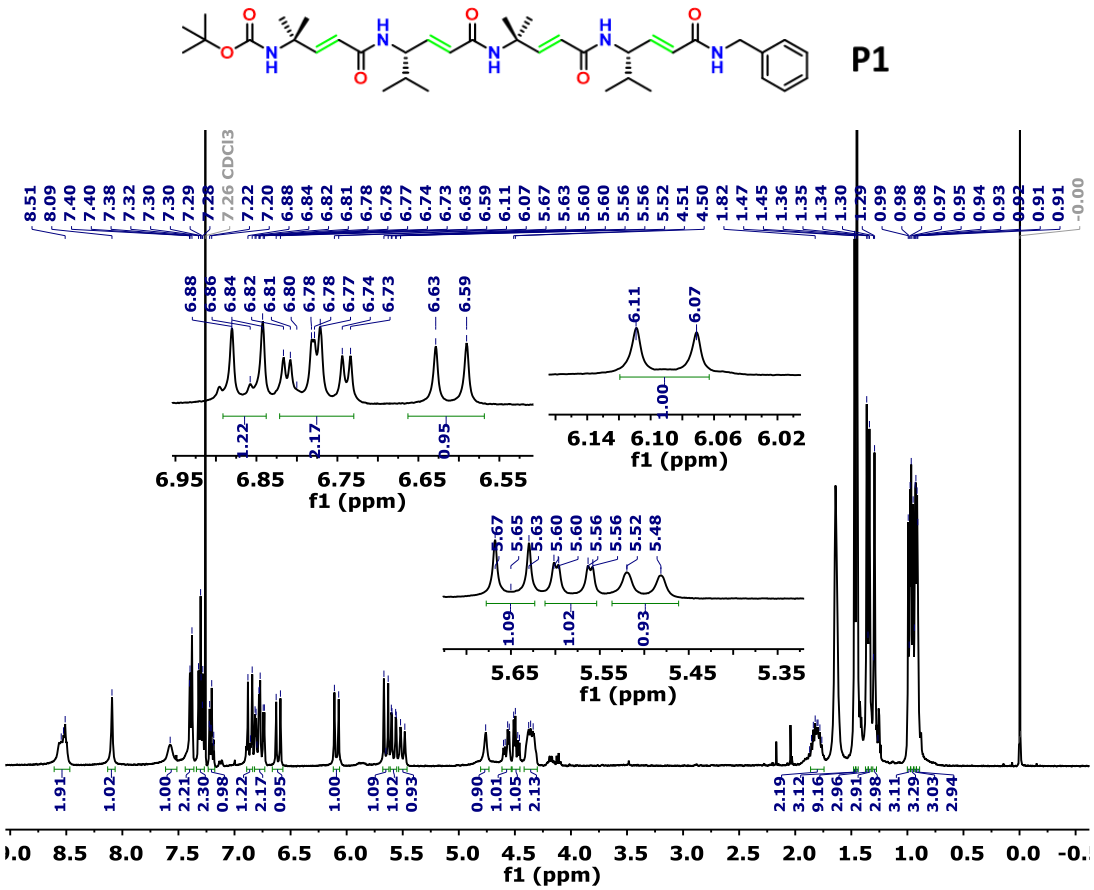

165.72 165.55 150.04 142.59 128.78 128.72 128.29 128.25 127.47 124.28 120.60 77.46 77.04 76.63 55.29 53.01 43.68 32.51 28.56 27.91 19.13 18.50
170 160 150 140 130 120 110 100 90 80 70 60 50 40 30 20 10 0
f1 (ppm)

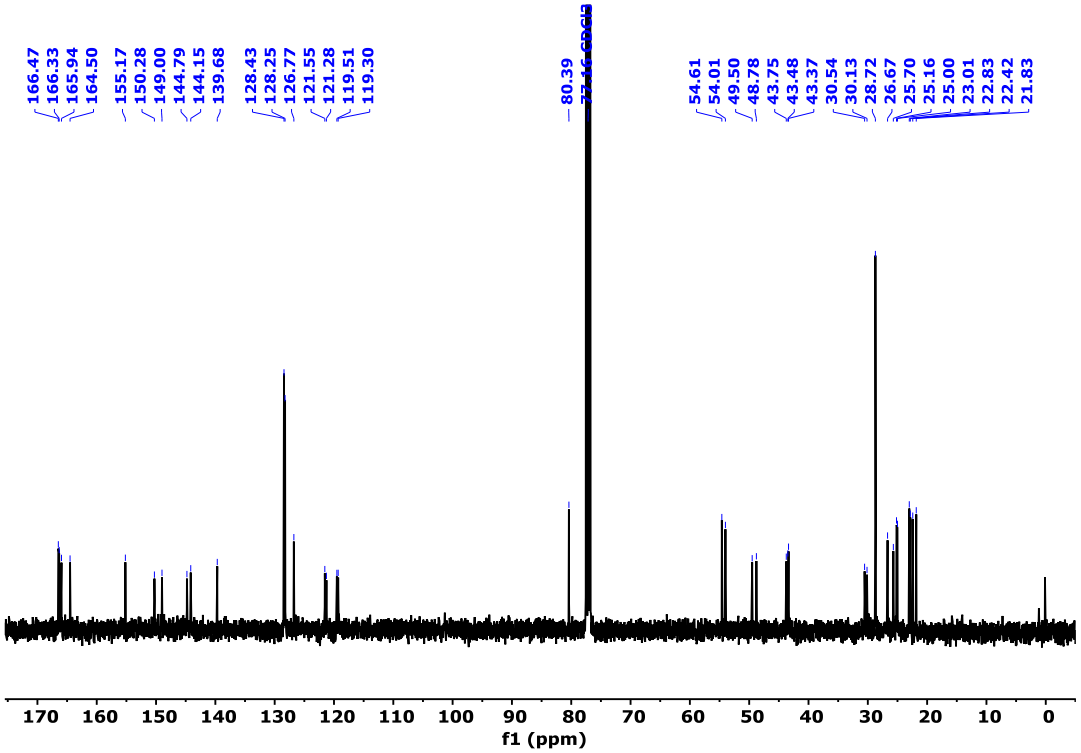


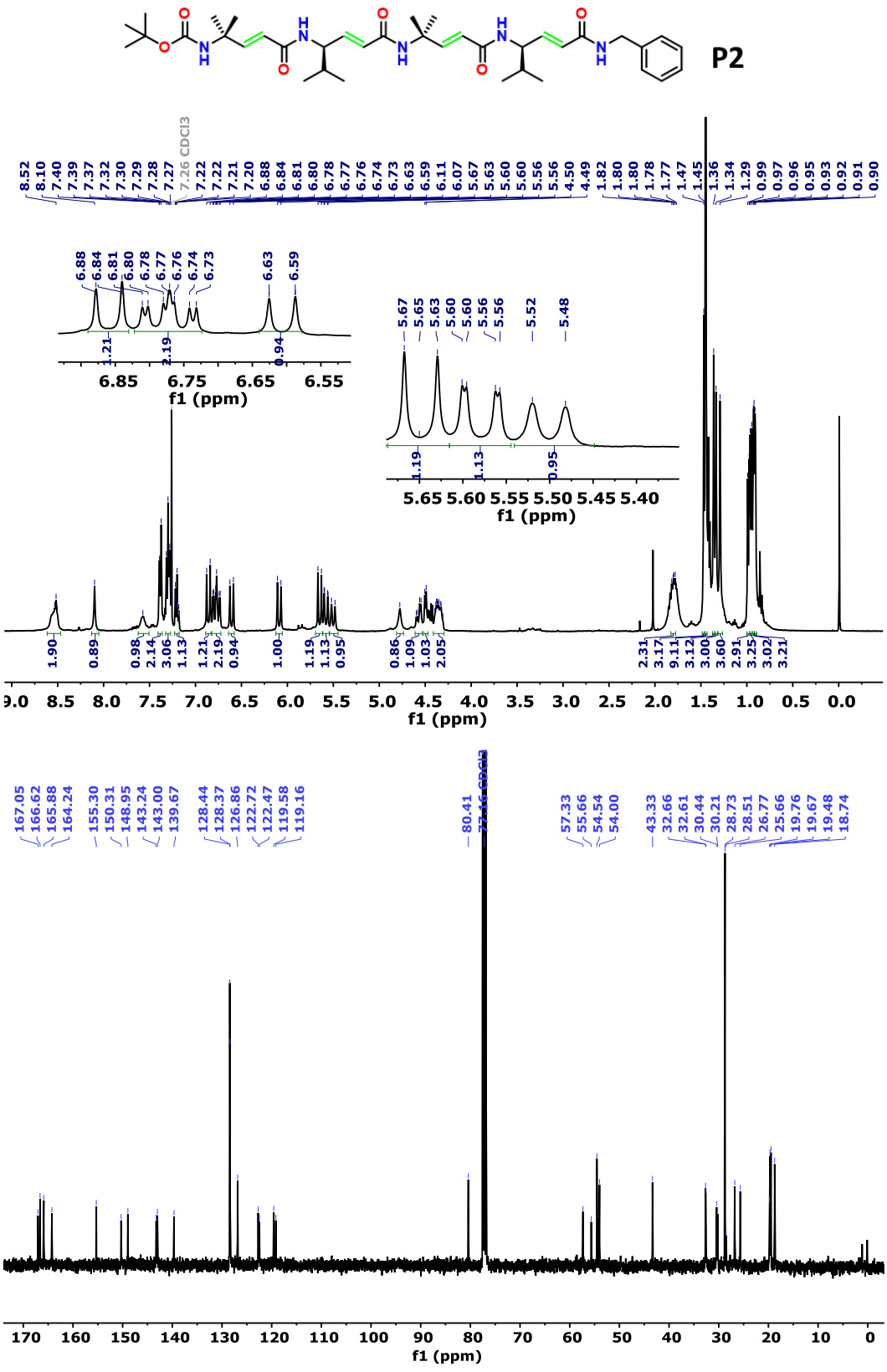
P3

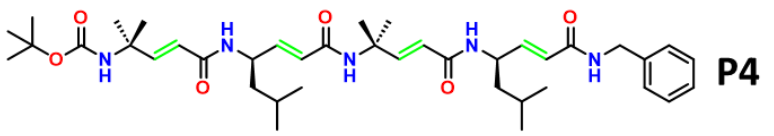


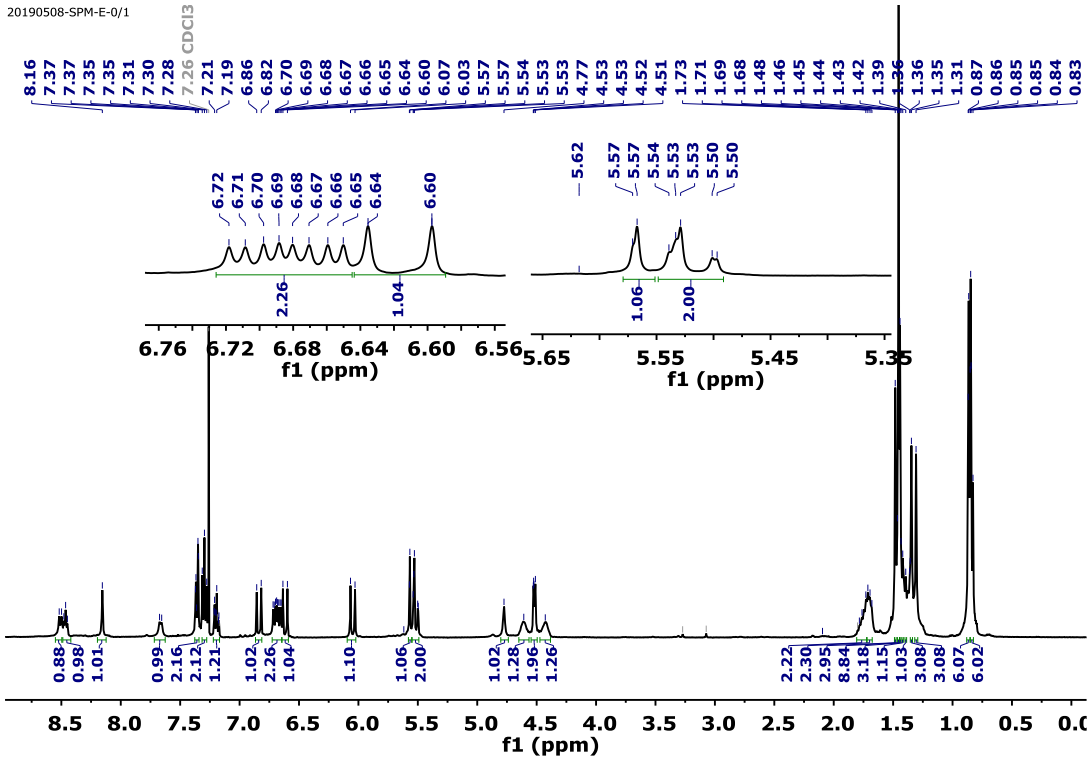


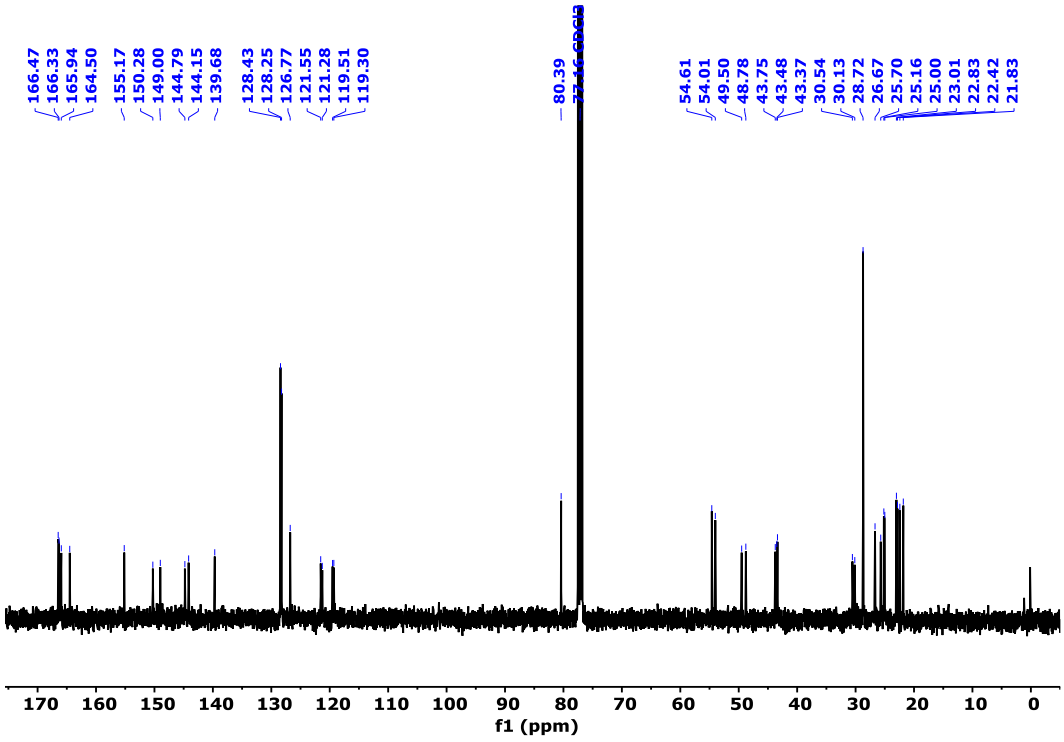

P1
f1 (ppm)

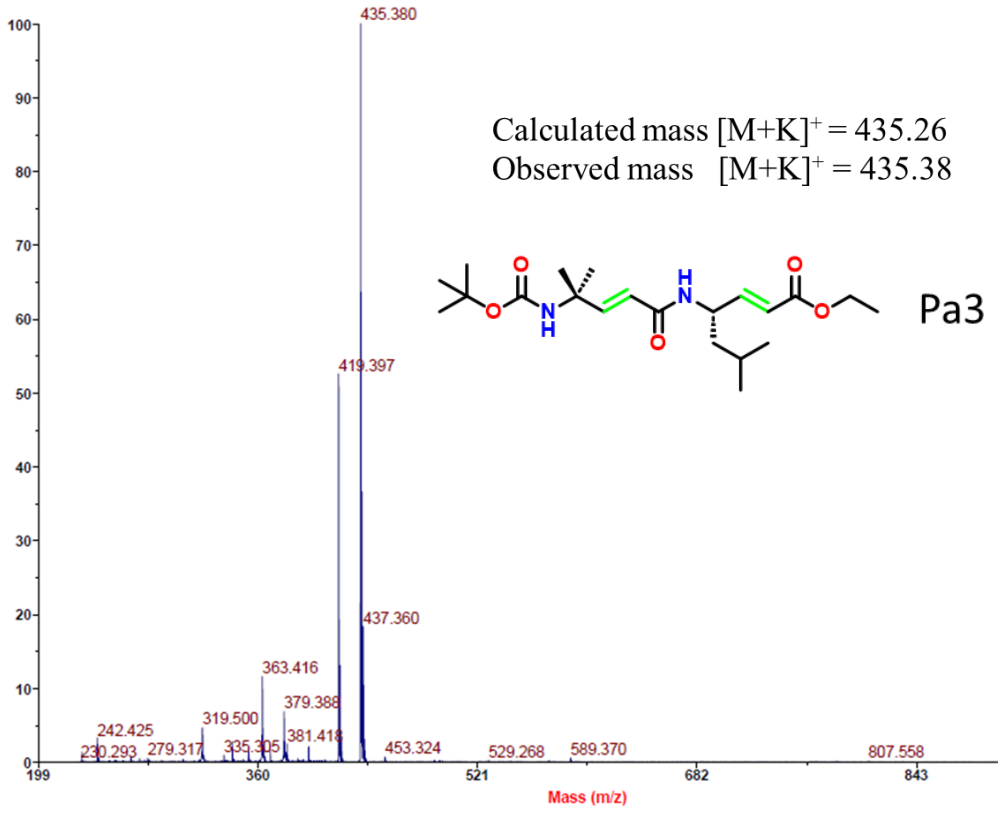

f1 (ppm)


P2
f1 (ppm)


P4

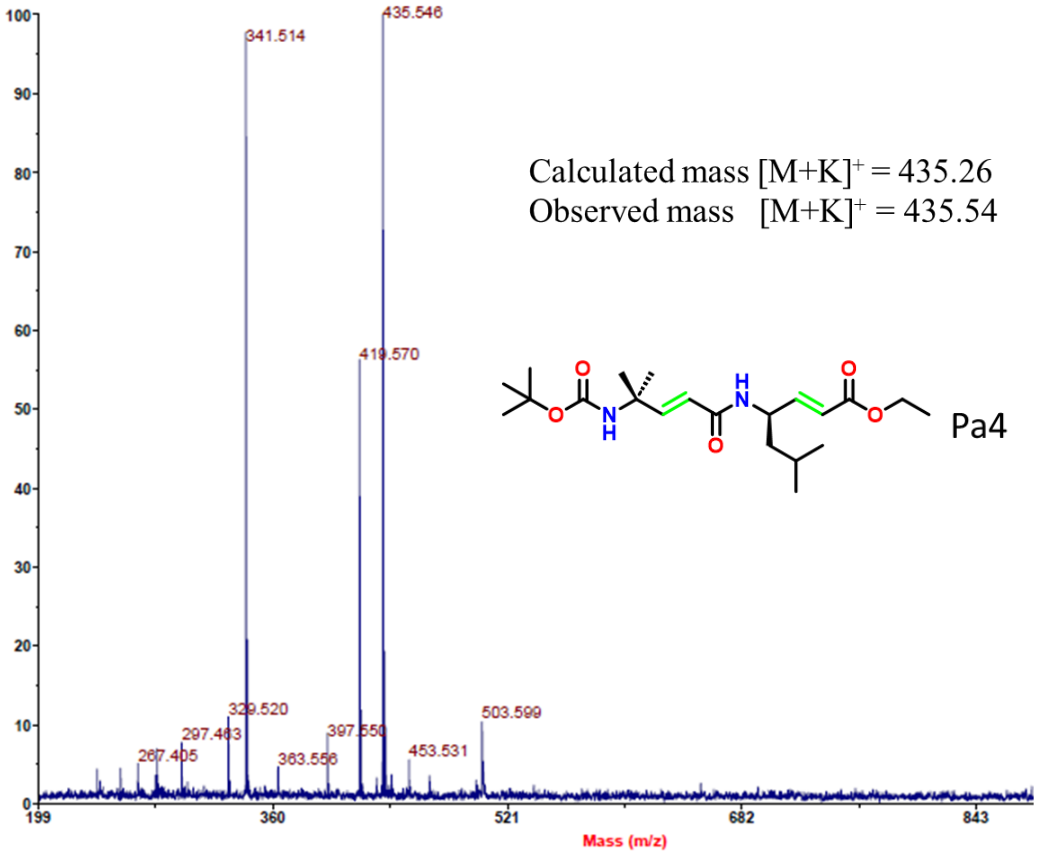

20190508-SPM-E-0/1
f1 (ppm)


f1 (ppm)



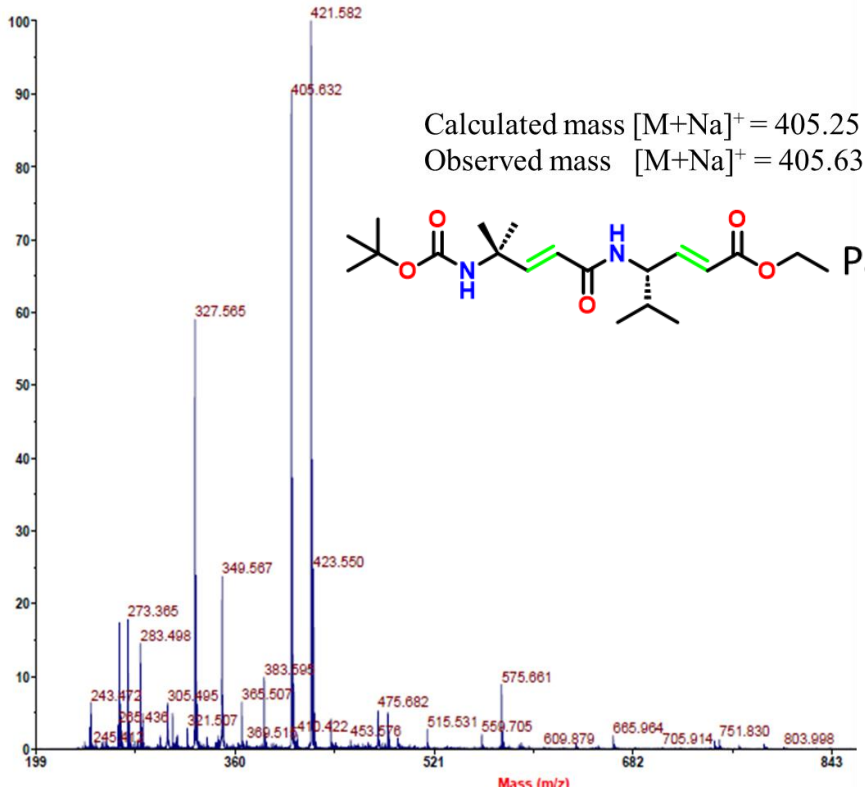
Calculated mass $[M+K]^+ = 435.26$
Observed mass $[M+K]^+ = 435.38$

Pa3



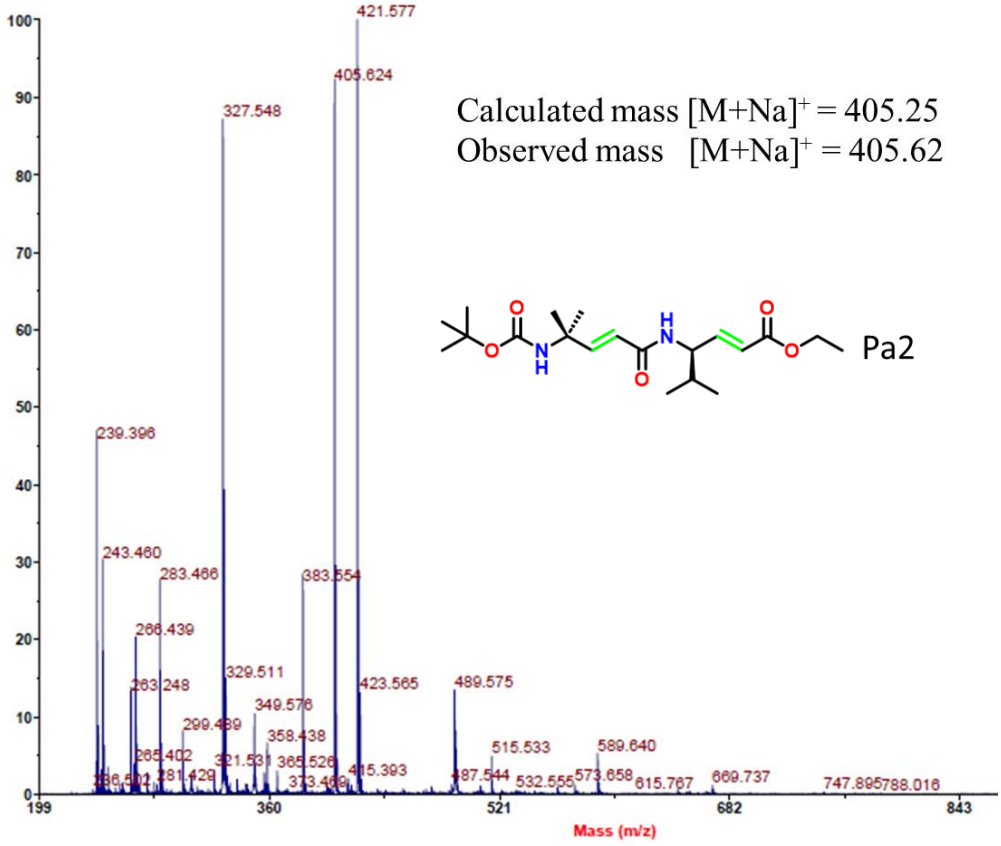
Calculated mass $[M+K]^+ = 435.26$
Observed mass $[M+K]^+ = 435.54$

Pa4



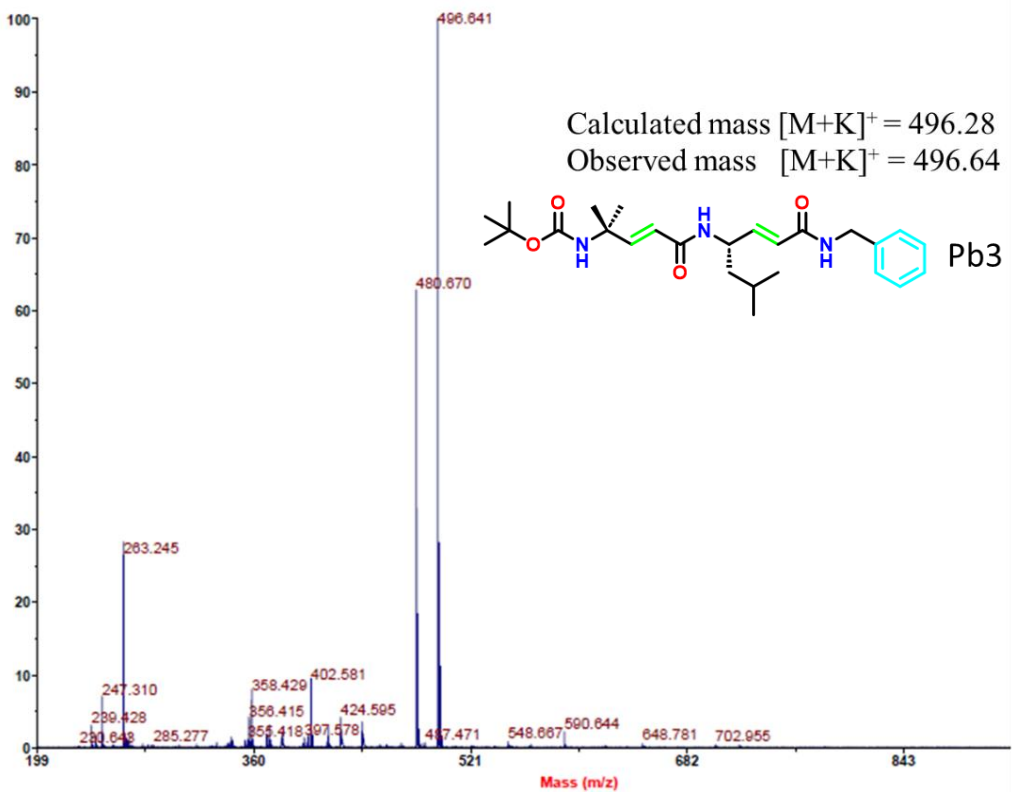
Calculated mass $[M+Na]^+ = 405.25$
Observed mass $[M+Na]^+ = 405.63$

Pa1



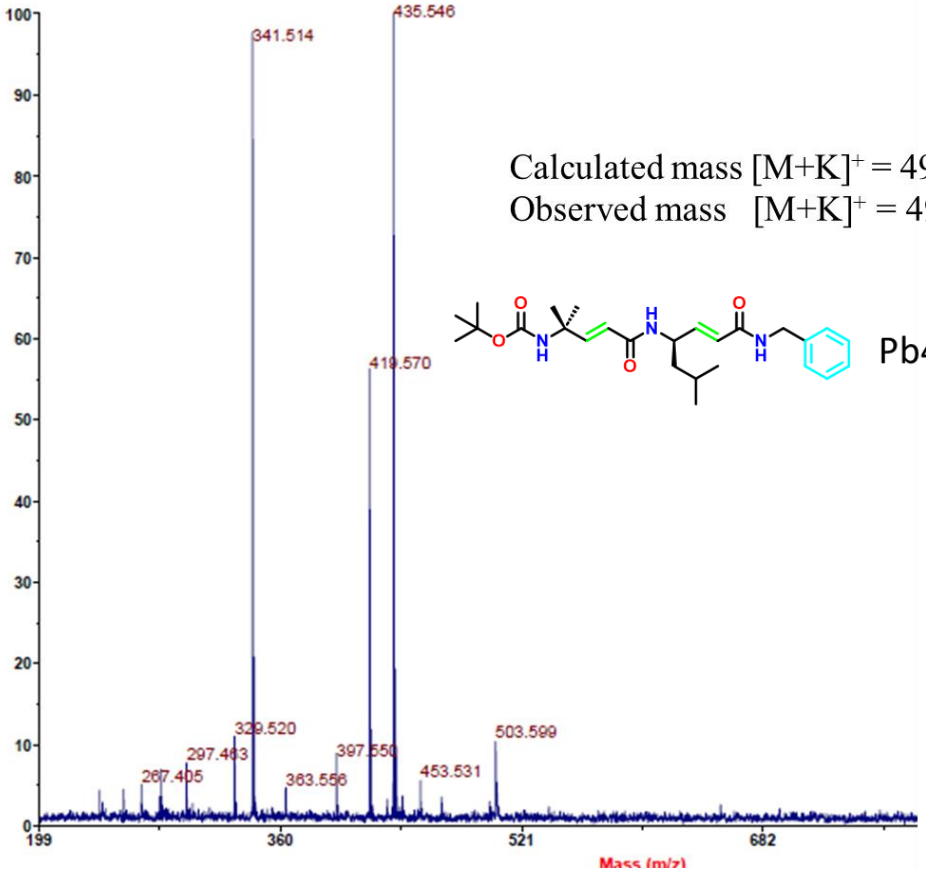
Calculated mass $[M+Na]^+ = 405.25$
Observed mass $[M+Na]^+ = 405.62$

Pa2



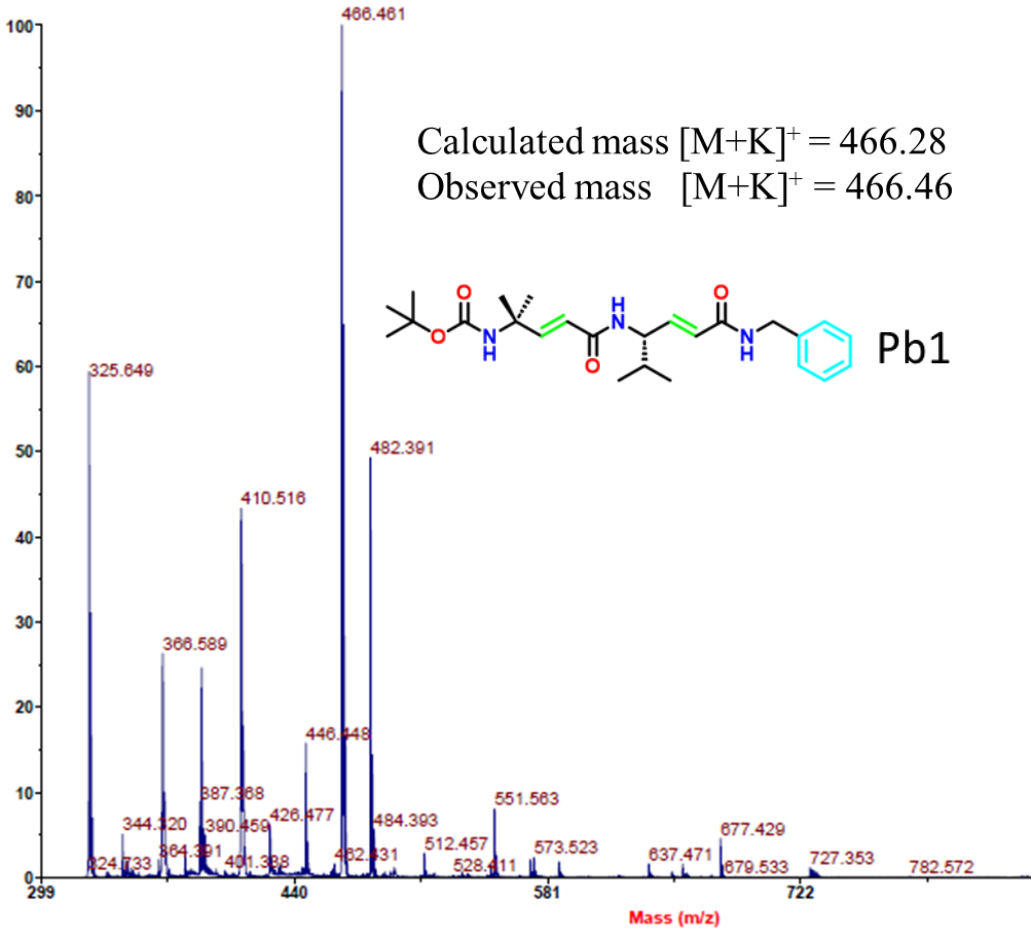
Calculated mass $[M+K]^+ = 496.28$
Observed mass $[M+K]^+ = 496.64$

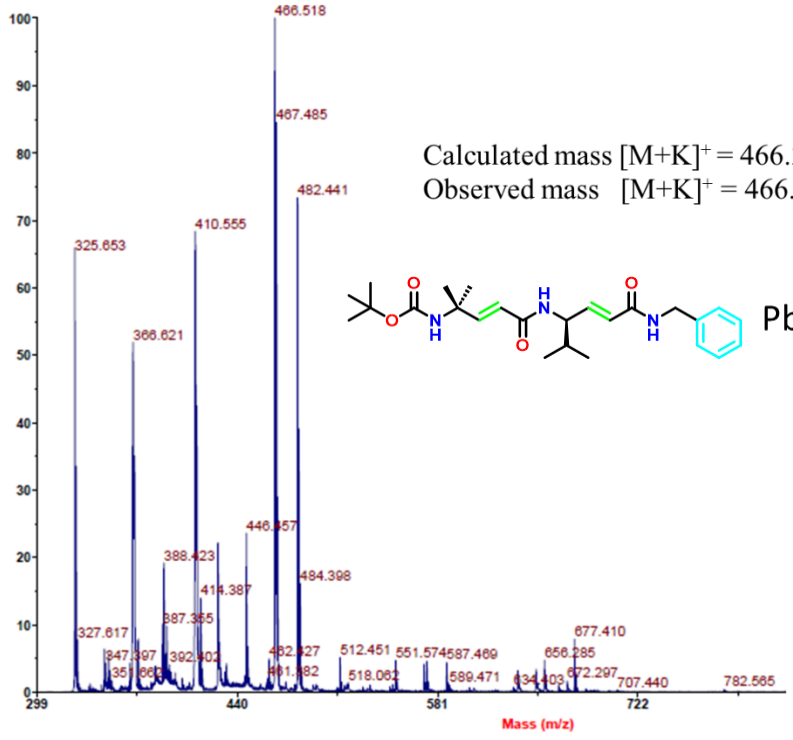
Pb3

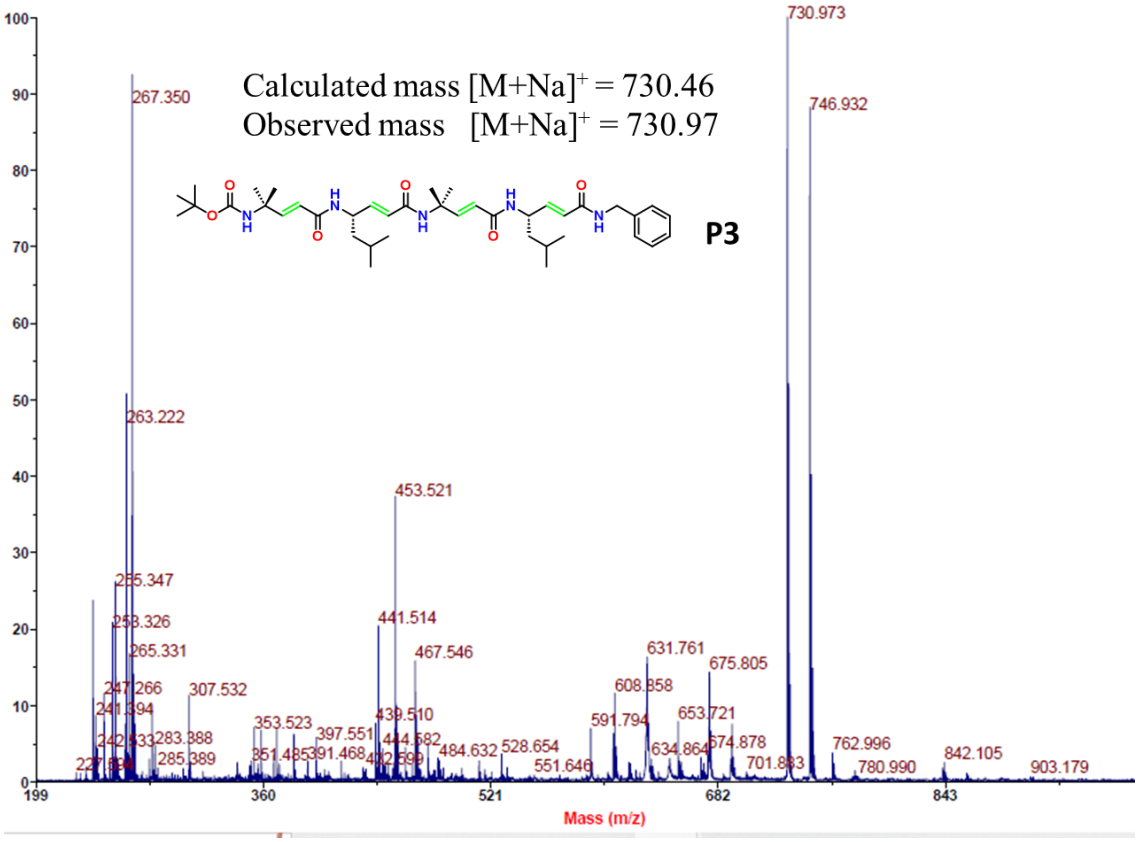


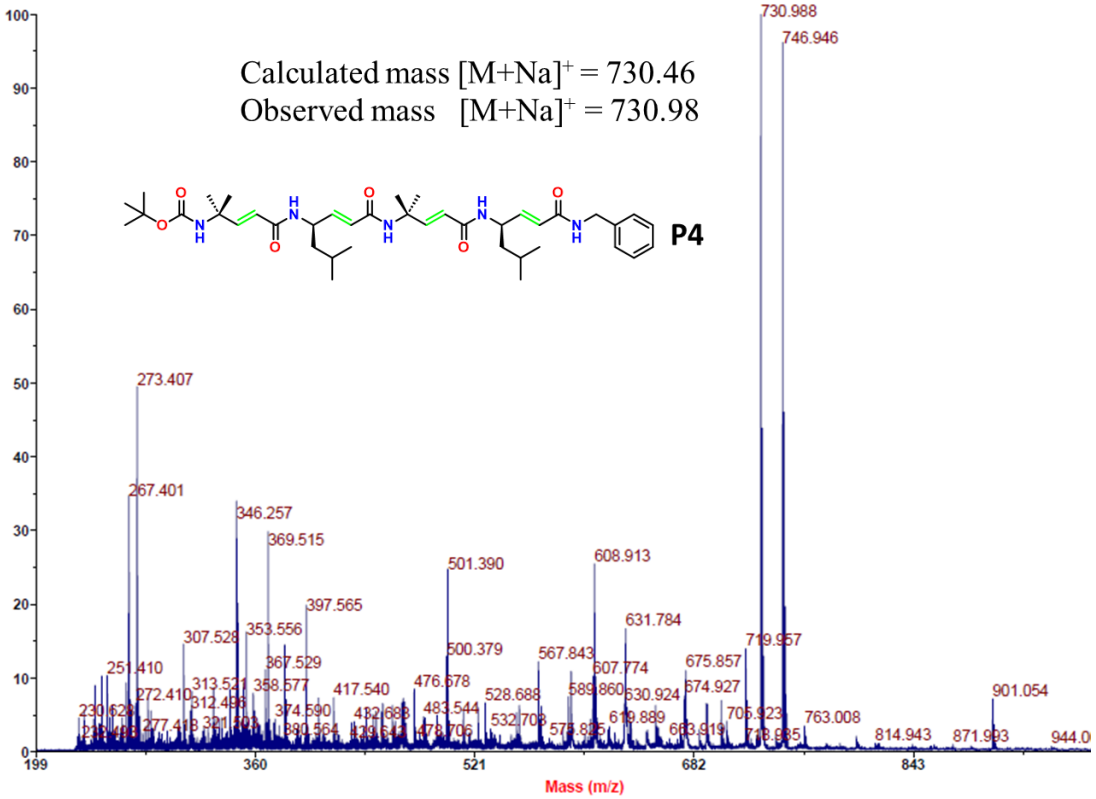
Calculated mass $[M+K]^+ = 496.29$
Observed mass $[M+K]^+ = 496.54$

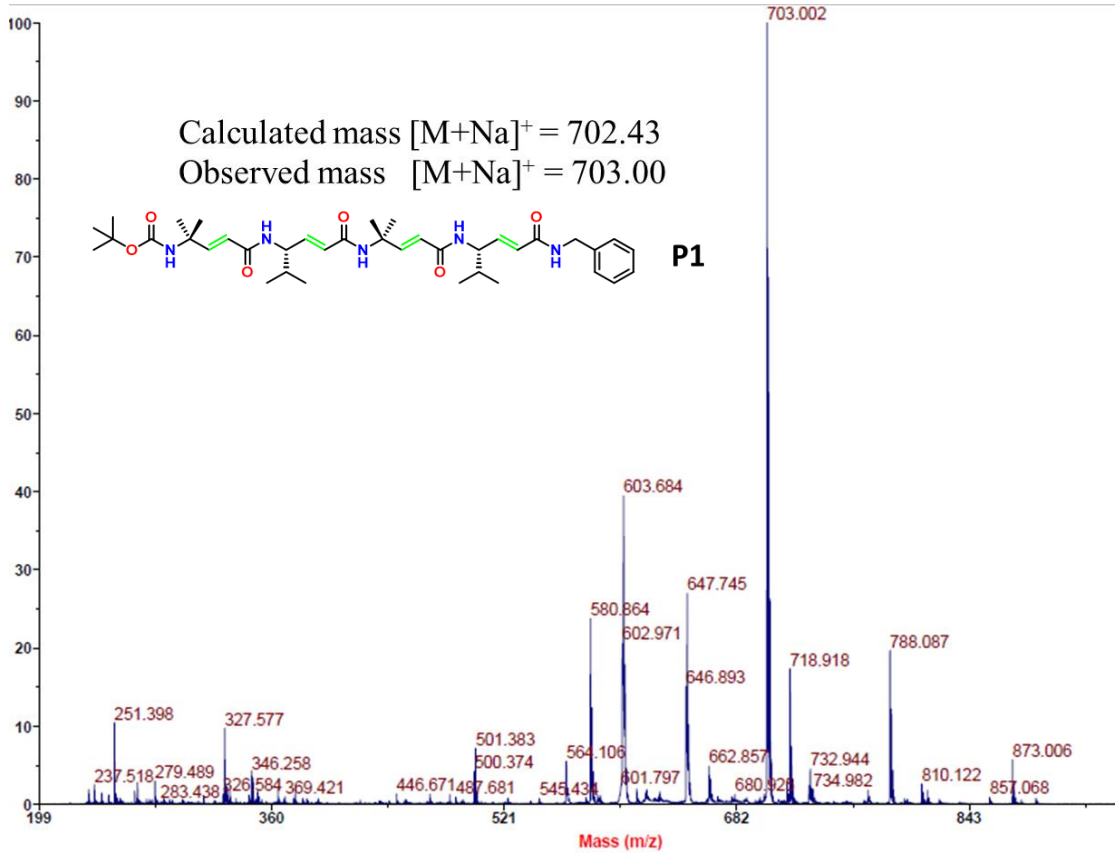
Pb4

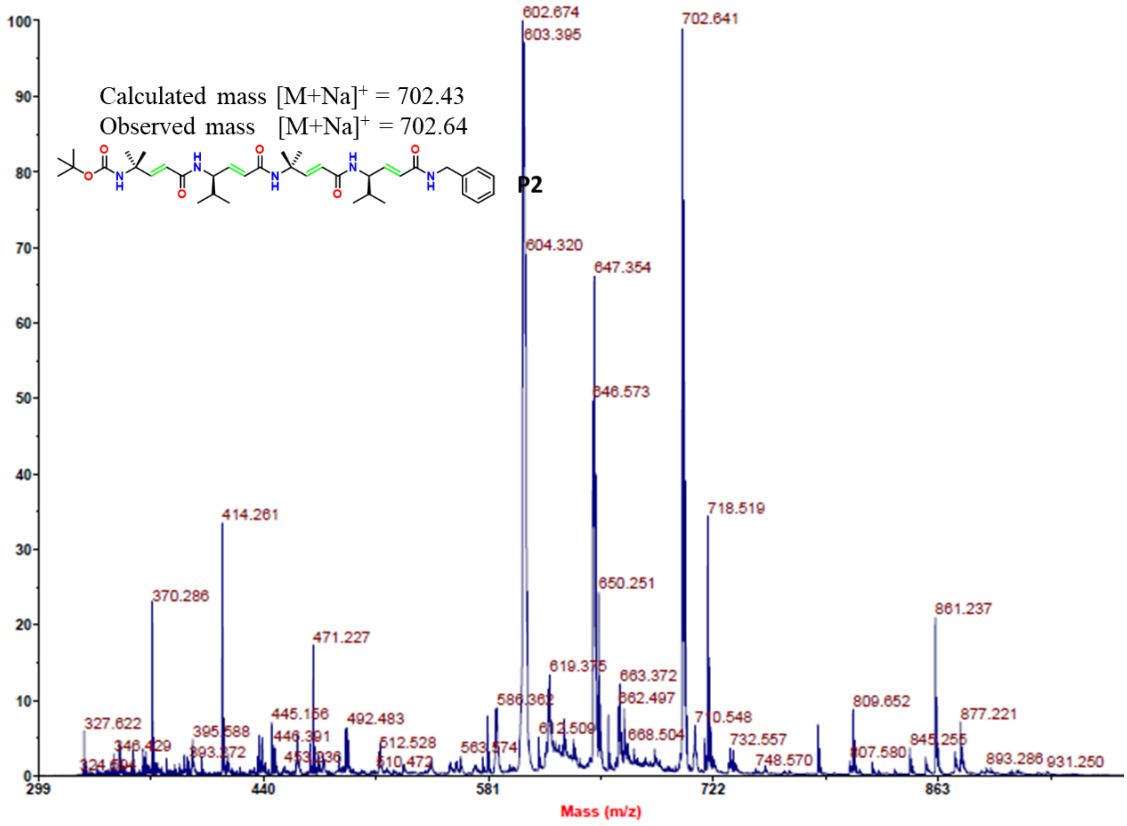

Calculated mass [M+K]+ = 466.28
Observed mass [M+K]+ = 466.46
Pb1
Mass (m/z)


Calculated mass [M+K]+ = 466.28
Observed mass [M+K]+ = 466.51
Pb2
Mass (m/z)


Calculated mass [M+Na]+ = 730.46
Observed mass [M+Na]+ = 730.97
P3
730.973
746.932
267.350
263.222
453.521
255.347
253.326
441.514
265.331
467.546
631.761
675.805
608.858
247.266
307.532
241.394
653.721
591.794
439.510
353.523
397.551
444.582
674.878
762.996
283.388
484.632
528.654
634.864
842.105
285.389
551.646
701.883
780.990
903.179
Mass (m/z)


Calculated mass [M+Na]+ = 730.46
Observed mass [M+Na]+ = 730.98
P4
730.988
746.946
273.407
267.401
346.257
369.515
501.390
608.913
397.565
631.784
307.528
353.556
500.379
719.957
567.843
607.774
675.857
251.410
367.529
476.678
674.927
272.410
358.577
417.540
528.688
589.860
630.924
901.054
763.008
814.943
871.993
944.0
Mass (m/z)


Calculated mass [M+Na]+ = 702.43
Observed mass [M+Na]+ = 703.00
P1
703.002
603.684
647.745
580.864
602.971
646.893
718.918
788.087
251.398
327.577
501.383
500.374
564.106
662.857
732.944
734.982
810.122
873.006
857.068
346.258
369.421
Mass (m/z)


Calculated mass [M+Na]+ = 702.43
Observed mass [M+Na]+ = 702.64
P2
602.674
603.395
702.641
604.320
647.354
646.573
414.261
718.519
650.251
370.286
861.237
471.227
619.375
663.372
662.497
586.362
809.652
877.221
327.622
445.156
492.483
710.548
732.557
668.504
748.570
845.255
893.286
931.250
512.528
Mass (m/z)

Chapter 3

Modulating β-Sheet Mimetics: Influence of Substituents on the Transformation of (*E*)-Vinylogous γ-Amino Acid Oligomers into β-Double Helix and C_{14}-Helix

3.1. Introduction

One of the most common secondary structural motif of proteins is β-sheet and it plays a fundamental role on the stability of the three dimensional structure of proteins.[1] β-sheets are characterized by the alignment of multiple peptide strands, which can be either parallel or antiparallel to each other, stabilized inter-strand hydrogen bonds between the amide functionalities of peptide backbone. The similar kind of inter-strand hydrogen bonding is observed in the double helical structure of DNA where two antiparallel strands intertwined through the hydrogen bonding between the conjugate base pairs.[2] It is evident that the formation of duplex structures is not confined to the exact molecular composition present in DNA and RNA. Various analogs of nucleic acids have been synthesized in which modifications have been made to the phosphate diester,[3] the bases,[4] and the sugar components,[5] and all of these oligomers establish enduring duplex structures. Motivated by the structural and functional significance of nucleic acids, researchers have endeavored to engineer duplex structures using various building blocks. This has been achieved through supramolecular assembly facilitated by hydrogen bonds,[6] metal ion coordination,[7] ionic interactions,[8] aromatic π–π stacking,[9] or a combination of these forces.[10] Nevertheless, the presence of a double helical structure is not commonly observed in proteins and peptides, with only two notable examples found in natural antibiotics: gramicidin A[11] and feglymycin.[12] These double helical structures are built by alternating α_L- and α_D- amino acids, forming a double helical arrangement in organic solvents. However, in the lipid bilayer environment, they adopt a β-helical structure.[13] Inspired by the duplex structures of gramicidin A, efforts have been made to mimic this double helical structure and functions from the synthetic peptides composed of alternating L- and D- amino acids.[14] In comparison to the double helical structures, the β-pleated structure is also generally constructed from predominately β-branched residues.[15] β-sheets can be assembled from oligomers of either L- or D-amino acids[16] (with D-amino acids being used in synthetic peptides), and Pauling's insights further proposed that more effective β-sheet structures could be achieved by combining racemic L- and D-polypeptide β-strands.[17] Even though the double helical structures and β-sheet structures have resembles in intermolecular hydrogen bonding, the conformational difference between these two structures is rarely studied in literature.

3.2. Object of the Present Work

We have been working on the design of foldamers constructed from (*E*)-α,β-unsaturated γ-amino acids. The first systematic study exploring the preferred conformation of (*E*)-vinylogous γ-amino acids was carried out in the early 1990s by Schreiber and colleagues, revealing that dipeptides constructed from (*E*)-vinylogous γ-amino acids adopt a β-sheet structure.[18] Over the years from our labs, we have developed various secondary and super secondary structures such as β-hairpin[19], β-meander,[20]planar structure,[21] 3-stranded hairpin motif[22] from (*E*)-vinylogous γ-amino acids. The crystal structures of all sheet-type foldamer are shown in Figure 1.

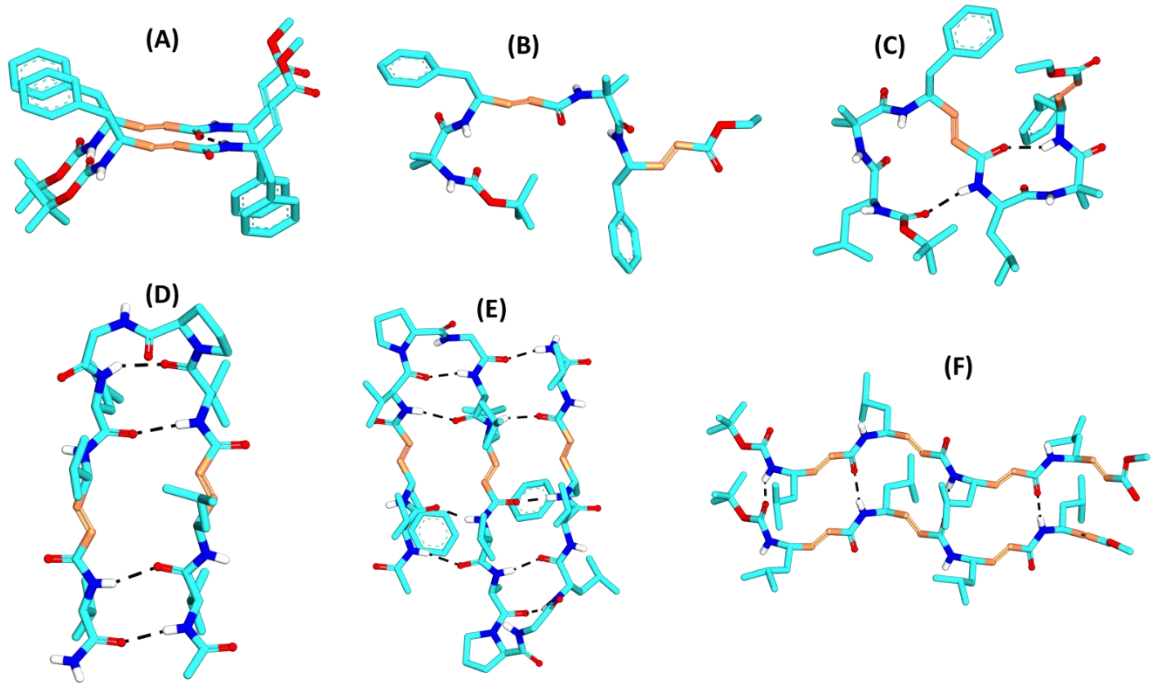


Figure 1: (A) Dipeptide-based β-sheet structure. (B) Planar structure. (C) β-meander structure. (D) β-hairpin structure. (E) 3-stranded β-hairpin structure. (F) β-sheet structure from oligomer of dγLeu residues

In all these structures, (*E*)-vinylogous γ-amino acids attain similar torsion angle values about ϕ = 120°, θ_1=120°, θ_2 =180° and ψ=180. Because of the 1,3-allylic strain, the γ-H atom resides within the plane of the enamide, leading to a preference for the *s-cis* conformation along the C^{α}. Due to this *s-cis* conformation, the θ_2 and ψ- values are fixed, however, the ϕ and θ_1-values can differ depending on the substituents on the C^{γ}-position. Keeping this in mind, we have recently developed β-double helical structures from the monomers of 4,4-gem-dialkyl substituted-(*E*)-

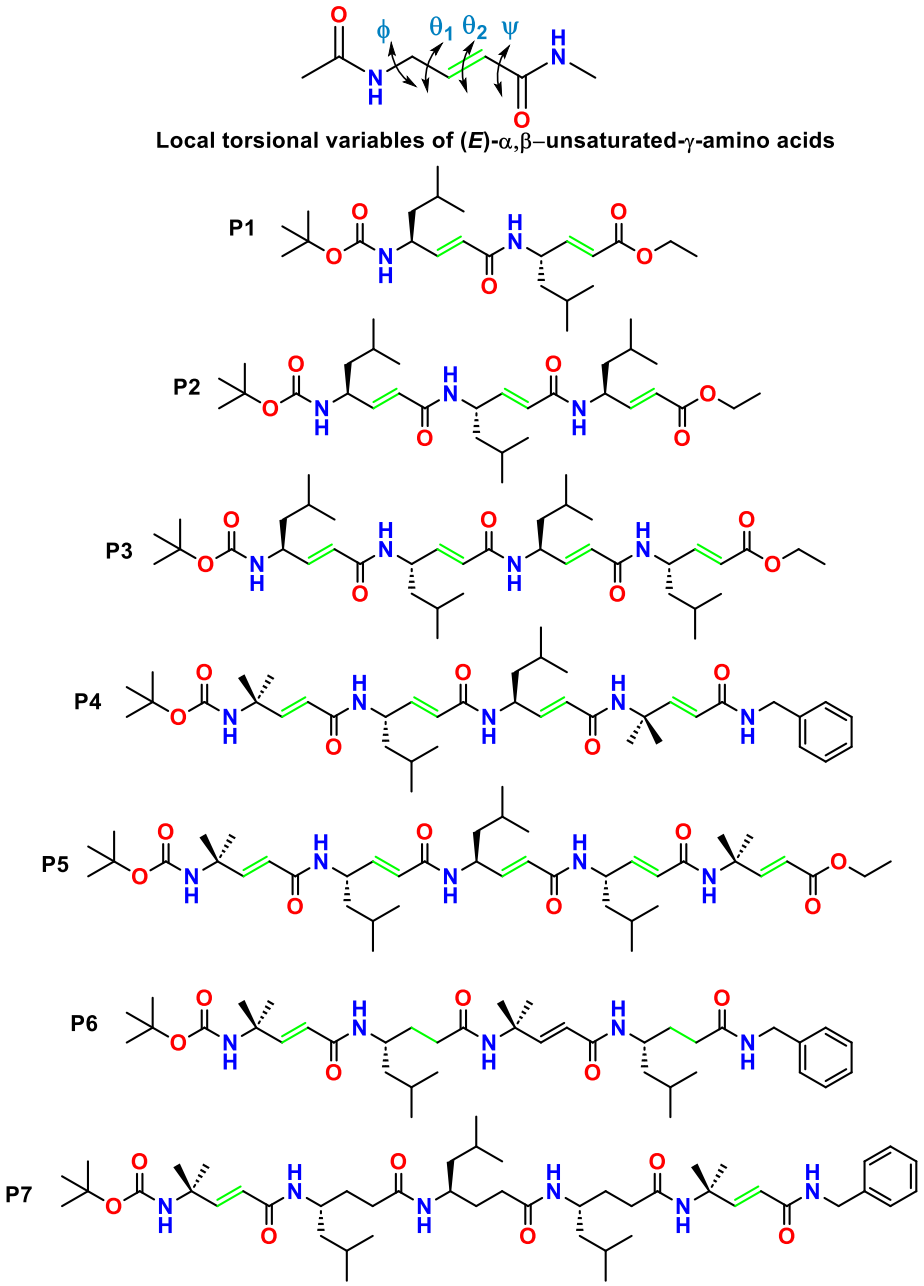
vinylogous γ-amino acids.[23] The substitution of the C^{γ}-H with a methyl group in an (*E*)-vinylogous γ-alanine residue largely impacted the torsion angles ϕ and θ_1 which leads to the double helical structure. A comprehensive study of this work has been recently reported by our group. In Chapter 2, we demonstrated the designing of chiral β-double helices where we incorporated consecutively (*E*)-vinylogous γAic amino acids and chiral (*E*)-vinylogous γ-Leu/Val amino acids. We have shown that, the double helical structures can be constructed by incorporating chiral (*E*)-vinylogous γ-amino acids, which are accommodated into a β-double helical structure by changing its torsion angles at ϕ and θ_1 to the values similar to that of the values adopted by gem-dialkyl residues.[24] In our current study we further explored the possibility of transforming a sheet structure into a β-double helical structure by sandwiching the sheet structures in between two gem-dialkyl groups. We further explored the formation of the β-double helical structure by removing the double bond constraints of the (*E*)-vinylogous γ-amino acids in a consecutive manner. Along with this, we further incorporated the saturated γ-amino acids in between the two gem-dialkyl (*E*)-vinylogous γ-amino acids and carried out their structural analysis.

3.3. Results and Discussion

To explore the impact of substituents on the conformations of (*E*)-vinylogous γ-amino acid homo-oligomers, we synthesized peptides **P1**-**P7.** Sequences of the peptides are shown in Scheme 1. Peptides **P1**, **P2,** and **P3** are the sequences of β-sheet type structures where the γ^4-position is substituted by a single-side chain leucine group. In peptides **P4** and **P5,** we have incorporated **P1** and **P3** *i.e.* singly substituted α,β-unsaturated-γ^4 residues in between two doubly substituted α,β-unsaturated-$\gamma^{4,4}$-residues. In peptide **P6**, we have incorporated saturated γ-Leu amino acids in between two doubly substituted α,β-unsaturated-$\gamma^{4,4}$dimethyl amino acids (dγAic). Finally, in **P7** we have incorporated consecutive saturated γ^4 residues in between the α,β-unsaturated-$\gamma^{4,4}$ dimethyl amino acids. We utilized solution-phase peptide synthesis methods to synthesize all peptides and the α,β-unsaturated γ-amino acids were prepared using previously established procedures.[25]

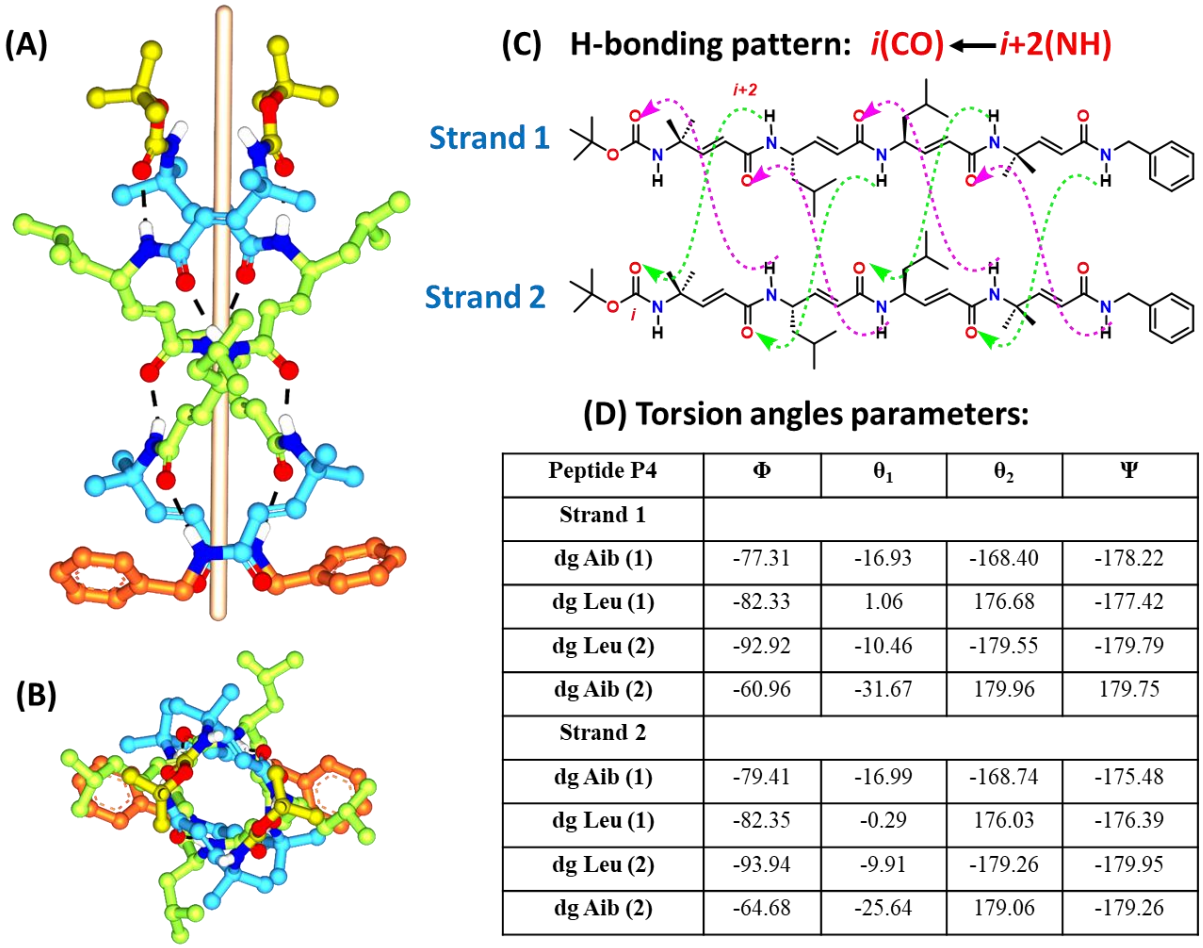
3.3.1 Crystal Structure Analysis of P4

To gain insights into the conformational characteristics of the peptides, we subjected them to crystallization using different solvent combinations. Crystals of **P4** were successfully obtained in a solvent mixture of $CHCl_3$/ toluene, and the X-ray diffraction structure is illustrated in Figure 2.



Scheme 1: Sequences of the peptides composed of (*E*)-vinylogous γ-amino acids

Despite the presence of a dipeptide residue favoring β-sheet formation, the peptide, within the single crystals, adopted a β-double helix structure. This conformation was characterized by the intertwining of two individual peptides through the formation of intermolecular hydrogen bonds. The stability of this double helix structure was maintained through the presence of eight intermolecular hydrogen bonds, which formed between the amide carbonyl (CO) of the (*i*) residue in strand 1 and the amide NH of the (*i*+2) residue in strand 2.



(D) Torsion angles parameters:

Peptide P4	Φ	θ_1	θ_2	Ψ
Strand 1				
dg Aib (1)	-77.31	-16.93	-168.40	-178.22
dg Leu (1)	-82.33	1.06	176.68	-177.42
dg Leu (2)	-92.92	-10.46	-179.55	-179.79
dg Aib (2)	-60.96	-31.67	179.96	179.75
Strand 2				
dg Aib (1)	-79.41	-16.99	-168.74	-175.48
dg Leu (1)	-82.35	-0.29	176.03	-176.39
dg Leu (2)	-93.94	-9.91	-179.26	-179.95
dg Aib (2)	-64.68	-25.64	179.06	-179.26

Figure 2: (A) Single crystal structure of **P4.** An imaginary rod is inserted along the crystal axis for a better view of the double-helical structure. (B) Top view of the **P4. (C)** Hydrogen bonding pattern observed in **P4.** (D) Torsion angle parameters of strand 1 and strand 2 of **P4**.

The amide NH groups of the N-terminal, protected with Boc groups, participated in intermolecular hydrogen bonds with the exposed amide CO groups at the C-terminal end of the other double helix, resulting in a continuous assembly of double helices. The hydrogen bonding pattern observed in **P4** is shown in Figure 2C. Each strand of the peptide **P4** adopted a right-handed helical shape without forming any hydrogen bonds wherein these two strands intertwined through H-bonding to form the right-handed (*P*)-β-double helix conformation in the single crystals. The H-bond parameters of **P4** are tabulated in Table 1. The H-bonds parameters are within the standard limits observed earlier report.[23] Using the torsion variables depicted in Scheme 1, we measured the torsion angles of α, and β-unsaturated amino acids. The torsion angle analysis revealed that α,β-unsaturated 4,4-dimethyl γ-amino acids displayed average ϕ, θ_1, θ_2, and ψ angles of -70.59°±8°, -

22.80°±6°, ±174°±5°, and ±178.17°±1.65°, respectively. The torsion angles θ_1 displayed a value near zero whereas θ_2, and ψ displayed a value close to 180°.

Table 1: The H-bond parameters of **P4** double helix.

Donor (D)	Acceptor (A)	D.... A (Å)	DH.... A (Å)	∡NH.... O (°)
N2	O8	2.866	2.022	160.52
N3	O9	2.809	1.979	156.60
N4	O10	2.819	1.97	161.49
N5	O11	2.871	2.001	169.74
N7	O2	2.822	1.97	162.73
N8	O3	2.803	1.971	157.35
N9	O4	2.835	1.991	160.04
N10	O5	2.929	2.070	165.46

The values exhibited by the α,β-unsaturated 4,4-dimethyl γ-amino acid residues align with the characteristics seen in previously observed β-double helix structures. As the middle two dγLeu residues are the fragments of β-sheet residue, so they generally tend to attain the ϕ and θ_1 value of 120° same as observed in the case of sheet structure. But, to accommodate into a double helical structure the ϕ and θ_1 value attains almost the same as observed in the case of dγAic units. The average value of ϕ and θ_1 for dγLeu units are -87.88°±5° and -4.89°±5° respectively. The average values of θ_2 and ψ also attain extended conformation with average values ±177.88°±1.54°, and ±178.38°±1.52°, respectively.

To compare with our previously reported[23]tetrapeptide structure comprised of oligomers of α,β-unsaturated leucine amino acids, in the present study we have seen that by incorporating α,β-unsaturated 4,4-dimethyl γ-amino acid residues at both N and C terminal interconvert the β-sheet structure into the β-double helical structure. In general, the torsion parameters ϕ and θ_1 play a key role in shaping the β-sheet and β-double helix structures in (*E*)-vinylogous γ-amino acid homo-oligomers. The presence of γ-disubstitution restricts the rotational freedom of ϕ and θ_1 of the sheet

promoting residues and thus compelling the peptides to take on the β-double helix conformation. To gain more insights into our sheet to double helical transition, we have synthesized peptide **P5** where we incorporated three of α,β-unsaturated leucine amino acids keeping β-unsaturated 4,4-dimethyl γ-amino acid at N and C terminal. However, we did not obtain good-quality crystals of **P5**.

3.3.2. Conformational Analysis of Peptides P4 and P5 in Solution State

To get a deeper understanding of the conformation of **P4** and **P5** in solution, we subjected both peptides to the solution NMR analysis. The ^{1}H-NMR analysis revealed that **P4** and **P5** in $CDCl_3$ gave well-resolved spectra conforming to one set of protons. To investigate the double helix structure in **P4** and **P5** in solution, temperature-dependent ^{1}H-NMR and DMSO-d_6 titration experiments were carried out.

3.3.3. DMSO-d_6 Titration Experiment for P4 and P5

The titration experiments using DMSO-d_6 indicated that, except for the N-terminal Boc amide NH, negligible changes in the chemical shift positions were observed for the other amide NH protons in peptides **P4** and **P5** as the concentration of DMSO-d_6 increased. Figures 3 and 4 depict the results of the DMSO-d_6 titration for **P4** and **P5**, respectively.

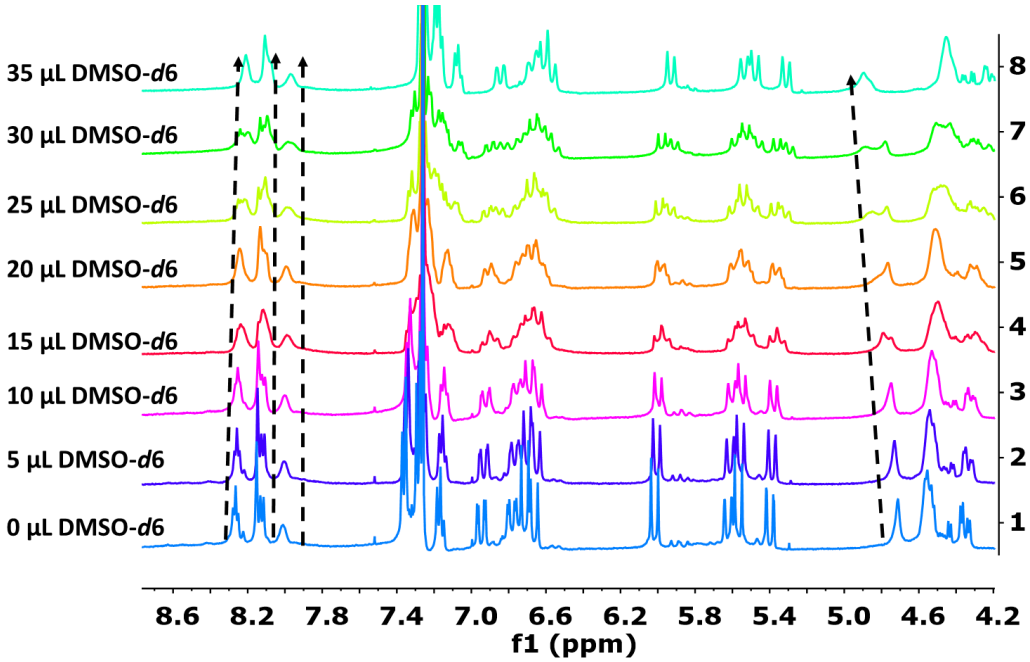


Figure 3: DMSO-d_6 ^{1}H-NMR titration plot for **P4** in $CDCl_3$

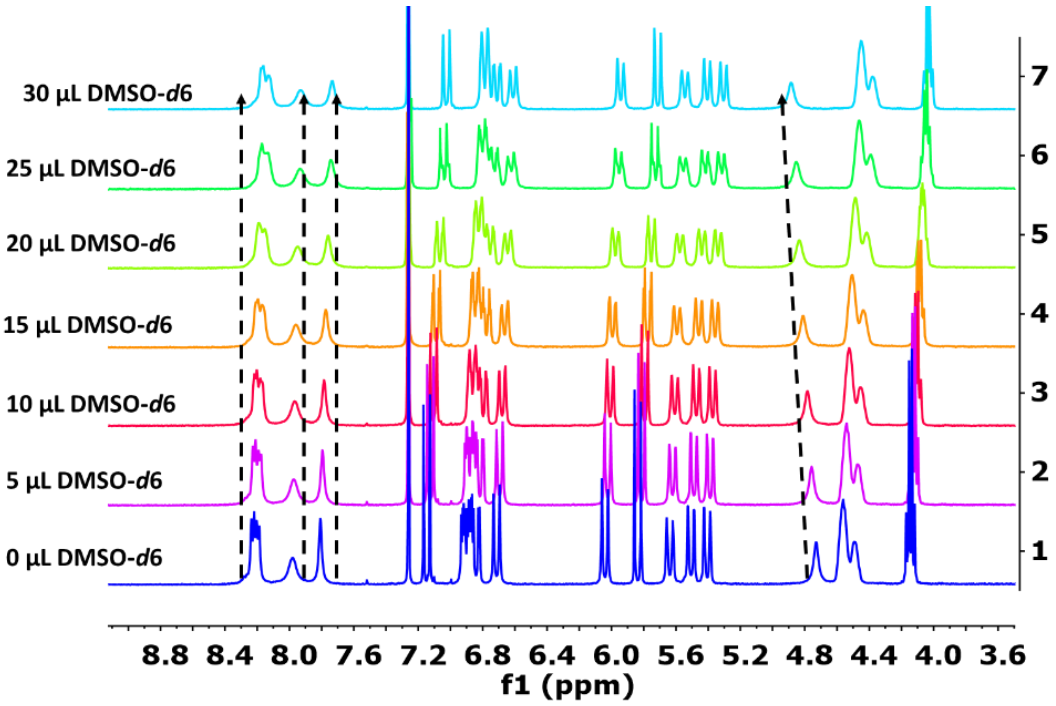


Figure 4: DMSO-d_6 ^{1}H-NMR titration plot for **P5** in $CDCl_3$

These findings strongly suggest the involvement of backbone amide NH and CO groups in intermolecular hydrogen bonding between peptide strands within the double helix. However, a notable downfield shift was observed for Boc-NH protons as the concentration of DMSO-d_6 increased, indicating the exposure of N-terminal NH protons in both **P4** and **P5** to the solvent for hydrogen bonding. This indirect evidence supports the conclusion that both peptides adopt double helical conformations in solution.

3.3.4. Temperature-Dependent ^{1}H Experiments of P4 and P5

The analysis of temperature dependence in **P4** and **P5** indicated a progressive up-field shift in chemical shifts for all amide NH groups as the temperature increased from 298 K to 378 K, excluding the Boc amide NH, which exhibited minimal alterations in chemical shift values. The gradual shifting of chemical shift in the amide NH-regions for peptides **P4** and **P5** are shown in Figures 5 and 6 respectively. The gradual up-field shift of the amide NH-protons except for Boc-NH, suggests possible breaking of H-bonding leads to the dissociation of the intertwined double helical strands into a single strand.

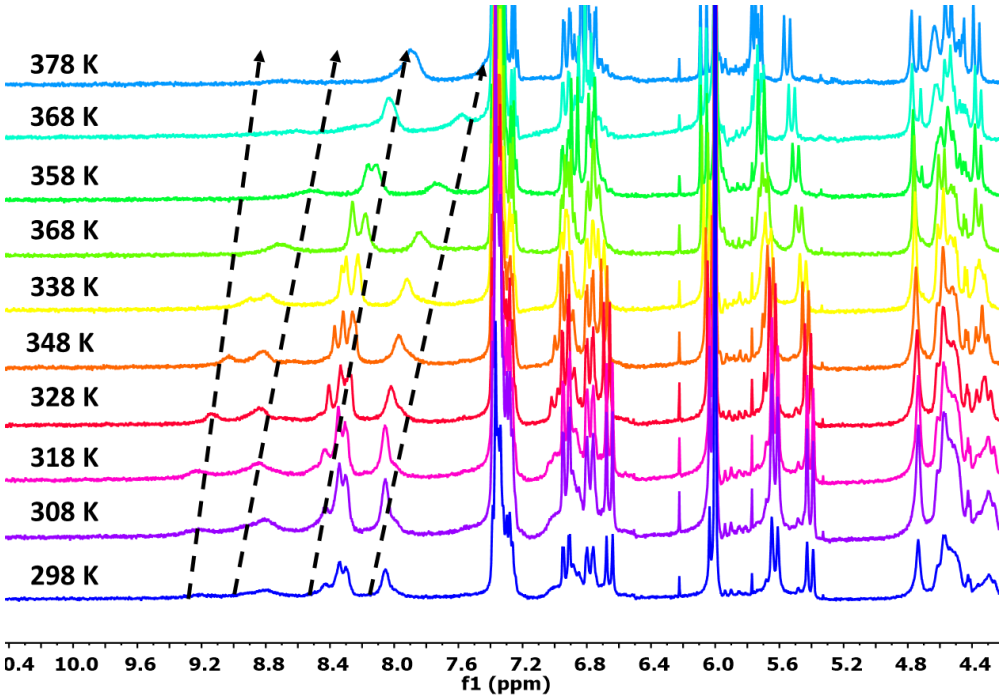


Figure 5: Temperature-dependent ^{1}H-NMR of **P4** in $C_2D_2Cl_4$ with increasing temperature

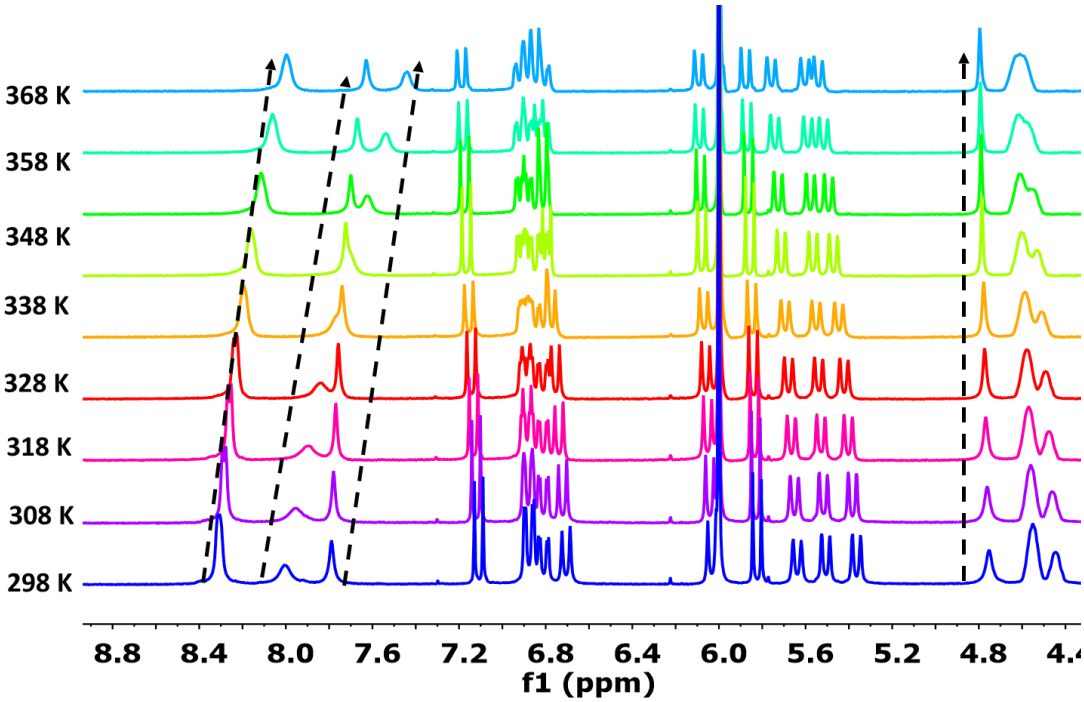


Figure 6: Temperature-dependent ^{1}H-NMR of **P5** in $C_2D_2Cl_4$ with increasing temperature

These results indirectly suggest that along with **P4**, peptide **P5** also assumes a β-double helical conformation in solution.

3.3.5 Circular Dichroism Analysis

Circular dichroism is an important tool for comprehending the secondary structure of polypeptides in solution. To understand the solution conformation of these peptides we subjected them for CD analysis in chloroform, tetrachloroethane, THF, and 1,4-dioxane solvents. All the peptides give distinct CD signals. CD analysis of peptides **P4** and **P5** in chloroform shows a CD maximum at 242 nm which is similar to our previous chapter double helices. This in turn also proves that they form a double helical structure in solution as well. However, the peptides **P1**, **P2,** and **P3** show a large CD minimum at 242 nm. All the CD spectra for peptides **P1** to **P5** are shown in Figure 7.

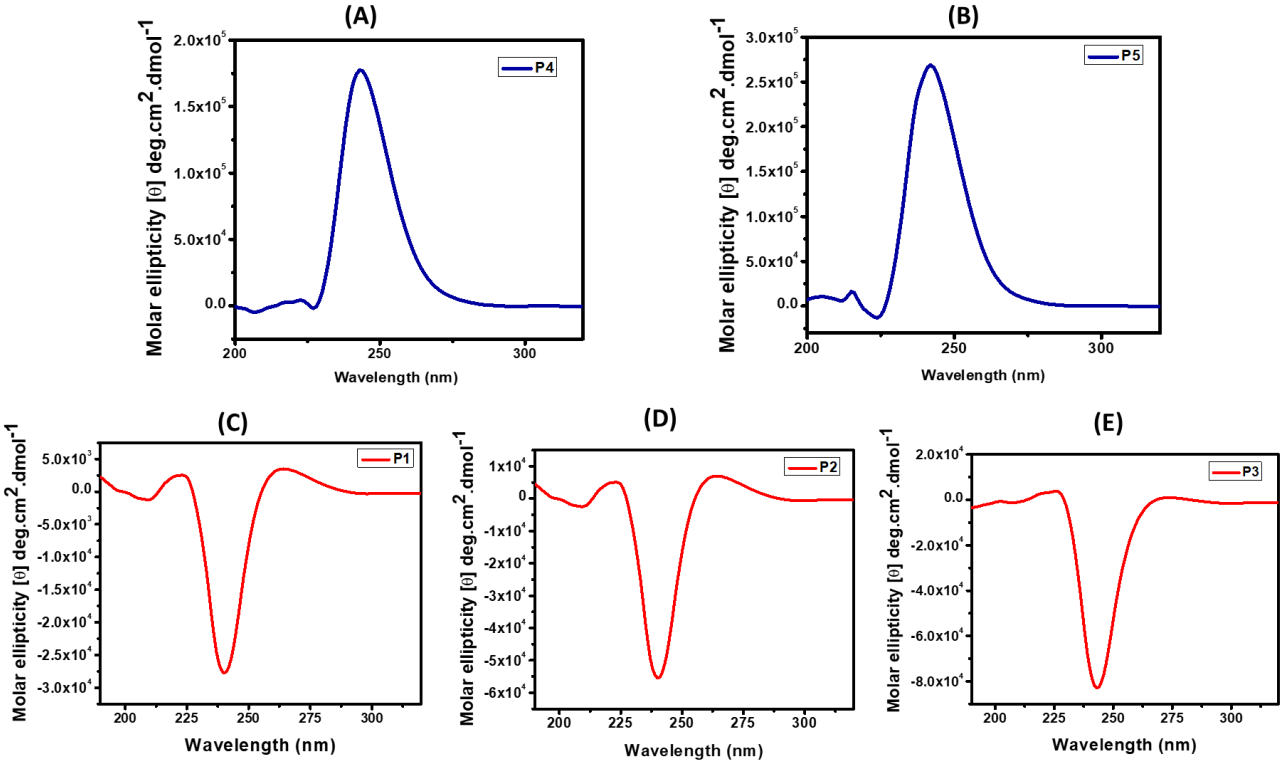


Figure 7: (A) CD spectra of **P4** in $CHCl_3$. (B) CD spectra of **P5** in $CHCl_3$. (C) CD spectra of **P1** in $CHCl_3$. (D) CD spectra of **P2** in $CHCl_3$. (E) CD spectra of **P3** in $CHCl_3$. In all the cases we have used 0.25 mM concentration of peptides.

The temperature-dependent CD spectra recorded in 1,1,2,2-tetrachloroethane solvent for peptides **P4** and **P5** show a gradual decrease of CD maximum intensity with increasing temperature. The possible breaking of interstrand hydrogen bonds between the two strands of the double helices gave rise to the decrease of CD maximum intensity. However, even at elevated temperature

peptides still retain their double helical characteristic. The temperature-dependent CD spectra for **P4** and **P5** are shown in Figures 8A and 8C respectively. We further carry out the melting temperature (T_m) of the double helices by normalizing the ellipticity at 242 nm and plotting against temperature. For **P4** and **P5**, we got the melting temperature 67.56 ± 1.99 °C and 69.37± 2.07 °C respectively.

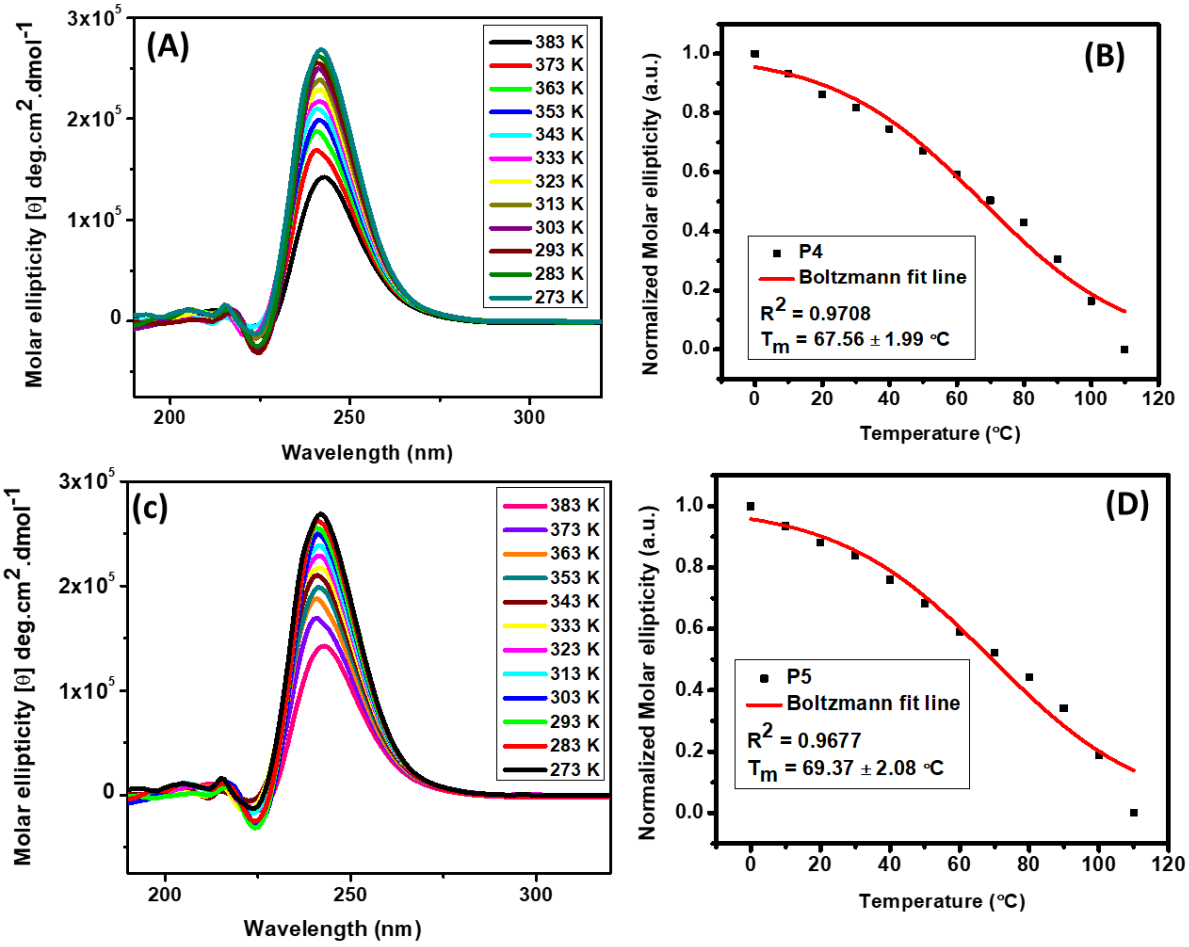


Figure 8: (A) Temperature-dependent CD spectra for peptide **P4.** (B) Melting temperature (T_m) calculation plot for **P4.** (C) Temperature-dependent CD spectra for peptide **P5.** (B) Melting temperature (T_m) calculation plot for **P5**. In all cases concentration of peptides was 0.25 mM.

However, the temperature-dependent CD spectra for β-sheet peptides **P1**, **P2,** and **P3** in 1,1,2,2-tetrachloroethane show no significant change in their λ_{min} values with increasing temperature. The temperature-dependent plots for peptides **P1**, **P2,** and **P3** are shown in Figure 9. This observation signifies their sheet structure in solution.

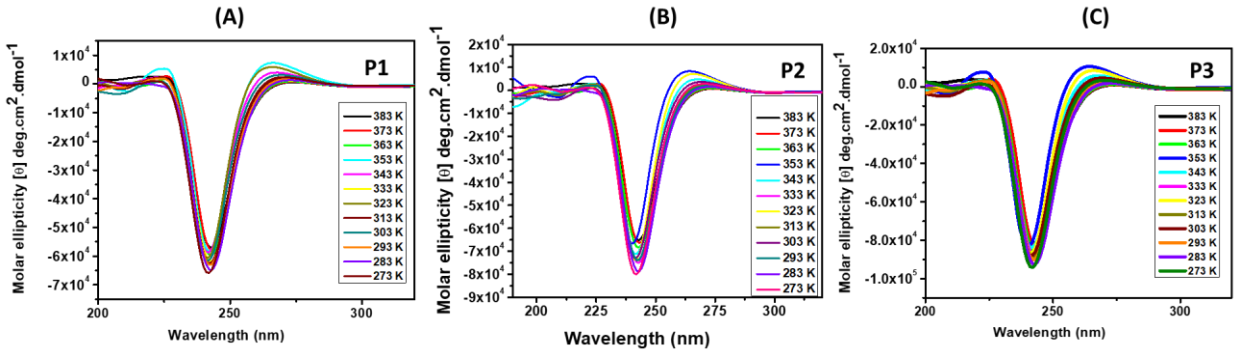


Figure 9: (A) Temperature-dependent CD spectra for peptide **P1.** (B) Temperature-dependent CD spectra for peptide **P2.** (C) Temperature-dependent CD spectra for peptide **P3.** In all cases concentration of peptides was 0.25 mM.

From the above plot, we have seen that CD signals of β-double helical peptides **P4** and **P5** are different from those of the β-sheet promoting peptides **P1**, **P2,** and **P3**. To explore the influence of solvents on the stability of the double helices, additional CD spectra were recorded in both THF and 1,4-dioxane solvents. The β-sheet peptides **P1**, **P2,** and **P3** show a CD minimum at 230 nm in THF. The CD spectra of **P1**-**P3** are shown in Figure 10.

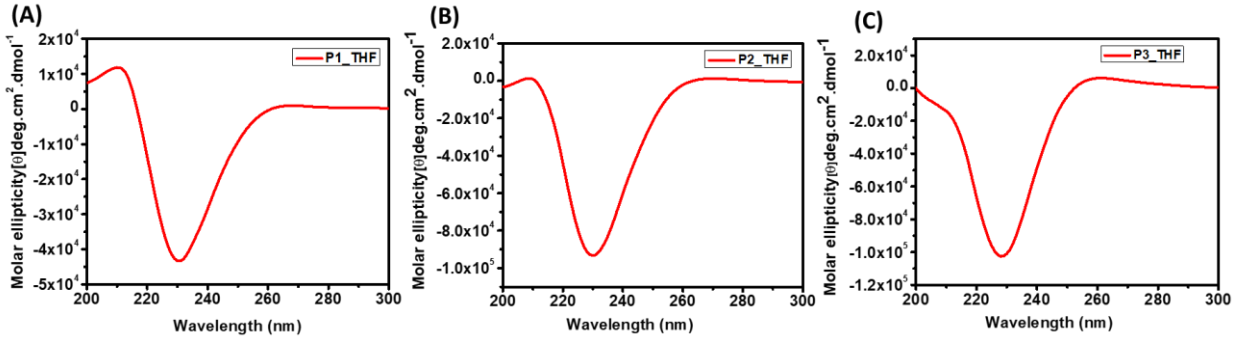


Figure 10: (A) CD spectra of peptide **P1** in THF. (B) CD spectra of peptide **P2** in THF. (C) CD spectra of peptide **P3** in THF. In all cases concentration of peptides was 0.25 mM.

In contrast to the β-sheet peptides, peptide **P4**, which forms a β-double helical structure exhibits a completely different CD signal. **P4** shows a large CD maximum at 240 nm and a small minimum at 222 nm. The peptide **P5** also exhibited a similar CD signal as we observed in **P4.** The CD spectra of **P4** and **P5** in THF are depicted in Figure 11.

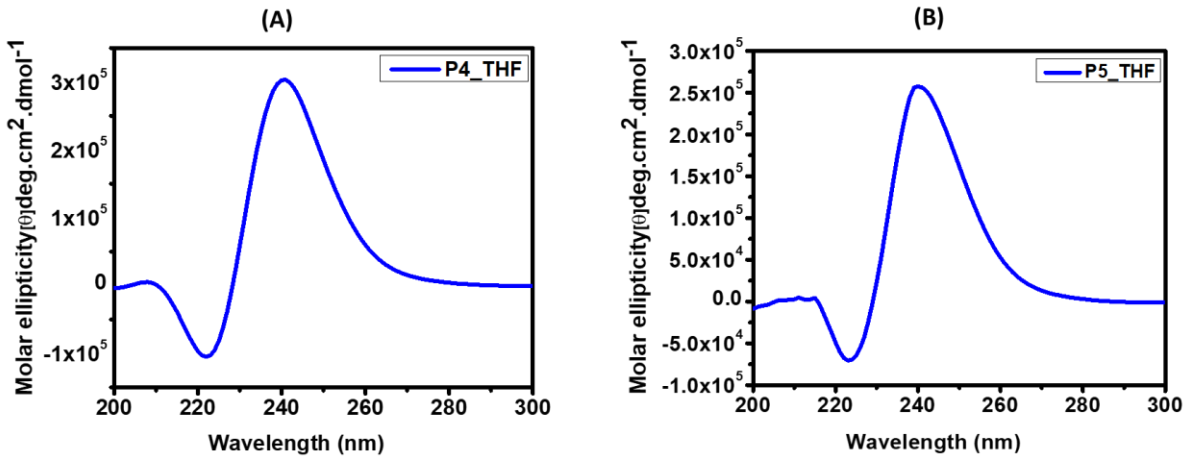


Figure 11: (A) CD spectra of peptide **P4** in THF. (B) CD spectra of peptide **P5** in THF. In all cases concentration of peptides was 0.25 mM.

We further recorded the temperature-dependent CD spectra were recorded in the 1,4-dioxane solvent. The CD spectra of all these peptides in 1,4-dioxane resemble the CD spectra recorded in the THF solution. The temperature-dependent CD spectra of peptides **P1**, **P2,** and **P3** show that there is no significant change in the CD spectra of the peptides as observed in 1,1,2,2-tetrachloroethane. (see Figure 12).

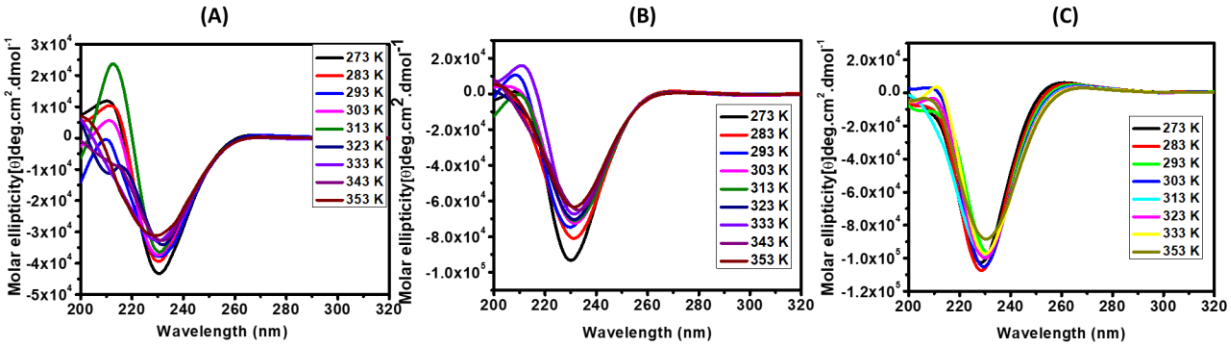


Figure 12: Temperature-dependent CD spectra of peptide**s** in 1,4-dioxane (A) **P1** (B) **P2** (C) **P3**. In all cases concentration of peptides was 0.25 mM.

However, we observed significant changes in the CD spectra of the double-helical peptides **P4** and **P5**. The 240 nm maximum gradually decreases with increasing temperature. This indicates that peptides **P4** and **P5** form a distinct double helical structure. As the temperature rises, the intermolecular hydrogen bonds between them weaken, leading to the destabilization of the double helical structure. The temperature-dependent CD spectra for **P4** and **P5** are depicted in Figure 13.

However, the fall of the CD maximum intensity is much faster in 1,4-dioxane rather in 1,1,2,2-tetrachloroethane for both **P4** and **P5**. We proceeded to determine the melting temperature (T_m) of the double helices. The ellipticity values at 242 nm with different temperatures were normalized and plotted against the respective temperatures. The obtained melting temperatures for **P4** and **P5** were found to be 53.71 ± 0.79 °C and 58.27 ± 3.74 °C, respectively. The reduced melting temperature implies that the double helices may experience less stabilization in THF or 1,4-dioxane compared to chloroform.

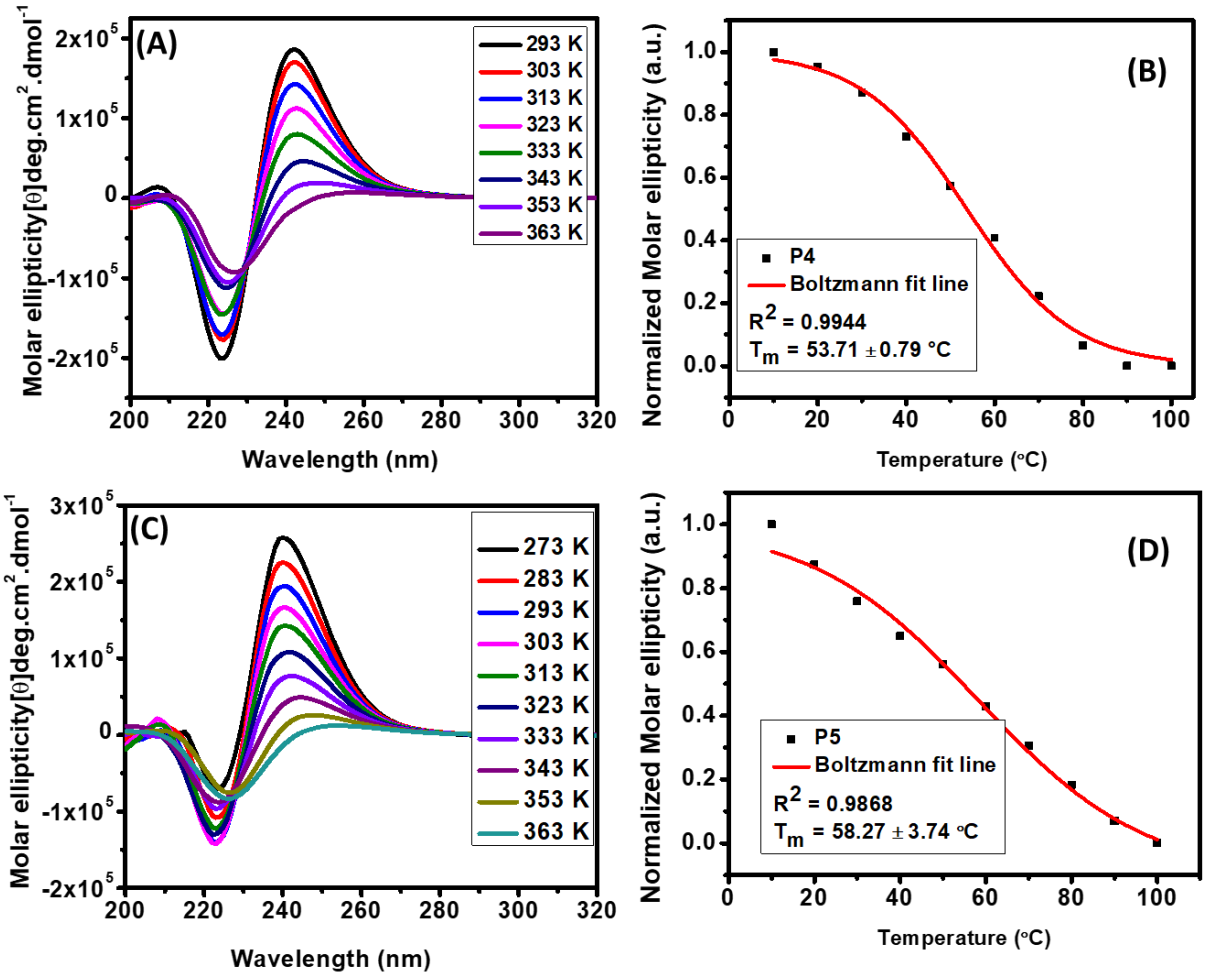


Figure 13: (A) Temperature-dependent CD spectra for peptide **P4**. (B) Melting temperature (T_m) calculation plot for **P4.** (C) Temperature-dependent CD spectra for peptide **P5**. (D) Melting temperature (T_m) calculation plot for **P5**. In all cases concentration of peptides was 0.25 mM.

The combined CD plot in Figure 14 representing sheet-promoting peptides **P1**-**P3** and double-helical peptides **P4** and **P5** reveals two discernible CD signals. The study thus indicates that the

CD signals in solution can be effectively employed to differentiate between β-sheet and β-double helical structures. The similar spectra of **P4** and **P5** suggest that the sheet structure of **P2** and **P3** can be converted to double helical structure by incorporating sterically hindered α,β-unsaturated 4,4-dimethyl γ-amino acid residue at the two terminals.

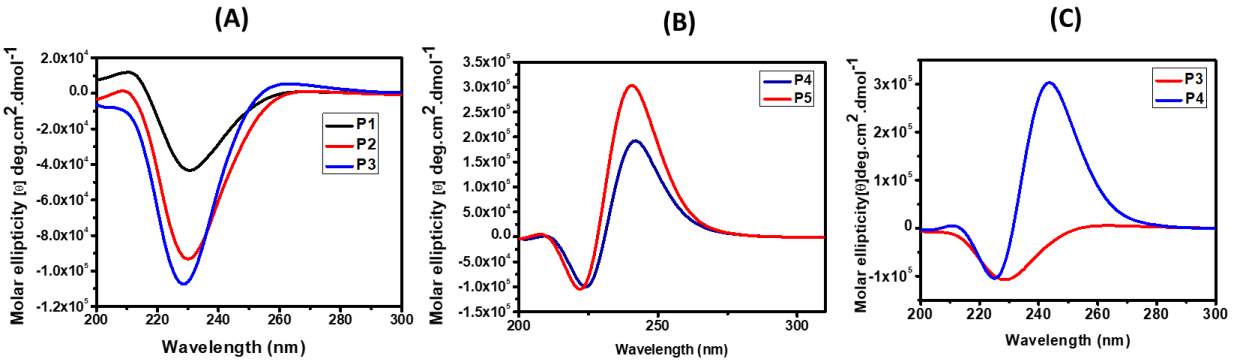
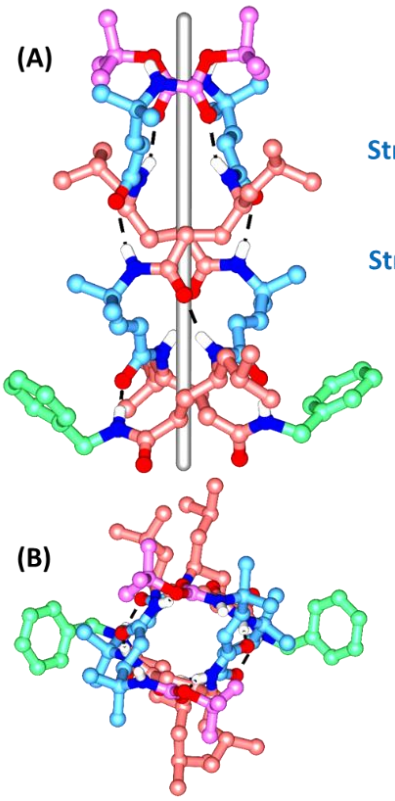


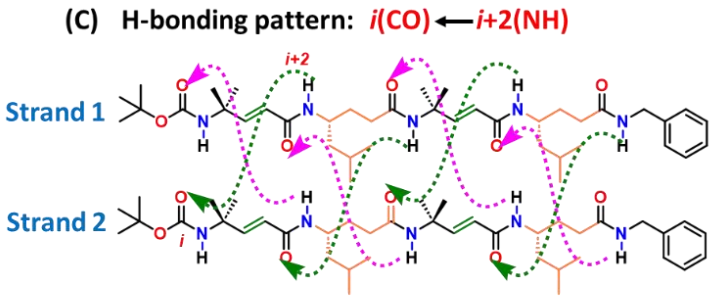
Figure 14: (A) Combined spectra of β-sheet peptides **P1**, **P2** and **P3** in THF. (B) Combined spectra of β-double helix peptides **P4** and **P5** in THF. (C) Combined spectra of **P3** and **P4** show the difference in CD signals for sheet and double helical peptides.

Based on the current findings, it is evident that the presence of a gem-dialkyl group plays a significant role in shaping the β-sheet or β-double helical structure. Now our current understanding is the importance of double bonds in the formation of β-double helical structures. In this connection, we have synthesized peptide **P6**, where we incorporated 1:1 alternating 4,4-dialkyl γ-amino acids (dγAic) and saturated γ-amino acids (γLeu).

3.3.6. Crystal Structure Analysis of P6

We got the single crystals of **P6** in a chloroform/acetonitrile solvent mixture by slow evaporation. The X-ray diffracted single crystal structure of peptide **P6** is shown in Figure 15. It is fascinating to see that peptide **P6** accommodated into a β-double helical structure as observed in the crystal structure. Even though the double bond has been removed, the γLeu residues are nicely accommodated into the double helical structure. Peptide strands 1 and 2 are interwoven through hydrogen bonds between them, and the stability of the β-double helix structure is maintained by a total of eight inter-strand hydrogen bonds. In strand 2, the amide CO group of residue *i* forms a hydrogen bond with the amide NH group of residue *i*+2 in strand 1 ($i \rightarrow i+2$).





(D) Torsion angles parameters:

Peptide P6	Φ	θ_1	θ_2	Ψ
Strand 1				
dγ Aic (1)	-71.65	-11.91	-172.69	175.64
γ Leu (1)	-86.94	-50.49	-169.42	-155.78
dγ Aic (2)	-71.01	-6.01	-177.51	173.98
γ Leu (2)	-112.81	63.52	173.72	104.09
Strand 2				
dγ Aic (1)	-70.82	-18.55	-171.01	179.62
γ Leu (1)	-81.54	-66.12	-174.97	-138.77
dγ Aic (2)	-75.57	-5.47	-173.91	177.79
γ Leu (2)	-120.06	64.45	175.92	105.81

Figure 15: (A) Single crystal structure of **P6.** An imaginary rod is inserted along the crystal axis for a better view of the double-helical structure. (B) Top view of the **P6. (C)** Hydrogen bonding pattern observed in **P6.** (D) Torsion angle parameters of strand 1 and strand 2 of **P6**.

Similarly, within strand 1, the amide CO group of residue *i* establishes hydrogen bonding with the amide NH group of residue *i*+2 in strand 2 ($i \rightarrow i+2$). The NH groups of the N-terminal Boc-amide and the CO groups of the C-terminal benzylamine do not participate in inter-strand hydrogen bonding interactions within their β-double helix structure. However, they do engage in intermolecular hydrogen bonding with other β-double helices. A diagram illustrating the inter-strand hydrogen bonds identified in **P3** is depicted in Figure 15C. The H-bond characteristics of the **P3** double helix are summarized in Table 2. The properties of the observed hydrogen bonds fall within the standard range of H-bond parameters. A thorough structural examination of **P6** uncovered a noteworthy pattern in its torsion angle parameters. The dγAic residues exhibited torsion angle parameters that closely resembled those observed in the crystal structure of **P4**. The average torsion angle parameters of dγAic are ϕ = -72.26°±2°, θ_1= -10.49°±5° θ_2= -173.77°±2,° and ψ = +176.75°±2°. In contrast to the dγAic residues, the γLeu residues exhibited distinct torsion

angle parameters. On average, these parameters were as follows: ϕ = -100.33°±16°, θ_1 = ±61.14°±6°, θ_2 = ±173.5°±3°, and ψ = ±126°±22°.

Table 2: The H-bond parameters of **P6** double helix

Donor (D)	Acceptor (A)	D.... A (Å)	DH.... A (Å)	∡NH.... O (°)
N2	O8	2.933	2.149	151.11
N3	O9	2.889	2.044	167.59
N4	O10	2.821	1.986	163.21
N5	O11	2.780	1.948	162.44
N7	O2	2.947	2.148	154.61
N8	O3	2.940	2.096	166.63
N9	O4	2.737	1.956	150.55
N10	O5	2.749	1.909	165.01

It is interesting to see that the torsion angles and ψ displayed are -100° and ±126°, respectively which are completely different from the dγAic residues. Notably, θ_1 typically hovers around 0°, but in the case of γLeu, it assumes a value of ±61.14°±6° and adopts the gauche conformation along the N-**C$^{\gamma}$**-**C$^{\beta}$**-C$^{\alpha}$ bond. The torsion angles are given in Figure 15D. In summary, these findings indicate that γLeu residues can fit well within the double helix structure with minimal deviation from the overall double helix conformation.

3.3.7. Conformational Analysis of Peptides P6 in Solution State

To get a deeper understanding of the conformation of **P6** in solution, we subjected peptide **P6** to the solution NMR analysis. The ^{1}H-NMR analysis revealed that **P6** in $CDCl_3$ gave well-resolved spectra conforming to one set of protons. To investigate the double helix structure in **P6** in solution, temperature-dependent ^{1}H-NMR and DMSO-d_6 titration experiments were carried out.

3.3.7.1. DMSO-d_6 Titration Experiment for P6

The titration experiments using DMSO-d_6 indicated that, except for the N-terminal Boc amide NH, negligible changes in the chemical shift positions were observed for the other amide NH protons in peptides **P6** as the concentration of DMSO-d_6 increased. Figure 16 depicts the results of the DMSO-d_6 titration for **P6**.

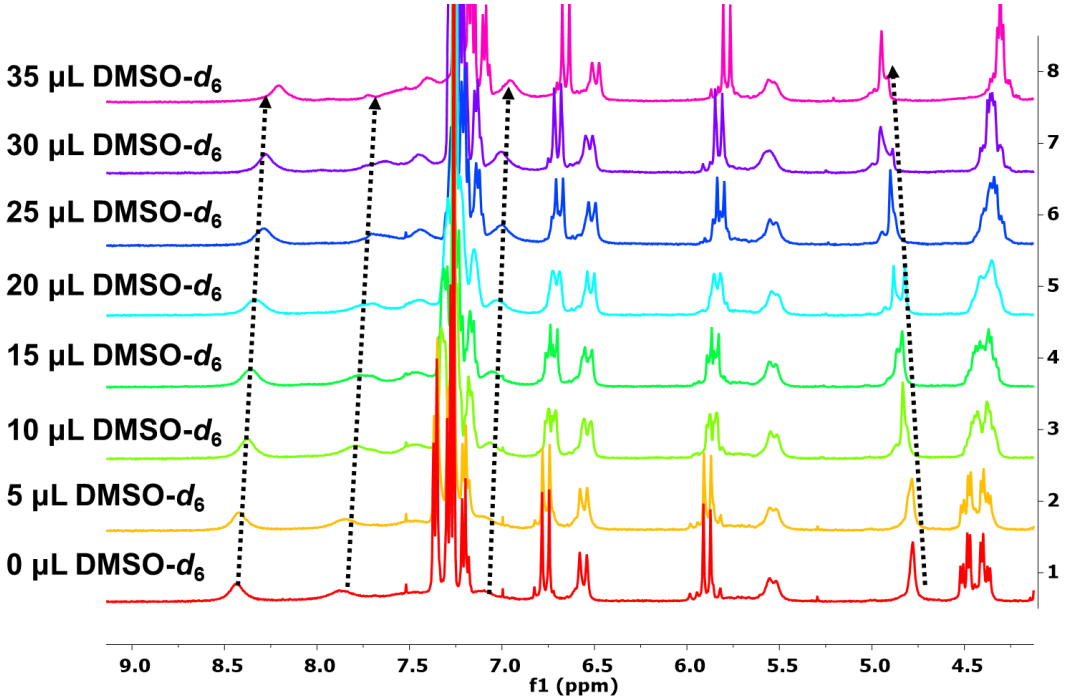


Figure 16: DMSO-d_6 ^{1}H-NMR titration plot for **P6** in $CDCl_3$

These findings strongly suggest the involvement of backbone amide NH and CO groups in intermolecular hydrogen bonding between peptide strands within the double helix. However, a notable downfield shift was observed for Boc-NH protons as the concentration of DMSO-d_6 increased, indicating the exposure of N-terminal NH protons in **P6** to the solvent for hydrogen bonding. This indirect evidence supports the conclusion that **P6** adopts double helical conformations in solution.

3.3.7.2. Temperature-dependent experiments of P6

The temperature-dependent analysis of **P6** demonstrated a gradual up-field shift in chemical shifts for all amide NH groups as the temperature increased from 298 K to 378 K, except for the Boc amide NH, which exhibited minimal changes in chemical shift values. The gradual shift of

chemical shift in the amide NH-regions for peptide **P6** is shown in Figure 17. The gradual upfield shift of the amide NH-protons except for Boc-NH, suggests possible breaking of H-bonding leads to the dissociation of the intertwined double helical strands into a single strand.

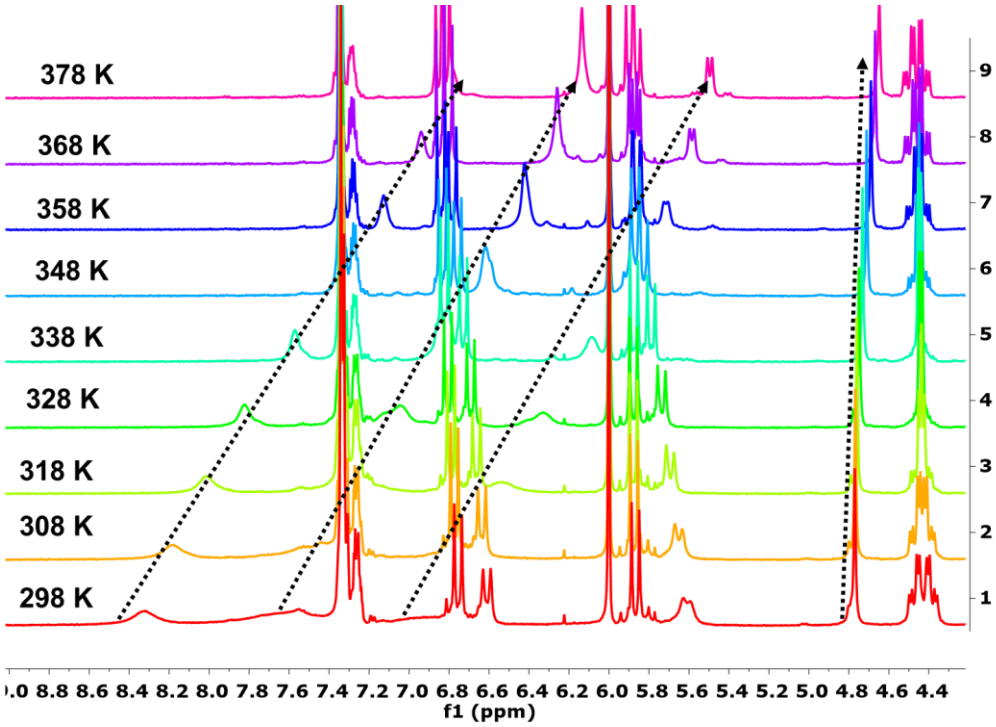


Figure 17: Temperature-dependent ^{1}H-NMR of **P6** in $C_2D_2Cl_4$ with increasing temperature

Overall, the temperature-dependent study indicates, that **P6** forms a double helical structure in solution as well. An intriguing observation is that the NH chemical shift in peptide **P6** experiences a more rapid up-field shift compared to the cases of peptides **P4** and **P5**. This investigation implies that while **P6** forms a double-helical conformation, the stability of these double helices is lower than those constructed from all unsaturated γ-amino acids in peptides **P4** and **P5**.

3.3.8. Circular Dichroism Analysis of P6

To comprehend the solution conformation of peptide **P6**, we conducted CD analysis in chloroform, tetrachloroethane, THF, and 1,4-dioxane solvents. All peptides exhibited distinct CD signals. Notably, the CD analysis of peptide **P6** in chloroform revealed a CD maximum at 242 nm, akin to our earlier observed double helices. This further substantiates that **P6** indeed adopts a double helical structure in solution. The CD spectra for peptide **P6** in chloroform are depicted in Figure 18A. Further temperature-dependent CD spectra in 1,1,2,2-tetrachloroethane were also recorded

for peptide **P6** which is depicted in Figure 18B. The temperature-dependent CD spectra revealed a gradual decrease in the CD maximum at 242 nm with increasing temperature. This phenomenon can be attributed to the weakening of interstrand hydrogen bonds as the temperature rises, leading to the reduction of the CD maximum. Similar to temperature-dependent ^{1}H-NMR experiments, we observed that in CD analysis, the gradual decrease of the maximum in peptide **P6** occurs at a faster rate compared to the double helices of **P4** and **P5**. The lower melting temperature (57.56± 1.45 °C) further indicates the lower stability of the double helices formed by **P6** compared to those constructed from all unsaturated γ-amino acids (Figure 18C).

The CD spectra recorded in THF show a CD maximum at 242 nm along with a CD minimum at 225 nm, which is similar to peptides **P4** and **P5** (Figure 18D). The temperature-dependent CD analysis in 1,4-dioxane also followed a similar trend as discussed above (Figure 18E). The melting temperature calculated for peptide **P6** in 1,4-dioxane solvent was found to be 50.91± 1.22 °C, which is lower than that of peptides **P4** and **P5** (Figure 18F).

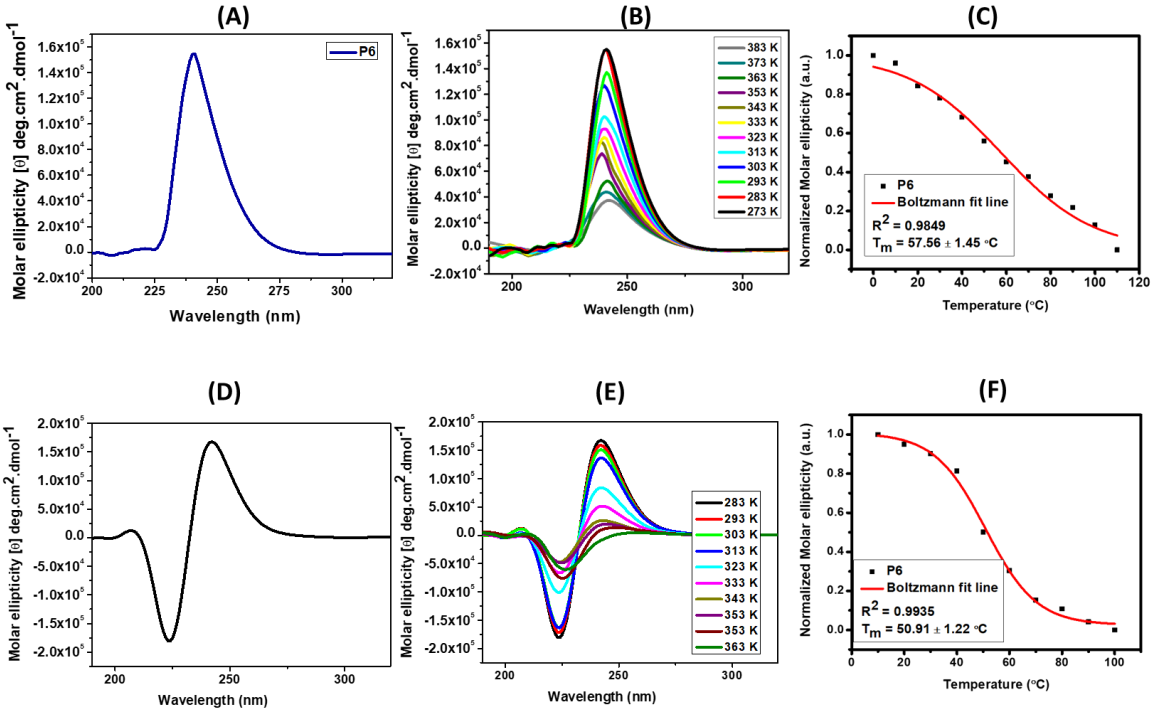


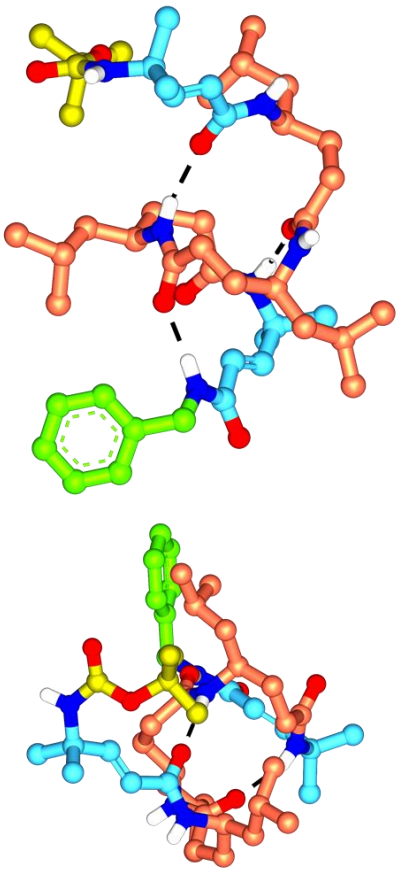
Figure 18: (A) CD spectra of **P6** in chloroform. (B) Temperature-dependent CD spectra for peptide **P6** in 1,1,2,2-tetrachloroethane. (C) Melting temperature (T_m) calculation plot for **P6.** (D) CD spectra of **P6** in THF. (E) Temperature-dependent CD spectra for peptide **P6** in 1,4-dioxane. (F) Melting temperature (T_m) calculation plot for **P6**. In all cases concentration of peptides was 0.25 mM.

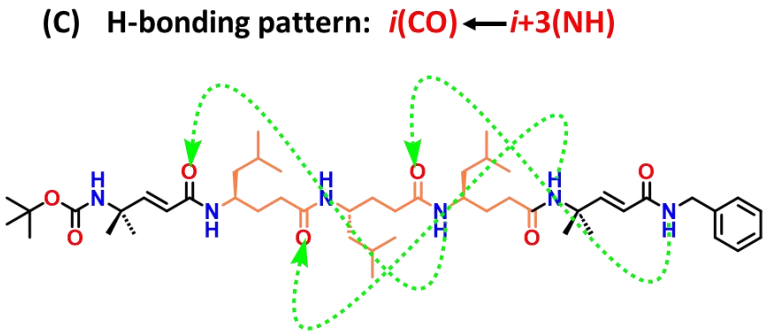
The above investigations clearly demonstrate that peptides constructed from the conjugation of α,β-unsaturated 4,4-dialkyl γ-amino acids with saturated γ-amino acids have the potential to form double helices. However, it is noteworthy that the stability of these double helices in solution is diminished compared to peptides constructed from exclusively unsaturated γ-amino acids.

In the previous section, we observed that introducing consecutive α,β-unsaturated monosubstituted γ-amino acids between the α,β-unsaturated disubstituted γ-amino acids results in the formation of a β-double helical structure. We also observed that peptides consisting of a 1:1 ratio of dγAic and γLeu amino acids can promote the β-double helical structure. Therefore, our current investigation aims to determine whether the inclusion of consecutive γLeu units between dγAic units can also induce the formation of a double helical structure or not. In this context, we have designed peptide **P7**, wherein we maintained dγAic residues at both the N-terminal and C-terminal positions while introducing three γLeu residues in between.

3.3.9. Crystal Structure Analysis of P7

As a single crystal structure gives unequivocal information regarding the conformation of the peptide, we subjected **P7** for crystallization in different solvent mixtures. We got the single crystal of **P7** from the slow evaporation of its solution from the methanol/water system. The x-ray diffracted single crystal of **P7** is shown in Figure 19. Interestingly **P7** didn't form a double helical structure instead it adopted a C_{14}-helical conformation. Structural analysis reveals that it formed a right-handed helical conformation. The carbonyl group of *i* -residue hydrogen bonded with the NH of (*i*+3) residue. The C_{14}-helix is stabilized by three independent hydrogen bonds. The hydrogen bonding parameters are shown in Table 3. The hydrogen bonding pattern is schematically shown in Figure 19B. The Boc-NH, NH(*i*+1), and NH(*i*+2) didn't participate in hydrogen bonding in the formation of 14-membered hydrogen bonding pseudo cycles. Instead, they form intermolecular hydrogen bonding to the other helix. Similarly, the carbonyl carbon of the Boc group, CO(*i*), CO(*i*+4) also does not participate in intramolecular hydrogen bonding, but rather forms intermolecular hydrogen bonding. The local conformation of all residues is characterized by the backbone torsion angles ϕ(N-C$^{\gamma}$), θ_1(C$^{\gamma}$-C$^{\beta}$), θ_2(C$^{\beta}$-C$^{\alpha}$), and ψ(C$^{\alpha}$-C=O). An analysis of the torsion values observed in the peptide **P7** indicates that the presence of gauche-gauche conformations around the central C-C bonds (C$^{\gamma}$-C$^{\beta}$ and C$^{\beta}$-C$^{\alpha}$) in the gamma (γ) residues (*i+1, i+2, i+3)* is a defining feature of a consistent C_{14} helical structure.





(D) Torsion angles parameters:

Peptide P7	Φ	θ_1	θ_2	Ψ
dγ Aic (1)	-47.14	150.56	-175.34	-177.58
γLeu (1)	-126.19	56.39	64.39	-164.81
γLeu (2)	-116.44	62.96	73.19	-147.88
γLeu (3)	-136.21	55.24	61.96	-150.65
dγ Aic (2)	-81.26	1.05	-176.65	172.84

Figure 19: (A) Single crystal structure of **P7.** (B) Top view of the **P7. (C)** Hydrogen bonding pattern observed in **P7.** (D) Torsion angle parameters of **P7**.

Table 3: H-bond Parameters of **P7**

Donor (D)	Acceptor (A)	D.....A (Å)	DH.....A (Å)	∡NH....O (°)
N4	O3	2.954	2.088	167.69
N5	O4	2.926	2.079	161.32
N6	O5	2.803	1.929	172.27

However, the penultimate dγAic residue has taken an eclipsed conformation along the C^{γ}-C^{β} bond with torsion angle θ_1 = 1.05° and trans conformation along the C^{β}-C^{α} bond with torsion angle θ_2 = -176.65°. The average backbone torsion angles calculated for the C_{14} helical structures originating from the central part of the helices are as follows: ϕ = -126.28° ± 8°, θ_1 = 58.19° ± 3.4°, θ_2 = 66.51° ± 4.82°, and ψ = -154.44° ± 7.4°. It's quite intriguing to observe that even when the C-

terminal dγAic residue possesses a trans double bond geometry, it can still fit within the helical conformation. Overall these results suggested that the incorporation of consecutive γ-amino acids in between the 4,4-dialkyl α,β-unsaturated γ-amino acids may not form a double helical structure but lead to a C_{14}-helical structure.

3.4. Conclusion

In conclusion, our investigation has demonstrated the remarkable ability to convert a β-sheet structure into a β-double helical configuration through the strategic incorporation of (*E*)-α,β-unsaturated 4,4-dialkyl γ-amino acid residues at both the N and C termini of the peptides. The presence of $\gamma^{4,4}$-dialkyl-substituted (*E*)-vinylogous γ-amino acids effectively compels the accommodation of these residues into a β-double helical structure. This structural transition is distinctly reflected in the circular dichroism spectra, offering clear differentiation between the solution-state conformations of β-sheet and β-double helical peptides. Moreover, our structural analysis indicates that γ-amino acids can be intricately positioned within the β-double helix through various torsion angles. However, it is noteworthy that the consecutive integration of γ-amino acids does not yield a double helical structure; instead, it gives rise to a C_{14}-helical conformation. In summary, our findings underscore the critical role played by (*E*)-α,β-unsaturated 4,4-dialkyl γ-amino acid residues in facilitating the formation of a double helical structure in γ-peptide foldamers. Additionally, this study underscores the significance of the double bond in driving the generation of the double helical structure. Overall, this research elucidates the indispensable conditions for the formation of a double helix from γ-peptide foldamers.

3.5. Experimental Section

3.5.1 Materials and Methods

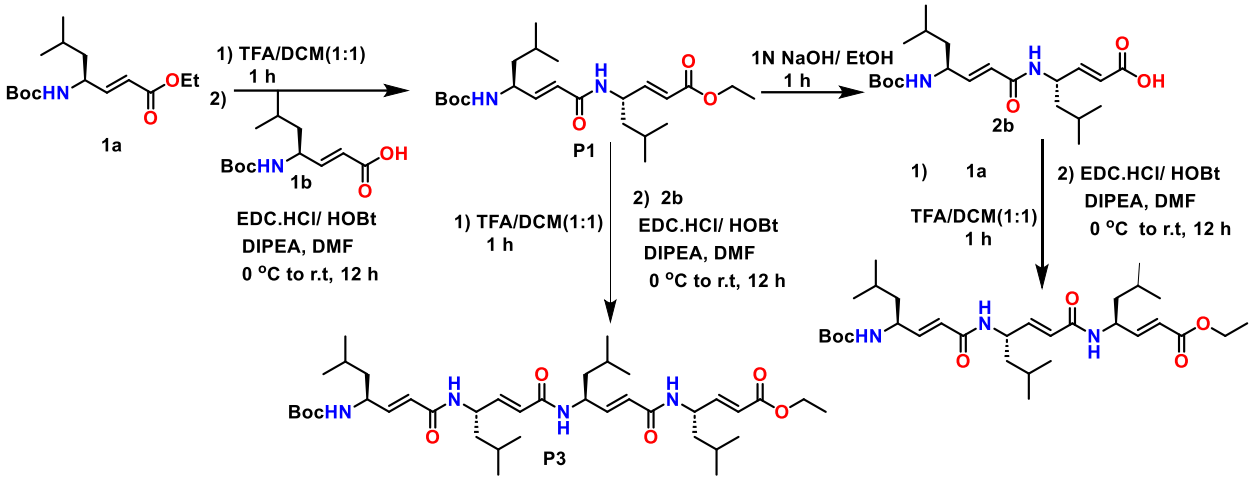
All reagents and solvents were used without further purification. Column chromatography was performed over silica gel. Final peptides were purified through reverse phase HPLC (C_{18} column, MeOH/H_2O 95:5 as a gradient with flow rate 2.00 mL/min). All the reactions were monitored by analytical thin-layered chromatography. The TLC visualization was done through UV light, $KMNO_4$ stain, and ninhydrin stain. ^1H NMR and ^{13}C NMR were performed through deuterated solvent on 400 MHz and 101 MHz respectively. We used a Matrix Assisted LASER Desorption Ionization mass spectrometer (MALDI-TOF/TOF) to calculate the accurate mass of our peptides. Fluorescence data was measured through the Spectrofluorometer instrument. X-ray crystal

structures were determined through APEX(III) DUO X-ray diffractometer using Mo-Kα (λ=0.71073 Å) graphite monochromatic radiation.

3.5.2 Synthetic Procedures for Peptides

BocNH-dγAic-OEt, BocHN-dγLeu(L)-OEt, BocNH-γLeu-OEt, Boc-NH-dγAic-OH, BocNH-dγLeu(L)-OH and BocNH-γLeu(L)-OH were synthesized using previously reported procedures.[23,24] The conventional solution phase method, employing the fragment condensation technique, was employed for peptide synthesis.

3.5.3. Synthesis of Peptide P1, P2 and P3



Scheme 2: Synthesis of peptides **P1**, **P2** and **P3**

3.5.3.1. Synthesis of Peptide P1

The Boc group of **1a** (8 mmol 2.28 g) was deprotected by using 8 mL 1:1 TFA: DCM for 1h. Subsequently, trifluoroacetic acid (TFA) and dichloromethane (DCM) solvent were evaporated, and 5-6 additional cycles of adding DCM followed by evaporation were performed to eliminate any remaining traces of TFA. The resulting crude material constituted the trifluoroacetic acid (TFA) salt of the amine of **1a** and to this 2 mL of DMF and 2 mL, of DIPEA were added to make it free amine. BocNH-dγLeu(L)-OH (**1b)** (2.04 g, 8 mmol) was dissolved in 7 mL of DMF and cooled to 0 °C under a nitrogen atmosphere. Following this, EDC.HCl (1.7 g, 8.8 mmol), HOBt (1.08 g, 8 mmol), and DIPEA (4.18 mL, 24 mmol) were added to the reaction mixture, and the stirring continued for 10 minutes. Subsequently, compound TFA.NH_2-dγLeu(L)-OEt was added,

and the reaction proceeded overnight, with TLC used to monitor the progress of the reaction. After the reaction reached completion, the mixture was diluted with 300 mL of ethyl acetate and subjected to washing with 10% HCl (150 mL × 2), 10% Na_2CO_3 solution (150 mL × 2), and brine solution (150 mL × 2). The organic layer was dried using anhydrous sodium sulfate (Na_2SO_4) and concentrated under reduced pressure, resulting in a crude powder. The crude material was then purified through column chromatography, yielding the white crystalline dipeptide, **P1**, with a 72% yield.

3.5.3.2. Synthesis of Peptide P2

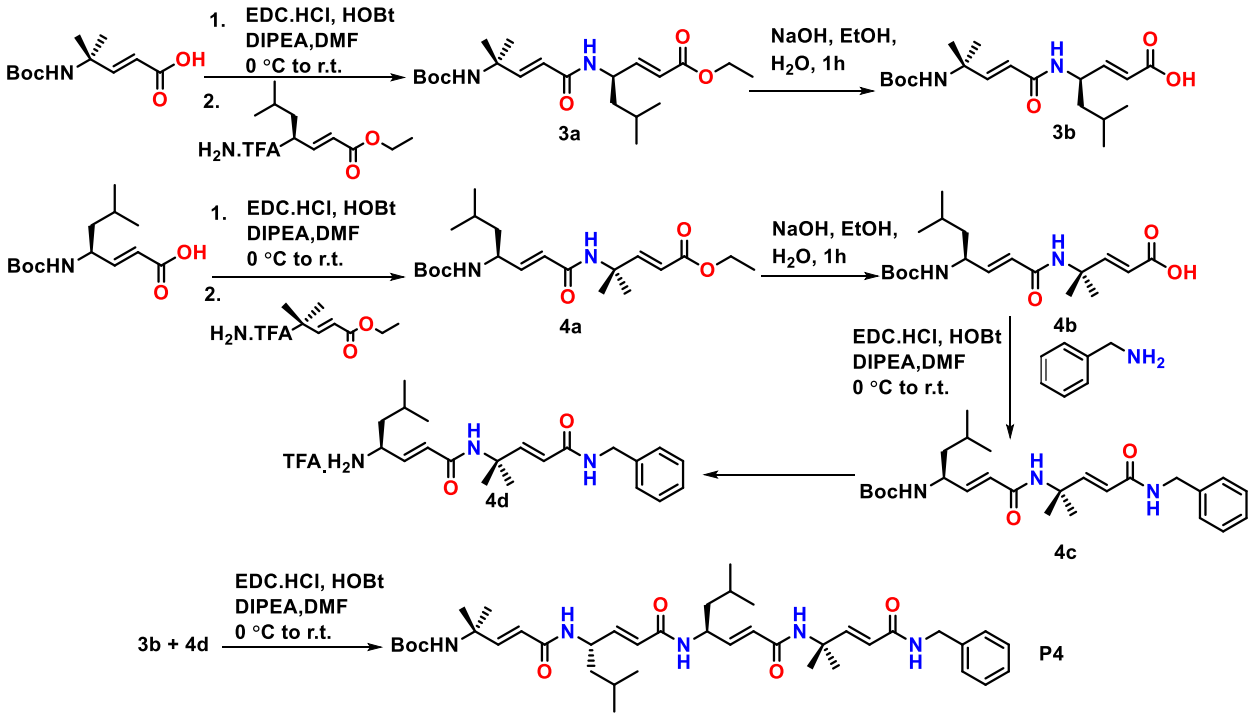
P1 (6 mmol, 2.54 g) was dissolved in 30 mL of ethanol, and 20 mL of 1N NaOH was added dropwise to the solution over 3 minutes. The reaction mixture was stirred for 30 minutes until the hydrolysis was complete. Afterward, the reaction mixture was acidified with 1N aqueous HCl solution and then extracted with ethyl acetate. The organic layer underwent washing with brine solution (3 x 100 mL) and was subsequently dried over anhydrous sodium sulfate (Na_2SO_4). The combined organic layer containing **2b** was concentrated under vacuum and was further employed for the subsequent coupling reaction. BocNH-dγLeu(L)-dγLeu(L)-OH (**2b**) (1.584 g, 4 mmol) was dissolved in DMF (5 mL) and cooled to 0 °C under a nitrogen atmosphere. Following this, EDC.HCl (0.85 g, 4.4 mmol), HOBt (0.5 g, 4 mmol), and DIPEA (2 mL, 12 mmol) were added to this solution. This reaction mixture was stirred for 5 min and subsequently, compound TFA.NH_2-dγLeu(L)-OEt (1.2 g, 4 mmol) was added, and the reaction proceeded overnight, with TLC used to monitor the progress of the reaction. After the reaction reached completion, the reaction mixture was diluted with 180 mL of ethyl acetate and subjected to washing with 10% HCl (125 mL × 2), 10% Na_2CO_3 solution (125 mL × 2), and brine solution (125 mL × 2). The organic layer was dried using anhydrous Na_2SO_4 and concentrated under reduced pressure, resulting in a crude powder. The crude material was then purified through column chromatography, yielding the white crystalline product, **P2**, with a 70% yield.

3.5.3.3. Synthesis of Peptide P3

The Boc group of **P1** (2 mmol 0.84 g) was deprotected by using 2 mL 1:1 TFA: DCM for 1h. Subsequently, trifluoroacetic acid (TFA) and dichloromethane (DCM) solvent were evaporated, and 5-6 additional cycles of adding DCM followed by evaporation were performed to eliminate any remaining traces of TFA. The resulting crude material constituted the trifluoroacetic acid

(TFA) salt of the amine of **P1** and to this 1.5 mL of DMF and 0.7 mL, of DIPEA were added to make it free amine. BocNH-dγLeu(L)-dγLeu(L)-OH (**2b**) (0.798 g, 1 mmol) was dissolved in DMF (3 mL) and cooled to 0 °C under a nitrogen atmosphere. Following this, EDC.HCl (0.4 g, 2.2 mmol), HOBt (0.25 g, 2 mmol), and DIPEA (1.4 mL, 8 mmol) were added to this solution. This reaction mixture was stirred for 5 min and subsequently, compound TFA.NH_2-dγLeu(L)-dγLeu(L)-OEt was added, and the reaction proceeded overnight, with TLC used to monitor the progress of the reaction. After the reaction reached completion, the mixture was diluted with 100 mL of ethyl acetate and subjected to washing with 10% HCl (75 mL × 2), 10% Na_2CO_3 solution (75 mL × 2), and brine solution (75 mL × 2). The organic layer was dried using anhydrous Na_2SO_4 and concentrated under reduced pressure, resulting in a crude powder. The crude material was then purified through column chromatography, yielding the white crystalline product, **P3**, with a 60% yield.

3.5.4. Synthesis of Peptide P4



Scheme 3: Synthesis of peptide **P4.**

Boc-dγAic-OH (6.5 mmol, 1.49 g) was dissolved in 7 mL of DMF and cooled to 0 °C under a nitrogen atmosphere. Following this, EDC.HCl (7.205 mmol, 1.38 g) HOBt (6.5 mmol, 880 mg),

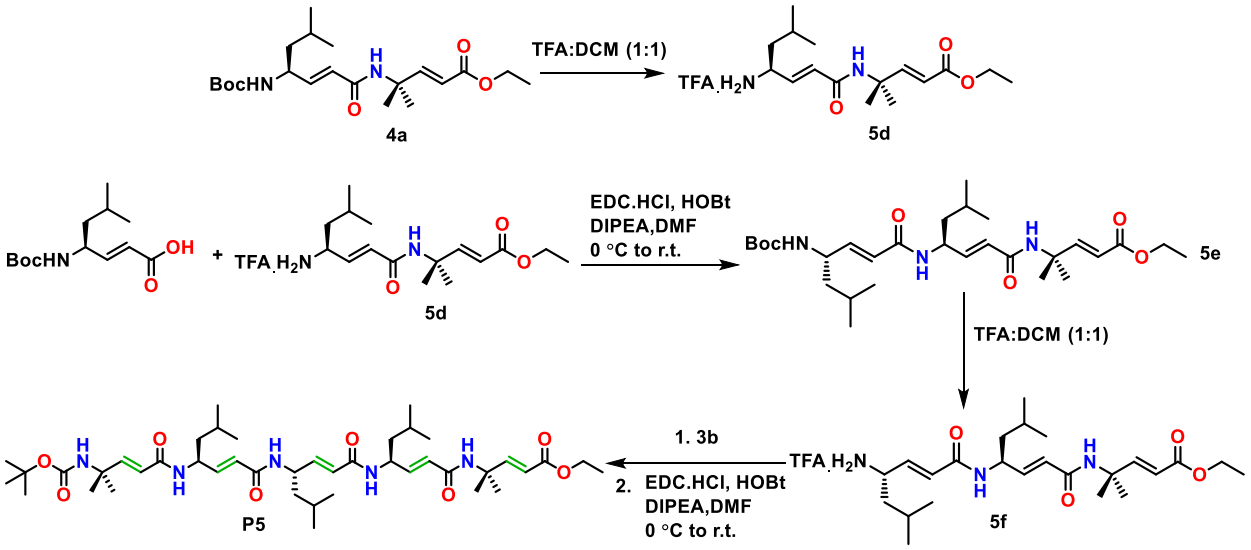
and DIPEA (19.65 mmol, 3.52 mL) were added to the reaction mixture, and the stirring continued for 10 minutes. Subsequently, compound TFA.NH_2-dγLeu(L)-OEt was added, and the reaction proceeded overnight, with TLC used to monitor the progress of the reaction. After the reaction reached completion, the mixture was diluted with 300 mL of ethyl acetate and subjected to washing with 10% HCl (150 mL × 2), 10% Na_2CO_3 solution (150 mL × 2), and brine solution (150 mL × 2). The organic layer was dried using anhydrous sodium sulfate (Na_2SO_4) and concentrated under reduced pressure, resulting in a crude powder. The crude material was then purified through column chromatography, yielding the white crystalline dipeptide, **3a**, with a 72% yield. The hydrolysis of **3a** was carried out by using 1 N NaOH solution following the previously mentioned procedure 3.5.3.2 and hydrolysis product **3b** was generated.

Following the above-mentioned procedure, dipeptide **4a** was also synthesized. The hydrolysis of **4a** to generate hydrolysis product **4b** was also carried out by the previously mentioned procedure in 3.5.3.2. The peptide BocHN-dγLeu-dγAic-OH (**4b**) (2 mmol, 0.736 g), EDC.HCl (2.2 mmol, 422 mg) and HOBt (2 mmol, 270 mg) were dissolved together in DMF (5 mL). To this solution (6 mmol, 1.0 mL) DIPEA was added. After stirring the reaction mixture for about 10 minutes at ice-cold conditions, benzylamine (5 mmol, 0.54 mL) was added and the reaction mixture was left for stirring overnight at room temperature. Upon finishing the reaction (verified by TLC), the compound underwent extraction with ethyl acetate, followed by sequential washes with 10% HCl (3 × 40 mL), 10% Na_2CO_3 (3× 40 mL), and brine solution (3 × 40 mL). The organic layer was dried by using anhydrous Na_2SO_4 and then condensed under reduced pressure. The crude product **4c** underwent purification through silica gel column chromatography employing an EtOAc/Hexane solvent system. The overall yield amounted to 68% (1.36 mmol, 0.62 g).

The Boc-deprotection of **4c** was further carried out by using TFA: DCM in a 1:1 ratio by following the previously mentioned procedure in 3.5.3.1. The synthesis of peptide Boc-dγAic-dγLeu(L)-dγLeu(L)-dγAic-NHBn (**P4**) involved a [2+3] condensation. For the coupling reaction, Boc-dγAic-dγLeu-OH (**3b**) (1.3 mmol, 0.48 g), EDC.HCl (1.43 mmol, 275 mg), and HOBt (6.5 mmol, 175 mg) were combined in DMF (3 mL). To this mixture, DIPEA (3.9 mmol, 0.9 mL) was added. After stirring the reaction mixture for approximately 5 minutes under ice-cold conditions, TFA.H_2N-dγLeu(L)-dγAic-NHBn (**4d**) (1.3 mmol, 0.59 mg) was introduced. The reaction mixture was stirred overnight at room temperature. Upon completion of the reaction (monitored by TLC), the

compound underwent extraction with ethyl acetate, followed by successive washings with 10% HCl (3 × 40 mL), 10% Na_2CO_3 (3 × 40 mL), and brine solution (3 × 40 mL). The combined organic layer was then dried over anhydrous Na_2SO_4 and concentrated under reduced pressure. The final peptide **P4** was purified through reverse-phase HPLC using a C_{18} column with MeOH/H_2O (95:5) as the gradient and a flow rate of 2.00 mL/min.

3.5.5. Synthesis of Peptide P5

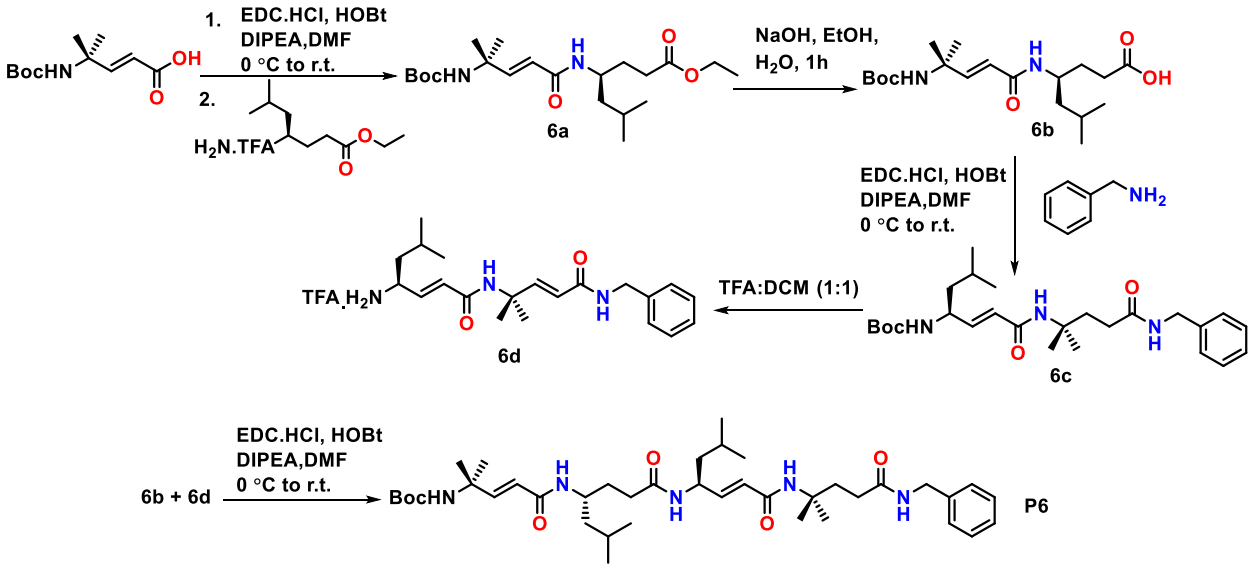


Scheme 4: Synthesis of peptide **P5**

The deprotection of the Boc group of the dipeptide **4a** was carried out by following the previously mentioned procedure in 3.5.3.1. In a typical coupling reaction, Boc-dγLeu(L)-OH (3 mmol, 0.768 g) and TFA·dγLeu(L)-dγAic-OEt (**5d**) (3 mmol, 1.1 g) were dissolved in 4 mL of DMF. EDC.HCl (3.3 mmol, 0.63 g) and HOBt (3 mmol, 405 mg) were added, and the mixture was cooled at 0 °C for 10 minutes. Subsequently, DIPEA (12 mmol, 2 mL) was introduced, and the reaction was allowed to reach room temperature. TLC was employed to monitor the reaction progress, which took approximately 24 hours. After completion, the mixture was diluted with 250 mL of ethyl acetate and subjected to washes with 5% HCl (3 × 80 mL), 10% sodium carbonate solution (3 × 80 mL), and brine (3 × 100 mL). The organic layer was dried with Na_2SO_4, evaporated under reduced pressure, and the crude product was purified through silica gel column chromatography using an EtOAc/Hexane solvent system. The overall yield of the product **5e** was 72% (2.16 mmol, 1.2 g).

Boc deprotection of tripeptide **5e** was carried out by following the procedure in 3.5.3.1. The peptide Boc-dγAic-dγLeu-dγLeu-dγLeu-dγAic-OEt (**P5**) was synthesized via a [2+3] condensation. In the coupling reaction, BocHN-dγAic-dγLeu(L)-OH (1.5 mmol, 0.55 g), EDC.HCl (1.65 mmol, 316 mg), and HOBt (1.5 mmol, 203 mg) were dissolved in 3 mL of DMF. DIPEA (6 mmol, 1 mL) was added to this solution, and after stirring for approximately 10 minutes under ice-cold conditions, TFA.H_2N-dγLeu(L)-dγLeu(L)-dγAic-OEt was introduced. The reaction mixture was stirred overnight at room temperature, and its completion was verified by TLC. The compound was then extracted with ethyl acetate and washed successively with 10% HCl (3 × 40 mL), 10% Na_2CO_3 (3 × 40 mL), and brine solution (3 × 40 mL). The combined organic layer was dried with anhydrous Na_2SO_4 and concentrated under reduced pressure. The final peptide **P5** was purified using reverse phase HPLC (C_{18} column, MeOH/H_2O 95:5 as a gradient, with a flow rate of 2.00 mL/min).

3.5.6. Synthesis of Peptide P6



Scheme 5: Synthesis of peptide **P6**

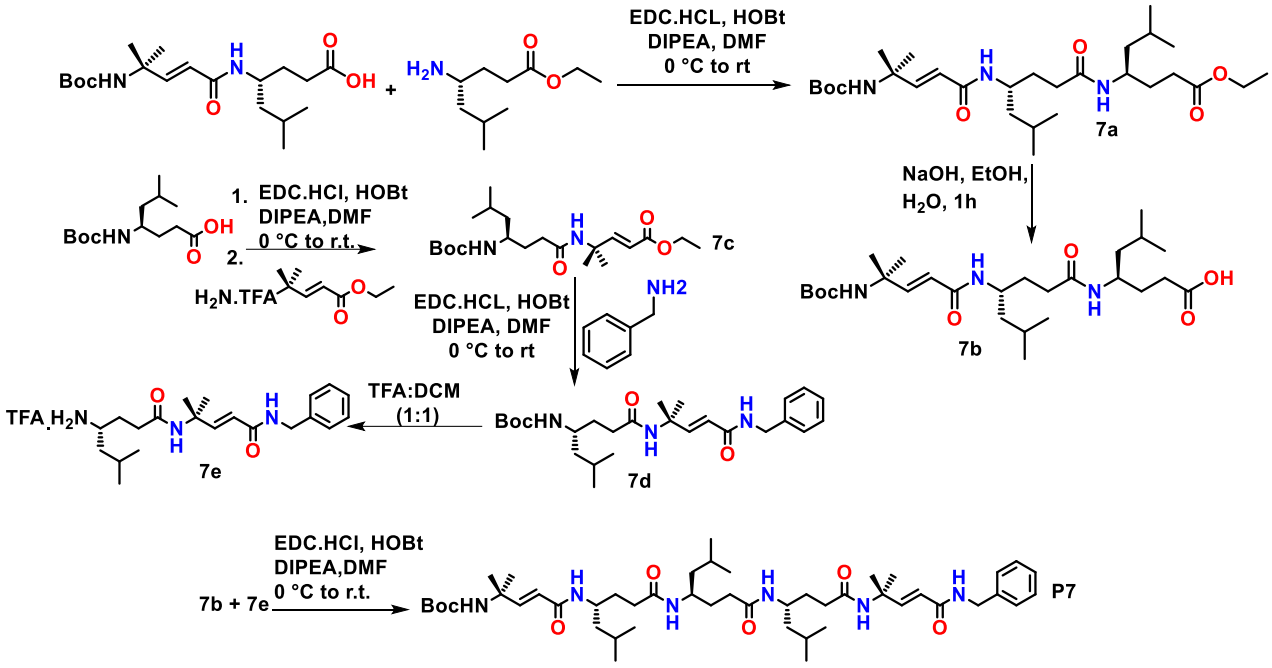
For the coupling reaction, Boc-dγAic-OH (6.5 mmol, 1.49 g) and TFA·H_2N-γLeu(L)-OEt (6.5 mmol, 1.12 g) were dissolved in DMF (6 mL). EDC.HCl (7.205 mmol, 1.38 g) and HOBt (6.5 mmol, 880 mg) were added to the solution, and the reaction mixture was cooled at 0 °C for 5 minutes. Subsequently, DIPEA (19.65 mmol, 3.52 mL) was introduced, and the reaction mixture was allowed to reach room temperature with stirring. The progress of the reaction was monitored by TLC. After approximately 24 hours, the reaction mixture was diluted with 250 mL of ethyl

acetate and washed with 10% HCl (3 × 80 mL), 10% sodium carbonate solution (3 × 80 mL), followed by brine (3 x 100 mL). The organic layer was dried over Na_2SO_4 and evaporated under reduced pressure. The crude product underwent purification on a silica gel column chromatography using an EtOAc/Hexane solvent system. The overall yield of the dipeptide 6a was 72% (4.68 mmol, 1.79 g).

Hydrolysis of BocHN-dγ-Aic-γLeu(L)-OEt was performed following the previously mentioned procedure (3.5.3.2.). The peptide BocHN-dγAic-γLeu(L)-OH (4 mmol, 1.062 g), EDC.HCl (4.4 mmol, 843 mg) and HOBt (4 mmol, 540 mg) were dissolved together in DMF (6 mL). To this solution (12 mmol, 1.5 mL) DIPEA was added. After stirring the reaction mixture for about 10 minutes at ice-cold conditions, benzylamine (9 mmol, 1.0 mL) was added. The reaction mixture was stirred overnight at room temperature. After completion of the reaction (monitored by TLC), the compound was extracted with ethyl acetate followed by successive washings with 10% HCl (3 × 40), 10% Na_2CO_3 (3× 40 mL) and brine solution (3× 40 mL). The combined organic layer was dried over anhydrous Na_2SO_4 and concentrated under reduced pressure. The crude product **6c** was purified on silica gel column chromatography using an EtOAc/Hexane solvent system Overall yield was 68% (2.72 mmol, 1.21 g).

Boc deprotection of BocHN-dγAic-γLeu(L)-NHBn (**6c**) was carried out following the previously mentioned procedure (3.5.3.1.). The peptide Boc-dγAic-γLeu(L)-dγAic-γLeu(L)-NHBn (**P6)** was prepared by [2+3] condensation. For the coupling reaction, BocHN-dγAic-γLeu(L)-OH (1.5 mmol, 0.55 g), EDC.HCl (1.65 mmol, 316 mg), and HOBt (1.5 mmol, 203 mg) were dissolved together in DMF (6 mL). To this solution, DIPEA (6 mmol, 4 mL) was added. After stirring the reaction mixture for approximately 10 minutes under ice-cold conditions, TFA.H_2N-γ Leu(L)-OEt was introduced. The reaction mixture was stirred overnight at room temperature. Upon completion of the reaction (monitored by TLC), the compound was extracted with ethyl acetate, followed by successive washings with 10% HCl (3 × 40 mL), 10% Na_2CO_3 (3× 40 mL), and brine solution (3 × 40 mL). The combined organic layer was then dried over anhydrous Na_2SO_4 and concentrated under reduced pressure. The final peptide **P6** underwent purification through reverse-phase HPLC using a C_{18} column with MeOH/H_2O (95:5) as the gradient and a flow rate of 2.00 mL/min.

3.5.7. Synthesis of Peptide P7



Scheme 6: Synthesis of peptide **P7**

For the coupling reaction, BocNH-dγAic-γLeu(L)-OH (**6a**) (3 mmol, 1.1 g) and TFA·H_2N-γLeu(L)-OEt (3 mmol, 0.89 g) were dissolved in 4 mL of DMF. Subsequently, EDC.HCl (3.3 mmol, 630 mg) and HOBt (3 mmol, 405 mg) were added to the mixture. The reaction mixture was allowed to cool at 0°C for 10 minutes. Following this, DIPEA (12 mmol, 2 mL) was introduced to the reaction mixture under stirring conditions, and the reaction mixture was allowed to return to room temperature. The monitoring of the reaction's progress was carried out by TLC. After the completion of the reaction (approximately 24 hrs), the reaction mixture was diluted with 250 mL of ethyl acetate and subjected to washing with 10% HCl (3 × 80 mL), 10% Na_2CO_3 solution in water (3 × 80 mL), followed by brine (3 x 100 mL). The organic layer was then dried over anhydrous sodium sulfate and concentrated under reduced pressure. The crude product **7a** was purified on a silica gel column chromatography using an EtOAc/Hexane solvent system. The overall yield of product **7a** was found to be 72% (2.16 mmol, 1.79 g).

The synthesis of peptide **7c** was carried out by following the above-mentioned coupling reaction procedure. The hydrolysis of **7c** was performed by following the procedure mentioned in 3.5.3.2. The peptide BocHN-γLeu(L)-dγAic-OH (**7c**) (4 mmol, 1.062 g), along with EDC.HCl (4.4 mmol, 843 mg) and HOBt (4 mmol, 540 mg), were dissolved in 6 mL of DMF. To this solution, DIPEA

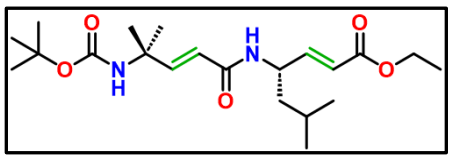
(12 mmol, 1.5 mL) was added. After stirring the reaction mixture for approximately 5 minutes under ice-cold conditions, benzylamine (9 mmol, 1.0 mL) was introduced. The reaction mixture was stirred overnight at room temperature. Upon completion of the reaction (monitored by TLC), the compound was extracted with ethyl acetate, followed by successive washings with 10% HCl (3 × 40 mL), 10% Na_2CO_3 (3× 40 mL), and brine solution (3 × 40 mL). The combined organic layer was dried over anhydrous Na_2SO_4 and concentrated under reduced pressure. The crude product **7d** was purified on a silica gel column chromatography using an EtOAc/Hexane solvent system. The overall yield was 68%.

The Boc group deprotection of BocHN-γLeu(L)-dγAic-NHBn (**7d**) was carried out as previously. The resulting gummy product, TFA.H_2N-γLeu(L)-dγAic-NHBn (**7e)** was subsequently utilized for coupling. The hydrolysis of BocHN-dγ-Aic-γLeu(L)-γLeu(L)-OEt (**7a**) was carried out following the previously mentioned procedure (5.2.1.1).

The peptide BocHN-dγ-Aic-γLeu(L)-γLeu(L)-γLeu(L)-dγAic-NHBn (**P7**) was synthesized through a [3+3] condensation. For the coupling reaction, Boc-dγAic-γLeu(L)-γLeu(L)-OH (1 mmol, 0.51 gm), along with EDC.HCl (1.1 mmol, 211 mg) and HOBt (1.0 mmol, 135 mg), were dissolved in 3 mL of DMF. To this solution, DIPEA (5 mmol, 1 ml) was added. After stirring the reaction mixture for about 10 minutes under ice-cold conditions, TFA.H_2N-γLeu(L)-dγAic-NHBn (**7e**) was added. The reaction mixture was stirred overnight at room temperature. Upon completion of the reaction (monitored by TLC), the compound was extracted with ethyl acetate, followed by successive washings with 10% HCl (3 × 40 mL), 10% Na_2CO_3 (3× 40 mL), and brine solution (3 × 40 mL). The combined organic layer was dried over anhydrous Na_2SO_4 and concentrated under reduced pressure. The final peptide was purified through reverse-phase HPLC (C_{18} column, MeOH/H_2O 95:5 as a gradient with a flow rate of 2.00 mL/min.

3.6. Characterization of Monomer and Peptides

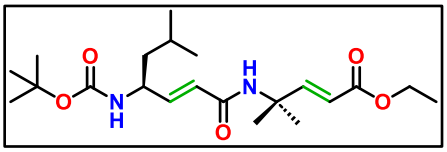
BocNH-dγAic-dγLeu-OEt (3a):



^{1}H NMR (400 MHz, $CDCl_3$) δ 6.88 – 6.84 (m, 1H), 6.84 – 6.80 (m, 1H), 5.92 (dd, *J* = 15.7, 1.6 Hz, 1H), 5.83 (d, *J* = 15.5 Hz, 1H), 5.72 (d, *J* = 7.8 Hz, 1H), 4.81 – 4.73 (m, 1H), 4.71 (s, 1H),

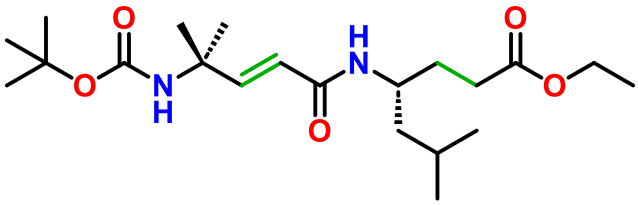
4.18 (q, *J* = 7.1 Hz, 2H), 1.66 (dq, *J* = 13.4, 6.7 Hz, 1H), 1.46 (d, *J* = 7.3 Hz, 2H), 1.43 (s, 9H), 1.41 (d, *J* = 2.2 Hz, 6H), 1.28 (t, *J* = 7.1 Hz, 3H), 0.94 (s, 3H), 0.93 (s, 3H). **^{13}C NMR** (101 MHz, $CDCl_3$) δ 166.51, 165.37, 154.50, 149.83, 148.20, 120.95, 120.56, 79.55, 60.56, 52.92, 48.50, 43.56, 28.50, 27.50, 24.86, 22.82, 22.28, 14.32. **MALDI TOF/TOF** m/z calculated value for $C_{21}H_{36}N_2O_5$ $[M+K]^+$ = 435.26 and observed $[M+K]^+$ = 435.38

BocNH- dγLeu -dγAic-OEt (4a):



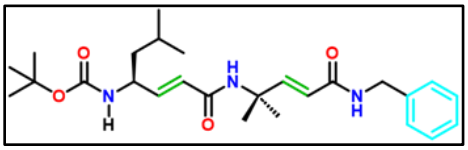
^{1}H NMR (400 MHz, $CDCl_3$) δ 7.03 (dd, *J* = 15.9, 1.1 Hz, 1H), 6.61 (dd, *J* = 15.3, 6.2 Hz, 1H), 5.84 (ddd, *J* = 15.8, 4.2, 1.5 Hz, 2H), 5.64 (s, 1H), 4.49 (s, 1H), 4.26 (d, *J* = 8.0 Hz, 1H), 4.17 (qd, *J* = 7.2, 1.9 Hz, 2H), 1.48 (d, *J* = 1.7 Hz, 6H), 1.43 (d, *J* = 1.9 Hz, 9H), 1.36 (t, *J* = 7.4 Hz, 2H), 1.27 (td, *J* = 7.1, 1.8 Hz, 3H), 0.92 (dd, *J* = 6.6, 2.0 Hz, 6H). **^{13}C NMR** (101 MHz, $CDCl_3$) δ 166.69, 164.60, 155.18, 152.54, 152.50, 144.64, 123.39, 118.82, 79.63, 77.35, 77.04, 76.72, 60.45, 53.80, 49.87, 44.02, 28.41, 27.15, 27.11, 24.65, 22.59, 22.31, 14.24. **MALDI TOF/TOF** m/z calculated value for $C_{21}H_{36}N_2O_5$ $[M+K]^+$ = 435.26 and observed $[M+K]^+$ = 435.22

BocNH-dγAic-γLeu-OEt (6a):



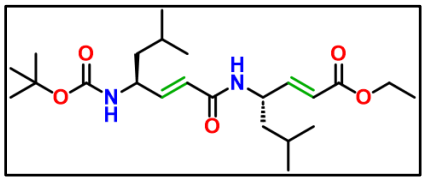
^{1}H NMR (400 MHz, CDCl3) δ 6.77 (d, J = 15.5 Hz, 1H), 5.74 (d, J = 15.5 Hz, 1H), 5.59 (d, J = 9.3 Hz, 1H), 4.71 (s, 1H), 4.07 (q, J = 7.2 Hz, 3H), 2.32 (ddd, J = 8.2, 6.9, 3.2 Hz, 2H), 1.89 – 1.79 (m, 1H), 1.67 – 1.52 (m, 2H), 1.36 (s, 6H), 1.33 – 1.29 (m, 1H), 1.25 (dt, J = 6.9, 5.2 Hz, 2H), 1.20 (t, J = 7.1 Hz, 3H), 0.87 (dd, J = 6.6, 3.4 Hz, 6H). **^{13}C NMR** (101 MHz, $CDCl_3$) δ 174.26, 165.95, 154.69, 149.31, 121.28, 79.72, 77.80, 77.48, 77.16, 60.84, 53.20, 47.61, 45.22, 31.45, 31.12, 28.77, 27.78, 27.77, 25.29, 23.42, 22.65, 14.58. MALDI TOF/TOF m/z calculated value for $C_{21}H_{38}N_2O_5$ $[M+K]^+$ = 437.28 and observed $[M+K]^+$ = 437.26

BocNH- dγLeu -dγAic-NHBn (4c):



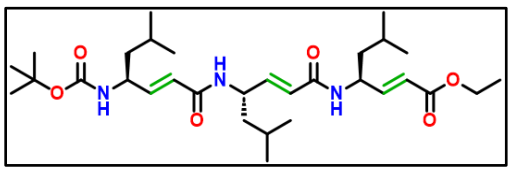
^{1}H NMR (400 MHz, $CDCl_3$) δ 7.63 (s, 1H), 7.29 (t, *J* = 2.0 Hz, 4H), 7.19 (td, *J* = 6.3, 2.9 Hz, 1H), 6.89 (s, 1H), 6.73 (d, *J* = 15.4 Hz, 1H), 6.63 (dd, *J* = 15.2, 4.4 Hz, 1H), 5.77 (dd, *J* = 15.4, 1.8 Hz, 1H), 5.63 (d, *J* = 15.4 Hz, 1H), 4.56 (d, *J* = 8.1 Hz, 1H), 4.44 (d, *J* = 5.4 Hz, 2H), 4.25 (s, 1H), 1.95 – 1.82 (m, 2H), 1.64 (h, *J* = 7.7 Hz, 1H), 1.45 (d, *J* = 12.6 Hz, 9H), 1.39 – 1.32 (m, 6H), 0.89 (dd, *J* = 9.3, 6.5 Hz, 6H). **^{13}C NMR** (101 MHz, $CDCl_3$) δ 165.68, 164.33, 156.06, 147.05, 144.86, 138.68, 128.72, 128.42, 128.12, 127.87, 127.54, 126.93, 122.27, 120.74, 80.36, 54.24, 50.23, 44.07, 43.76, 43.67, 38.62, 29.10, 28.51, 27.19, 26.46, 24.92, 23.27, 22.77, 21.73. **MALDI TOF/TOF** m/z calculated value for $C_{26}H_{39}N_3O_4$ $[M+K]^+$ = 496.29 and observed $[M+K]^+$ = 496.282.

BocNH-dγLeu-dγLeu-OEt (P2):



^{1}H NMR (400 MHz, $CDCl_3$) δ 6.82 (dd, *J* = 15.7, 5.7 Hz, 1H), 6.69 (d, *J* = 15.0 Hz, 1H), 5.89 (ddd, *J* = 15.3, 4.5, 1.5 Hz, 2H), 5.50 (s, 1H), 4.75 (p, *J* = 7.1 Hz, 1H), 4.38 (d, *J* = 74.3 Hz, 2H), 4.17 (qd, *J* = 7.1, 1.6 Hz, 2H), 1.67 – 1.64 (m, 4H), 1.44 (d, *J* = 1.2 Hz, 9H), 1.38 (t, *J* = 7.4 Hz, 2H), 0.93 (dd, *J* = 6.7, 2.2 Hz, 12H). **^{13}C NMR** (101 MHz, CDCl3) δ 166.33, 164.87, 147.83, 120.97, 77.35, 77.23, 77.03, 76.71, 60.50, 48.44, 44.03, 43.54, 28.40, 28.17, 24.79, 24.66, 22.72, 22.66, 22.19, 14.23. **MALDI TOF/TOF** m/z calculated value for $C_{23}H_{40}N_2O_5$ $[M+K]^+$ = 463.29 and observed $[M+K]^+$ = 463.297.

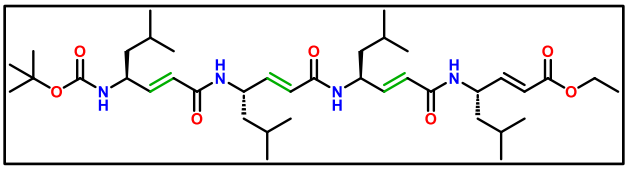
BocNH- dγLeu - dγLeu- dγLeu-OEt (P2):



^{1}H NMR (400 MHz, $CDCl_3$) δ 7.19 (s, 1H), 6.87 (dd, *J* = 15.8, 5.5 Hz, 1H), 6.82 – 6.78 (m, 1H), 6.78 – 6.68 (m, 2H), 5.94 – 5.85 (m, 2H), 5.64 (d, *J* = 15.2 Hz, 1H), 4.78 – 4.56 (m, 3H), 4.27 (d,

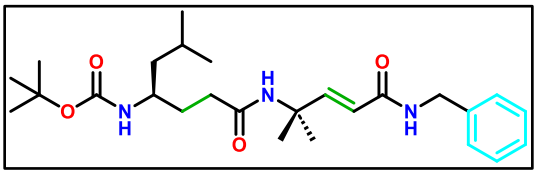
J = 6.8 Hz, 1H), 4.17 (q, *J* = 7.1 Hz, 2H), 1.70 (dt, *J* = 14.0, 6.9 Hz, 3H), 1.49 (d, *J* = 5.2 Hz, 9H), 1.47 – 1.37 (m, 6H), 1.28 (t, *J* = 7.1 Hz, 3H), 0.95 – 0.89 (m, 18H). **^{13}C NMR** (101 MHz, $CDCl_3$) δ 166.39, 164.98, 155.62, 148.35, 144.93, 143.84, 122.22, 121.98, 120.29, 79.60, 60.10, 49.79, 48.41, 48.18, 43.61, 43.26, 43.17, 40.48, 40.27, 40.06, 39.85, 39.65, 39.44, 28.30, 24.59, 24.40, 22.72, 22.65, 22.57, 22.01, 21.78, 21.58, 21.39, 14.09**. MALDI TOF/TOF** m/z calculated value for $C_{31}H_{35}N_3O_6$ $[M+K]^+$ = 602.39 and observed $[M+K]^+$ = 602.399

BocNH- dγLeu - dγLeu- dγLeu- dγLeu -OEt (P3):



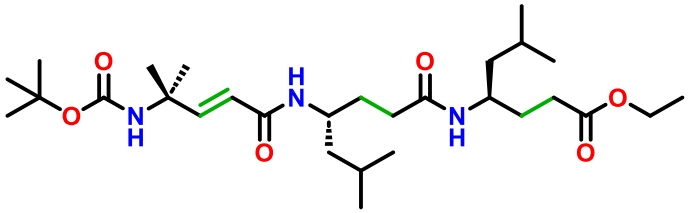
^{1}H NMR (400 MHz, CDCl3) δ 8.10 (d, J = 8.2 Hz, 2H), 7.80 (s, 1H), 7.00 – 6.76 (m, 4H), 6.04 – 5.91 (m, 2H), 5.49 (t, J = 13.7 Hz, 2H), 4.78 (d, J = 7.5 Hz, 2H), 4.50 (s, 2H), 4.17 (q, J = 7.1 Hz, 2H), 1.73 (dt, J = 13.6, 6.9 Hz, 4H), 1.51 (d, J = 6.5 Hz, 9H), 1.49 – 1.35 (m, 8H), 1.30 – 1.26 (m, 3H), 0.96 – 0.90 (m, 24H). **^{13}C NMR** (151 MHz, $C_2D_2Cl_4$) δ 166.72, 165.15, 165.00, 164.90, 156.40, 148.60, 146.05, 145.53, 144.59, 123.41, 120.77, 120.32, 80.82, 74.04, 73.96, 73.78, 73.60, 60.25, 50.32, 49.53, 48.23, 43.49, 43.31, 42.71, 28.35, 25.13, 24.78, 24.75, 23.05, 22.93, 22.70, 22.52, 22.35, 21.99, 21.48, 14.29. **MALDI TOF/TOF** m/z calculated value for $C_{39}H_{66}N_4O_7$ $[M+K]^+$ = 741.49 and observed $[M+K]^+$ = 741.509

BocNH- γLeu -dγAic-NHBn (7d):



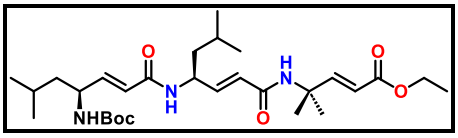
^{1}H NMR (400 MHz, $CDCl_3$) δ 7.31 (s, 1H), 7.27 (s, 3H), 7.26 – 7.16 (m, 2H), 6.82 (d, *J* = 15.5 Hz, 1H), 6.55 (s, 1H), 5.98 (d, *J* = 15.5 Hz, 1H), 4.58 (d, *J* = 9.7 Hz, 1H), 4.51 – 4.38 (m, 2H), 3.62 (h, *J* = 4.0 Hz, 1H), 2.22 – 2.09 (m, 2H), 1.89 – 1.76 (m, 1H), 1.66 – 1.55 (m, 1H), 1.47 (s, 4H), 1.36 (s, 3H), 1.35 (s, 9H), 1.29 – 1.15 (m, 3H), 0.85 (dd, *J* = 6.7, 4.8 Hz, 6H). **^{13}C NMR** (101 MHz, $CDCl_3$) δ 171.86, 171.20, 166.23, 156.38, 147.75, 138.56, 128.53, 128.44, 127.85, 127.10, 120.94, 79.17, 53.91, 47.98, 45.57, 45.50, 43.43, 32.99, 31.69, 28.35, 28.13, 26.88, 24.88, 22.98, 22.62, 22.37, 22.17. **MALDI TOF/TOF** m/z calculated value for $C_{26}H_{41}N_3O_4$ $[M+K]^+$ = 482.31 and observed $[M+K]^+$ = 482.32

BocNH- dγAic -γLeu- γLeu-OEt (7a):



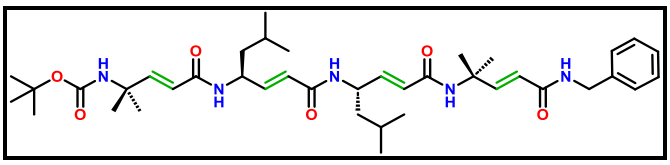
^{1}H NMR (400 MHz, $CDCl_3$) δ 7.17 – 6.97 (m, 1H), 6.76 (d, *J* = 15.5 Hz, 1H), 6.33 (s, 1H), 5.82 (d, *J* = 15.5 Hz, 1H), 4.90 (s, 1H), 4.07 (dd, *J* = 7.1, 3.0 Hz, 2H), 3.97 (ddp, *J* = 17.9, 8.9, 4.1 Hz, 2H), 2.31 (ddd, *J* = 8.7, 6.7, 1.9 Hz, 2H), 2.10 (dddd, *J* = 13.7, 10.0, 7.2, 4.0 Hz, 2H), 1.89 – 1.75 (m, 2H), 1.70 – 1.42 (m, 6H), 1.38 (s, 9H), 1.37 (s, 6H), 1.29 – 1.24 (m, 2H), 1.19 (d, *J* = 7.1 Hz, 3H), 0.86 – 0.83 (m, 12H). **^{13}C NMR** (101 MHz, CDCl3) δ 173.92, 173.85, 173.81, 173.65, 172.94, 172.85, 170.02, 166.20, 120.84, 79.54, 77.40, 77.08, 76.77, 60.35, 52.96, 47.43, 46.89, 44.97, 44.24, 31.16, 30.90, 29.65, 29.61, 28.39, 27.53, 27.37, 24.98, 24.91, 24.86, 23.05, 23.03, 23.00, 22.29, 22.22, 22.14, 22.05, 14.19. MALDI TOF/TOF m/z calculated value for $C_{29}H_{53}N_3O_6$ [M+K]+ = 578.39 and observed [M+K]+ = 578.39

BocNH- dγLeu - dγLeu- dγAic-OEt (5e):



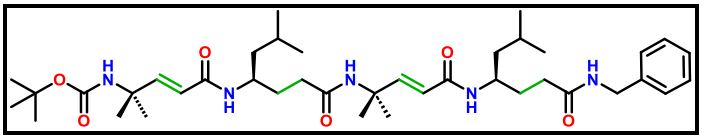
^{1}H NMR (400 MHz, CDCl3) δ 7.20 (s, 1H), 7.08 (d, J = 15.9 Hz, 1H), 7.04 (s, 1H), 6.79 (dd, J = 15.1, 3.6 Hz, 1H), 6.73 (dd, J = 15.1, 4.0 Hz, 1H), 5.90 (dd, J = 15.2, 2.0 Hz, 1H), 5.83 (d, J = 16.0 Hz, 1H), 5.52 (d, J = 15.0 Hz, 1H), 4.57 (d, J = 8.7 Hz, 2H), 4.27 (s, 1H), 4.18 – 4.12 (m, 2H), 1.72 (qt, J = 13.1, 6.6 Hz, 3H), 1.63 – 1.58 (m, 3H), 1.42 (s, 6H), 1.29 – 1.25 (m, 3H), 0.95 – 0.90 (m, 12H). **^{13}C NMR** (101 MHz, CDCl3) δ 167.08, 165.10, 164.46, 156.24, 154.04, 146.00, 143.69, 122.13, 121.06, 118.05, 80.49, 77.34, 77.23, 77.03, 76.71, 60.25, 53.64, 50.31, 49.16, 43.60, 43.14, 28.49, 27.60, 26.11, 24.99, 24.84, 22.93, 22.89, 21.70, 21.47, 14.28.

BocNH- dγAic-dγLeu- dγLeu- dγAic-NHBn (P4):



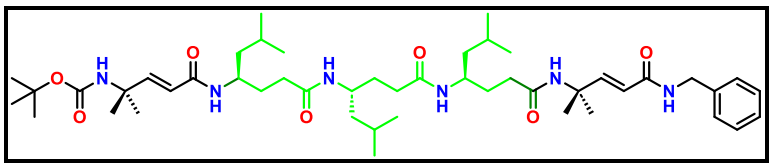
^{1}H NMR (400 MHz, $CDCl_3$) δ 8.26 (t, *J* = 5.7 Hz, 1H), 8.23 – 8.06 (m, 2H), 8.01 (s, 1H), 7.40 – 7.32 (m, 2H), 7.29 (d, *J* = 7.5 Hz, 2H), 7.21 – 7.12 (m, 1H), 6.95 (dd, *J* = 15.1, 3.5 Hz, 1H), 6.81 – 6.62 (m, 3H), 6.02 (d, *J* = 15.1 Hz, 1H), 5.67 – 5.51 (m, 2H), 5.40 (dd, *J* = 15.2, 1.8 Hz, 1H), 4.71 (s, 1H), 4.54 (d, *J* = 9.7 Hz, 2H), 4.49 – 4.23 (m, 2H), 1.90 – 1.74 (m, 2H), 1.63 – 1.53 (m, 2H), 1.50 (s, 9H), 1.46 (s, 3H), 1.45 – 1.37 (m, 6H), 1.34 (d, *J* = 4.4 Hz, 6H), 1.30 – 1.22 (m, 4H), 0.92 – 0.84 (m, 12H). **^{13}C NMR** (151 MHz, $C_2D_2Cl_4$) δ 171.19, 165.85, 165.68, 164.66, 154.61, 149.13, 147.85, 146.33, 145.40, 138.95, 128.66, 128.58, 128.22, 128.00, 127.58, 127.49, 126.67, 120.71, 120.42, 119.51, 118.67, 80.18, 60.39, 53.86, 53.65, 49.60, 48.90, 43.54, 43.37, 42.95, 42.20, 34.34, 31.10, 30.18, 28.40, 25.98, 25.35, 25.22, 24.67, 24.10, 23.22, 23.10, 22.86, 22.40, 22.04, 21.11, 14.17. **MALDI TOF/TOF** m/z calculated value for $C_{40}H_{61}N_5O_6$ $[M+K]^+$ = 746.46 and observed $[M+K]^+$ = 746.47

BocNH- dγAic-dγLeu- γAic- γLeu-NHBn:



^{1}H NMR (400 MHz, $CDCl_3$) δ 8.49 (s, 1H), 7.95 (s, 1H), 7.39 – 7.27 (m, 4H), 7.22 – 7.17 (m, 1H), 6.76 (d, *J* = 15.3 Hz, 1H), 6.55 (d, *J* = 15.2 Hz, 1H), 5.89 (d, *J* = 15.3 Hz, 1H), 5.52 (s, 1H), 4.78 (s, 1H), 4.44 (ddd, *J* = 48.3, 14.8, 5.9 Hz, 2H), 4.03 (s, 1H), 3.96 (s, 1H), 2.27 – 1.83 (m, 8H), 1.64 – 1.56 (m, 2H), 1.47 (s, 3H), 1.45 (s, 9H), 1.43 (d, *J* = 2.3 Hz, 4H), 1.42 (s, 3H), 1.39 (s, 2H), 1.36 (d, *J* = 8.5 Hz, 6H), 1.30 – 1.16 (m, 4H), 0.86 – 0.81 (m, 12H). **^{13}C NMR** (101 MHz, $CDCl_3$) δ 173.22, 172.20, 166.14, 154.79, 148.27, 139.56, 128.35, 128.00, 126.77, 120.40, 80.06, 77.35, 77.23, 77.03, 76.71, 54.22, 53.57, 47.91, 47.90, 44.86, 43.18, 32.99, 31.27, 30.26, 28.56, 28.51, 24.89, 24.75, 23.00, 22.77, 22.55, 22.25. **MALDI TOF/TOF** m/z calculated value for $C_{40}H_{65}N_5O_6$ $[M+Na]^+$ = 734.49 and observed $[M+Na]^+$ = 734.50

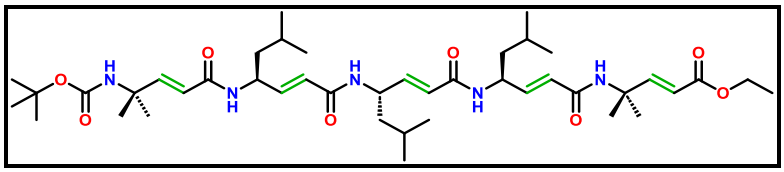
BocNH- dγAic-γLeu-γLeu- γLeu-dγAic-NHBn (P7):



^{1}H NMR (400 MHz, $CDCl_3$) δ 7.62 (s, 1H), 7.36 (s, 1H), 7.34 – 7.26 (m, 4H), 7.20 (t, *J* = 7.0 Hz, 1H), 7.06 (s, 1H), 6.77 (dd, *J* = 15.5, 4.4 Hz, 2H), 6.39 (s, 1H), 5.95 (d, *J* = 15.4 Hz, 1H), 5.83 (dd, *J* = 15.4, 1.4 Hz, 1H), 4.73 (s, 1H), 4.59 – 4.38 (m, 2H), 4.19 – 3.81 (m, 3H), 2.18 – 1.96 (m, 6H),

1.59 (dq, *J* = 20.8, 6.7 Hz, 3H), 1.42 (d, *J* = 2.6 Hz, 9H), 1.38 (s, 6H), 1.33 (s, 6H), 1.29 – 1.11 (m, 4H), 1.06 – 0.74 (m, 18H). **^{13}C NMR** (101 MHz, $CDCl_3$) δ 172.81, 172.31, 172.12, 166.31, 166.08, 147.55, 138.94, 128.37, 127.93, 126.92, 120.88, 120.61, 54.07, 46.57, 45.05, 43.38, 32.79, 32.34, 30.94, 28.56, 28.43, 25.04, 25.00, 23.16, 23.08, 22.95, 22.59, 22.48, 22.16. **MALDI TOF/TOF** m/z calculated value for $C_{48}H_{80}N_6O_7[M+Na]^+$ = 891.61 and observed $[M+Na]^+$ = 891.75

BocNH- dγAic-dγLeu-dγLeu- dγLeu-dγAic-OEt (P5):



^{1}H NMR (400 MHz, CDCl3) δ 8.22 (dd, J = 13.1, 6.6 Hz, 2H), 7.99 (s, 1H), 7.81 (s, 1H), 7.15 (d, J = 15.9 Hz, 1H), 6.93 (dd, J = 6.3, 3.5 Hz, 1H), 6.91 – 6.81 (m, 2H), 6.72 (d, J = 15.1 Hz, 1H), 6.05 (d, J = 15.1 Hz, 1H), 5.84 (d, J = 15.9 Hz, 1H), 5.64 (dd, J = 15.1, 1.9 Hz, 1H), 5.51 (dd, J = 15.2, 1.9 Hz, 1H), 5.41 (dd, J = 15.2, 1.9 Hz, 1H), 4.74 (s, 1H), 4.62 – 4.45 (m, 3H), 4.15 (q, J = 7.1 Hz, 2H), 1.87 (dq, J = 21.2, 9.7 Hz, 3H), 1.62 (qd, J = 8.3, 3.8 Hz, 4H), 1.51 (s, 9H), 1.49 (d, J = 1.4 Hz, 6H), 1.48 – 1.38 (m, 6H), 1.30 – 1.24 (m, 6H), 1.01 – 0.87 (m, 18H). **^{13}C NMR** (101 MHz, CDCl3) δ 167.27, 165.96, 165.69, 164.63, 154.98, 154.86, 149.47, 146.09, 143.88, 141.98, 137.18, 130.29, 121.51, 119.82, 119.03, 117.63, 80.30, 60.07, 54.09, 53.36, 49.71, 49.17, 42.96, 42.81, 42.70, 40.26, 40.05, 39.84, 28.58, 27.54, 25.79, 25.67, 25.37, 25.06, 24.87, 22.95, 22.66, 22.37, 22.08, 21.54, 14.28, **MALDI TOF/TOF** m/z calculated value for $C_{43}H_{71}N_5O_8[M+Na]^+$ = 824.53 and observed $[M+K]^+$ = 824.55

3.7. Appendix

3.7.1. ORTEP Diagrams

3.7.1.1. **ORTEP Diagram of Peptide P4**

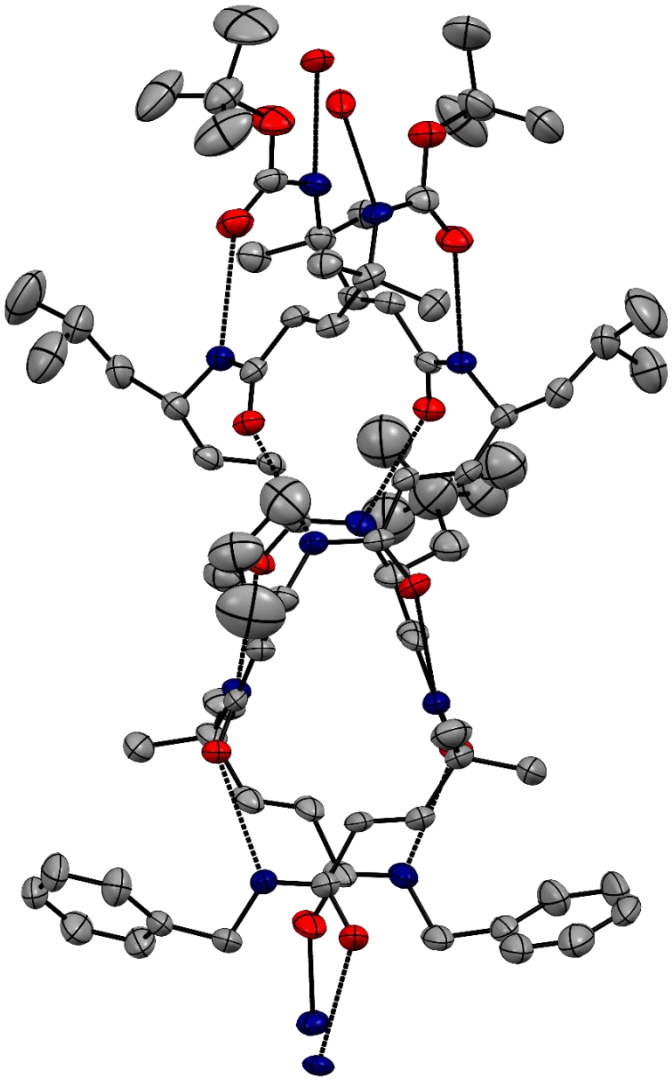


Figure 20: ORTEP diagram of peptide **P4.** H-bonds are shown in dotted lines. H-atoms are omitted for clarity. Ellipsoids are drawn at 50% probability. CCDC no 2295105

3.7.1.2. ORTEP Diagram of Peptide P6

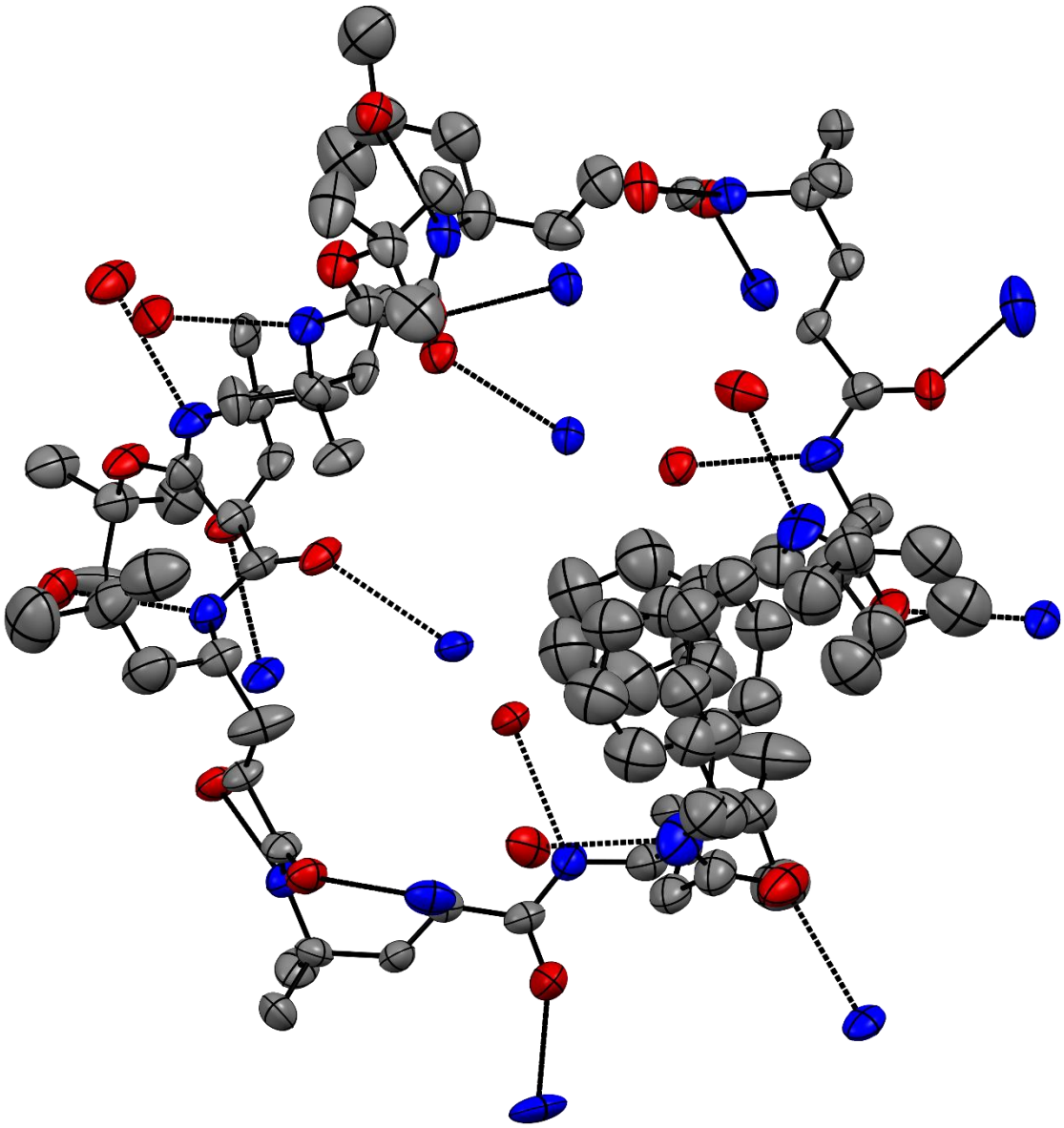


Figure 21: ORTEP diagram of peptide **P6**. H-bonds are shown in dotted lines. H-atoms are omitted for clarity. Ellipsoids are drawn at 50% probability. CCDC no 2295105

3.7.1.3. ORTEP Diagram of Peptide P7

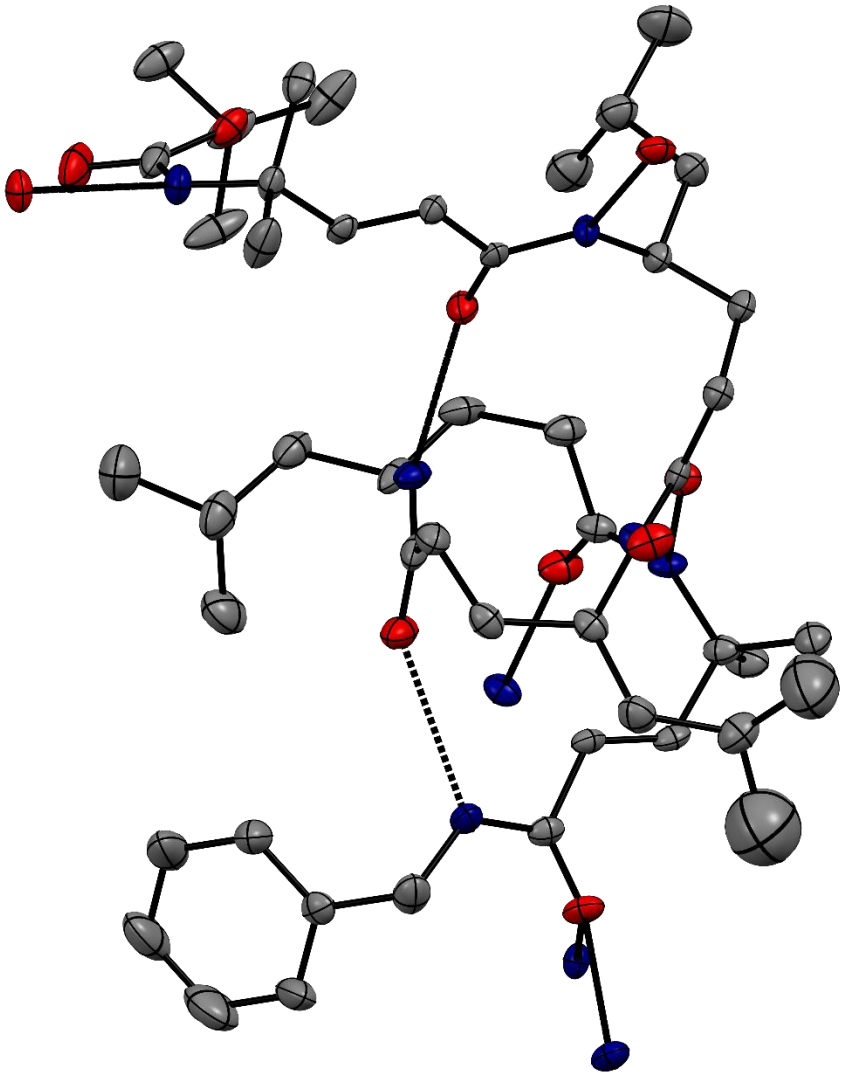


Figure 22: ORTEP diagram of peptide **P7.** H-bonds are shown in dotted lines. H-atoms are omitted for clarity. Ellipsoids are drawn at 50% probability. CCDC no 2295107

3.8. Crystal Structure Information of the Peptides

Crystal structure analysis of P4: Crystals were grown from chloroform/toluene solution by slow evaporation. A single crystal (0.28 × 0.09 × 0.15 mm) was mounted on a loop with a small amount of the paraffin oil. The X-ray data were collected at 150 K temperature using Mo K_α radiation (λ = 1.54178 Å), ω-scans (2θ = 130.216), for a total of 8544 independent reflections. Space group 'P 21 21 2', a = 21.8730(19), b = 34.755(3), c = 11.9812(11), α = 90, β = 90, γ = 90 V = 9108.1(14)Å^3, orthorhombic, Z = 4 for chemical formula C_{40} H_{61} N_5 O_6, with two molecules in asymmetric unit; ρcalcd = 1.027 gcm^{-3}, μ = 0.555mm^{-1}, F (000) = 3044, The structure was obtained by direct methods using SHELXS- 97.[1] The final R value was 0.0624 (wR2 = 0.1700) 14849 observed reflections ($F_0 \geq 4\sigma$ (|F_0|))and 951 variables, S = 1.009.

Crystal structure analysis of P6: Crystals were grown from chloroform/Ethyl acetate solution by slow evaporation. A single crystal (0.28 × 0.1 × 0.2 mm) was mounted on a loop with a small amount of the paraffin oil. The X-ray data were collected at 150 K temperature using Mo K_α radiation (λ = 0.71073 Å), ω-scans (2θ = 49.992), for a total of 8383 independent reflections. Space group 'P 61', a = 17.70(7), b = 17.07(7), c = 53.9(3), α = 90, β = 90, γ = 120 V = 14624(142)Å^3, hexagonal, Z = 6 for chemical formula C_{80} H_{124} N_{10} O_{12}, with two molecules in asymmetric unit; ρcalcd = 0.966 gcm^{-3}, μ = 0.065 mm^{-1}, F (000) = 4620, The structure was obtained by direct methods using SHELXS- 97.[1] The final R value was 0.1445 (wR2 = 0.4418) 17160 observed reflections ($F_0 \geq 4\sigma$ (|F_0|))and 987 variables, S = 1.380.

Crystal structure analysis of P7: Crystals were grown from chloroform/Ethyl acetate solution by slow evaporation. A single crystal (0.2 × 0.75 × 0.2 mm) was mounted on a loop with a small amount of the paraffin oil. The X-ray data were collected at 150 K temperature using Mo K_α radiation (λ = 0.71073 Å), ω-scans (2θ = 49.65), for a total of 7737 independent reflections. Space group 'P 21 21 21', a = 11.761(2), b = 17.751(4), c = 24.416(5), α = 90, β = 90, γ = 90 V = 5097.3(18)Å^3, orthorhombic, Z = 4 for chemical formula C_{48} H_{80} N_6 O_7, with one molecule in asymmetric unit; ρcalcd = 1.112 gcm^{-3}, μ = 0.074 mm^{-1}, F (000) = 1864, The structure was obtained by direct methods using SHELXS- 97.[1] The final R value was 0.053 (wR2 = 0.1379) 8740 observed reflections ($F_0 \geq 4\sigma$ (|F_0|))and 563 variables, S = 1.034.

3.9. References

1. Creighton T. E., *Proteins: structure and molecular properties*, W. H. Freeman and Co., New York, 2nd edn, 1993
2. (a) Watson J. D. and Crick F. H. C., *Nature*, **1953**, *171*, 964; (b) Watson J. D. and Crick F. H. C., *Nature*, **1953**, *171*, 737
3. (a) Isobe, H.; Fujino, T.; Yamazaki, N.; Guillot-Nieckowski, M.; Nakamura, E. *Org. Lett.* **2008**, *10*, 3729. (b) Burgess, K.; Gibbs, R. A.; Metzker, M. L.; Raghavachari, R. *J. Chem. Soc. Chem. Commun.* **1994**, 8, 915. (c) Appella, D. H. *Curr. Opin. Chem. Biol.* **2009**, *13*, 687.
4. (a) Liu, H.; Gao, J.; Lynch, S. R.; Saito, Y. D.; Maynard, L.; Kool, E. T. *Science*, **2003**, *302*, 868. (b) Delaney, J. C.; Gao, J.; Liu, H.; Shrivastav, N.; Essigmann, J. M.; Kool, E. T. *Angew. Chemie Int. Ed.* **2009**, *48*, 4524. (c) Zhang, L.; Yang, Z.; Sefah, K.; Bradley, K. M.; Hoshika, S.; Kim, M.-J.; Kim, H.-J.; Zhu, G.; Jiménez, E.; Cansiz, S.; Teng, I.-T.; Champanhac, C.; McLendon, C.; Liu, C.; Zhang, W.; Gerloff, D. L.; Huang, Z.; Tan, W.; Benner, S. A. *J. Am. Chem. Soc.* **2015**, *137*, 6734. (d) Schweitzer, B. A.; Kool, E. T. *J. Org. Chem.* **1994**, *59*, 7238.
5. (a) Gerber, A.; Leumann, C. J. *Chem. – A Eur. J.* **2013**, *19*, 6990. (b) Obika, S.; Nanbu, D.; Hari, Y.; Morio, K.; In, Y.; Ishida, T.; Imanishi, T. *Tetrahedron Lett.* **1997**, *38*, 8735. (c) Schöning, K.-U.; Scholz, P.; Guntha, S.; Wu, X.; Krishnamurthy, R.; Eschenmoser, A. *Science*, **2000**, *290*, 1347. (d) Koshkin, A. A.; Singh, S. K.; Nielsen, P.; Rajwanshi, V. K.; Kumar, R.; Meldgaard, M.; Olsen, C. E.; Wengel, J. *Tetrahedron* **1998**, *54*, 3607. (e) Zhang, L.; Peritz, A.; Meggers, E. *J. Am. Chem. Soc.* **2005**, *127*, 4174. (f) Aerschot Van, A.; Verheggen, I.; Hendrix, C.; Herdewijn, P. *Angew. Chemie Int. Ed.*, **1995**, *34*, 1338.
6. (a) Yang, Y.; Yang, Z.-Y.; Yi, Y.-P.; Xiang, J.-F.; Chen, C.-F.; Wan, L.-J.; Shuai, Z.-G. *J. Org. Chem.* **2007**, *72*, 4936. (b) Gong, H.; Krische, M. J. *J. Am. Chem. Soc.* **2005**, *127*, 1719. (c) Stross, A. E.; Iadevaia, G.; Núñez-Villanueva, D.; Hunter, C. A. *J. Am. Chem. Soc.* **2017**, *139*, 12655. (d) Bisson, A. P.; Carver, F. J.; Eggleston, D. S.; Haltiwanger, R. C.; Hunter, C. A.; Livingstone, D. L.; McCabe, J. F.; Rotger, C.; Rowan, A. E. *J. Am. Chem. Soc.* **2000**, *122*, 8856.
7. (a) Kramer, R.; Lehn, J. M.; Marquis-Rigault, A. *Proc. Natl. Acad. Sci.* **1993**, *90*, 5394. (b) Taylor, P. N.; Anderson, H. L. *J. Am. Chem. Soc.* **1999**, *121*, 11538.

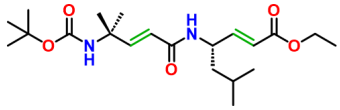
8. (a) Tanaka, Y.; Katagiri, H.; Furusho, Y.; Yashima, E. *Angew. Chemie Int. Ed.* **2005**, *44*, 3867. (b) Ito, H.; Furusho, Y.; Hasegawa, T.; Yashima, E. *J. Am. Chem. Soc.* **2008**, *130*, 14008.
9. (a) Berl, V.; Huc, I.; Khoury, R. G.; Krische, M. J.; Lehn, J.-M. *Nature* **2000**, *407*, 720. (b) Ferrand, Y.; Gan, Q.; Kauffmann, B.; Jiang, H.; Huc, I. *Angew. Chemie Int. Ed.* **2011**, *50*, 7572. (C) Shang, J.; Gan, Q.; Dawson, S. J.; Rosu, F.; Jiang, H.; Ferrand, Y.; Huc, I. *Org. Lett.* **2014**, *16* , 4992. (d) Gan, Q.; Wang, X.; Kauffmann, B.; Rosu, F.; Ferrand, Y.; Huc, I. *Nat. Nanotechnol.* **2017**, *12*, 447. (e) Gan, Q.; Ferrand, Y.; Chandramouli, N.; Kauffmann, B.; Aube, C.; Dubreuil, D.; Huc, I. *J. Am. Chem. Soc.* **2012**, *134*, 15656.
10. (a) Yashima, E.; Maeda, K.; Furusho, Y. *Acc. Chem. Res.* **2008**, *41*, 1166. (b) Koert, U.; Harding, M. M.; Lehn, J.-M.; *Nature* **1990**, *346*, 339. (c) Gabriel, G. J.; Iverson, B. L. *J. Am. Chem. Soc*., **2002**, *124*, 15174. (d) Lokey, R. S.; Iverson, B. L. *Nature* **1995**, *375*, 303. (e) Ikkanda, B. A.; Iverson, B. L. *Chem. Commun.* **2016**, *52*, 7752. (f) Yashima, E.; Ousaka, N.; Taura, D.; Shimomura, K.; Ikai, T.; Maeda, K. *Chem. Rev.* **2016**, *116*, 13752. (g) Wang, J.; Meersman, F.; Esnouf, R.; Froeyen, M.; Busson, R.; Heremans, K.; Herdewijn, P. *Helv. Chim. Acta*. **2001**, *84*, 2398; (i) Wang, Y.; He, Y.; Yu, Z.; Gao, J.; Brinck, S. Ten.; Slebodnick, C.; Fahs, G. B.; Zanelotti, C. J.; Hegde, M.; Moore, R. B.; Ensing, B.; Dingemans, T. J.; Qiao, R.; Madsen, L. A.; *Nat. Commun.* **2019**, *10*, 801. (j) Hu, Y.; Teat, S.J.; Gong, W.; Zhou, Z.; Jin, Y.; Chen, H.; Wu, J.; Cui, Y.; Jiang, T.; Cheng, X.; Zhang, W. *Nat. Chem.* **2021**, *13*, 660. (k) Liu, C.; Koppireddi, S.; Wang, H.; Zhang, D.; Li, Z. *Angew. Chem. Int. Ed.* **2019**, *58*, 226.
11. (a) Langes, D. A. *Science* **1988**, *241*, 188. (b) Urry, D. W.; Glickson, J. D.; Mayers, D. F.; Haider, J. *Biochemistry* **1972,** *11*, 487. c) Wallace, B. A.; Ravikumar, K. *Science* **1988**, *241*, 182. (c) Wallace, B. *J. Struct. Biol.* **1998**, *121*, 123.
12. (a) Vertesy, L.; Aretz, W.; Knauf, M.; Markus, A.; Vogel, M.; Wink, J. J. *Antibiot.* **1999**, *52*, 374. (b) Bunkóczi, G.; Vértesy, L.; Sheldrick, G. M.; *Angew. Chem. Int. Ed.* **2005**, *44*, 1340. (c) F. Dettner, A. Hänchen, D. Schols, L. Toti, A. Nußer, R. D. Süssmuth, *Angew. Chem. Int. Ed.* **2009**, *48*, 1856. (d) Férir, G.; Hänchen, A.; François, K. O.; Hoorelbeke, B.; Huskens, D.; Dettner, F.; Süssmuth, R. D.; Schols, D. *Virology* **2012**, *433*, 308. (e) Rausch, S.; Hänchen, A.; Denisiuk, A.; Löhken, M.; Schneider, T.; Süssmuth, R. D. *ChemBioChem*

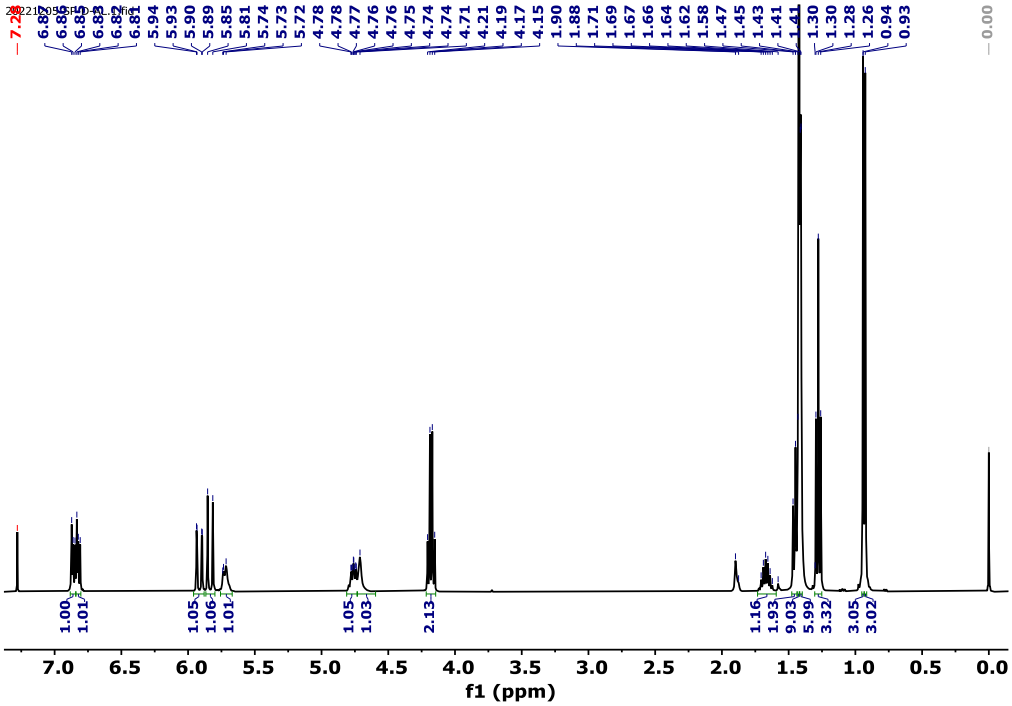
2011, *12*, 1171. (f) Fuse, S.; Mifune, Y.; Nakamura, H.; Tanaka, H. *Nat. Commun.* **2016**, *7*, 13491.

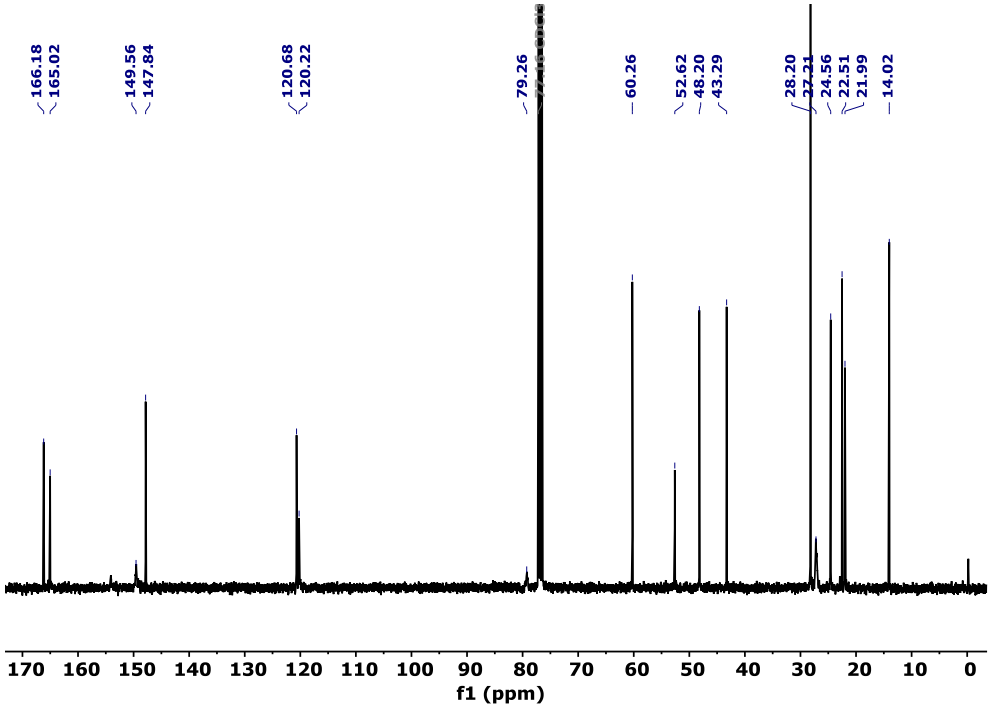
13. (a) Zhang, Z.; Pascal, S. M.; Cross, T. A. *Biochemistry* **1992**, *31*, 8822. (b) Arsemev, A. S.; Barsukov, I. L.; Bystrov, V. F. *FEBS. Lett.* **1984,** 1*80*, 33. (c) Roux, B.; Bruschweiler, R.; Ernst, R. R. *Eur. J. Biochem.* **1990**, *194*, 57. (d) Pascal, S. M.; Cross, T. A. *J. Biomol. NMR* **1993**, *3*, 495. (e) Langs D. A. *Biopolymers* **1989**, *28*, 259. (f) Woolley, G. A.; Wallace, B. A. *J. Membr. Biol*. **1992**, *129*, 109. (g) Ketchem, R. R.; Hu, W.; Cross, T. A. *Science* **1993**, *261*, 1457. (h) Kovacs, F.; Quine, J.; Cross, T. A. *Proc. Natl. Acad. Sci. USA.* **1999**, *96*, 7910. (i) Sychev, S. V.; Barsukov, L. I.; Ivanov V. T.; *J. Pept. Sci.* **2013**, *19*, 452. (j) Sychev, S.V.; Barsukov, L. I.; Ivanov, V. T. *Eur. Biophys. J.* **1993**, *22*, 279.
14. (a) Benedetti, E.; Di Blasio, B.; Pedone, C.; Lorenzi, G. P.; Tomasic, L.; Gramlich, V. *Nature* **1979**, *282*, 630. (b) Di Blasio, B.; Benedetti, E.; Pavone, V.; Pedone, C.; Gerber, C.; Lorenzi, G. P. *Biopolymers* **1989**, *28*, 203. (c) Kulp, J. L.; Clark, T. D. *Chem. Eur. J.* **2009,** *15*, 11867. (d) Navarro, E.; Fenude, E.; Celda, B. *Biopolymers* **2004**, *73*, 229. (e) Sastry, M.; Brown, C.; Wagner, G.; Clark, T. D. *J. Am. Chem. Soc*. **2006,** *128*, 10650. (f) Schramm, P.; Hofmann, H. -J. *J. Pept. Sci.* **2010**, *16*, 276. (e) Jadhav, K. B.; Lichtenecker, R. J.; Bullach, A.; Mandal, B.; Arndt, H. -D. *Chem. Eur. J*. **2015**, *21*, 5898.
15. (a) Janin, J.; Wodak, S.; Levitt, M.; Maigret, B. *J. Mol. Biol.*, **1978**, *125*, 357. (b) Joo H.; Tsai J. *Proteins,* **2014,** *82*, 2128. (c) Nowick, J. S. *Acc. Chem. Res.,* **2008**, *41*, 1319. (d) Kung V. M.; Cornilescu G.; Gellman S. H. *Angew. Chem., Int. Ed*., **2015**, *54*, 14336.
16. (a) Smith, C. K.; Regan L. *Acc. Chem. Res*., **1997**, *30*, 153. (b) Hecht, M. H. *Proc. Natl. Acad. Sci. U. S. A.*, **1994**, *91*, 8729. (c) Marcos, E.; Chidyausiku, T. M.; McShan, A. C.; Evangelidis, T.; Nerli, S.; Carter, L.; Nivón, L. G.; Davis, A.; Oberdorfer, G.; Tripsianes, K.; Sgourakis, N. G. *Nat. Struct. Biol*., **2018**, *25*, 1028. (d) Loughlin, W. A.; Tyndall, J. D. A.; Glenn, M. P.; Fairlie, D. P. *Chem. Rev.*, **2004**, *104*, 6085.
17. (a) Pauling, L.; Corey, R. B. *Proc. Natl. Acad. Sci. U. S. A.* **1953**, *39*, 253. (b) Pauling L.; Corey, R. B. *Proc. Natl. Acad. Sci. U. S. A.*, **1951**, *37*, 251. (c) Pauling L.; Corey R. B. *Proc. Natl. Acad. Sci. U. S. A.* **1951,** *37*, 256.
18. Hagihara, M.; Anthony, N. J.; Stout, T. J.; Clardy, J.; Schreiber, S. L. *J. Am. Chem. Soc*., **1992**, *114*, 6568.

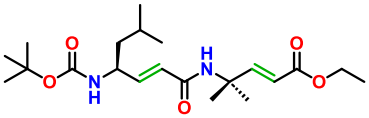
19. (a) Ganesh Kumar, M.; Mali, S. M.; Raja, K. M. P.; Gopi, H. N. *Org. Lett.* **2015**, *17*, 230. (b) Bandyopadhyay, A.; Mali, S. M.; Lunawa, P.; Raja, K. M.; Gopi, H. N. *Org. Lett.* **2011**, *13*, 4482.
20. Ganesh Kumar, M.; Benke, S. N.; Poopathi Raja, K. M.; Gopi, H. N. *Chem. Commun.* **2015**, *51*, 13397.
21. Bandyopadhyay, A.; Gopi, H. N. *Org. Lett.* **2012**, *14*, 2770.
22. Bandyopadhyay, A.; Misra, R.; Gopi, H. N. *Chem. Commun.* **2016**, *52*, 4938.
23. (a) Misra, R.; Dey, S.; Reja, R. M.; Gopi, H. N. *Angew. Chem., Int. Ed.* **2018**, *57*, 1057. (b) K. Veeresh, M. Singh, H. N. Gopi, *Org Biomol Chem* **2019**, *17*, 9226.
24. Pahan, S.; Dey, S.; George, G.; Panda Mahapatra, S.; Puneeth Kumar, DR.; Gopi, H. N. *Angew. Chemie Int. Ed.* **2023**, e202316309
25. Mali, S. M.; Bandyopadhyay, A.; Jadhav, S. V.; Ganesh Kumar, M.; Gopi, H. N. *Org. Biomol. Chem.* **2011**, *9*, 6566.

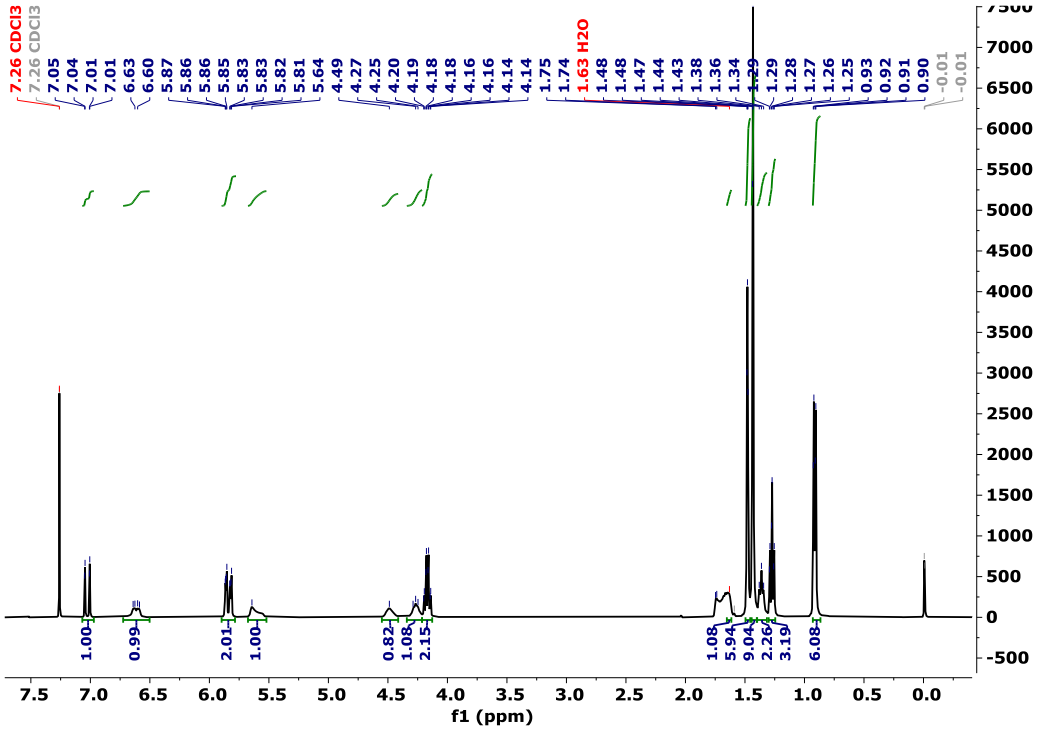
3.10. ^{1}H, ^{13}C NMR and Mass Spectra of Peptides P1-P7

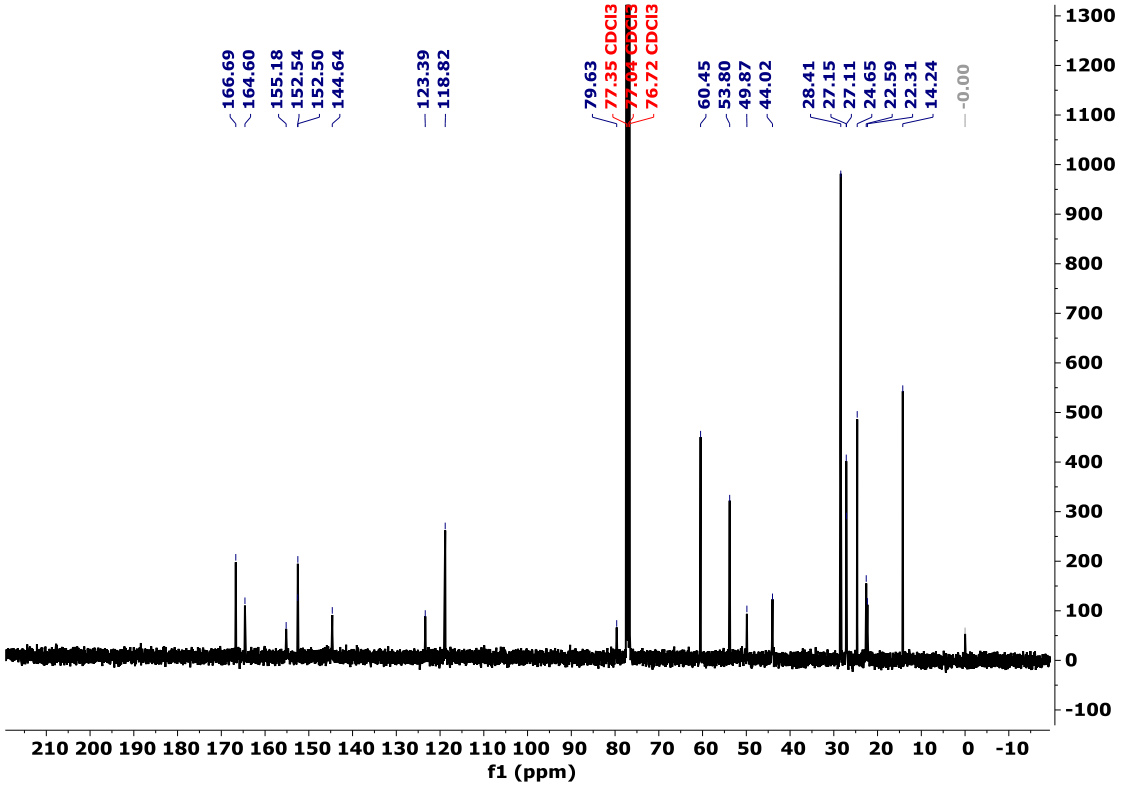


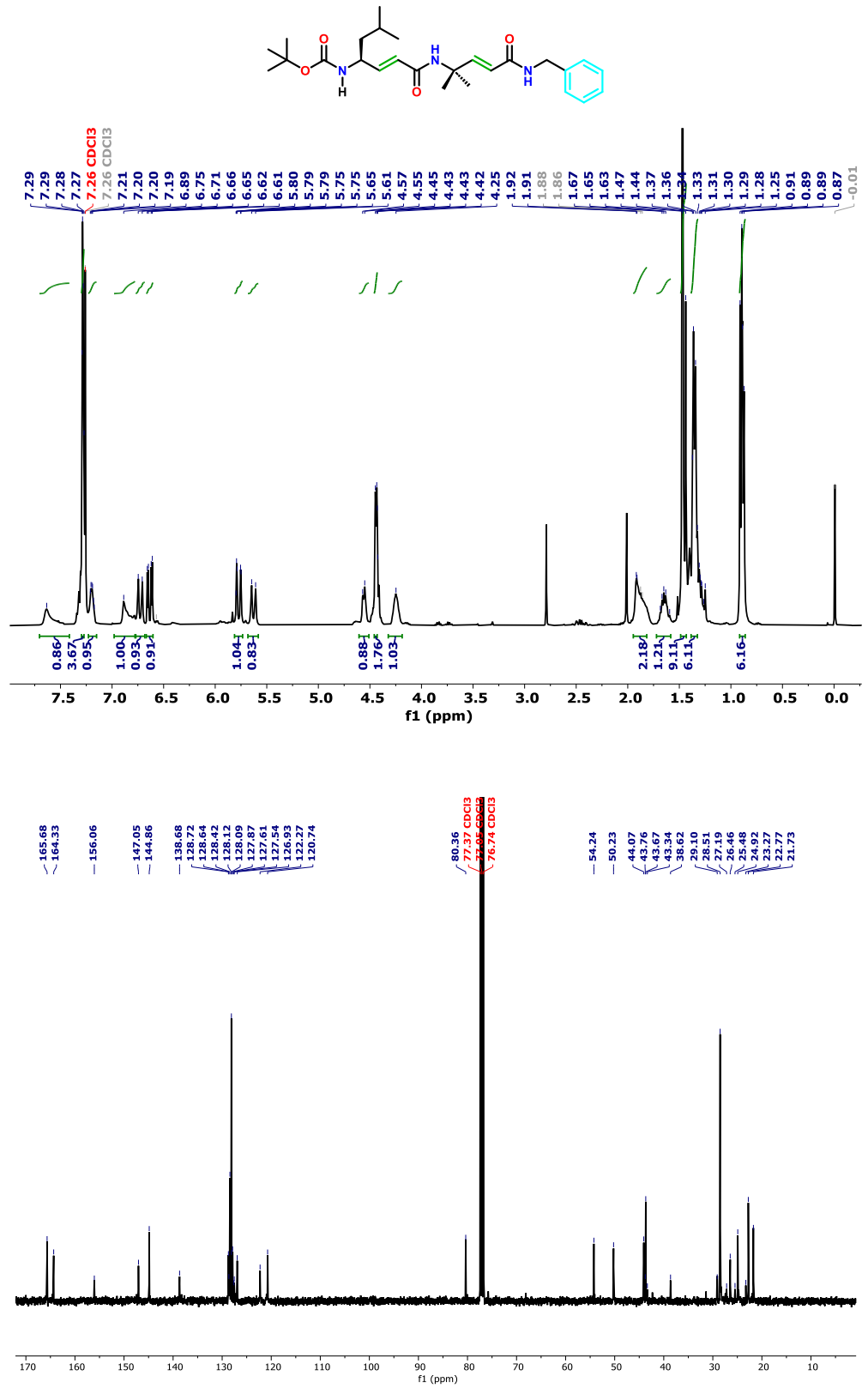


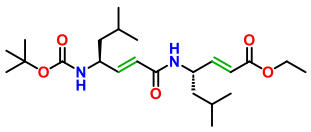


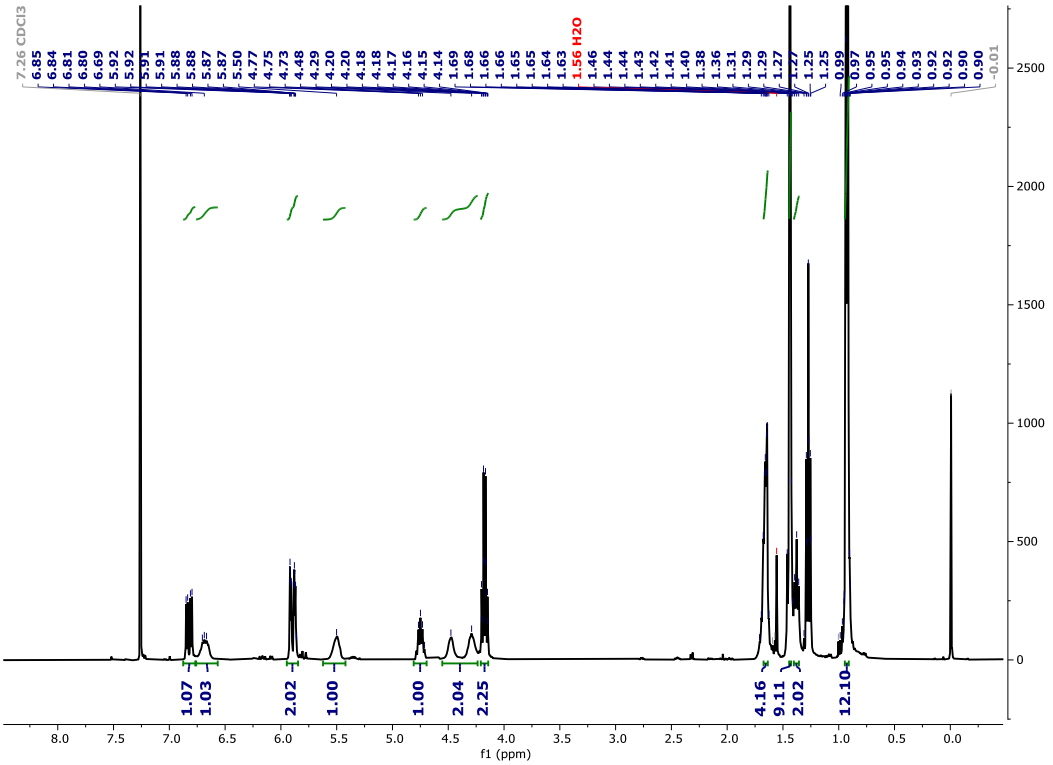


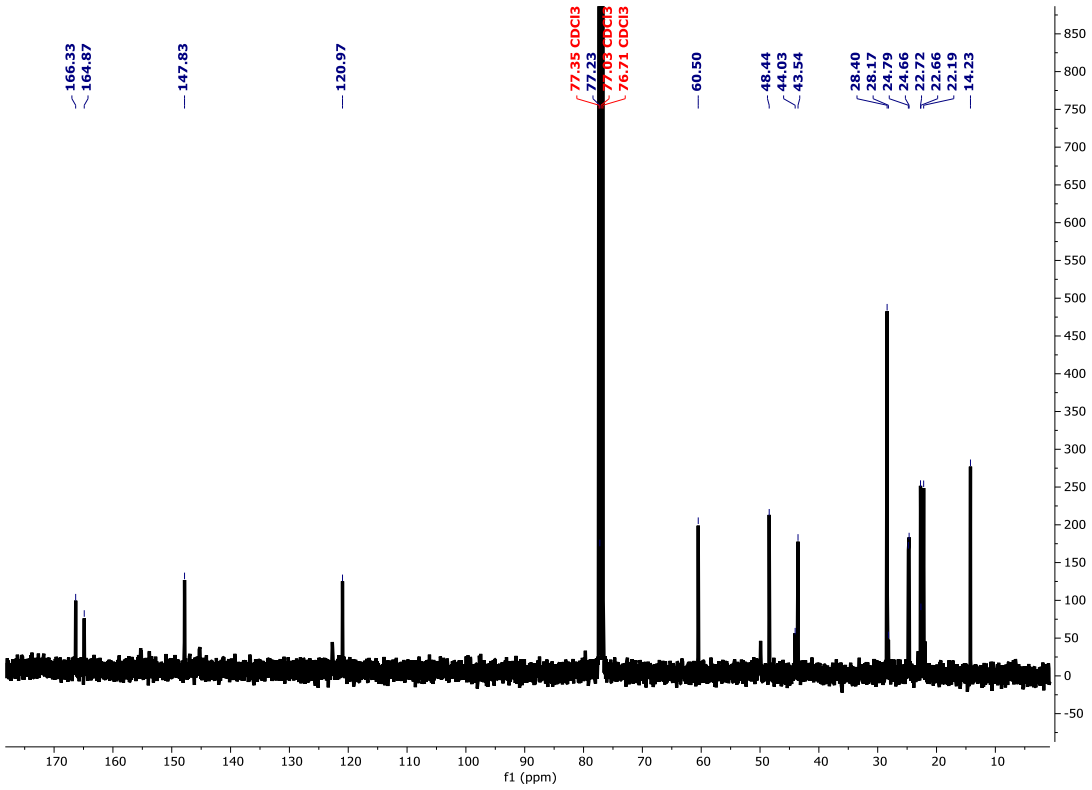

7.26 CDCl3
7.26 CDCl3
7.05
7.04
7.01
7.01
6.63
6.60
5.87
5.86
5.86
5.85
5.83
5.83
5.82
5.81
5.64
4.49
4.27
4.25
4.20
4.19
4.18
4.18
4.16
4.16
4.14
4.14
1.75
1.74
1.63 H2O
1.48
1.48
1.47
1.44
1.43
1.38
1.36
1.34
1.29
1.29
1.28
1.27
1.26
1.25
0.93
0.92
0.91
0.90
-0.01
-0.01
1.00
0.99
2.01
1.00
0.82
1.08
2.15
1.08
5.94
9.04
2.26
3.19
6.08
f1 (ppm)

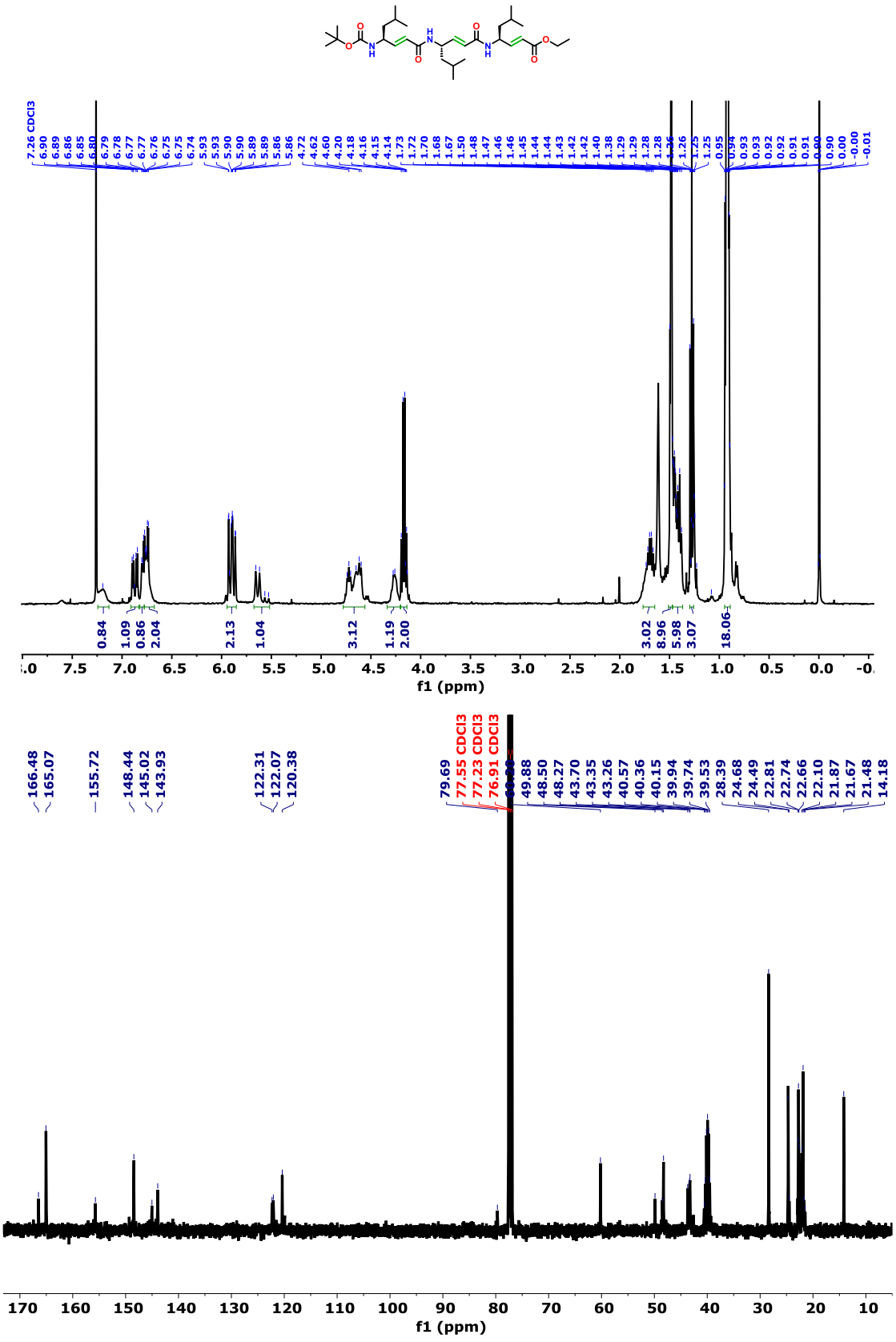

166.69
164.60
155.18
152.54
152.50
144.64
123.39
118.82
79.63
77.35 CDCl3
77.04 CDCl3
76.72 CDCl3
60.45
53.80
49.87
44.02
28.41
27.15
27.11
24.65
22.59
22.31
14.24
-0.00
f1 (ppm)

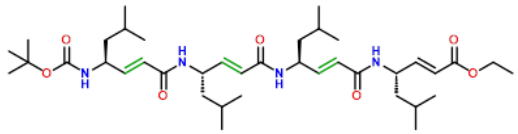


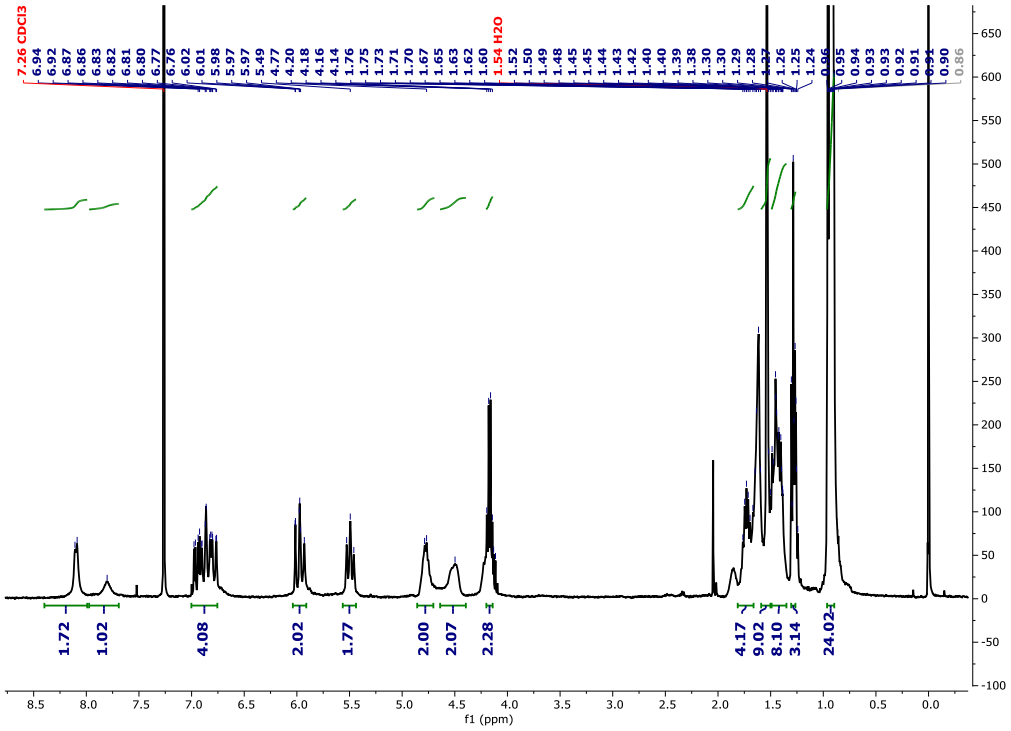


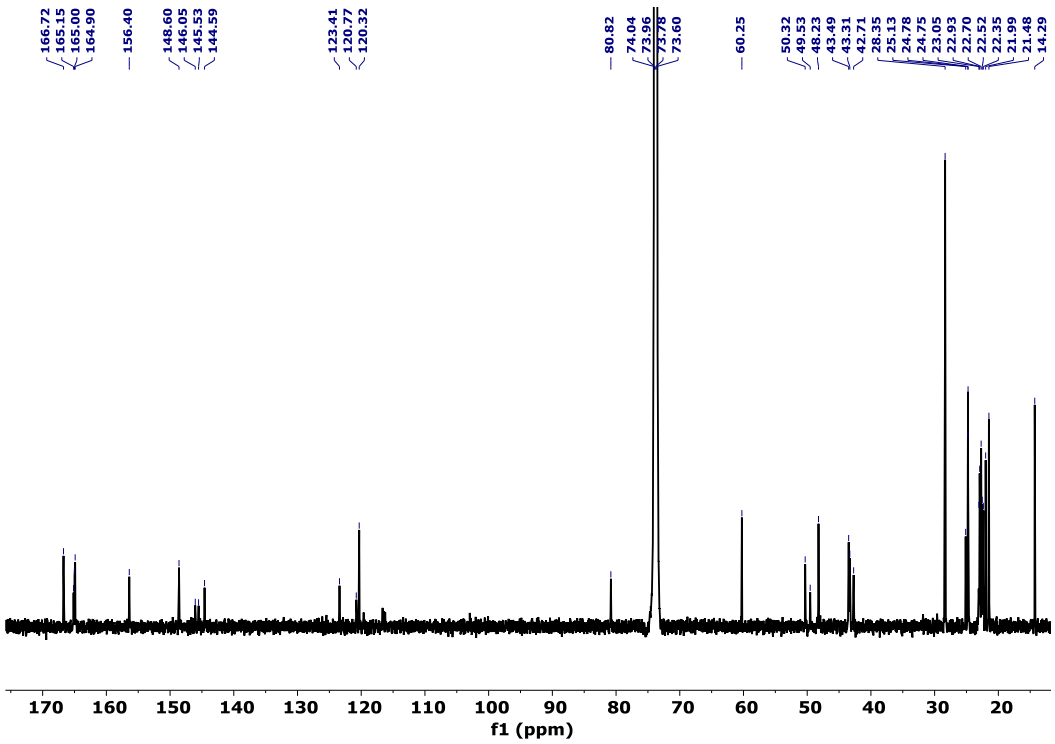

7.26 CDCl3
6.85 6.84 6.81 6.80 6.69 5.92 5.92 5.91 5.91 5.88 5.88 5.87 5.87 5.50 4.77 4.75 4.73 4.48 4.29 4.20 4.20 4.18 4.18 4.17 4.16 4.15 4.14 1.69 1.68 1.66 1.66 1.65 1.65 1.64 1.63
1.56 H2O
1.46 1.44 1.44 1.43 1.42 1.41 1.40 1.38 1.36 1.31 1.29 1.29 1.27 1.27 1.25 1.25 0.99 0.97 0.95 0.95 0.94 0.93 0.92 0.92 0.90 0.90 -0.01
1.07 1.03 2.02 1.00 1.00 2.04 2.25 4.16 9.11 2.02 12.10
f1 (ppm)

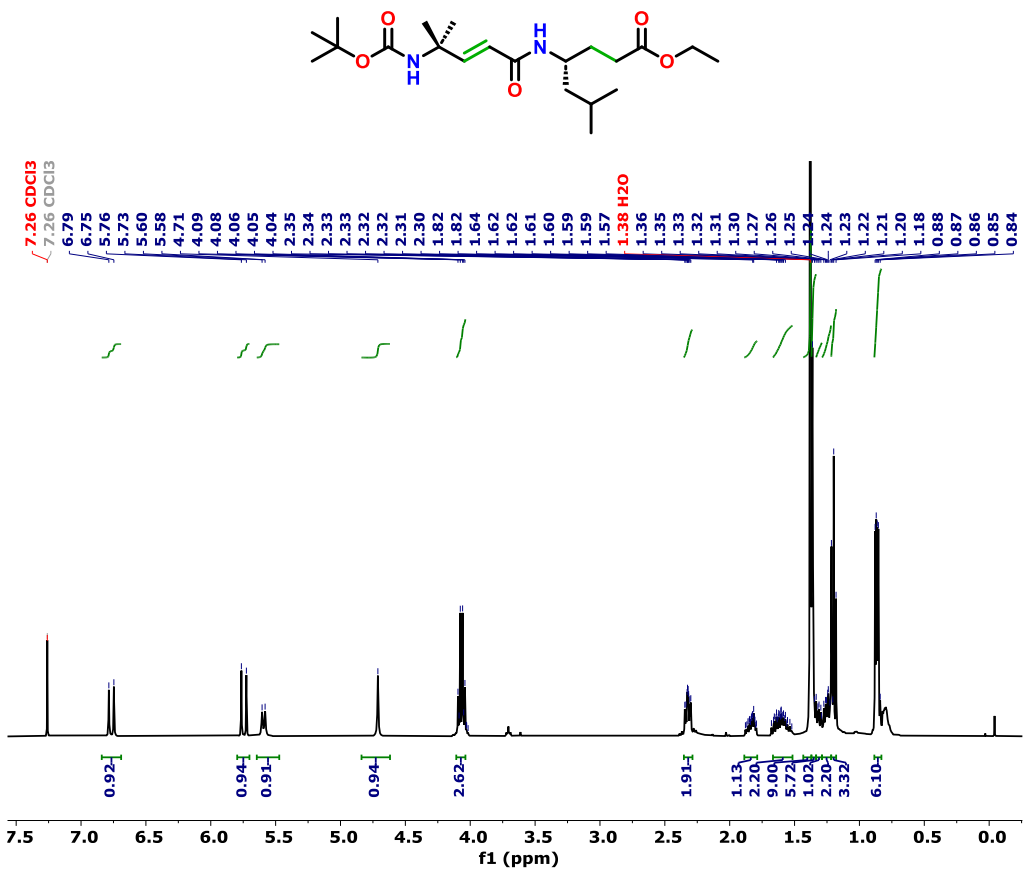

166.33 164.87 147.83 120.97
77.35 CDCl3 77.23 77.03 CDCl3 76.71 CDCl3
60.50 48.44 44.03 43.54
28.40 28.17 24.79 24.66 22.72 22.66 22.19 14.23
f1 (ppm)

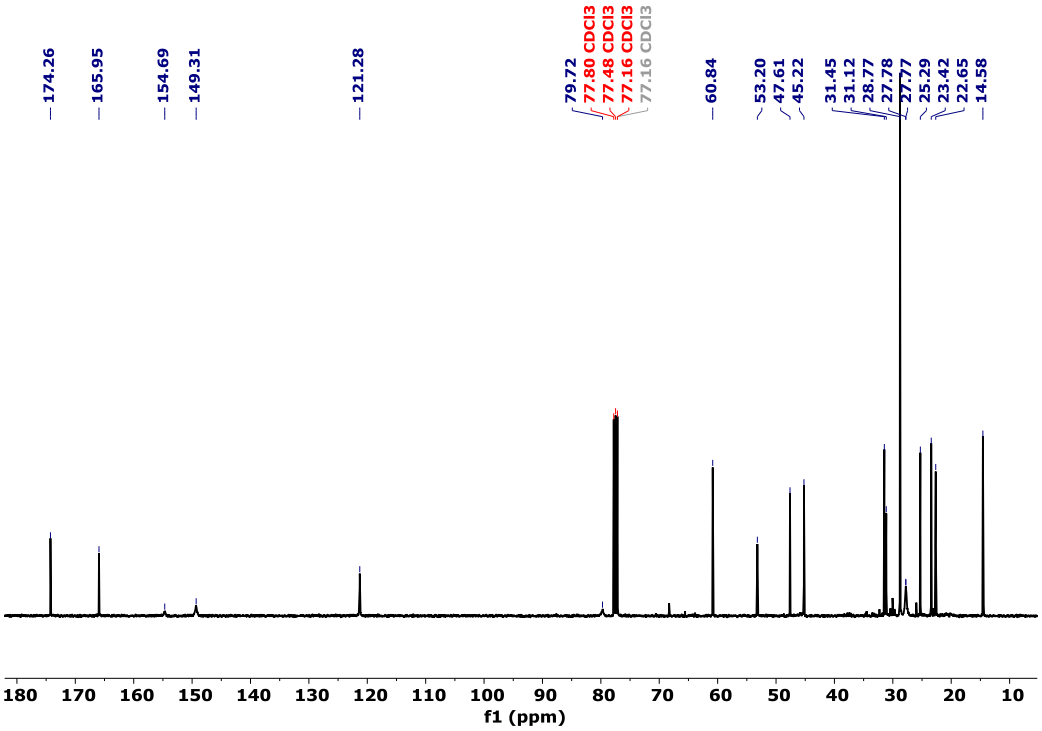

7.26 CDCl3
6.90
6.89
6.86
6.85
6.80
6.79
6.78
6.77
6.77
6.76
6.75
6.75
6.74
5.93
5.93
5.90
5.90
5.89
5.89
5.86
5.86
4.72
4.62
4.60
4.20
4.18
4.16
4.15
4.14
1.73
1.72
1.70
1.68
1.67
1.50
1.48
1.47
1.46
1.46
1.45
1.44
1.44
1.43
1.42
1.42
1.40
1.38
1.29
1.29
1.28
1.28
1.26
1.26
1.25
1.25
0.95
0.94
0.93
0.93
0.92
0.92
0.91
0.91
0.90
0.90
0.00
-0.00
-0.01
0.84
1.09
0.86
2.04
2.13
1.04
3.12
1.19
2.00
3.02
8.96
5.98
3.07
18.06
f1 (ppm)
166.48
165.07
155.72
148.44
145.02
143.93
122.31
122.07
120.38
79.69
77.55 CDCl3
77.23 CDCl3
76.91 CDCl3
49.88
48.50
48.27
43.70
43.35
43.26
40.57
40.36
40.15
39.94
39.74
39.53
28.39
24.68
24.49
22.81
22.74
22.66
22.10
21.87
21.67
21.48
14.18
f1 (ppm)

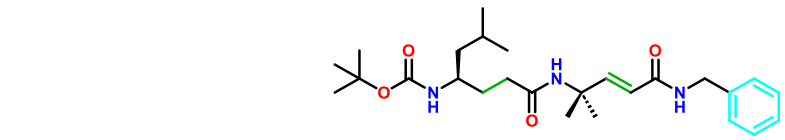


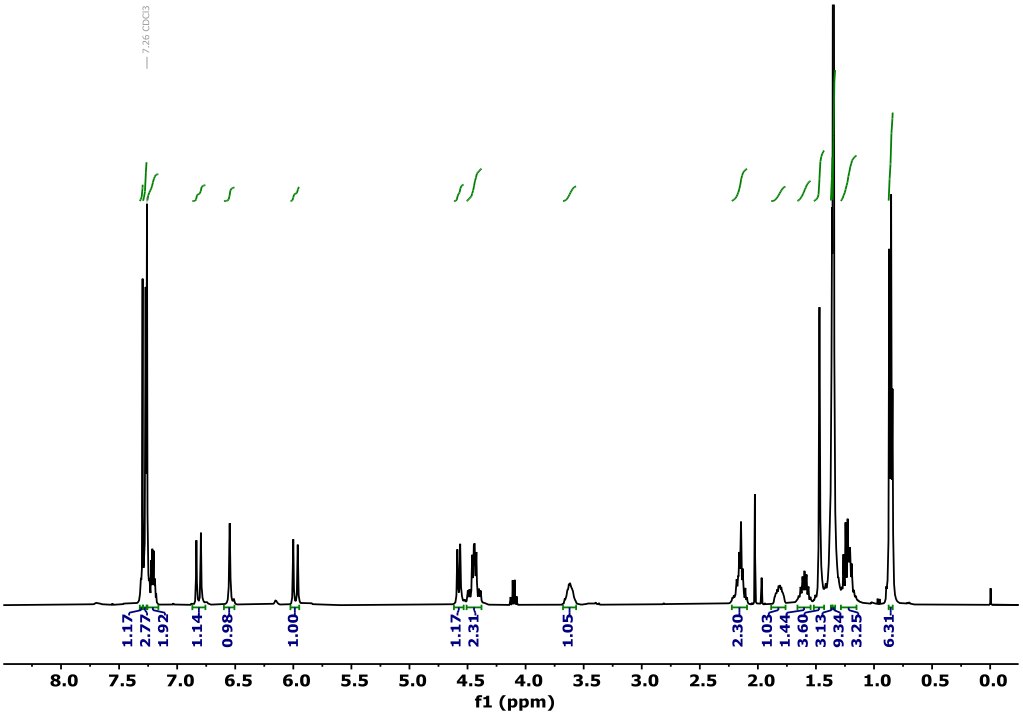

7.26 CDCl3
1.54 H2O
1.72
1.02
4.08
2.02
1.77
2.00
2.07
2.28
4.17
9.02
8.10
3.14
24.02
f1 (ppm)

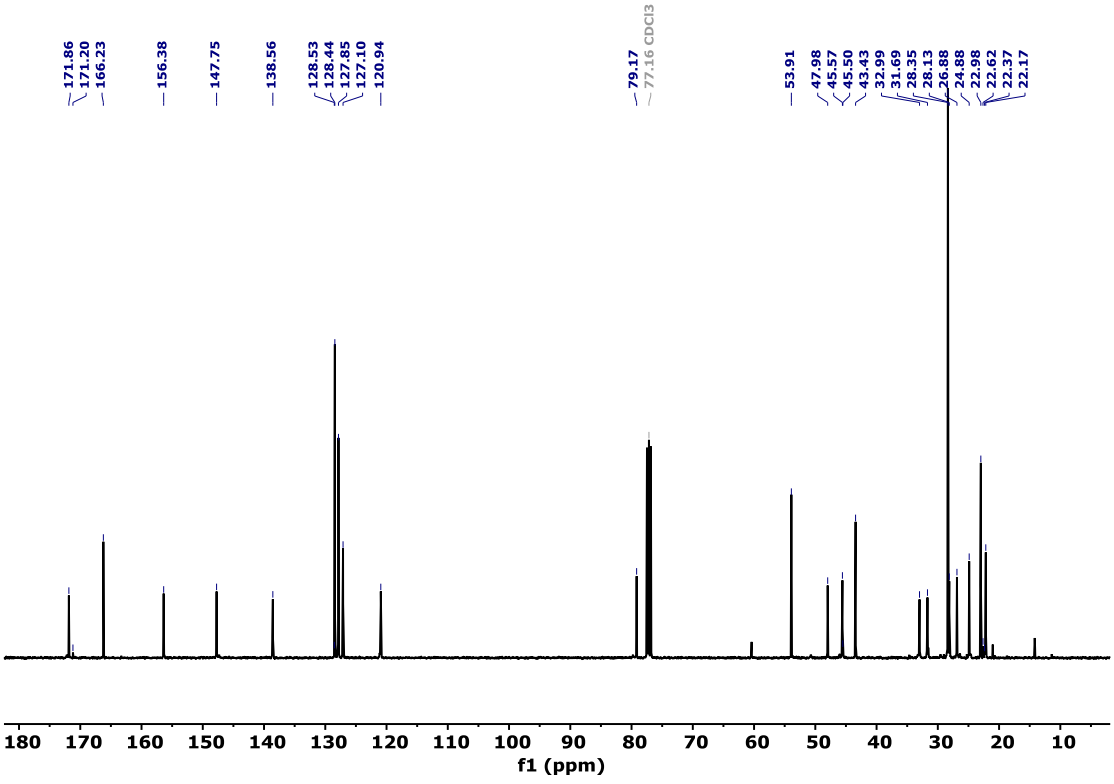

166.72
165.15
165.00
164.90
156.40
148.60
146.05
145.53
144.59
123.41
120.77
120.32
80.82
74.04
73.96
73.78
73.60
60.25
50.32
49.53
48.23
43.49
43.31
42.71
28.35
25.13
24.78
24.75
23.05
22.93
22.70
22.52
22.35
21.99
21.48
14.29
f1 (ppm)

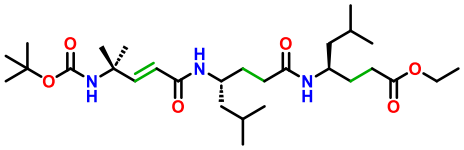

7.26 CDCl3
7.26 CDCl3
6.79
6.75
5.76
5.73
5.60
5.58
4.71
4.09
4.08
4.06
4.05
4.04
2.35
2.34
2.33
2.33
2.32
2.32
2.31
2.30
1.82
1.82
1.64
1.62
1.62
1.61
1.60
1.59
1.59
1.57
1.38 H2O
1.36
1.35
1.33
1.32
1.31
1.30
1.27
1.26
1.25
1.24
1.24
1.23
1.22
1.21
1.20
1.18
0.88
0.87
0.86
0.85
0.84
0.92
0.94
0.91
0.94
2.62
1.91
1.13
2.20
9.00
5.72
1.02
2.20
3.32
6.10
7.5
7.0
6.5
6.0
5.5
5.0
4.5
4.0
3.5
3.0
2.5
2.0
1.5
1.0
0.5
0.0
f1 (ppm)

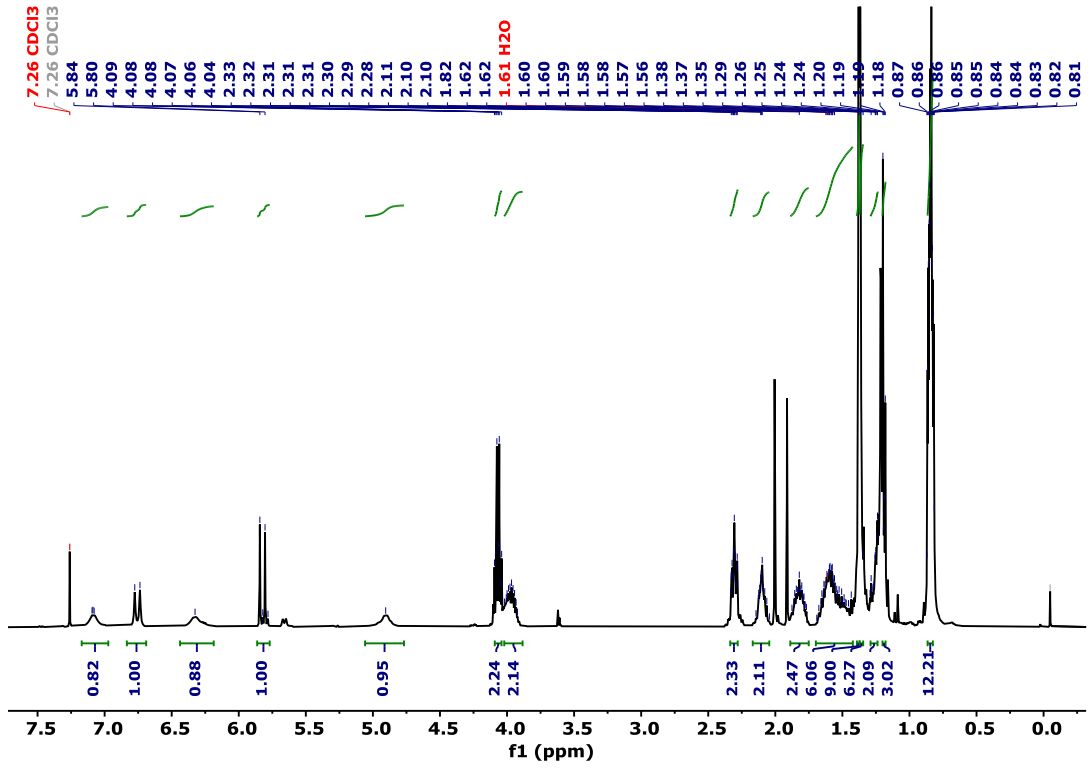

174.26
165.95
154.69
149.31
121.28
79.72
77.80 CDCl3
77.48 CDCl3
77.16 CDCl3
77.16 CDCl3
60.84
53.20
47.61
45.22
31.45
31.12
28.77
27.78
27.77
25.29
23.42
22.65
14.58
180
170
160
150
140
130
120
110
100
90
80
70
60
50
40
30
20
10
f1 (ppm)

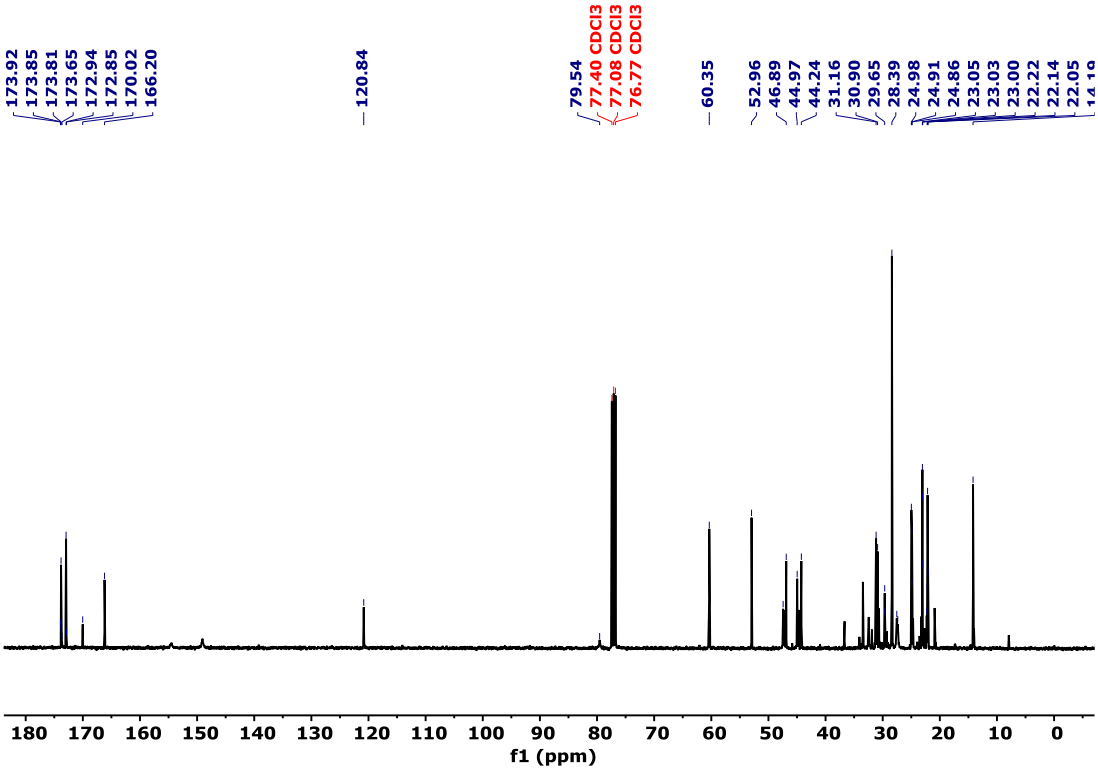


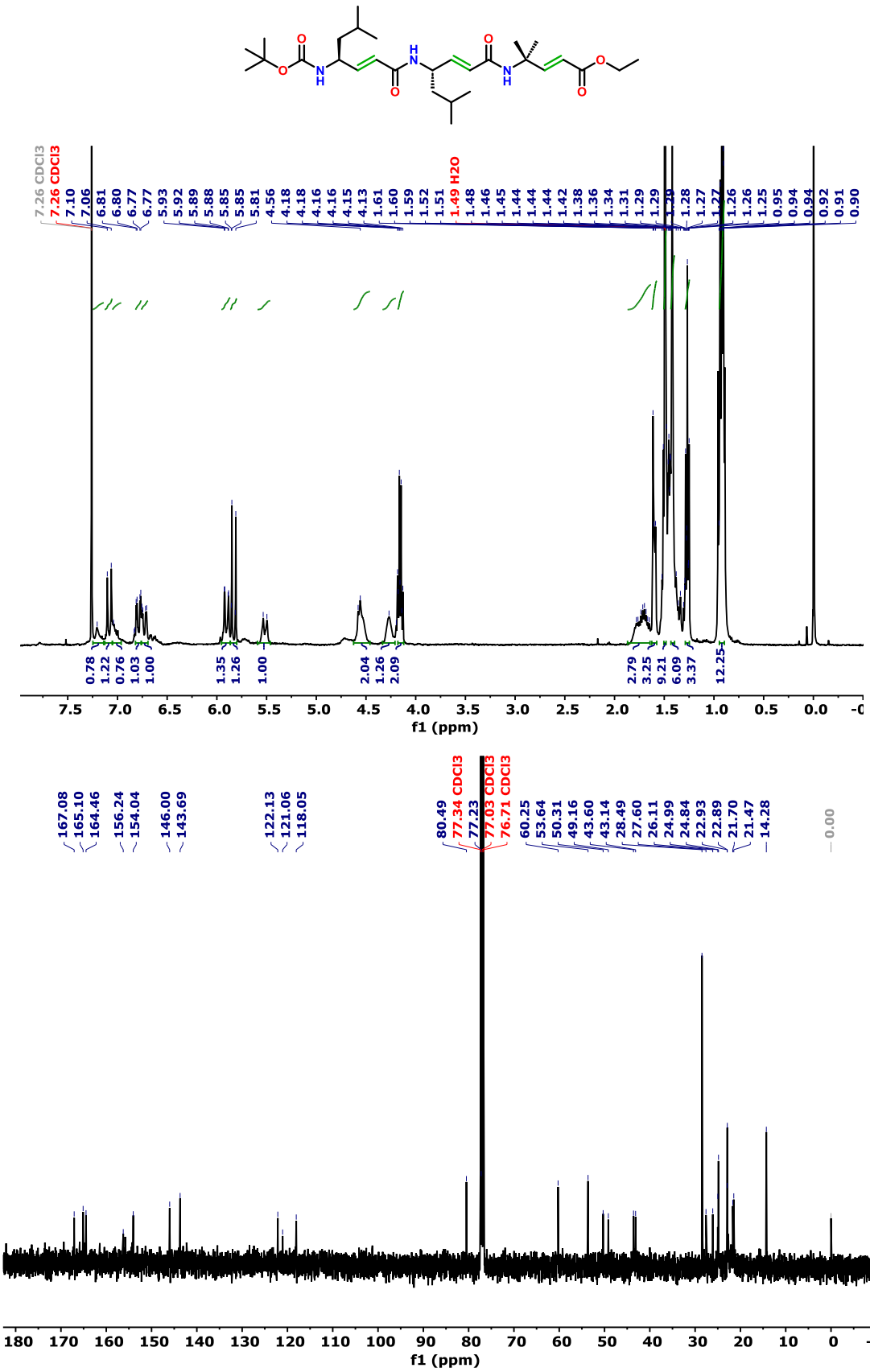

7.26 CDCl3
1.17
2.77
1.92
1.14
0.98
1.00
1.17
2.31
1.05
2.30
1.03
1.44
3.60
3.13
9.34
3.25
6.31
8.0 7.5 7.0 6.5 6.0 5.5 5.0 4.5 4.0 3.5 3.0 2.5 2.0 1.5 1.0 0.5 0.0
f1 (ppm)

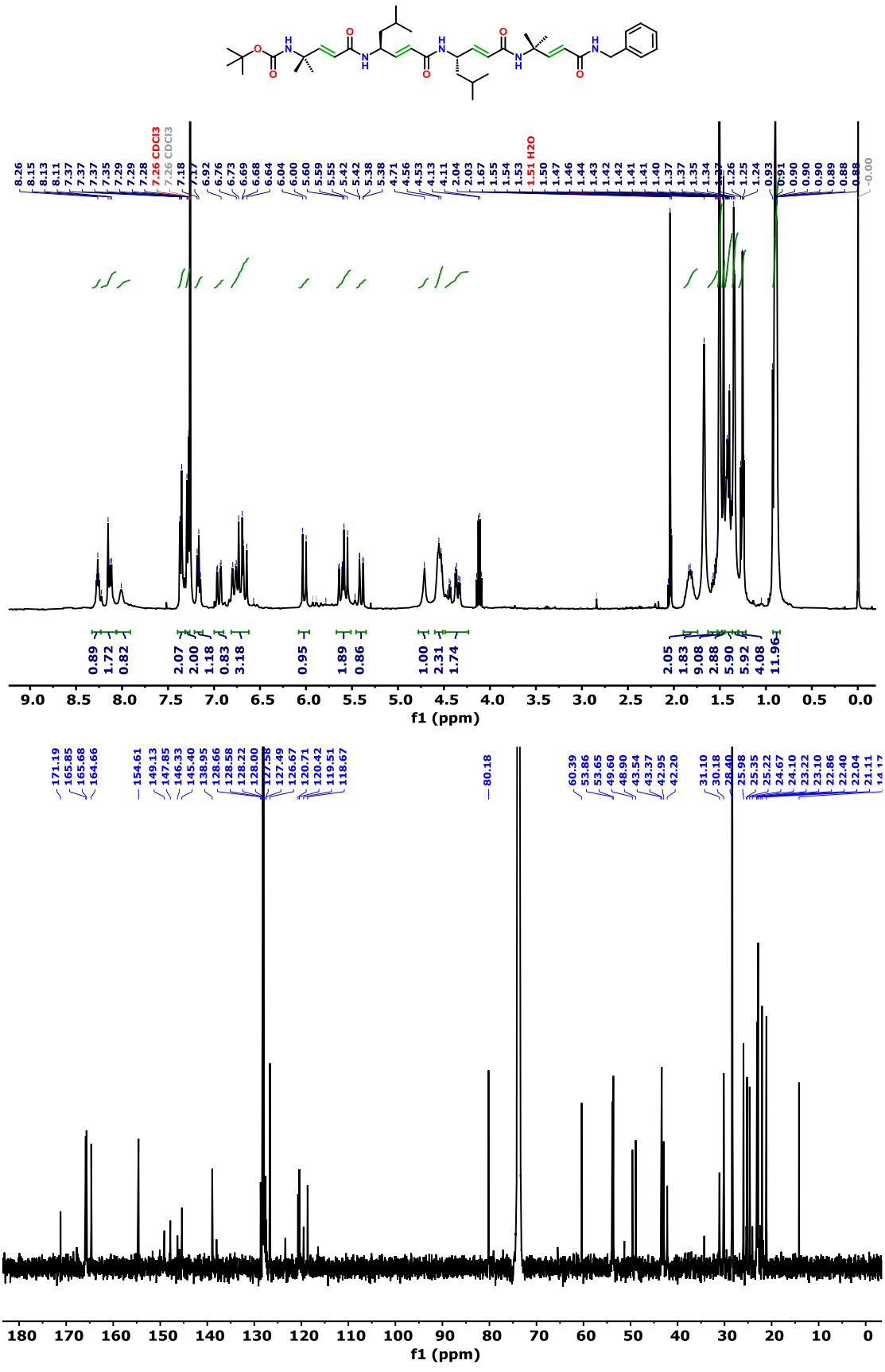

171.86
171.20
166.23
156.38
147.75
138.56
128.53
128.44
127.85
127.10
120.94
79.17
77.16 CDCl3
53.91
47.98
45.57
45.50
43.43
32.99
31.69
28.35
28.13
26.88
24.88
22.98
22.62
22.37
22.17
180 170 160 150 140 130 120 110 100 90 80 70 60 50 40 30 20 10
f1 (ppm)

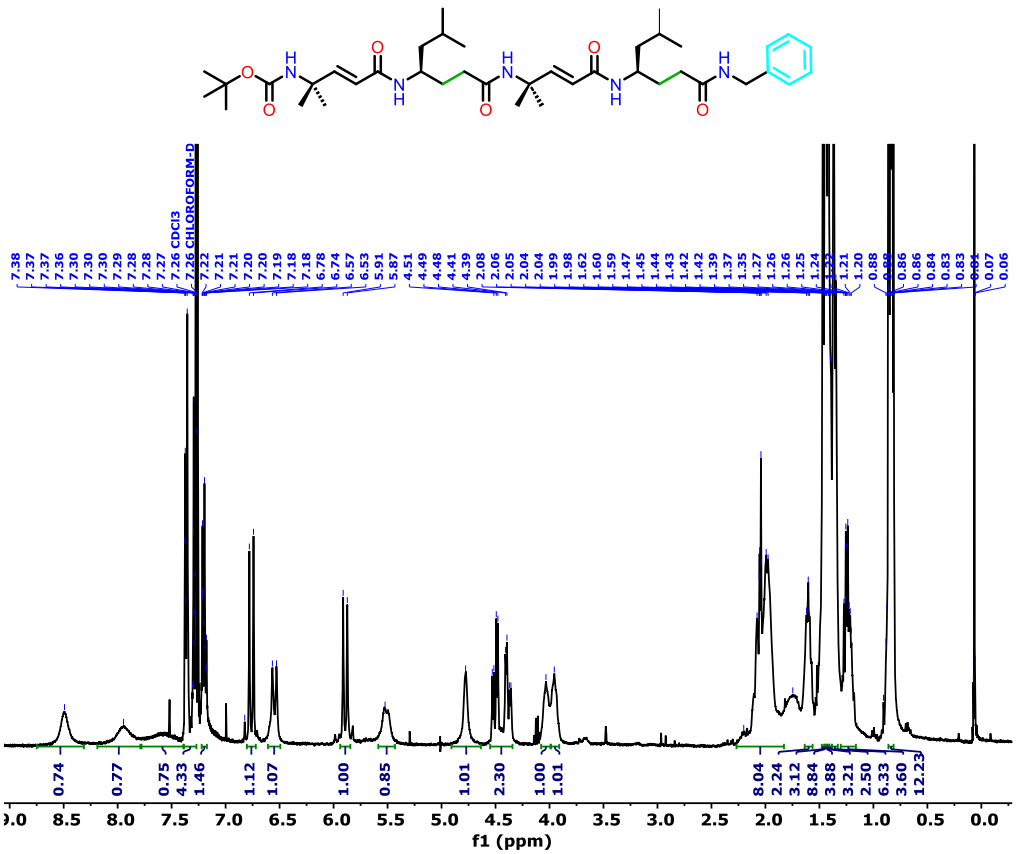


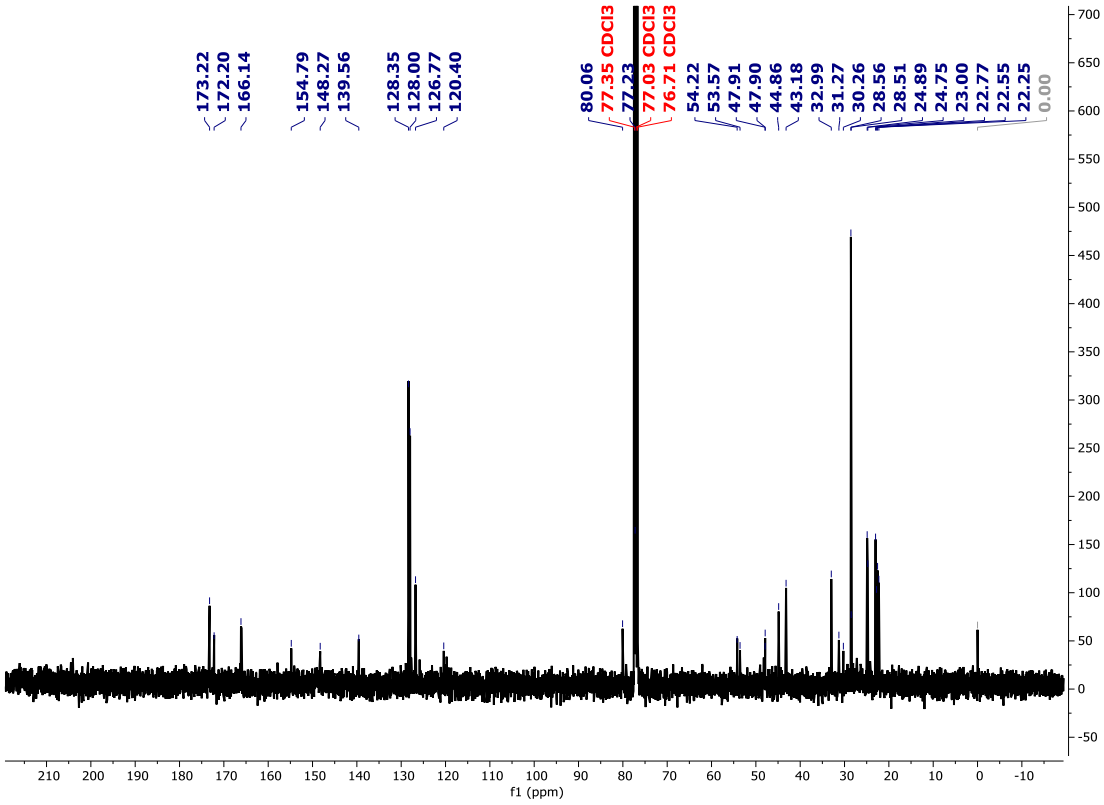

7.26 CDCl3
7.26 CDCl3
1.61 H2O
f1 (ppm)

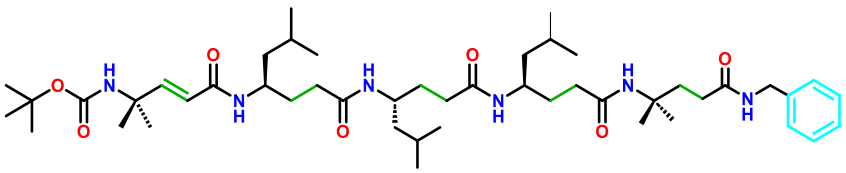

173.92
173.85
173.81
173.65
172.94
172.85
170.02
166.20
120.84
79.54
77.40 CDCl3
77.08 CDCl3
76.77 CDCl3
60.35
52.96
46.89
44.97
44.24
31.16
30.90
29.65
28.39
24.98
24.91
24.86
23.05
23.03
23.00
22.22
22.14
22.05
f1 (ppm)

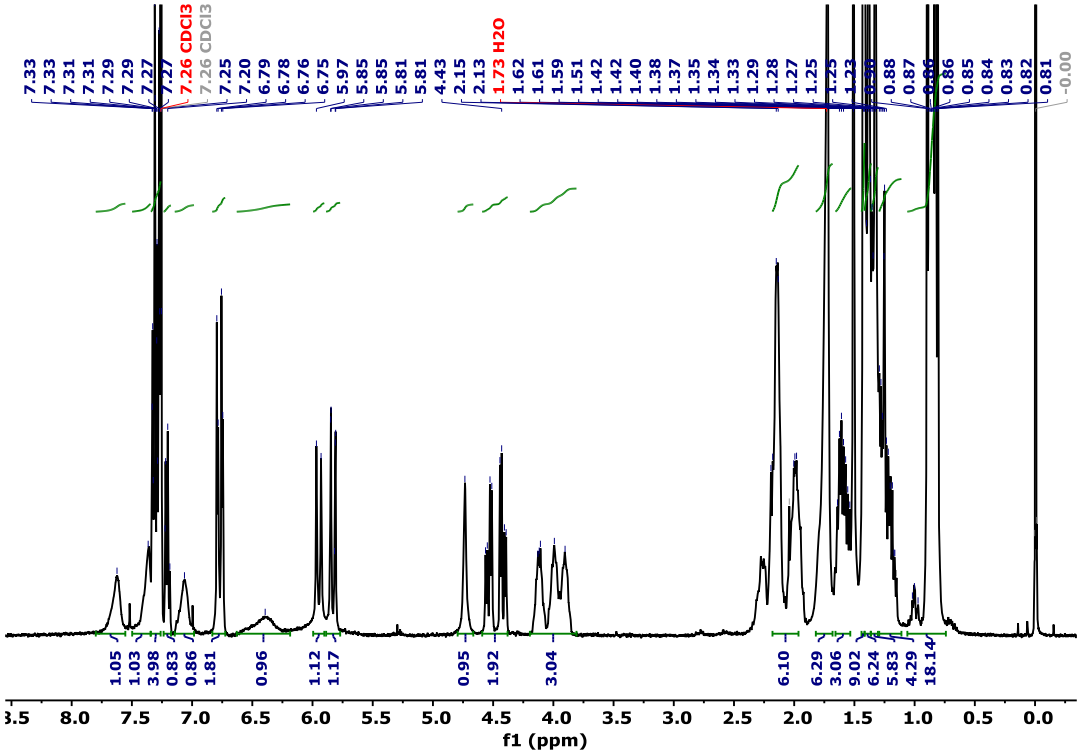

7.26 CDCl3
7.26 CDCl3
7.10
7.06
6.81
6.80
6.77
6.77
5.93
5.92
5.89
5.88
5.85
5.85
5.81
4.56
4.18
4.18
4.16
4.16
4.15
4.13
1.61
1.60
1.59
1.52
1.51
1.49 H2O
1.48
1.46
1.45
1.44
1.44
1.44
1.42
1.38
1.36
1.34
1.31
1.29
1.29
1.28
1.27
1.27
1.26
1.26
1.25
0.95
0.94
0.94
0.92
0.91
0.90
0.78
1.22
0.76
1.03
1.00
1.35
1.26
1.00
2.04
1.26
2.09
2.79
3.25
9.21
6.09
3.37
12.25
7.5
7.0
6.5
6.0
5.5
5.0
4.5
4.0
3.5
3.0
2.5
2.0
1.5
1.0
0.5
0.0
f1 (ppm)
167.08
165.10
164.46
156.24
154.04
146.00
143.69
122.13
121.06
118.05
80.49
77.34 CDCl3
77.23
77.03 CDCl3
76.71 CDCl3
60.25
53.64
50.31
49.16
43.60
43.14
28.49
27.60
26.11
24.99
24.84
22.93
22.89
21.70
21.47
14.28
0.00
180
170
160
150
140
130
120
110
100
90
80
70
60
50
40
30
20
10
0
-1
f1 (ppm)

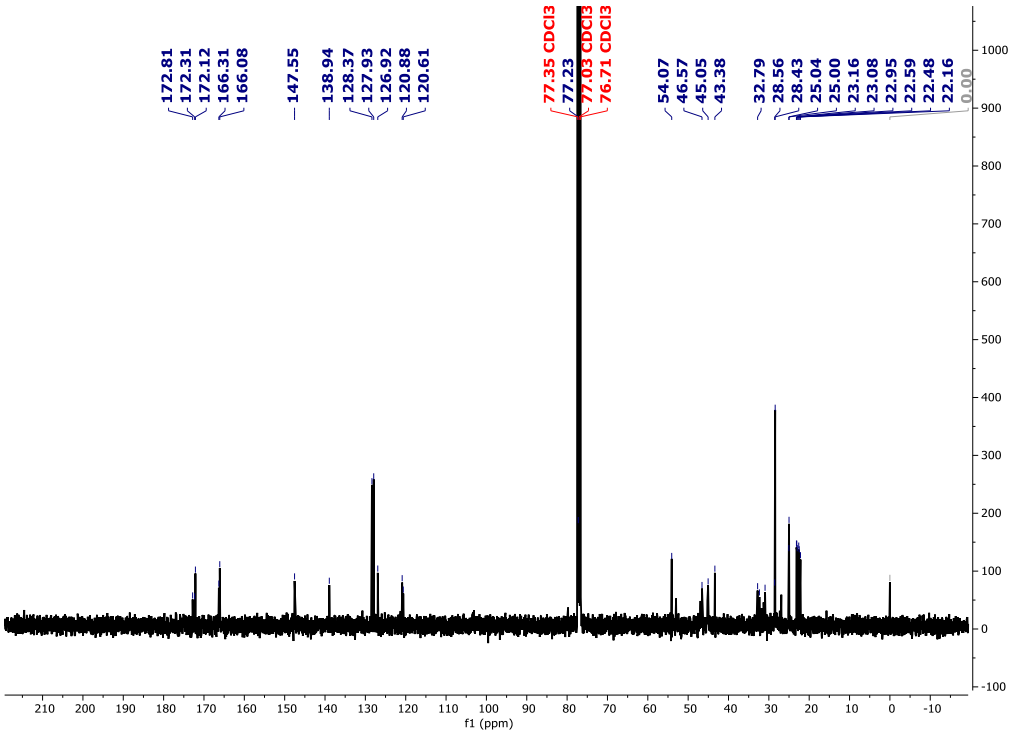


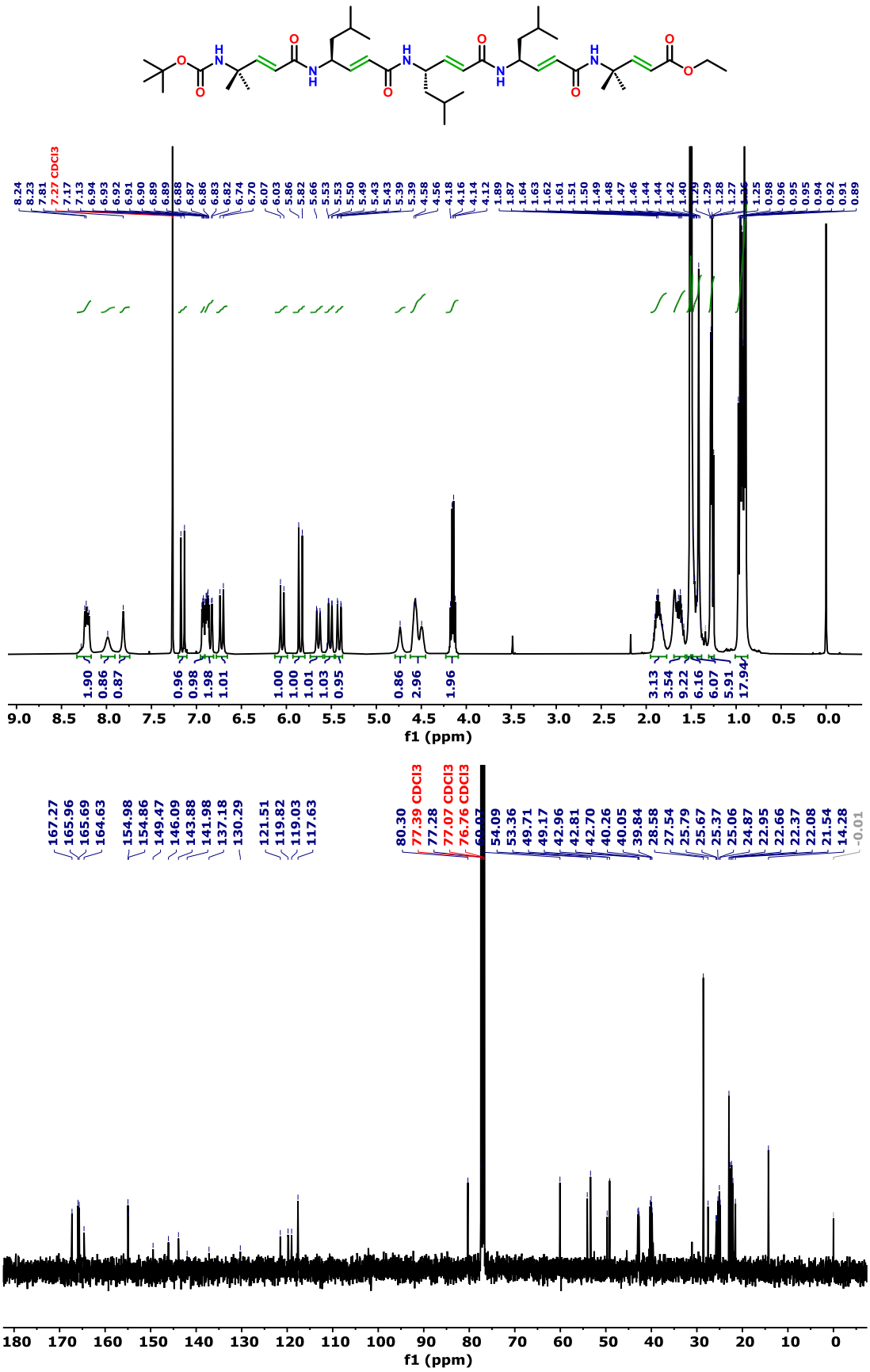

7.38 7.37 7.37 7.36 7.30 7.30 7.29 7.28 7.28 7.27 7.26 CDCl3 7.26 CHLOROFORM-D 7.22 7.21 7.21 7.20 7.20 7.19 7.18 7.18 6.78 6.74 6.57 6.53 5.91 5.87 4.51 4.49 4.48 4.41 4.39 2.08 2.06 2.05 2.04 2.04 1.99 1.98 1.62 1.60 1.59 1.47 1.45 1.44 1.43 1.42 1.42 1.39 1.37 1.35 1.27 1.26 1.26 1.25 1.24 1.21 1.20 0.88 0.86 0.86 0.84 0.83 0.83 0.07 0.06
0.74 0.77 0.75 4.33 1.46 1.12 1.07 1.00 0.85 1.01 2.30 1.00 1.01 8.04 2.24 3.12 8.84 3.88 3.21 2.50 6.33 3.60 12.23
f1 (ppm)

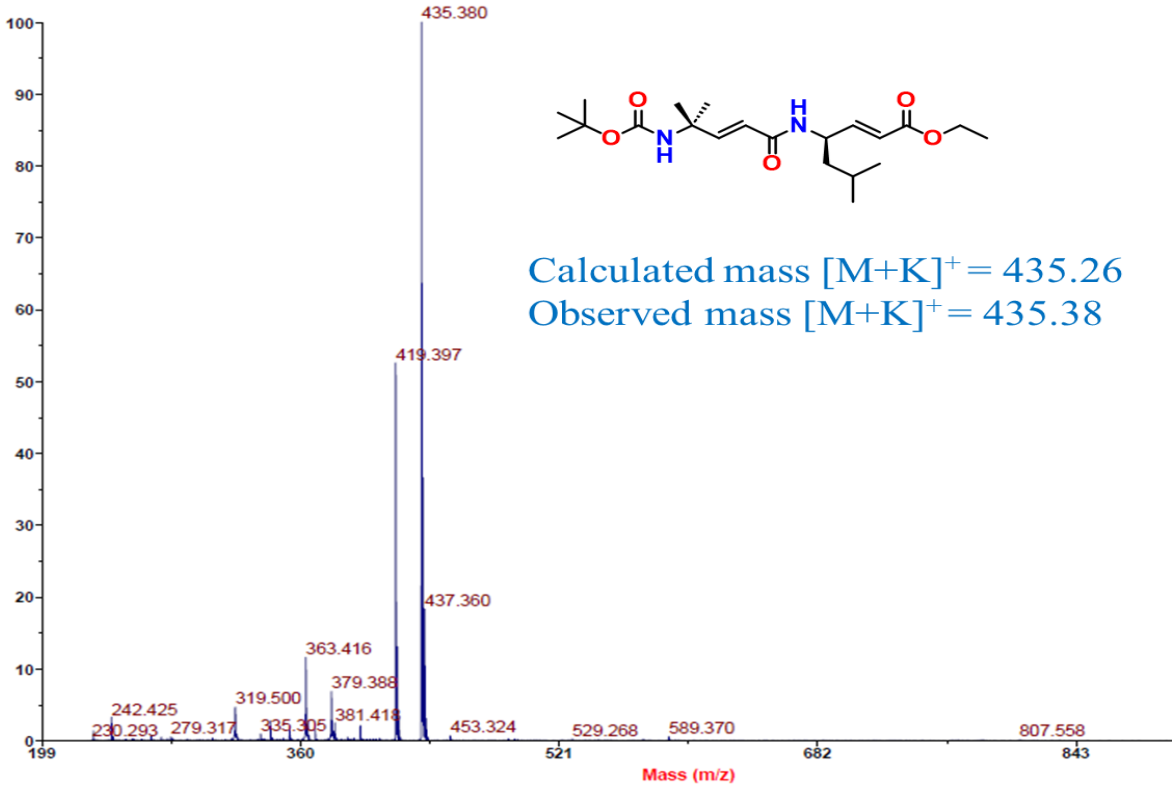

173.22 172.20 166.14 154.79 148.27 139.56 128.35 128.00 126.77 120.40 80.06 77.35 CDCl3 77.23 77.03 CDCl3 76.71 CDCl3 54.22 53.57 47.91 47.90 44.86 43.18 32.99 31.27 30.26 28.56 28.51 24.89 24.75 23.00 22.77 22.55 22.25 0.00
f1 (ppm)



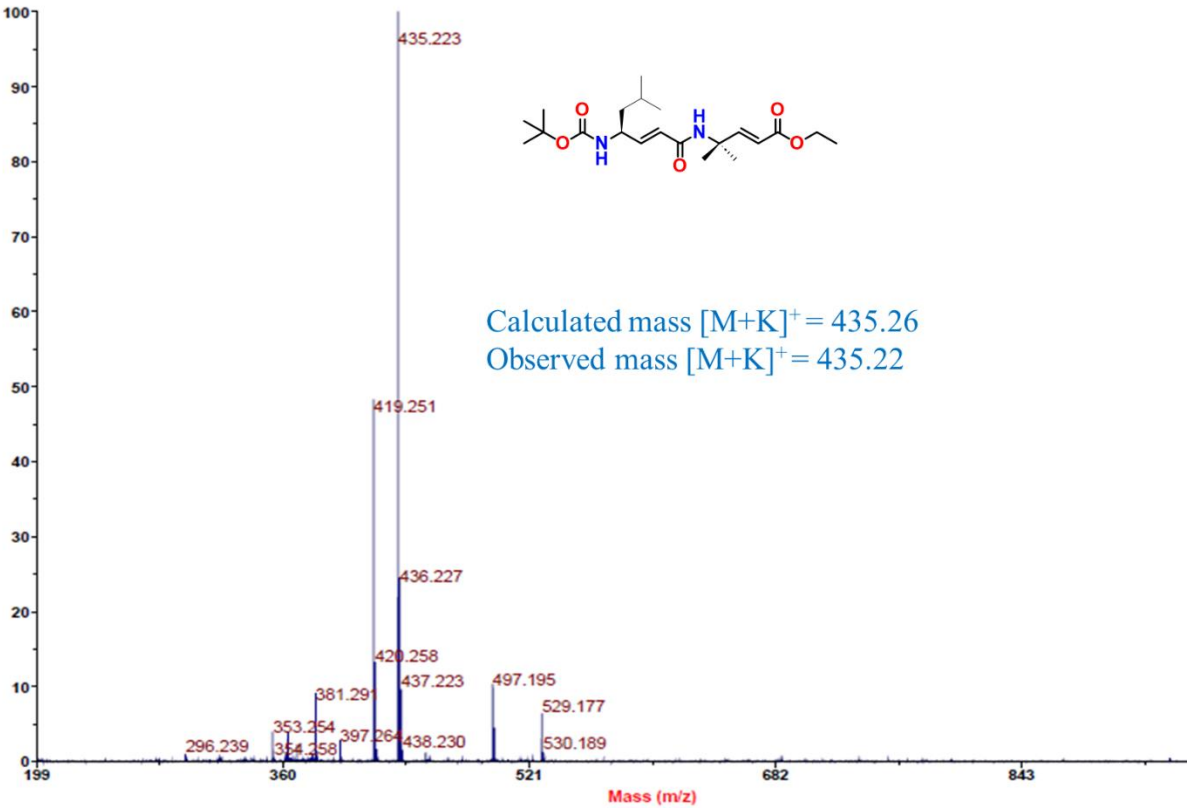

7.33 7.33 7.31 7.31 7.29 7.29 7.27 7.27 7.26 CDCl3 7.26 CDCl3 7.25 7.20 6.79 6.78 6.76 6.75 5.97 5.85 5.85 5.81 5.81 4.43 2.15 2.13 1.73 H2O 1.62 1.61 1.59 1.51 1.42 1.42 1.40 1.38 1.37 1.35 1.34 1.33 1.29 1.28 1.27 1.25 1.25 1.23 0.88 0.87 0.86 0.86 0.85 0.84 0.83 0.82 0.81 -0.00
1.05 1.03 3.98 0.83 0.86 1.81 0.96 1.12 1.17 0.95 1.92 3.04 6.10 6.29 3.06 9.02 6.24 5.83 4.29 18.14
f1 (ppm)


172.81 172.31 172.12 166.31 166.08 147.55 138.94 128.37 127.93 126.92 120.88 120.61 77.35 CDCl3 77.23 77.03 CDCl3 76.71 CDCl3 54.07 46.57 45.05 43.38 32.79 28.56 28.43 25.04 25.00 23.16 23.08 22.95 22.59 22.48 22.16 0.00
f1 (ppm)

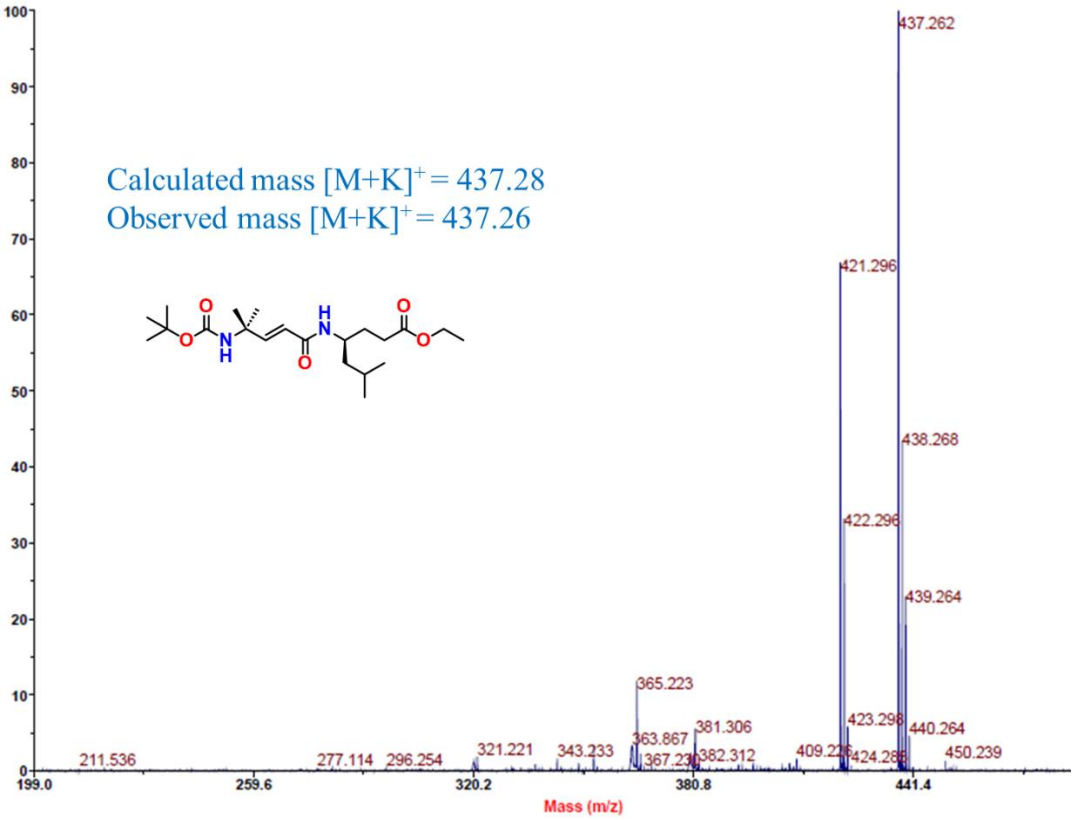


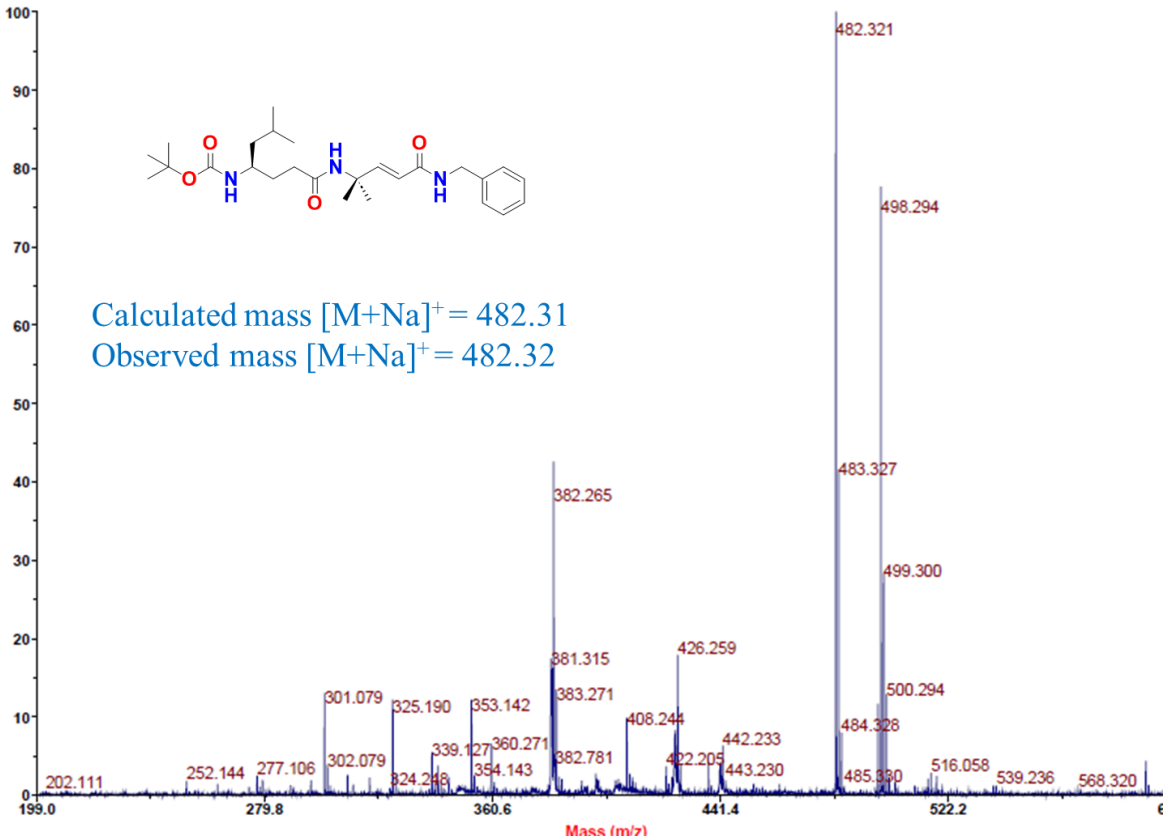


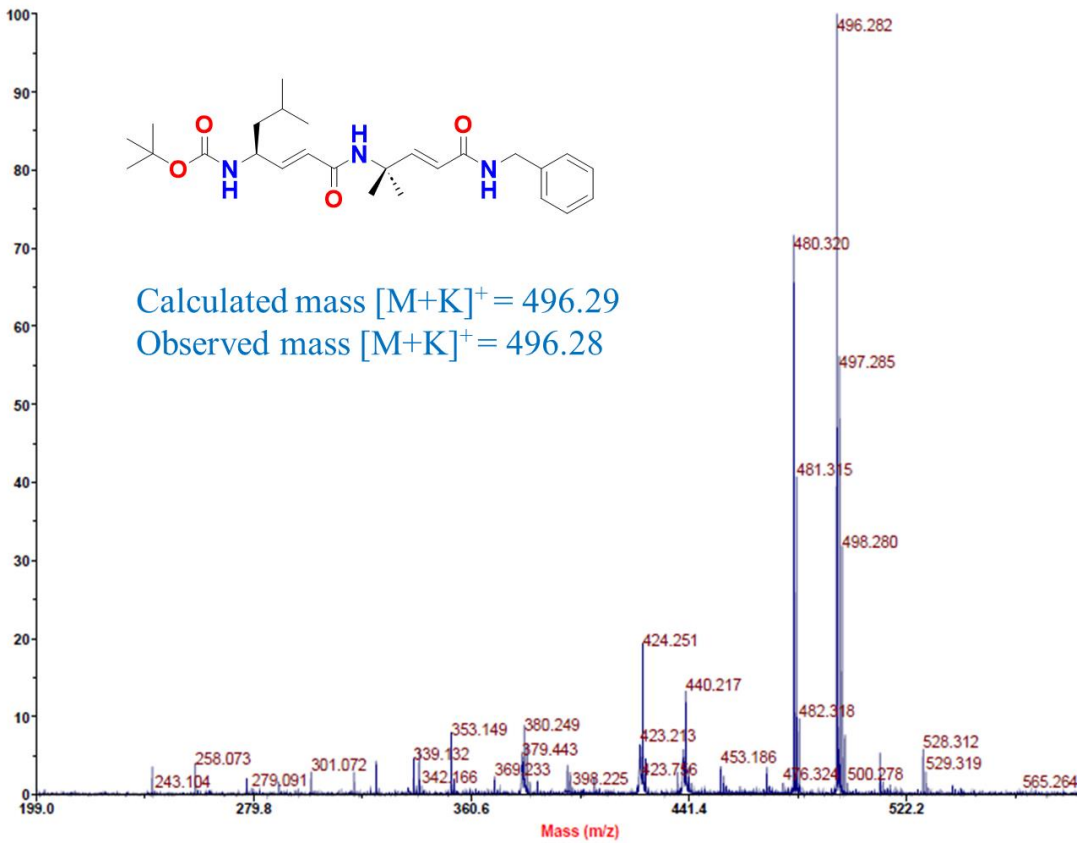
Calculated mass $[M+K]^+ = 435.26$
Observed mass $[M+K]^+ = 435.38$

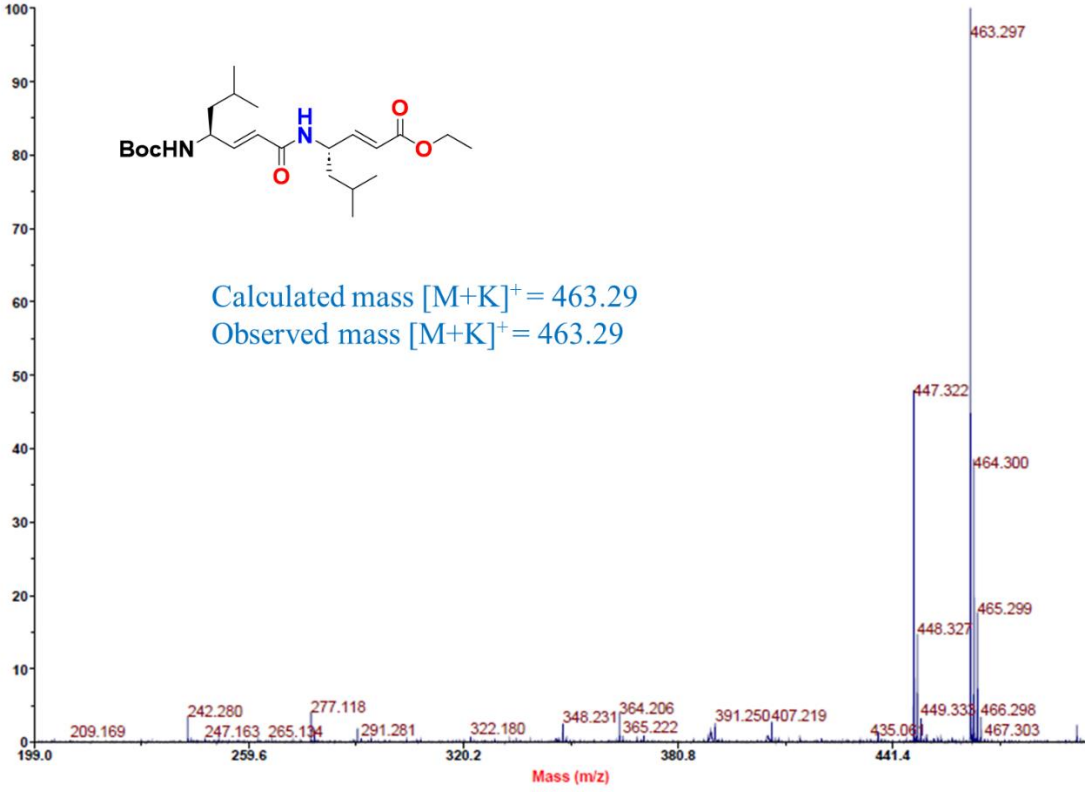


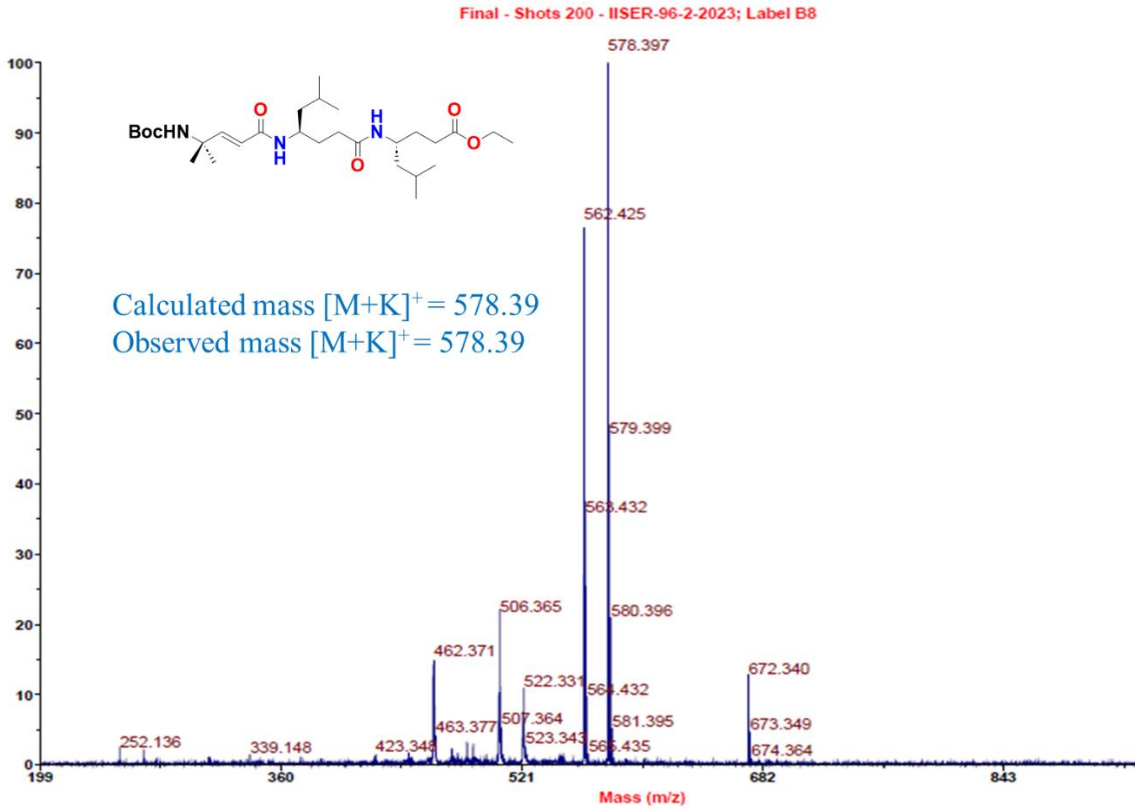
Calculated mass $[M+K]^+ = 435.26$
Observed mass $[M+K]^+ = 435.22$

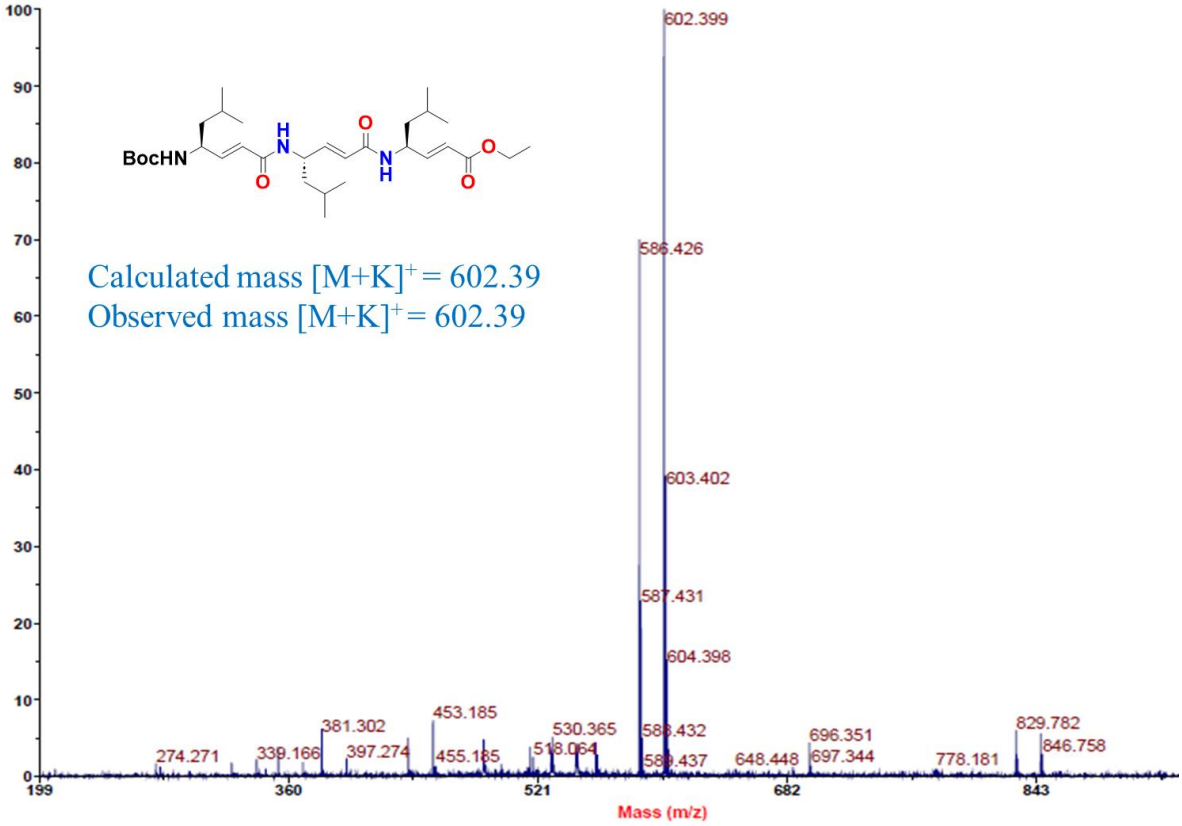

Calculated mass [M+K]+ = 437.28
Observed mass [M+K]+ = 437.26
437.262
421.296
438.268
422.296
439.264
365.223
423.298
440.264
381.306
363.867
211.536
277.114
296.254
321.221
343.233
367.230
382.312
409.226
424.286
450.239
Mass (m/z)

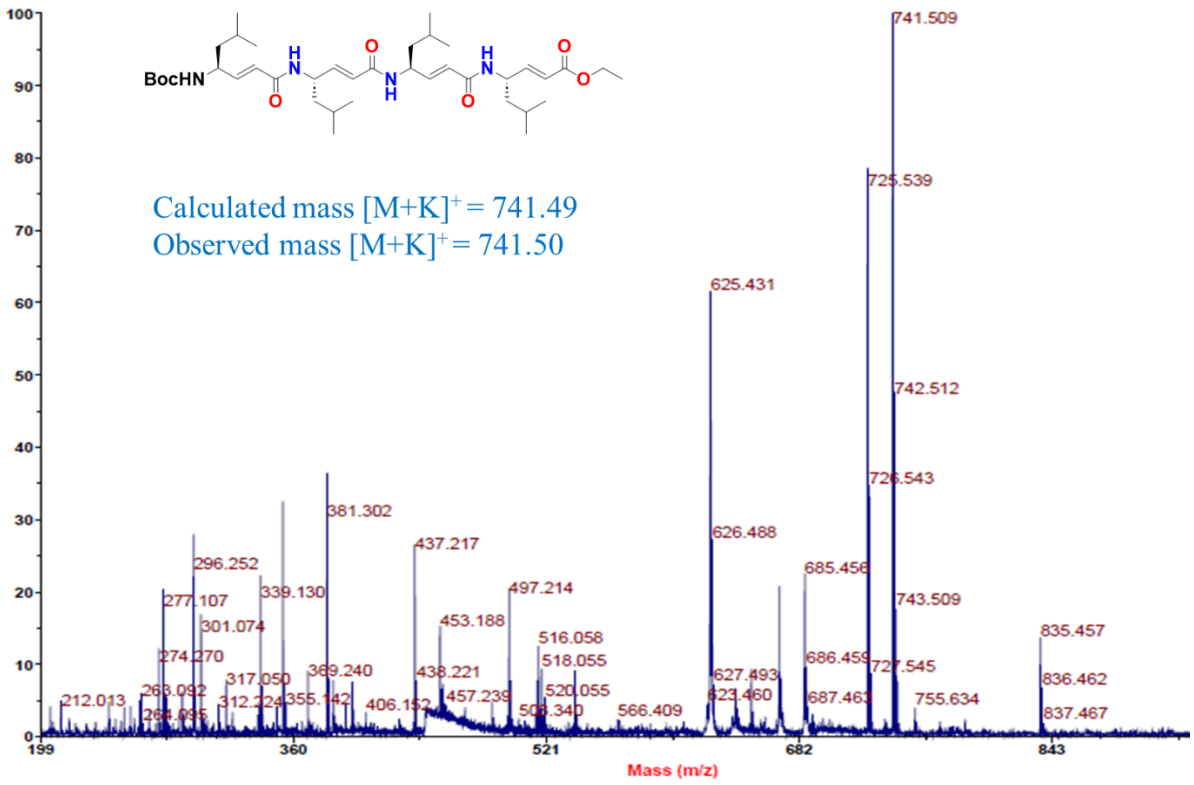

Calculated mass [M+Na]+ = 482.31
Observed mass [M+Na]+ = 482.32
482.321
498.294
483.327
382.265
499.300
381.315
426.259
500.294
301.079
325.190
353.142
383.271
408.244
484.328
442.233
339.127
360.271
302.079
382.781
422.205
443.230
485.330
516.058
539.236
568.320
202.111
252.144
277.106
324.248
354.143
Mass (m/z)

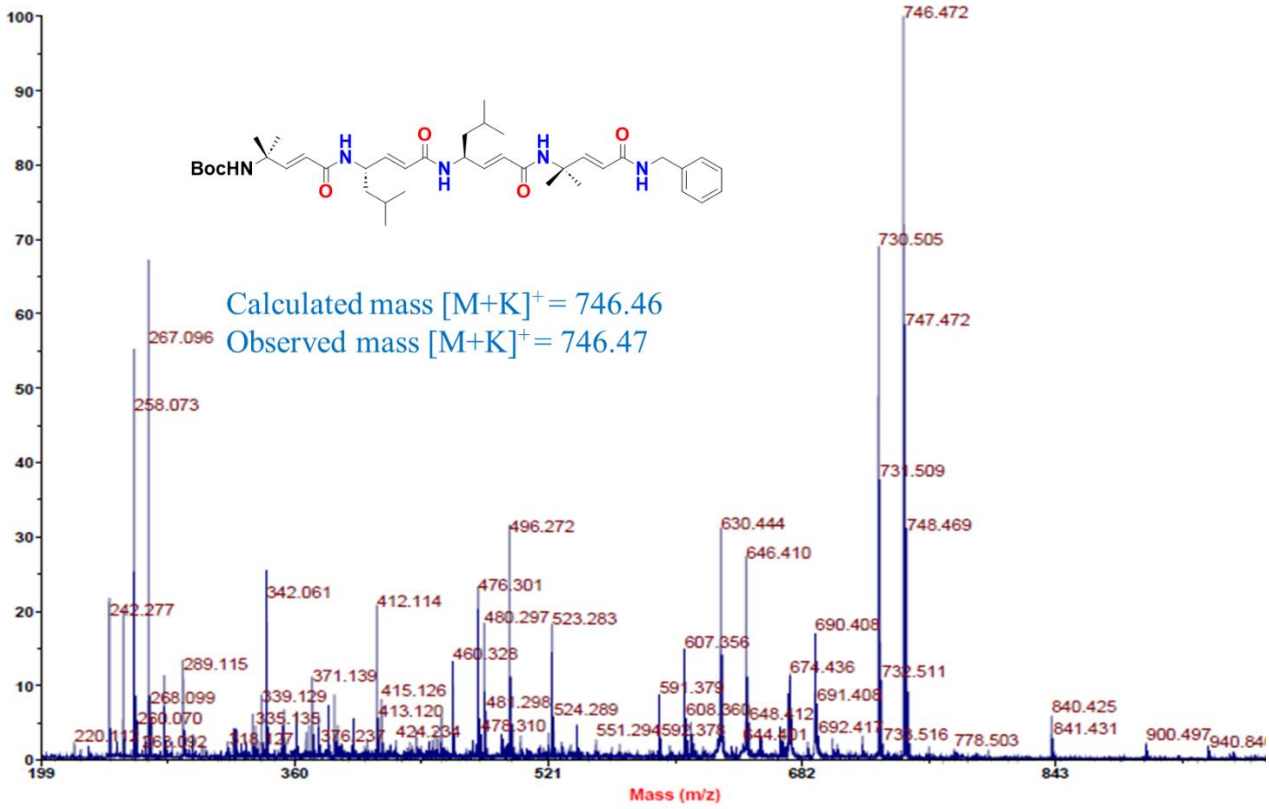

Calculated mass [M+K]+ = 496.29
Observed mass [M+K]+ = 496.28
Mass (m/z)

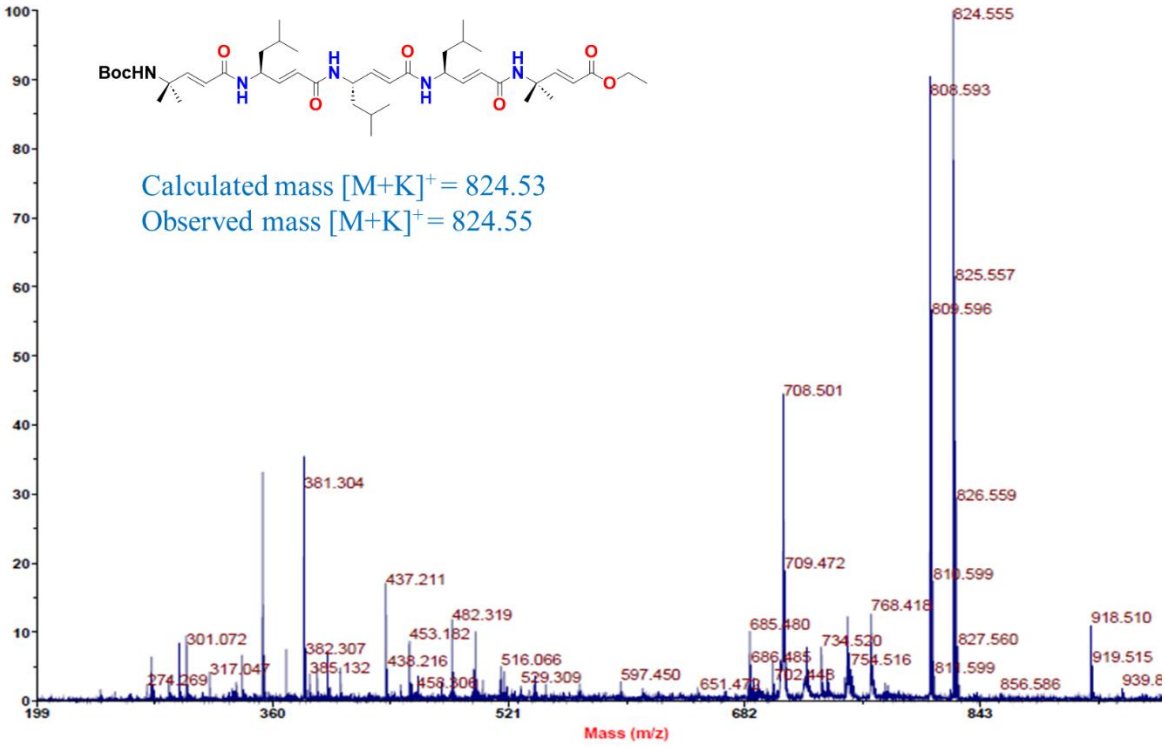

BocHN
Calculated mass [M+K]+ = 463.29
Observed mass [M+K]+ = 463.29
Mass (m/z)

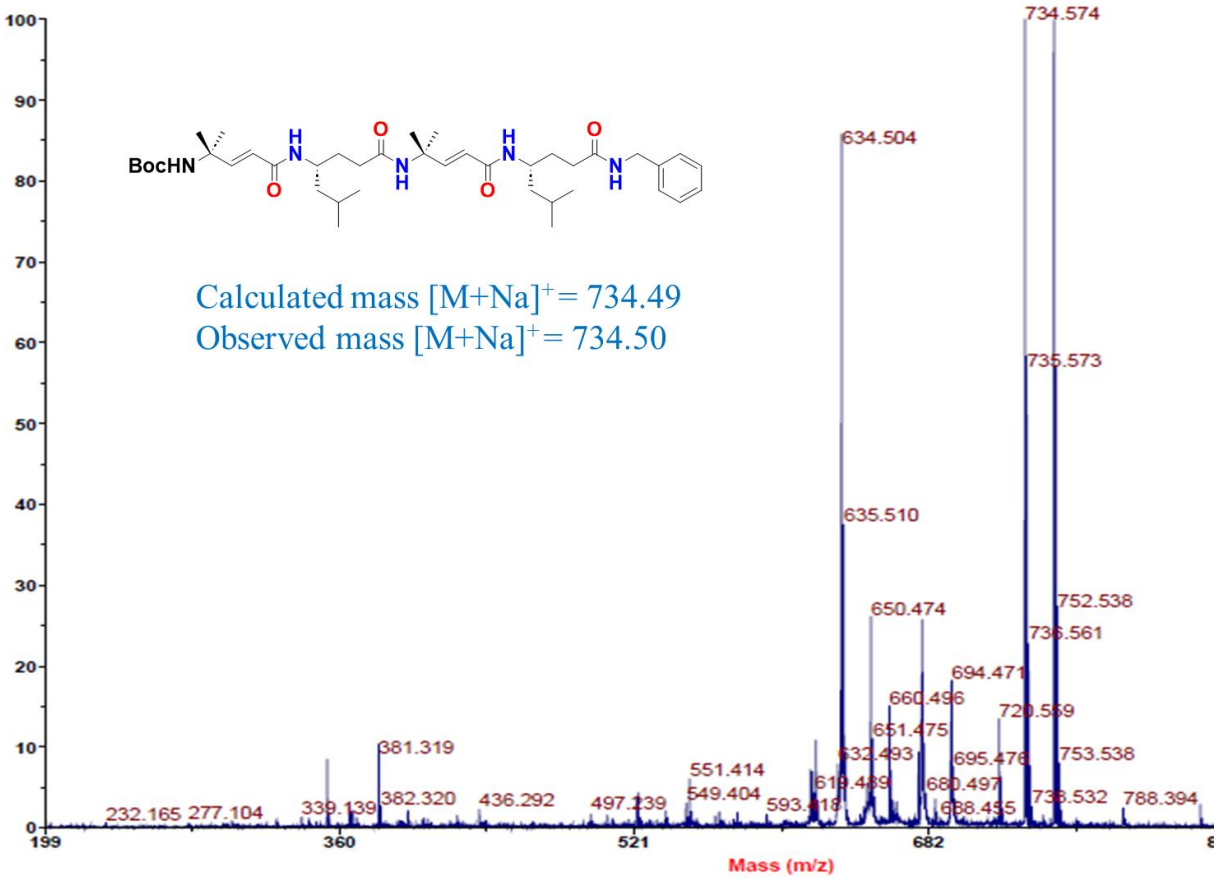

Final - Shots 200 - IISER-96-2-2023; Label B8
BocHN
Calculated mass [M+K]+ = 578.39
Observed mass [M+K]+ = 578.39
578.397
562.425
579.399
563.432
506.365
580.396
462.371
672.340
522.331
564.432
507.364
581.395
673.349
463.377
523.343
565.435
674.364
252.136
339.148
423.348
Mass (m/z)

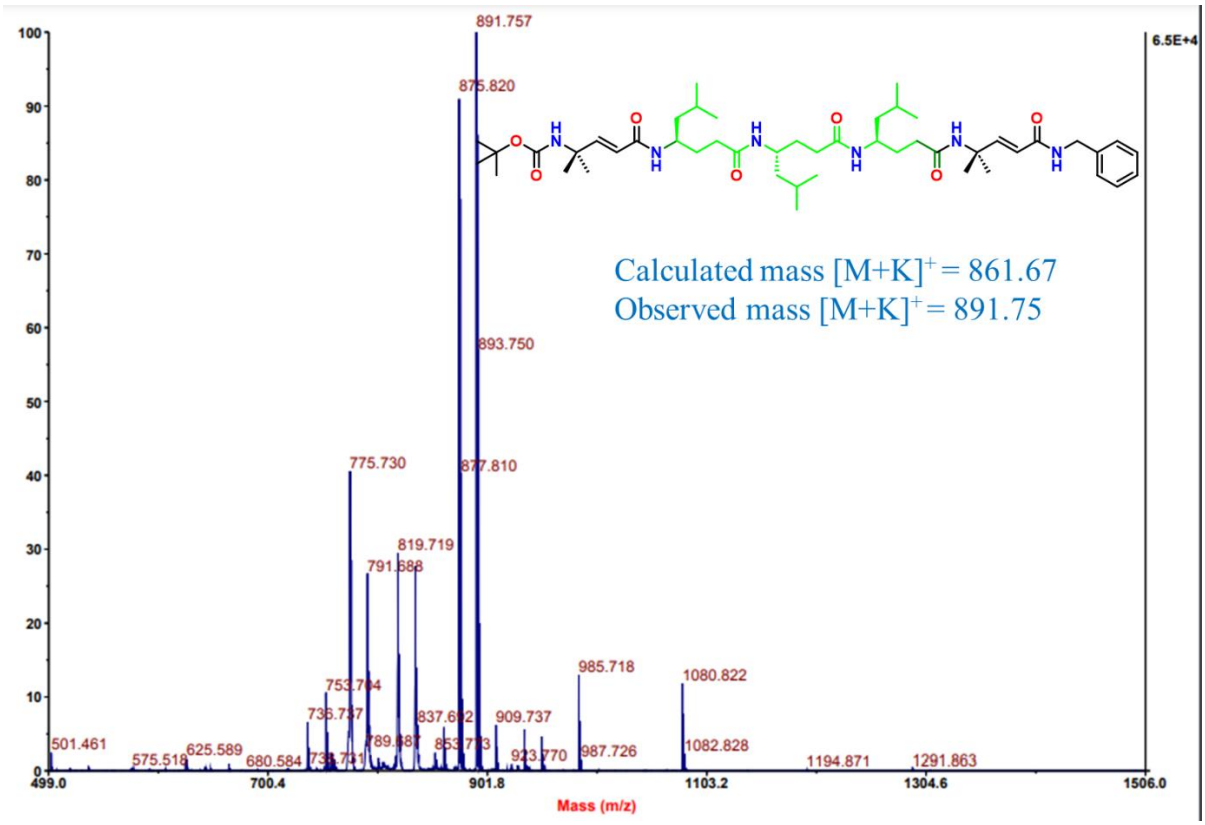

BocHN
Calculated mass [M+K]+ = 602.39
Observed mass [M+K]+ = 602.39
602.399
586.426
603.402
587.431
604.398
453.185
381.302
530.365
588.432
696.351
829.782
274.271
339.166
397.274
455.185
697.344
846.758
648.448
778.181
Mass (m/z)


BocHN
Calculated mass [M+K]+ = 741.49
Observed mass [M+K]+ = 741.50
Mass (m/z)


BocHN
Calculated mass [M+K]+ = 746.46
Observed mass [M+K]+ = 746.47
Mass (m/z)


BocHN
Calculated mass [M+K]+ = 824.53
Observed mass [M+K]+ = 824.55
Mass (m/z)


BocHN
Calculated mass [M+Na]+ = 734.49
Observed mass [M+Na]+ = 734.50
Mass (m/z)


891.757
875.820
893.750
775.730
877.810
819.719
791.688
985.718
1080.822
753.704
736.737
837.692
909.737
501.461
575.518
625.589
680.584
789.687
853.773
923.770
987.726
1082.828
1194.871
1291.863
6.5E+4
100
90
80
70
60
50
40
30
20
10
0
499.0
700.4
901.8
1103.2
1304.6
1506.0
Mass (m/z)
Calculated mass [M+K]+ = 861.67
Observed mass [M+K]+ = 891.75

Chapter 4

Porous Frameworks of Double Helical Peptide Foldamers

4.1. Introduction

The concept of drawing inspiration from the self-organization of biomolecules, such as proteins and peptides, to create innovative supramolecular structures with unique functionalities is a fascinating and promising area of research.[1-4] Despite the intricate nature of modern proteins, there is growing evidence to suggest that they originated from the spontaneous supramolecular self-assembly of much shorter and simpler peptides, typically consisting of fewer than 40-50 amino acids.[5-10] This theory presents an intriguing design principle for developing advanced and versatile materials that can be applied in various fields, including catalysis, separations, and drug delivery.[11-15] This approach aims to bridge the gap between small-molecule compounds and large protein assemblies. The significance of this concept lies in its potential to unlock new possibilities in the field of materials science and molecular engineering. Over the last decade, there has been a significant upsurge in enthusiasm for achieving higher-level self-assembly of synthetic peptide-based porous framework structures, to emulate the remarkable functions observed in biological systems. This emerging field represents a cutting-edge intersection of materials science and bioinspired molecular design. Peptides, as well as peptidomimetic building blocks, offer an extensive range of structural possibilities.[16] Their intrinsic chirality (handedness) and flexibility make them exceptionally well-suited for creating advanced porous-peptide frameworks. These frameworks have exhibited remarkable versatility and have found applications in several diverse areas such as gas storage, catalysis, sensing, bio-imaging, specific organelle-based drug delivery, chiral separation, chiral recognition, etc.[17-32] From the pioneering work from Rosseinsky and Fujita group, the field of designing metal-peptide frameworks (MPFs) has made considerable strides albeit it continues to grapple with a persistent challenge: the construction of extended peptide-based porous networks that are assembled primarily through supramolecular interactions like hydrogen bonding, halogen bonding, π-interactions, and host-guest interactions. Acknowledging the vast uncharted potential in this research area, our goal is to harness peptides with well-defined secondary structures to strategically design and employ these peptides for creating supramolecular peptide frameworks (SPFs) primarily based on non-covalent interactions.

4.2. Object of the Present Work

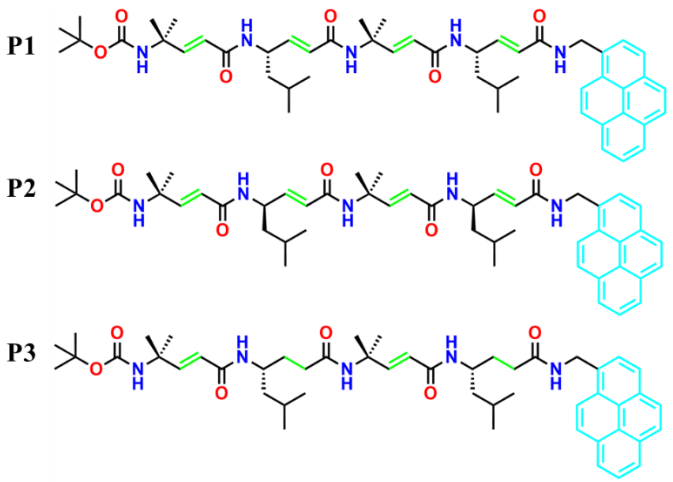
Among various secondary structures of proteins (such as helix, sheet, and turn) DNA possesses a unique double helical structure composed of two complementary polynucleotide strands linked by

numerous hydrogen bonds. Additional stability is provided by π–π stacking interactions between the covalently attached nucleobase pairs on the strands. Double-helical structures are uncommon in many natural biopolymers; however, Gramicidin A-D and feglymicin, linear natural polypeptides with alternating amino acid configuration, produced by *Bacillus brevis* have been shown to adopt double helix conformation.[33-39] In addition, synthetic peptides with alternating α_L and α_D amino acids have also been shown to adopt double helix structures.[40-44] Extensive efforts have been made over the decades to design double helical structures from different building blocks.[45] Recently, we have demonstrated the design of β-double helices, from the (*E*)-α, β-unsaturated 4, 4-dialkyl substituted γ-amino acids.[46] We also developed the strategy to create chiral double helices by incorporating (*E*)-α, β-unsaturated γ-amino acids in combination with the (*E*)-α, β-unsaturated 4, 4-dialkyl substituted γ-amino acids.[47] These double helices show remarkable conformational stability both in solid and solution states. This work focused on investigating the conformation of double helical motifs in solution by incorporating a fluorescence-active group, pyrene methyl amine, at the C-terminal. Additionally, we explored the self-assembly of these motifs in the solid state. Our report describes the construction of pyrene-appended double helical peptides and their self-assembly into a luminescent hydrogen-bonded framework governed by aromatic stacking and hydrogen bonding. These porous frameworks, being chiral and featuring a luminescent group, exhibit circularly polarized luminescence (CPL) properties.[48] This research holds promise for the development of peptide-based functional materials in optoelectronics and photonics.

4.3. Results and Discussions

The sequences of our peptides **P1**, **P2,** and **P3** are given in scheme 1. Peptide **P1** is the combination of achiral 4,4-gem-dimethyl α,β-unsaturated γ-amino acid (NH_2-dγAic-OH) and chiral (*S, E*)-α,β-unsaturated γ-Leu(L) amino acid (NH_2-dγLeu(L)-OH) and **P2** is the enantiomer of **P1** where we used (*R, E*)-α,β- unsaturated γ-Leu(D) amino acid (NH_2-dγLeu(D)-OH). In peptide **P3** where in place of *trans*-α, β-unsaturated γ-Leu, we used saturated γLeu(D) amino acid. The synthesis of all the saturated and unsaturated γ-amino acids was accomplished by initiating the Wittig reaction from the N-Boc-Aib aldehyde, N-Boc-Leu (L/or D) aldehyde following a previously documented procedure.[49] The three peptides were synthesized in solution through conventional Boc-chemistry, employing EDC·HCl and HOBt as coupling agents and purified through RP-HPLC. As crystal

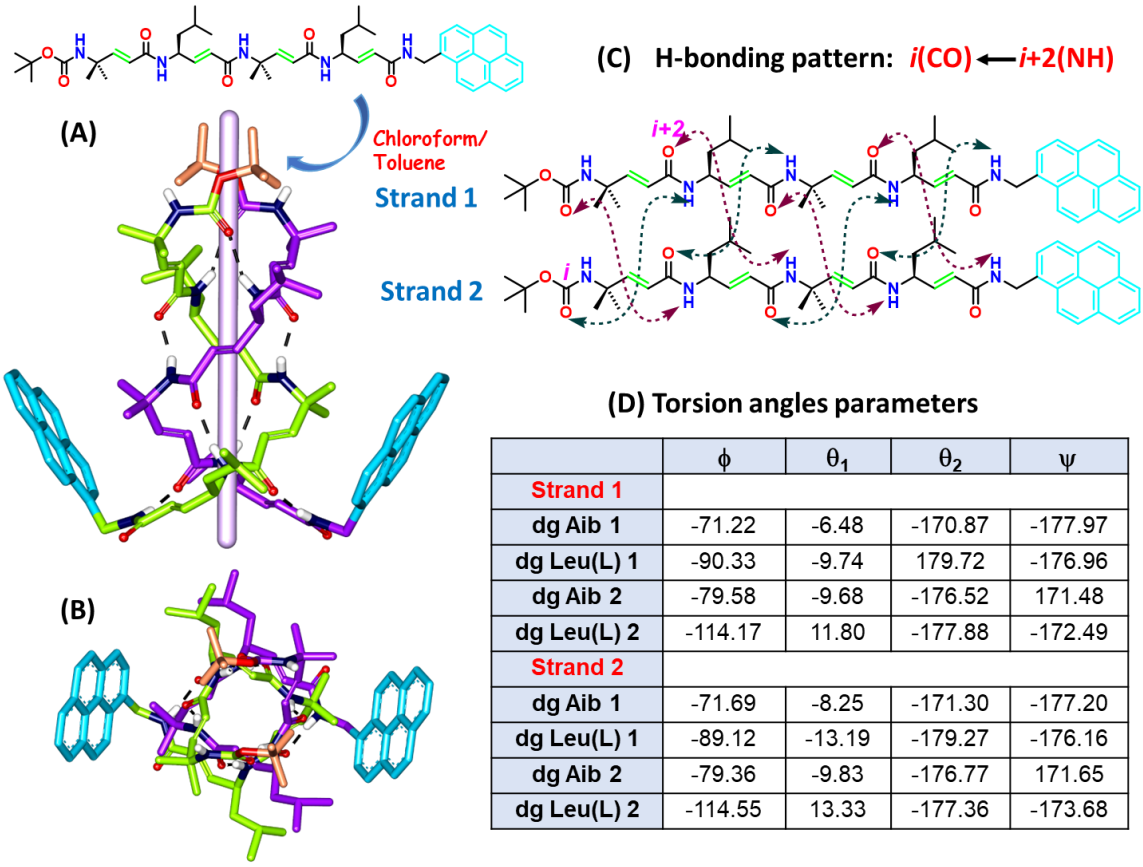
structures give unambiguous information about the solid-state conformation of the peptides, we subjected all three peptides for crystallization in different solvent combination mixtures.



Scheme 1: Sequences of pyrene appended peptides **P1, P2,** and **P3**

4.3.1. Crystal Structure Analysis of Peptide P1

We got diffraction quality crystals for **P1** from slow evaporation of chloroform/toluene mixture and solved in a tetragonal crystal system with space group *I*4. In the asymmetric unit, two molecules of P1 were identified, each independently adopting a right-handed helical conformation without forming intramolecular hydrogen bonds. All amide NH and carbonyl groups were exposed for intermolecular hydrogen bonding. The peptide engaged in self-assembly with another molecule, by involving all amide NH groups and CO groups for intermolecular hydrogen bonds, except the first NH and penultimate C-terminal CO group. The double helical structure of **P1** is shown in Figure 1A. The stability of this double helix structure was maintained through the presence of eight intermolecular hydrogen bonds, which formed between the amide carbonyl (CO) of the (*i*) residue in strand 1 and the amide NH of the (*i*+2) residue in strand 2. The hydrogen bonding pattern observed in **P1** is shown in Figure 1C. Overall, peptide **P1** adopted a right-handed (*P*)-β-double helix conformation in single crystals. The hydrogen bond distances fall within the span of 1.94–2.15 Å (with an average N-O distance of 2.77–3.07 Å) resulting in an average value of ∢N-H-O, 170°. The H-bond parameters of **P1** are tabulated in Table 1. The analysis of torsion angles indicated that achiral α,β-unsaturated 4,4-dimethyl γ-amino acids(dγAic) exhibited mean angles of approximately –75.46°±4° for ϕ, -8.9°±1° for θ_1, about -173° ± 2° for θ_2, and approximately ±174.57°±3° for ψ.



(D) Torsion angles parameters

	ϕ	θ_1	θ_2	ψ
Strand 1				
dg Aib 1	-71.22	-6.48	-170.87	-177.97
dg Leu(L) 1	-90.33	-9.74	179.72	-176.96
dg Aib 2	-79.58	-9.68	-176.52	171.48
dg Leu(L) 2	-114.17	11.80	-177.88	-172.49
Strand 2				
dg Aib 1	-71.69	-8.25	-171.30	-177.20
dg Leu(L) 1	-89.12	-13.19	-179.27	-176.16
dg Aib 2	-79.36	-9.83	-176.77	171.65
dg Leu(L) 2	-114.55	13.33	-177.36	-173.68

Figure 1: (A) Single crystal structure of **P1.** An imaginary rod is inserted along the crystal axis for a better view of the double-helical structure. (B) Top view of the **P1.** (C) Hydrogen bonding pattern observed in **P1.** (D) Torsion angle parameters of strand 1 and strand 2 of **P1**.

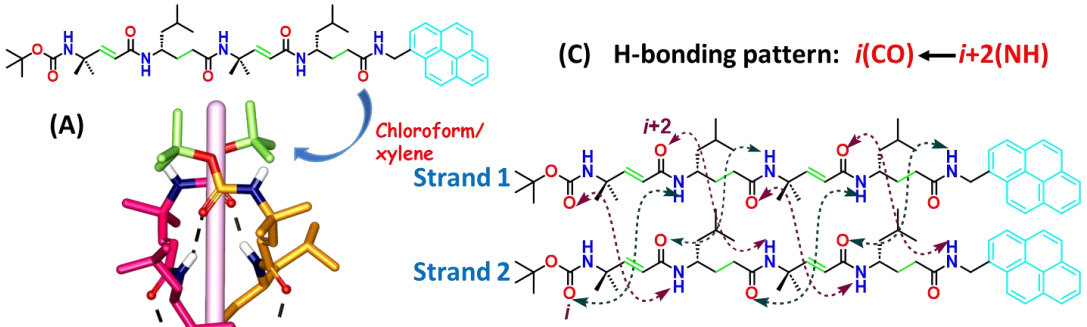
Table 1: The H-bond parameters of the **P1** double helix.

Donor (D)	Acceptor (A)	D.... A (Å)	DH.... A (Å)	∡NH....O (°)
N2	O8	2.866	2.022	160.52
N3	O9	2.809	1.979	156.60
N4	O10	2.819	1.97	161.49
N5	O11	2.871	2.001	169.74
N7	O2	2.822	1.97	162.73
N8	O3	2.803	1.971	157.35
N9	O4	2.835	1.991	160.04
N10	O5	2.929	2.070	165.46

The average torsional angles of θ_1 are close to 0, and θ_2 and ψ attain an angle close to 180°. The initial three torsion variables exhibited negative values, while ψ showed a negative value for the first dγAic residue and the second dγAic attained a positive value. The average torsion angles of the dγLeu acids ϕ, θ_1, θ_2, and ψ were found to be -102.04°±12°, ±0.55°±12°, ±178.55°±1°, and ±174.82°±2°, respectively. The sign remains uniform for the torsion variables ϕ and θ_1, but it varies in the case of fully extended θ_2 and ψ. All torsions variables are tabulated and shown in Figure 1D. Overall, **P1** adopted a right-handed double helical structure. Even though we got the crystals of peptide **P2**, but quality of the crystals was not good for diffraction.

4.3.2. Crystal Structure Analysis of P3

However, we got diffraction quality crystals for **P3** from slow evaporation of chloroform/xylene mixture and solved in orthorhombic crystal system with space group *I*222 and the X-ray diffracted structure is illustrated in Figure 2.



(D) Torsion angles parameters

	ϕ	θ_1	θ_2	ψ
Strand 1				
dγ Aic 1	73.58	4.14	171.67	-178.44
γLeu() 1	107.72	-47.89	-161.66	-136.74
dγ Aic 2	70.65	10.14	174.86	-170.81
γLeu(D) 2	125.92	-71.58	175.95	-136.75
Strand 2				
dγ Aic 1	75.91	5.37	172.58	178.54
γLeu() 1	70.06	61.23	-173.46	134.74
dγ Aic 2	71.22	-149.59	-168.05	-8.42
γLeu(D) 2	113.02	-66.03	179.71	-125.30

Figure 2: (A) Single crystal structure of **P3.** An imaginary rod is inserted along the crystal axis for a better view of the double-helical structure. (B) Top view of the **P3.** (C) Hydrogen bonding pattern observed in **P3.** (D) Torsion angle parameters of strand 1 and strand 2 of **P3**.

It is fascinating to see that peptide **P3** accommodated into a β-double helical structure as observed in the crystal structure. Even though the double bond has been removed, the γLeu residues are nicely accommodated into the double helical structure. Peptide strands 1 and 2 are interwoven through hydrogen bonds between them, and the stability of the β-double helix structure is maintained by a total of eight inter-strand hydrogen bonds. In strand 2, the amide CO group of residue *i* forms a hydrogen bond with the amide NH group of residue *i*+2 in strand 1 (*i*→ *i+2*). Similarly, within strand 1, the amide CO group of residue *i* establishes hydrogen bonding with the amide NH group of residue *i*+2 in strand 2 (*i*→ *i+2*). The NH groups of the N-terminal Boc-amide and the CO groups of the C-terminal pyrenyl amine NH do not participate in inter-strand hydrogen bonding interactions within their β-double helix structure. However, they do engage in intermolecular hydrogen bonding with other β-double helices. A diagram illustrating the inter-strand hydrogen bonds identified in **P3** is depicted in Figure 2C. The H-bond characteristics of the **P3** double helix are summarized in Table 2. The properties of the observed hydrogen bonds fall within the standard range of H-bond parameters. Due to the presence of γLeu amino residues in between the α,β-unsaturated 4,4-dimethyl gamma-amino acids, the torsional angles are not quite similar to our previous structure **P1**. The average torsional angles ϕ for dγAic and γLeu are 72.84° ± 2° and 104.96±20° respectively, which is well in accord with structure **P1**. But the differences arise in θ_1, and ψ values.

Table 2: The H-bond parameters of the **P3** double helix.

Donor (D)	Acceptor (A)	D.... A (Å)	DH.... A (Å)	∡NH....O (°)
N2	O8	2.906	2.074	157.13
N3	O9	2.780	1.902	176.66
N4	O10	2.818	1.982	158.86
N5	O11	2.771	1.884	172.68
N7	O2	2.808	1.968	157.32
N8	O3	2.818	1.952	168.11
N9	O4	2.809	1.990	154.23
N10	O5	2.824	1.973	162.31

The θ_1 torsion values are nearly zero for achiral dγAic units same as **P1**, except the 2nd dγAic residue of strand B with a value of -149.59°. But in the case of γLeu residues, the average torsion angle θ_1 deviates from the previous structure and attains a value of $\pm 60.18° \pm 11°$. The average torsion angle θ_2 for dγAic and γLeu is $\pm 171.79° \pm 2°$ and $\pm 172.69° \pm 7°$ respectively, which is almost the same as **P1**, forming an extended conformation. In the case of the torsional angle ψ, the values are also same as dγAic units of **P1** except the 2nd dγAic residue of strand 2 with a value of -8.42, which is quite unusual compared to our previously reported double helices. There is also a difference in torsion angles ψ for the γLeu units in both strands with an average torsion value of $\pm 133.38° \pm 5°$, which is quite a deviation from **P1**. Even though there is quite a difference in torsion values of peptides **P1** and **P2**, but still both peptides form a double helical structure. Peptide **P2** rearranges its torsion angles to accommodate the γ-residues in the backbone. This proves the plasticity of our double helical structures.

4.3.3. Self-Assembly of Peptides P1 and P3

After characterizing the peptides' double-helical conformation, our subsequent objective is to delve into their self-assembly within the solid state, with a specific focus on crystal packing analysis. Notably, in our crystal structure examination, we observed that the NH groups of the N-terminal Boc-amide and the CO groups of the C-terminal pyrenyl amine do not engage in inter-strand hydrogen bonding interactions within their β-double helix structure. Instead, these groups remain exposed for potential hydrogen bonding with other double helices in the crystal lattice. Upon scrutiny of the crystal packing, a significant finding emerges: the Boc-NH groups of a double helix actively participate in intermolecular hydrogen bonding with the C-terminus C=O groups of another double helical moiety. This intermolecular hydrogen bonding interaction between two distinct double helices is visually depicted in Figure 3B.

The head-to-tail concomitant hydrogen bonding observed among the double helices extends its influence within the *a-b* plane. As illustrated in Figure 3C, the self-assembly process involves the coordination and alignment of four double helical entities through hydrogen bonding interactions. This molecular arrangement leads to the creation of a distinctive supramolecular macrocycle structure, resembling a tetrameric rosette. In this assembly, the hydrogen bonding interactions play a crucial role in stabilizing the connections between the double helical entities.

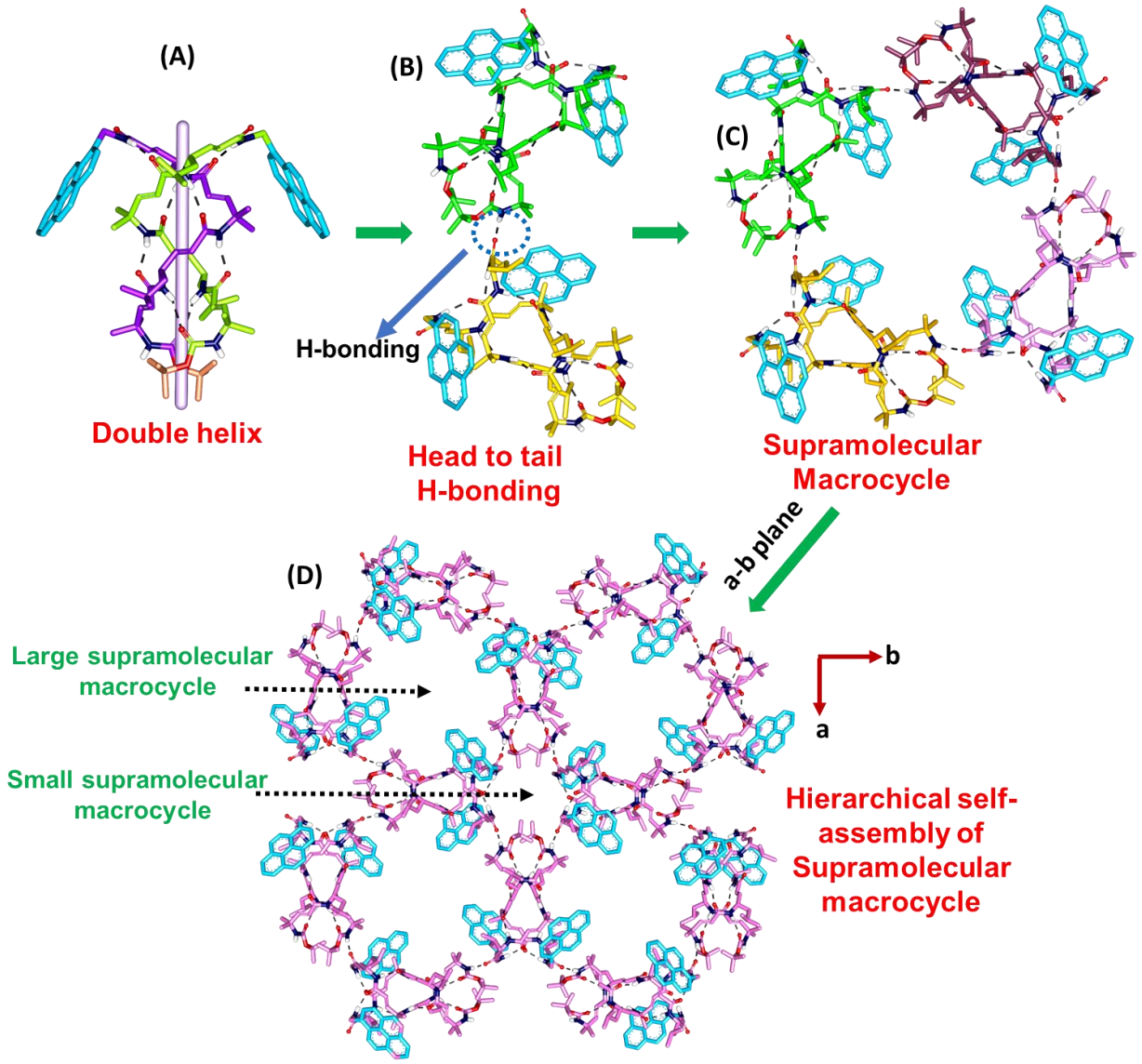


Figure 3: (A) Double helical structure of peptide **P1**. (B) Intermolecular hydrogen bonding between two double helices through Boc-NH of one double helix with the carbonyl group of another double helix at (*i* + 5) position. (C) Formation of supramolecular macrocycles by self-assembly of four double helices. (D) The two-dimensional network of supramolecular macrocycles shows a large and small macrocycle.

This leads to the creation of a larger, cyclic structure. The tetrameric rosette configuration highlights the organized and cooperative nature of the hydrogen bonding interactions, which contribute to the overall stability and integrity of the supramolecular macrocycle. The four double helices are positioned relative to each other with their double helical axes oriented at a 90° angle. This macrocycle, in turn, engages in further self-assembly with additional double helical moieties

through hydrogen bonding interactions. The assembly is shown in Figure 3D. The careful analysis shows the formation of two different kinds of macrocycles. The large macrocycles have a diameter of approximately 9.923 Å, while the small supramolecular macrocycles have a diameter of approximately 6.94 Å.

The supramolecular self-assembly further results in a two-dimensional intricate network of supramolecular macrocycles that spans the *a*-*b* crystal plane, as depicted in Figure 4.

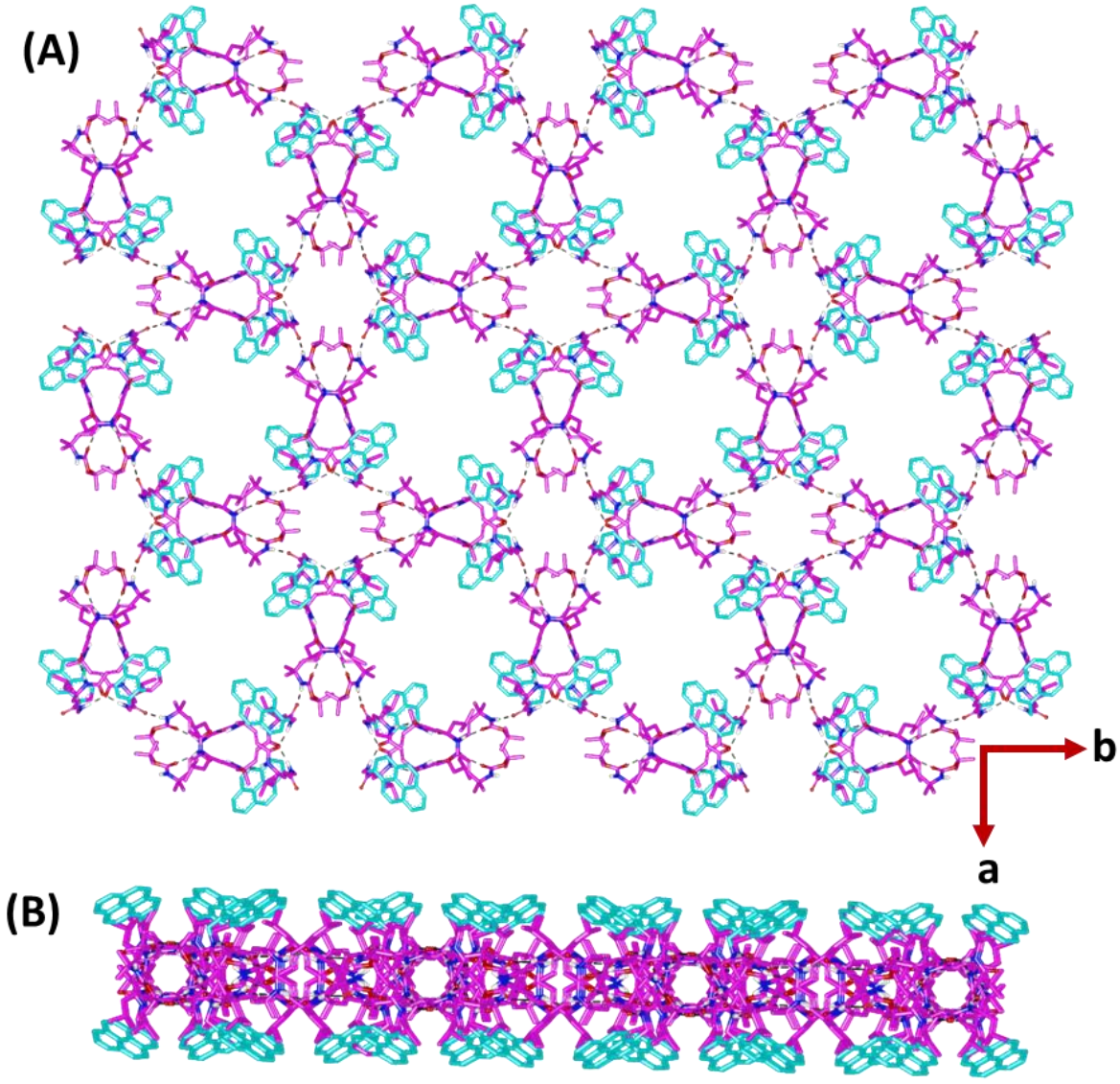


Figure 4: (A) The supramolecular two-dimensional self-assembly of macrocycles in *a*-*b* plane. (B) The side view of the assembly.

As the supramolecular two-dimensional assembly in the *a*-*b* plane is solely facilitated by the intermolecular hydrogen bonding interactions between the double helical moieties, we further sought to investigate the role of pyrene moieties in the self-assembly process in different directions. Due to the substantial π-aromatic surface of pyrene moieties, pyrene moieties additionally contribute to π-π stacking interactions. The tetrameric rosette kind of supramolecular macrocyclic structures are further self-assembled through π-π interaction between the pyrene moieties along the *c*-direction.

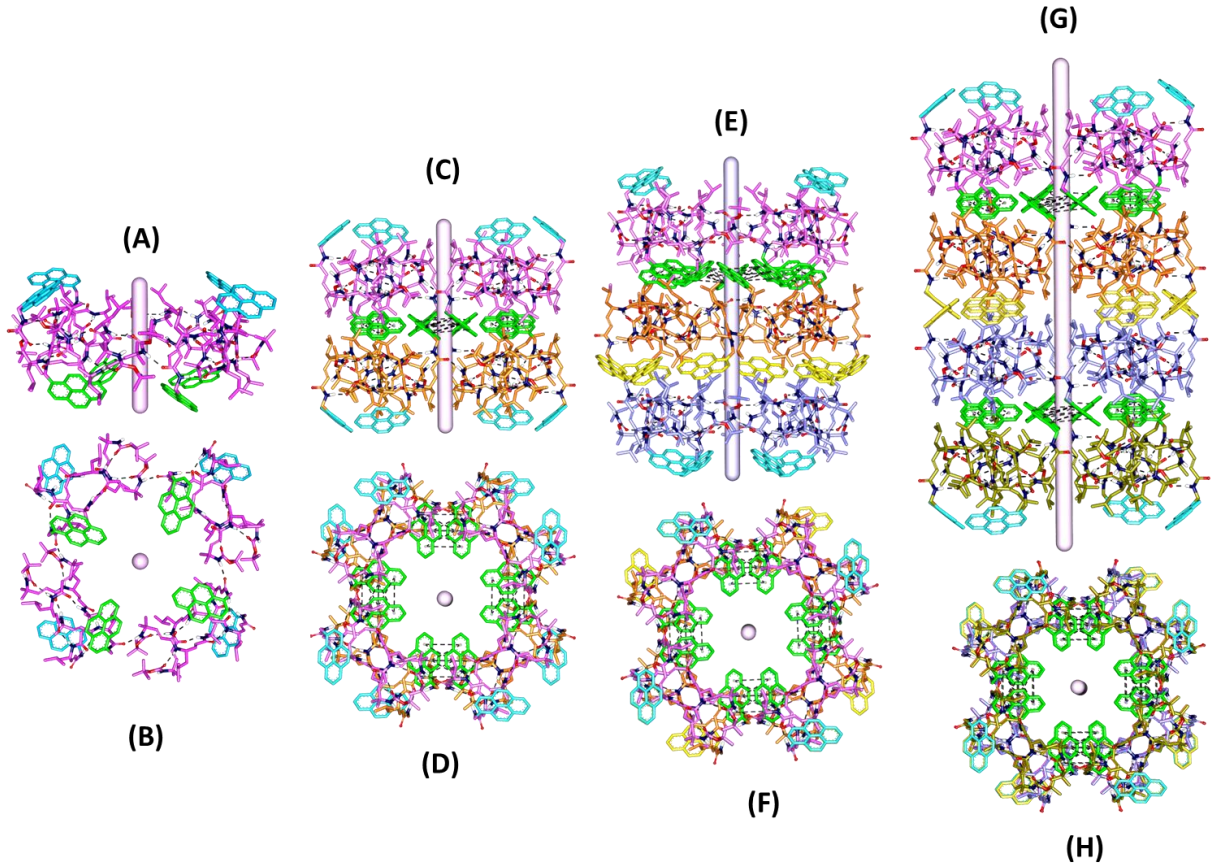


Figure 5: (A) A single tetrameric double helix-based macrocycle shown along the *c*-axis (B) Top view of the macrocyclic structure. (C) Two macrocycle rings self-assembled through π-π stacking interaction between the pyrene moieties. (D) Top view of the self-assembled structure. (E) Three macrocycle rings self-assembled through π-π stacking and CHπ-CHπ interaction between the pyrene moieties. (F) Top view of the self-assembled structures. (G) Four macrocycle rings self-assembled through π-π stacking and CHπ-CHπ interaction between the pyrene moieties. (H) Top view of the self-assembled structures.

In Figure 5A, the side view of the tetrameric structure reveals the formation of a macrocyclic ring-like architecture. This macrocyclic ring, oriented along the crystal *c*-axis, undergoes further self-assembly with another macrocyclic ring through π-π interactions involving the green-colored pyrene moieties. The self-assembly process extends along the *c*-direction, where the third macrocyclic ring engages in self-assembly with the second ring through CH-π and CH-π interactions, as illustrated by the yellow-colored pyrene moieties. A similar pattern continues, with yet another macrocyclic ring aligning below the third ring and self-assembling through π-π interactions among the pyrene moieties. This self-propagating process along the c-axis demonstrates the successive assembly of each macrocyclic ring structure. The interactions involved include both π-π interactions and CH-π interactions between the pyrene moieties. Through this orchestrated combination of forces, a supramolecular 1D-channel-like structure emerges. The resulting architecture is characterized by a continuous arrangement of these macrocyclic rings, with each ring contributing to the overall formation of the channel-like structure through the specific interactions between their pyrene moieties.

In the self-assembly process, a higher level of complexity was achieved as the supramolecular channel architecture interconnects along the *c*-axis in the *a*-*b* plane through intermolecular H-bonding interactions. This extended self-assembly culminates in the formation of a precisely defined 3D-porous network structure, as depicted in Figure 6.

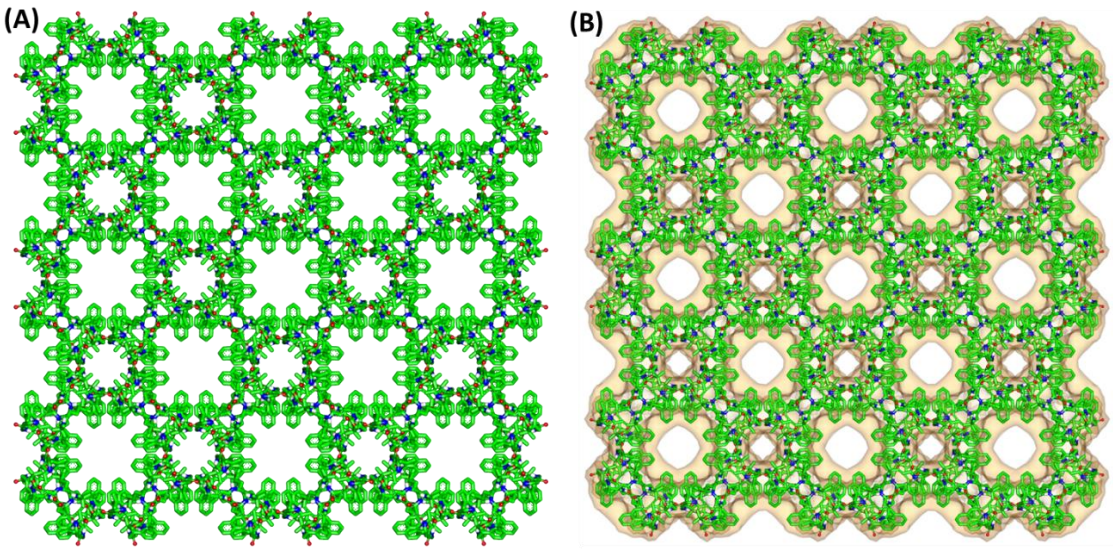


Figure 6: (A) The 3D crystal packing of **P1** observed along the c axis (B) The space-fill framework packing structure of **P1**

The solvent-accessible void volume, calculated to be approximately 2997 Å^3, indicates the presence of empty spaces within the porous network.

Having this exciting assembly in mind, we also want to investigate how peptide **P3** is self-assembled in the solid state. Excitingly, we have seen that **P3** also forms a macrocycle similar to what we observed in **P1** along the *b*-*c* crystal plane (Figure 7A). Likewise, extended 2D self-assembly of macrocycles is happening for **P3** with a large supramolecular macrocycle having a diameter of 10.128 Å and a small supramolecular macrocycle with a diameter of 7.23 Å (Figure 7B). Through self-assembly of these supramolecular macrocycles along the *a*-axis gives a channel-like supramolecular architecture through π-π interactions and CH-π interactions (Figure 7C).

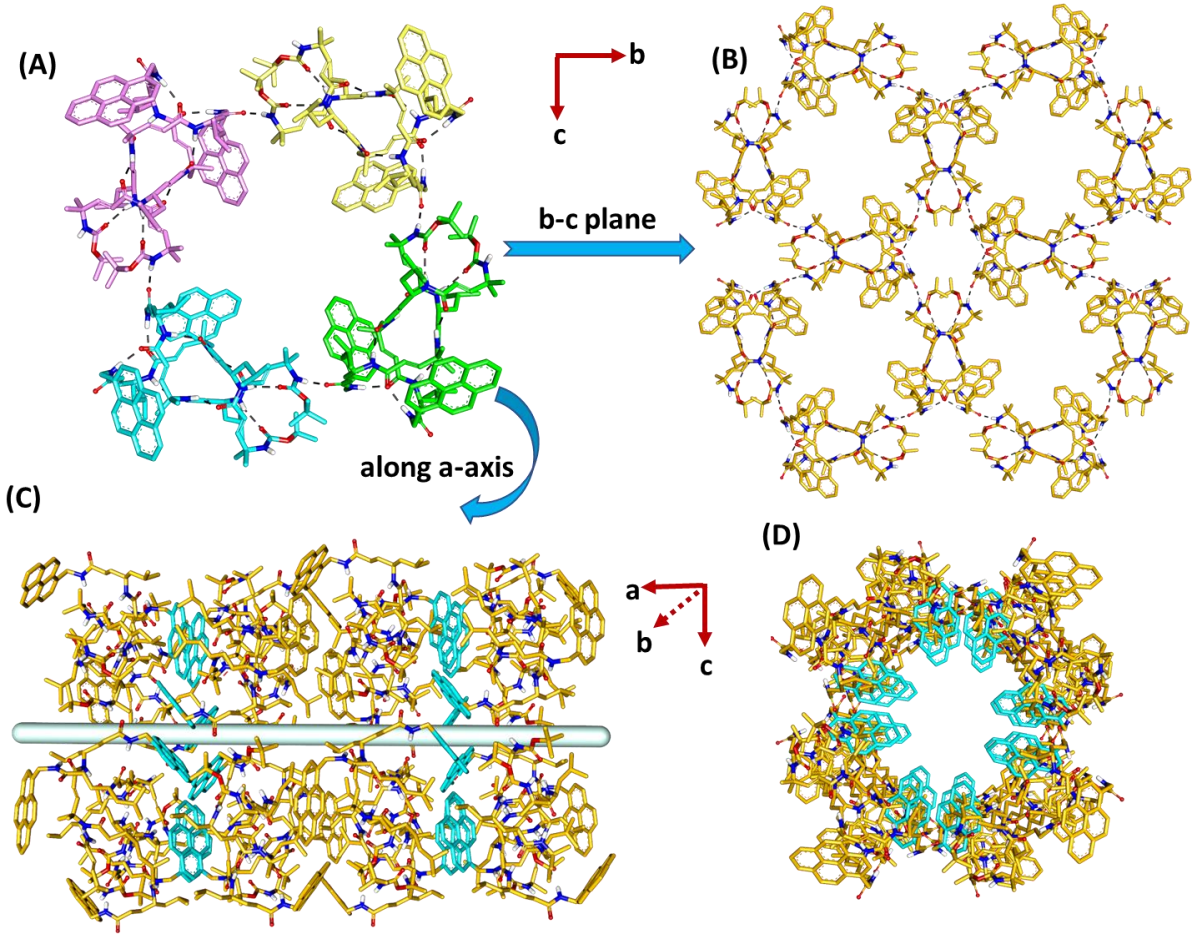


Figure 7: (A) supramolecular macrocycle formation by **P3** four double helical units. (B) self-assembly between the tetrameric core. (C) Side view of the large channel formed through π-π stacking and CHπ- CHπ interactions among each macrocyclic subunit. (D) Top view of the channel.

Similar to **P1**, a supramolecular porous framework was generated for **P3** by self-assembly of these supramolecular channels through inter-double helix hydrogen bonding and pi-pi stacking between the pyrene units. The porous structure is shown in Figure 8. The solvent accessible void volume in in case of **P3** is 2867 $Å^3$.

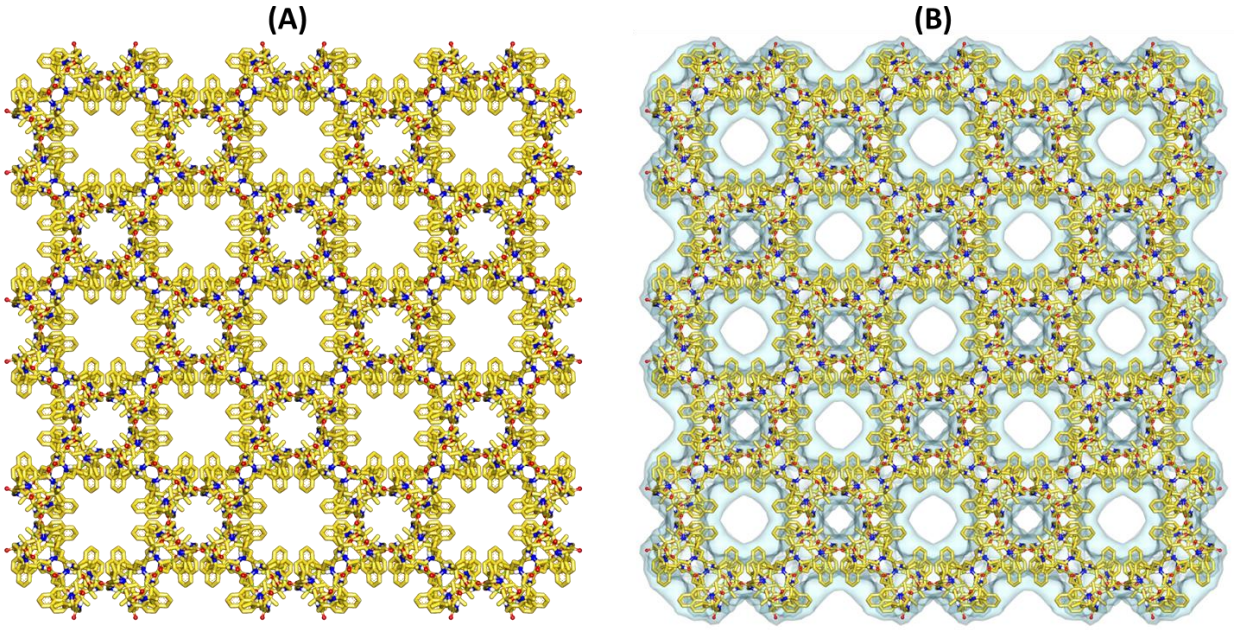
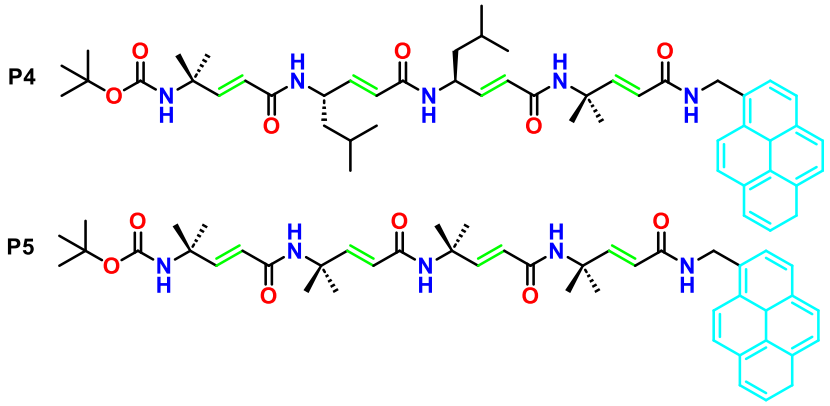


Figure 8: (A) The 3D crystal packing of **P3** observed along the c axis (B) The space-fill framework packing structure of **P3**

The success of these intermolecular forces in guiding the formation of the 3D-porous network structure attests to their cooperative and synergistic action. The controlled interplay between hydrogen bonding and π-π stacking interactions enables the stepwise progression from the initial double helical entities to the more complex supramolecular channels and, ultimately, to the intricate 3D-porous network. This success is indicative of the delicate balance achieved in harnessing these forces to create a precisely defined and organized architecture, showcasing the potential for tailored design and applications in diverse fields such as materials science and nanotechnology.

To further confirm how the sequences of the peptides impact the abovementioned self-assembly, we have synthesized peptides **P4** and **P5**. In peptide **P4,** we interchanged the dγAic and dγLeu residues at the very end and kept the dγAic unit at the C-terminal of the peptide **P4**. In peptide **P5**, we have synthesized the peptide having all the dγAic amino acids in the peptide backbone.

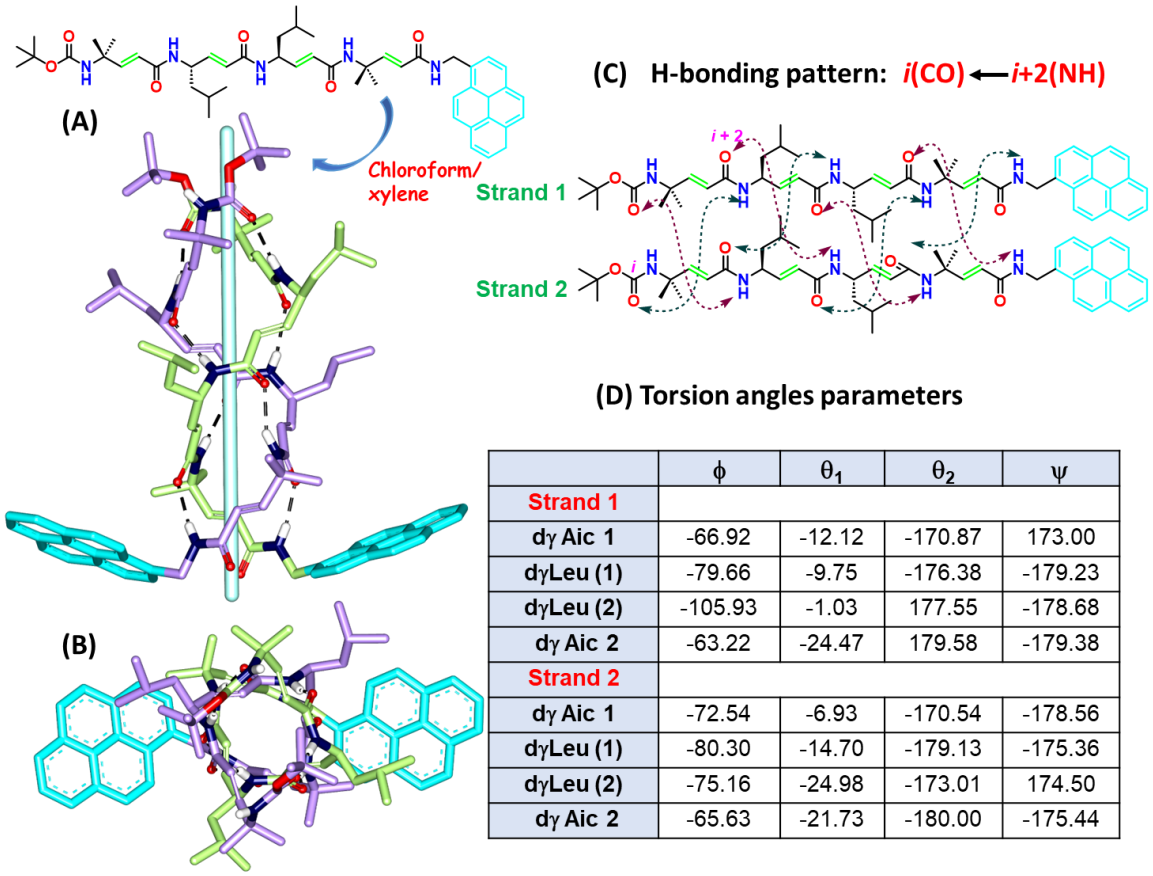


Scheme 2: Sequences of the peptide **P4** and **P5**

All these two peptides were synthesized through solution phase peptide synthesis by using conventional Boc-chemistry. As crystal structures give unambiguous conformational information about their solid-state structure, we subjected all these two peptides to crystallization in different solvent mixtures.

4.3.4. Crystal Structure of Peptide P4

We got diffraction quality crystals for **P4** from slow evaporation of chloroform/toluene mixture and solved in a tetragonal crystal system with space group $P2_12_12_1$. The single crystal structure of **P4** is shown in Figure 9A. In the asymmetric unit, two molecules of **P4** molecules were identified, each independently assuming a right-handed helical conformation without forming intramolecular hydrogen bonds. All amide NH and carbonyl groups were accessible for intermolecular hydrogen bonding. The peptide engaged in self-assembly with another molecule, utilizing all amide NH groups and CO groups for intermolecular hydrogen bonds, excluding the first NH and the penultimate C-terminal CO group. The stability of this double helix structure was maintained through the presence of eight intermolecular hydrogen bonds, which formed between the amide carbonyl (CO) of the (*i*) residue in strand 1 and the amide NH of the (*i*+2) residue in strand 2. The hydrogen bonding pattern observed in **P4** is shown in Figure 9C. Overall, peptide **P4** adopted a right-handed (*P*)-β-double helix conformation in the single crystals. The hydrogen bond distances fall within standard limits as observed in our previous structures. The H-bond parameters of **P4** are tabulated in Table 3. The analysis of torsion angles indicated that achiral α,β-unsaturated 4,4-dimethyl γ-amino acids(dγAic) exhibited mean angles of approximately –67.07°±4° for ϕ, -16.31°±7° for θ_1, about ±175.24±4.5° for θ_2, and approximately ±176.59°±2° for ψ.



	ϕ	θ_1	θ_2	ψ
Strand 1				
dγ Aic 1	-66.92	-12.12	-170.87	173.00
dγLeu (1)	-79.66	-9.75	-176.38	-179.23
dγLeu (2)	-105.93	-1.03	177.55	-178.68
dγ Aic 2	-63.22	-24.47	179.58	-179.38
Strand 2				
dγ Aic 1	-72.54	-6.93	-170.54	-178.56
dγLeu (1)	-80.30	-14.70	-179.13	-175.36
dγLeu (2)	-75.16	-24.98	-173.01	174.50
dγ Aic 2	-65.63	-21.73	-180.00	-175.44

Figure 9: (A) Single crystal structure of **P4.** An imaginary rod is inserted along the crystal axis for a better view of the double-helical structure. (B) Top view of the **P4.** (C) Hydrogen bonding pattern observed in **P4.** (D) Torsion angle parameters of strand 1 and strand 2 of **P4**.

Table 3: The H-bond parameters of **P4** double helix.

Donor (D)	Acceptor (A)	D.... A (Å)	DH.... A (Å)	∡NH.... O (°)
N2	O8	2.938	2.081	175.27
N3	O9	2.857	2.060	153.68
N4	O10	2.901	2.042	177.12
N5	O11	2.867	2.017	169.93
N7	O2	2.878	2.039	164.82
N8	O3	2.951	2.152	154.34
N9	O4	2.931	2.134	153.85
N10	O5	2.884	2.030	171.59

The average torsional angles of θ_1 are close to 0, and θ_2 and ψ attain an angle close to 180°. The average torsion angles of the dγLeu acids ϕ, θ_1, θ_2, and ψ were found to be -85.26°±12°, ±12.61°±8°, ±176.51°±2.24°, and ±1746.94°±2°, respectively. The sign remains uniform for the torsion variables ϕ and θ_1, but it varies in the case of the fully extended θ_2 and ψ. All the torsions variables are tabulated in Figure 9D. Overall, **P4** adopted a right-handed double helical structure.

The peptide proceeded to self-assemble by utilizing the exposed Boc-amide NH and the CO groups attached to the C-terminal pyrene. Within a single double helical unit, the two Boc-amide NHs established hydrogen bonds with the penultimate CO group of two other double helices, resulting in the formation of a continuous assembly of a double helical structure. The self-assembly is schematically depicted below.

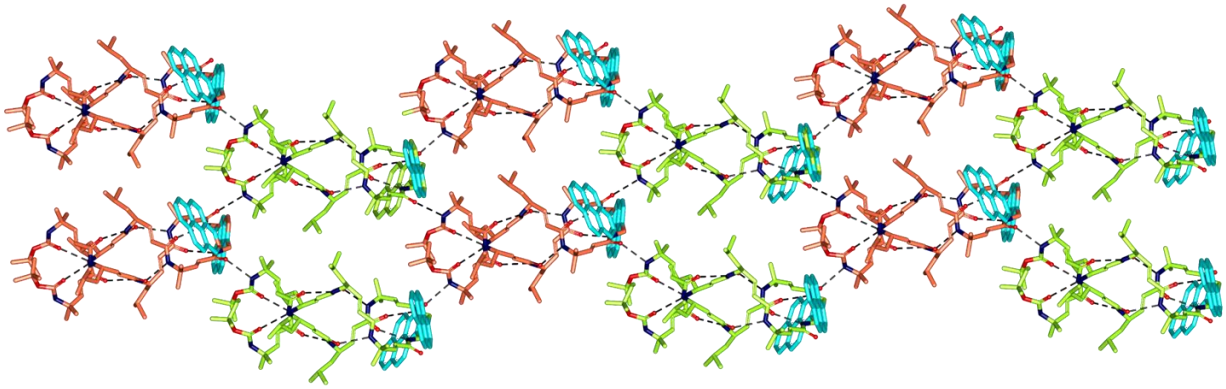
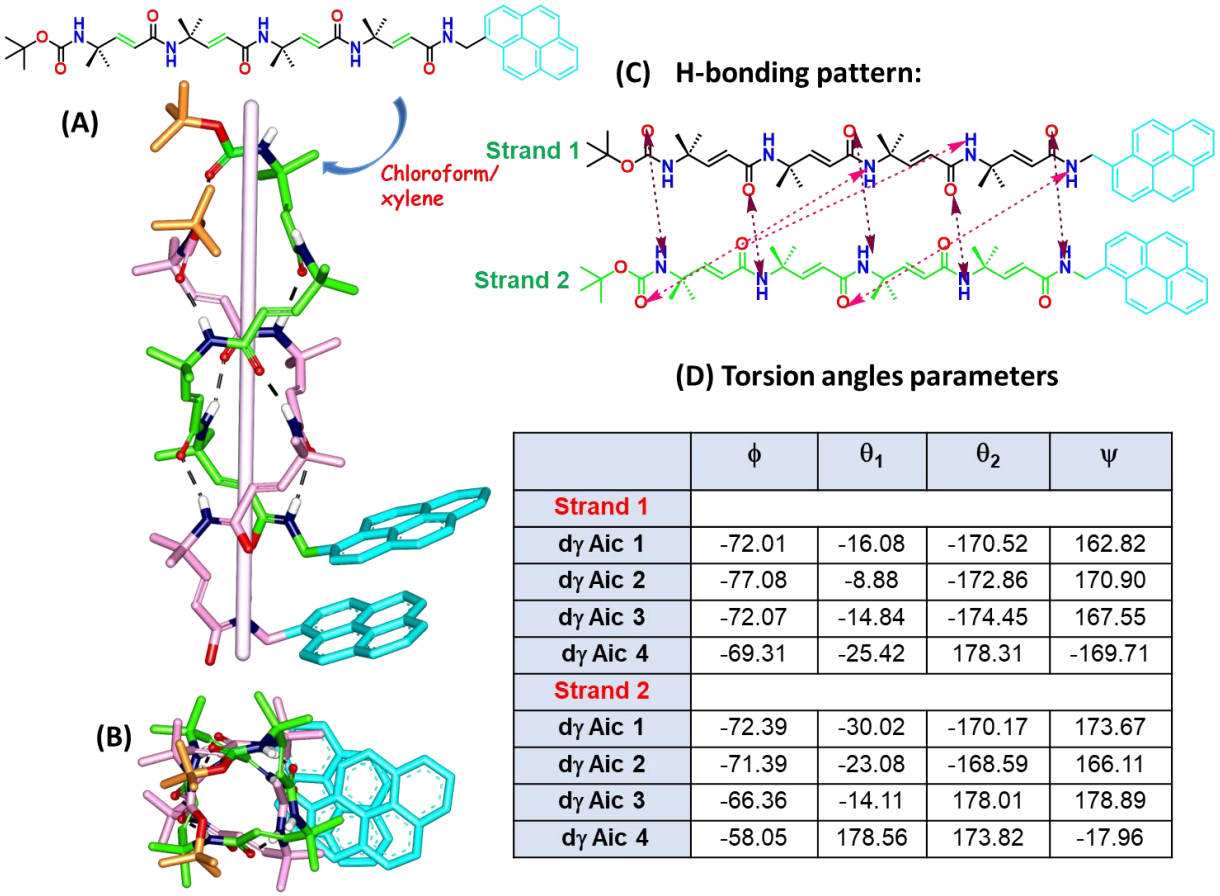


Figure 10: The continuous self-assembly of peptide **P4**

4.3.5. Crystal Structure of Peptide P5

We got diffraction quality crystals for **P5** from the slow evaporation of chloroform/toluene mixture and solved them in a triclinic crystal system with space group *P*-1. The X-ray structure is depicted in Figure 11A and peptide **P5** adopted a parallel β-double helical structure. Here, we have seen that one γ-peptide strand lags behind the other, and the spatially proximate pyrenyl moieties at the C-terminus of the double helix are stabilized by π–π interactions. Due to this the hydrogen bonding pattern also differs from what we observed in our earlier structure. The structure is stabilized by eight independent interstrand H-bonds. Specifically, the amide CO group in residue *i* of strand 1 participates in a hydrogen bond with the amide NH group of residue *i*+1 in strand 2 (*i*→*i*+1). Additionally, the amide CO group of residue *i* in strand 2 engages in a hydrogen bond with the amide NH group of residue *i*+3 in strand 1.



(D) Torsion angles parameters

	ϕ	θ_1	θ_2	ψ
Strand 1				
dγ Aic 1	-72.01	-16.08	-170.52	162.82
dγ Aic 2	-77.08	-8.88	-172.86	170.90
dγ Aic 3	-72.07	-14.84	-174.45	167.55
dγ Aic 4	-69.31	-25.42	178.31	-169.71
Strand 2				
dγ Aic 1	-72.39	-30.02	-170.17	173.67
dγ Aic 2	-71.39	-23.08	-168.59	166.11
dγ Aic 3	-66.36	-14.11	178.01	178.89
dγ Aic 4	-58.05	178.56	173.82	-17.96

Figure 11: (A) Single crystal structure of **P5.** An imaginary rod is inserted along the crystal axis for a better view of the double-helical structure. (B) Top view of the **P5.** (C) Hydrogen bonding pattern observed in **P5.** (D) Torsion angle parameters of strand 1 and strand 2 of **P5**.

This arrangement results in a distinctive pattern of hydrogen bonds within the structure. Notably, two N-terminal amide NH groups of strand 1 and two C-terminal CO groups of strand 2 do not participate in interstrand hydrogen bonds. The configuration of intermolecular hydrogen bonds between strand 1 and strand 2 is illustrated in Figure 11C. The hydrogen bond parameters of the **P5** double helix are given in Table 4, and these observed parameters fall within the standard limits reported in the literature for hydrogen bonds.

The analysis of torsion angles indicated that achiral α,β-unsaturated 4,4-dimethyl γ-amino acids(dγAic) in strand 1 exhibited mean angles of approximately –72.61°±3° for ϕ, -16.84°±7° for θ_1, about ±174° ± 3° for θ_2, and approximately ±167.74°±3.56° for ψ. The average torsional angles of θ_1 are close to 0, and θ_2 and ψ attain an angle close to 180°. The average torsion angles

of the dγAic residues in strand 2 were found to be -67.04°±6.55°, ±22.4°±8°, ±172.64°±4.2°, and ±172.89°±6.42°, respectively for ϕ, θ_1, θ_2, and ψ. Nevertheless, in order to facilitate the positioning of the pyrene moieties atop each other through a sliding movement of one strand over the other along the double helical axis, the torsion angle θ_1 of the penultimate dγAic residue deviates from the typical value of almost 0°, instead taking a value of 178.56°. Similarly, for the same residue, the ψ value assumes an unusual value of almost 0° instead of the typical 180°. All the torsions variables are tabulated in Figure 11D. Overall, **P5** adopted a right-handed β-double helical structure.

Table 4: The H-bond parameters of the **P5** double helix.

Donor (D)	Acceptor (A)	D.... A (Å)	DH.... A (Å)	∡NH.... O (°)
N3	O8	2.826	1.983	166.73
N4	O9	2.809	2.006	162.61
N5	O10	2.937	2.097	165.53
N6	O2	2.918	2.002	160.62
N7	O3	2.833	1.978	172.69
N8	O4	2.808	1.956	171.27
N9	O5	2.871	2.033	164.88
N10	O6	2.974	2.130	167.48

As above we mentioned that the two N-terminal amide NH protons of strand 1 and two C-terminal CO groups of strand 2 do not participate in interstrand hydrogen bonds. However, they are involved in head-to-tail intermolecular hydrogen bonding with other β-double helices. This results in a linear self-assembly of the double helices along the c-axis. Additionally, the self-assembly progresses in parallel through CHπ…CHπ interactions. A visual representation of the self-assembly is provided in Figure 12.

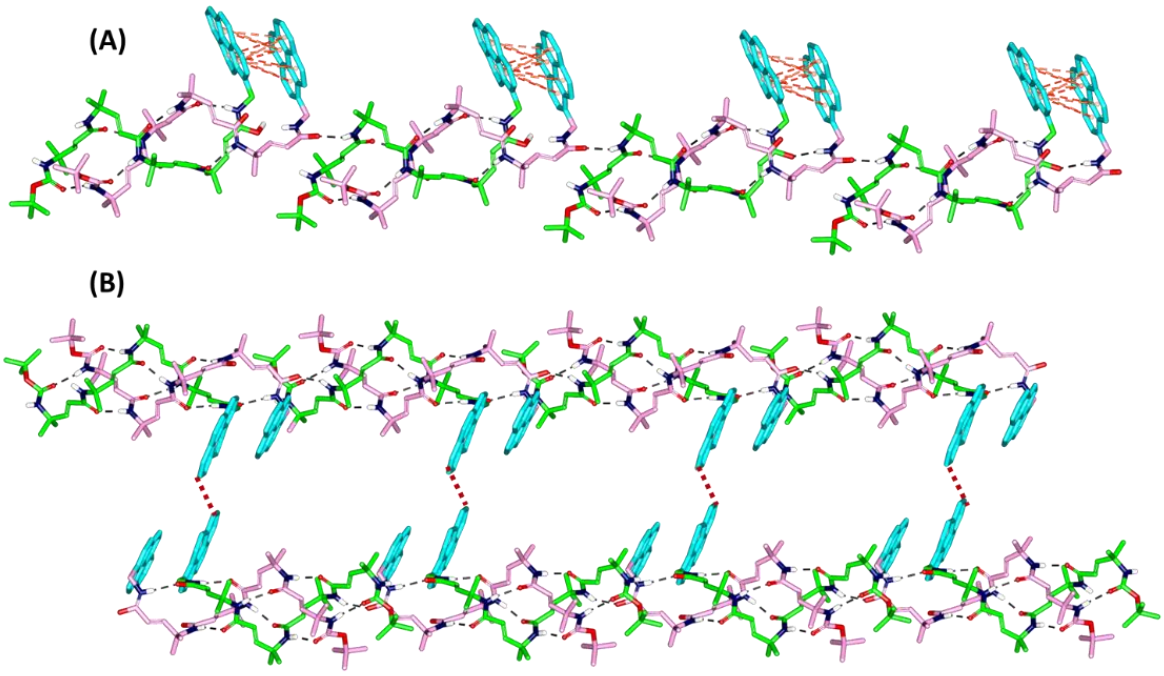


Figure 12: (A) Linear self-assembly of the double helix of **P5**. (B) The lateral self-assembly of the double helices of **P5**.

The cases of **P4** and **P5,** compared to **P1** and **P3** demonstrate that different amino acid sequences lead to distinct supramolecular structures. Even though all peptides exhibit a double helical conformation, the specific arrangement of amino acids within that double helix influences the overall structure and assembly. In summary, the sequence of amino acids here serves as a critical determinant in the formation of supramolecular porous network structure. Changes in this sequence lead to variations in the overall structure and properties of the self-assembled system, highlighting the intricate relationship between molecular structure and function in the realm of supramolecular chemistry.

4.3.6. Thermal Properties of Peptide P1 and P3

In addition to their structural attributes, these highly ordered porous peptide frameworks (PPFs) exhibited good thermal resilience, maintaining their stability even under heating conditions of up to 200 °C as demonstrated by thermogravimetric analysis (TGA). The respective TGA plots are shown in Figure 13. The remarkable thermal durability observed in these Highly Ordered Aromatic

Frameworks (HOAFs) can be attributed to robust intralayer π-π interactions and the presence of numerous interlayer hydrogen bonds.

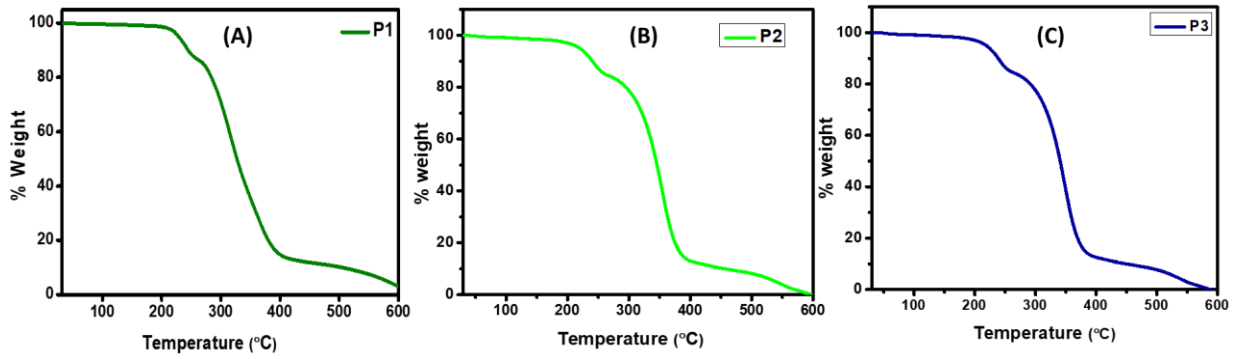


Figure 13: TGA plot for the peptide (A) **P1** (B) **P2** and (C) **P3**

4.3.7. Optical Properties of P1

The optical characteristics of **P1** were further assessed through UV-Vis absorption spectra, luminescence spectroscopy, and time-resolved luminescence lifetime in both solid and solution states. In a chloroform solution with varying concentrations, the UV-Vis spectra displayed a peak with the maximum wavelength at approximately 346 nm (as depicted in Figure 14A). The fluorescence emission of **P1** was recorded at different concentrations (as shown in Figure 14B). Just as observed in the crystal structure, where we observed pyrene-pyrene aromatic stacking, we also detected excimer fluorescence in the solution. This excimer fluorescence peak was centered around ~460 nm and coexisted with monomeric emission falling in the range of 350-400 nm. Notably, the excimer peak remained detectable even at very low concentrations, as low as 1 μM. This persistence suggests the structural integrity of the double helix in the solution. Furthermore, the solvent-dependent fluorescence spectra revealed that there was no shift in the maximum emission wavelength. This indirectly supports the formation of excimer complexes in the solution. The formation of excimers in the solution is significantly influenced by the polarity of the environment. The absence of an excimer peak in polar protic solvents such as MeOH and DMF indicates a potential disruption in the structural integrity of the double-helical framework. Conversely, an increase in the excimer intensity is observed in aromatic solvents, suggesting enhanced stabilization of excimer formation in these environments. Furthermore, we conducted temperature-dependent fluorescence spectra in tetrachloroethane solvent, and the results are presented in Figure 14D. As the temperature is raised from 283 K to 393 K, there is a gradual

reduction in excimer intensity. This decrease implies that the double helical assembly becomes less stable with increasing temperature.

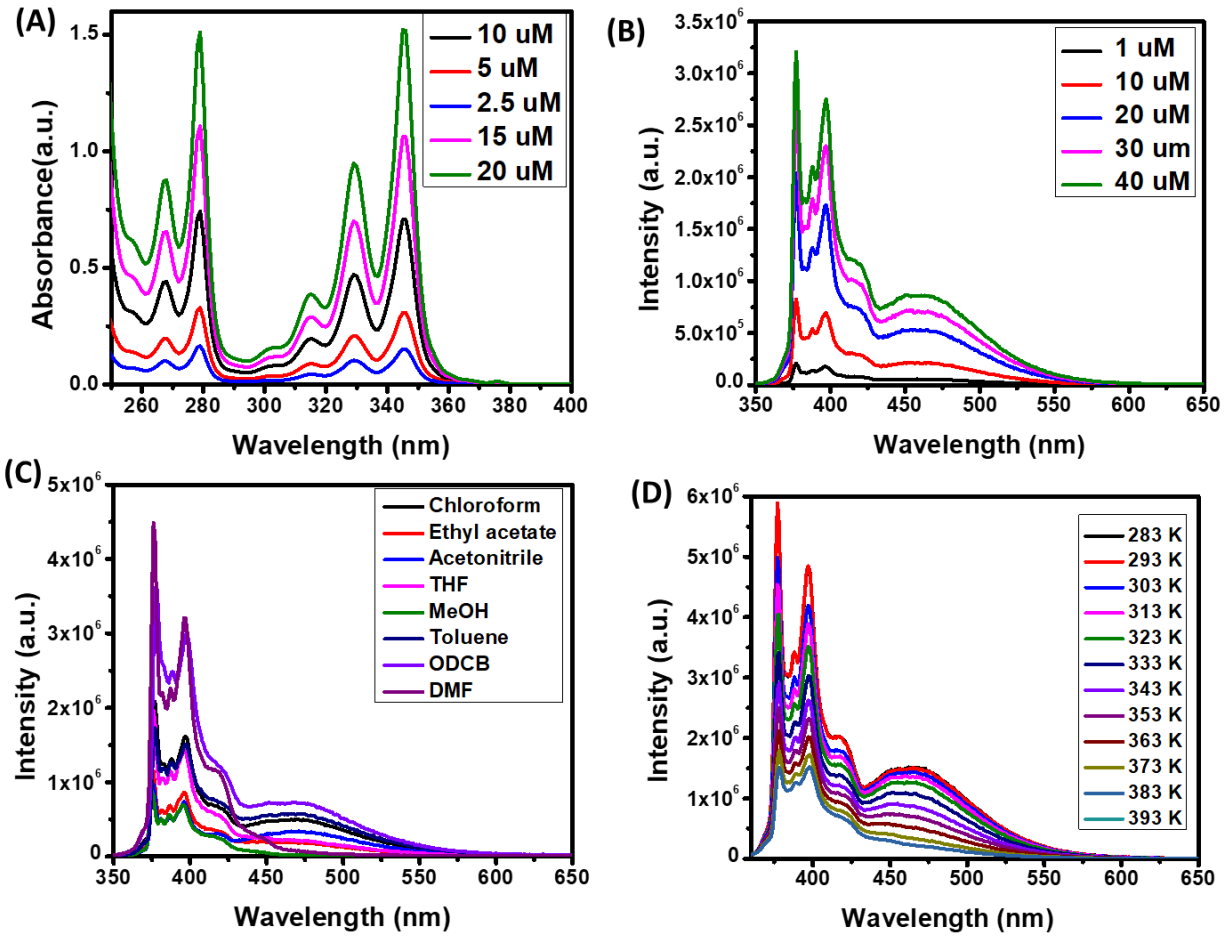


Figure 14: (A) The concentration-dependent UV-Vis spectra of **P1.** (B) The concentration-dependent fluorescence spectra. (C) Fluorescence spectra of **P1** in various solvents. (D) Fluorescence spectra of **P1** with variable temperature. The excitation wavelength is 345 nm.

In the solid-state photoluminescence (PL) emission, only the excimer peak is observed, leading to the solid emitting a cyan color, as depicted in Figure 15C. Additionally, the emission color in the solution is concentration-dependent. With increasing concentration, the faint blue color transitions to cyan, which further indicates excimer formation at higher concentrations. The peptide **P1** shows a relatively high absolute quantum yield of 24%. The fluorescence lifetime plot for the monomeric emission at 397 nm in chloroform displayed a triexponential decay with an average lifetime of 18.52 ns and that for excimer emission at 453 nm displayed also a triexponential decay with an average lifetime of 22.53 ns. The solid-state decay profile at 453 nm also follows a triexponential

decay with an average lifetime of 44.74 ns suggested in solid state due to proper framework structure the π-π stacking maximizes to give excimer emission.

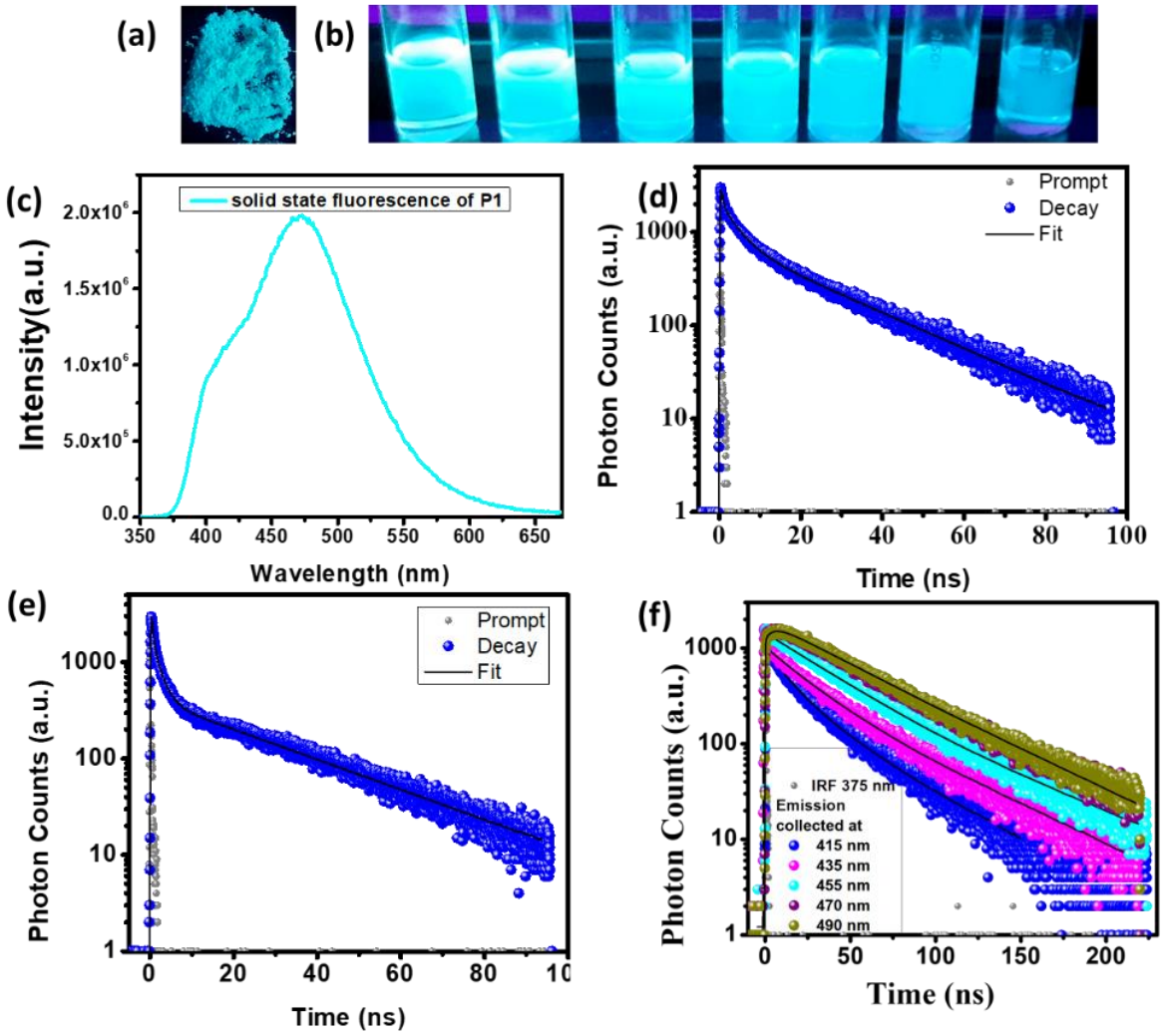


Figure 15: (A) Color of **P1** powder (B) Variable concentration color of **P1** under UV light. (C) Solid state PL spectra (D) Lifetime decay profile in solution for monomer collected at 397 nm. (E) Lifetime decay profile collected in solution at 455 nm. (F) Solid state lifetime decay profile of the excimer collected at variable excimer wavelengths.

4.3.8. Chiroptical Properties of Peptides P1 and P2

Since the peptides are inherently chiral, the chiroptical properties were further explored. The ground state chirality of the peptides **P1** and **P2** is analyzed using CD spectroscopy. The CD spectra in chloroform show a positive cotton effect for P1 at λ_{max} ~242 nm and **P2** which is the enantiomer of **P1** shows the opposite signal with a negative cotton effect at λ_{min} ~242 nm. The CD

spectra resemble our previous double helical CD spectra. As our peptides were CD active and there was a luminescent chromophore present, so we further looked for their excited state chiral properties through CPL spectroscopy. Interestingly clear mirror image CPL signal with a positive sign for **P1** and a negative sign for **P2** is observed upon excitation at 350 nm. The broad CPL signal arises at 478 nm which resembles the fluorescence emission of the pyrene excimer. Through the CPL study, it is evident that the chirality of the backbone transferred through pyrene chromophore due to excimer formation from pyrene-pyrene stacking interaction. The extent of chiral dissymmetry is quantified through the anisotropic factor (g_{lum}) which is given by $g_{lum} = 2(I_L - I_R)/ (I_L + I_R)$, where I_L and I_R are the left and right circularly polarized light intensities respectively.

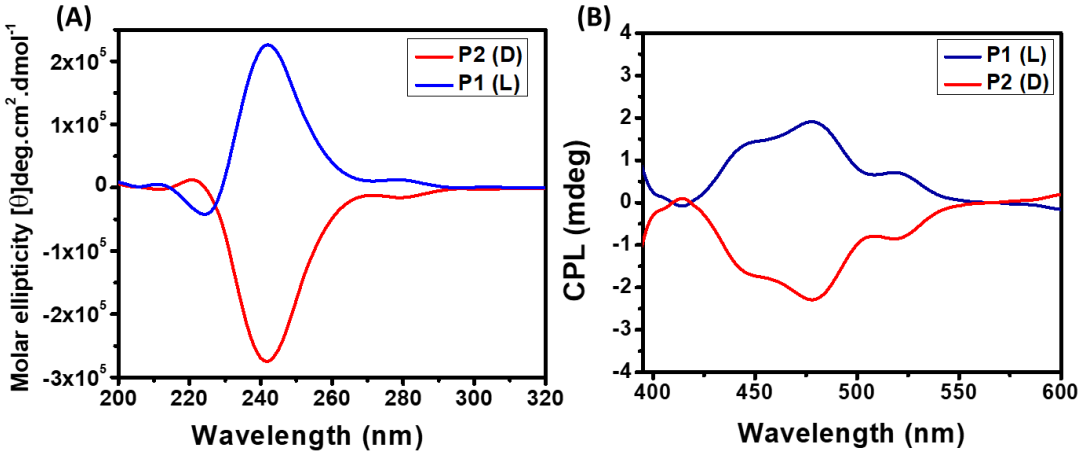


Figure 16: (A) CD spectra of P1(blue traces) and **P2** (red traces) and (B) CPL Spectra of Peptide of P1(blue traces) and **P2** (red traces)

The g_{lum} values for **P1** and **P2** are $+8.0 \times 10^{-3}$ and -8.3×10^{-3} at 478 nm which is well within the range of what has been reported for organic molecules.

4.4. Conclusion

In summary, the pyrene-appended peptides exhibit a sophisticated structural organization characterized by a β-double helical arrangement capable of accommodating substantial pyrenyl moieties. This structural motif undergoes hierarchical self-assembly, where the double helical units come together through a combination of hydrogen bonding, π-π stacking, and CHπ-CHπ

interactions. This multi-step self-assembly process results in the formation of a two-dimensional assembly of supramolecular macrocycles, primarily driven by hydrogen bonding, and a supramolecular channel-like architecture, predominantly influenced by π-π stacking and CHπ-CHπ interactions. The two-dimensional assembly of supramolecular macrocycles represents a significant structural feature arising from the hydrogen bonding interactions, contributing to the overall stability and organization of the system. Simultaneously, the supramolecular channels, formed through π-π stacking and CHπ-CHπ interactions, provide an additional layer of complexity by creating a framework with distinct nanoscale architectures. These supramolecular channels further self-assemble through hydrogen bonding interactions, culminating in the development of a crystalline porous framework. The porous nature of this framework holds considerable promise for various applications due to its ability to facilitate molecular interactions and selective binding. This aspect makes the structure well-suited for applications in chiral separation, catalysis, and sensing. The absence of additional covalent or noncovalent associations highlights the robustness of the π structure, underscoring the crucial role played by π-π stacking interactions in fortifying peptide-based porous supramolecular frameworks. This observation serves as compelling evidence of the significance of π-π stacking in providing structural integrity and stability to such systems. Furthermore, the framework exhibits a remarkable circularly polarized luminescence property with a chiroptical switch. This unique optical characteristic adds an extra dimension to the potential applications of the structure, making it particularly intriguing for advanced optical and sensing applications. In conclusion, the described pyrene-appended peptide framework, with its intricate hierarchical self-assembly and diverse supramolecular interactions, holds great promise for applications ranging from molecular separations to advanced optical technologies.

4.5. Experimental Section

4.5.1 Materials and Methods

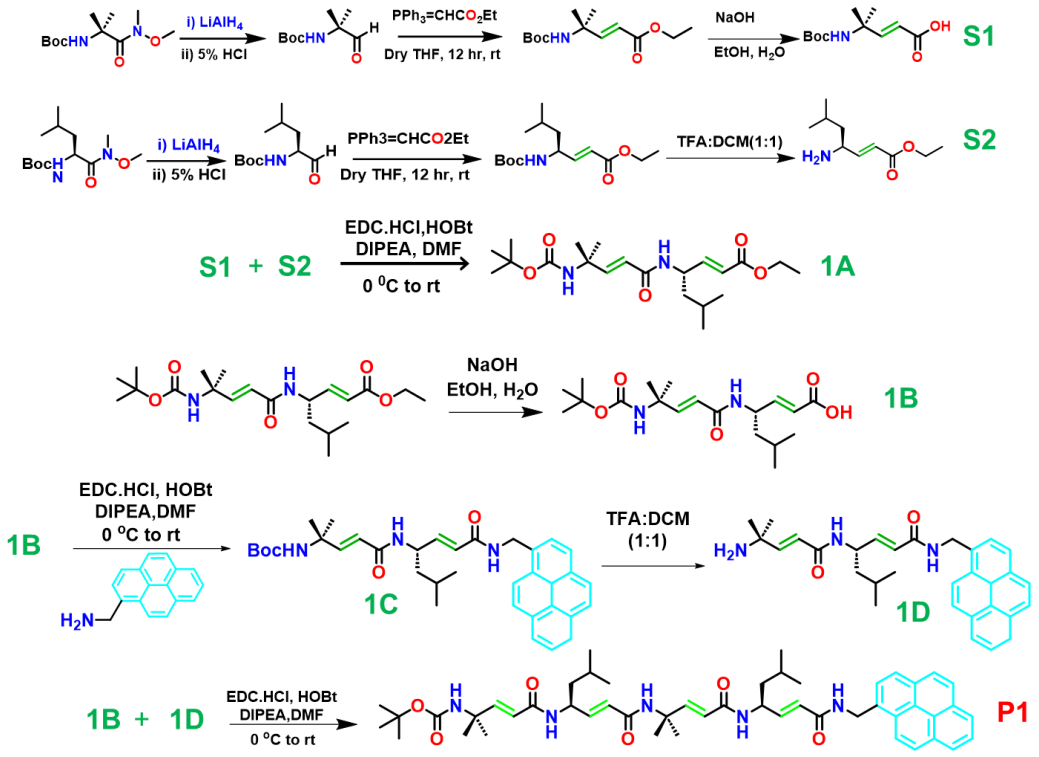
All reagents and solvents were used without further purification. Column chromatography was performed over silica gel. Final peptides were purified through reverse phase HPLC (C_{18} column, MeOH/H_2O 95:5 as a gradient with flow rate 2.00 mL/min). All the reactions were monitored by analytical thin-layered chromatography. The TLC visualization was done through UV light, $KMNO_4$ stain, and ninhydrin stain. ^1H NMR and ^{13}C NMR were performed through deuterated solvent on 400 MHz and 101 MHz respectively. We used a Matrix Assisted LASER Desorption

Ionization mass spectrometer (MALDI-TOF/TOF) to calculate the accurate mass of our peptides. Fluorescence data was measured through the Spectrofluorometer instrument. X-ray crystal structures were determined through APEX(III) DUO X-ray diffractometer using Mo-Kα (λ=0.71073 Å) graphite monochromatic radiation.

4.5.2 Synthesis Procedures for the Peptides

4.5.2.1. Synthesis of the Peptide P1

The schematic illustration depicting the synthesis process of peptide **P1** is presented below:



Scheme 3: Synthesis of peptide **P1**

Boc-dγAic-OEt and Boc-dγLeu(L)-OEt were synthesized following the protocol reported earlier. **1A** and **1B** were synthesized following the procedure described in Chapter 2. Boc-dγAic-dγLeu-OH (**1B**) weighing 846.4 mg (2.3 mmol) was dissolved in 5 mL of DMF and cooled to 0 °C under a nitrogen atmosphere. EDC.HCl (490 mg, 2.53 mmol), HOBt (310 mg, 2.3 mmol), and DIPEA (1.6 mL, 9.2 mmol) were then added to the reaction mixture, which was stirred for 10 minutes. Following this, pyrene-1-methyl amine (615 mg, 2.3 mmol) was introduced and the reaction was stirred overnight. TLC was employed to monitor the reaction progress. Upon completion, the

reaction mixture was diluted with 150 mL of ethyl acetate and subjected to washing with 10% HCl (75 mL × 2), 10% sodium carbonate solution (75 mL × 2), and brine solution (75 mL × 2). The organic layer was dried using anhydrous sodium sulfate (Na_2SO_4) and concentrated under reduced pressure, resulting in a crude powder. This material was then purified by column chromatography, yielding a white crystalline product, **1C**, with a yield of 82%.

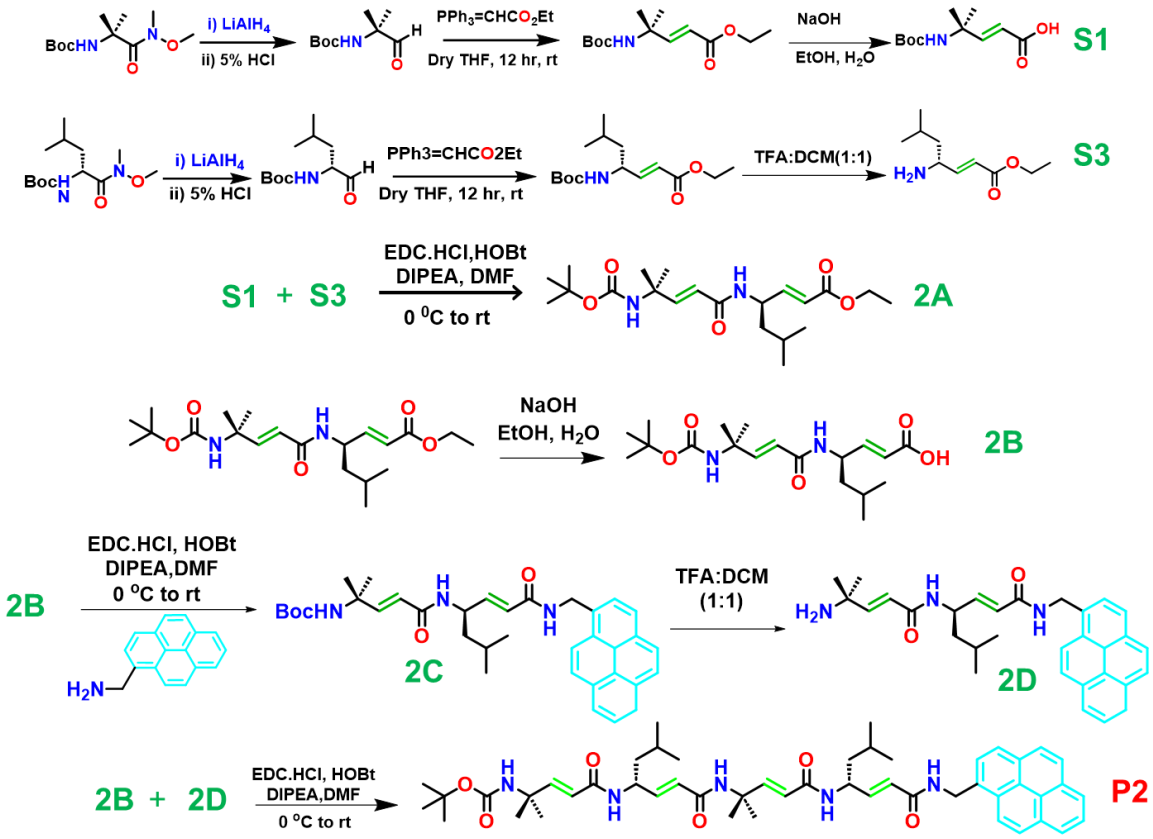
The Boc group of **1C** (1.2 mmol 0.7 g) was deprotected by using 1.5 mL 1:1 TFA: DCM for 1h. Subsequently, trifluoroacetic acid (TFA) and dichloromethane (DCM) solvent were evaporated, and 5-6 additional cycles of adding DCM followed by evaporation were performed to eliminate any remaining traces of TFA. The resulting crude material constituted the trifluoroacetic acid (TFA) salt of the amine of **1C** and to this 0.5 mL of DMF and 0.5 ml, of DIPEA were added to make it free amine **1D**. The compound **1B** (0.44 g, 1.2 mmol) was dissolved in 3 mL of DMF and cooled to 0 °C under a nitrogen atmosphere. Following this, EDC.HCl (253 mg, 1.32 mmol), HOBt (162 mg, 1.2 mmol), and DIPEA (0.625 mL, 3.6 mmol) were added to the reaction mixture, and the stirring continued for 10 minutes. Subsequently, compound **1D** was added, and the reaction proceeded overnight, with TLC used to monitor the progress. After the reaction reached completion, the mixture was diluted with 125 mL of ethyl acetate and subjected to washing with 10% HCl (75 mL × 2), 10% Na_2CO_3 solution (75 mL × 2), and brine solution (75 mL × 2). The organic layer was dried using anhydrous Na_2SO_4 and concentrated under reduced pressure, resulting in a crude powder. The crude material was then purified through column chromatography, yielding the white crystalline product, **P1**, with a 59% yield.

4.5.2.2. Synthesis of the Peptide P2

Boc-dγAic-OEt and Boc-dγLeu(D)-OEt were synthesized following the protocol reported earlier. **2A** and **2B** were synthesized following the procedure described in Chapter 2. Boc-dγAic-dγLeu(D)-OH (**2B**) weighing 846.4 mg (2.3 mmol) was dissolved in 5 mL of DMF and cooled to 0 °C under a nitrogen atmosphere. EDC.HCl (490 mg, 2.53 mmol), HOBt (310 mg, 2.3 mmol), and DIPEA (1.6 mL, 9.2 mmol) were then added to the reaction mixture, which was stirred for 10 minutes. Following this, pyrene-1-methyl amine (615 mg, 2.3 mmol) was introduced and the reaction was stirred overnight. TLC was employed to monitor the reaction progress. Upon completion, the reaction mixture was diluted with 150 mL of ethyl acetate and subjected to washing with 10% HCl (75 mL × 2), 10% sodium carbonate solution (75 mL × 2), and brine

solution (75 mL × 2). The organic layer was dried using anhydrous sodium sulfate (Na_2SO_4) and concentrated under reduced pressure, resulting in a crude powder. This material was then purified by column chromatography, yielding a white crystalline product, **2C**, with a yield of 82%.

The schematic illustration depicting the synthesis process of peptide **P2** is presented below:



Scheme 4: Synthesis of peptide **P2**

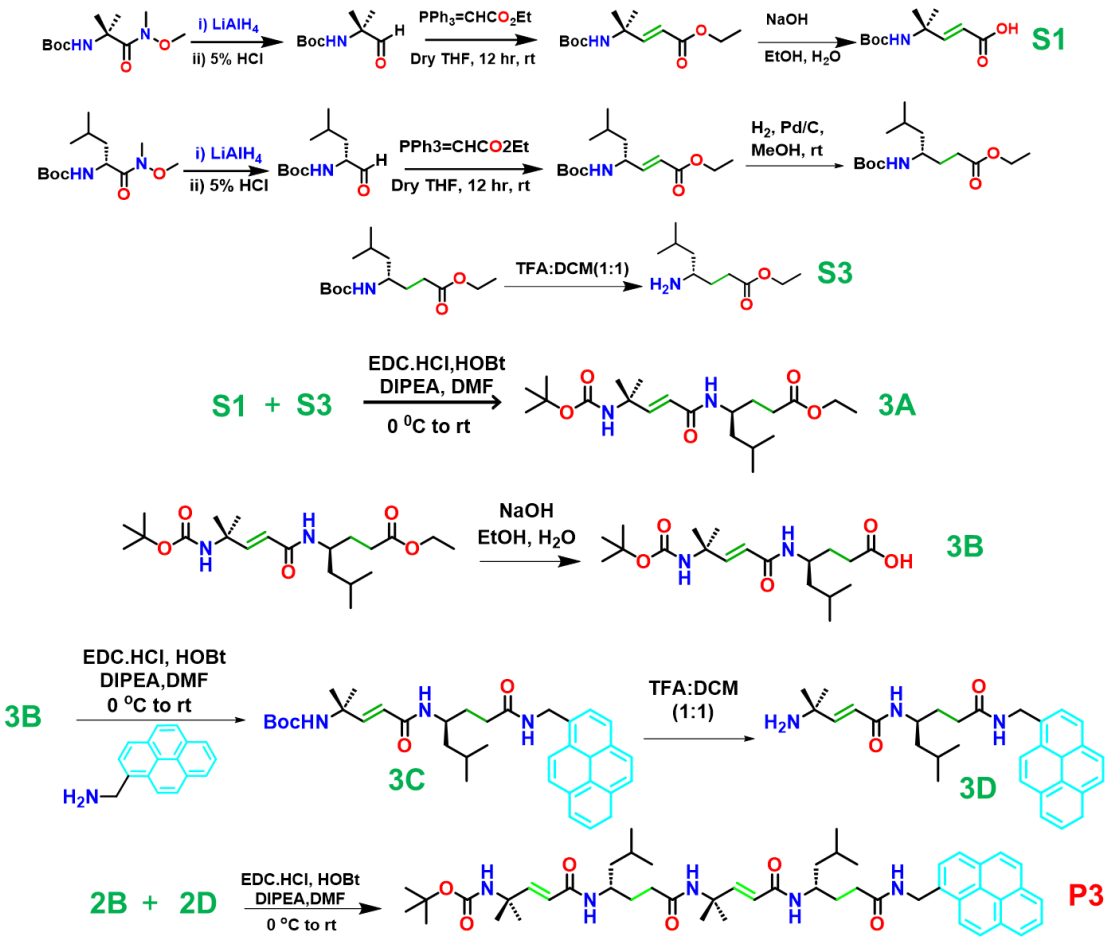
The Boc group of **2C** (1.2 mmol 0.7 g) was deprotected by using 1.5 mL 1:1 TFA: DCM for 1h. Subsequently, trifluoroacetic acid (TFA) and dichloromethane (DCM) solvent were evaporated, and 5-6 additional cycles of adding DCM followed by evaporation were performed to eliminate any remaining traces of TFA. The resulting crude material constituted the trifluoroacetic acid (TFA) salt of the amine of **2C** and to this 0.5 mL of DMF and 0.5 mL, of DIPEA were added to make it free amine **2D.** The compound **2B** (0.44 g, 1.2 mmol) was dissolved in 3 mL of DMF and cooled to 0 °C under a nitrogen atmosphere. Following this, EDC.HCl (253 mg, 1.32 mmol), HOBt (162 mg, 1.2 mmol), and DIPEA (0.625 mL, 3.6 mmol) were added to the reaction mixture, and the stirring continued for 10 minutes. Subsequently, compound **2D** was added, and the reaction

proceeded overnight, with TLC used to monitor the progress. After the reaction reached completion, the mixture was diluted with 125 mL of ethyl acetate and subjected to washing with 10% HCl (75 mL × 2), 10% Na_2CO_3 solution (75 mL × 2), and brine solution (75 mL × 2). The organic layer was dried using anhydrous Na_2SO_4 and concentrated under reduced pressure, resulting in a crude powder. The crude material was then purified through column chromatography, yielding the white crystalline product, **P2**, with a 59% yield.

4.5.2.3. Synthesis of the Peptide P3

Boc-dγAic-OEt and Boc-γLeu(D)-OEt were prepared using the previously documented procedure. The synthesis of **3A** and **3B** adhered to the methodology outlined in Chapter 3. Boc-dγAic-γLeu(D)-OH (**3B**) weighing 846 mg (2.3 mmol) was dissolved in 5 mL of DMF and cooled to 0 ℃ under a nitrogen atmosphere. EDC.HCl (490 mg, 2.53 mmol), HOBt (310 mg, 2.3 mmol), and DIPEA (1.6 mL, 9.2 mmol) were then added to the reaction mixture, which was stirred for 10 minutes. Following this, pyrene-1-methyl amine (615 mg, 2.3 mmol) was introduced and the reaction was stirred overnight. TLC was employed to monitor the reaction progress. Upon completion, the reaction mixture was diluted with 150 mL of ethyl acetate and subjected to washing with 10% HCl (75 mL × 2), 10% sodium carbonate solution (75 mL × 2), and brine solution (75 mL × 2). The organic layer was dried using anhydrous sodium sulfate (Na_2SO_4) and concentrated under reduced pressure, resulting in a crude powder. This material was then purified by column chromatography, yielding a white crystalline product, **3C**, with a yield of 80%.

The Boc group of **3C** (1.25 mmol, 0.7 g**)** was deprotected by using 1.5 mL 1:1 TFA: DCM for 1h. Subsequently, trifluoroacetic acid (TFA) and dichloromethane (DCM) solvent were evaporated, and 5-6 additional cycles of adding DCM followed by evaporation were performed to eliminate any remaining traces of TFA. The resulting crude material constituted the trifluoroacetic acid (TFA) salt of the amine of **3C** and to this 0.5 mL of DMF and 0.5 mL, of DIPEA were added to make it free amine **3D.** The compound **3B** (0.44 g, 1.2 mmol) was dissolved in 3 mL of DMF and cooled to 0 °C under a nitrogen atmosphere. Following this, EDC.HCl (253 mg, 1.32 mmol), HOBt (162 mg, 1.2 mmol), and DIPEA (0.625 mL, 3.6 mmol) were added to the reaction mixture, and the stirring continued for 10 minutes. Subsequently, compound **3D** was added, and the reaction proceeded overnight, with TLC used to monitor the progress. After the reaction reached completion, the mixture was diluted with 125 mL of ethyl acetate and subjected to washing with



Scheme 5: Synthesis of peptide **P3**

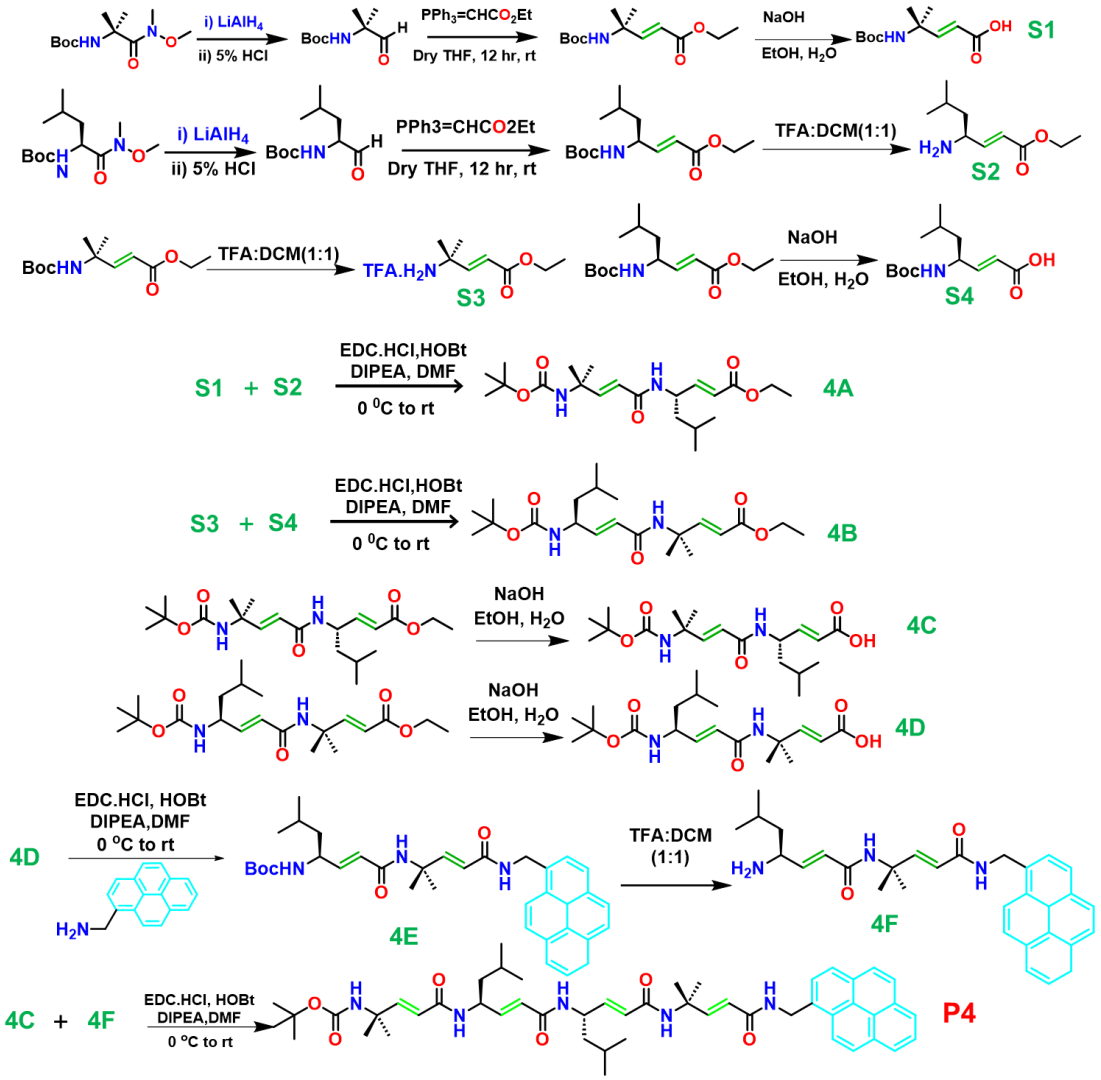
10% HCl (75 mL × 2), 10% Na_2CO_3 solution (75 mL × 2), and brine solution (75 mL × 2). The organic layer was dried using anhydrous Na_2SO_4 and concentrated under reduced pressure, resulting in a crude powder. The crude material was then purified through column chromatography, yielding the white crystalline product, **P3**, with a 65% yield.

4.5.2.4. Synthesis of the Peptide P4

Boc-dγAic-OEt and Boc-dγLeu(L)-OEt were synthesized following the protocol reported earlier. **4A, 4B, 4C,** and **4D** were synthesized following the procedure described in Chapter 2 and Chapter 3. Boc-dγAic-dγLeu(D)-OH (**4B**) weighing 846 mg (2.3 mmol) was dissolved in 5 mL of DMF and cooled to 0 °C under a nitrogen atmosphere. EDC.HCl (490 mg, 2.53 mmol), HOBt (310 mg, 2.3 mmol), and DIPEA (1.6 mL, 9.2 mmol) were then added to the reaction mixture, which was

stirred for 10 minutes. Following this, pyrene-1-methyl amine (615 mg, 2.3 mmol) was introduced and the reaction was stirred overnight.

The schematic illustration depicting the synthesis process of peptide **P4** is presented below:



Scheme 6: Synthesis of peptide **P4**

TLC was employed to monitor the reaction progress. Upon completion, the reaction mixture was diluted with 150 mL of ethyl acetate and subjected to washing with 10% HCl (75 mL × 2), 10% sodium carbonate solution (75 mL × 2), and brine solution (75 mL × 2). The organic layer was dried using anhydrous sodium sulfate (Na_2SO_4) and concentrated under reduced pressure, resulting in a crude powder. This material was then purified by column chromatography, yielding a white crystalline product, **4E**, with a yield of 79%.

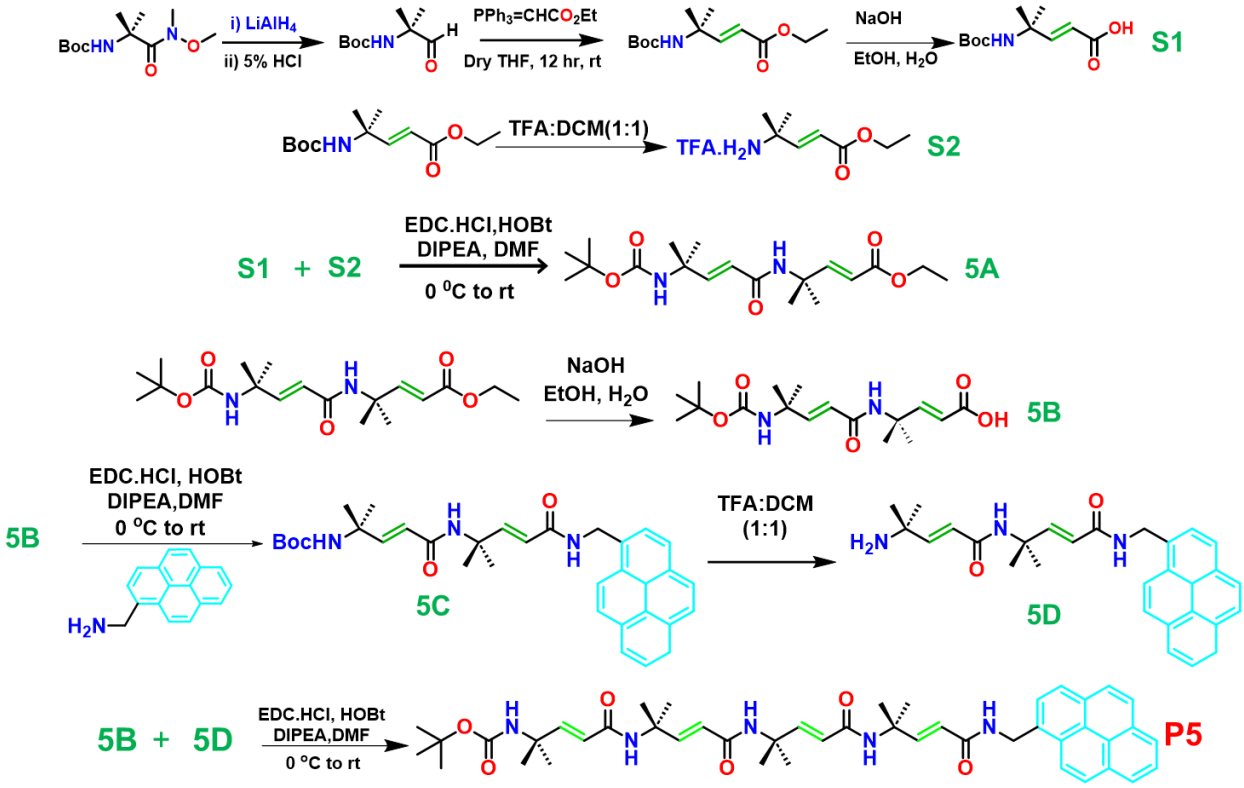
The Boc group of **4E** (1.25 mmol, 0.7 g**)** was deprotected by using 1.5 mL 1:1 TFA: DCM for 1h. Subsequently, trifluoroacetic acid (TFA) and dichloromethane (DCM) solvent were evaporated, and 5-6 additional cycles of adding DCM followed by evaporation were performed to eliminate any remaining traces of TFA. The resulting crude material constituted the trifluoroacetic acid (TFA) salt of the amine of **4E**. To this 0.5 mL of DMF and 0.5 mL, of DIPEA were added to make it free of amine **4F.** The compound **4D** (0.44 g, 1.2 mmol) was dissolved in 3 mL of DMF and cooled to 0 °C under a nitrogen atmosphere. Following this, EDC.HCl (253 mg, 1.32 mmol), HOBt (162 mg, 1.2 mmol), and DIPEA (0.625 mL, 3.6 mmol) were added to the reaction mixture, and the stirring continued for 10 minutes. Subsequently, compound **4F** was added, and the reaction proceeded overnight, with TLC used to monitor the progress. After the reaction reached completion, the mixture was diluted with 125 mL of ethyl acetate and subjected to washing with 10% HCl (75 mL × 2), 10% Na_2CO_3 solution (75 mL × 2), and brine solution (75 mL × 2). The organic layer was dried using anhydrous Na_2SO_4 and concentrated under reduced pressure, resulting in a crude powder. The crude material was then purified through column chromatography, yielding the white crystalline product, **P4**, with a 62% yield.

4.5.2.5. Synthesis of the Peptide P5

Boc-dγAic-OEt was synthesized following the protocol reported earlier. For the coupling reaction, Boc-dγAic-OH (6.5 mmol, 1.49 g) and TFA·H2N-dγAic-OEt (6.5 mmol, 1.05 g) were combined in DMF (6 mL). EDC.HCl (7.205 mmol, 1.38 g) and HOBt (6.5 mmol, 880 mg) were added to the solution. The reaction mixture was allowed to cool at 0 °C for 5 minutes, and then DIPEA (19.65 mmol, 3.52 mL) was introduced while stirring. The reaction proceeded at room temperature, and TLC was employed to monitor its progress. After completion of the reaction (approximately 24 hours), the mixture was diluted with 250 mL of ethyl acetate and subjected to washing with 10% HCl (3 × 80 mL), 10% Na_2CO_3 solution in water (3 × 80 mL), and brine (3 × 100 mL). The organic layer was dried over Na_2SO_4 and evaporated under reduced pressure. The crude product underwent purification via silica gel column chromatography using an Ethyl acetate/Hexane solvent system. The overall yield of **5A** was 72% (4.68 mmol, 1.72 g).

An amount of 1.1 g **5A** (3 mmol) was dissolved in 30 mL of ethanol, and a 10 mL portion of 1N NaOH was gradually added dropwise to the solution over a period of 3 minutes. The reaction mixture was then stirred for 30 minutes until the hydrolysis process reached completion.

The schematic illustration depicting the synthesis process of peptide **P5** is presented below:



Scheme 7: Synthesis of peptide **P5**

Subsequently, the reaction mixture was acidified using 1N aqueous HCl solution and then subjected to extraction with ethyl acetate. The organic layer underwent washing with a brine solution (3 × 100 mL) and was dehydrated using anhydrous sodium sulfate (Na_2SO_4). The combined organic layer, containing the hydrolyzed product **5B**, was concentrated under vacuum and further employed for coupling.

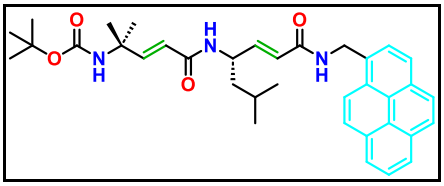
Boc-dγAic-dγAic-OH (**3B**) weighing 782 mg (2.3 mmol) was dissolved in 5 mL of DMF, which was then cooled to 0 °C under a nitrogen atmosphere. EDC.HCl (490 mg, 2.53 mmol), HOBt (310 mg, 2.3 mmol), and DIPEA (1.6 mL, 9.2 mmol) were subsequently added, and the reaction mixture was stirred for 10 minutes. Following this, pyrene-1-methyl amine (615 mg, 2.3 mmol) was introduced and left to stir overnight. The progression of the reaction was monitored through TLC. Upon completion, the reaction mixture was diluted with 180 mL of ethyl acetate and subjected to washing with 10% HCl (75 mL × 2), 10% Na_2CO_3 solution (75 mL × 2), and finally brine solution (75 mL × 2). The organic layer was then dried and dehydrated using anhydrous Na_2SO_4 and

concentrated under reduced pressure, resulting in a crude powder. Subsequently, the crude product underwent purification through column chromatography, yielding a white crystalline product, **5C**, with a notable yield of 82%.

The deprotection of **5C** (1.25 mmol, 0.94 g) involved the use of a mixture of 1.5 mL each of TFA and DCM (1:1) for a duration of 1 hour. Subsequently, the solvent DCM and TFA were evaporated, and the residue was treated with DCM multiple times to eliminate any remaining traces of TFA. The resulting crude material constituted the TFA-salt of the amine derived from **5C**. To convert it into the free amine, 0.5 mL each of DMF and DIPEA were added to the TFA-salt.

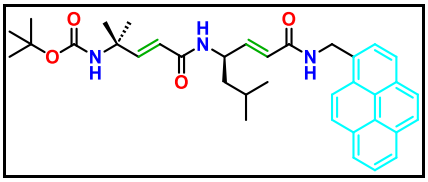
In parallel, the compound **5B** (0.77 g, 1.2 mmol) was dissolved in 3 mL of DMF and cooled to 0 °C under a nitrogen atmosphere. EDC.HCl (253 mg, 1.32 mmol), HOBt (162 mg, 1.2 mmol), and DIPEA (0.625 mL, 3.6 mmol) were introduced, and the reaction mixture was stirred for 10 minutes. Subsequently, compound **3D** was added, and the reaction continued overnight with TLC monitoring. Upon completion, the reaction mixture was diluted with 125 mL of ethyl acetate and subjected to washing with 10% HCl (75 mL × 2), 10% Na_2CO_3 solution (75 mL × 2), and brine solution (75 mL × 2). The organic layer was dried with anhydrous Na_2SO_4 and concentrated under reduced pressure, resulting in a crude powder. This material underwent purification through column chromatography, yielding the white crystalline product **P5** with a yield of 63%.

4.6. Characterization of Peptides P1-P5

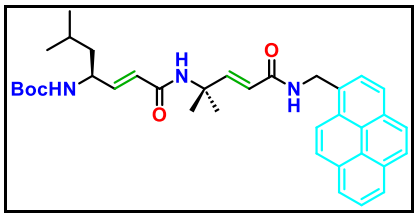


^{1}H NMR (400 MHz, Chloroform-*d*) δ 8.52 – 8.35 (m, 1H), 8.30 (d, *J* = 9.3 Hz, 1H), 8.14 (d, *J* = 7.6 Hz, 1H), 8.09 (dd, *J* = 7.7, 2.5 Hz, 2H), 8.07 – 8.01 (m, 2H), 7.98 (d, *J* = 17.2 Hz, 3H), 6.66 (ddd, *J* = 16.2, 9.9, 4.6 Hz, 1H), 6.54 (dd, *J* = 40.1, 10.2 Hz, 1H), 6.17 (d, *J* = 8.1 Hz, 1H), 5.72 – 5.56 (m, 1H), 5.37 (dd, *J* = 14.5, 6.5 Hz, 1H), 5.04 (d, *J* = 14.6 Hz, 1H), 4.83 (s, 1H), 4.49 (s, 1H), 1.41 (dt, *J* = 13.7, 6.8 Hz, 1H), 1.30 (d, *J* = 11.0 Hz, 9H), 1.19 (dd, *J* = 9.1, 5.8 Hz, 2H), 1.13 (d, *J* = 17.8 Hz, 3H), 0.85 (d, *J* = 19.8 Hz, 3H), 0.71 (td, *J* = 19.7, 19.0, 6.5 Hz, 6H). **^{13}C NMR** (101

MHz, Chloroform-d) δ 165.37, 165.09, 149.54, 144.13, 132.26, 131.23, 130.97, 130.64, 128.91, 127.86, 127.75, 127.43, 127.20, 125.90, 125.14, 125.05, 124.93, 124.86, 124.71, 123.64, 122.38, 52.63, 48.02, 43.76, 41.69, 28.35, 27.55, 25.80, 24.56, 22.68, 21.73. **MALDI TOF/TOF** m/z calculated value for $C_{36}H_{43}N_3O_4$[M+Na]$^+$ = 604.33 and observed [M+Na]$^+$ = 604.48

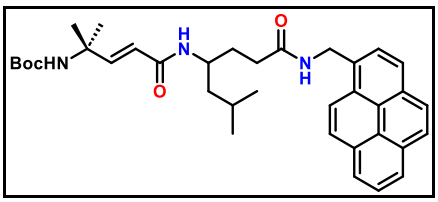


^{1}H NMR (400 MHz, Chloroform-*d*) δ 8.52 – 8.35 (m, 1H), 8.30 (d, *J* = 9.3 Hz, 1H), 8.15 – 7.87 (m, 9H), 6.66 (ddd, *J* = 16.2, 9.9, 4.6 Hz, 1H), 6.54 (dd, *J* = 40.1, 10.2 Hz, 1H), 6.17 (d, *J* = 8.1 Hz, 1H), 5.69 (dd, *J* = 15.3, 2.0 Hz, 1H), 5.37 (dd, *J* = 14.5, 6.5 Hz, 1H), 5.04 (d, *J* = 14.6 Hz, 1H), 4.83 (s, 1H), 4.49 (s, 1H), 1.41 (dt, *J* = 13.7, 6.8 Hz, 1H), 1.30 (d, *J* = 11.0 Hz, 9H), 1.19 (dd, *J* = 9.1, 5.8 Hz, 2H), 1.13 (d, *J* = 17.8 Hz, 3H), 0.85 (d, *J* = 19.8 Hz, 3H), 0.71 (td, *J* = 19.7, 19.0, 6.5 Hz, 6H). **^{13}C NMR** (101 MHz, Chloroform-*d*) δ 165.37, 165.09, 149.54, 144.13, 132.26, 131.23, 130.97, 130.64, 128.91, 127.86, 127.75, 127.43, 127.20, 125.90, 125.14, 125.05, 124.93, 124.86, 124.71, 123.64, 122.38, 52.63, 48.02, 43.76, 41.69, 28.35, 27.55, 25.80, 24.56, 22.68, 21.73. **MALDI TOF/TOF** m/z calculated value for $C_{36}H_{43}N_3O_4$ [M+Na]$^+$ = 604.33 and observed [M+Na]$^+$ = 604.48

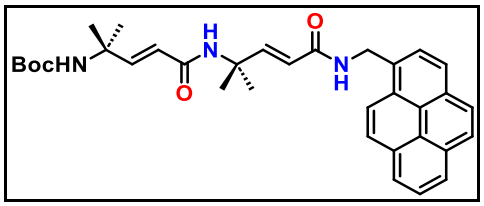


^{1}H NMR (400 MHz, Chloroform-*d*) δ 8.39 – 7.90 (m, 9H), 7.75 (s, 1H), 6.83 (dd, *J* = 15.4, 8.9 Hz, 1H), 6.65 (s, 1H), 6.49 (dd, *J* = 15.2, 4.6 Hz, 1H), 5.88 – 5.60 (m, 2H), 5.32 – 4.99 (m, 2H), 4.53 – 4.37 (m, 1H), 4.11 (h, *J* = 7.2 Hz, 1H), 1.50 – 1.42 (m, 1H), 1.37 (d, *J* = 11.2 Hz, 9H), 1.29 (d, *J* = 7.6 Hz, 3H), 1.25 (d, *J* = 5.2 Hz, 3H), 1.18 – 1.09 (m, 2H), 0.76 (td, *J* = 13.0, 12.1, 6.8 Hz, 6H). **^{13}C NMR** (101 MHz, Chloroform-d) δ 165.61, 164.16, 155.88, 147.31, 144.69, 132.05, 131.20, 130.81, 128.95, 127.65, 127.57, 127.45, 126.94, 125.67, 124.92, 124.80, 124.75, 123.52, 122.24, 120.83, 80.20, 54.14, 50.07, 43.89, 41.73, 29.71, 28.43, 26.44, 24.73, 22.54, 21.64.

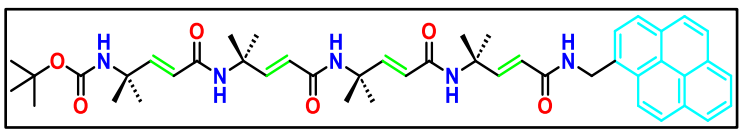
MALDI TOF/TOF m/z calculated value for $C_{36}H_{45}N_3O_4[M+Na]^+$ = 604.33 and observed $[M+Na]^+$ = 604.49



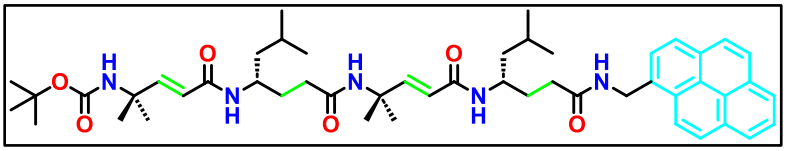
^{1}H NMR (400 MHz, Chloroform-*d*) δ 8.39 – 8.07 (m, 5H), 8.04 – 7.95 (m, 4H), 7.55 – 7.28 (m, 1H), 6.72 – 6.52 (m, 1H), 5.88 – 5.74 (m, 1H), 5.70 (d, *J* = 15.4 Hz, 1H), 5.14 (qd, *J* = 14.6, 5.6 Hz, 2H), 4.57 (s, 1H), 3.99 (tq, *J* = 12.5, 4.5 Hz, 1H), 2.29 – 2.16 (m, 2H), 2.10 – 1.84 (m, 2H), 1.64 – 1.47 (m, 2H), 1.42 (d, *J* = 6.0 Hz, 2H), 1.35 (s, 9H), 1.31 (t, *J* = 4.9 Hz, 2H), 1.26 (s, 6H), 1.21 – 1.20 (m, 1H), 0.77 (d, *J* = 6.6 Hz, 3H), 0.68 (d, *J* = 6.5 Hz, 3H). **^{13}C NMR** (101 MHz, Chloroform-*d*) δ 172.82, 166.05, 139.29, 131.23, 130.92, 130.80, 128.88, 127.89, 127.38, 127.21, 127.18, 125.88, 125.10, 124.95, 124.78, 124.76, 123.25, 120.59, 114.08, 52.88, 47.51, 44.95, 41.64, 33.43, 32.35, 31.94, 30.32, 28.36, 24.83, 22.96, 22.71, 21.90. **MALDI TOF/TOF m/z** calculated value for $C_{36}H_{45}N_3O_4$ $[M+Na]^+$ = 606.76 and observed $[M+Na]^+$ = 606.49



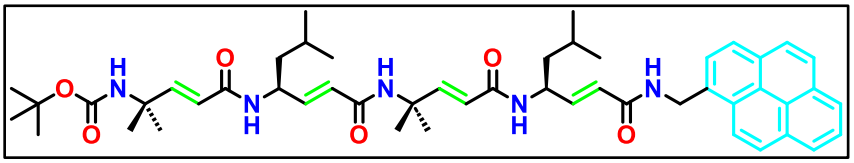
^{1}H NMR (400 MHz, Chloroform-*d*) δ 8.24 (d, *J* = 9.2 Hz, 1H), 8.14 (d, *J* = 7.6 Hz, 2H), 8.11 – 8.06 (m, 2H), 8.01 – 7.93 (m, 4H), 6.88 (d, *J* = 15.5 Hz, 1H), 6.68 (d, *J* = 15.5 Hz, 1H), 6.60 (s, 1H), 5.83 (d, *J* = 15.5 Hz, 2H), 5.73 (d, *J* = 15.5 Hz, 1H), 5.14 (d, *J* = 5.4 Hz, 2H), 4.60 (s, 1H), 1.43 (s, 6H), 1.30 (d, *J* = 2.5 Hz, 9H). **^{13}C NMR** (101 MHz, Chloroform-*d*) δ 165.70, 164.98, 147.99, 131.19, 131.08, 130.73, 128.98, 128.08, 127.36, 127.33, 125.91, 125.18, 124.91, 124.76, 124.67, 123.04, 121.10, 53.96, 52.77, 41.93, 28.31, 27.33. **MALDI TOF/TOF m/z** calculated value for $C_{36}H_{45}N_3O_4$ $[M+Na]^+$ = 576.29 and observed $[M+Na]^+$ = 576.41



^{1}H NMR (400 MHz, Chloroform-*d*) δ 8.40 (d, *J* = 103.3 Hz, 4H), 7.94 (d, *J* = 60.8 Hz, 9H), 6.93 (d, *J* = 15.5 Hz, 1H), 6.60 (dd, *J* = 41.6, 15.1 Hz, 3H), 5.89 (dd, *J* = 23.6, 15.3 Hz, 2H), 5.61 (dd, *J* = 33.4, 15.2 Hz, 2H), 5.50 – 4.82 (m, 2H), 4.54 (d, *J* = 187.9 Hz, 1H), 1.64 – 0.96 (m, 33H). **^{13}C NMR** (101 MHz, Chloroform-*d*) δ 166.43, 165.03, 164.99, 164.85, 154.76, 147.94, 130.45, 130.45, 128.87, 127.45, 127.28, 126.47, 125.27, 124.73, 124.59, 124.58, 124.36, 123.79, 121.49, 121.07, 121.01, 120.74, 80.06, 54.38, 54.35, 53.98, 53.74, 53.58, 41.52, 30.53, 29.71, 28.96, 28.65, 26.20. **MALDI TOF/TOF m/z** calculated value for $C_{46}H_{57}N_5O_6$ $[M+Na]^+$ = 798.43 and observed $[M+Na]^+$ = 798.66

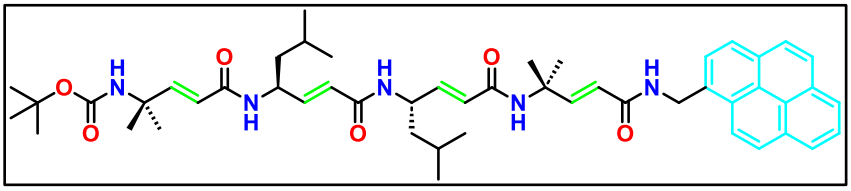


^{1}H NMR (400 MHz, Chloroform-*d*) δ 8.75 (s, 1H), 8.54 – 7.86 (m, 9H), 7.64 (s, 1H), 7.05 (s, 1H), 6.66 (dd, *J* = 23.6, 15.2 Hz, 1H), 6.26 (d, *J* = 79.8 Hz, 1H), 5.79 (dd, *J* = 15.2, 9.8 Hz, 1H), 5.30 (s, 2H), 5.18 – 4.98 (m, 1H), 4.95 (s, 1H), 4.72 (s, 1H), 3.90 (s, 2H), 2.14 – 1.76 (m, 8H), 1.52 (tt, *J* = 12.8, 6.0 Hz, 3H), 1.41 (s, 9H), 1.37 (d, *J* = 13.9 Hz, 3H), 1.33 – 1.24 (m, 6H), 1.21 – 0.90 (m, 6H), 0.87 – 0.72 (m, 12H). **^{13}C NMR** (151 MHz, Chloroform-*d*) δ 172.99, 171.76, 165.84, 131.25, 130.89, 130.68, 128.88, 127.76, 127.59, 127.45, 127.08, 126.92, 125.79, 125.67, 124.91, 124.80, 79.97, 62.03, 54.07, 53.26, 47.69, 44.93, 41.23, 33.38, 33.10, 32.86, 29.69, 28.51, 28.45, 24.88, 24.81, 24.69, 23.00, 22.93, 22.74, 22.33, 22.17, 22.00. **MALDI TOF/TOF m/z** calculated value for $C_{46}H_{57}N_5O_6$[$M+Na]^+$ = 858.33 and observed $[M+Na]^+$ = 858.704

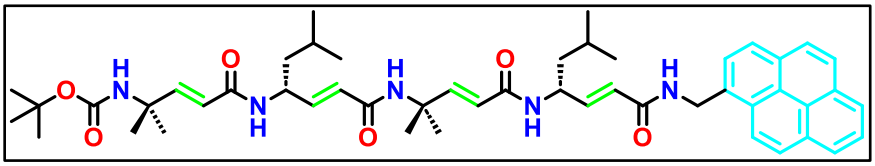


^{1}H NMR (400 MHz, Chloroform-*d*) δ 8.85 (t, *J* = 5.6 Hz, 1H), 8.49 (d, *J* = 9.3 Hz, 1H), 8.29 (d, *J* = 7.9 Hz, 1H), 8.23 – 7.83 (m, 9H), 7.57 (d, *J* = 6.9 Hz, 1H), 6.71 (d, *J* = 15.2 Hz, 1H), 6.65 (dd, *J* = 15.3, 3.4 Hz, 1H), 6.54 (dd, *J* = 15.2, 3.9 Hz, 1H), 6.24 (d, *J* = 15.3 Hz, 1H), 5.96 (d, *J* = 15.2 Hz, 1H), 5.57 (dd, *J* = 15.4, 1.9 Hz, 1H), 5.42 – 5.34 (m, 2H), 5.33 (d, *J* = 8.3 Hz, 1H), 5.20 (dd, *J* = 14.8, 5.2 Hz, 1H), 4.69 (s, 1H), 4.46 (s, 1H), 4.24 (s, 1H), 1.76 – 1.61 (m, 2H), 1.57 – 1.47 (m, 2H), 1.41 (s, 12H), 1.33 (d, *J* = 4.6 Hz, 1H), 1.27 (d, *J* = 10.2 Hz, 6H), 1.13 (d, *J* = 6.8 Hz, 1H),

1.09 (s, 3H), 0.79 (dd, *J* = 6.6, 3.7 Hz, 6H), 0.71 (d, *J* = 6.6 Hz, 3H), 0.57 (d, *J* = 6.5 Hz, 3H). **^{13}C NMR** (151 MHz, Chloroform-*d*) δ 174.72, 166.41, 166.21, 164.50, 155.29, 150.28, 148.97, 144.82, 144.62, 133.36, 131.64, 130.97, 129.25, 127.96, 127.86, 127.10, 125.95, 125.26, 125.20, 125.01, 124.26, 121.55, 119.60, 119.23, 80.56, 70.64, 65.54, 63.69, 54.57, 54.19, 49.61, 48.70, 43.94, 43.57, 41.82, 34.52, 32.29, 31.80, 30.41, 30.06, 30.01, 29.96, 29.81, 29.73, 29.61, 29.49, 28.90, 26.73, 25.47, 25.28, 25.21, 25.14, 23.10, 23.06, 22.29, 21.96, 14.49. **MALDI TOF/TOF m/z** calculated value for $C_{50}H_{65}N_5O_6$ $[M+Na]^+$ = 854.49 and observed $[M+Na]^+$ = 854.64



^{1}H NMR (400 MHz, Chloroform-*d*) δ 8.59 (s, 2H), 8.20 (s, 1H), 8.18 – 7.95 (m, 9H), 6.90 (s, 1H), 6.85 (d, *J* = 7.6 Hz, 1H), 6.68 – 6.63 (m, 1H), 6.63 – 6.57 (m, 1H), 5.97 (d, *J* = 15.1 Hz, 1H), 5.64 (d, *J* = 15.2 Hz, 1H), 5.55 (d, *J* = 15.3 Hz, 2H), 5.34 – 5.20 (m, 1H), 4.98 (s, 1H), 4.67 (s, 1H), 4.48 (s, 2H), 1.79 (s, 1H), 1.42 (s, 3H), 1.37 (dd, *J* = 10.1, 3.9 Hz, 2H), 1.31 (s, 3H), 1.27 (d, *J* = 8.6 Hz, 2H), 1.22 (s, 3H), 0.85 (d, *J* = 6.5 Hz, 6H), 0.79 (d, *J* = 6.6 Hz, 6H). **^{13}C NMR** (151 MHz, Chloroform-*d*) δ 166.22, 164.69, 155.10, 145.41, 133.40, 131.63, 131.36, 130.87, 129.45, 128.16, 127.98, 127.57, 126.91, 125.78, 125.26, 125.16, 125.04, 124.84, 121.29, 121.07, 119.86, 119.30, 80.66, 54.45, 54.10, 50.12, 49.35, 43.24, 42.00, 30.64, 28.90, 26.28, 25.82, 25.59, 25.19, 23.52, 23.06, 22.35, 21.63. **MALDI TOF/TOF m/z** calculated value for $C_{50}H_{65}N_5O_6$ $[M+Na]^+$ = 854.49 and observed $[M+Na]^+$ = 854.67



^{1}H NMR (400 MHz, Chloroform-*d*) δ 8.86 (t, *J* = 5.5 Hz, 1H), 8.49 (d, *J* = 9.3 Hz, 1H), 8.29 (d, *J* = 8.0 Hz, 1H), 8.20 – 7.86 (m, 9H), 7.57 (d, *J* = 7.1 Hz, 1H), 6.74 – 6.62 (m, 2H), 6.54 (dd, *J* = 15.2, 3.9 Hz, 1H), 6.24 (d, *J* = 15.2 Hz, 1H), 5.96 (d, *J* = 15.2 Hz, 1H), 5.57 (dd, *J* = 15.3, 1.9 Hz, 1H), 5.42 – 5.34 (m, 2H), 5.33 (d, *J* = 8.7 Hz, 1H), 5.20 (dd, *J* = 14.8, 5.2 Hz, 1H), 4.70 (s, 1H), 4.46 (s, 1H), 4.25 (s, 1H), 1.68 (dt, *J* = 12.7, 7.2 Hz, 1H), 1.57 – 1.47 (m, 1H), 1.41 (s, 12H), 1.35

– 1.26 (m, 6H), 1.25 – 1.10 (m, 2H), 1.09 (s, 3H), 0.94 – 0.81 (m, 2H), 0.80 (dd, *J* = 7.1, 3.4 Hz, 6H), 0.71 (d, *J* = 6.6 Hz, 3H), 0.57 (d, *J* = 6.5 Hz, 3H). **^{13}C NMR** (151 MHz, Chloroform-*d*) δ 174.72, 166.41, 166.21, 164.50, 155.29, 150.28, 148.97, 144.82, 144.62, 133.36, 131.64, 130.97, 129.25, 127.96, 127.86, 127.10, 125.95, 125.26, 125.20, 125.01, 124.26, 121.55, 119.60, 119.23, 80.56, 70.64, 65.54, 63.69, 54.57, 54.19, 49.61, 48.70, 43.94, 43.57, 41.82, 34.52, 32.29, 31.80, 30.41, 30.06, 30.01, 29.96, 29.81, 29.73, 29.61, 29.49, 28.90, 26.73, 25.47, 25.28, 25.21, 25.14, 23.10, 23.06, 22.29, 21.96, 14.49. **MALDI TOF/TOF m/z** calculated value for $C_{50}H_{65}N_5O_6$ $[M+Na]^+$ = 854.49 and observed $[M+Na]^+$ = 854.64

4.7. Appendix

4.7.1. ORTEP Diagrams

4.7.1.1. ORTEP Diagram of Peptide P1

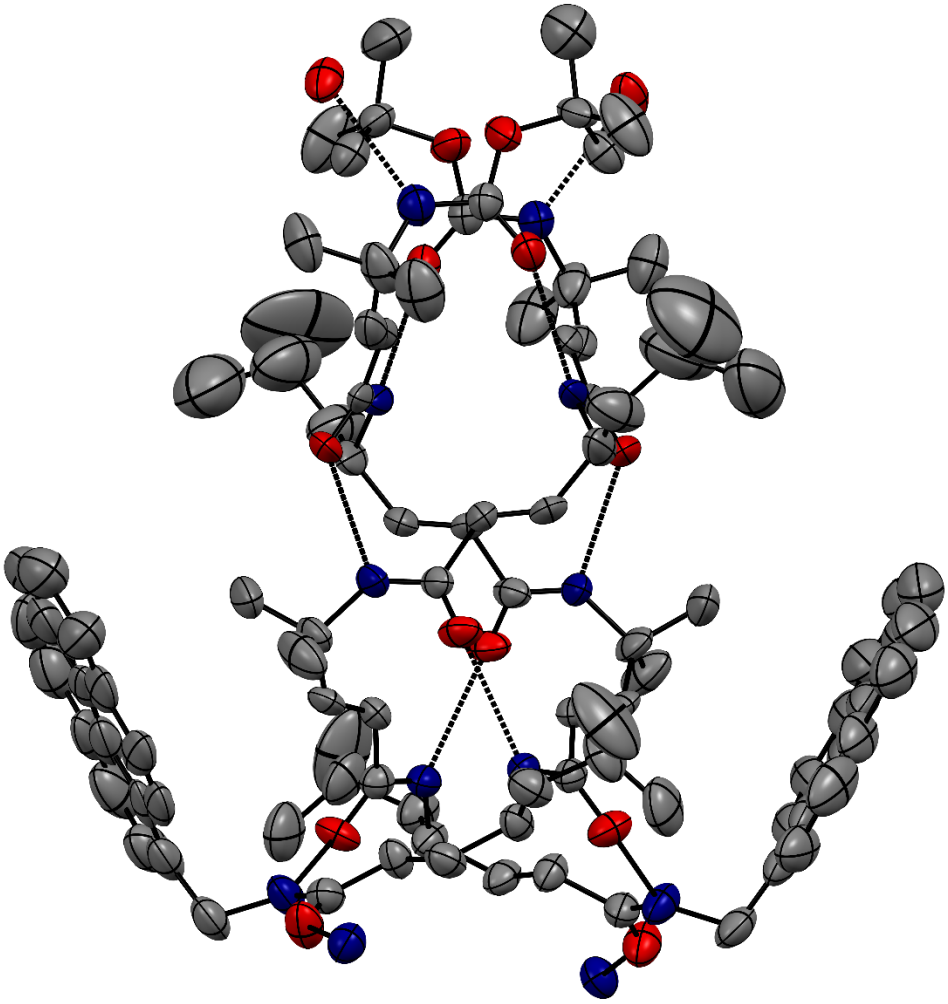


Figure 17: ORTEP diagram of peptide **P1.** H-bonds are shown in dotted lines. H-atoms are omitted for clarity. Ellipsoids are drawn at 50% probability.

4.7.1.2. ORTEP Diagram of Peptide P3

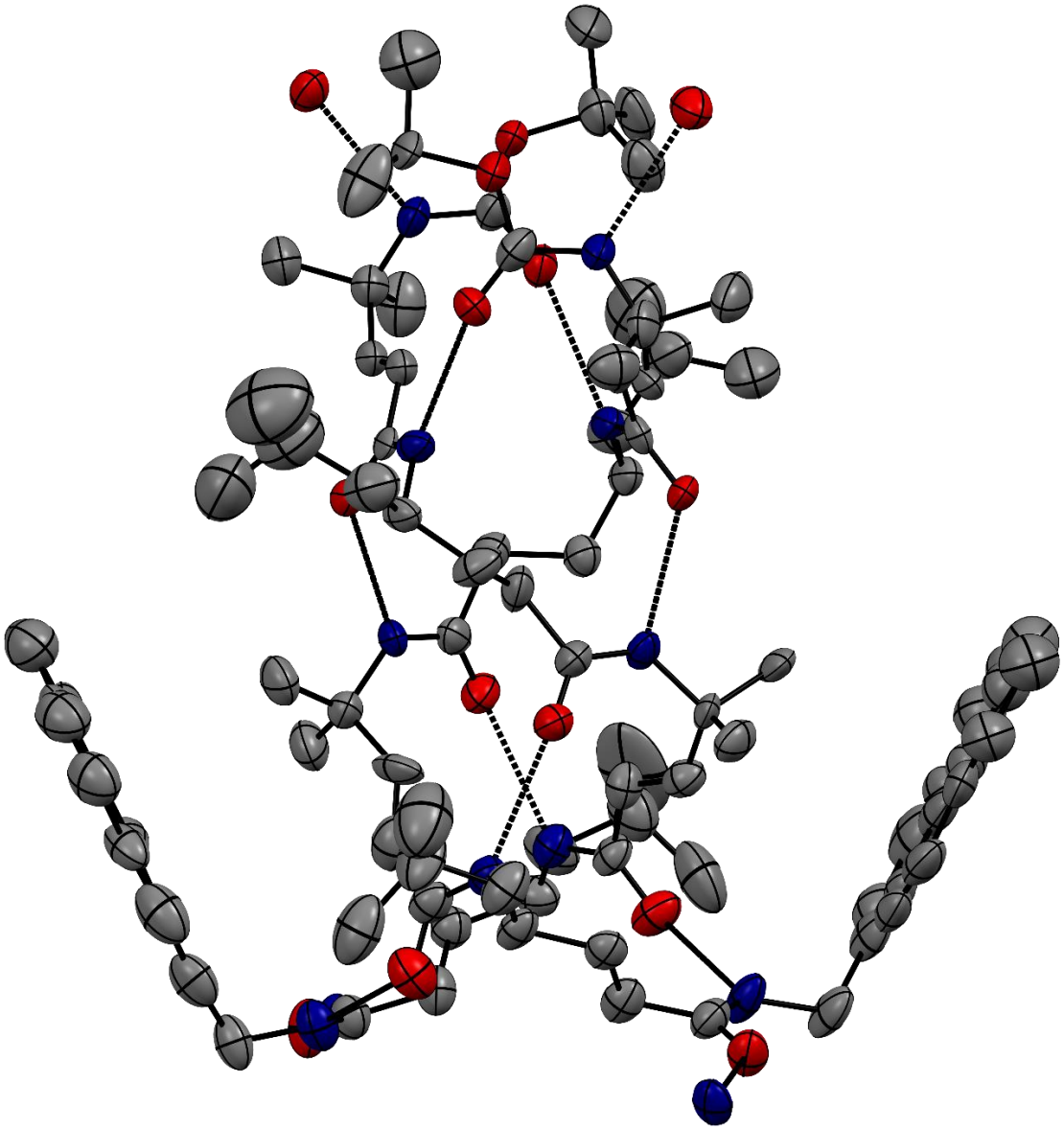


Figure 18: ORTEP diagram of peptide **P3.** H-bonds are shown in dotted lines. H-atoms are omitted for clarity. Ellipsoids are drawn at 50% probability.

4.7.1.3. ORTEP Diagram of peptide P4

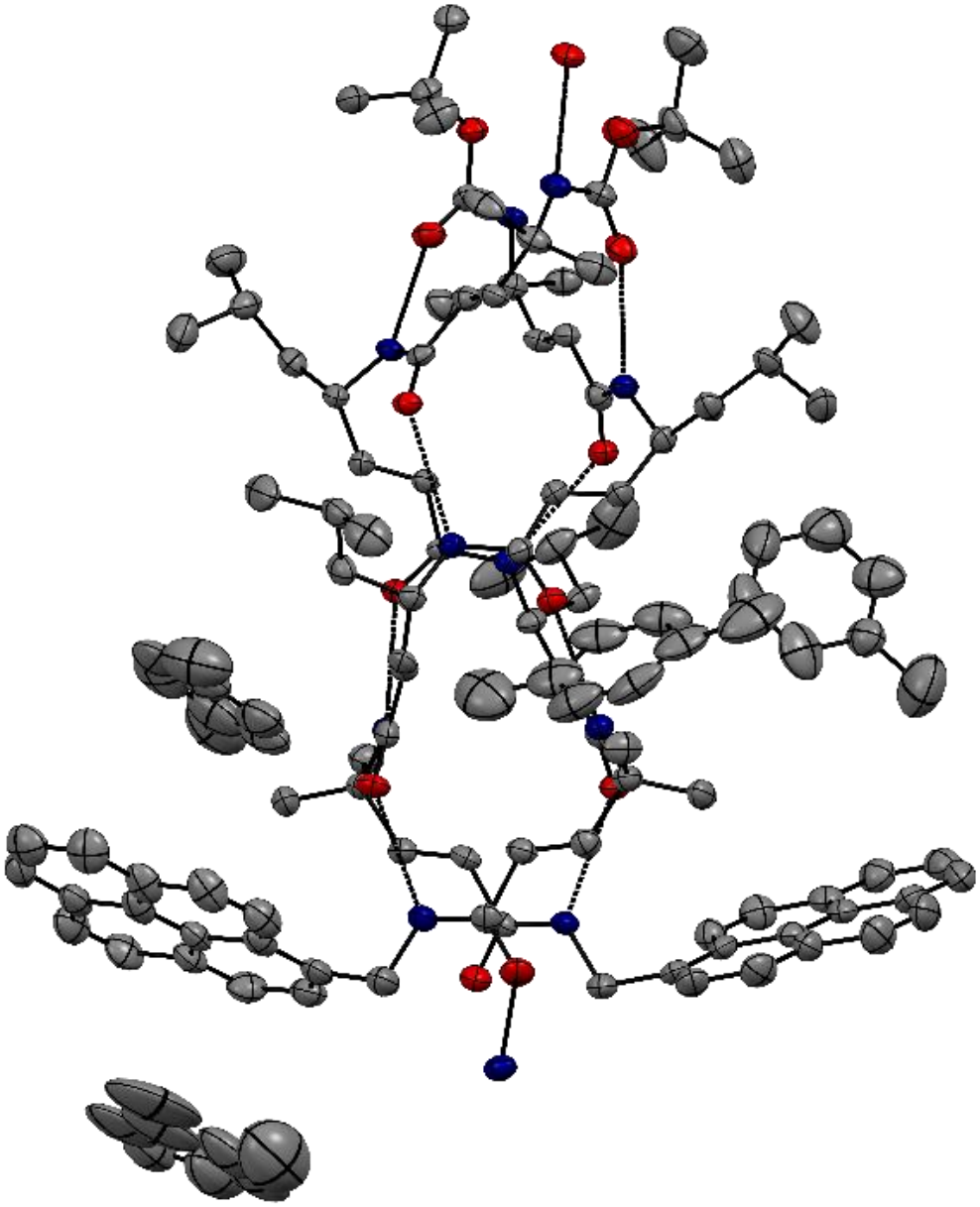


Figure 19: ORTEP diagram of peptide **P4.** H-bonds are shown in dotted lines. H-atoms are omitted for clarity. Ellipsoids are drawn at 50% probability.

4.7.1.4 ORTEP Diagram of Peptide P5

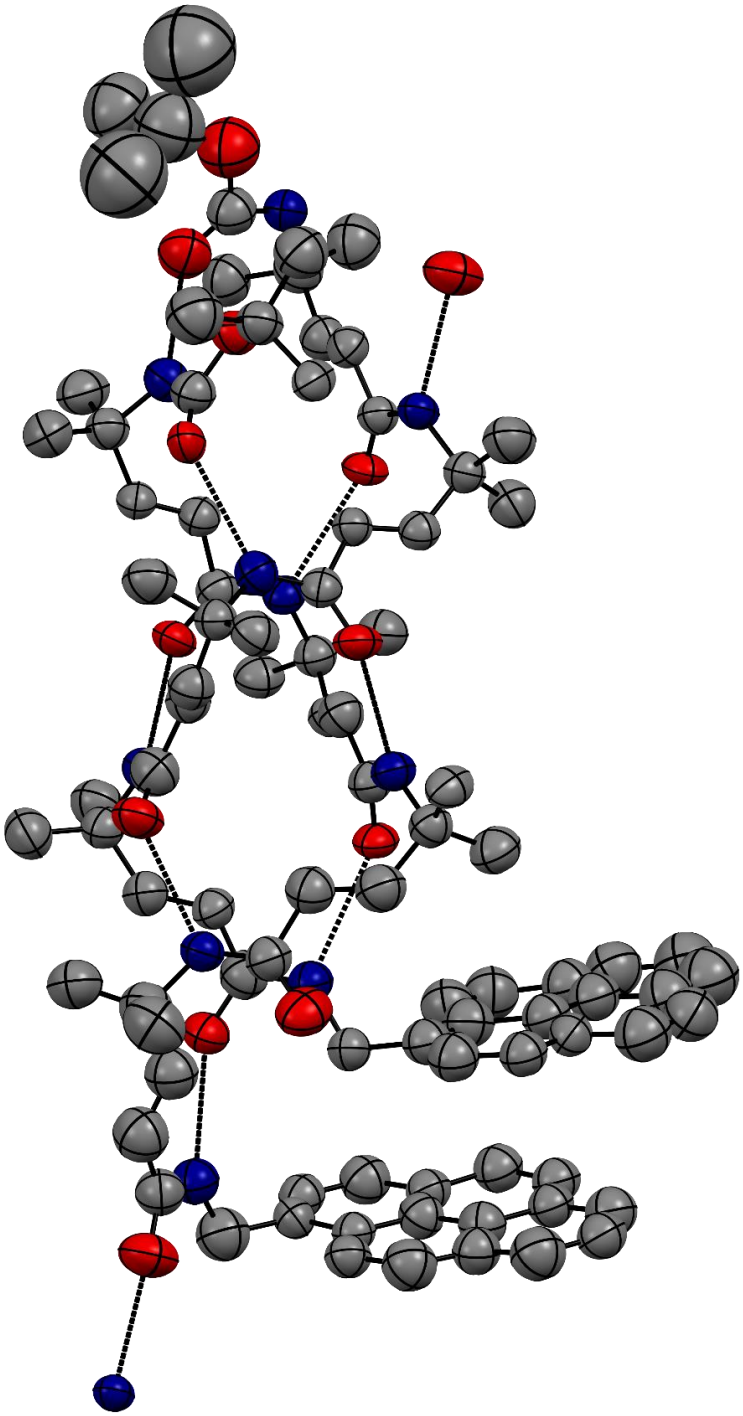


Figure 20: ORTEP diagram of peptide **P5.** H-bonds are shown in dotted lines. H-atoms are omitted for clarity. Ellipsoids are drawn at 50% probability.

4.8. Crystal Structure Information

Crystal structure identification table for P1

Identification code	**P1**	
Empirical formula	'C50 H65 N5 O6 [+ solvent]'	
Formula weight	832.07	
Temperature	150(2) K	
Wavelength	0.71073 Å	
Crystal system	Tetragonal	
Space group	I4	
Unit cell dimensions	a = 32.880(3) Å	α= 90°.
	b = 32.880(3) Å	β= 90°.
	c = 24.805(4) Å	γ = 90°.
Volume	26816(7) $Å^3$	
Z	16	
Density (calculated)	0.824 Mg/m^3	
Absorption coefficient	0.054 mm^{-1}	
F(000)	7168	
Crystal size	0.300 x 0.200 x 0.200 mm^3	
Theta range for data collection	1.959 to 24.812°.	
Index ranges	-38<=h<=38, -38<=k<=37, -29<=l<=29	
Reflections collected	288261	
Independent reflections	14233 [R(int) = 0.0732]	
Completeness to theta = 24.000°	99.9 %	
Absorption correction	Semi-empirical from equivalents	
Max. and min. Data/restraints5 and 0.987		
Refinement method	Full-matrix least-squares on F^2	
Data/restraints/parameters	23025 / 226 / 1121	
Goodness-of-fit on F^2	1.04	
Final R indices [I>2sigma(I)]	R1 = 0.0732, wR2 = 0.1847	
R indices (all data)	R1 = 0.1310, wR2 = 0.2156	
Absolute structure parameter	0.1(2)	
Extinction coefficient	n/a	
Largest diff. peak and hole	0.383 and -0.218 $e.Å^{-3}$	

Crystal structure identification table for P3

Identification code	**P3**	
Empirical formula	'C_{50} H_{69} N_5 O_6 [+ solvent]'	
Formula weight	836.10	
Temperature	150(2) K	
Wavelength	0.71073 Å	
Crystal system	Orthorhombic	
Space group	I 2 2 2	
Unit cell dimensions	a = 24.73(5) Å	α= 90°.
	b = 32.10(6) Å	β= 90°.
	c = 33.24(5) Å	γ = 90°.
Volume	26390(83) $Å^3$	
Z	16	
Density (calculated)	0.842 Mg/m^3	
Absorption coefficient	0.055 mm^{-1}	
F(000)	7232	
Crystal size	0.30 x 0.200 x 0.100 mm^3	
Theta range for data collection	2.39 to 13.75°.	
Index ranges	-29<=h<=29, -38<=k<=38, -39<=l<=39	
Reflections collected	327092	
Independent reflections	9813 [R(int) = 0.0865]	
Completeness to theta = 24.000°	99.9 %	
Absorption correction	Semi-empirical from equivalents	
Max. and min. transmission	0.995 and 0.987	
Refinement method	Full-matrix least-squares on F^2	
Data/restraints/parameters	23322 / 126 / 1121	
Goodness-of-fit on F^2	1.002	
Final R indices [I>2sigma(I)]	R1 = 0.0865, wR2 = 0.2247	
R indices (all data)	R1 = 0.2303, wR2 = 0.3061	
Absolute structure parameter	0.6(7)	
Extinction coefficient	n/a	
Largest diff. peak and hole	0.376 and -0.266 $e.Å^{-3}$	

Crystal Structure Identification table for P4

Identification code	**P4**	
Empirical formula	C131 H168 N10 O12	
Formula weight	2074.75	
Temperature	150(2) K	
Wavelength	0.71073 Å	
Crystal system	Orthorhombic	
Space group	P 21 21 21	
Unit cell dimensions	a = 13.254(2) Å	α= 90°.
	b = 26.712(5) Å	β= 90°.
	c = 34.729(5) Å	γ = 90°.
Volume	12296(4) $Å^3$	
Z	4	
Density (calculated)	1.121 Mg/m^3	
Absorption coefficient	0.071 mm^{-1}	
F(000)	4480	
Crystal size	0.125 x 0.200 x 0.225 mm^3	
Theta range for data collection	2.39 to 13.75°.	
Index ranges	-16<=h<=16, -33<=k<=33, -43<=l<=43	
Reflections collected	334254	
Independent reflections	14045 [R(int) = 0.0865]	
Completeness to theta = 24.000°	99.9 %	
Absorption correction	Semi-empirical from equivalents	
Max. and min. transmission	0.995 and 0.987	
Refinement method	Full-matrix least-squares on F^2	
Data/restraints/parameters	25370 / 918 / 1371	
Goodness-of-fit on F^2	1.017	
Final R indices [I>2sigma(I)]	R1 = 0.0831, wR2 = 0.2071	
R indices (all data)	R1 = 0.1681, wR2 = 0.2602	
Absolute structure parameter	-0.3(5)	
Extinction coefficient	n/a	
Largest diff. peak and hole	1.605 and -0.391 $e.Å^{-3}$	

Crystal structure identification table for P5

Identification code	**P5**	
Empirical formula	'C92 H113 N10 O12 [+ solvent]'	
Formula weight	1550.92	
Temperature	150(2) K	
Wavelength	0.71073 Å	
Crystal system	triclinic	
Space group	P-1	
Unit cell dimensions	a = 15.179(16) Å	α= 106.317°.
	b = 18.39(2) Å	β= 97.232°.
	c = 19.40(2) Å	γ = 102.430°.
Volume	4974(9) $Å^3$	
Z	2	
Density (calculated)	01.036 Mg/m^3	
Absorption coefficient	0.069 mm^{-1}	
F(000)	1662	
Crystal size	0.25 x 0.200 x 0.300 mm^3	
Theta range for data collection	2.3 to 21.31°.	
Index ranges	-29<=h<=29, -38<=k<=38, -39<=l<=39	
Reflections collected	114944	
Independent reflections	17391 [R(int) = 0.0865]	
Completeness to theta = 24.000°	99.9 %	
Absorption correction	Semi-empirical from equivalents	
Max. and min. transmission	0.410 and 0.745	
Refinement method	Full-matrix least-squares on F^2	
Data/restraints/parameters	17391 / 684 / 1036	
Goodness-of-fit on F^2	0.989	
Final R indices [I>2sigma(I)]	R1 = 0.1882, wR2 = 0.4076	
R indices (all data)	R1 = 0.5737, wR2 = 0.5889	
Absolute structure parameter	0.6(7)	
Extinction coefficient	n/a	
Largest diff. peak and hole	1.018 and -0.334 $e.Å^{-3}$	

4.9. References

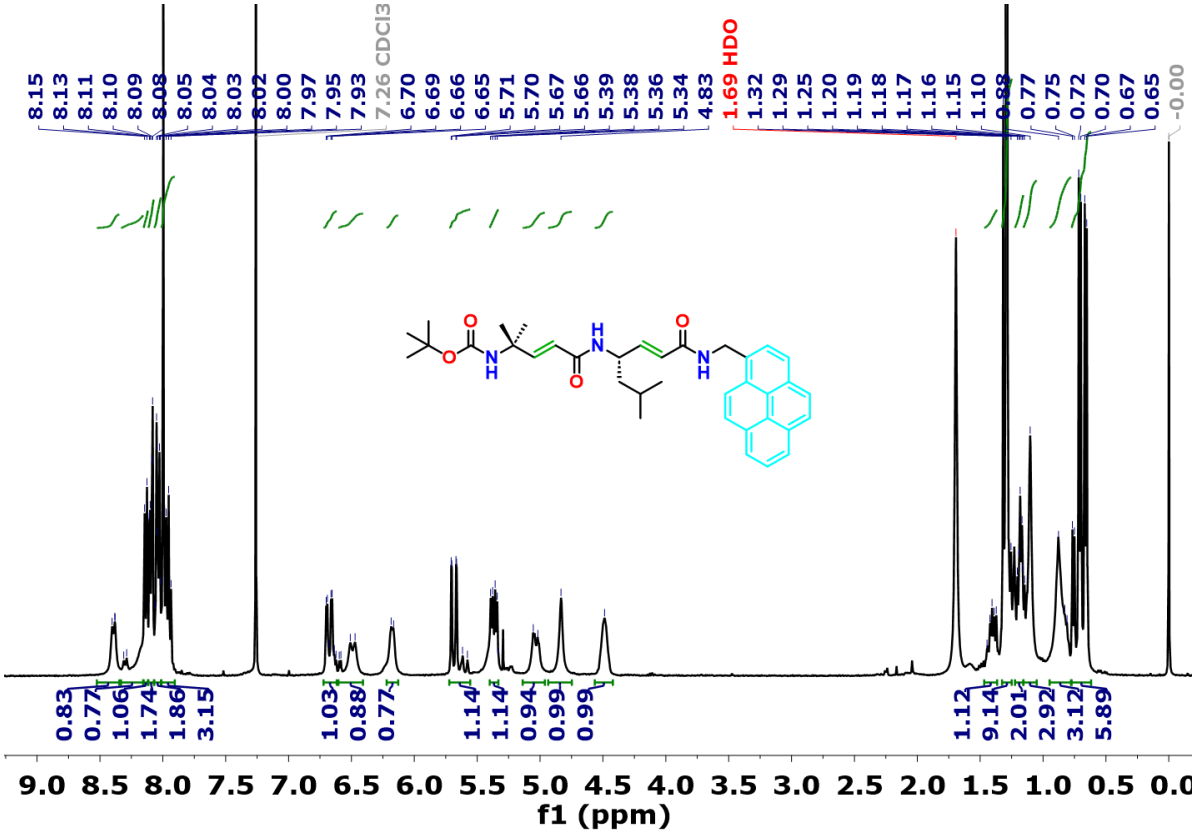
1. Whitesides GM, Grzybowski B. *Science* **2002**, *295* 2418.
2. Zhang, *Nat. Biotechnol.* **2003**, *21*, 1171.
3. S. Zhang, *Biotechnol. Adv.* **2002**, *20*, 321
4. Lawrence DS, Jiang T, Levett M. *Chemical Reviews.* **1995**, *95*, 2229
5. Otvos, L.; Wade, J. D. *Frontiers in Chemistry* **2014**, *2*, 62
6. Eck, R. V.; Dayhoff, M. O. *Science* **1966**, *152*, 363.
7. Romero Romero, M. L.; Rabin, A.; Tawfik, D. S. *Angew. Chem., Int. Ed.* **2016**, 55, 15966.
8. D'Alessio, G. *Prog. Biophys. Mol. Biol.* **1999**, 72, 271.
9. Alva, V.; Lupas, A. N. *Curr. Opin Struct Biol.* **2018**, *48*, 103.
10. Yadid, I.; Kirshenbaum, N.; Sharon, M.; Dym, O.; Tawfik, D. S. *Proc. Natl. Acad. Sci. U.S.A.* **2010**, *107*, 7287.
11. Rufo, C. M.; Moroz, Y. S.; Moroz, O. V.; Stöhr, J.; Smith, T. A.; Hu, X.; DeGrado, W. F.; Korendovych, I. V. *Nature Chem.* **2014**, 6, 303.
12. Zastrow, M. L.; Peacock, A. F. A.; Stuckey, J. A.; Pecoraro, V. L. *Nature Chem.* **2012**, *4*, 118.
13. Matthew J. Webber, E. Thomas Pashuck *Advanced Drug Delivery Reviews* 2021, *172*, 275.
14. Levin, A; Hakala, T. A.; Schnaider, L.; Bernardes, G. J. L.; Gazit, E.; Knowles, T. P. J. *Nat. Rev. Chem*. **2020**, *4*, 615.
15. Morimoto, M.; Bierschenk, S. M.; Xia, K. T.; Bergman, R. G.; Raymond, K. N.; Toste, F. D. *Nat. Catal* **2020**, 3, 969.
16. (a) Fletcher, J. M.; Harniman, R. L.; Barnes, F. R. H.; Boyle, A. L.; Collins, A.; Mantell, J.; Sharp, T. H.; Antognozzi, M.; Booth, P. J.; Linden, N.; Miles, M. J.; Sessions, R. B.; Verkade, P.; Woolfson, D. N. *Science* **2013**, *340*, 595. (b) Padilla, J. E.; Colovos, C.; Yeates, T. O. *Proc. Natl. Acad. Sci. U.S.A.* **2001**, *98*, 2217. (c) Ryadnov, M. G.; Woolfson, D. N. *Nat. Mater*. **2003**, *2*, 329; (d) Lai, Y.-T.; Cascio, D.; Yeates, T. O. *Science* **2012**, *336*, 1129.
17. Zhou, H.-C.; Long, J. R.; Yaghi, O. M. *Chem. Rev.* **2012**, *112*, 673.
18. Zhu, J.; Avakyan, N.; Kakkis, A.; Hoffnagle, A. M.; Han, K.; Li, Y.; Zhang, Z.; Choi, T. S.; Na, Y.; Yu, C.-J.; Tezcan, F. A. *Chem. Rev*. **2021**, *121*, 13701.

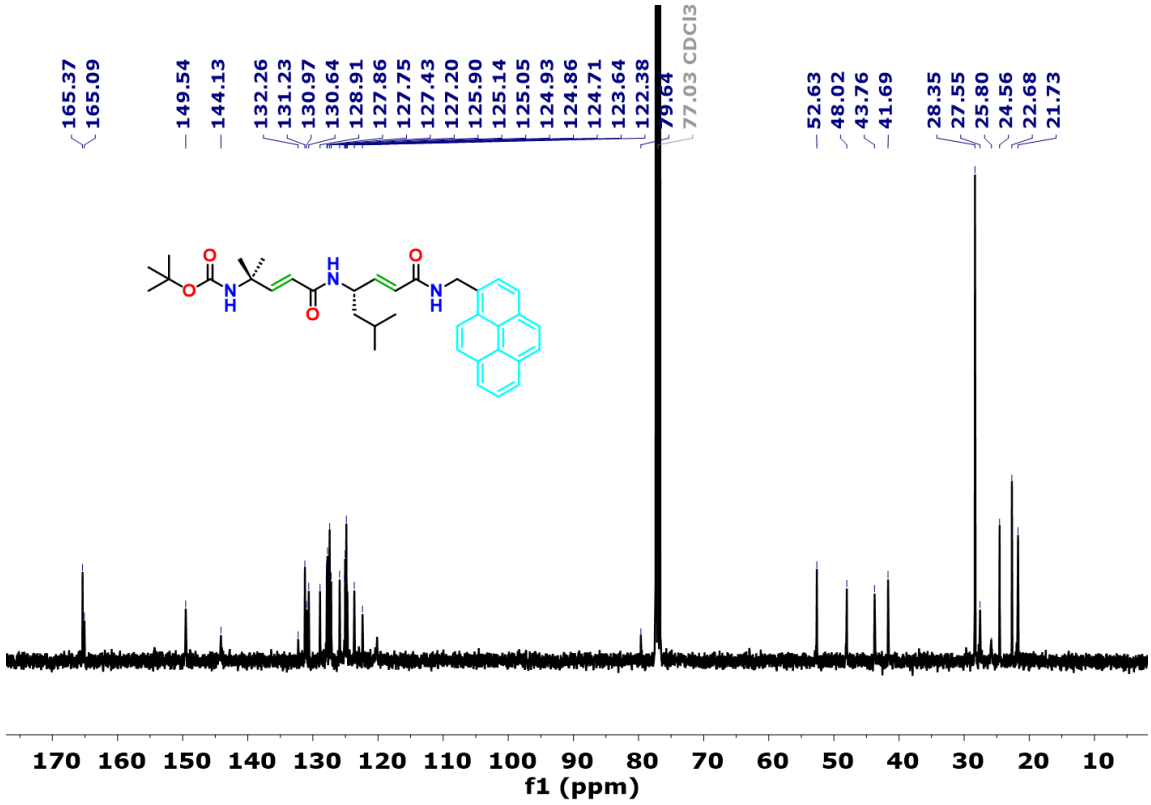
19. Schnitzer, T.; Paenurk, E.; Trapp, N.; Gershoni-Poranne, R.; Wennemers, H. *J. Am. Chem. Soc.* **2021**, *143*, 644.
20. Saito, A.; Sawada, T.; Fujita, M. *Angew. Chem. Int. Ed.* **2020**, 59, 20367.
21. Sawada, T.; Matsumoto, A.; Fujita, M. *Angew. Chem.* **2014**, *126*, 7356.
22. Navarro-Sánchez, J.; Argente-García, A. I.; Moliner-Martínez, Y.; Roca-Sanjuán, D.; Antypov, D.; Campíns-Falcó, P.; Rosseinsky, M. J.; Martí-Gastaldo, C. J. *Am. Chem. Soc.* **2017**, 139, 4294.
23. Rabone, J.; Yue, Y.-F.; Chong, S. Y.; Stylianou, K. C.; Bacsa, J.; Bradshaw, D.; Darling, G. R.; Berry, N. G.; Khimyak, Y. Z.; Ganin, A. Y.; Wiper, P.; Claridge, J. B.; Rosseinsky, M. J. *Science* **2010**, *329*, 1053.
24. Martí-Gastaldo, C.; Antypov, D.; Warren, J. E.; Briggs, M. E.; Chater, P. A.; Wiper, P. V.; Miller, G. J.; Khimyak, Y. Z.; Darling, G. R.; Berry, N. G.; Rosseinsky, M. J. *Nat. Chem.* **2014**, *6*, 343.
25. Katsoulidis, A. P.; Antypov, D.; Whitehead, G. F. S.; Carrington, E. J.; Adams, D. J.; Berry, N. G.; Darling, G. R.; Dyer, M. S.; Rosseinsky, M. J. *Nature* **2019**, *565*, 213.
26. Yan, Y.; Carrington, E. J.; Pétuya, R.; Whitehead, G. F. S.; Verma, A.; Hylton, R. K.; Tang, C. C.; Berry, N. G.; Darling, G. R.; Dyer, M. S.; Antypov, D.; Katsoulidis, A. P.; Rosseinsky, M. J. *J. Am. Chem. Soc.* **2020**, *142*, 14903.
27. Misra, R.; Saseendran, A.; Dey, S.; Gopi, H. N. *Angew. Chem., Int. Ed.* **2019**, 58, 2251.
28. Mantion, A.; Massüger, L.; Rabu, P.; Palivan, C.; McCusker, L. B.; Taubert, A. *J. Am. Chem. Soc.* **2008**, 130, 2517.
29. Miyake, R.; Tashiro, S.; Shiro, M.; Tanaka, K.; Shionoya, M. *J. Am. Chem. Soc.* **2008**, 130, 5646.
30. Sawada, T.; Saito, A.; Tamiya, K.; Shimokawa, K.; Hisada, Y.; Fujita, M. *Nat. Commun.* **2019**, *10*, 921
31. Chen, Y.; Yang, Y.; Orr, A. A.; Makam, P.; Redko, B.; Haimov, E.; Wang, Y.; Shimon, L. J. W.; Rencus-Lazar, S.; Ju, M.; Tamamis, P.; Dong, H.; Gazit, E. *Angew. Chem., Int. Ed.* **2021**, *60*, 17164.
32. Chen, Y.; Guerin, S.; Yuan, H.; O'Donnell, J.; Xue, B.; Cazade, P.-A.; Haq, E. U.; Shimon, L. J. W.; Rencus-Lazar, S.; Tofail, S. A. M.; Cao, Y.; Thompson, D.; Yang, R.; Gazit, E. *J. Am. Chem. Soc.* **2022**, *144*, 3468.

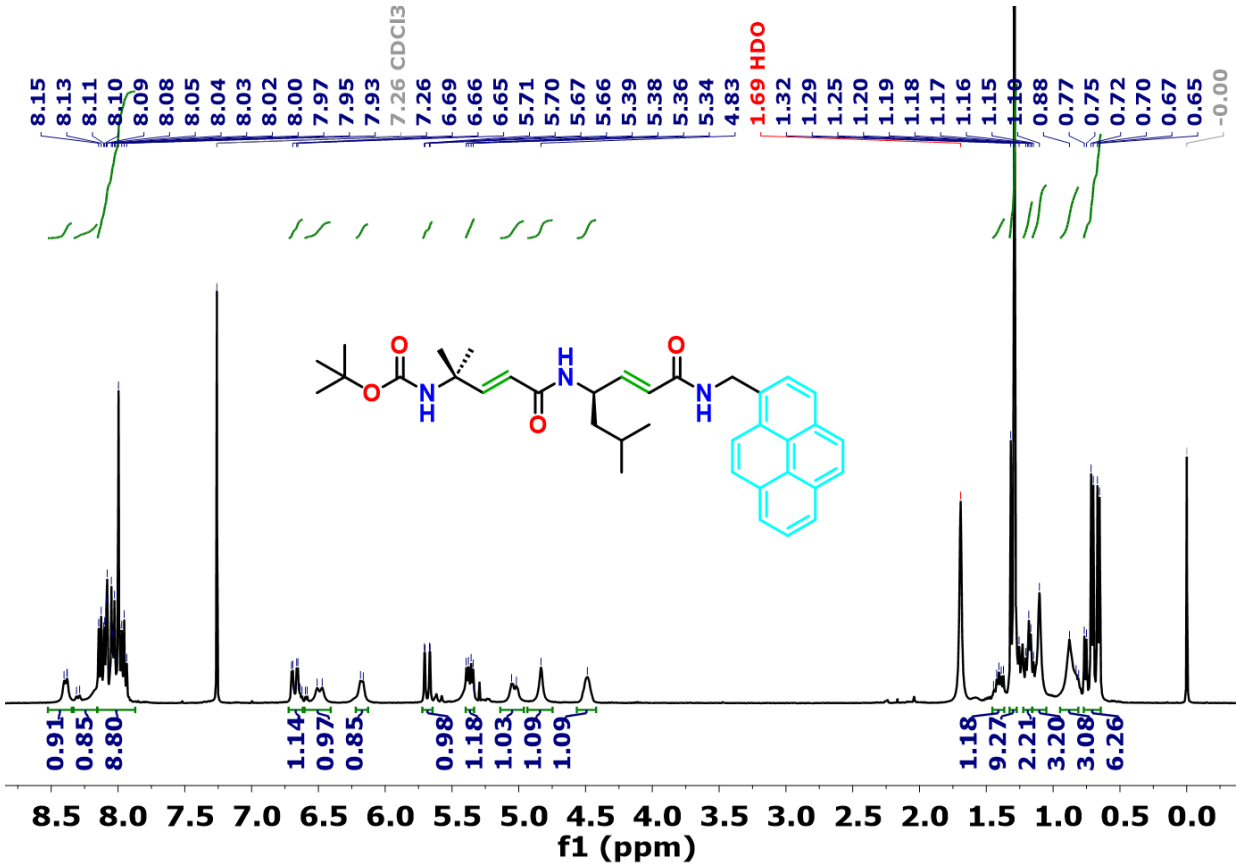
33. Langes, D. A. *Science* **1988**, *241*, 188.
34. Urry, D. W.; Glickson, J. D.; Mayers, D. F.; Haider, J. *Biochemistry* **1972**, *11*, 487.
35. Wallace, B. A.; Ravikumar, K. *Science* **1988**, *241*, 182.
36. Sychev, S. V.: Barsukov, L. I.; Ivanov, V. T. *J. Pept. Sci.* **2013**, *19*, 452.
37. Kelkar, D. A.; Chattopadhyay, A. *Biochim. Biophys. Acta Biomembr.* **2007**, *1768*, 2011.
38. F. Dettner, A. Hänchen, D. Schols, L. Toti, A. Nußer, R. D. Süssmuth, *Angew. Chem. Int. Ed.* **2009**, *48*, 1856;
39. Sychev, S.V.; Barsukov, L. I.; Ivanov, V. T. *Eur. Biophys. J.* **1993**, *22*, 279.
40. Benedetti, E.; Di Blasio, B.; Pedone, C.; Lorenzi, G. P.; Tomasic, L.; Gramlich, V. *Nature* **1979**, *282*, 630
41. Di Blasio, B.; Benedetti, E.; Pavone, V.; Pedone, C.; Gerber, C.; Lorenzi, G. P. *Biopolymers* **1989**, *28*, 203
42. Kulp, J. L.; Clark, T. D. *Chem. Eur. J.* **2009,** *15*, 11867.
43. Navarro, E.; Fenude, E.; Celda, B. *Biopolymers* **2004**, *73*, 229.
44. Jadhav, K. B.; Lichtenecker, R. J.; Bullach, A.; Mandal, B.; Arndt, H.-D. *Chem. Eur. J.* **2015**, *21*, 5898.
45. (a) Berl, V.; Huc, I.; Khoury, R. G.; Krische, M. J.; Lehn, J. -M. *Nature* **2000**, *407*, 720. (b) Gan, Q.; Wang, X.; Kauffmann, B.; Rosu, F.; Ferrand, Y.; Huc. I. *Nature Nanotech.* **2017**, *12*, 447. (c) Wang, X.; Wicher, B.; Ferrand, Y.; Huc, I. *J. Am. Chem. Soc*. **2017**, *139*, 9350. (d) Li, X.; Markandeya, N.; Jonusauskas, G.; McClenaghan, N. D.; Maurizot, V.; Denisov, S. A.; Huc, I. *J. Am. Chem. Soc*. **2016**, *138*, 13568. (e) Denisov, S. A.; Gan, Q.; Wang, X.; Scarpantonio, L.; Ferrand, Y.; Kauffmann, B.; Jonusauskas, G.; Huc, I.; McClenaghan, N. D. *Angew. Chem. Int. Ed*. **2016**, *55*, 1328. (f) Shang, J.; Gan, Q.; Dawson, S. J.; Rosu, F.; Jiang, H.; Ferrand, Y.; Huc I. *Org. Lett*. **2014**, *16*, 4992. (g) Denisov, S. A.; Gan, Q.; Wang, X.; Scarpantonio, L.; Ferrand, Y.; Kauffmann, B.; Jonusauskas, G.; Huc, I.; McClenaghan, N. D. *Angew. Chem. Int. Ed.* **2016**, *55*, 1328. (h) Denisov, S. A.; Gan, Q.; Wang, X.; Scarpantonio, L.; Ferrand, Y.; Kauffmann, B.; Jonusauskas, G.; Huc, I.; McClenaghan, N. D. *Angew. Chem. Int. Ed.* **2016**, *55*, 1328. (i) Maurizot, V.; J. Léger, M.; Guionneau, P.; Huc, I. *Russ.Chem.Bull. Int.Ed.* **2004**, *53*, 1572. (j) Zhan, C.; Léger, J.-M.; Huc, I. *Angew. Chem. Int. Ed.* **2006**, *45*, 4625. (k) Haldar, D.; Jiang, H.; Léger, J.-M.; Huc, I. *Angew. Chem. Int. Ed.* **2006**, *45*, 5483.

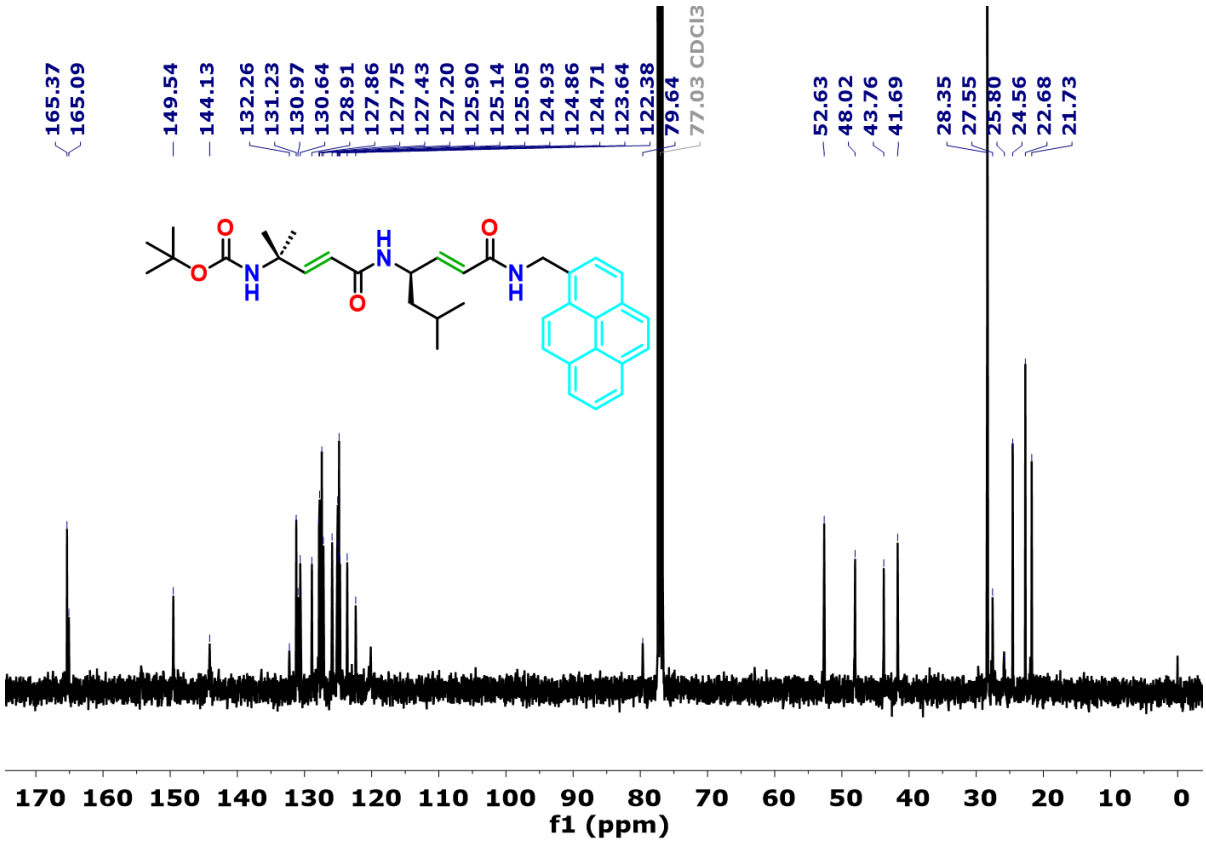
46. Misra, R.; Dey, S.; Reja, R. M.; Gopi, H. N. *Angew. Chem., Int. Ed.* **2018**, *57*, 1057.
47. Pahan, S.; Dey, S.; George, G.; Panda Mahapatra, S.; Puneeth Kumar, DR.; Gopi, H. N. *Angew. Chemie Int. Ed.* **2023**, *e202316309*
48. (a) Zullo, V.; Iuliano, A.; Pescitelli, G.; Zinna, F. *Chem. Eur. J.* **2022**, *28*, e202104226. (b) Takaishi, K.; Murakami, S.; Iwachido, K.; Ema, T. *Chem. Sci.* **2021**, *12*, 14570. (c) Liu, Z.; Jiang, Y.; Jiang, J.; Yuan, C.; Wang, D.; Liu, M. *RSC Adv.* **2020**, *10*, 6772. (d) Gao, Y.; Ren, C.; Lin, X.; He, T. *Front. Chem.* **2020**, *8*, 458. (e) Ohishi, Y.; Inouye, M. *Tetrahedron Lett.* **2019**, *60*, 151232. (f) Yang, D.; Duan, P.; Zhang, L.; Liu, M. *Nat. Commun.* **2017**, *8*, 15727. (g) Zhang, Y.; Yang, D.; Han, J.; Zhou, J.; Jin, Q.; Liu, M.; Duan, P. *Langmuir* **2018**, *34*, 5821. (h) Feng, X.; Wang, X.; Redshaw, C.; Tang, B. Z. *Chem. Soc. Rev.* **2023**, *52*, 6715.
49. Mali, S. M.; Bandyopadhyay, A.; Jadhav, S. V.; Ganesh Kumar, M.; Gopi, H. N. *Org. Biomol. Chem.* **2011**, *9*, 6566.

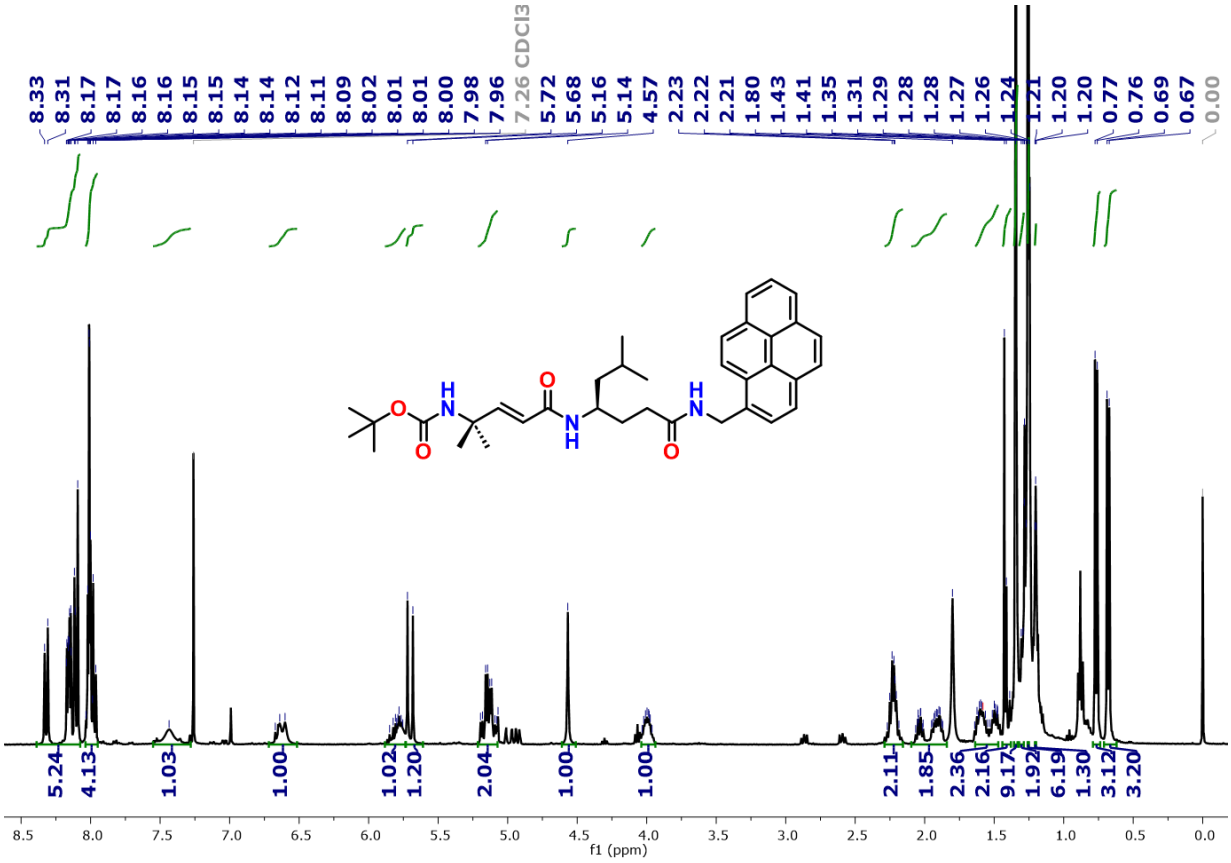
4.10. ^{1}H, ^{13}C NMR and Mass Spectra of Peptides P1-P5

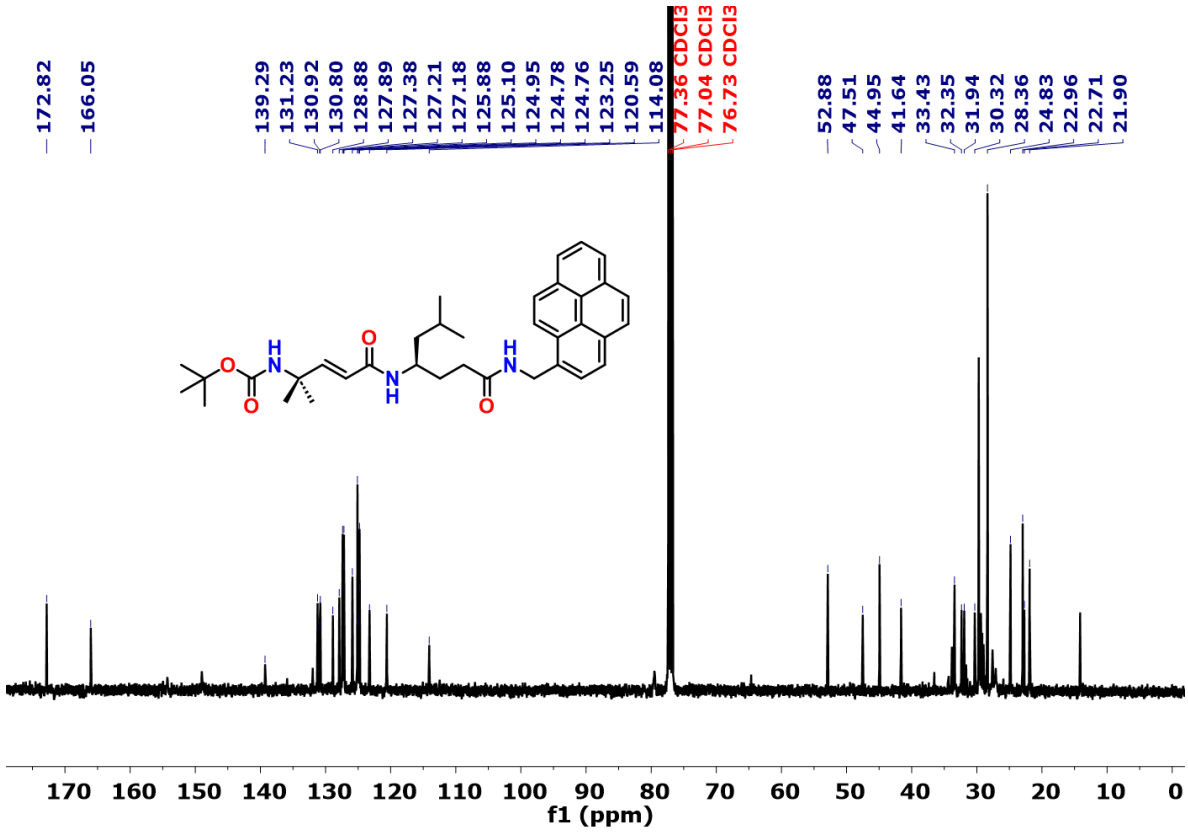


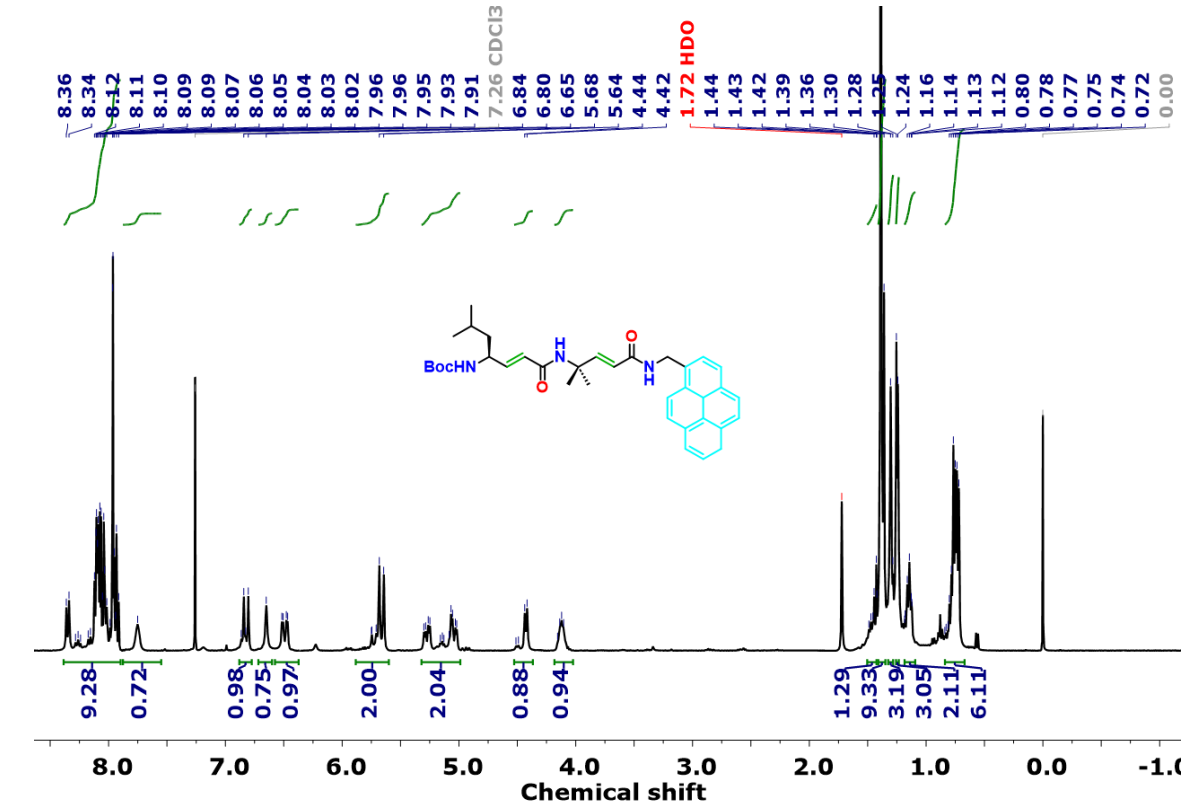


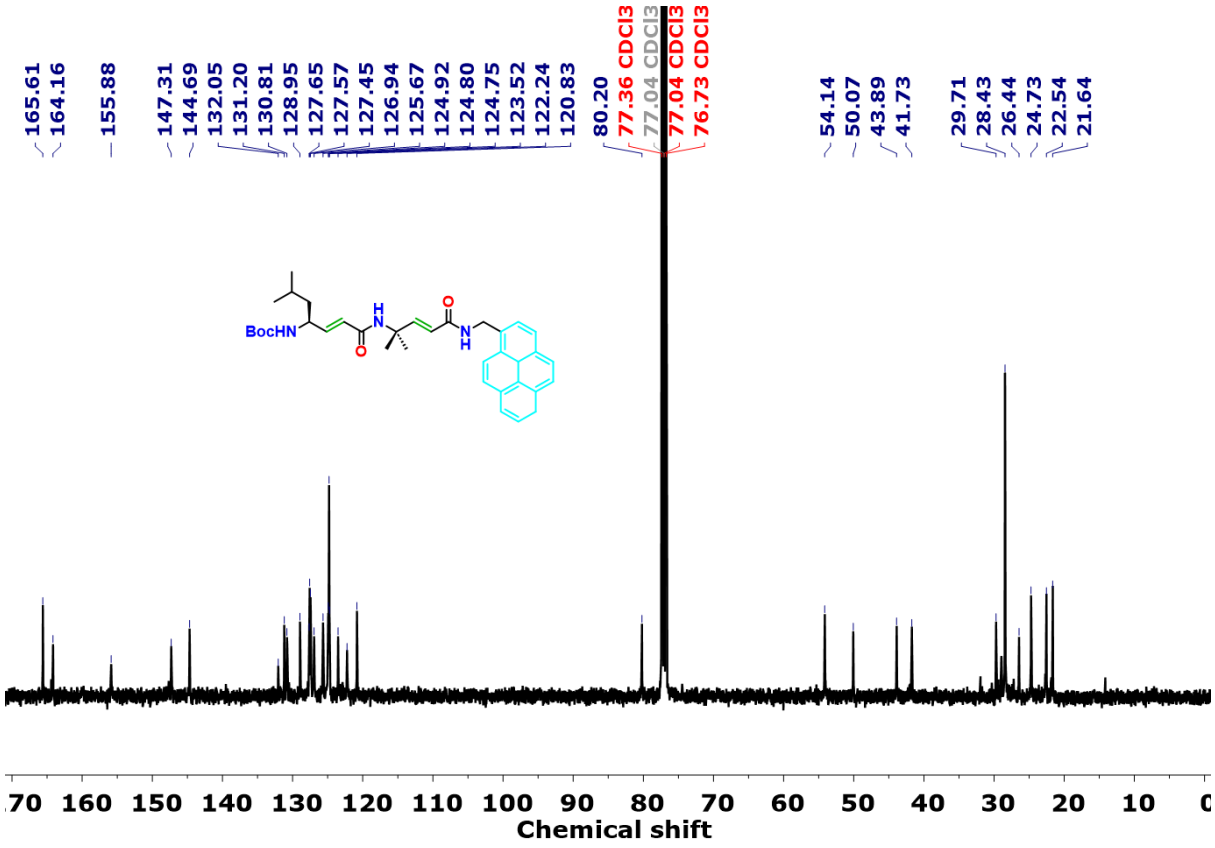

8.15 8.13 8.11 8.10 8.09 8.08 8.05 8.04 8.03 8.02 8.00 7.97 7.95 7.93 7.26 CDCl3 7.26 6.69 6.66 6.65 5.71 5.70 5.67 5.66 5.39 5.38 5.36 5.34 4.83 1.69 HDO 1.32 1.29 1.25 1.20 1.19 1.18 1.17 1.16 1.15 1.10 0.88 0.77 0.75 0.72 0.70 0.67 0.65 -0.00
0.91 0.85 8.80 1.14 0.97 0.85 0.98 1.18 1.03 1.09 1.09 1.18 9.27 2.21 3.20 3.08 6.26
8.5 8.0 7.5 7.0 6.5 6.0 5.5 5.0 4.5 4.0 3.5 3.0 2.5 2.0 1.5 1.0 0.5 0.0
f1 (ppm)

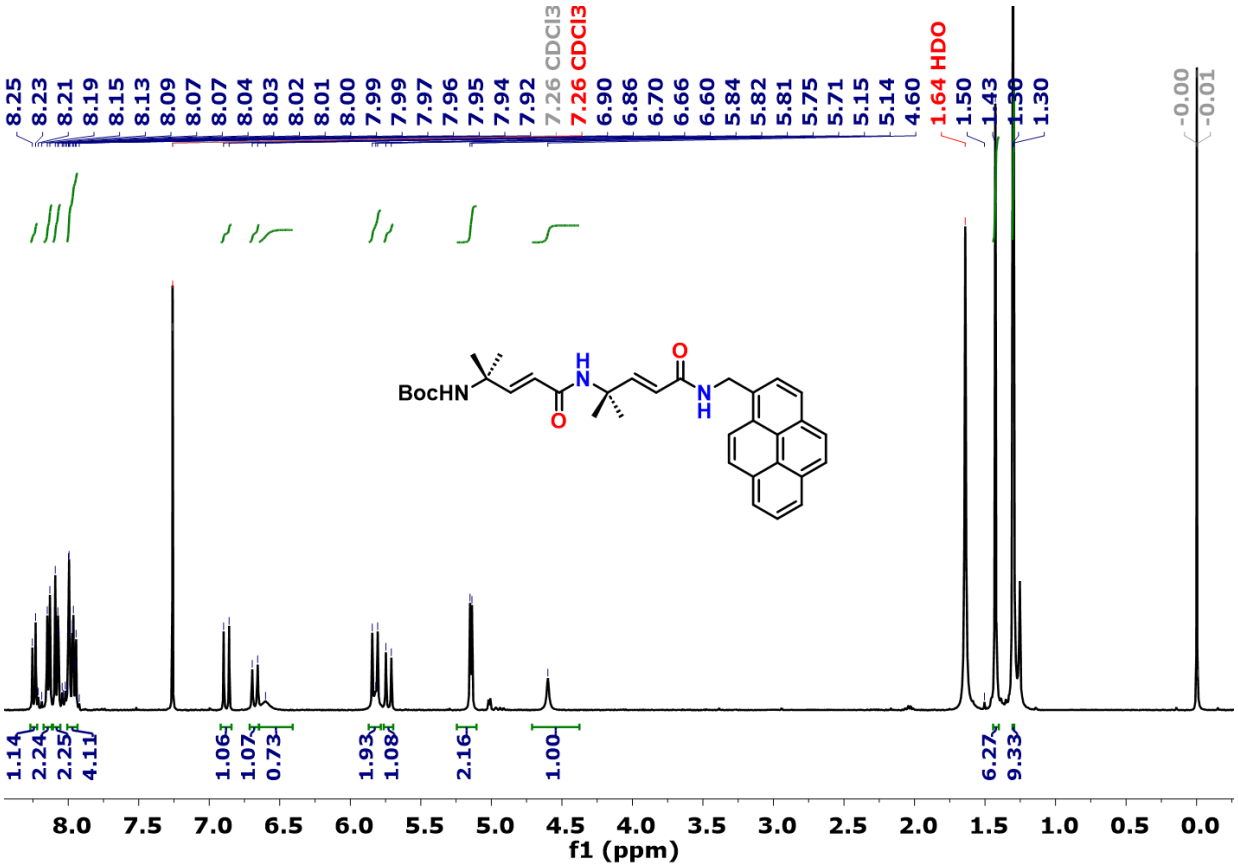

165.37 165.09 149.54 144.13 132.26 131.23 130.97 130.64 128.91 127.86 127.75 127.43 127.20 125.90 125.14 125.05 124.93 124.86 124.71 123.64 122.38 79.64 77.03 CDCl3 52.63 48.02 43.76 41.69 28.35 27.55 25.80 24.56 22.68 21.73
170 160 150 140 130 120 110 100 90 80 70 60 50 40 30 20 10 0
f1 (ppm)

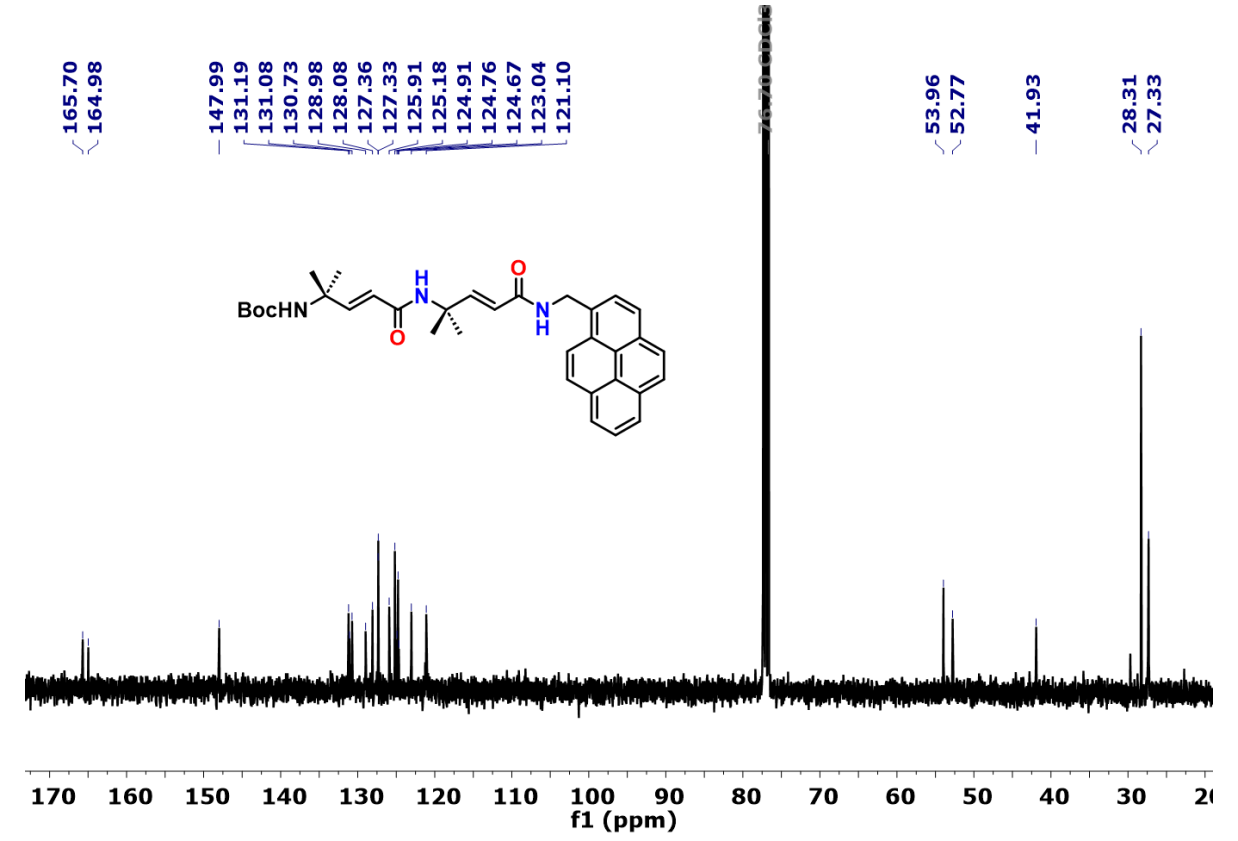

8.33 8.31 8.17 8.17 8.16 8.16 8.15 8.15 8.14 8.14 8.12 8.11 8.09 8.02 8.01 8.01 8.00 7.98 7.96 7.26 CDCl3 5.72 5.68 5.16 5.14 4.57 2.23 2.22 2.21 1.80 1.43 1.41 1.35 1.31 1.29 1.28 1.28 1.27 1.26 1.24 1.21 1.20 1.20 0.77 0.76 0.69 0.67 0.00
5.24 4.13 1.03 1.00 1.02 1.20 2.04 1.00 1.00 2.11 1.85 2.36 2.16 9.17 1.92 6.19 1.30 3.12 3.20
8.5 8.0 7.5 7.0 6.5 6.0 5.5 5.0 4.5 4.0 3.5 3.0 2.5 2.0 1.5 1.0 0.5 0.0
f1 (ppm)

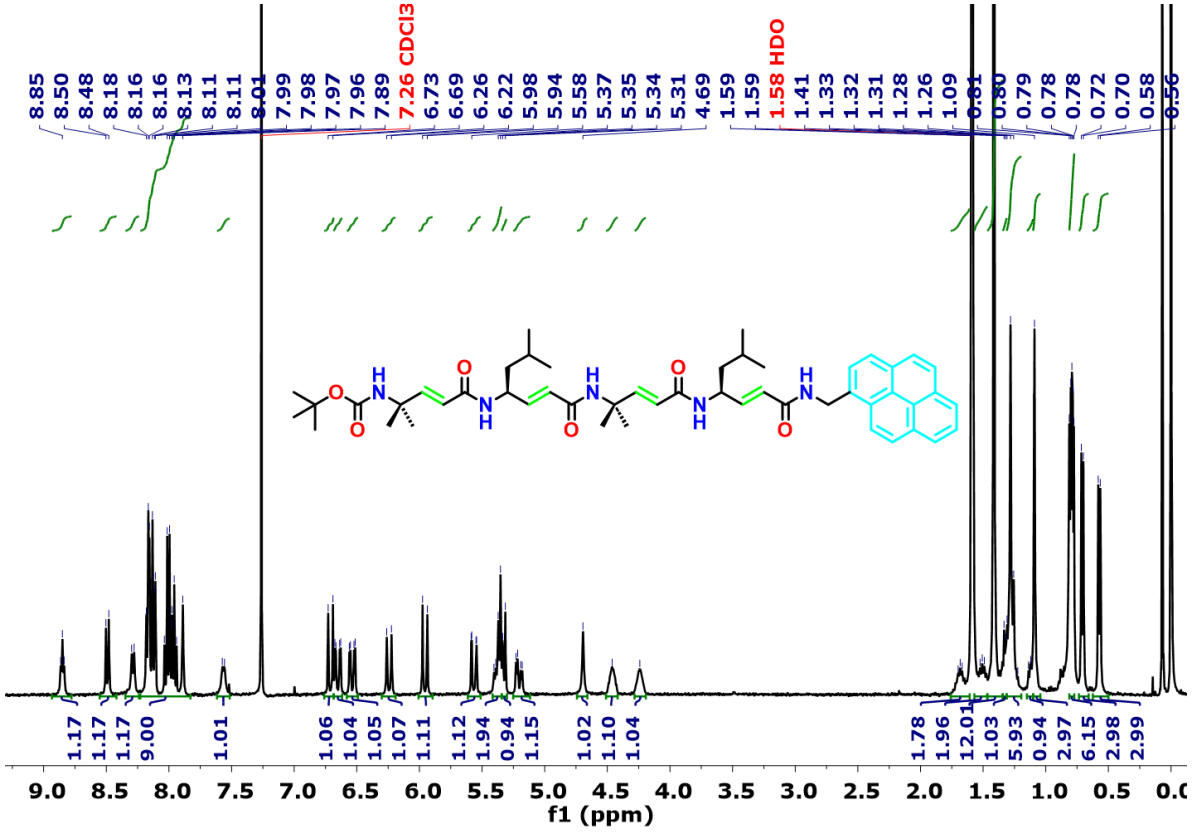

172.82 166.05 139.29 131.23 130.92 130.80 128.88 127.89 127.38 127.21 127.18 125.88 125.10 124.95 124.78 124.76 123.25 120.59 114.08 77.36 CDCl3 77.04 CDCl3 76.73 CDCl3 52.88 47.51 44.95 41.64 33.43 32.35 31.94 30.32 28.36 24.83 22.96 22.71 21.90
170 160 150 140 130 120 110 100 90 80 70 60 50 40 30 20 10 0
f1 (ppm)

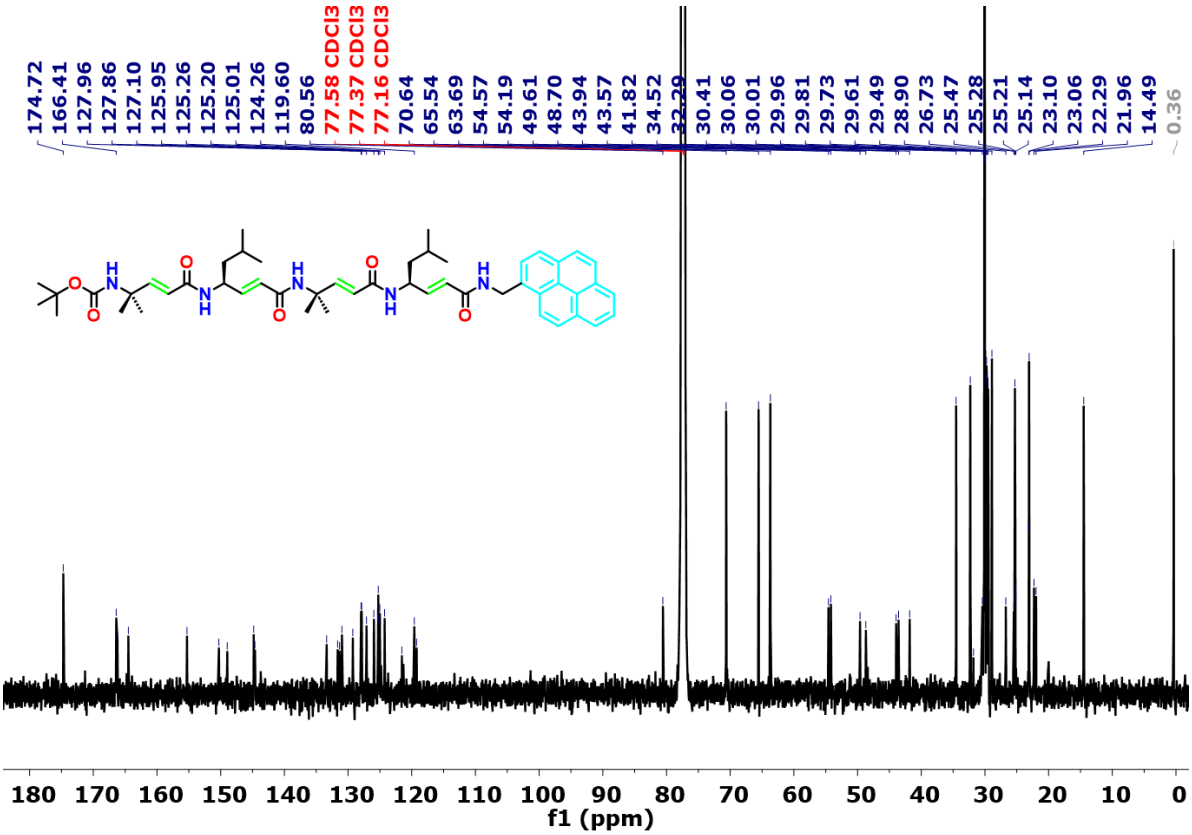

8.36 8.34 8.12 8.11 8.10 8.09 8.09 8.07 8.06 8.05 8.04 8.03 8.02 7.96 7.96 7.95 7.93 7.91 7.26 CDCl3 6.84 6.80 6.65 5.68 5.64 4.44 4.42 1.72 HDO 1.44 1.43 1.42 1.39 1.36 1.30 1.28 1.25 1.24 1.16 1.14 1.13 1.12 0.80 0.78 0.77 0.75 0.74 0.72 0.00
BocHN
9.28 0.72 0.98 0.75 0.97 2.00 2.04 0.88 0.94 1.29 9.33 3.19 3.05 2.11 6.11
8.0 7.0 6.0 5.0 4.0 3.0 2.0 1.0 0.0
Chemical shift

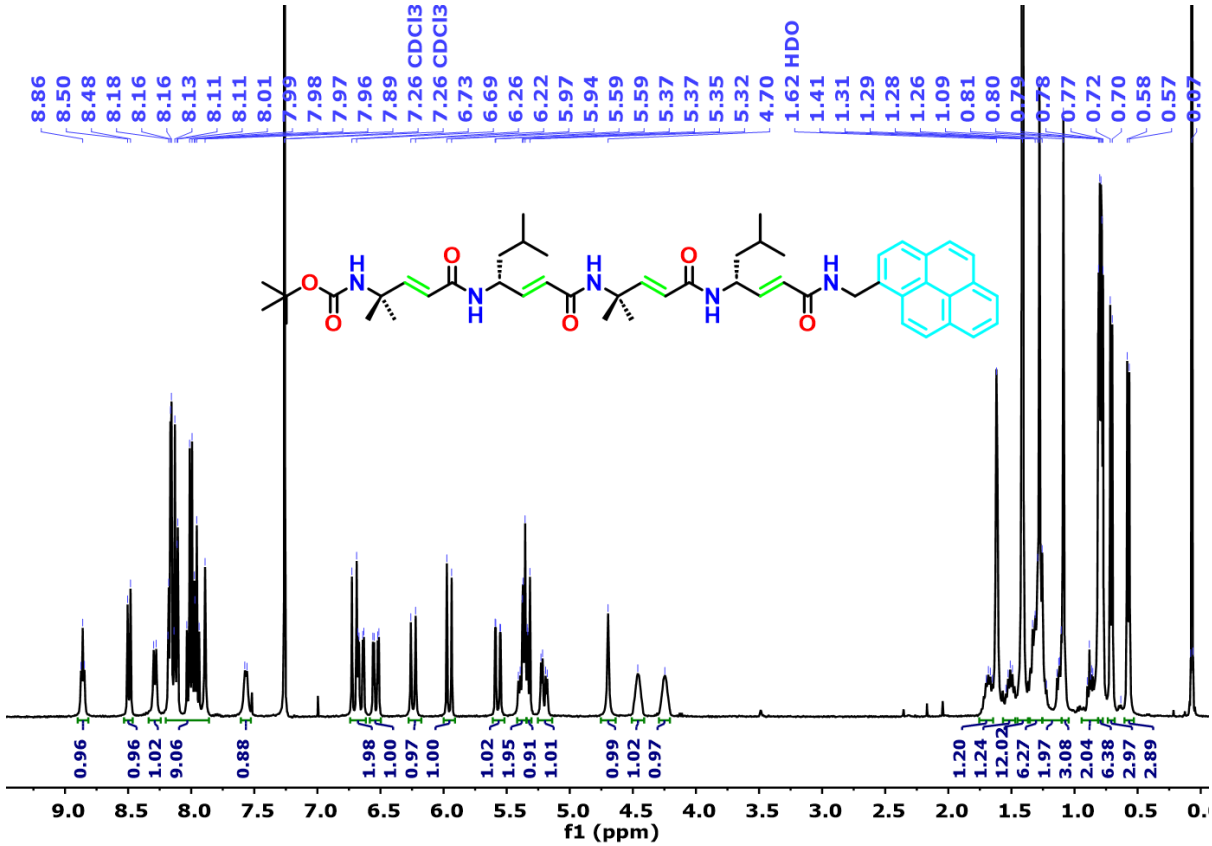

165.61 164.16 155.88 147.31 144.69 132.05 131.20 130.81 128.95 127.65 127.57 127.45 126.94 125.67 124.92 124.80 124.75 123.52 122.24 120.83 80.20 77.36 CDCl3 77.04 CDCl3 77.04 CDCl3 76.73 CDCl3 54.14 50.07 43.89 41.73 29.71 28.43 26.44 24.73 22.54 21.64
BocHN
70 160 150 140 130 120 110 100 90 80 70 60 50 40 30 20 10
Chemical shift

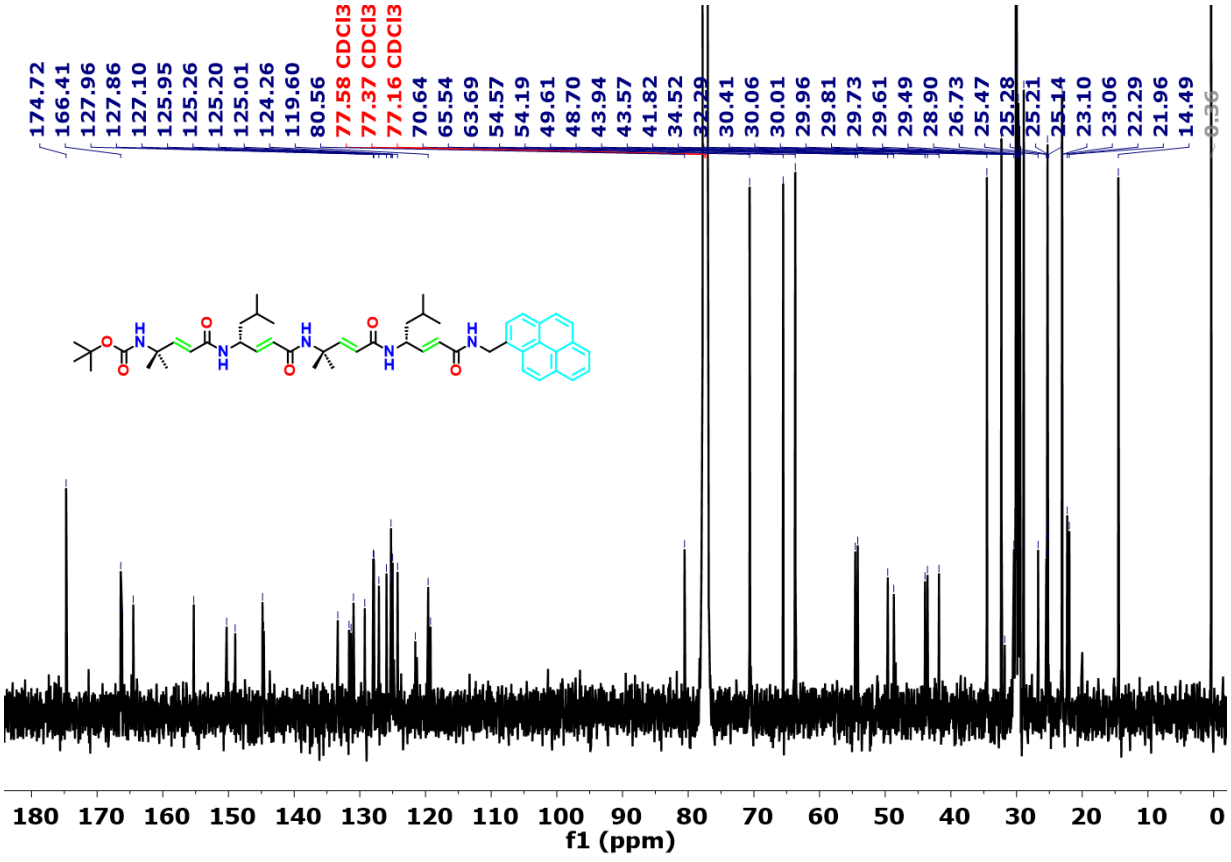

8.25 8.23 8.21 8.19 8.15 8.13 8.09 8.07 8.07 8.04 8.03 8.02 8.01 8.00 7.99 7.99 7.97 7.96 7.95 7.94 7.92 7.26 CDCl3 7.26 CDCl3 6.90 6.86 6.70 6.66 6.60 5.84 5.82 5.81 5.75 5.71 5.15 5.14 4.60 1.64 HDO 1.50 1.43 1.30 1.30 -0.00 -0.01
BocHN
1.14 2.24 2.25 4.11 1.06 1.07 0.73 1.93 1.08 2.16 1.00 6.27 9.33
8.0 7.5 7.0 6.5 6.0 5.5 5.0 4.5 4.0 3.5 3.0 2.5 2.0 1.5 1.0 0.5 0.0
f1 (ppm)

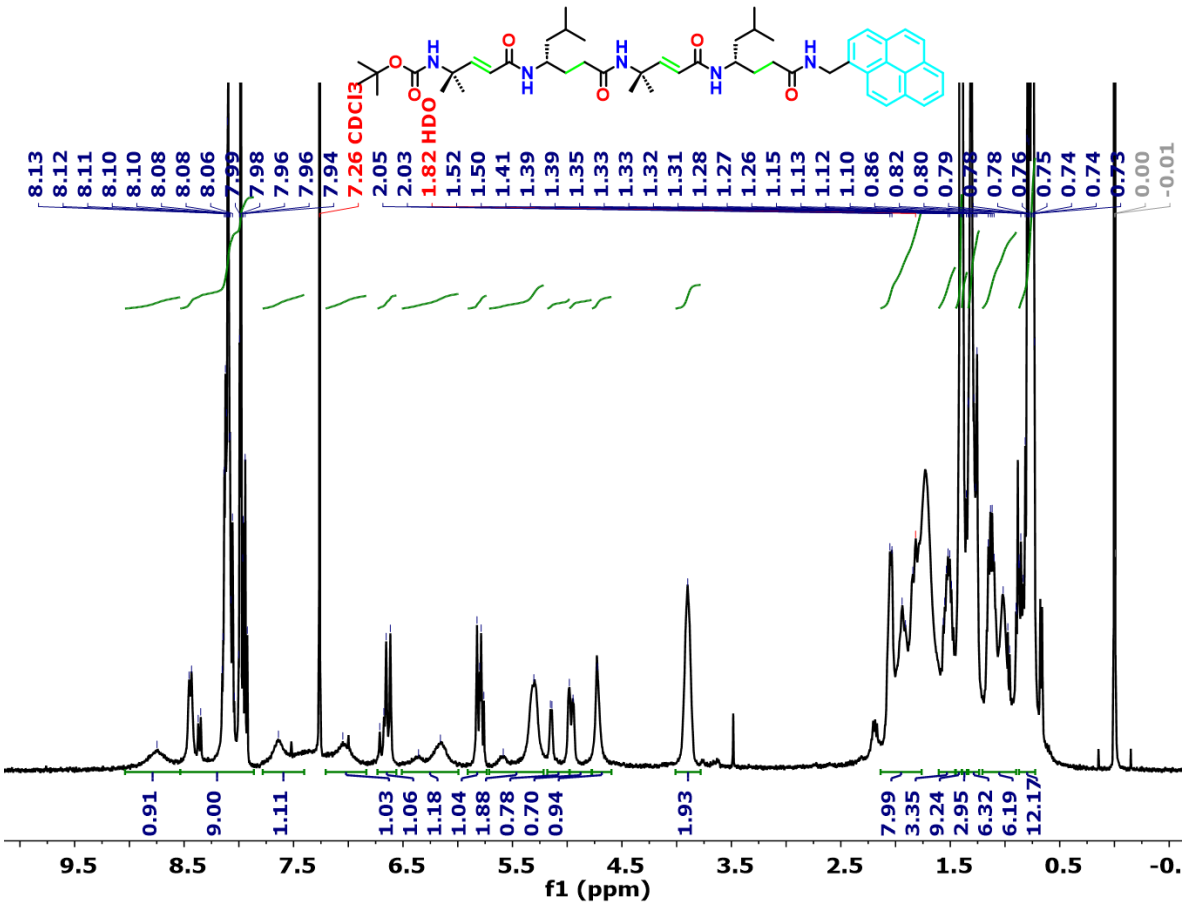

165.70 164.98 147.99 131.19 131.08 130.73 128.98 128.08 127.36 127.33 125.91 125.18 124.91 124.76 124.67 123.04 121.10 53.96 52.77 41.93 28.31 27.33
BocHN
170 160 150 140 130 120 110 100 90 80 70 60 50 40 30
f1 (ppm)

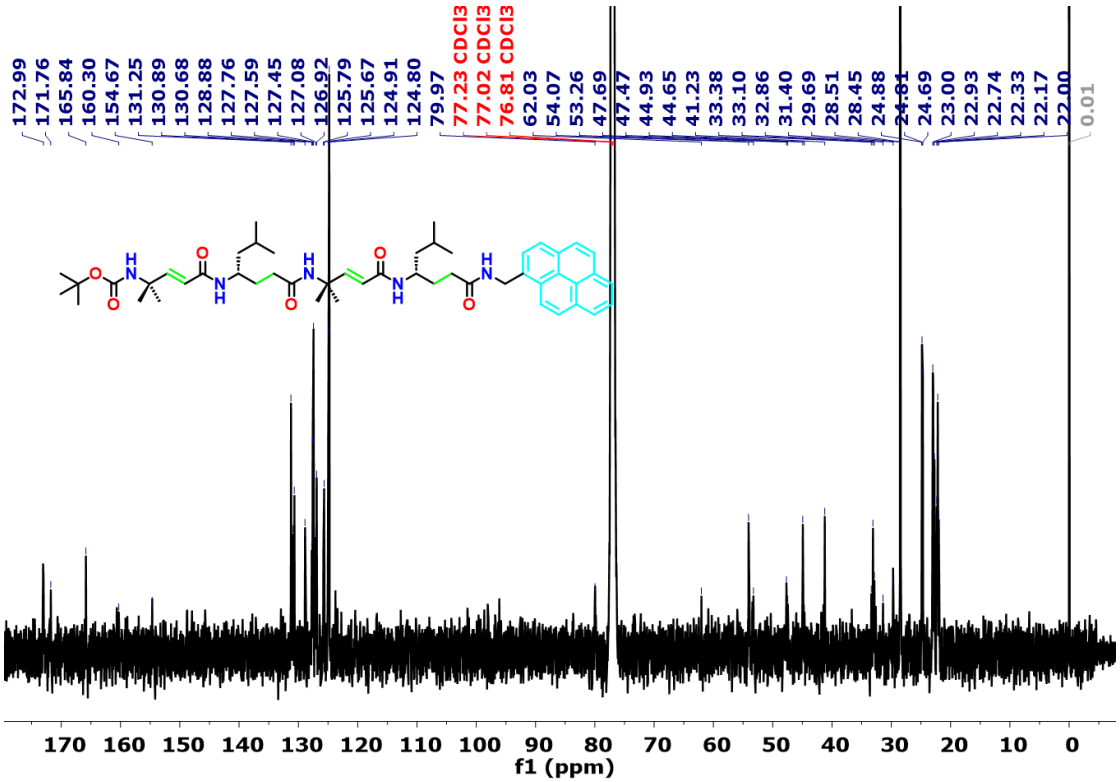

8.85 8.50 8.48 8.18 8.16 8.16 8.13 8.11 8.11 8.01 7.99 7.98 7.97 7.96 7.89 7.26 CDCl3 6.73 6.69 6.26 6.22 5.98 5.94 5.58 5.37 5.35 5.34 5.31 4.69 1.59 1.59 1.58 HDO 1.41 1.33 1.32 1.31 1.28 1.26 1.09 0.81 0.80 0.79 0.78 0.78 0.72 0.70 0.58 0.56
1.17 1.17 1.17 9.00 1.01 1.06 1.04 1.05 1.07 1.11 1.12 1.94 0.94 1.15 1.02 1.10 1.04 1.78 1.96 12.01 1.03 5.93 0.94 2.97 6.15 2.98 2.99
9.0 8.5 8.0 7.5 7.0 6.5 6.0 5.5 5.0 4.5 4.0 3.5 3.0 2.5 2.0 1.5 1.0 0.5 0.0
f1 (ppm)

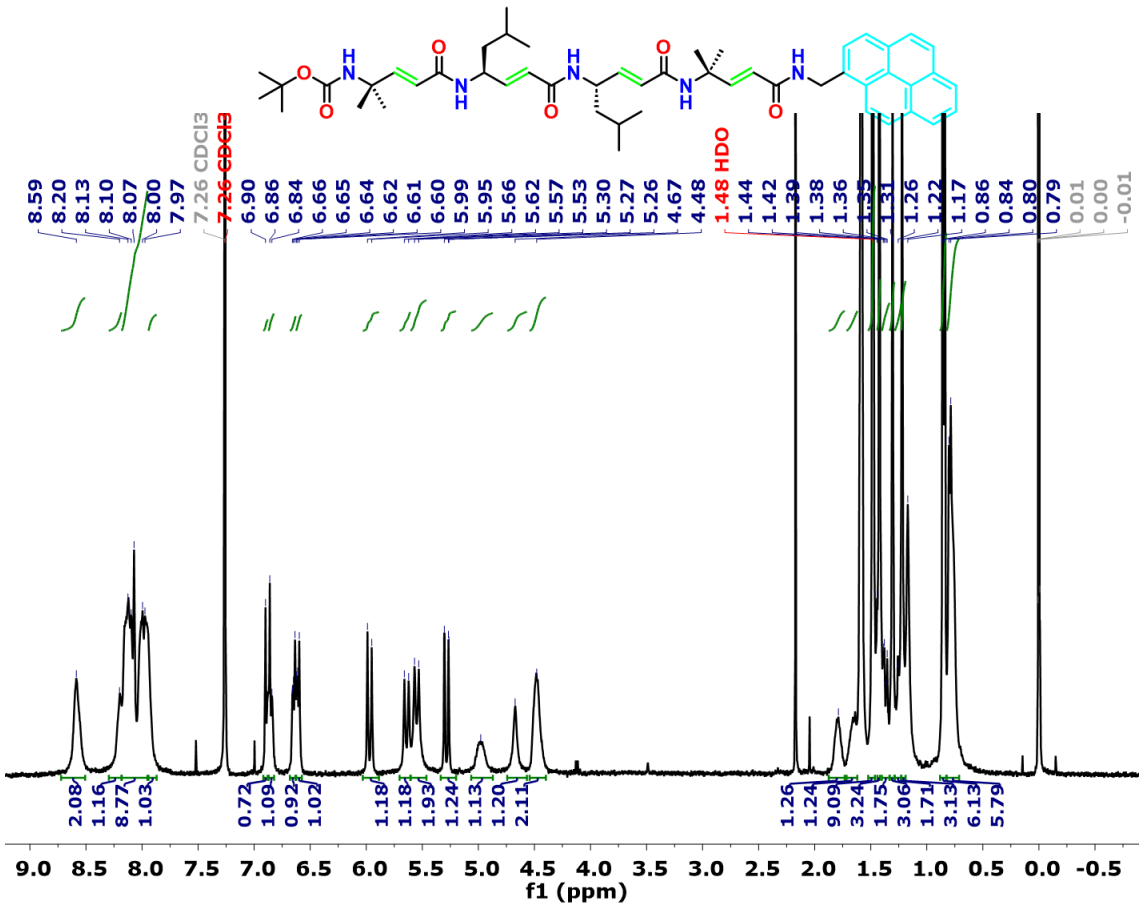

174.72 166.41 127.96 127.86 127.10 125.95 125.26 125.20 125.01 124.26 119.60 80.56 77.58 CDCl3 77.37 CDCl3 77.16 CDCl3 70.64 65.54 63.69 54.57 54.19 49.61 48.70 43.94 43.57 41.82 34.52 32.29 30.41 30.06 30.01 29.96 29.81 29.73 29.61 29.49 28.90 26.73 25.47 25.28 25.21 25.14 23.10 23.06 22.29 21.96 14.49 0.36
180 170 160 150 140 130 120 110 100 90 80 70 60 50 40 30 20 10 0
f1 (ppm)

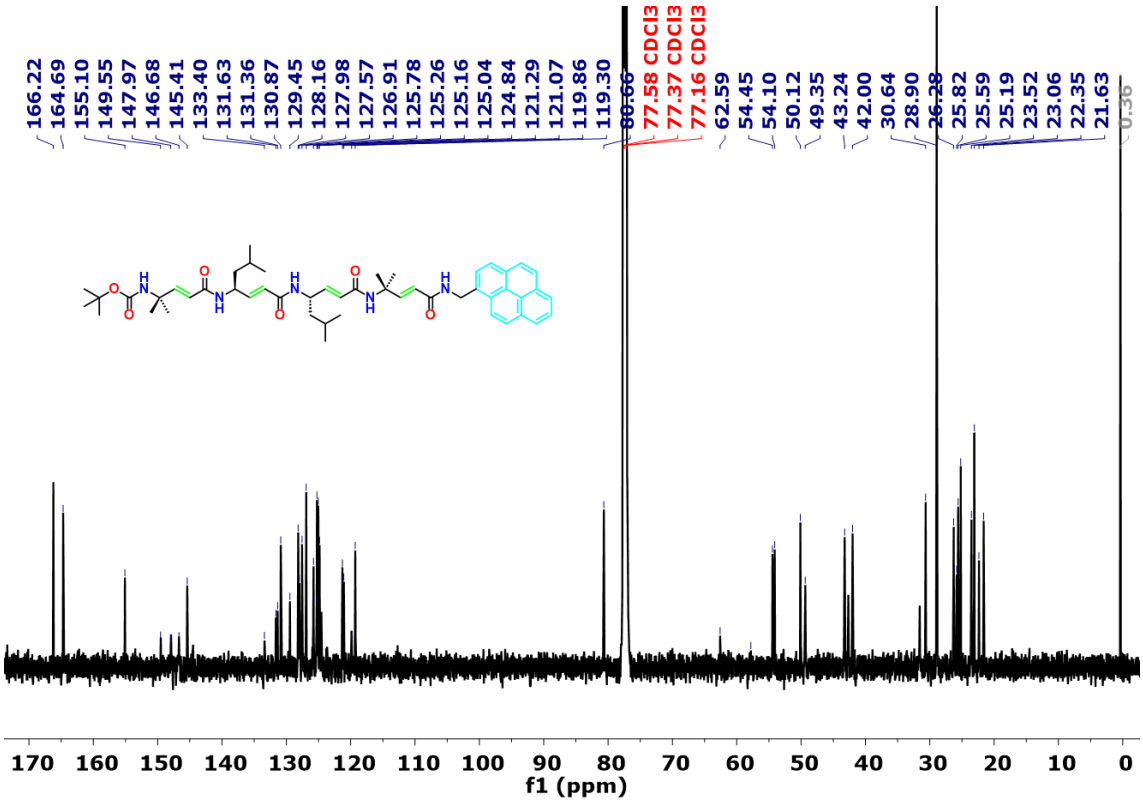

8.86 8.50 8.48 8.18 8.16 8.16 8.13 8.11 8.11 8.01 7.99 7.98 7.97 7.96 7.89 7.26 CDCl3 7.26 CDCl3 6.73 6.69 6.26 6.22 5.97 5.94 5.59 5.59 5.37 5.37 5.35 5.32 4.70 1.62 HDO 1.41 1.31 1.29 1.28 1.26 1.09 0.81 0.80 0.79 0.78 0.77 0.72 0.70 0.58 0.57 0.07
0.96 0.96 1.02 9.06 0.88 1.98 1.00 0.97 1.00 1.02 1.95 0.91 1.01 0.99 1.02 0.97 1.20 1.24 12.02 6.27 1.97 3.08 2.04 6.38 2.97 2.89
f1 (ppm)

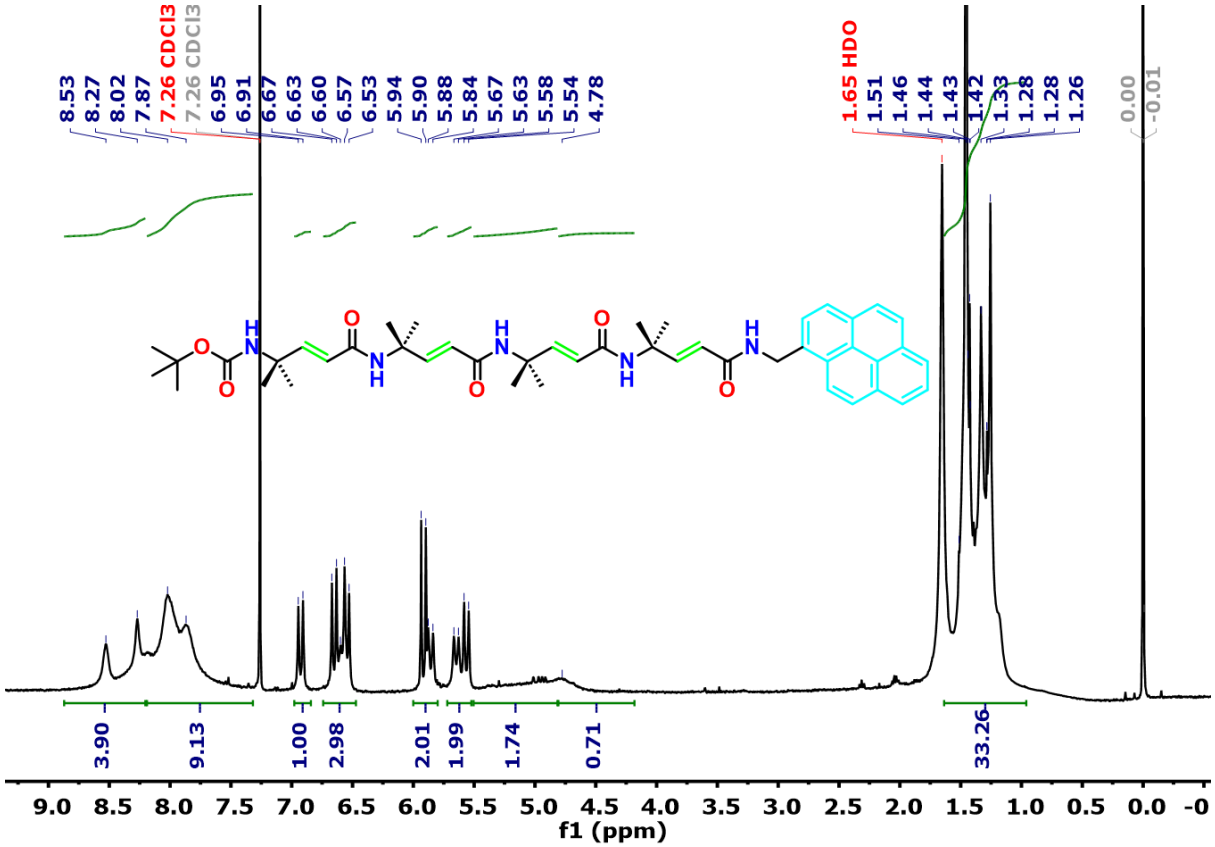

174.72 166.41 127.96 127.86 127.10 125.95 125.26 125.20 125.01 124.26 119.60 80.56 77.58 CDCl3 77.37 CDCl3 77.16 CDCl3 70.64 65.54 63.69 54.57 54.19 49.61 48.70 43.94 43.57 41.82 34.52 32.29 30.41 30.06 30.01 29.96 29.81 29.73 29.61 29.49 28.90 26.73 25.47 25.28 25.21 25.14 23.10 23.06 22.29 21.96 14.49
f1 (ppm)

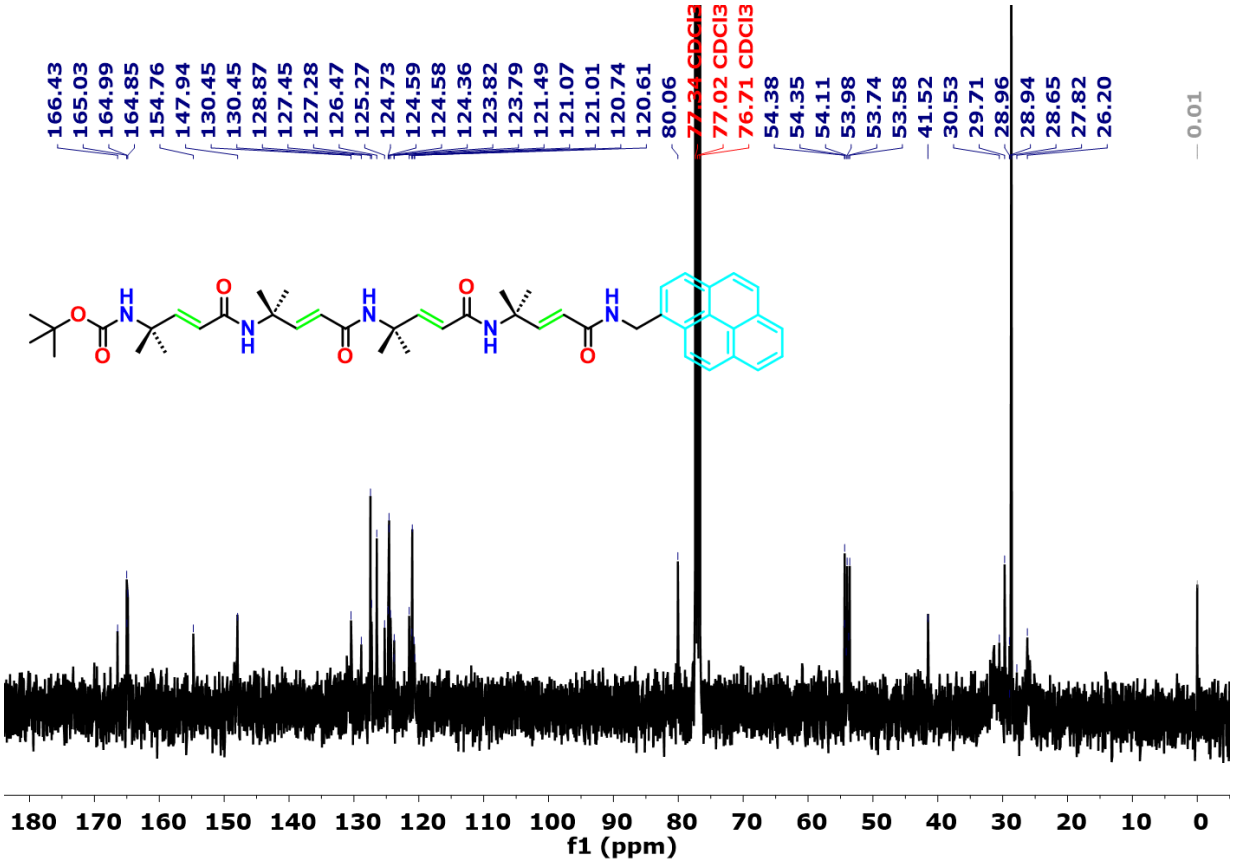

8.13 8.12 8.11 8.10 8.10 8.08 8.08 8.06 7.99 7.98 7.96 7.96 7.94 7.26 CDCl3 2.05 2.03 1.82 HDO 1.52 1.50 1.41 1.39 1.39 1.35 1.33 1.33 1.32 1.31 1.28 1.27 1.26 1.15 1.13 1.12 1.10 0.86 0.82 0.80 0.79 0.78 0.78 0.76 0.75 0.74 0.74 0.73 0.00 -0.01
0.91 9.00 1.11 1.03 1.06 1.18 1.04 1.88 0.78 0.70 0.94 1.93 7.99 3.35 9.24 2.95 6.32 6.19 12.17
9.5 8.5 7.5 6.5 5.5 4.5 3.5 2.5 1.5 0.5 -0.
f1 (ppm)

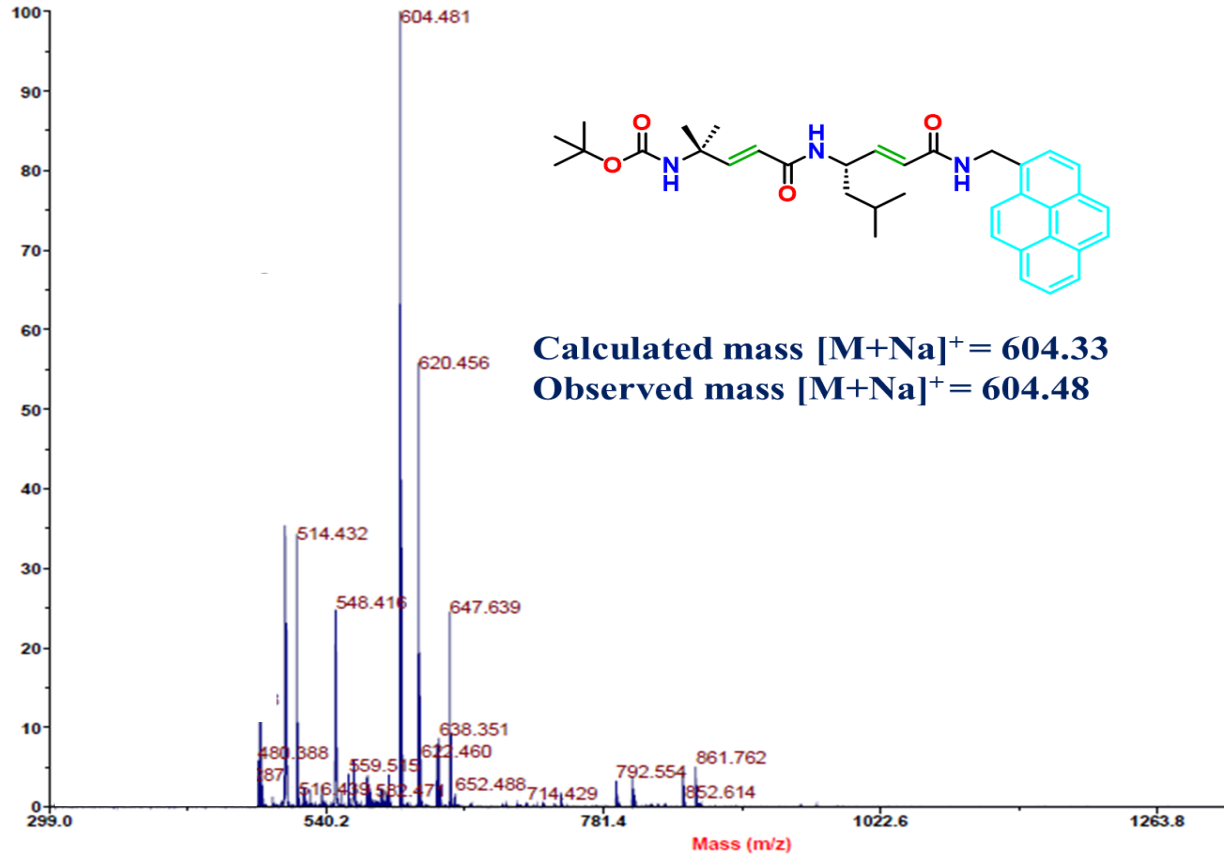

172.99 171.76 165.84 160.30 154.67 131.25 130.89 130.68 128.88 127.76 127.59 127.45 127.08 126.92 125.79 125.67 124.91 124.80 79.97 77.23 CDCl3 77.02 CDCl3 76.81 CDCl3 62.03 54.07 53.26 47.69 47.47 44.93 44.65 41.23 33.38 33.10 32.86 31.40 29.69 28.51 28.45 24.88 24.81 24.69 23.00 22.93 22.74 22.33 22.17 22.00 0.01
170 160 150 140 130 120 110 100 90 80 70 60 50 40 30 20 10 0
f1 (ppm)


8.59 8.20 8.13 8.10 8.07 8.00 7.97 7.26 CDCl3 7.26 CDCl3 6.90 6.86 6.84 6.66 6.65 6.64 6.62 6.61 6.60 5.99 5.95 5.66 5.62 5.57 5.53 5.30 5.27 5.26 4.67 4.48 1.48 HDO 1.44 1.42 1.39 1.38 1.36 1.35 1.31 1.26 1.22 1.17 0.86 0.84 0.80 0.79 0.01 0.00 -0.01
2.08 1.16 8.77 1.03 0.72 1.09 0.92 1.02 1.18 1.18 1.93 1.24 1.13 1.20 2.11 1.26 1.24 9.09 3.24 1.75 3.06 1.71 3.13 6.13 5.79
9.0 8.5 8.0 7.5 7.0 6.5 6.0 5.5 5.0 4.5 4.0 3.5 3.0 2.5 2.0 1.5 1.0 0.5 0.0 -0.5
f1 (ppm)

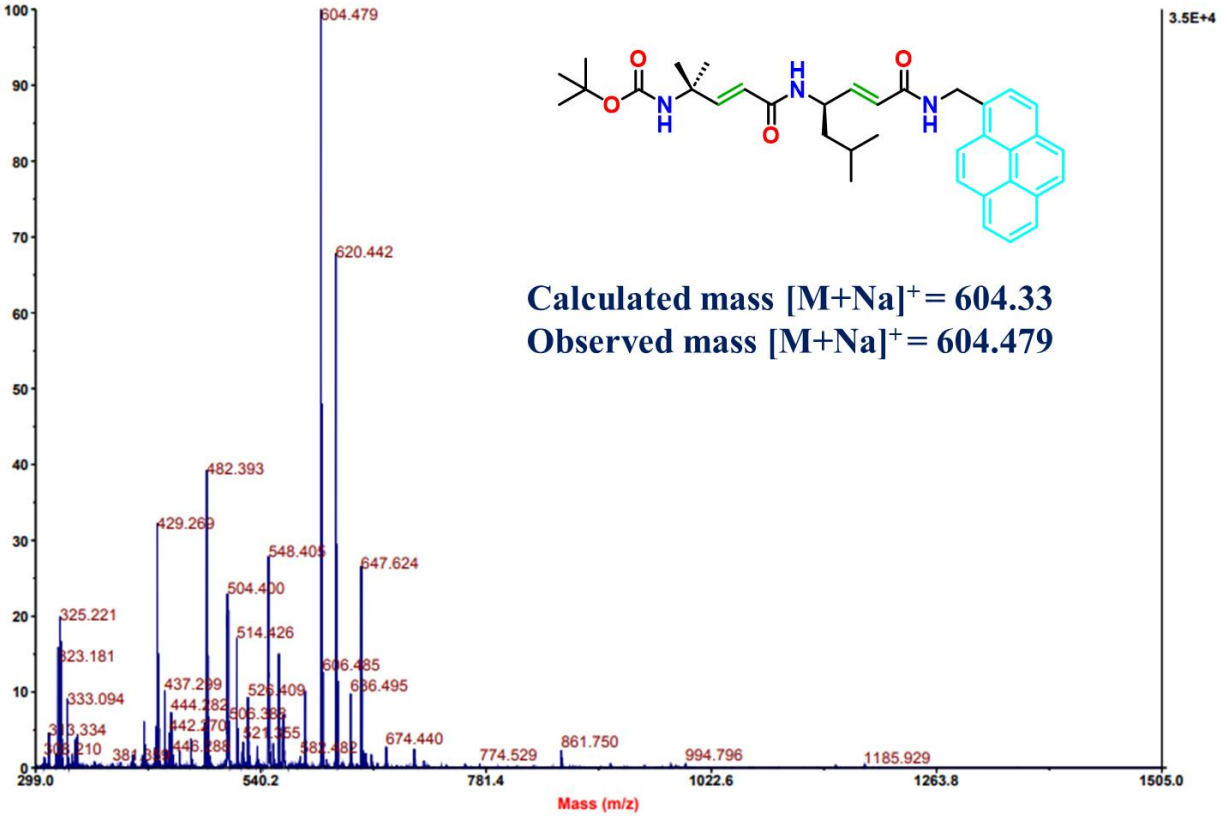

166.22 164.69 155.10 149.55 147.97 146.68 145.41 133.40 131.63 131.36 130.87 129.45 128.16 127.98 127.57 126.91 125.78 125.26 125.16 125.04 124.84 121.29 121.07 119.86 119.30 80.66 77.58 CDCl3 77.37 CDCl3 77.16 CDCl3 62.59 54.45 54.10 50.12 49.35 43.24 42.00 30.64 28.90 26.28 25.82 25.59 25.19 23.52 23.06 22.35 21.63 0.36
170 160 150 140 130 120 110 100 90 80 70 60 50 40 30 20 10 0
f1 (ppm)


8.53
8.27
8.02
7.87
7.26 CDCl3
7.26 CDCl3
6.95
6.91
6.67
6.63
6.60
6.57
6.53
5.94
5.90
5.88
5.84
5.67
5.63
5.58
5.54
4.78
1.65 HDO
1.51
1.46
1.44
1.43
1.42
1.33
1.28
1.28
1.26
0.00
-0.01
3.90
9.13
1.00
2.98
2.01
1.99
1.74
0.71
33.26
9.0 8.5 8.0 7.5 7.0 6.5 6.0 5.5 5.0 4.5 4.0 3.5 3.0 2.5 2.0 1.5 1.0 0.5 0.0 -0
f1 (ppm)

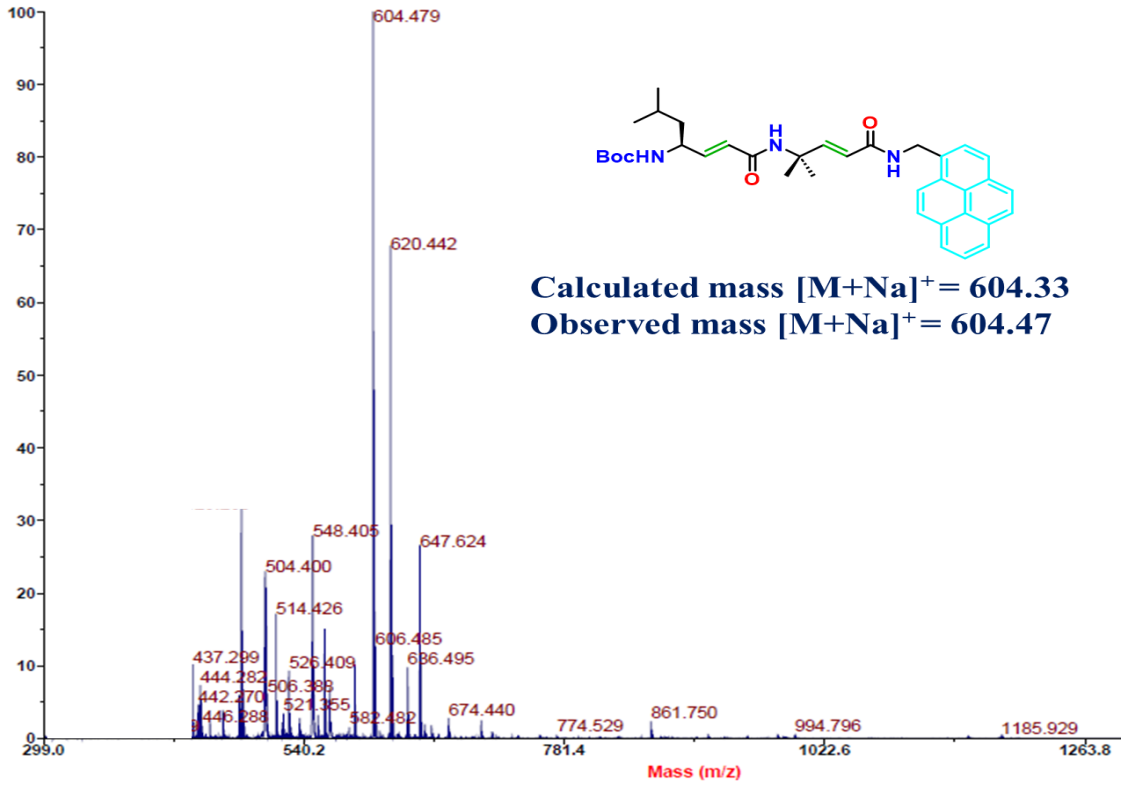

166.43
165.03
164.99
164.85
154.76
147.94
130.45
130.45
128.87
127.45
127.28
126.47
125.27
124.73
124.59
124.58
124.36
123.82
123.79
121.49
121.07
121.01
120.74
120.61
80.06
77.34 CDCl3
77.02 CDCl3
76.71 CDCl3
54.38
54.35
54.11
53.98
53.74
53.58
41.52
30.53
29.71
28.96
28.94
28.65
27.82
26.20
0.01
180 170 160 150 140 130 120 110 100 90 80 70 60 50 40 30 20 10 0
f1 (ppm)

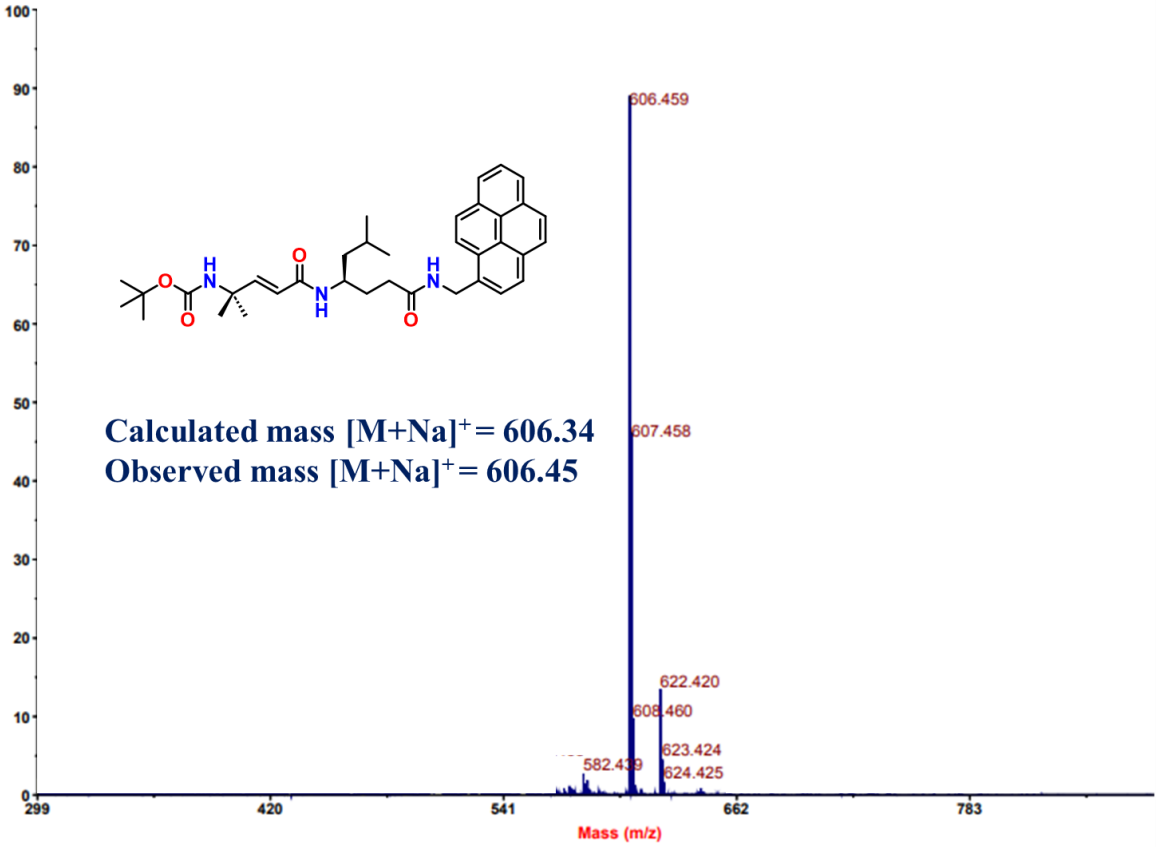


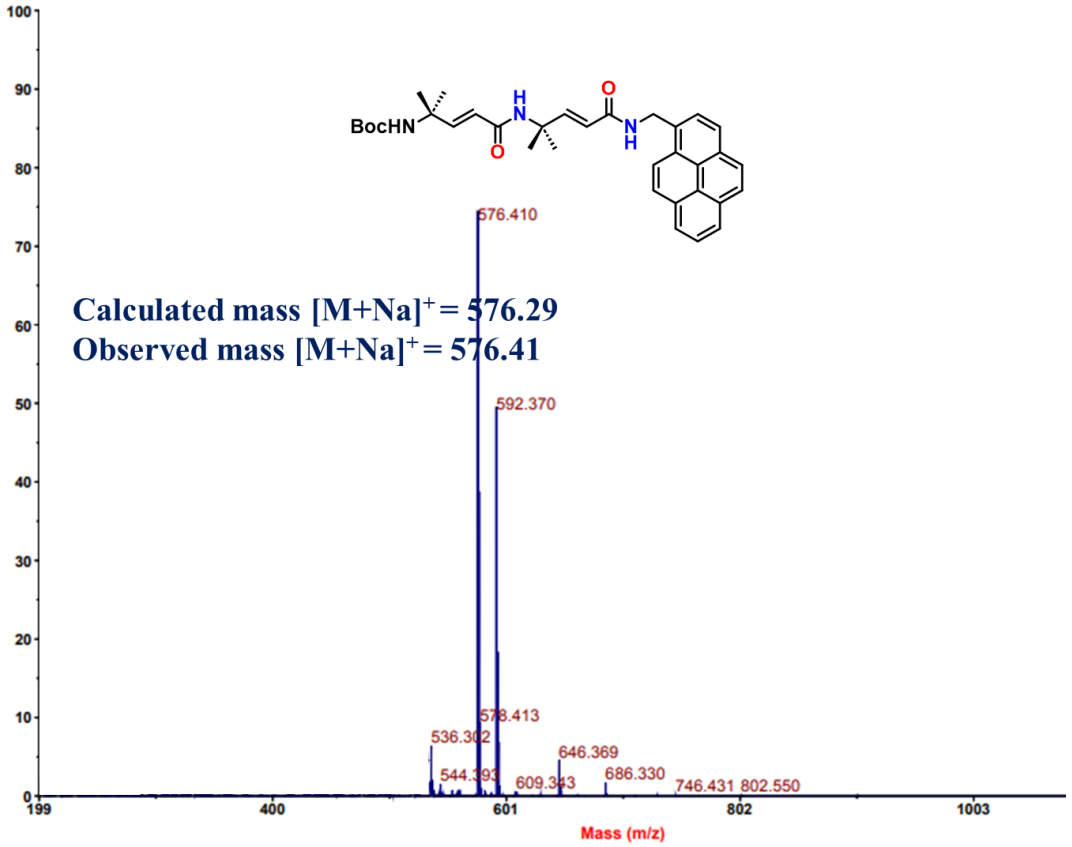
Calculated mass $[M+Na]^+ = 604.33$
Observed mass $[M+Na]^+ = 604.48$

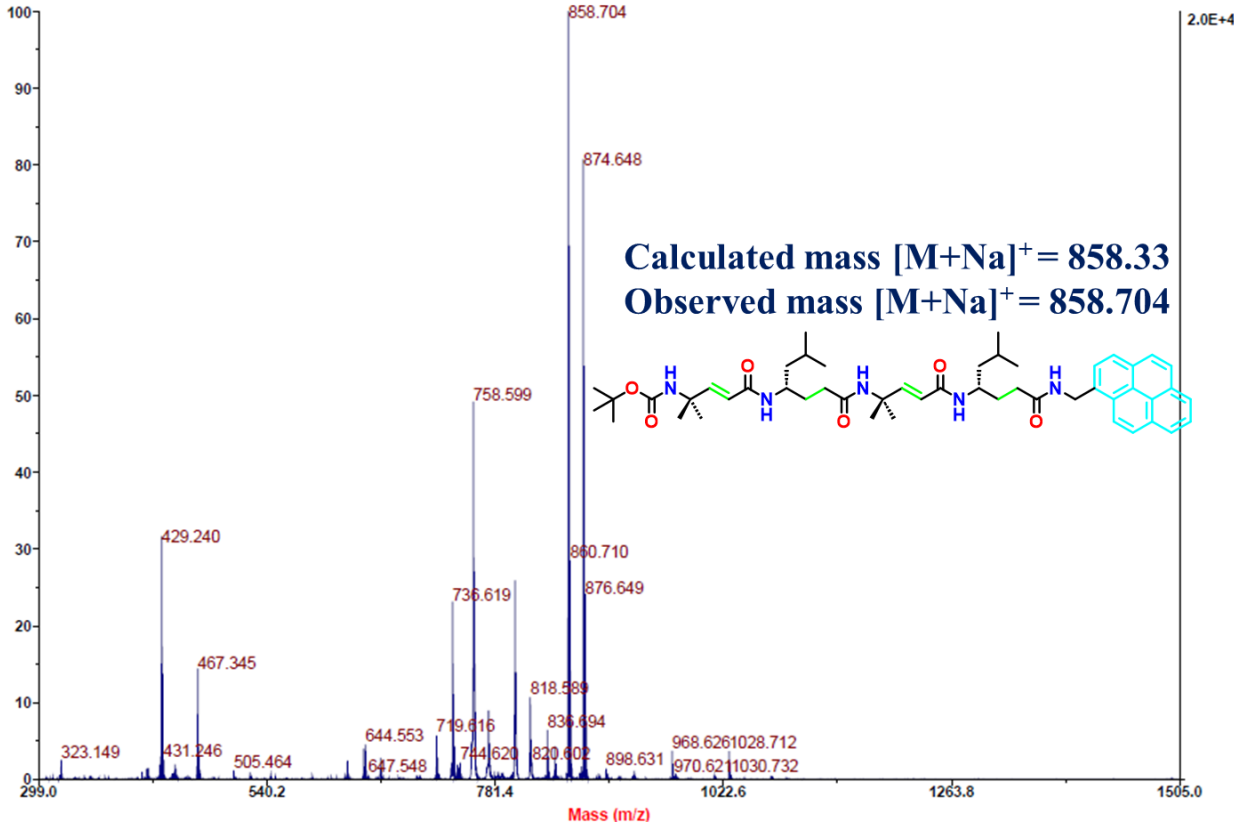


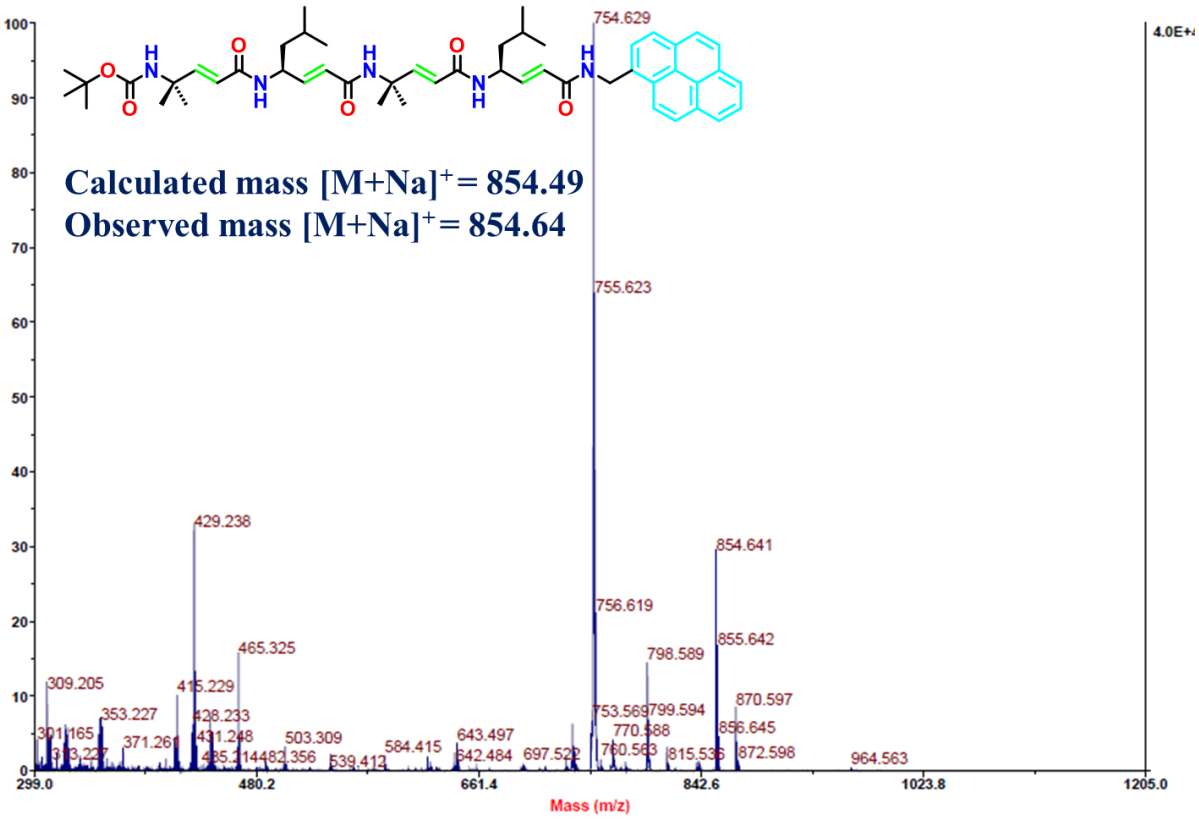
Calculated mass $[M+Na]^+ = 604.33$
Observed mass $[M+Na]^+ = 604.479$

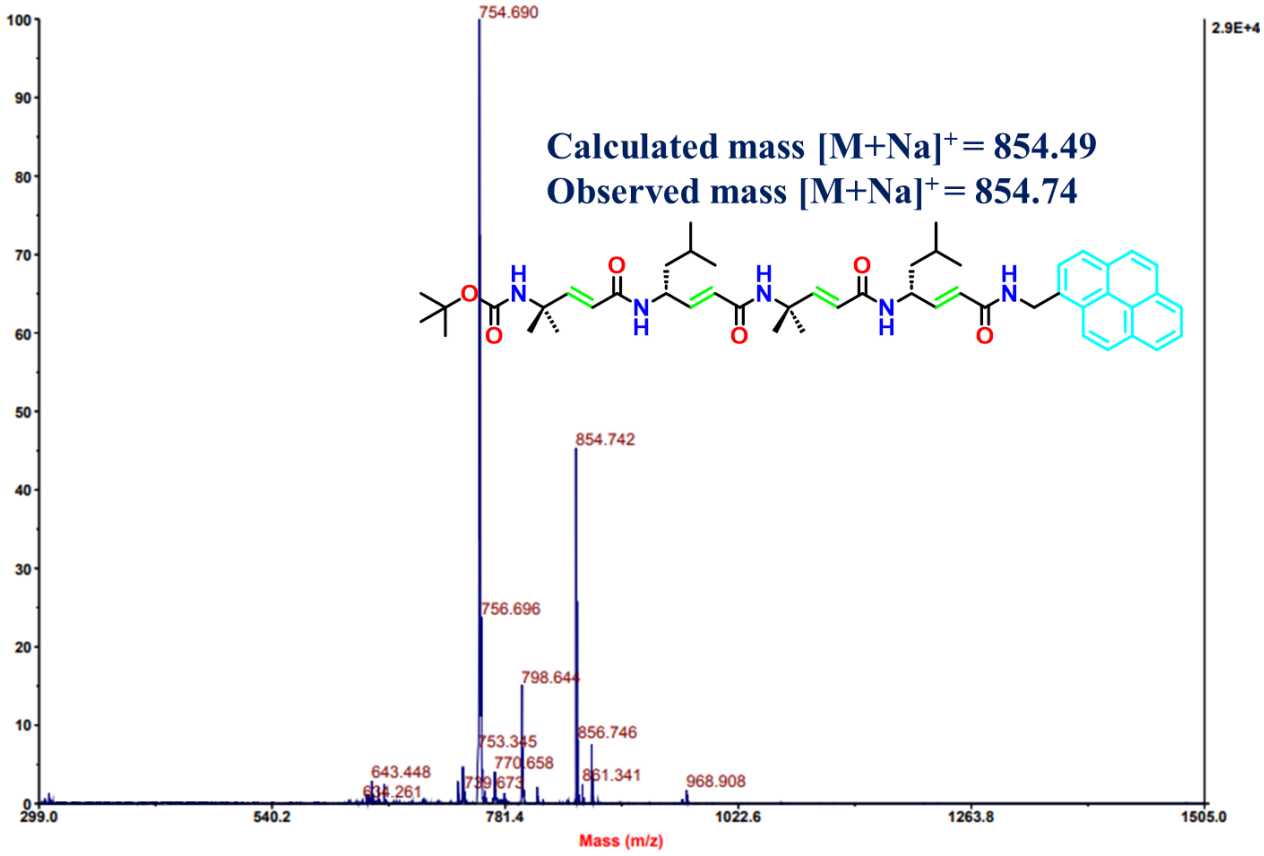

604.479
620.442
548.405
647.624
504.400
514.426
606.485
636.495
437.299
526.409
444.282
506.388
442.270
521.355
582.482
674.440
774.529
861.750
994.796
1185.929
299.0
540.2
781.4
1022.6
1263.8
Mass (m/z)
BocHN
Calculated mass [M+Na]+= 604.33
Observed mass [M+Na]+= 604.47

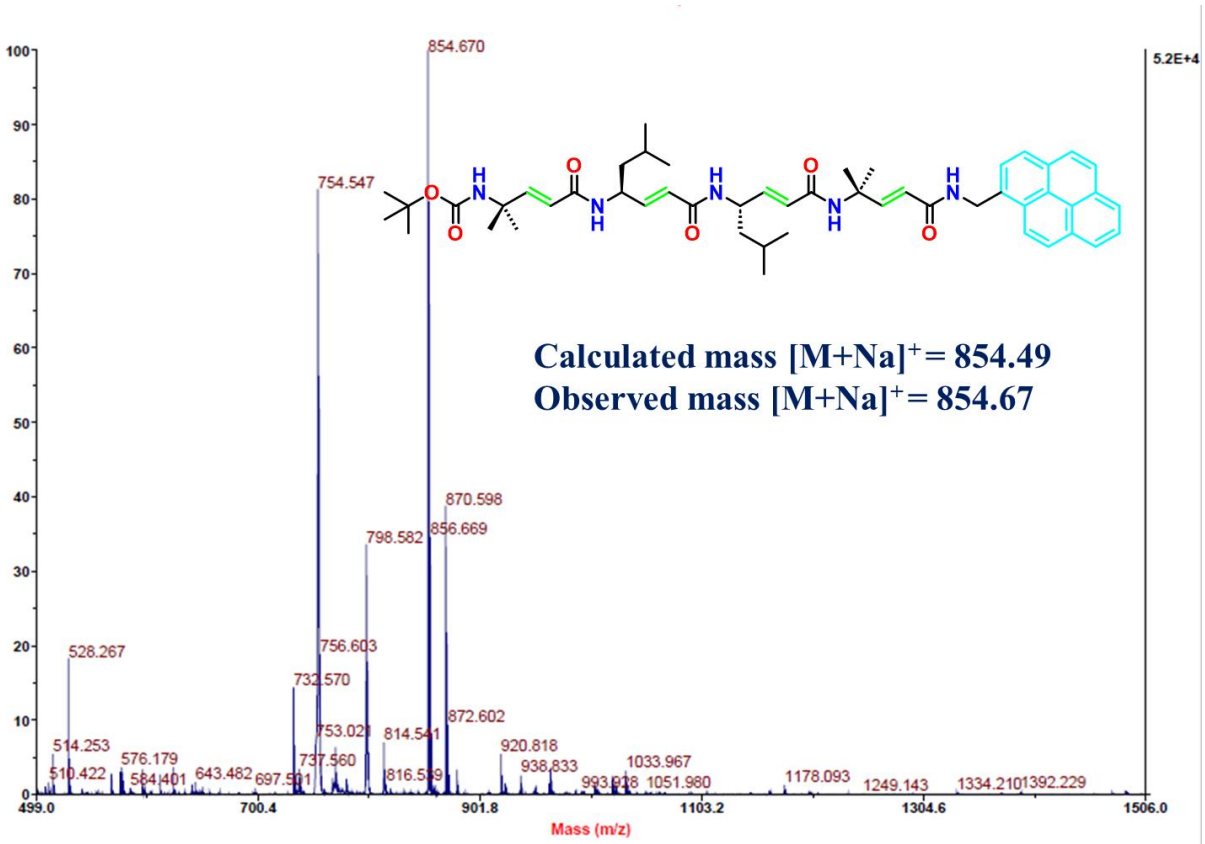

606.459
607.458
622.420
608.460
623.424
624.425
582.439
299
420
541
662
783
Mass (m/z)
Calculated mass [M+Na]+= 606.34
Observed mass [M+Na]+= 606.45

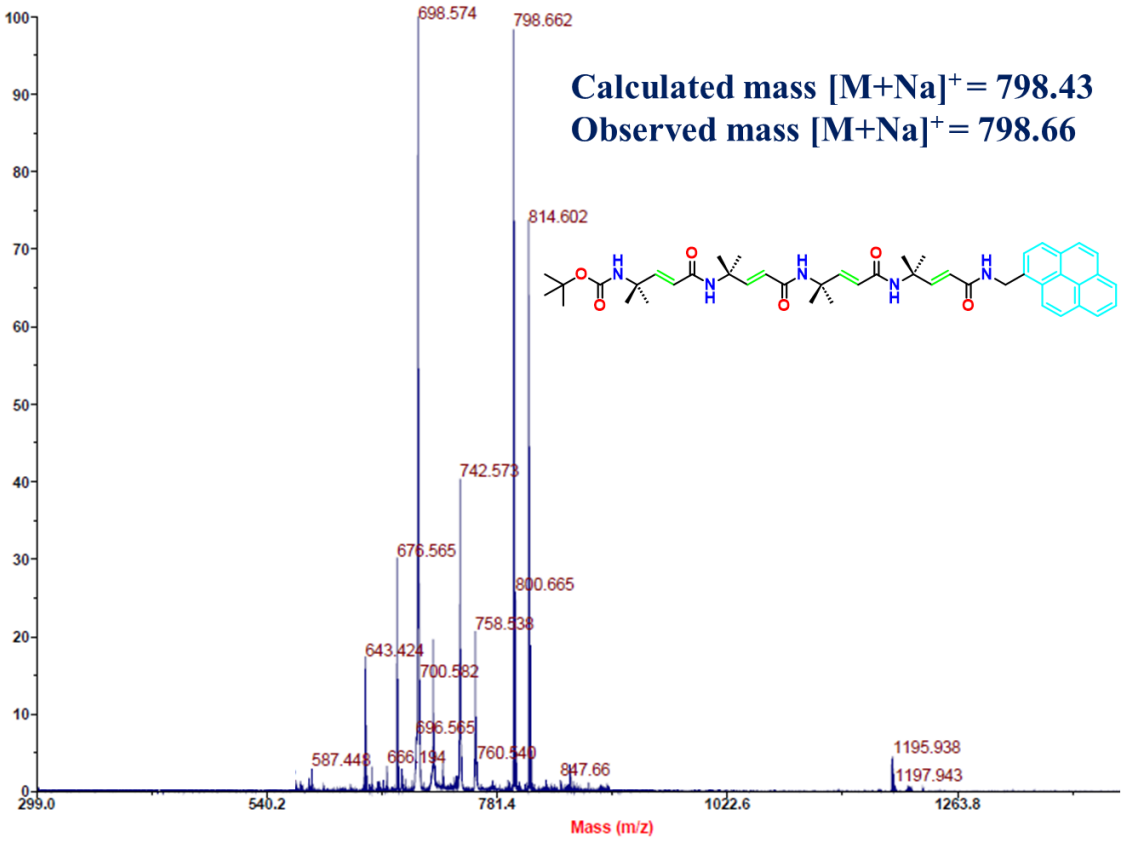

BocHN
Calculated mass [M+Na]+ = 576.29
Observed mass [M+Na]+ = 576.41
576.410
592.370
578.413
536.302
646.369
544.393
609.343
686.330
746.431
802.550
Mass (m/z)


Calculated mass [M+Na]+ = 858.33
Observed mass [M+Na]+ = 858.704
858.704
874.648
758.599
429.240
860.710
876.649
736.619
467.345
818.589
836.694
644.553
719.616
323.149
431.246
505.464
647.548
744.620
820.602
898.631
968.626
1028.712
970.621
1030.732
Mass (m/z)


Calculated mass [M+Na]+= 854.49
Observed mass [M+Na]+= 854.64
754.629
755.623
429.238
854.641
756.619
855.642
798.589
465.325
309.205
415.229
870.597
353.227
428.233
753.569
799.594
856.645
301.165
431.248
503.309
770.588
872.598
371.261
584.415
643.497
760.563
815.536
964.563
697.522
Mass (m/z)


Calculated mass [M+Na]+= 854.49
Observed mass [M+Na]+= 854.74
754.690
854.742
756.696
798.644
856.746
753.345
770.658
643.448
861.341
968.908
Mass (m/z)


854.670
754.547
Calculated mass [M+Na]+= 854.49
Observed mass [M+Na]+= 854.67
870.598
856.669
798.582
528.267
756.603
732.570
872.602
753.021
814.541
920.818
514.253
576.179
737.560
938.833
1033.967
1178.093
1249.143
1334.2101392.229
Mass (m/z)


698.574
798.662
Calculated mass [M+Na]+= 798.43
Observed mass [M+Na]+= 798.66
814.602
742.573
676.565
800.665
758.538
643.424
700.582
696.565
760.540
1195.938
1197.943
Mass (m/z)

Chapter 5

Supramolecular Assemblies and Optoelectronic Properties of β-Double Helices Appended with Donor-Acceptor Groups

5.1. Introduction

The potential of molecular self-assembly to influence research at the convergence of biology, chemistry, and material science is vast, given its capability to effortlessly create a variety of nanostructures.[1-6] Among the various biocompatible and biodegradable constituents, the self-assembly of peptides and proteins stands out due to its significant capacity to adjust functions depending on the characteristics of their assembly patterns.[7-13] From the nano-scale creation of collagen proteins to the macro-scale development of cytoskeletons, a broad spectrum of natural structural variations has been witnessed through the self-assembly of proteins. Due to the prevalence of protein self-assembly in the natural world, there is considerable enthusiasm within the fields of materials science and biomedicine for the molecular self-assembly of oligopeptides, a keen interest that has persisted since the initial demonstration of short self-assembled peptides.[14-15] Furthermore, considering that the polypeptide serves as a biologically active substance engaged in diverse cellular functions within living organisms, it exhibits favorable biocompatibility, non-toxicity, high abundance, self-healing properties, antimicrobial properties, and controllable degradation when compared to the majority of organic polymers. Consequently, the molecular self-assembly of oligopeptides holds significant potential for a wide array of applications in biomedicine[16-19] and biochemical materials[20-24], surpassing many other self-assembled systems in terms of their advantages. Moreover, factors like pH, temperature, light, ionic strength, solvent interactions, and salt concentration are recognized for their significant influence on the aggregation pathways, mechanisms, and morphologies of peptide assemblies.[25-30] Crucially, the self-assembly of peptides is primarily governed by the nuanced interplay among various attractive non-covalent interactions (such as aromatic, van der Waals, hydrogen bonding, and electrostatic interactions) and repulsive interactions (like electrostatic repulsions between similar charges and steric effects).[31,32] In the realm of non-covalent interactions, aromatic interactions play a significant role in influencing the self-assembly processes of peptides and simultaneously contribute to balancing the hydrophobicity of the systems.[33-35] The deliberate choice of amino acid sequences, diverse protein secondary structures such as 3_{10}- and α-helices, β-strands[36], β-hairpin motifs and super-secondary structures, such as two-helix motifs,[37,38] helix-hairpin motifs,[39] multi-stranded beta-sheets,[40,41] and beta -meander structure[42] have been documented. The aromatic group-assisted self-assembly of peptide secondary structures refers to a process where the presence of aromatic groups plays a crucial role in facilitating the spontaneous organization of peptide molecules into defined

structural patterns. Lately, there has been substantial interest in the utilization of peptide amphiphiles incorporating chromophores like pyrene,[43] naphthalene,[44,45] anthracene,[46] perylene diimide,[47] and naphthalene diimide[48] for the stepwise creation of adjustable luminescent nanomaterials. However, understanding the relationship between aromatic interactions and mechanistic pathways of peptide self-assembly remains elusive.[49] The aromatic groups not only enhance the self-assembly process but also impart unique properties to the resulting structures, making them of interest in various applications, including materials science, nanotechnology, and biomedicine. This approach leverages the specific characteristics of aromatic interactions, such as π-π stacking and other non-covalent forces, to drive the ordered assembly of peptides into functional and potentially tunable structures with diverse applications.

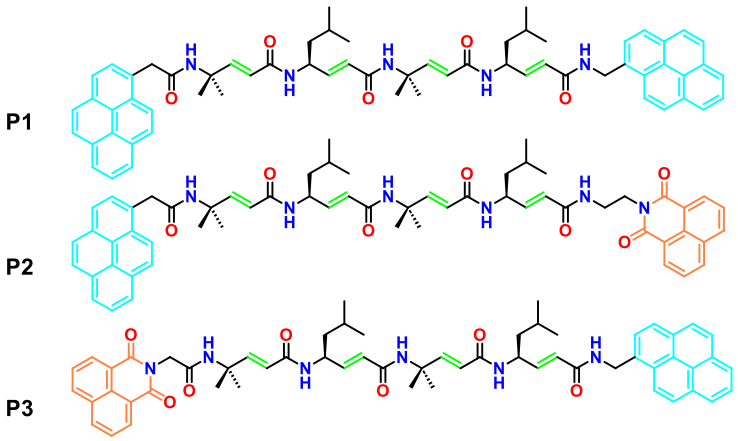
5.2. Objective of the Present Work

Among various secondary structures in protein, the double helical structures are very rare and have only been seen in the case of synthetic peptides with alternating α_L and α_D amino acids.[50,51] Recently we have demonstrated the formation of double helical foldamers from oligomers of (*E*)-α, β-unsaturated γ-amino acids. We also further demonstrated that the pyrene appended double helical moiety can be self-assembled into a porous 3D structure through π-π stacking interactions and hydrogen bonding. To get further insights into the self-assembly of the double-helical motifs, we rationalized that a double helix attached both C and N terminals with electron donor pyrene and electron acceptor NMI dyads (Scheme 1). Pyrene's aromatic nature facilitates pi-pi stacking interactions, contributing to the stabilization and self-assembly of the peptide chains.[52] Simultaneously, NMI imparts unique electronic properties, potentially influencing charge transfer processes within the molecular system.[53] The combination of pyrene and NMI in double-helical peptides holds promise for applications in various domains, including materials science, nanotechnology, and optoelectronics. The distinct attributes of pyrene and NMI integrated double helical peptides create a self-assembled molecular architecture that can further show various optoelectronic properties.

5.3. Results and Discussions

To understand the molecular conformation and self-assembly of the PY-NMI attached peptides, we have synthesized the following peptides **P1**, **P2,** and **P3**. The peptide sequences are illustrated in Scheme 1. Peptide **P1** is composed of two pyrene groups attached to both the C- and N-terminal

of the peptides while in the case of **P2**, we have attached a C-terminal carboxyl group with the NMI unit with an ethylene diamine spacer and N-terminal is appended with pyrene acetic acid. Peptide **P2** is a unique construction as here electron-rich pyrene and electron-deficient NMI consists of a single peptide.



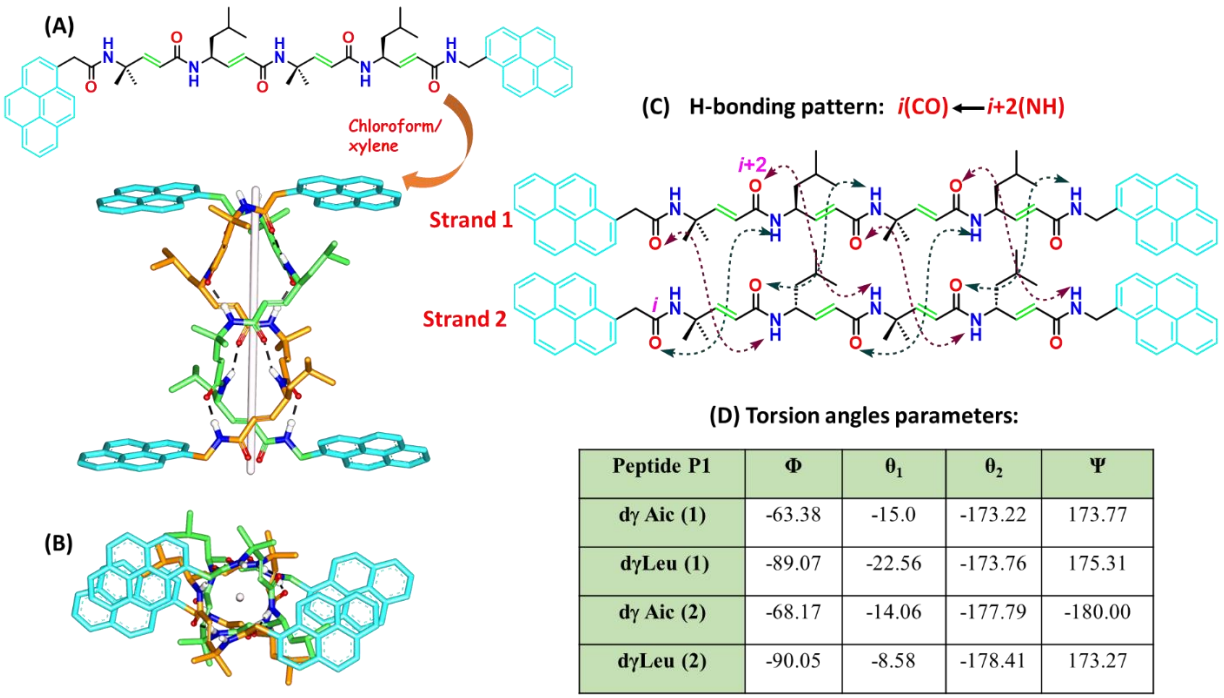
Scheme 1: Sequences of peptides under investigation.

To get further insights into their conformational identity and supramolecular assembly, we designed peptide **P3**, where we have interchanged the pyrene and NMI position from N- to C-terminal and vice versa. All peptides were synthesized through solution phase peptide synthesis and purified through revere phase HPLC and authenticated by MALDI-TOF analysis. The pyrene acetic acid and pyrene methyl amine were directly used from commercial sources. The N-mono Boc-protected ethylene diamine and glycine were coupled to the 1,8-Naphthalic anhydride to get NMI-based linkers. As crystal structures often give explicit information about the molecular structure, all peptides were subjected to crystallization with various solvent mixtures.

5.3.1. Crystal Structure Analysis of P1

We got diffraction quality crystals for **P1** from slow evaporation from chloroform/toluene mixture and solved in an orthorhombic crystal system with space group $P2_12_12$. In the asymmetric unit, a single molecule of **P1** was identified, accompanied by four chloroform and two water molecules. The peptide exhibited a right-handed helical conformation, devoid of any intramolecular hydrogen bonds. All amide NH and carbonyl groups were exposed, facilitating intermolecular hydrogen bonds. The peptide engaged in self-assembly with another molecule, utilizing all amide NH groups and CO groups for intermolecular hydrogen bonding, except for the initial NH and penultimate C-

terminal CO group. The double helical structure of **P1** is shown in Figure 1A. The stability of this double helix structure was maintained through the presence of eight intermolecular hydrogen bonds, which formed between the amide carbonyl (CO) of the (*i*) residue in strand 1 and the amide NH of the (*i*+2) residue in strand 2. The hydrogen bonding pattern observed in **P1** is shown in Figure 1C.



(D) Torsion angles parameters:

Peptide P1	Φ	θ_1	θ_2	Ψ
dγ Aic (1)	-63.38	-15.0	-173.22	173.77
dγLeu (1)	-89.07	-22.56	-173.76	175.31
dγ Aic (2)	-68.17	-14.06	-177.79	-180.00
dγLeu (2)	-90.05	-8.58	-178.41	173.27

Figure 1: (A) Single crystal structure of **P1.** An imaginary rod is inserted along the crystal axis for a better view of the double-helical structure. (B) Top view of the **P1.** (C) Hydrogen bonding pattern observed in **P1.** (D) Torsion angle parameters of strand 1 and strand 2 of **P1**.

Overall, peptide **P1** adopted a right-handed (*P*)-β-double helix conformation in the single crystals. The H-bond parameters of **P1** are tabulated in Table 1.

The torsion angle analysis revealed that α,β-unsaturated 4,4-dimethyl γ-amino acids displayed averageϕ, θ_1, θ_2, and ψ angles of -65.77°±2.38°, -14.58°±0.52°, ±175.5°±2.2°, and ±178.17°±1.65°, respectively. The torsion angles θ_1 displayed a value near to zero whereas θ_2, and ψ displayed a value close to 180°. The first three torsion variables displayed negative signs, whereas ψ displayed a positive sign, with the exception of the second residue. The values displayed by the achiral residues are consistent with previously observed β-double helix structures. The average torsion angles of the dγLeu amino acids ϕ, θ_1, θ_2, and ψ were found to be -89.56°±0.49°,

-15.57°±7°, -176.08°±2.3°, and +174.29°±1°, respectively. The observed sign here for ϕ, θ_1, θ_2, and ψ is respectively (-, -, -, +).

Table 1: The H-bond parameters of **P1** double helix

Donor (D)	Acceptor (A)	D.....A (Å)	DH....A (Å)	∡NH....O (°)
N2 (strand 1)	O1 (strand 2)	2.869	2.014	172.13
N3 (strand 1)	O2 (strand 2)	2.900	2.06	160.53
N4 (strand 1)	O3 (strand 2)	2.854	2.045	156.44
N5 (strand 1)	O4 (strand 2)	2.845	1.963	171.18
N2 (strand 2)	O1 (strand 1)	2.869	2.014	172.13
N3 (strand 2)	O2 (strand 1)	2.900	2.06	160.53
N4 (strand 2)	O3 (strand 1)	2.854	2.045	156.44
N5 (strand 2)	O4 (strand 1)	2.845	1.963	171.18

5.3.2 Self-Assembly of P1

Developing supramolecular helical structures to mimic natural helices, such as the DNA double helix and protein α-helix, is a valuable strategy for uncovering the fundamental principles underlying the construction and interactions of these helical forms. This approach holds the potential to pave the way for creating innovative artificial supramolecular helices with a diverse range of structures and functions. In the case of helicity, the DNA double helix achieves its overall helical structure through the stacking of base pairs in a columnar fashion. This serves as a source of inspiration for designing supramolecular helical assemblies by organizing planar π-conjugated building blocks in a columnar, helical fashion. Examples of such building blocks encompass trialkylbenzene-1,3,5-tricarboxamide discotics,[54] porphyrins,[55] perylene bisimides,[56] and merocyanine dyes.[57] This concept offers a novel perspective for creating robust supramolecular helical structures by utilizing helical building blocks assembled into supramolecular helices through head-to-tail intermolecular interactions.

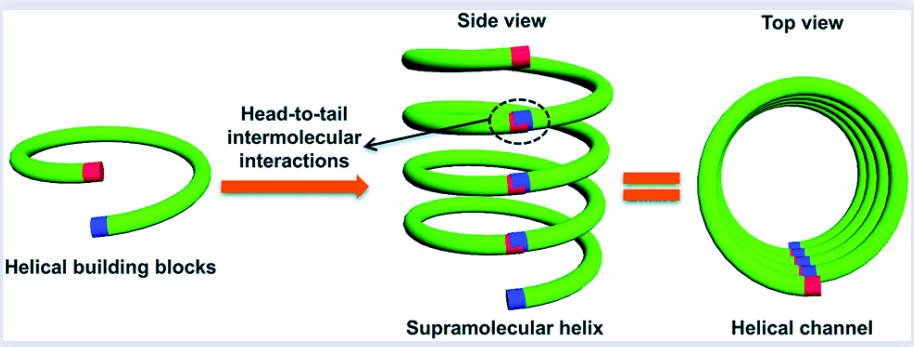


Figure 2: The formation of a supramolecular helix involves helical building blocks linked by head-to-tail intermolecular interactions. This arrangement may result in the creation of a helical channel.

A variety of helical building components, including helical aromatic foldamers and short peptides with helical structures, have proven effective in constructing supramolecular helices through intermolecular interactions such as π–π stacking, hydrogen bonding, and metal coordination. This versatile approach opens avenues for creating diverse and functional supramolecular helices, contributing to the broader understanding of helical structures and their potential applications in various fields.

With this concept in mind, we thought of analyzing the self-assembly characteristic of our pyrene-attached double helical peptide **P1**. This is because the peptide **P1** fulfills all the criteria such as having a double helical structure and appended with large aromatic pyrene moieties to self-assemble into higher order structure. Notably, in our current investigation, we observed that the pyrene units are oriented nearly perpendicular, approximately 90 degrees, to the double helical axis (Figure 1). This is in contrast to our earlier study, where the pyrene units, attached solely at the C-terminal of the peptides, exhibited an angle of approximately 45 degrees. A detailed analysis of the crystal structure uncovered intriguing features. Specifically, the first amide NH of the N-terminus and the CO group at the C-terminus of **P1** were observed not to form hydrogen bonds with the intertwined strands. Instead, they engaged in intermolecular hydrogen bonding with another double helix along the helix axis, fostering a continuous columnar assembly of the double helices. The primary driving force behind this columnar supramolecular assembly was identified as π–π stacking between the pyrene units at both ends of the double-helical moieties. The head-to-tail self-assembly of the double helices is illustrated in Figure 3A, with the average intermolecular

pyrene-pyrene distance calculated at 3.75 Å. Moreover, the top view of the columnar assembly reveals a channel-like structure, as depicted in Figure 3B.

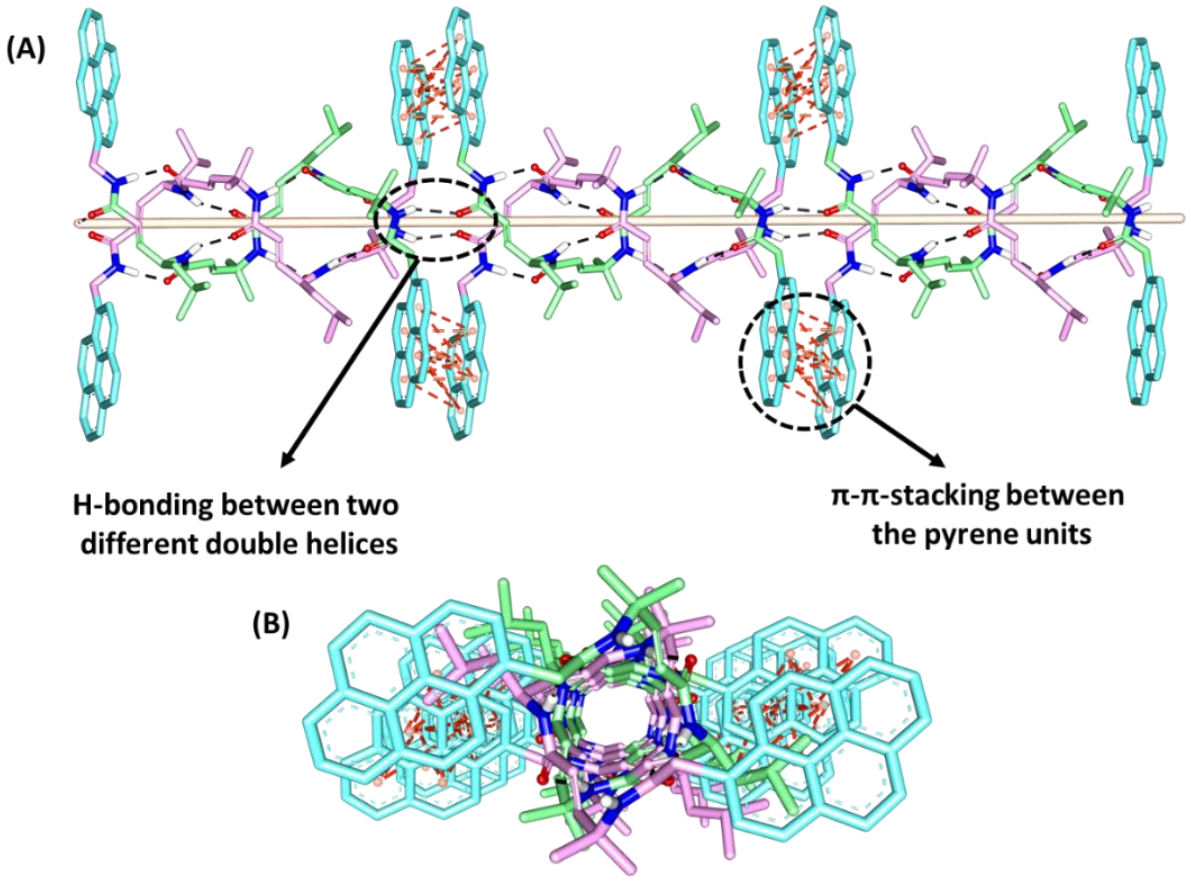


Figure 3: (A) columnar packing of the double helices **P1.** (B) Top view of the columnar packing.

This assembly, formed through the head-to-tail self-assembly of the double helices, showcases a well-defined channel, suggesting potential applications in molecular recognition or encapsulation processes. Overall, the intricate interplay of hydrogen bonding and π–π stacking drives the formation of this columnar supramolecular assembly, providing valuable insights into the unique self-assembly characteristics of the pyrene-attached double helical peptide **P1**.

In the vertical direction along the *b*-axis, the π-π interactions play a crucial role in stabilizing the tubular assembly. This involves the stacking of pyrene moieties, creating a cohesive structure along this crystallographic axis. Simultaneously, the horizontal assembly involves CH-π interactions between adjacent pyrene units, enhancing the lateral connectivity and stability of the

tubular structures. Figure 4 illustrates these interactions, showcasing the interplay of π-π and CH-π interactions responsible for the tubular assembly in the crystal lattice.

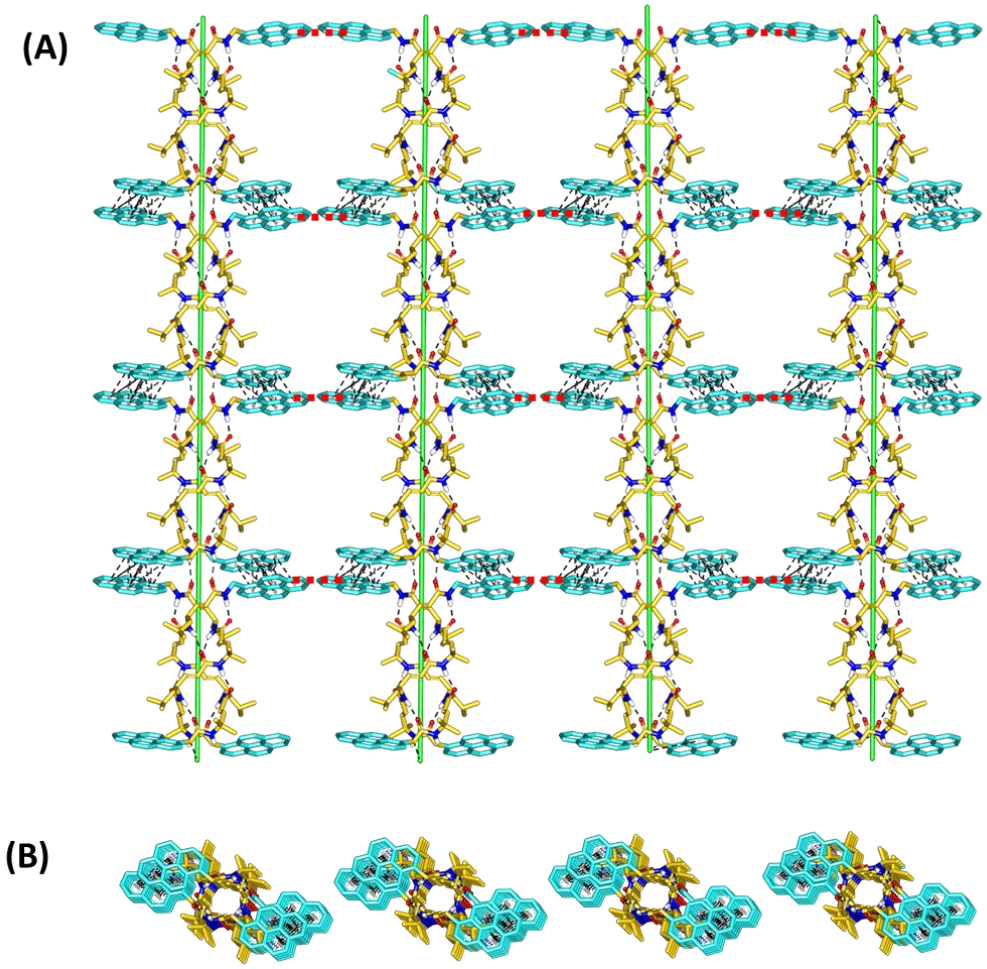


Figure 4: (A) The columnar packing along the *c*-axis of **P1**. The black dotted lines indicate π-π interactions and the red lines indicate CH-π..CH-π interactions. (B) The top view of the columnar packing shows a channel-type architecture.

This comprehensive view reveals the spatial arrangement of the tubular structures in the crystal lattice, providing insights into the overall architecture of the three-dimensional supramolecular assembly. The combination of π-π and CH-π interactions in different directions contributes to the formation of a complex, yet well-defined, crystal structure, demonstrating the versatility and specificity of intermolecular forces in guiding the assembly of the pyrene-attached double helical peptide **P1**.

The overall crystal packing along the *a*-axis and *c*-axis is shown in below in Figure 5.

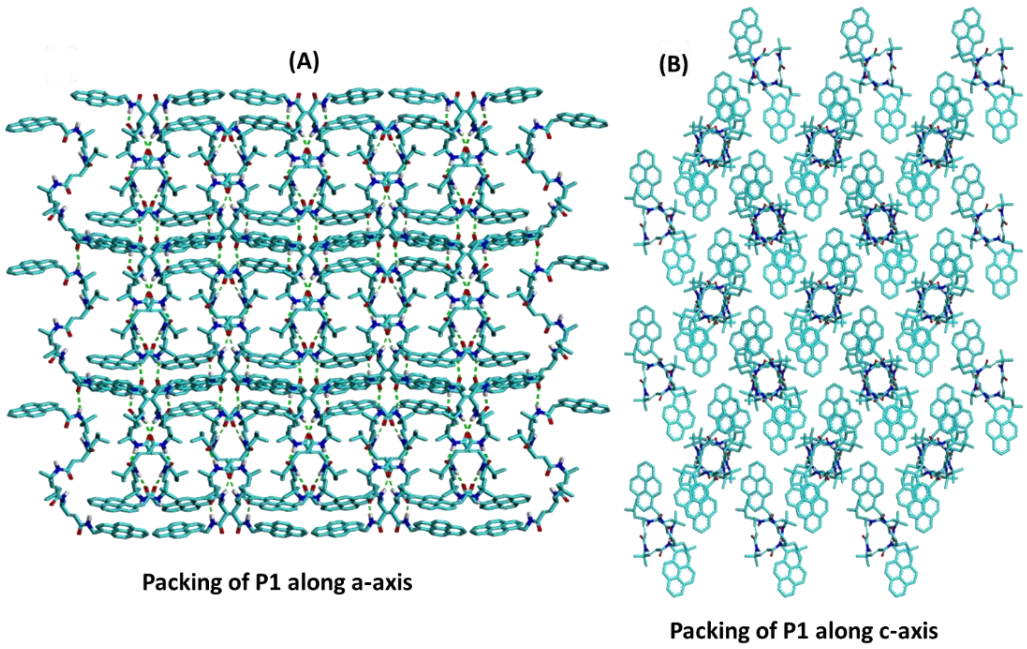
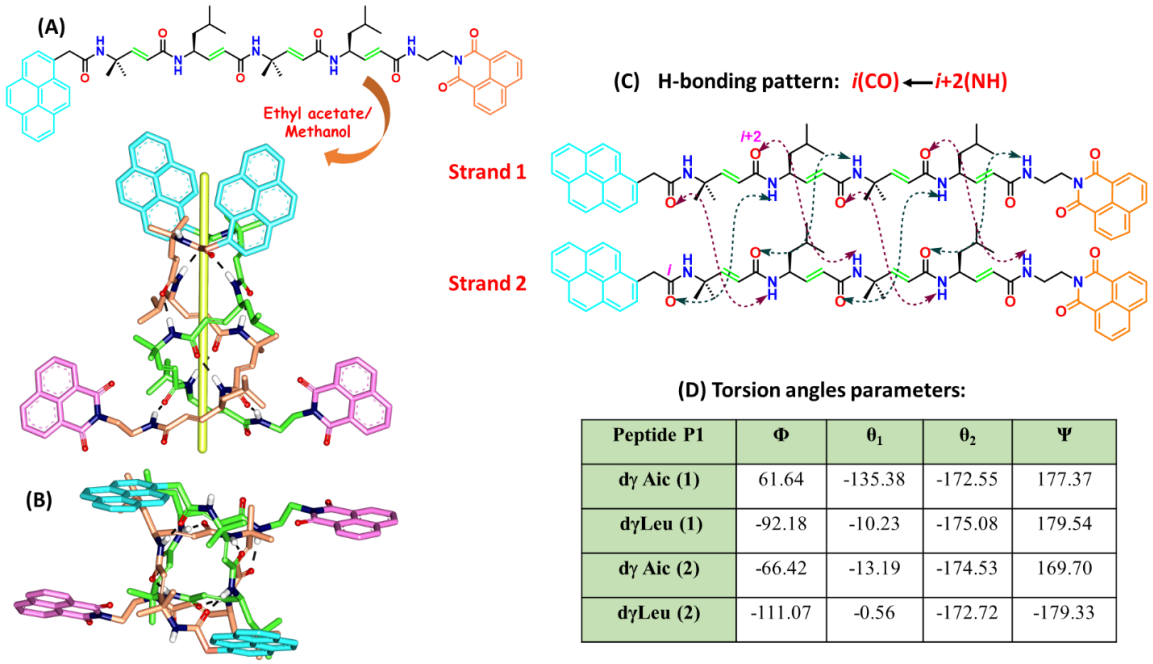


Figure 5: (A) Crystal packing of **P1** along *a*-axis. (B) Crystal packing of **P1** along the *c*-axis

5.3.3. Crystal Structure Analysis of P2

The single crystals obtained for peptide **P2** from slow evaporation from ethyl acetate/methanol solvent mixture and solved in a tetragonal crystal system with space group $P4_12_12$. The structure of **P2** is shown in Figure 6. The structure of **P2** also adopts a double helical structure carrying a pyrene unit at the N-terminal and an NMI unit at the C-terminal of the double helix sequences. In the asymmetric unit, a single **P2** molecule coexisted with four ethyl acetate molecules. The peptide adopted a right-handed helical conformation, lacking intramolecular hydrogen bonds. All amide NH and carbonyl groups were exposed, facilitating intermolecular hydrogen bonds. The peptide engaged in self-assembly with another molecule, utilizing all amide NH groups and CO groups for intermolecular hydrogen bonding, excluding the Boc NH and C-terminal CO groups. The stability of this double helix structure was upheld through the presence of eight intermolecular hydrogen bonds. These bonds were formed between the amide carbonyl (CO) of the (*i*) residue in strand 1 and the amide NH of the (*i*+2) residue in strand 2. The hydrogen bonding pattern observed in **P2** is shown in Figure 6C. Overall, peptide **P2** adopted a right-handed (*P*)-β-double helix conformation in the single crystals. The NMI units are stayed perpendicular to the helix axis whereas pyrene units are parallel to the double helical peptide axis. The H-bond parameters of **P2** are tabulated in Table 2.



Peptide P1	Φ	θ_1	θ_2	Ψ
dγ Aic (1)	61.64	-135.38	-172.55	177.37
dγLeu (1)	-92.18	-10.23	-175.08	179.54
dγ Aic (2)	-66.42	-13.19	-174.53	169.70
dγLeu (2)	-111.07	-0.56	-172.72	-179.33

Figure 6: (A) Single crystal structure of **P2.** An imaginary rod is inserted along the crystal axis for a better view of the double-helical structure. (B) Top view of the **P2.** (C) Hydrogen bonding pattern observed in **P2.** (D) Torsion angle parameters of strand 1 and strand 2 of **P2**.

Table 2: The H-bond parameters of **P2** double helix

Donor (D)	Acceptor (A)	D.....A (Å)	DH....A (Å)	∡NH....O (°)
N2 (strand 1)	O1 (strand 2)	2.821	1.871	173.83
N3 (strand 1)	O2 (strand 2)	2.815	1.880	178.77
N4 (strand 1)	O3 (strand 2)	2.813	1.879	174.24
N5 (strand 1)	O4 (strand 2)	2.806	1.934	157.83
N2 (strand 2)	O1 (strand 1)	2.821	1.871	173.83
N3 (strand 2)	O2 (strand 1)	2.815	1.880	178.77
N4 (strand 2)	O3 (strand 1)	2.813	1.879	174.24
N5 (strand 2)	O4 (strand 1)	2.806	1.934	157.83

The torsion angle analysis revealed that the first dγAic residue took quite a different torsion value for and θ_1. The value in this case is 61.64° with a positive sign and instead of taking observed

torsion angles 0°, θ_1 has taken a value -135.38°. This could be attributed to the need to align the pyrene components in the same direction as the double helix's axis to fit them properly. The alteration in the torsion angles is ascribed to the flexible nature of γ-peptide strands, enabling them to adapt to the presence of bulky pyrenyl moieties along the double helix. The ϕ, θ_1, θ_2, and ψ values for second dγAic residue are -66.42°,-13.19°,-174.53°, and +169.70° respectively. The average values of torsion angles ϕ, θ_1, θ_2, and ψ for dγLeu residues were found to be -101.62°±9°, -5.39°±4.43°, -173.9°±1.18°, and +179.43°, respectively. The observed sign here for ϕ, θ_1, θ_2, and ψ is respectively (-, -, -, ±).

5.3.4. Self-Assembly of P2

In the end-group attached donor-acceptor-based peptide assembly, scientists create synthetic peptides by adding electron-rich (donor) and electron-poor (acceptor) parts at the ends of the peptide molecules. These chosen end groups strategically foster non-covalent interactions, driving the peptides to self-assemble into specific, well-defined structures or supramolecular architectures.[58] These donor and acceptor groups enable non-covalent interactions like hydrogen bonding, π-π stacking, or electrostatic forces. Incorporating them at the peptide ends allows precise control over folding and assembly. These assemblies can possess unique traits like increased stability, responsiveness to external factors, or selective molecule binding. End-group attached donor-acceptor-based peptide assemblies represent a vibrant research field at the crossroads of chemistry, materials science, and nanotechnology, with wide-ranging potential applications.

Akin to the concept mentioned above, our design of peptide **P2** follows a similar principle as donor-acceptor-based peptide foldamers. In this design, we incorporate an NMI unit as the acceptor molecule, and pyrene serves as the donor molecule. This setup is reminiscent of the donor-acceptor concept, where NMI acts as the electron-poor (acceptor) component, and pyrene serves as the electron-rich (donor) component. The inclusion of NMI and pyrene at the C-terminus and N-terminus in peptide **P2** is strategically chosen to facilitate non-covalent interactions between them, such as π-π stacking or other intermolecular forces. These interactions drive the folding and self-assembly of the peptide into well-defined structures or supramolecular architectures. The NMI unit's electron-poor nature complements the electron-rich properties of pyrene, allowing for effective donor-acceptor interactions, akin to those found in donor-acceptor-based peptide foldamers.

Analyzing the supramolecular assembly process of **P2**, we have seen that there is indeed a donor-acceptor interaction is happening between the pyrene and NMI units. Each double helical unit bears two pyrene units at the N-terminus and two NMI units at the C-terminus, which are further interconnected to another four double helical moieties through donor-acceptor-based π-π interaction along crystallographic plane *b*-*c*. The representative supramolecular assembly is shown in Figure 7**.**

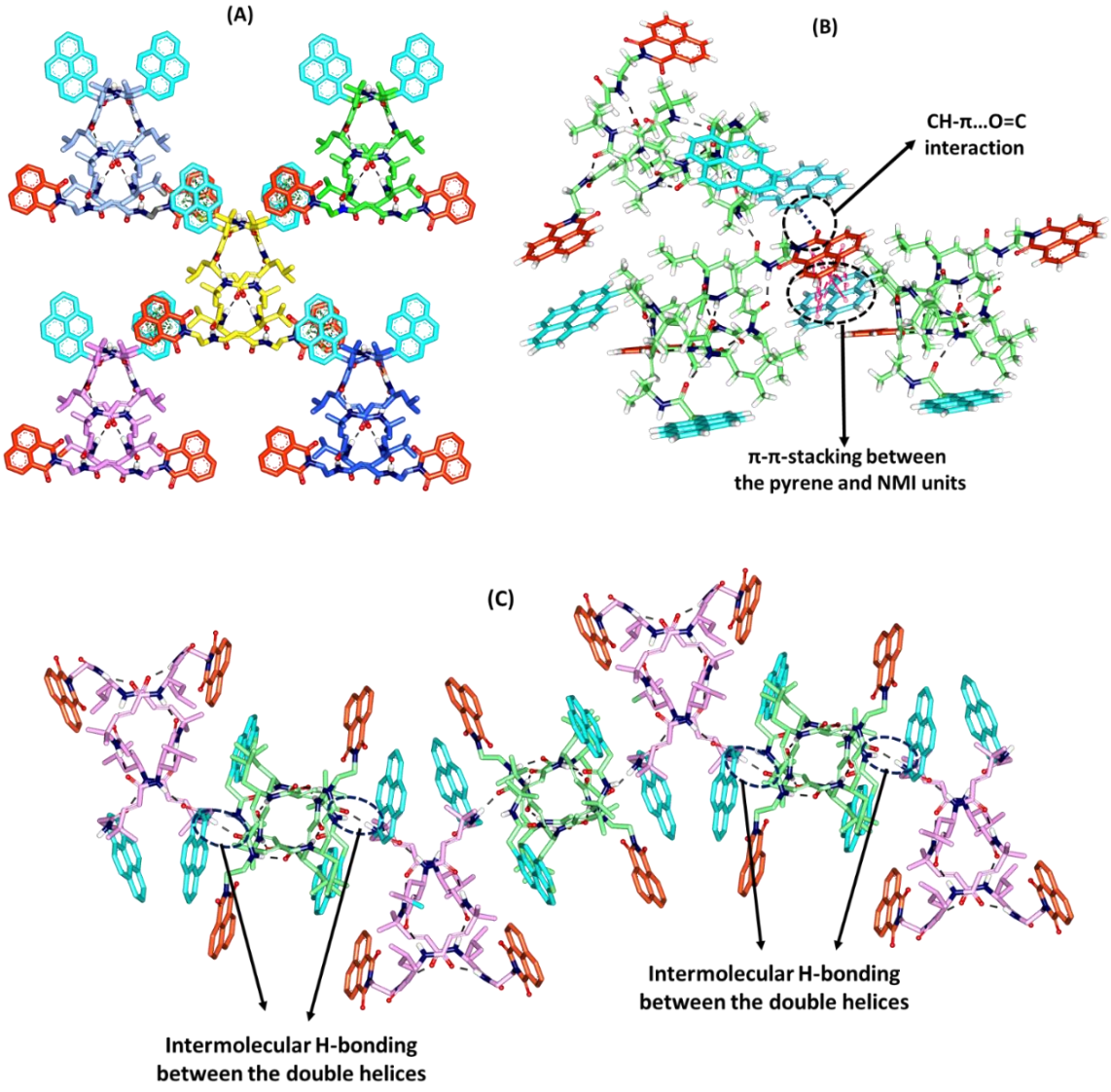


Figure 7: (A) The supramolecular assembly of the double helical structures. The central double helix (depicted in yellow) is linked to four additional double helices through stacking interactions involving pyrene and NMI groups. (B) The π-π and CH-π…O=C interactions were observed between the pyrene and NMI groups. (C) Intermolecular H-bonding was observed among the double helices.

The average intermolecular Py-NMI distance calculated is 3.584 Å which is similar to the reported this kind of interaction. In addition to the π-π stacking interactions, we observed CH-π…O=C interactions occurring between the carbonyl groups of NMI units and the pyrene ring of other double helical moieties. Careful analysis of the crystal structure shows that the first amide hydrogen attached to the N-side pyrene acetic acid group of each double helical unit and the CO group at the C-terminal of the **P2**, are not hydrogen bonded with the intertwined strands. Instead, they form a hydrogen bond with the adjacent double helices, leading to the overall supramolecular assembly. The intermolecular hydrogen bonding between the double helices is shown in Figure 8C.

Overall, the self-assembly of pyrene NMI-attached double helical moieties through donor-acceptor interactions results in the formation of a two-dimensional supramolecular network structure along the *a*-*b* plane. The overall two-dimensional supramolecular network structure is shown below in Figure 8**.**

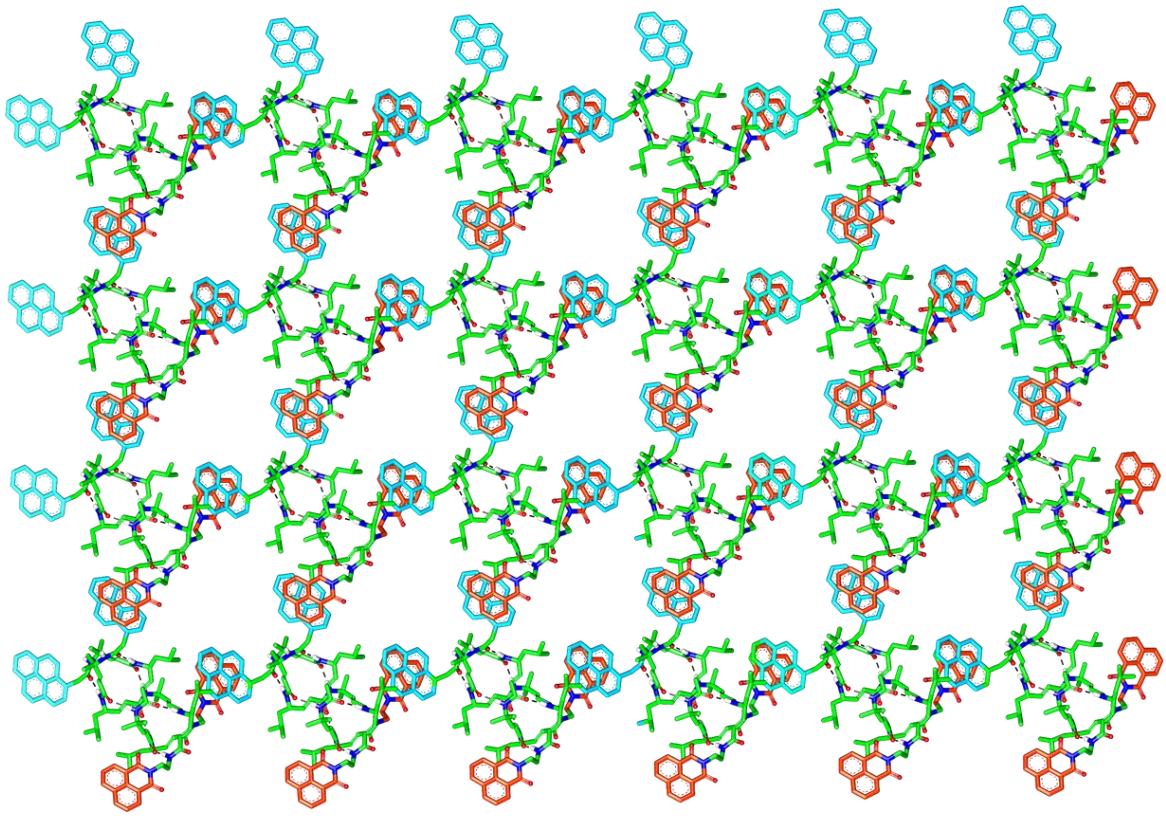
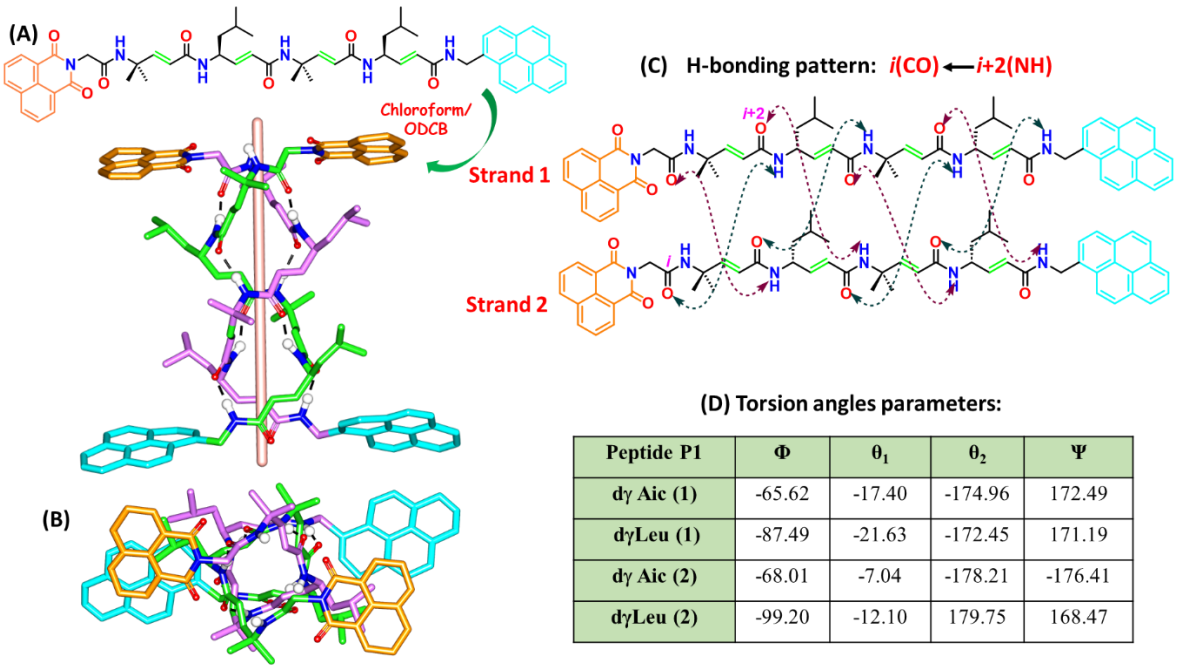


Figure 9: (A) The supramolecular network assembly of **P2.** Top view of the network assembly of **P2**.

The donor-acceptor interactions between these units play a crucial role in guiding the assembly process. The resulting two-dimensional supramolecular network consists of a periodic arrangement of pyrene-NMI double helices, with each double helix interacting with adjacent ones. The controlled and specific interactions between the pyrene and NMI units contribute to the stability and functionality of this supramolecular structure.

5.3.5. Crystal Structure Analysis of P3

We also obtained the crystal of **P3** from the $CHCl_3$/1,2-dichlorobenzene solvent system through slow evaporation and solved in an orthorhombic crystal system with space group $P2_12_12$. One molecule of **P3** was found in the asymmetric unit along with one molecule of 1,2-dichlorobenzene. The single crystal structure of **P3** is shown in Figure 10A.



(D) Torsion angles parameters:

Peptide P1	Φ	θ_1	θ_2	Ψ
dγ Aic (1)	-65.62	-17.40	-174.96	172.49
dγLeu (1)	-87.49	-21.63	-172.45	171.19
dγ Aic (2)	-68.01	-7.04	-178.21	-176.41
dγLeu (2)	-99.20	-12.10	179.75	168.47

Figure 10: (A) Single crystal structure of **P3.** An imaginary rod is inserted along the crystal axis for a better view of the double-helical structure. (B) Top view of the **P3.** (C) Hydrogen bonding pattern observed in **P3.** (D) Torsion angle parameters of strand 1 and strand 2 of **P3**.

The peptide assumed a conformation resembling a right-handed helix, devoid of any intramolecular hydrogen bonds. All amide NH and carbonyl groups were externally exposed, enabling the formation of intermolecular hydrogen bonds. The peptide underwent self-assembly with another molecule, utilizing all amide NH groups and CO groups for intermolecular hydrogen

bonding, with the exception of the initial NH and penultimate C-terminal CO groups. The stability of this double helix structure was upheld through the presence of eight intermolecular hydrogen bonds. These bonds were established between the amide carbonyl (CO) of the (*i*) residue in strand 1 and the amide NH of the (*i*+2) residue in strand 2. The hydrogen bonding pattern observed in **P3** is shown in Figure 10C. Overall, peptide **P3** adopted a right-handed (*P*)-β-double helix conformation in the single crystals. The H-bond parameters are similar to that of our previously reported structure. The H-bond parameters of **P3** are tabulated in Table 3.

Table 3: The H-bond parameters of the **P3** double helix.

Donor (D)	Acceptor (A)	D.....A (Å)	DH....A (Å)	∡NH....O (°)
N2 (strand 1)	O1 (strand 2)	2.807	2.033	150.61
N3 (strand 1)	O2 (strand 2)	2.808	1.987	177.37
N4 (strand 1)	O3 (strand 2)	2.867	1.985	170.22
N5 (strand 1)	O4 (strand 2)	2.857	2.212	146.67
N2 (strand 2)	O1 (strand 1)	2.807	2.033	150.61
N3 (strand 2)	O2 (strand 1)	2.808	1.987	177.37
N4 (strand 2)	O3 (strand 1)	2.867	1.985	170.22
N5 (strand 2)	O4 (strand 1)	2.857	2.212	146.67

The torsion angle analysis revealed that α,β-unsaturated 4,4-dimethyl γ-amino acids displayed average ϕ, θ_1, θ_2, and ψ angles of -65.77°±2.38°, -14.58°±0.52°, ±175.5°±2.2°, and ±178.17°±1.65°, respectively. The torsion angles θ_1 displayed a value near to zero whereas θ_2, and ψ displayed a value close to 180°. The initial three torsion variables exhibited negative values, while ψ had a positive value, except for the second residue. The characteristics observed in achiral residues align with known β-double helix structures. For the dγLeu amino acids, the mean torsion angles for ϕ, θ_1, θ_2, and ψ were determined as -89.56°±0.49°, -15.57°±7°, -176.08°±2.3°, and +174.29°±1°, respectively.

5.3.6. Self-Assembly of P3

In peptide **P3**, we incorporated a donor pyrene and an acceptor NMI group, and we were interested in exploring their self-assembly within a crystal. We decided to switch the positions of the NMI and pyrene residues, moving them from the N-terminus to the C-terminus of the peptide **P3**. We anticipated that this rearrangement might lead to a different self-assembled structure. However, when we analyzed the single crystal structure, we observed that it closely resembled the structure of peptide **P1**. Akin to **P1**, the pyrene and NMI units in **P3** maintained a perpendicular orientation concerning the double helical axis. This unexpected similarity in the self-assembled structures suggests that the specific arrangement of these units within the peptide and their interactions led to consistent crystal structures, regardless of the pyrene-pyrene or pyrene-NMI diads. Here, also careful analysis of the crystal structure shows that the first amide hydrogen attached to the N-side pyrene acetic acid group of each double helical unit and the CO group at the C-terminal of the **P3,** are not hydrogen bonded with the intertwined strands. Instead, they make the intermolecular hydrogen bonding with another double helix along the double helix axis leading to a continuous columnar assembly of the double helices (Figure 11A).

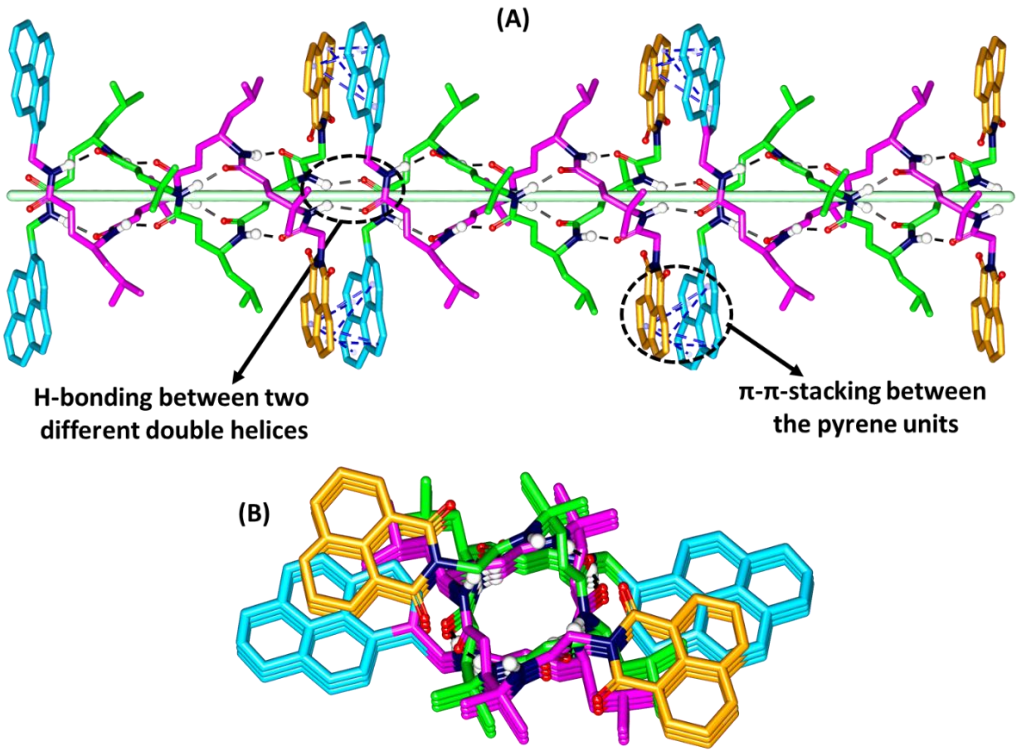


Figure 11: (A) columnar packing of the double helices **P3.** (B) Top view of the columnar packing.

Along with the hydrogen bonding, this columnar supramolecular assembly is formed through π–π stacking between the donor pyrene units and acceptor NMI units of the double-helical moieties. The columnar assembly is formed through the head-to-tail self-assembly of the double helices. The average distance between the pyrene and NMI units is 3.5 Å. The top view of the columnar assembly shows a channel-like structure depicted in Figure 11B.

The assembly along the *b*-axis is driven by a combination of π-π interactions between the pyrene and NMI moieties in a vertical arrangement and CH-π interactions that occur between the pyrene units in a horizontal orientation, as depicted in Figure 12A. In the case of the π-π interactions, the pyrene molecules, which serve as the donor units, are stacked vertically with the acceptor NMI units on top of each other. This stacking arrangement is a result of the attractive forces between the electron-rich pyrene rings and electron-deficient NMI units, which align in a head-to-tail fashion. These π-π interactions play a significant role in stabilizing the assembly along the *c*-axis, effectively forming the columnar self-assembly. Additionally, the CH-π interactions occur horizontally between adjacent pyrene units along the *a*-axis. These interactions involve the electron-rich regions of one pyrene ring engaging with the electron-poor regions of neighboring pyrene rings. This CH-π interaction contributes to the lateral stability of the assembly, connecting the pyrene columns together.

The top view of the assembly reveals the formation of a remarkable channel-type architecture, which is a result of the columnar assembly of the constituent molecules. Figure 12B depicts the top view of the columnar assembly of **P3**. The formation of a "channel-type" architecture indicates that there are voids or open spaces between these columns. These spaces or channels can be thought of as pathways or tunnels running through the assembly. This architecture is characterized by its structural regularity and the presence of these channels, which can be significant in various applications. The existence of channels in the assembly has functional implications. In materials science and nanotechnology, such channel architectures are of interest because they can be harnessed for applications such as guest molecule encapsulation, ion transport, or creating functional materials with specific properties. The ability of the columnar assembly to form such a well-structured channel-type architecture highlights the precision and control achieved in the self-assembly process. It underscores the potential utility of these supramolecular structures in various fields, including molecular transport, sensor development, and the design of advanced materials.

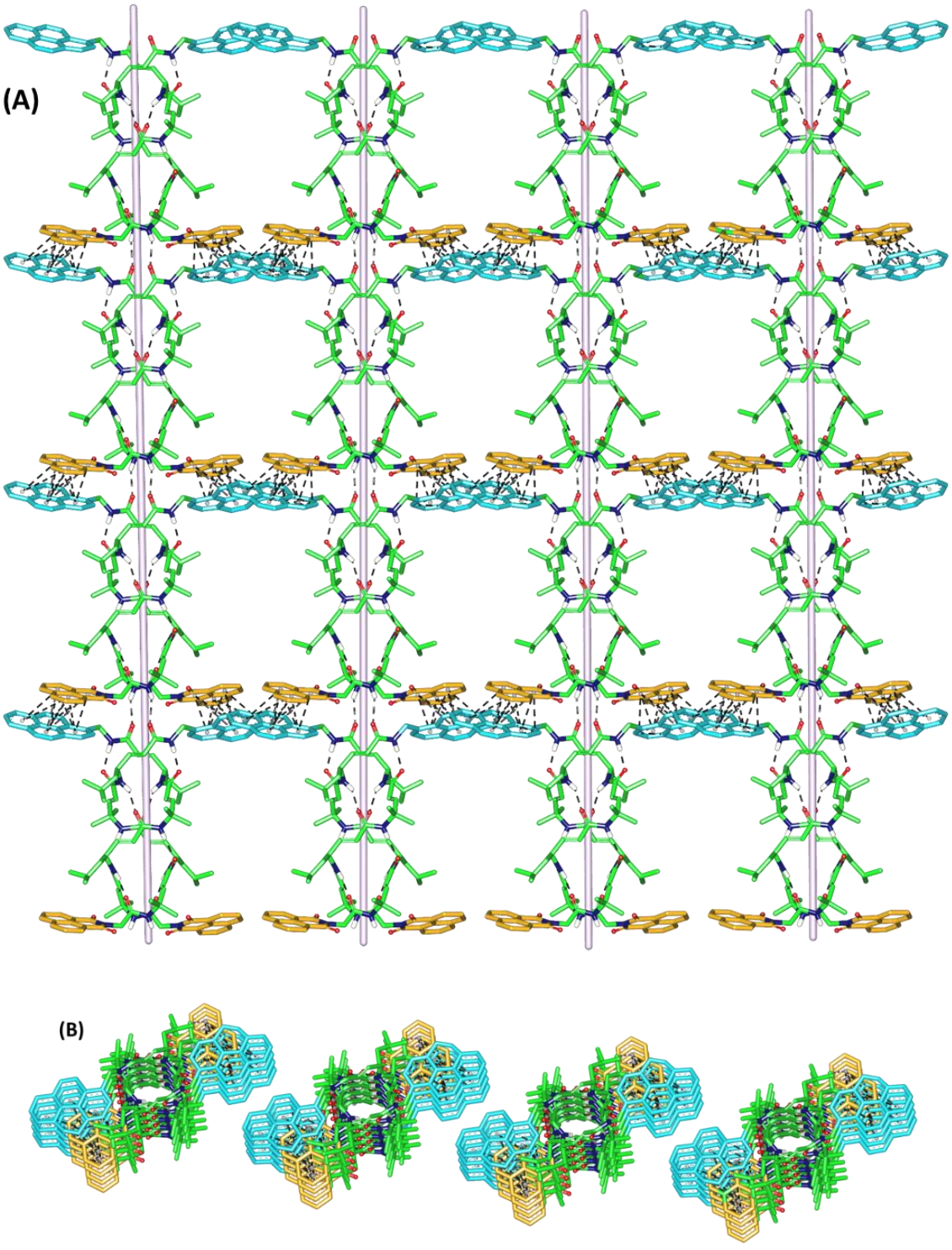


Figure 12: (A) Columnar assembly of the peptide **P3.** (B) The top view of the columnar assembly shows a channel-like architecture.

Understanding the crystal packing along different axes is crucial for characterizing the three-dimensional structure of a crystal. It helps in determining the symmetry and periodicity of the crystal lattice and provides insights into how the molecules interact with one another to form the overall solid-state structure. The crystal packing along the a-axis shows a specific pattern, and provides insight into how the molecules are ordered side by side in this particular direction. The crystal packing is shown in Figure 13A. The top view of the three-dimensional crystal packing along the *c*-axis and in the *a*-*b* plane reveals a distinctive zig-zag assembly pattern between the columnar architecture. The "zig-zag" assembly pattern indicates that the columns are not aligned in a perfectly straight manner. Instead, they exhibit a zig-zag or serpentine arrangement, where adjacent columns have an alternating left-to-right or right-to-left orientation. This zig-zag pattern is characteristic of the molecular arrangement within the crystal lattice. The assembly is shown in Figure 13B. This complex three-dimensional assembly is essential for the overall stability and structural integrity of the crystal lattice, and it reflects the intricate interplay of various non-covalent interactions that contribute to the formation of this supramolecular structure.

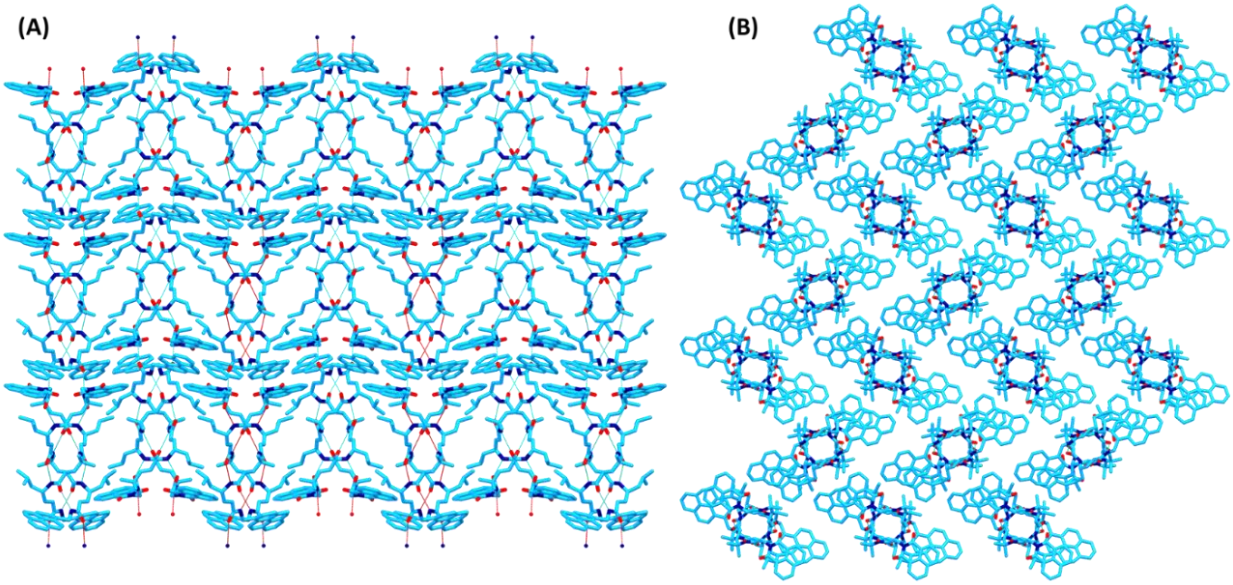


Figure 13: (A) 3-D crystal packing of the peptide **P3** along *a*-direction. (B) The crystal packing along the *c*-direction.

Understanding these interactions is vital for designing and engineering materials with specific properties in the fields of chemistry, materials science, and nanotechnology.

5.3.7. Photophysical Properties of the Peptides

Steady-state UV-visible absorption and fluorescence spectroscopy in both dilute solutions and solvent-free liquids were employed to establish a direct correlation between molecular structure and the interactions among pyrene and NMI moieties. The UV-Vis spectra observed in a chloroform ($CHCl_3$) solution with different concentrations exhibit a peak with a maximum wavelength at ~ 346 nm for all three peptides. The concentration-dependent absorption spectra for **P1**, **P2** and **P3** are shown in Figure 14**.**

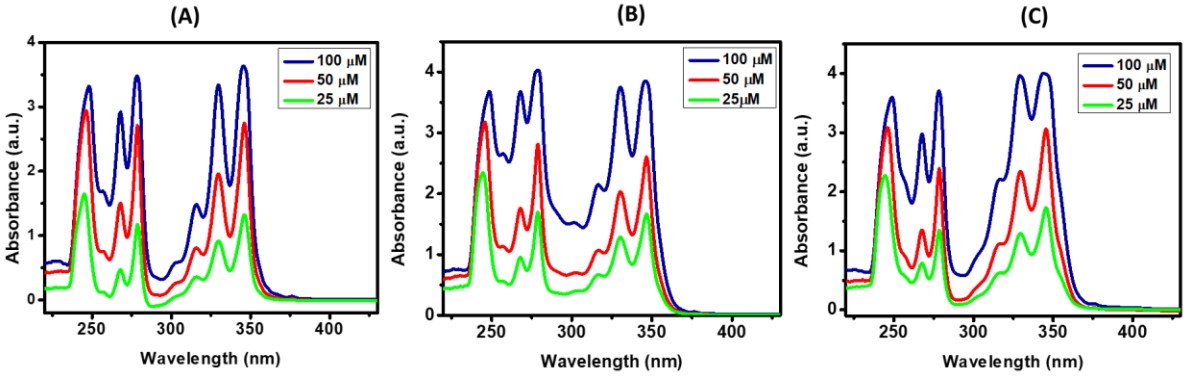


Figure 14: UV-Vis spectra of peptide (A) **P1** (B) **P2** and (C) **P3** in chloroform

In the crystal structure analysis, we observed aromatic stacking between pyrene moieties in **P1**. Similarly, in solution, we identified the presence of an excimer fluorescence peak for **P1** centered around ~460 nm, in addition to the monomeric emission range of 350-400 nm. Notably, the excimer peak remained detectable even at very low concentrations, specifically at 1μM, indicating the persistence of double helical structural integrity in the solution phase. The concentration-dependent fluorescence spectra of **P1**, illustrated in Figure 15A, further support this observation. Even at varying concentrations, the excimer peak consistently appeared, underscoring the stability and structural characteristics of the formed excimer complex in solution. Additionally, when examining the fluorescence spectra of **P1** in different solvents, we noted that there was no shift in the maximum emission wavelength at 460 nm. This lack of shift indirectly implies the presence of the excimer complex in solution, suggesting that the interaction between pyrene molecules leading to excimer formation remains consistent across different solvents.

In chloroform, the fluorescence spectra of **P2** reveal a distinctive broad emission peak centered around 540 nm, as illustrated in Figure 16A.

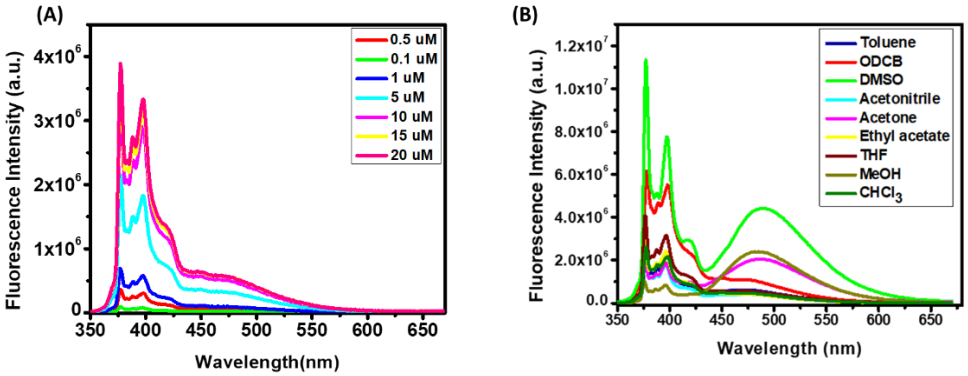


Figure 15: (A) Concentration-dependent fluorescence spectra of **P1** in chloroform. (B) Solvent-dependent fluorescence spectra of **P1**

To provide a comprehensive comparison, Figure 16B depicts the fluorescence spectra of peptides containing only pyrene, only NMI, and **P2**, where both pyrene and NMI units are present Notably, the λ_{max} value of the broad band observed for peptide **P2** differs significantly from the λ_{max} values seen in cases involving only pyrene (excimer band at 460 nm) or only NMI (excimer band due to NMI-NMI stacking interaction at 470 nm). The red-shifted band observed in **P2**'s spectrum is indicative of a charge transfer process occurring between the pyrene and NMI units. The concentration-dependent spectra in chloroform offer further insights. With an increase in peptide concentration, the intensity of the complex, characterized by the charge transfer band, exhibits a corresponding augmentation. This concentration-dependent increase suggests that the charge transfer process becomes more pronounced and significant at higher peptide concentrations. The presence of the charge transfer band even at very low concentrations supports the idea of supramolecular assembly at these lower concentration levels.

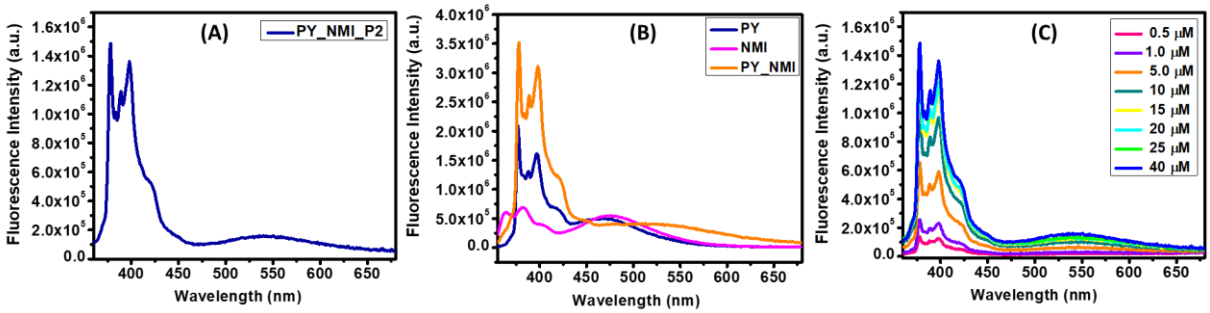


Figure 16: (A) Emission spectra of **P2** in chloroform. (B) Combine spectra of a peptide containing only pyrene, only NMI, and Pyrene-NMI (**P2**) together. (C) Concentration-dependent emission spectra of **P2** in chloroform

Additionally, the solvent-dependent emission spectra of **P2** demonstrate variations in λ_{max}, further implying the formation of a solvent-dependent charge transfer complex indirectly. However, a more profound understanding of the intermolecular charge transfer complex is obtained through the concentration-dependent fluorescence spectra of **P2** in toluene solution. Here, the observation that the intensity of the charge transfer band surpasses the intensity of monomeric emission with increasing peptide concentration indicates that, as more molecules come closer, a charge transfer-based supramolecular assembly is formed.

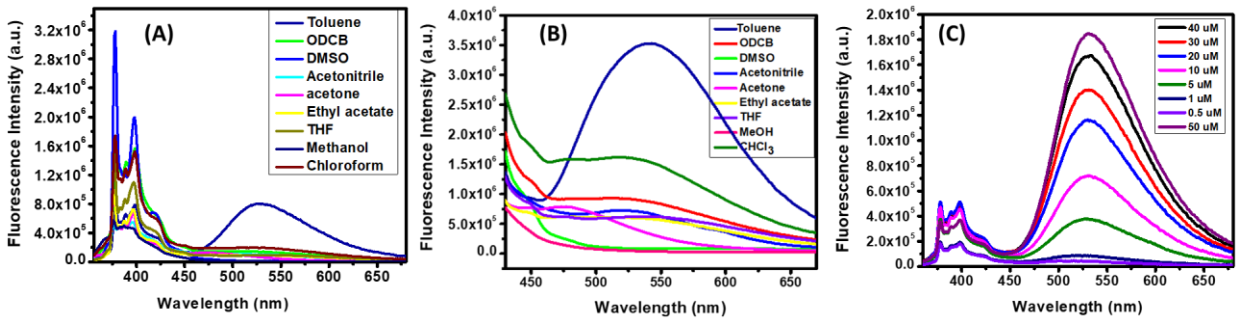


Figure 17: (A) solvent-dependent emission spectra of **P2**. (B) The zoom region of the charge-transfer band observed in **P2** (C) Concentration-dependent emission spectra of **P2** in toluene.

In summary, the red-shifted emission band in **P2**'s spectra, concentration-dependent behavior, and solvent-dependent variations collectively support the presence of a charge transfer complex between pyrene and NMI units, highlighting the dynamic nature of supramolecular assemblies influenced by both concentration and solvent conditions.

The emission spectra of peptide **P3** in chloroform, as illustrated in Figure 18, exhibit a notable broad peak at approximately 475 nm, in addition to the monomeric emission. This broad peak is attributed to the pyrene-NMI stacking interaction, which gives rise to an excimer-type complex rather than a charge transfer complex. The formation of this excimer complex is responsible for the observed broad peak in the emission spectra. The solvent-dependent emission spectra of **P3** provide additional evidence supporting the excimer formation. The absence of significant changes in the λ_{max} values of the broad peak across different solvents indicates the stability of the excimer complex in various environmental conditions. This consistent behavior in different solvents aligns with the observation made in the crystal structure, indicating that **P3** exhibits similar characteristics both in the solid state and in solution. In summary, the broad peak at ~475 nm in the emission spectra of **P3** in chloroform, coupled with the lack of significant changes in λ_{max} values across

different solvents, underscores the formation of an excimer-type complex through pyrene-NMI stacking interaction. The similarity in behavior between the crystal structure and the solution phase further reinforces the notion that **P3** maintains consistent characteristics across different states, emphasizing the stability and reproducibility of its excimer-forming interactions.

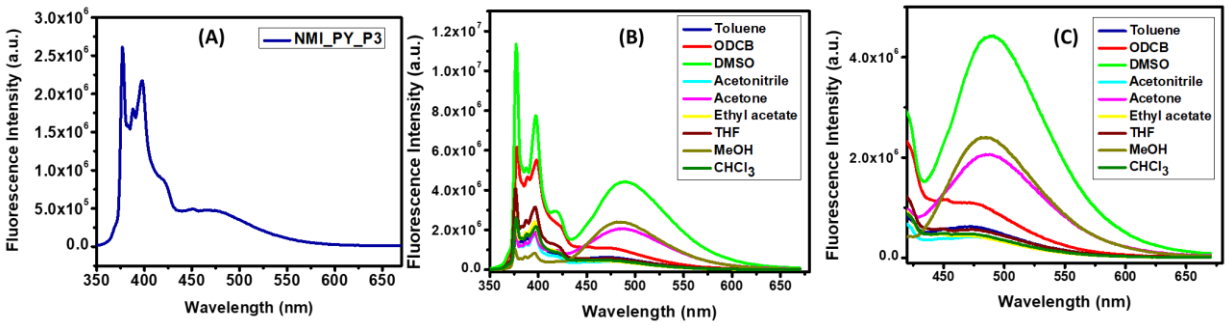


Figure 18: (A) Emission spectra of **P3** in chloroform. (B) solvent-dependent emission spectra of **P3** (C) The zoom region of the broad band observed in **P3.**

5.3.8. Circular Dichroism Analysis of Peptides

Circular dichroism is an important tool for comprehending the secondary structure of polypeptides in solution. CD analysis of the peptides **P1**, **P2,** and **P3** were carried out in chloroform. **P1** showed a positive cotton effect at λ_{max}= 243 nm and a negative cotton effect at λ_{min}= 226 nm. **P2** showed a positive cotton effect at λ_{max}= 248 nm and a negative cotton effect at λ_{min}= 225 nm. **P3** showed a positive cotton effect at λ_{max}= 245 nm and a negative cotton effect at λ_{min}= 223 nm. The CD signals are similar to our previously observed β-double helical signals. This study also proves that peptides adopt a β-double helical conformation in solution as well. The representative CD plot for **P1**, **P2,** and **P3** is given below.

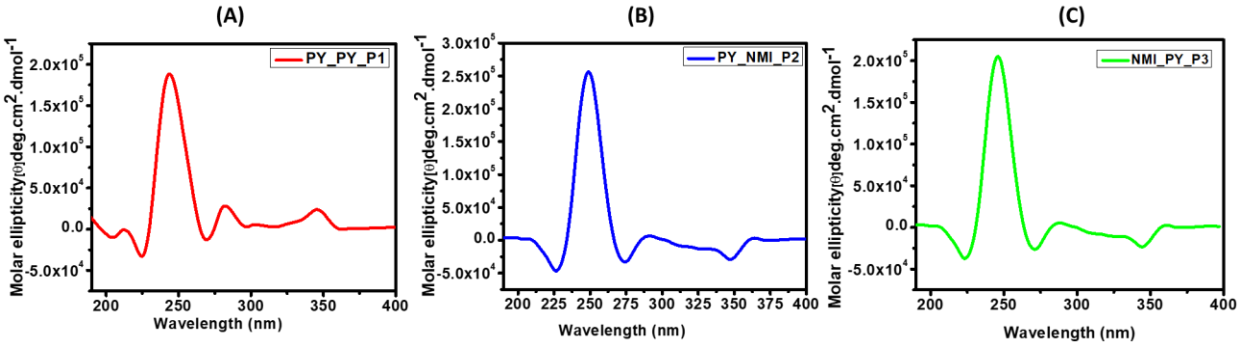


Figure 19: (A) CD-spectra of **P1** (B) CD-spectra of **P2** (C) CD-spectra of peptide **P3**.

5.3.9. Current-Voltage Study of the Peptides

Pyrene and Naphthalenediimide (NDI) are organic molecules that, when combined, can form a semiconducting material.[59] Their unique electronic properties along with their ability to self-assemble into well-defined structures make them promising candidates for applications in organic electronics and optoelectronics.[60,61] The use of peptides for semiconducting materials is an emerging field in materials science.[62] Peptides are advantageous due to their tunable structures, self-assembly properties, and potential for bio-compatibility. The key to creating a semiconducting material is the controlled self-assembly of these peptides. When pyrene and NMI units are alternately arranged in the peptide sequence, they can stack through π-π interactions. This π-π stacking facilitates charge transport through the assembly, creating a pathway for charge carriers, which is a fundamental characteristic of semiconductors. In this context, we were curious to investigate whether the peptides in the current study appended with pyrene and NMI groups can show semiconducting properties.

In the crystal structures of peptides **P1** we have seen a specific arrangement of pyrene units in between the double helical motifs and also, we observed a π-stacking interaction between the pyrene units. Again, in the case of **P2** and **P3**, we observed a donor-acceptor-based supramolecular assembly of the double-helical units. As this kind of well-structured assembly helps in keeping the electron donor pyrene and electron acceptor NMI units, they can further improve the semiconducting behavior of these materials. The bulk electrical conductivities of the peptides **P1**, **P2** and **P3** were measured by current–voltage study. We prepared the experimental samples by drop-casting the solutions onto an ITO glass and then sealing them with another ITO strip. Before the experiment, we maintained the samples in a vacuum for 24 hours to eliminate any moisture that could potentially impact their electrical properties. To measure the current, we gradually changed the voltage from -5 V to +5 V. The *I-V* plot for all three peptides is presented in Figure 20. It was found that the increment of current concerning the voltage applied shows a non-ohmic nature for the peptides. This indicates the semiconducting nature of these peptide molecules. In Figure 20, we can see that at +4 V, **P1**, **P2**, and **P3** exhibit current values of 7.8 × 10^-5 μA, 1.7 × 10^-4 μA, and 1.87 × 10^-4 μA, respectively. Notably, the current values of **P2** and **P3** at +4 V were nearly 10 times higher than that of **P1**. This interesting phenomenon can be attributed to the formation of charge-transfer complexes by the pyrene-NMI units.[63] These complexes, in turn,

facilitate the mobility of both electrons and holes within the peptide structures. This increased charge mobility is likely responsible for the significantly higher currents observed in **P2** and **P3** compared to **P1**.

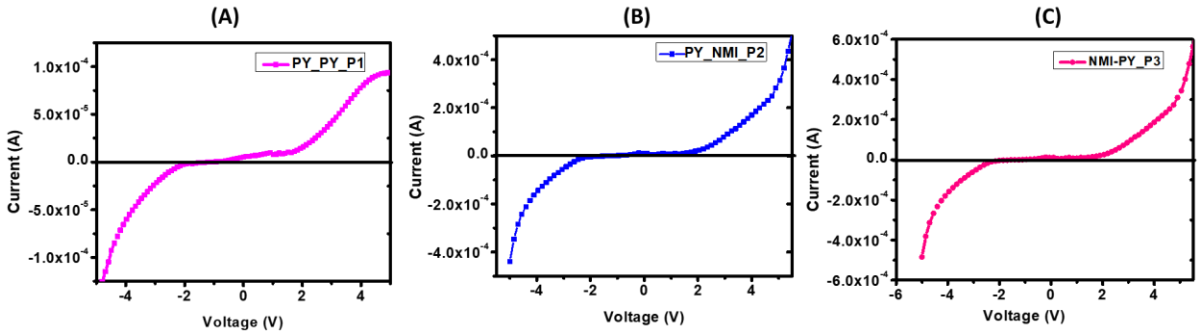


Figure 20: The *I-V* plot for the peptides (A) **P1** (B) **P2** (C) **P3**

5.3.10. Photo-Switching Property

A composite system that incorporates both donor and acceptor moieties can exhibit a strong ability to respond to light. The responsiveness of a system to light, particularly in terms of switching photocurrent, is evaluated by conducting measurements with and without the presence of light. In the context of this study, we conducted photocurrent measurements on peptides **P1** and **P2** to explore and assess their photo-switching properties. The time vs photocurrent plot is given below in Figure 21.

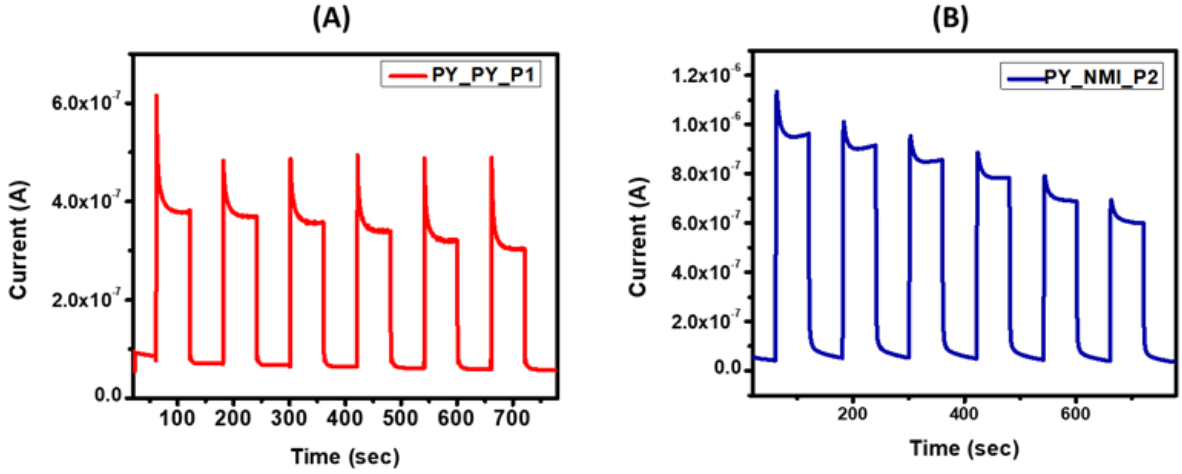


Figure 21: Photo-response behavior by turning on/off light on devices made of (A) **P1** (B) **P2**

In this experiment, as a light source, we used 365 nm blue LED. Based on the data presented in Figure 21, it becomes apparent that **P1** exhibits photo-switching behavior, characterized by a photocurrent gain (I_{on}/I_{off}) value of 4.5, while **P2** displays a significantly higher photocurrent gain of 24.5, both at a fixed bias of +0.5 V. This substantial difference in photocurrent gain for **P2** can be attributed to the formation of a charge transfer complex between the pyrene and NMI moieties within the peptide structure. This complex enhances the mobility of charges within the system, resulting in the significantly elevated photocurrent observed in **P2** compared to **P1**. In essence, the charge transfer complex contributes to the improved photo-switching properties of **P2**.

5.4. Conclusion

In conclusion, this work has presented a comprehensive exploration of the design and synthesis of a novel pyrene and NMI-appended β-double helix. The investigation of its self-assembly behavior has unveiled diverse packing arrangements, showcasing its versatility in forming columnar structures and two-dimensional network structures. Notably, the formation of an acceptor charge transfer complex has been successfully achieved, highlighting the potential for intriguing electronic interactions within the system. The significance of π-π stacking interactions in the self-assembly process has been emphasized, shedding light on the structural intricacies that govern the organization of the pyrene and NMI-appended double helices. This work has also delved into the photophysical properties of the synthesized structure, providing valuable insights into its optical behavior and photoelectronic properties. Furthermore, the exploration of semiconductor properties has opened new avenues for potential applications in electronic devices. The ability to modulate the electronic characteristics of the material through controlled self-assembly suggests promising implications for the field of organic electronics. This multidimensional analysis contributes to our understanding of the structure-property relationships and offers a foundation for the development of innovative materials with tailored functionalities for diverse applications in electronic and optoelectronic devices.

5.5. Experimental Section

5.5.1 Materials and Methods

All reagents and solvents were used without further purification. Column chromatography was performed over silica gel. Final peptides were purified through reverse phase HPLC (C_{18} column, MeOH/H_2O 95:5 as a gradient with flow rate 2.00 mL/min). All the reactions were monitored by

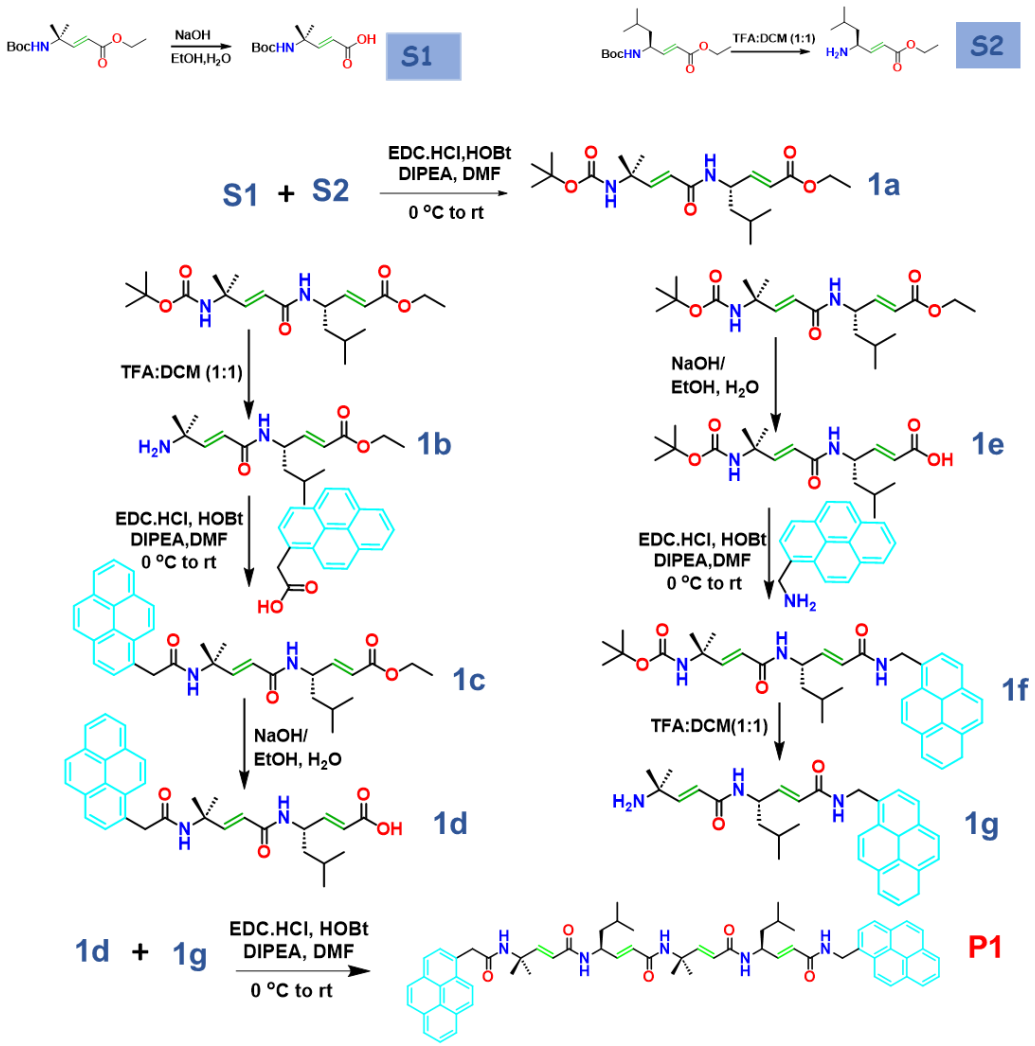
analytical thin-layered chromatography. The TLC visualization was done through UV light, $KMNO_4$ stain, and ninhydrin stain. ^1H NMR and ^{13}C NMR were performed through deuterated solvent on 400 MHz and 101 MHz respectively. We used a Matrix Assisted LASER Desorption Ionization mass spectrometer (MALDI-TOF/TOF) to calculate the accurate mass of our peptides. Fluorescence data was measured through the Spectrofluorometer instrument. X-ray crystal structures were determined through APEX(III) DUO X-ray diffractometer using Mo-Kα (λ=0.71073 Å) graphite monochromatic radiation.

5.5.2. Synthesis Procedures for the Peptides

5.5.2.1. Synthesis of the Peptide P1

Boc-dγAic-OEt and Boc-dγLeu-OEt were synthesized using a previously reported method. For the synthesis of **1a**, **1b**, and **1e**, the procedure outlined in Chapter 2 was followed. Pyrene acetic acid (600 mg, 2.3 mmol) was dissolved in 5 mL of DMF and cooled to 0°C under a nitrogen atmosphere. EDC.HCl (490 mg, 2.53 mmol), HOBt (310 mg, 2.3 mmol), and DIPEA (1.6 ml, 9.2 mmol) were added, and the reaction mixture was stirred for 10 minutes. Subsequently, dipeptide amine **1b** was introduced, and the reaction was stirred overnight. TLC was used to monitor the reaction progress. After completion of the reaction, the mixture was diluted with 150 mL ethyl acetate and washed with first 10% HCl (75 ml × 2) and then 10% Na2CO3 solution (75 ml × 2), and brine solution (75 mL × 2). The organic layer was dried using anhydrous Na_2SO_4, and the resulting solution was concentrated under reduced pressure, leading to the formation of a crude powder. Column chromatography was used for the purification. Finally, we got crystalline product **1c** with a yield of 82%.

Compound **1f** was synthesized by following the procedure mentioned in the experimental section reported in Chapter 4. The hydrolysis of Pyrene-dγAic-dγLeu-OEt (1c) (1.2 mmol, 634 mg) was conducted in a mixture of ethanol and water (1:1) using 1.0 N NaOH as a base. Following complete hydrolysis, ethanol was removed by evaporation, and the resulting reaction mixture was acidified with a 1.0 N HCl solution. The mixture was then subjected to extraction with ethyl acetate and washed with a brine solution (75 mL × 2). The organic layer was dried using anhydrous Na_2SO_4 and concentrated under reduced pressure, yielding a crude powder (**1d**) that was directly utilized for the next step of the coupling reaction.



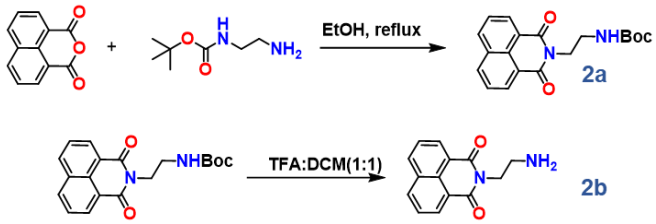
Scheme 2: Synthesis of peptide **P1**

The Boc group of **1f** (1.2 mmol 0.7 g) was deprotected by using 1.5 ml 1:1 TFA: DCM for 1h. Subsequently, trifluoroacetic acid (TFA) and dichloromethane (DCM) solvent were evaporated, and 5-6 additional cycles of adding DCM followed by evaporation were performed to eliminate any remaining traces of TFA. The resulting crude material constituted the trifluoroacetic acid (TFA) salt of the amine of **1f**. To convert it into the free amine **1g**, 0.5 ml of DMF, and 0.5 ml of DIPEA were introduced. Concurrently, compound **1d** (0.61 g, 1.2 mmol) was dissolved in 3 mL of DMF and chilled to 0 °C under a nitrogen atmosphere. In this step, EDC.HCl (253 mg, 1.32 mmol), HOBt (162 mg, 1.2 mmol), and DIPEA (0.625 ml, 3.6 mmol) were combined, and the resulting reaction mixture was stirred for 10 minutes. Subsequently, compound 1g was introduced into the reaction mixture and stirred overnight. The advancement of the reaction was observed

through thin-layer chromatography (TLC). Once the reaction reached completion, the mixture was diluted by adding 125 mL of ethyl acetate and subjected to washing with 10% HCl (75 mL × 2), 10% Na_2CO_3 solution (75 mL × 2), and, finally, a brine solution (75 mL × 2). The organic layer was dried using anhydrous Na_2SO_4 and concentrated under reduced pressure, resulting in a crude powder. This crude material was then subjected to purification via column chromatography to obtain a white crystalline product, **P1**, with a yield of 61%.

5.5.2.2. Synthesis of Peptide P2

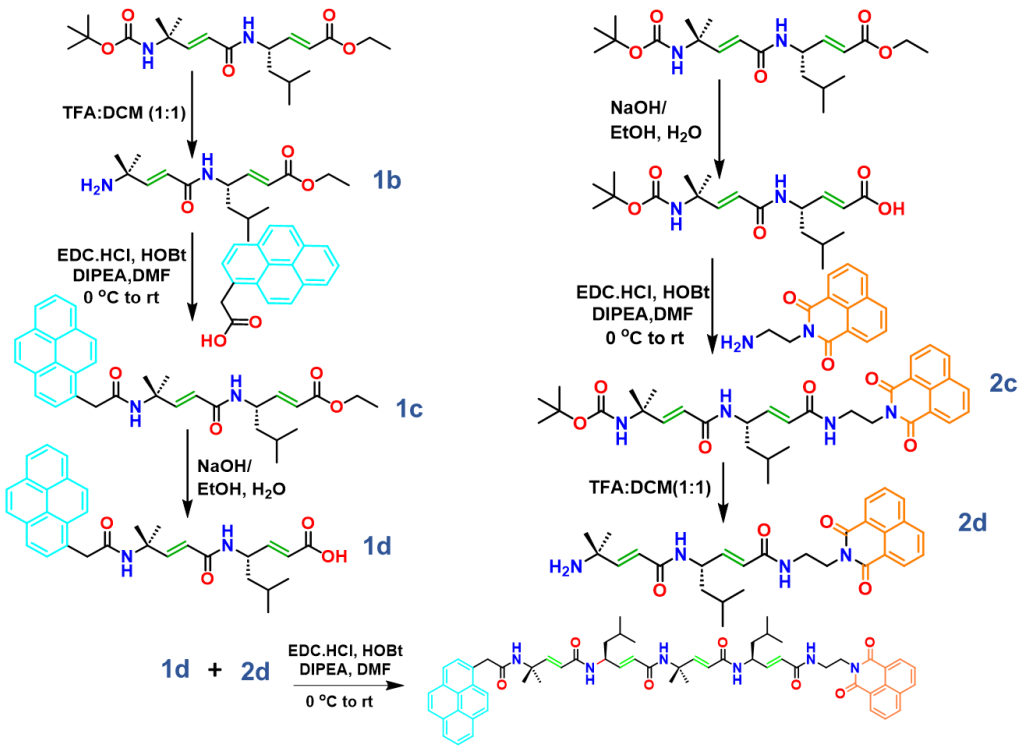
Ethylene diamine, protected with a single Boc group (1.6 g, 10 mmol), was placed into a round-bottomed flask, and 30 ml of ethanol was added. Following 5 minutes of stirring, 1,8-Naphthalic anhydride (2.0 g, 10 mol) was added, and the reaction was subjected to reflux for 1 hour. Subsequently, the reaction mixture was allowed to cool to room temperature solid formed was filtered, rinsed with cold ethanol, and subsequently dried under vacuum at 40 °C. This process resulted in the production of an off-white solid, **2a**. The overall yield of the process was 94%. After that, the Boc deprotection of **2a** was carried out following the procedure mentioned above to get **2b**.



Scheme 3: Synthesis of **2a** and **2b**

The dipeptide acid (**1e**) (0.85 g. 2.3 mmol) was dissolved in 3 mL of DMF and cooled to 0°C under a nitrogen atmosphere. EDC.HCl (490 mg, 2.53 mmol), HOBt (310 mg, 2.3 mmol), and DIPEA (1.6 ml, 9.2 mmol) were added, and the reaction mixture was stirred for 10 minutes. Subsequently, compound **2b** was introduced, and the reaction was stirred overnight. TLC was used to monitor the reaction progress. After completion of the reaction, the mixture was diluted with 150 mL ethyl acetate and washed with first 10% HCl (75 ml × 2) and then 10% Na2CO3 solution (75 ml × 2), and brine solution (75 mL × 2). The organic layer was dried using anhydrous Na_2SO_4, and the resulting solution was concentrated under reduced pressure, leading to the formation of a crude

powder. Column chromatography was used for the purification. Finally, we got crystalline product **2c** with a yield of 80%.

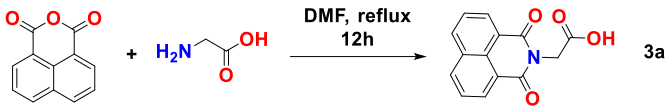


Scheme 4: Synthesis of peptide **P2**

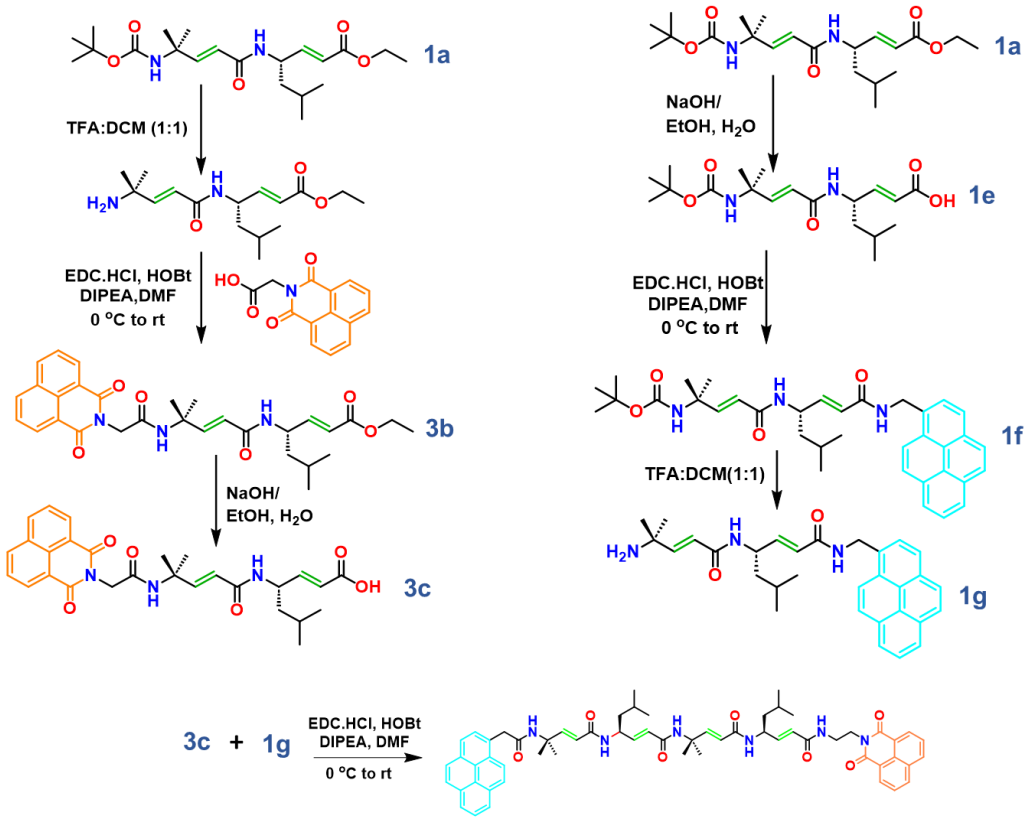
Boc-deprotection of **2c** (1.2 mmol 0.71 g) was carried out by using the method mentioned in the synthesis of **P1**. The resulting material in its crude form constituted the trifluoroacetic acid (TFA) salt of the amine in **2c**. To convert it into the free amine, 0.5 ml of DMF and 0.5 ml of DIPEA were added. Simultaneously, compound **1d** (0.61 g, 1.2 mmol) was dissolved in 3 mL of DMF and cooled to 0 °C under a nitrogen atmosphere. EDC.HCl (253 mg, 1.32 mmol), HOBt (162 mg, 1.2 mmol), and DIPEA (0.625 ml, 3.6 mmol) were introduced to the reaction mixture, which was stirred for 10 minutes. Subsequently, compound 2d was added and stirred overnight, with the reaction progress monitored by TLC. Upon completion, the mixture was diluted with 125 mL of ethyl acetate and washed with 10% HCl (75 mL × 2), 10% Na_2CO_3 solution (75 mL × 2), and finally, a brine solution (75 mL × 2). The organic layer was dried using anhydrous Na_2SO_4 and concentrated under reduced pressure, resulting in a crude powder. This material was then subjected to column chromatography for purification, yielding a yellowish-white product, **P2**, with a yield of 63%.

5.5.2.3. Synthesis of Peptide P3

Synthesis of NMI-Gly-OH: To produce the compound, 1,8-Naphthalic anhydride (5.0 mmol, 0.99 g) and glycine (7.0 mmol, 0.52 g) were dissolved in 15 mL of anhydrous dimethylformamide (DMF) and subjected to reflux under a nitrogen (N2) atmosphere for 12 hours using a heating mantle. Subsequently, the reaction mixture was cooled to room temperature. Filtration removed the insoluble fraction, and the resulting brown solution was introduced into 100 mL of distilled water. The resulting white precipitate was filtered and thoroughly rinsed with distilled water. The crude product was then allowed to air-dry. The yield of the product was 1.21 g (4.74 mmol, 95.3%).



Scheme 5: Synthesis of NMI-Gly-OH



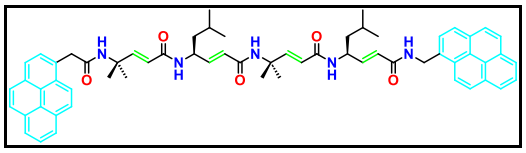
Scheme 6: Synthesis of peptide **P3**

The NMI-Gly-OH (0.58 g. 2.3 mmol) was dissolved in 3 mL of DMF and cooled to 0°C under a nitrogen atmosphere. EDC.HCl (490 mg, 2.53 mmol), HOBt (310 mg, 2.3 mmol), and DIPEA (1.6

ml, 9.2 mmol) were added, and the reaction mixture was stirred for 10 minutes. Subsequently, compound **1b** was introduced, and the reaction was stirred overnight. TLC was used to monitor the reaction progress. After completion of the reaction, the mixture was diluted with 150 mL ethyl acetate and washed with first 10% HCl (75 ml × 2) and then 10% Na_2CO_3 solution (75 ml × 2), and brine solution (75 mL × 2). The organic layer was dried using anhydrous Na_2SO_4, and the resulting solution was concentrated under reduced pressure, leading to the formation of a crude powder. Column chromatography was used for the purification. Finally, we got crystalline product **3b** with a yield of 82%.

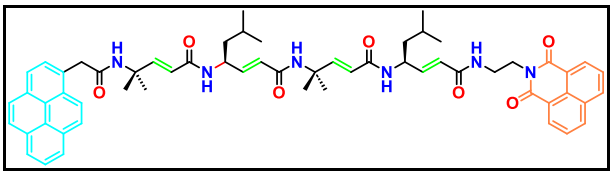
Hydrolysis of **3b** (1.2 mmol 0.63 g) was carried out by a previously reported method to give a crude powder (**3c**) which was used directly for the coupling. The compound **3c** (1.2 mmol, 0.6 g) was dissolved in 3 ml of DMF and cooled to 0 ℃. EDC.HCl (253 mg, 1.32 mmol), HOBt (162 mg, 1.2 mmol), and DIPEA (0.625 ml, 3.6 mmol) were then added to the reaction mixture, which was stirred for 10 minutes. Following this, compound **1g** was introduced and stirred overnight, with TLC used to monitor the reaction progress. Once the reaction was complete, the mixture was diluted with 125 mL of ethyl acetate and subjected to washing with 10% HCl (75 mL × 2), 10% Na_2CO_3 solution (75 mL × 2), and finally, a brine solution (75 mL × 2). The organic layer was dried using anhydrous Na_2SO_4 and concentrated under reduced pressure, resulting in a crude powder. This material was then subjected to column chromatography for purification, yielding a yellowish-white product, **P3**, with a yield of 64%.

5.6. Characterization of Peptides P1, P2 and P3

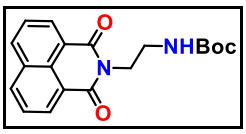


P1:**^{1}H NMR** (400 MHz, Chloroform-d) δ 8.84 (t, J = 5.6 Hz, 1H), 8.56 (d, J = 8.1 Hz, 1H), 8.52 (d, J = 9.2 Hz, 1H), 8.42 (d, J = 8.1 Hz, 1H), 8.27 – 7.88 (m, 18H), 7.85 (d, J = 7.8 Hz, 1H), 6.75 (d, J = 9.3 Hz, 1H), 6.70 (d, J = 3.5 Hz, 1H), 6.33 (d, J = 5.9 Hz, 1H), 6.29 (d, J = 6.1 Hz, 1H), 5.64 (dd, J = 15.3, 1.9 Hz, 1H), 5.60 – 5.53 (m, 2H), 5.45 (d, J = 15.4 Hz, 1H), 5.43 – 5.36 (m, 1H), 5.25 (dd, J = 14.7, 5.3 Hz, 1H), 4.58 (s, 1H), 4.30 (s, 1H), 4.20 – 4.06 (m, 2H), 1.62 – 1.29 (m, 6H), 1.23 (d, J = 23.7 Hz, 6H), 0.88 (d, J = 3.2 Hz, 6H), 0.80 (d, J = 6.6 Hz, 3H), 0.71 (dd, J = 12.8, 6.5 Hz, 6H), 0.56 (d, J = 6.5 Hz, 3H). **^{13}C NMR** (101 MHz, Chloroform-d) δ 171.42, 166.39,

166.33, 166.02, 164.42, 150.01, 148.63, 145.26, 144.68, 133.11, 131.49, 131.42, 131.36, 131.12, 130.79, 130.76, 129.47, 129.07, 128.99, 128.24, 128.12, 127.82, 127.72, 127.66, 127.37, 127.30, 126.93, 126.66, 126.06, 125.88, 125.77, 125.32, 125.08, 125.03, 124.83, 124.62, 124.03, 122.32, 121.25, 120.85, 120.63, 119.17, 54.55, 53.66, 49.11, 48.57, 43.93, 43.61, 43.13, 41.67, 29.98, 29.84, 29.52, 25.45, 25.11, 25.06, 23.25, 23.04, 22.74, 21.94. **MALDI TOF/TOF** m/z calculated value for $C_{63}H_{67}N_5O_5[M+Na]^+$ = 996.51 and observed $[M+Na]^+$ = 996.78

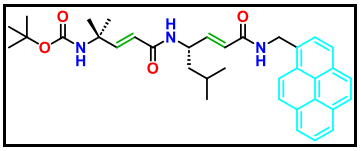


P2: ^{1}H NMR (400 MHz, Chloroform-d) δ 8.70 (d, J = 7.4 Hz, 2H), 8.50 (d, J = 7.9 Hz, 2H), 8.41 (s, 2H), 8.27 – 8.01 (m, 9H), 7.96 (d, J = 9.3 Hz, 1H), 7.90 (d, J = 7.8 Hz, 1H), 7.78 (t, J = 7.7 Hz, 2H), 6.86 – 6.75 (m, 2H), 6.70 (d, J = 15.3 Hz, 1H), 6.44 – 6.32 (m, 2H), 5.74 – 5.61 (m, 2H), 5.52 (d, J = 15.3 Hz, 1H), 5.44 (dd, J = 15.2, 1.9 Hz, 1H), 4.82 – 4.63 (m, 2H), 4.29 (dt, J = 12.6, 4.8 Hz, 1H), 4.24 – 4.14 (m, 2H), 3.91 (d, J = 9.0 Hz, 2H), 3.78 – 3.63 (m, 1H), 1.69 – 1.67 (m, 6H), 1.56 – 1.44 (m, 2H), 1.40 (s, 3H), 1.30 – 1.21 (m, 2H), 1.13 – 1.04 (m, 1H), 0.94 (s, 3H), 0.88 (t, J = 7.0 Hz, 1H), 0.81 (d, J = 6.5 Hz, 3H), 0.75 (d, J = 6.5 Hz, 3H), 0.70 (d, J = 6.5 Hz, 3H), 0.48 (d, J = 6.4 Hz, 3H). **^{13}C NMR** (101 MHz, Chloroform-d) δ 171.50, 166.64, 166.42, 164.46, 133.49, 131.62, 131.36, 130.80, 129.00, 128.33, 128.09, 127.37, 127.26, 125.33, 124.63, 122.99, 54.96, 53.76, 49.14, 44.06, 43.81, 40.08, 37.78, 30.62, 29.48, 25.86, 25.07, 23.34, 22.66, 22.09, 22.02. **MALDI TOF/TOF** m/z calculated value for $C_{60}H_{66}N_6O_7$ $[M+Na]^+$ = 1005.5 and observed $[M+Na]^+$ = 1005.85

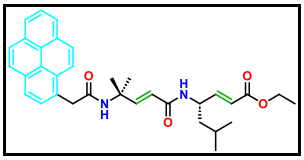


Compound 2a: ^{1}H NMR (400 MHz, Chloroform-d) δ 8.61 (dd, J = 7.3, 1.2 Hz, 2H), 8.22 (dd, J = 8.2, 1.1 Hz, 2H), 7.76 (dd, J = 8.2, 7.3 Hz, 2H), 4.98 (s, 1H), 4.37 (t, J = 5.8 Hz, 2H), 3.54 (q, J = 5.9 Hz, 2H), 1.29 (s, 9H). **^{13}C NMR** (101 MHz, Chloroform-*d*) δ 164.57, 156.06, 134.06, 131.57,

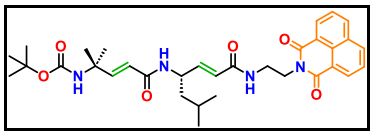
131.43, 128.25, 126.94, 122.50, 79.14, 39.83, 39.69, 28.21. **MALDI TOF/TOF** m/z calculated value for $C_{19}H_{20}N_2O_4[M+Na]^+$ = 363.28 and observed $[M+Na]^+$ = 363.21



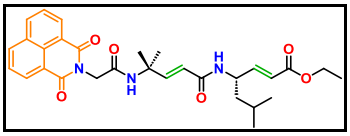
Compound 1f: **^{1}H NMR** (400 MHz, Chloroform-d) δ 8.49 – 8.33 (m, 1H), 8.30 – 7.86 (m, 9H), 6.66 (ddd, J = 16.2, 9.9, 4.6 Hz, 1H), 6.49 (d, J = 15.3 Hz, 1H), 6.17 (d, J = 8.1 Hz, 1H), 5.75 – 5.56 (m, 1H), 5.52 – 5.19 (m, 2H), 5.04 (d, J = 14.6 Hz, 1H), 4.83 (s, 1H), 4.49 (s, 1H), 1.41 (dt, J = 13.7, 6.8 Hz, 1H), 1.30 (d, J = 11.0 Hz, 9H), 1.24 – 1.17 (m, 2H), 1.13 (d, J = 17.8 Hz, 3H), 0.85 (d, J = 19.8 Hz, 3H), 0.71 (td, J = 19.7, 19.0, 6.5 Hz, 6H). **^{13}C NMR** (101 MHz, Chloroform-d) δ 165.41, 165.13, 149.54, 144.14, 143.96, 132.25, 131.23, 130.96, 130.64, 128.89, 127.98, 127.84, 127.74, 127.58, 127.42, 127.18, 125.89, 125.13, 125.04, 124.91, 124.85, 124.70, 123.63, 122.97, 122.37, 79.66, 52.63, 48.03, 43.74, 41.68, 31.93, 29.71, 29.37, 28.35, 27.55, 24.56, 22.71, 22.68, 21.95, 21.72, 14.14. **MALDI TOF/TOF** m/z calculated value for $C_{36}H_{43}N_3O_4[M+Na]^+$ = 604.33 and observed $[M+Na]^+$ = 604.48



Compound 1c: ^{1}H NMR (400 MHz, Chloroform-d) δ 8.31 – 7.90 (m, 9H), 6.65 (dd, J = 7.6, 1.5 Hz, 1H), 6.61 (dd, J = 7.8, 1.5 Hz, 1H), 5.69 (dq, J = 15.7, 1.5 Hz, 1H), 5.30 (dd, J = 14.8, 7.7 Hz, 1H), 5.21 – 5.04 (m, 1H), 4.69 (s, 1H), 4.54 (p, J = 7.6 Hz, 1H), 4.28 – 4.24 (m, 2H), 4.20 (qd, J = 7.1, 1.3 Hz, 2H), 1.41 (dq, J = 13.2, 6.7 Hz, 1H), 1.33 – 1.26 (m, 9H), 1.21 – 0.99 (m, 2H), 0.83 (dd, J = 6.6, 1.2 Hz, 6H).**^{13}C NMR** (101 MHz, Chloroform-d) δ 170.10, 166.29, 164.58, 148.70, 147.66, 131.33, 131.07, 130.63, 129.43, 129.02, 128.46, 128.31, 127.72, 127.43, 126.48, 125.78, 125.56, 125.43, 125.16, 124.54, 123.35, 120.74, 119.93, 60.46, 54.04, 48.00, 43.36, 43.20, 27.25, 27.06, 24.58, 22.62, 22.12, 14.29. **MALDI TOF/TOF** m/z calculated value for $C_{34}H_{38}N_2O_4[M+Na]^+$ = 561.28 and observed $[M+Na]^+$ = 561.486



Compound 2c: **^{1}H NMR** (400 MHz, Chloroform-*d*) δ 8.70 – 8.43 (m, 2H), 8.32 – 8.13 (m, 2H), 7.87 – 7.65 (m, 2H), 6.98 (d, *J* = 86.9 Hz, 1H), 6.78 (d, *J* = 15.6 Hz, 1H), 6.51 (ddd, *J* = 15.4, 12.1, 5.4 Hz, 1H), 6.12 (d, *J* = 58.0 Hz, 1H), 5.96 – 5.60 (m, 2H), 5.05 – 4.75 (m, 1H), 4.68 (d, *J* = 9.3 Hz, 1H), 4.45 – 4.22 (m, 1H), 3.76 – 3.56 (m, 1H), 3.48 (d, *J* = 3.2 Hz, 2H), 1.60 (dt, *J* = 13.0, 6.6 Hz, 1H), 1.42 – 1.32 (m, 15H), 1.29 – 1.19 (m, 2H), 0.89 (td, *J* = 7.8, 7.1, 4.5 Hz, 6H). **^{13}C NMR** (101 MHz, Chloroform-d) δ 165.89, 164.71, 134.35, 134.15, 131.53, 131.47, 128.21, 126.96, 122.38, 121.08, 48.02, 39.92, 28.42, 27.99, 24.72, 22.79, 22.24. **MALDI TOF/TOF** m/z calculated value for $C_{33}H_{42}N_4O_6[M+Na]^+$ = 613.7 and observed $[M+Na]^+$ = 613.51



Compound 3b: **^{1}H NMR** (400 MHz, Chloroform-d) δ 8.58 (dd, J = 7.3, 1.2 Hz, 2H), 8.23 (dd, J = 8.3, 1.1 Hz, 2H), 7.76 (dd, J = 8.2, 7.3 Hz, 2H), 6.86 (dd, J = 15.6, 5.6 Hz, 1H), 6.76 (d, J = 15.4 Hz, 1H), 6.03 (d, J = 15.4 Hz, 1H), 5.99 – 5.91 (m, 2H), 5.90 (s, 1H), 4.93 – 4.81 (m, 2H), 4.78 – 4.69 (m, 1H), 1.65 (s, 2H), 1.50 (d, J = 7.2 Hz, 6H), 1.47 – 1.40 (m, 2H), 1.28 (d, J = 9.8 Hz, 1H), 1.26 – 1.22 (m, 3H), 0.90 (dd, J = 6.6, 2.4 Hz, 6H). **^{13}C NMR** (101 MHz, Chloroform-d) δ 166.45, 166.21, 165.35, 164.22, 148.21, 147.17, 134.48, 131.63, 128.33, 126.98, 122.18, 121.20, 120.81, 60.42, 55.12, 48.31, 43.61, 43.44, 29.70, 27.67, 27.50, 24.71, 22.73, 22.22, 14.22. **MALDI TOF/TOF** m/z calculated value for $C_{30}H_{35}N_3O_6[M+Na]^+$ = 556.25 and observed $[M+Na]^+$ = 556.47

5.7. Appendix

5.7.1. ORTEP Diagrams

5.7.1.1. ORTEP Diagram of Peptide P1

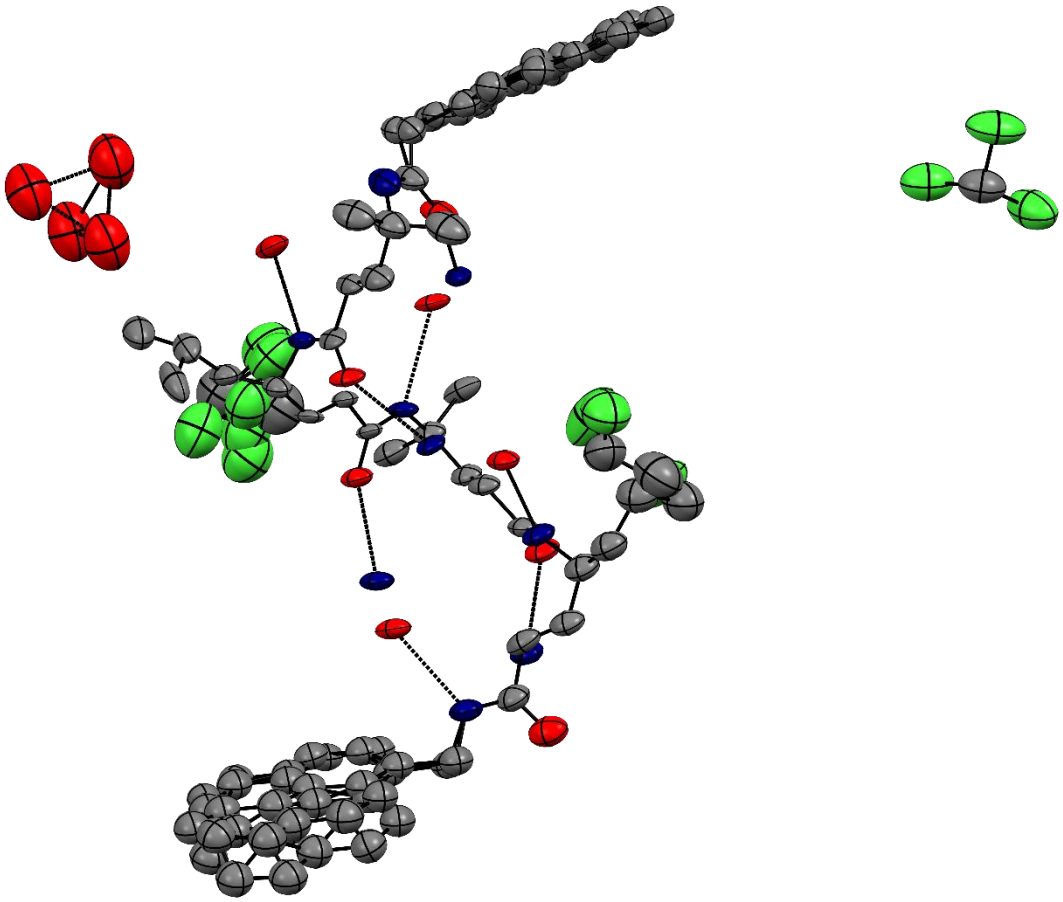


Figure 22: ORTEP diagram of peptide **P1.** H-bonds are shown in dotted lines. H-atoms are omitted for clarity. Ellipsoids are drawn at 50% probability.

5.7.1.2. ORTEP Diagram of peptide P2

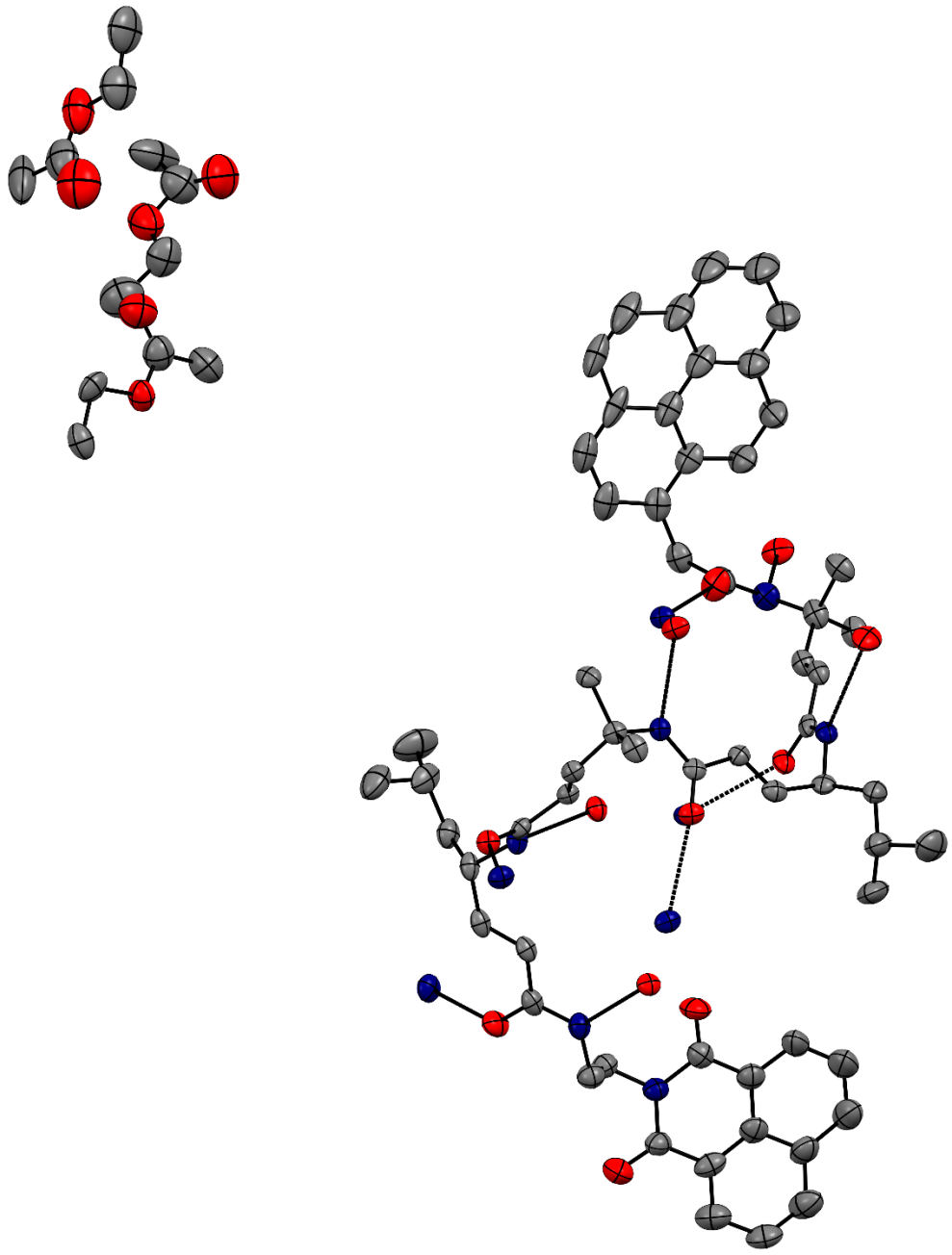


Figure 23: ORTEP diagram of peptide **P2.** H-bonds are shown in dotted lines. H-atoms are omitted for clarity. Ellipsoids are drawn at 50% probability.

5.7.1.3. ORTEP Diagram of Peptide P3

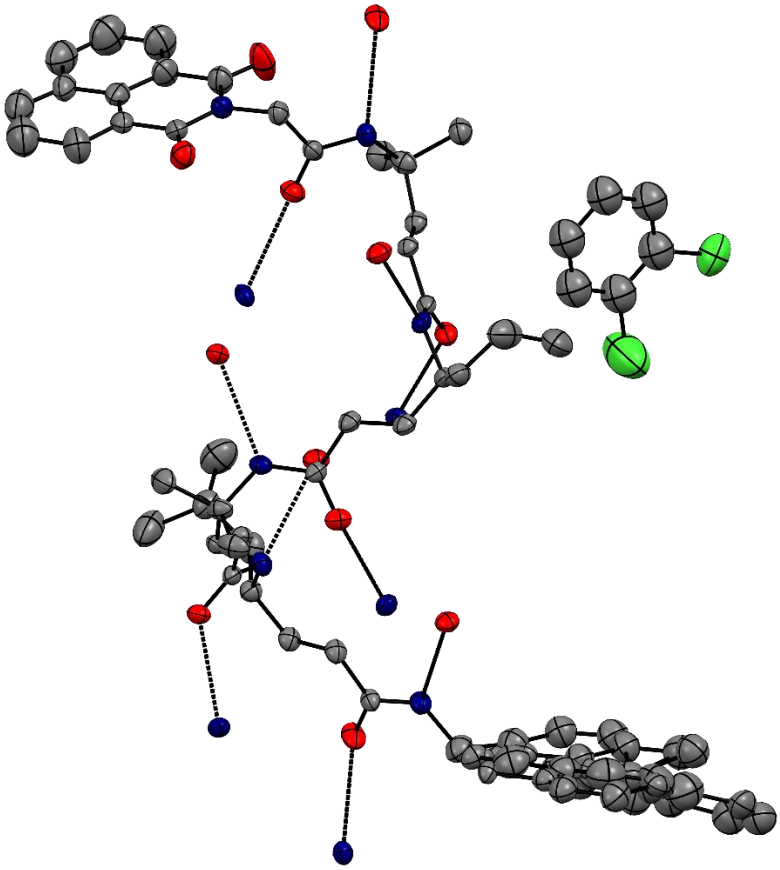


Figure 24: ORTEP diagram of peptide **P3.** H-bonds are shown in dotted lines. H-atoms are omitted for clarity. Ellipsoids are drawn at 50% probability.

5.8 Crystal Structure Information

Crystal structure identification table for P1

Empirical formula	$C_{65.50}H_{71.50}Cl_{7.50}N_5O_6$	
Formula weight	1290.65	
Temperature	296(2) K	
Wavelength	0.71073 Å	
Crystal system	Orthorhombic	
Space group	$P2_12_12$	
Unit cell dimensions	a = 17.322(4) Å	α= 90°.
	b = 22.305(5) Å	β= 90°.
	c = 18.437(4) Å	γ = 90°.
Volume	7124(3) $Å^3$	
Z	4	
Density (calculated)	1.203 Mg/m^3	
Absorption coefficient	0.347 mm^{-1}	
F(000)	2700	
Crystal size	0.300 x 0.200 x 0.200 mm^3	
Theta range for data collection	1.854 to 24.000°.	
Index ranges	-19<=h<=19, -25<=k<=25, -21<=l<=21	
Reflections collected	266829	
Independent reflections	11181 [R(int) = 0.1661]	
Completeness to theta = 24.000°	99.9 %	
Absorption correction	Semi-empirical from equivalents	
Max. and min. transmission	0.94 and 0.85	
Refinement method	Full-matrix least-squares on F^2	
Data/restraints/parameters	11181 / 4937 / 1139	
Goodness-of-fit on F^2	1.127	
Final R indices [I>2sigma(I)]	R1 = 0.1416, wR2 = 0.3343	
R indices (all data)	R1 = 0.2328, wR2 = 0.4229	
Absolute structure parameter	0.073(19)	
Largest diff. peak and hole	0.615 and -0.367 $e.Å^{-3}$	

Crystal structure identification table for P2

Empirical formula	C_{72} H_{90} N_6 O_{13}	
Formula weight	1247.49	
Temperature	296(2) K	
Wavelength	0.71073 Å	
Crystal system	Tetragonal	
Space group	$P4_12_12$	
Unit cell dimensions	a = 19.047(14) Å	α= 90°.
	b = 19.047 Å	β= 90°.
	c = 40.65(3) Å	γ = 90°.
Volume	14746(24) $Å^3$	
Z	8	
Density (calculated)	1.124 Mg/m^3	
Absorption coefficient	0.077 mm^{-1}	
F(000)	5344	
Crystal size	0.150 x 0.100 x 0.100 mm^3	
Theta range for data collection	1.844 to 25.000°.	
Index ranges	-22<=h<=22, -22<=k<=22, -48<=l<=48	
Reflections collected	579109	
Independent reflections	12981 [R(int) = 0.0881]	
Completeness to theta = 25.000°	99.9 %	
Absorption correction	Semi-empirical from equivalents	
Max. and min. transmission	0.99 and 0.91	
Refinement method	Full-matrix least-squares on F^2	
Data/restraints/parameters	12981 / 515 / 911	
Goodness-of-fit on F^2	1.092	
Final R indices [I>2sigma(I)]	R1 = 0.0948, wR2 = 0.2568	
R indices (all data)	R1 = 0.1106, wR2 = 0.2803	
Absolute structure parameter	-0.12(17)	
Largest diff. peak and hole	1.459 and -0.487 $e.Å^{-3}$	

Crystal structure identification table for P3

Empirical formula	$C_{65}\ H_{57}\ Cl_2\ N_6\ O_7$ [+ solvent]	
Formula weight	1105.07	
Temperature	150(2) K	
Wavelength	0.71073 Å	
Crystal system	orthorhombic	
Space group	$P2_12_12$	
Unit cell dimensions	a = 18.480(3) Å	α= 90°.
	b = 21.578(3) Å	β= 90°.
	c = 18.120(3) Å	γ = 90°.
Volume	7225.6 (17) $Å^3$	
Z	4	
Density (calculated)	1.016 Mg/m^3	
Absorption coefficient	0.138mm^{-1}	
F(000)	2316	
Crystal size	0.150 x 0.100 x 0.100 mm^3	
Theta range for data collection	1.844 to 25.000°.	
Index ranges	-22<=h<=21, -25<=k<=2, -21<=l<=20	
Reflections collected	164519	
Independent reflections	12802 [R(int) = 0.0881]	
Completeness to theta = 25.000°	99.9 %	
Absorption correction	Semi-empirical from equivalents	
Max. and min. transmission	0.99 and 0.91	
Refinement method	Full-matrix least-squares on F^2	
Data/restraints/parameters	12802 / 832 / 578	
Goodness-of-fit on F^2	1.041	
Final R indices [I>2sigma(I)]	R1 = 0.0893, wR2 = 0.2598	
R indices (all data)	R1 = 0.1077, wR2 = 0.2419	
Absolute structure parameter	0.2(2)	
Largest diff. peak and hole	1.135 and -0.519 $e.Å^{-3}$	

5.9. References

1. Lehn J M, Ball P. In*: The New Chemistry*. Hall N, editor. Cambridge, U.K.: Cambridge Univ. Press; **2000**. pp. 300–351
2. Philip D, Stoddart J F. *Angew. Chem. Int. Ed*. **1996**, *35*, 1155.
3. Whitesides, G. M.; Boncheva, M. *Proc. Natl. Acad. Sci.* **2002**, *99*, 4769.
4. Thomas, E. L. *Science* **1999**, *286*, 1307.
5. Zhang, S. *Nat. Biotechnol.* **2003**, *21*, 1171
6. Lazzari, M.; Rodríguez-Abreu, C.; Rivas, J.; López-Quintela, M. A. *J. Nanosci. Nanotechnol.* **2006**, *6*, 892.
7. Palmer, L. C.; Stupp, S. I. *Acc. Chem. Res.* **2008**, *41*, 1674.
8. Gazit, E. *Chem. Soc. Rev.* **2007**, *36*, 1263.
9. Levin, A.; Hakala, T. A.; Schnaider, L.; Bernardes, G. J. L.; Gazit, E.; Knowles, T. P. J. *Nat. Rev. Chem.* **2020**, *4*, 615.
10. Murai, K. *Polym. J.* **2023**, *55*, 817.
11. Gelain, F.; Luo, Z.; Rioult, M.; Zhang, S. *npj Regen. Med.* **2021**, *6*, 9.
12. Sun, H.; Marelli, B. *Nat. Commun.* **2020**, *11*, 351.
13. Ganewatta, M. S.; Wang, Z.; Tang, C. *Nat. Rev. Chem.* **2021**, *5*, 753.
14. Ghadiri, M. R.; Granja, J. R.; Milligan, R. A.; McRee, D. E.; Khazanovich, N. *Nature* **1993**, *366*, 324.
15. Zhang, S.; Holmes, T.; Lockshin, C; Rich, A. *Proc. Natl. Acad. Sci. U. S. A.* **1993**, *90*, 3334.
16. Melchionna, M.; Styan, K. E.; Marchesan, S. *Curr. Top. Med. Chem.* **2016**, *16*, 2009.
17. Sahab Negah, S.; Khaksar, Z.; Aligholi, H.; Mohammad Sadeghi, S.; Modarres Mousavi, S. M.; Kazemi, H.; Jahanbazi Jahan-Abad, A.; Gorji, A. *Mol. Neurobiol.* **2017**, *54*, 8050.
18. Ouberai, M. M.; Santos, A. L. G. D.; Kinna, S.; Madalli, S.; Hornigold, D. C.; Baker, D.; Naylor, J.; Sheldrake, L.; Corkill, D. J.; Hood, J. *Nat. Commun.* **2017**, *8*, 1026.
19. Tagalakis, A. D.; Maeshima, R.; Yu-Wai-Man, C.; Meng, J.; Syed, F.; Wu, L. P.; Aldossary,A. M.; Mccarthy, D.; Moghimi, S. M.; Hart, S. L. *Acta Biomater*. **2017**, *51*, 351.
20. Hu, K.; Jiang, Y.; Xiong, W.; Li, H.; Zhang, P. Y.; Yin, F.; Zhang, Q.; Geng, H.; Jiang, F.; Li, Z. *Sci. Adv.* **2018**, *4*, 5907.
21. Zhang, S.; Marini, D. M.; Hwang, W.; Santoso, S. *Curr. Opin. Chem. Biol.* **2002,** *6*, 865.

22. Matson, J. B.; Zha, R. H.; Stupp, S. I. *Curr. Opin. Solid St. M.* **2011**, *15*, 225.
23. Qian, Y.; Wang, W.; Wang, Z.; Jia, X.; Han, Q.; Rostami, I.; Wang, Y.; Hu, Z. *ACS Appl. Mater. Inter.* **2018**, *10*, 7871
24. Ghosh, G.; Barman, R.; Sarkar, J.; Ghosh, S. *J. Phys. Chem. B* **2019**, *123*, 5909.
25. Ghosh, G.; Fernández, G. *Beilstein J. Org. Chem.* **2020**, *16*, 2017.
26. Frisch, H.; Nie,Y.; Raunser, S.; Besenius, P. *Chem. Eur. J.* **2015**, *21*, 3304.
27. Bauri, k.; Nandi, N.; De, P. *Polym. Chem.* **2018**, *9*, 1257.
28. Falcone, N.; Kraatz, H. B. *Chem. Eur. J.* **2018**, *24*, 14316.
29. Korevaar, P. A.; Newcomb, C. J.; Meijer E. W.; Stupp, S. I. *J. Am. Chem. Soc.* **2014**, *136*, 8540.
30. Spitzer, D.; Rodrigues, L. L.; Straßburger, D.; Mezger, M.; Besenius, P. *Angew. Chem., Int. Ed*. **2017**, *56*, 15461.
31. Wang, J.; Liu, K.; Xing, R.; Yan, X. *Chem. Soc. Rev.* **2016**, *45*, 5589.
32. R. Otter, R.; Besenius, P. *Org. Biomol. Chem.* **2019**, *17*, 6719.
33. Dasgupta, A.; Das, D. *Langmuir* **2019**, *35*, 10704.
34. Fleming, S.; Ulijn, R. V. *Chem. Soc. Rev.* **2014**, *43*, 8150.
35. Ustinov, A.; Weissman, H.; Shirman, E.; Pinkas, I.; Zuo, X.; Rybtchinski, B. *J. Am. Chem. Soc.* **2011**, *133*, 16201.
36. Toniolo, C., Crisma, M., Formaggio, F. & Peggion, C. *Biopolym. Pept. Sci.* **2001**, *60*, 396.
37. Karle, I. L.; Banerjee, A.; Balaram, P. *Folding and Design* **1997**, 2, 203.
38. Banerjee, A.; Raghothama, S.; Balaram, P. *J. Chem. Soc., Perkin Trans.* **1997**, *2*, 2087.
39. Ramagopal, U. A.; Ramakumar, S.; Sahal, D.; Chauhan, V.S. *Proc. Natl. Acad. Sci. U.S.A.* **2001**, *98*, 870.
40. R.Sonti, R.; Gopi, H. N.; Muddegowda, U.; Ragothama, S.; Balaram, P. *Chem. Eur. J.* **2013**, *19*, 5955.
41. Bandyopadhyay, A.; Misra, R.; Gopi, H. N. *Chem. Commun*. **2016**, *52*, 4938.
42. Ganesh Kumar, M.; Benke, S. N.; Poopathi Raja, K. M.; Gopi, H. N. *Chem. Commun*. **2015**, *51*, 13397.
43. Pramanik, B.; Singha, N.; Das, D. *ACS Appl. Polym. Mater*. **2019**, *1*, 833.
44. Chen, L.; Morris, K.; Laybourn, A.; Elias, D.; Hicks, M. R.; Rodger, A.; Serpell, L.; Adams, D. J. *Langmuir*, **2010**, *26*, 5232.

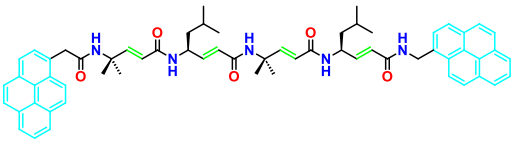
45. Das, A.; Ghosh, S. *Chem. Eur. J.* **2010**, *16*, 13622.
46. Gavel, P. K.; Dev, D.; Parmar, H. S.; Bhasin, S.; Das, A. K. *ACS Appl. Mater. Interfaces* **2018**, *10*, 10729.
47. Ahmed, S.; Amba Sankar, K. N.; Pramanik, B.; Mohanta, K.; Das, D. *Langmuir*, **2018**, *34*, 8355.
48. N. Singha, N.; Gupta, P.; Pramanik, B.; Ahmed, A.; Dasgupta, A.; Ukil, A.; Das, D. *Biomacromolecules*, **2017**, *18*, 3630.
49. Ogi, S.; Matsumoto, K.; Yamaguchi, S. *Angew. Chem., Int. Ed.* **2018**, *57*, 2339.
50. (a) Langes, D. A. *Science* **1988**, *241*, 188. (b) Urry, D. W.; Glickson, J. D.; Mayers, D. F.; Haider, J. *Biochemistry* **1972,** *11*, 487. c) Wallace, B. A.; Ravikumar, K. *Science* **1988**, *241*, 182; (c) Wallace, B. *J. Struct. Biol.* **1998**, *121*, 123.
51. (a) Benedetti, E.; Di Blasio, B.; Pedone, C.; Lorenzi, G. P.; Tomasic, L.; Gramlich, V. *Nature* **1979**, *282*, 630. (b) Di Blasio, B.; Benedetti, E.; Pavone, V.; Pedone, C.; Gerber, C.; Lorenzi, G. P. *Biopolymers* **1989**, *28*, 203. (c) Kulp, J. L.; Clark, T. D. *Chem. Eur. J.* **2009,** *15*, 11867. (d) Navarro, E.; Fenude, E.; Celda, B. *Biopolymers* **2004**, *73*, 229. (e) Sastry, M.; Brown, C.; Wagner, G.; Clark, T. D. *J. Am. Chem. Soc*. **2006,** *128*, 10650. (f) Schramm, P.; Hofmann, H. -J. *J. Pept. Sci.* **2010**, *16*, 276. (e) Jadhav, K. B.; Lichtenecker, R. J.; Bullach, A.; Mandal, B.; Arndt, H. -D. *Chem. Eur. J*. **2015**, *21*, 5898.
52. (a) Ronson, T. K.; Roberts, D. A.; Black, S. P.; Nitschke, J. R. *J. Am. Chem. Soc.* **2015**, *137*, 14502. (b) Feng, X.; Wang, X.; Redshaw, C.; Tang, B. Z. *Chem. Soc. Rev.* **2023**, *52* , 6715. (c) Zhang, K.; Wucher, P.; Marszalek, T.; Babics, M.; Ringk, A.; Blom, P. W. M.; Beaujuge, P. M.; Pisula, W. *Chem. Mater.* **2018**, *30*, 5032. (d) Haedler, A. T.; Misslitz, H.; Buehlmeyer, C.; Albuquerque, R. Q.; Köhler, A.; Schmidt, H. *ChemPhysChem* **2013**, *14*, 1818. (e) Niu, D.; Jiang, Y.; Ji, L.; Ouyang, G.; Liu, M. *Angew. Chemie Int. Ed.* **2019**, *58*, 5946. (f) Tovar, J. D.; Claussen, R. C.; Stupp, S. I. *J. Am. Chem. Soc.* **2005**, *127*, 7337
53. (a) Liu, S.; Li, F.; Wang, Y.; Li, X.; Zhu, C.; Cheng, Y. *J. Mater. Chem. C* **2017**, *5*, 6030. (b) Cheng, Q.; Hao, A.; Xing, P. *Nat. Commun.* **2021**, *12*, 6320. (c) Pham, Q. N.; Brosse, N.; Frochot, C.; Dumas, D.; Hocquet, A.; Jamart-Grégoire, B. *New J. Chem.* **2008**, *32*, 1131. (d) Zhylitskaya, H.; Stępień, M. *Org. Chem. Front.* **2018**, *5*, 2395. (e) Maurya, Y. K.; Chmielewski, P. J.; Cybińska, J.; Prajapati, B.; Lis, T.; Kang, S.; Lee, S.; Kim, D. *Adv. Sci.* **2022**, *9*, 2105886.

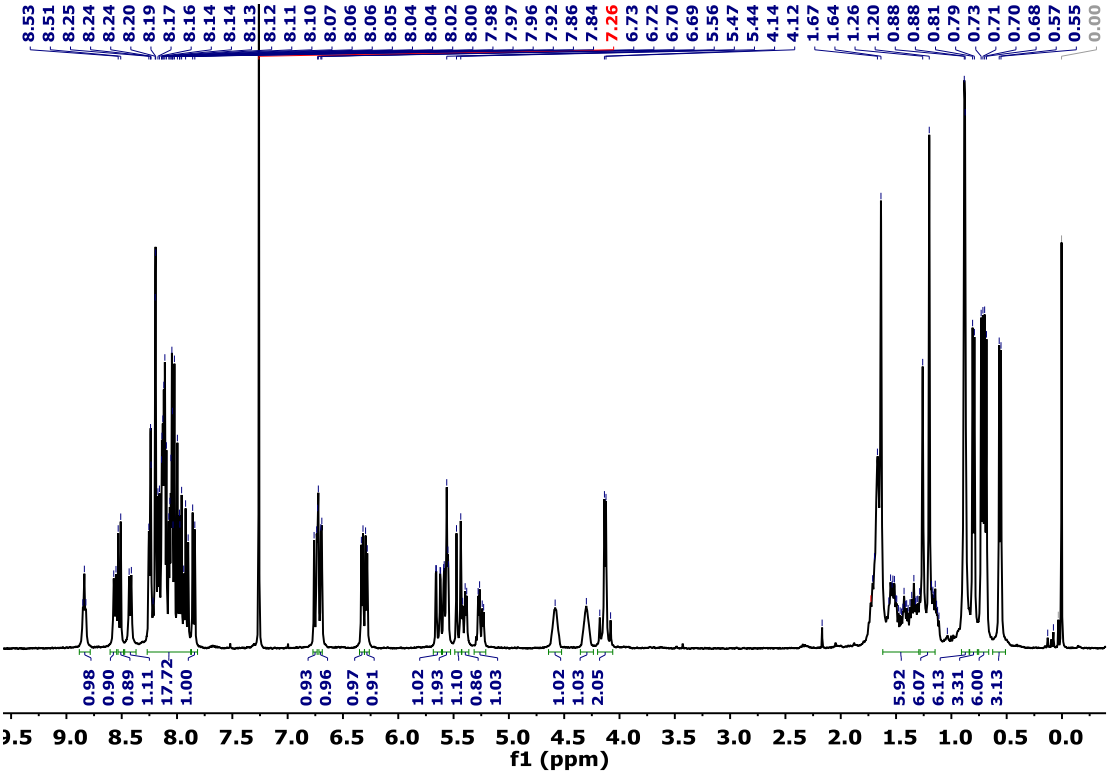
54. Cantekin, S.; de Greef, T. F. A.; Palmans, A. R. A. *Chem. Soc. Rev*. **2012**, *41*, 6125.
55. Helmich, E.; Smulders, M.M.; Lee, C. C.; Schenning, A. P.; Meijer, E. W. *J. Am. Chem. Soc.* **2011**, *133*, 12238.
56. Wu¨rthner, F.; Saha-Mo¨ller, C. R.; Fimmel, B.; Ogi, S.; Leowanawat, P.; Schmidt, D. *Chem. Rev.* **2016**, *116*, 962.
57. Lohr, A.; Wu¨rthner, F. *Angew. Chem., Int. Ed.* **2008**, *47*, 1232.
58. (a) Zhang, J.; Chen, W.; Kalytchuk, S.; Li, K. F.; Chen, R.; Adachi, C.; Chen, Z.; Rogach, A. L.; Zhu, G.; Yu, P. K. N.; Zhang, W.; Cheah, K. W.; Zhang, X.; Lee, C.-S. *ACS Appl. Mater. Interfaces* **2016**, *8*, 11355. (b) Rybtchinski, B.; Sinks, L. E.; Wasielewski, M. R. *J. Phys. Chem. A* **2004**, *108*, 7497. (c) Schwartz, P.-O.; Biniek, L.; Zaborova, E.; Heinrich, B.; Brinkmann, M.; Leclerc, N.; Méry, S. *J. Am. Chem. Soc.* **2014**, *136*, 5981. (d) Dhar, J.; Swathi, K.; Karothu, D. P.; Narayan, K. S.; Patil, S. *ACS Appl. Mater. Interfaces* **2015**, *7*, 670. (e) Mativetsky, J. M.; Kastler, M.; Savage, R. C.; Gentilini, D.; Palma, M.; Pisula, W.; Müllen, K.; Samorì, P. *Adv. Funct. Mater.* **2009**, *19*, 2486. (f) Gunderson, V. L.; Smeigh, A. L.; Kim, C. H.; Co, D. T.; Wasielewski, M. R. *J. Am. Chem. Soc.* **2012**, 134, 4363.
59. (a) Anthony, J. E.; Facchetti, A.; Heeney, M.; Marder, S. R.; Zhan, X. *Adv. Mater*.**2010**, *22*, 3876. (b) Avinash, M. B.; Govindaraju, T. *Adv. Mater.* **2012**, *24*, 3905. (c) Avinash, M. B.; Govindaraju, T.; *Acc. Chem. Res.* **2018**, *51*, 414. (d) Ivnitski, D.; Amit, M.; Silberbush, O.; Atsmon-Raz, Y.; Nanda, J.; CohenLuria, R.; Miller, Y.; Ashkenasy, G.; Ashkenasy, N. *Angew. Chem. Int. Ed.* **2016**, *55*, 9988. (e) Das, A.; Ghosh, S. *Chem. Commun.***2016**, *52*, 6860. (f) Kobaisi, M. K.;Bhosale, S.V.; Latham, K.; Raynor, A. M.; Bhosale, S. V. *Chem. Rev.* **2016**, *116*, 11685.
60. (a) Wu, Y.; Frasconi, M.; Gardner, D. M.; McGonigal, P. R.; Schneebeli, S. T.; Wasielewski, M. R.; Stoddart, J. F. *Angew. Chem. Int. Ed*. **2014**, *53*, 9476. (b) Wu, Y.; S. K. M Nalluri, S. K. M.; Young, R. M.; Krzyaniak, M. D.; Margulies, E. A.; Stoddart, J. F. Wasielewski, M. R. *Angew. Chem. Int. Ed.* **2015**, *54*, 11971. (c) Nalluri, S. K. M.; Liu, Z.; Wu, Y.; Hermann, K. R.; Samanta, A.; Kim, D. J.; Krzyaniak, M. D.; Wasielewski, M. R.; Stoddart, J. F. *J. Am. Chem. Soc.* **2016**, *138*, 5968.
61. (a) Pantos, G. D.; Pengo, P.; Sanders, J. K. M. *Angew. Chem., Int. Ed*. **2007**, *119*, 194. (b) Anderson, T. W.; Sanders, J. K. M.; Pantoş, G. D. *Org. Biomol. Chem.* **2010**, *8*, 4274. (c)

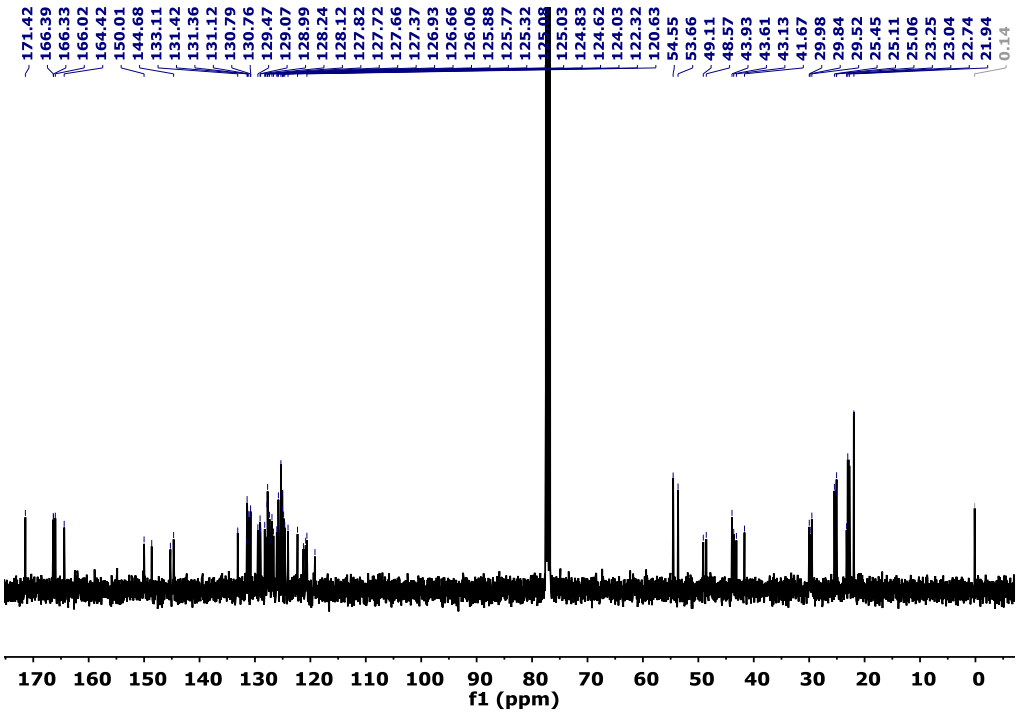
Anderson, T. W.; Pantoş, G. D.; Sanders, J. K. M. *Org. Biomol. Chem.* **2011**, *9*, 7547. (d) Pantoş, G. D.; Wietor, J. L.; Sanders, J. K. M. *Angew. Chem. Int. Ed.* **2007**, *46*, 2238. (e)Wietor, J. L.; Pantoş, G. D.; Sanders, K. M. *Angew. Chem. Int. Ed.* **2008**, *47*, 2689. (f) Ponnuswamy, N.; Pantos, G. D.; Smulders, M. M. J.; Sanders, J. K. M. *J. Am. Chem. Soc.* **2012**, *134*, 566.

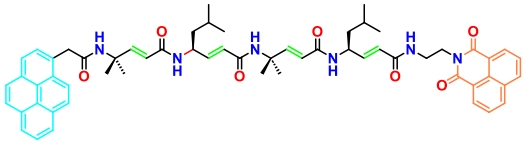
62. (a) Tovar, J. D. *Acc. Chem. Res.* **2013**, *46*, 1527. (b) Ardoña, H. A. M.; Tovar, J. D. *Bioconjugate Chem.* **2015**, *26*, 2290. (c) Avinash, M. B.; Govindaraju, T. *Adv. Funct. Mater.* **2011**, *21*, 3875. (d) Nandi, N.; Basak, S.; Kirkham, S.; Hamley, I. W.; Banerjee, A. *Langmuir* **2016**, *32*, 13226. (e) Avinash, M. B.; Govindaraju, T. *Nanoscale* **2014**, *6*, 13348. (f) Ardoña, H. A. M.; Draper, E. R.; Citossi, F. C.; Wallace, M.; Serpell, L. C.; Adams, D. J.; Tovar, J. D. *J. Am. Chem. Soc.* **2017**, *139*, 8685. (g) Panda, S. S.; Katz, H. E.; Tovar, J. D. *Chem. Soc. Rev.* **2018**, *47*, 3640. (h) Pandeeswar, M.; Khare, H.; Ramakumar, S.; Govindaraju, T.; *Chem. Commun.* **2015**, *51*, 8315.
63. (a) Das, A.; Ghosh, S. *Angew. Chem. Int. Ed.* **2014**, *53*, 1092. (b) Molla, M. R.: Gehrig, D.; Roy, L.; Kamm, V.; Paul, A.; Laquai, F.; Ghosh, S. *Chem. Eur. J.* **2014**, *20*, 760. (c) Bhattacharjee, S.; Maiti, B.; Bhattacharya, S. *Nanoscale* **2016**, *8*, 11224. d) Kumar, N. S. S.; Gujrati, M. D.; Wilson, J. N. *Chem. Commun*. **2010**, *46*, 5464.

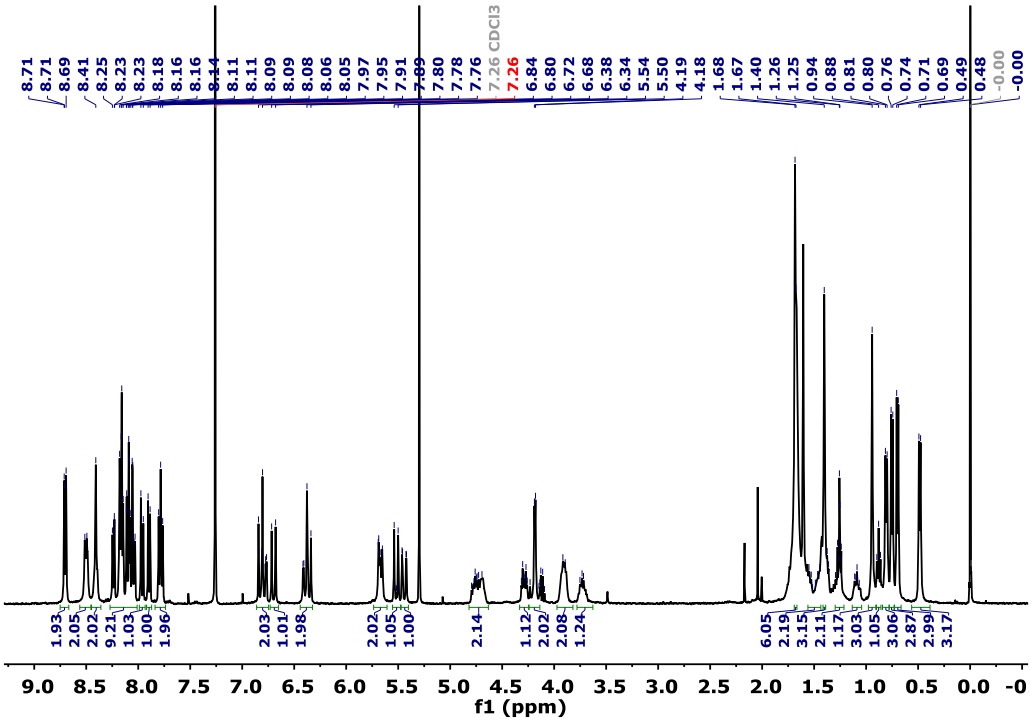
5.10. ^{1}H, ^{13}C NMR and Mass Spectra of Peptides P1-P3

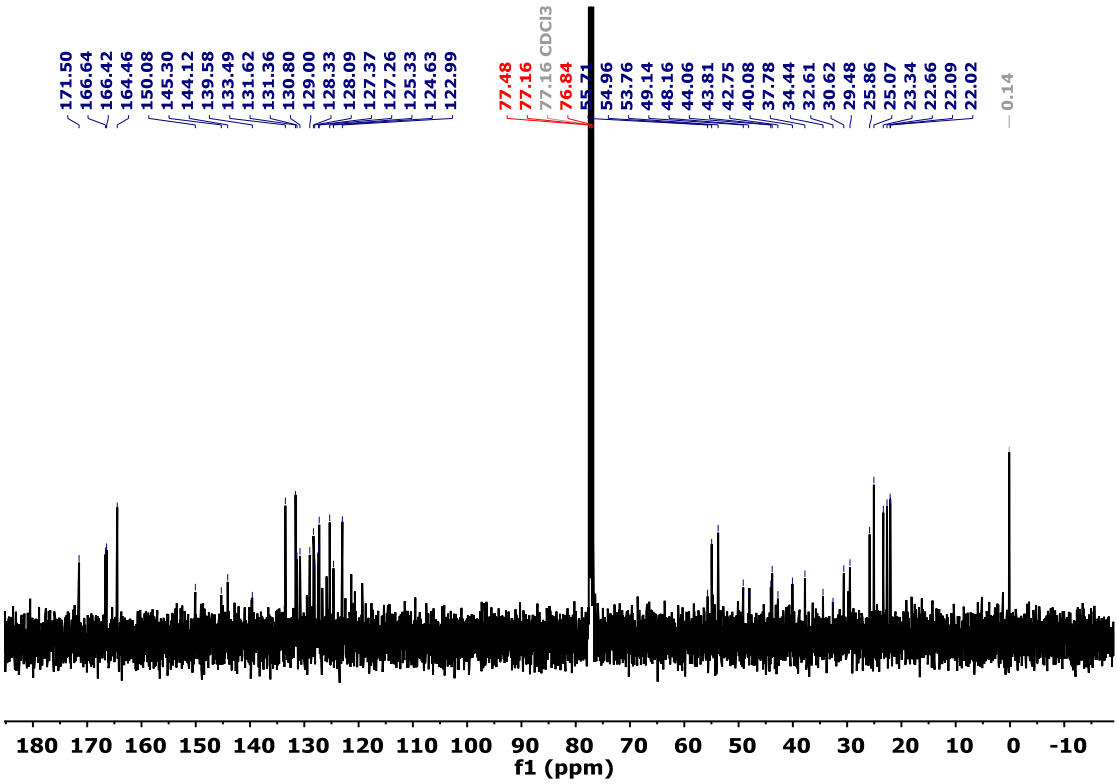


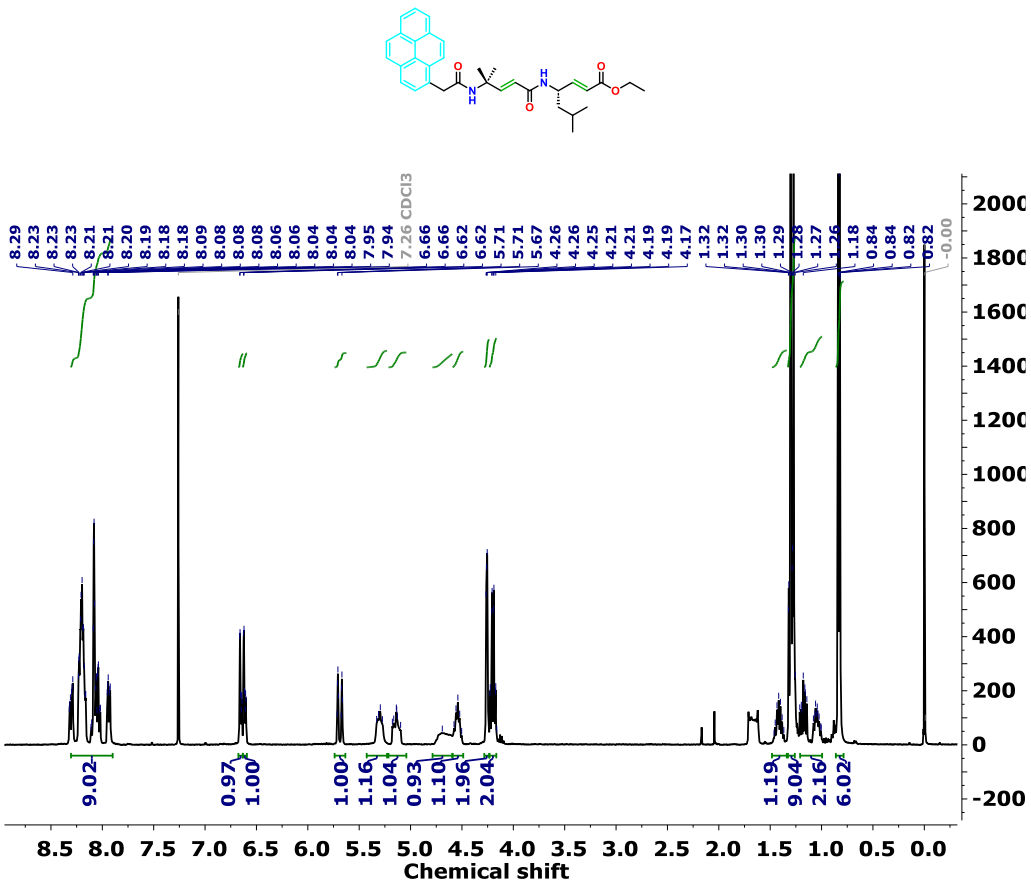


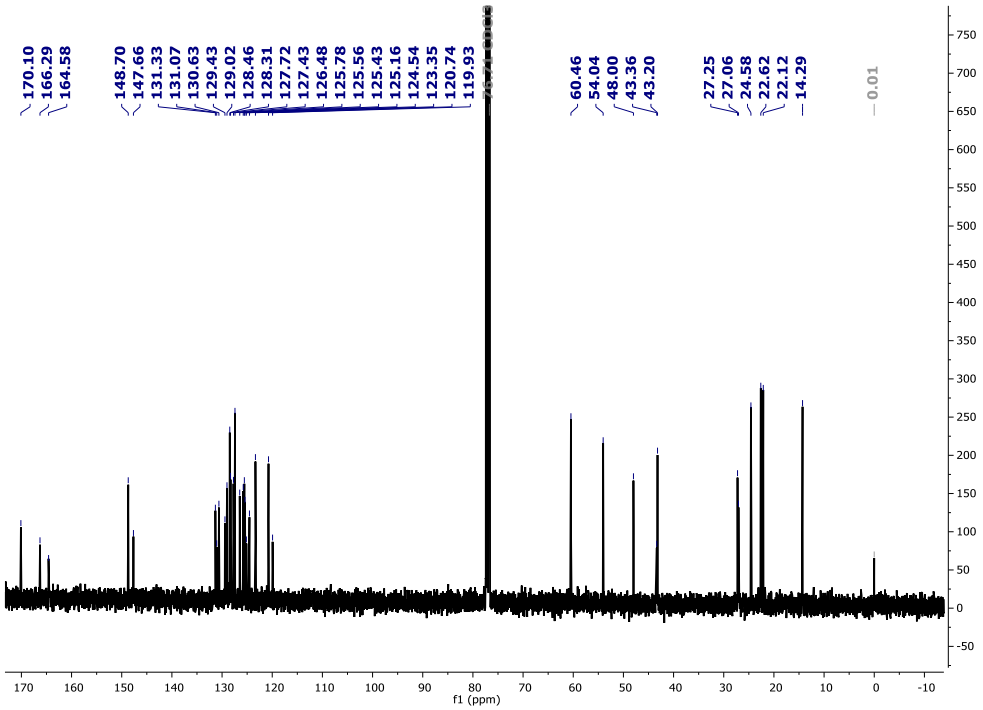


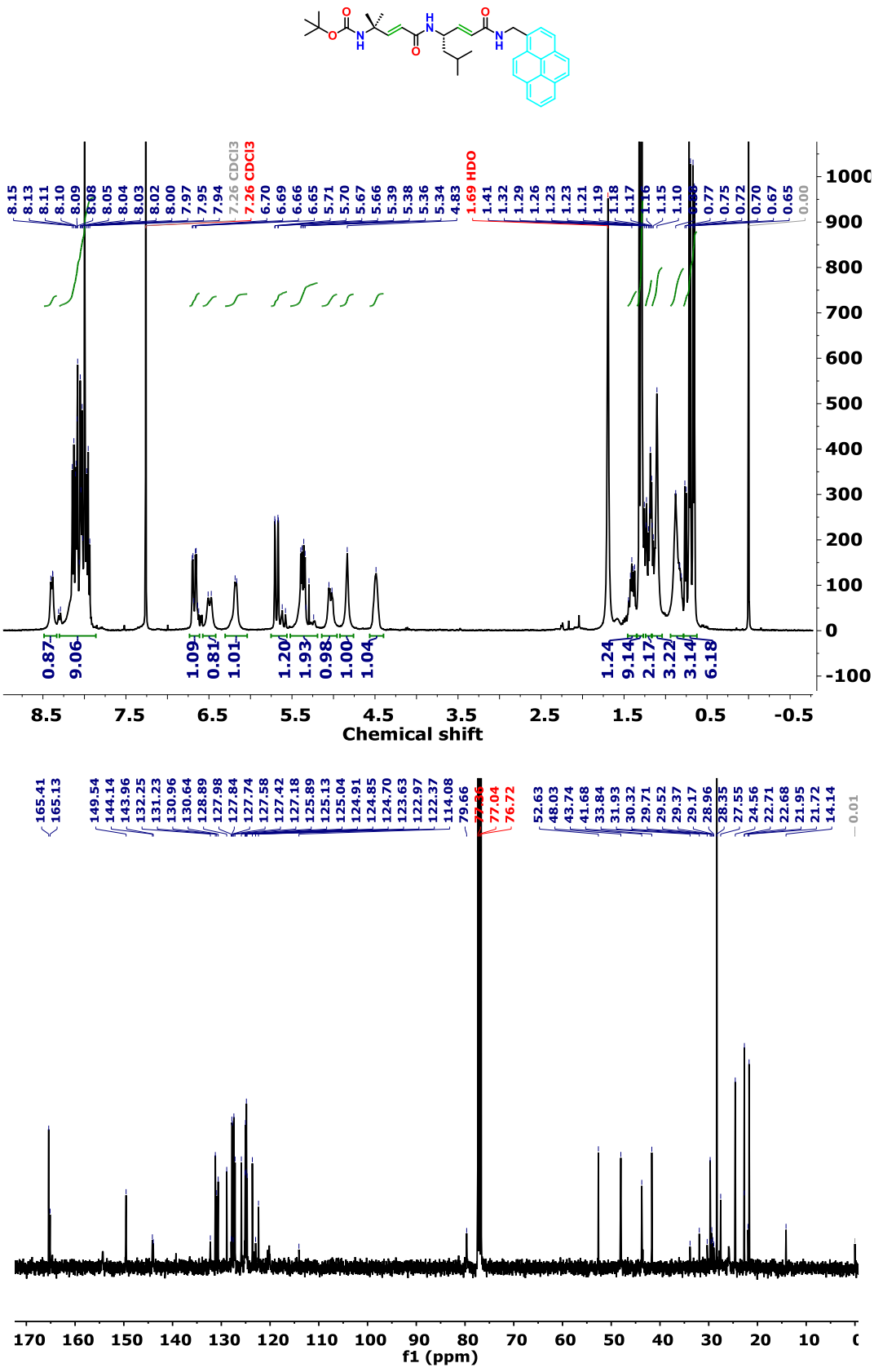


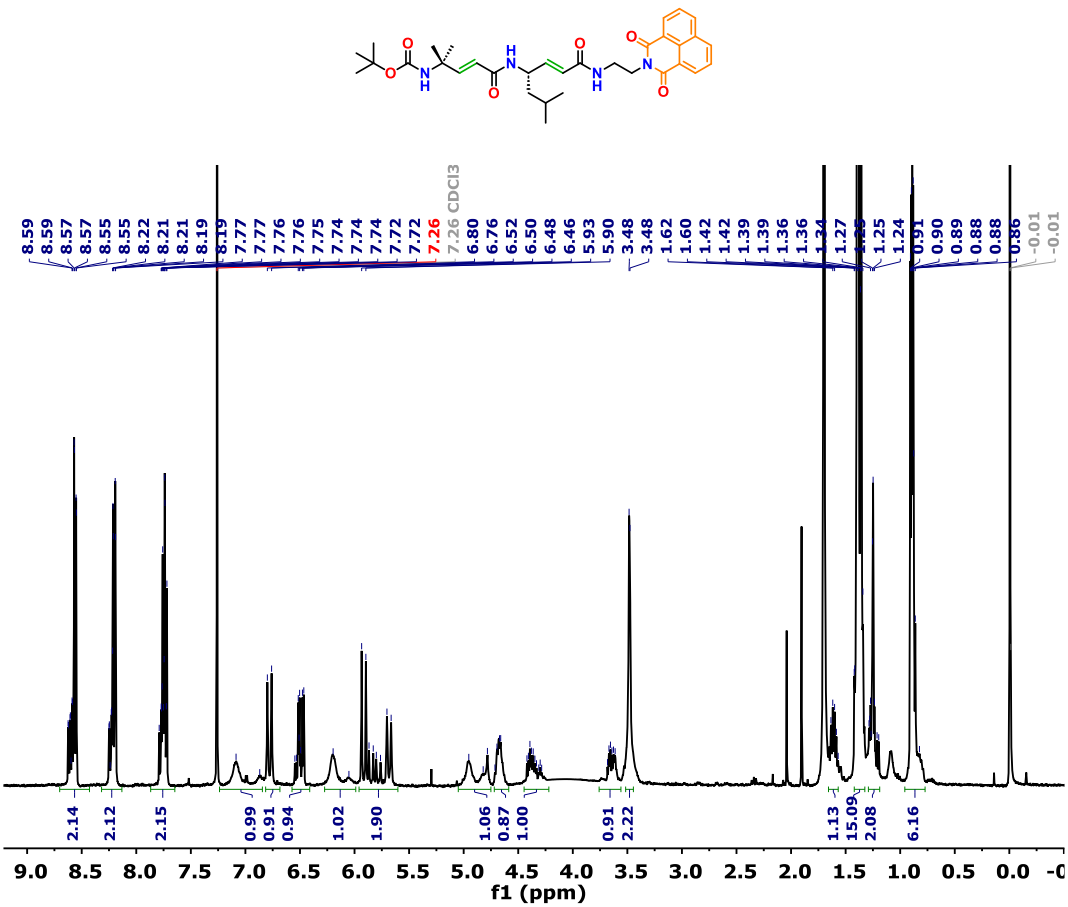

8.71 8.71 8.69 8.41 8.25 8.23 8.23 8.18 8.16 8.16 8.14 8.11 8.11 8.09 8.09 8.08 8.06 8.05 7.97 7.95 7.91 7.89 7.80 7.78 7.76 7.26 CDCl3 7.26 6.84 6.80 6.72 6.68 6.38 6.34 5.54 5.50 4.19 4.18 1.68 1.67 1.40 1.26 1.25 0.94 0.88 0.81 0.80 0.76 0.74 0.71 0.69 0.49 0.48 -0.00 -0.00
1.93 2.05 2.02 9.21 1.03 1.00 1.96 2.03 1.01 1.98 2.02 1.05 1.00 2.14 1.12 2.02 2.08 1.24 6.05 2.19 3.15 2.11 1.17 3.03 1.05 3.06 2.87 2.99 3.17
9.0 8.5 8.0 7.5 7.0 6.5 6.0 5.5 5.0 4.5 4.0 3.5 3.0 2.5 2.0 1.5 1.0 0.5 0.0 -0
f1 (ppm)

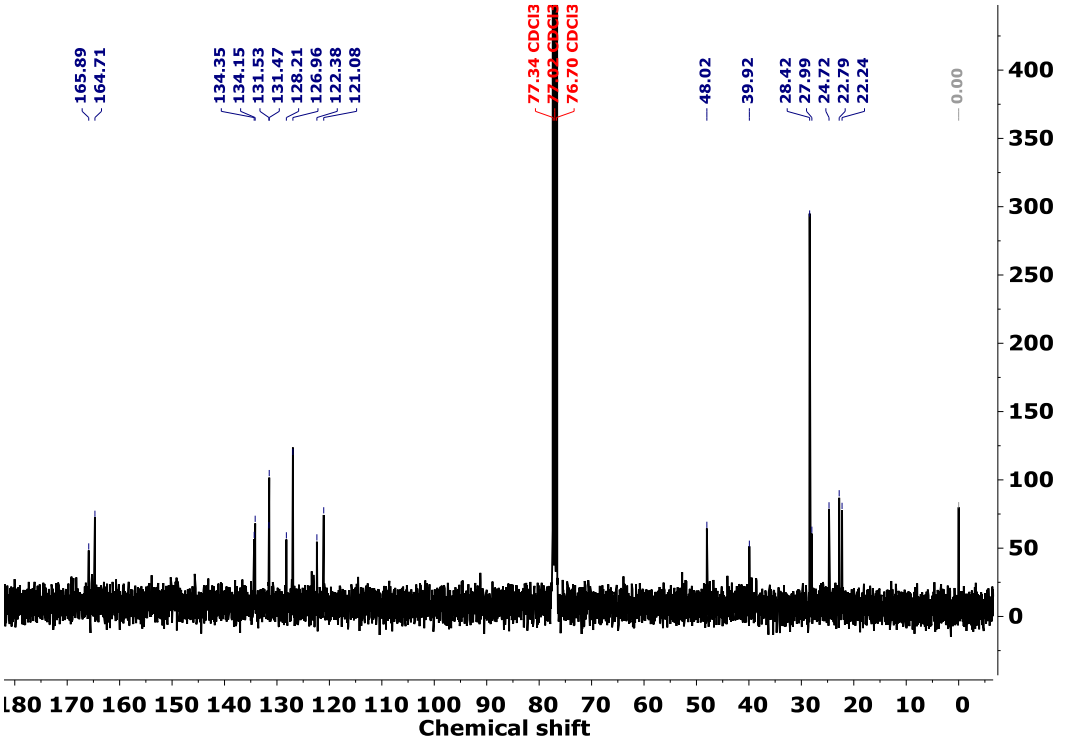

171.50 166.64 166.42 164.46 150.08 145.30 144.12 139.58 133.49 131.62 131.36 130.80 129.00 128.33 128.09 127.37 127.26 125.33 124.63 122.99 77.48 77.16 77.16 CDCl3 76.84 55.71 54.96 53.76 49.14 48.16 44.06 43.81 42.75 40.08 37.78 34.44 32.61 30.62 29.48 25.86 25.07 23.34 22.66 22.09 22.02 0.14
180 170 160 150 140 130 120 110 100 90 80 70 60 50 40 30 20 10 0 -10
f1 (ppm)

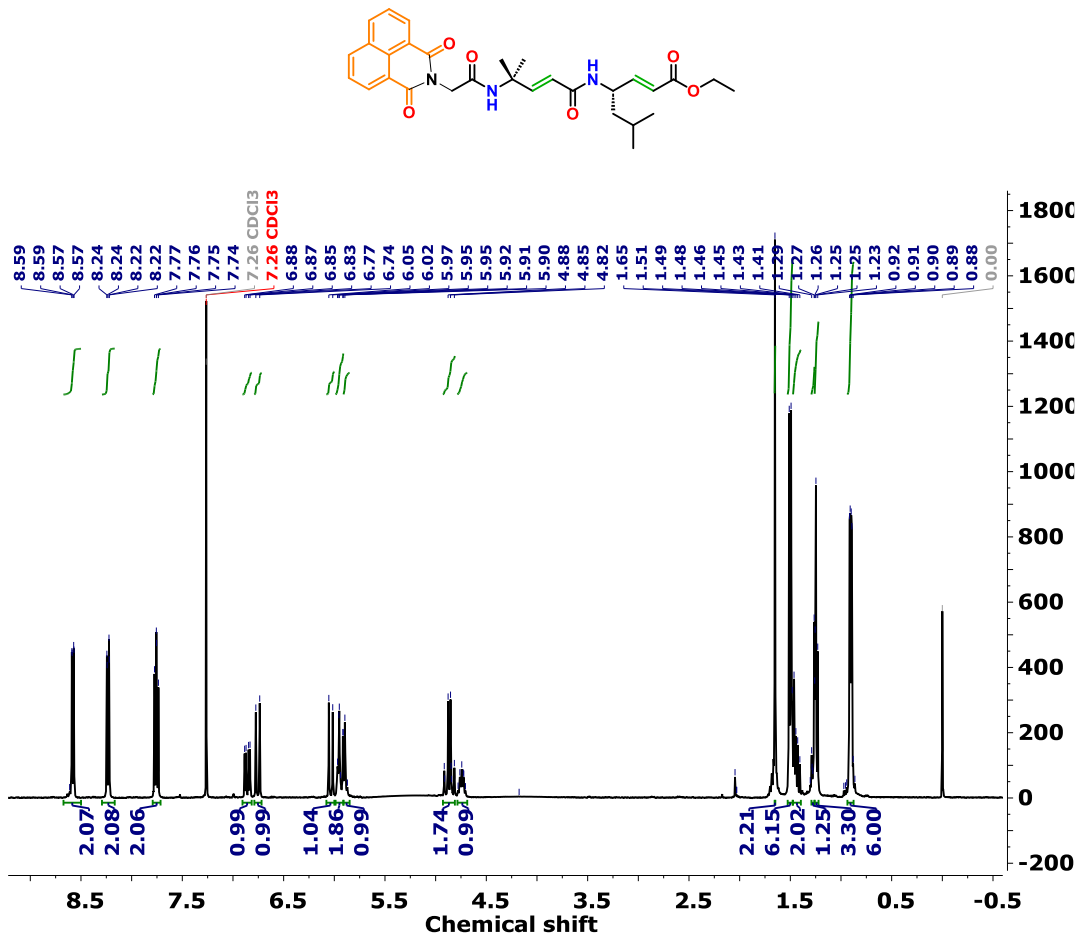

8.29 8.23 8.23 8.23 8.21 8.21 8.20 8.19 8.18 8.18 8.09 8.08 8.08 8.08 8.06 8.06 8.04 8.04 8.04 7.95 7.94 7.26 CDCl3 6.66 6.66 6.62 6.62 5.71 5.67 4.26 4.25 4.21 4.19 4.19 4.17 1.32 1.32 1.30 1.30 1.29 1.28 1.27 1.26 1.18 0.84 0.84 0.82 0.82 -0.00
9.02 0.97 1.00 1.00 1.16 1.04 0.93 1.10 1.96 2.04 1.19 9.04 2.16 6.02
Chemical shift

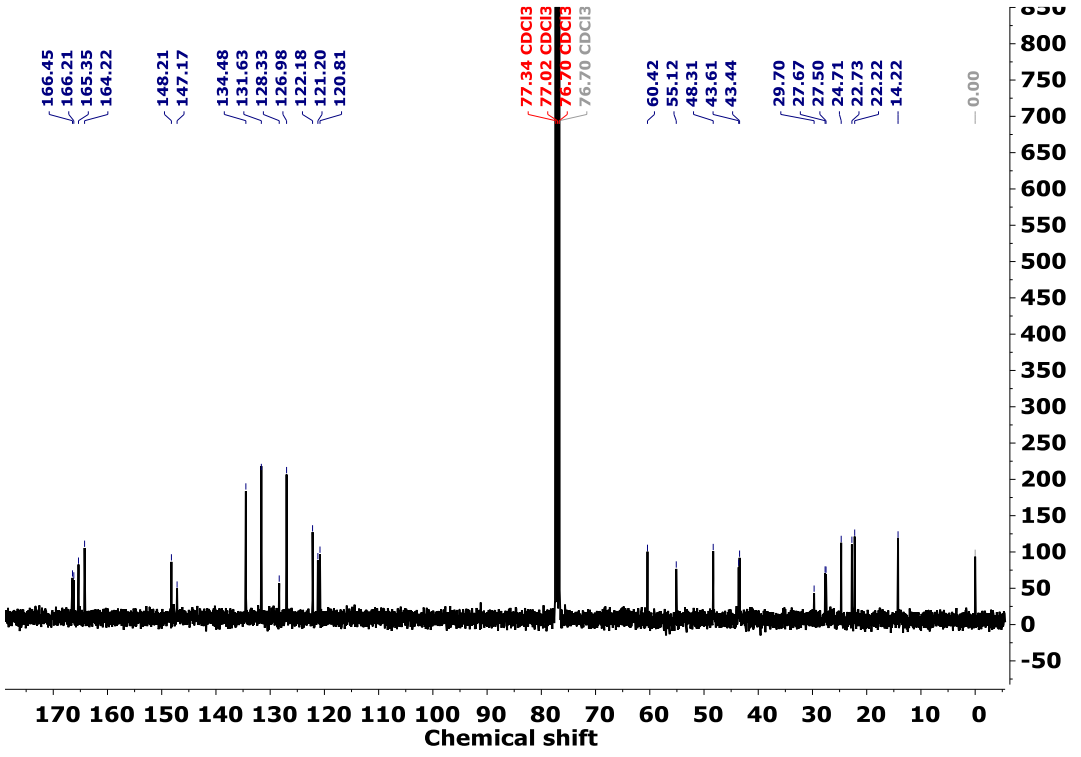

170.10 166.29 164.58 148.70 147.66 131.33 131.07 130.63 129.43 129.02 128.46 128.31 127.72 127.43 126.48 125.78 125.56 125.43 125.16 124.54 123.35 120.74 119.93 77.41 77.00 76.59 60.46 54.04 48.00 43.36 43.20 27.25 27.06 24.58 22.62 22.12 14.29 0.01
f1 (ppm)

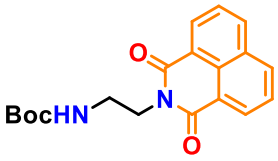

8.15 8.13 8.11 8.10 8.09 8.08 8.05 8.04 8.03 8.02 8.00 7.97 7.95 7.94 7.26 CDCl3 7.26 CDCl3 6.70 6.69 6.66 6.65 5.71 5.70 5.67 5.66 5.39 5.38 5.36 5.34 4.83 1.69 HDO 1.41 1.32 1.29 1.26 1.23 1.23 1.21 1.19 1.18 1.17 1.16 1.15 1.10 0.77 0.75 0.72 0.70 0.67 0.65 0.00
0.87 9.06 1.09 0.81 1.01 1.20 1.93 0.98 1.00 1.04 1.24 9.14 2.17 3.22 3.14 6.18
Chemical shift
165.41 165.13 149.54 144.14 143.96 132.25 131.23 130.96 130.64 128.89 127.98 127.84 127.74 127.58 127.42 127.18 125.89 125.13 125.04 124.91 124.85 124.70 123.63 122.97 122.37 114.08 79.66 77.04 76.72 52.63 48.03 43.74 41.68 33.84 31.93 30.32 29.71 29.52 29.37 29.17 28.96 28.35 27.55 24.56 22.71 22.68 21.95 21.72 14.14
f1 (ppm)

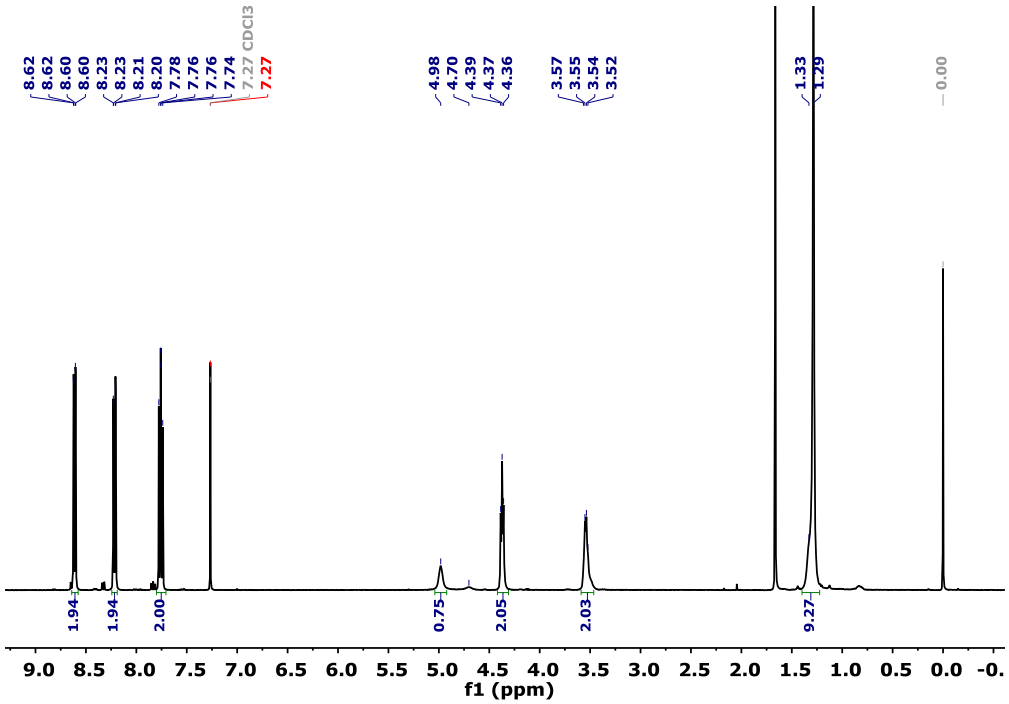

8.59 8.59 8.57 8.57 8.55 8.55 8.22 8.21 8.21 8.19 8.19 7.77 7.77 7.76 7.76 7.75 7.74 7.74 7.74 7.72 7.72 7.26 CDCl3 6.80 6.76 6.52 6.50 6.48 6.46 5.93 5.90 3.48 3.48 1.62 1.60 1.42 1.42 1.39 1.39 1.36 1.36 1.34 1.27 1.25 1.24 0.91 0.90 0.89 0.88 0.88 0.86 -0.01 -0.01
2.14 2.12 2.15 0.99 0.91 0.94 1.02 1.90 1.06 0.87 1.00 0.91 2.22 1.13 15.09 2.08 6.16
9.0 8.5 8.0 7.5 7.0 6.5 6.0 5.5 5.0 4.5 4.0 3.5 3.0 2.5 2.0 1.5 1.0 0.5 0.0
f1 (ppm)

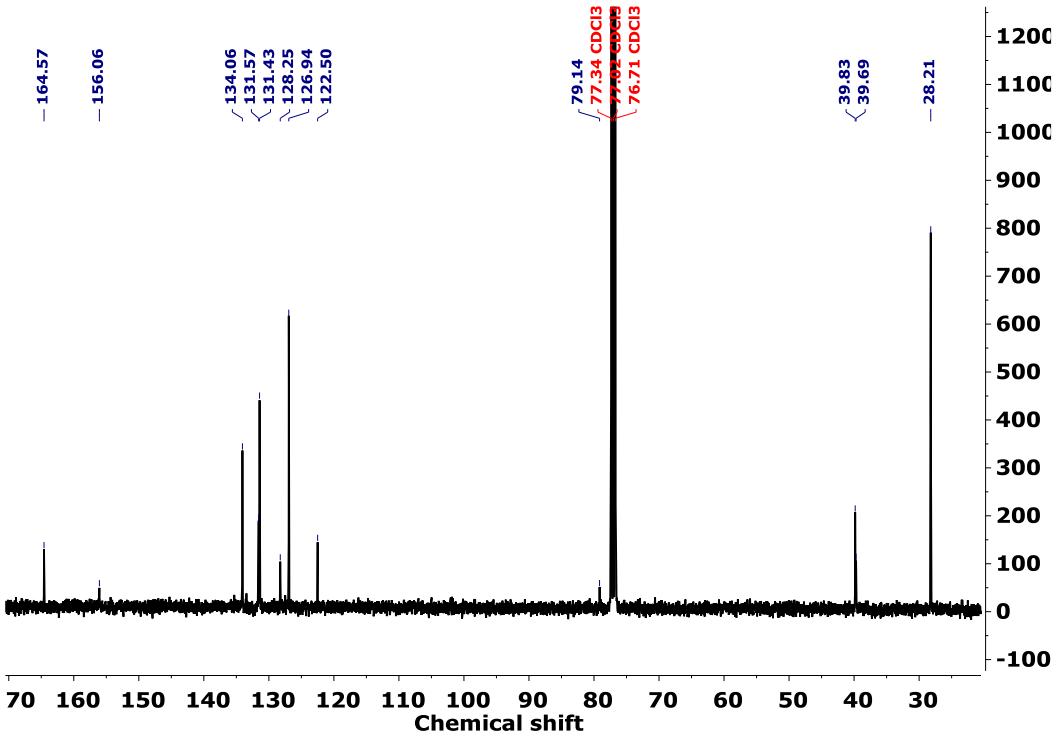

165.89 164.71 134.35 134.15 131.53 131.47 128.21 126.96 122.38 121.08 77.34 CDCl3 76.70 CDCl3 48.02 39.92 28.42 27.99 24.72 22.79 22.24 0.00
400 350 300 250 200 150 100 50 0
180 170 160 150 140 130 120 110 100 90 80 70 60 50 40 30 20 10 0
Chemical shift

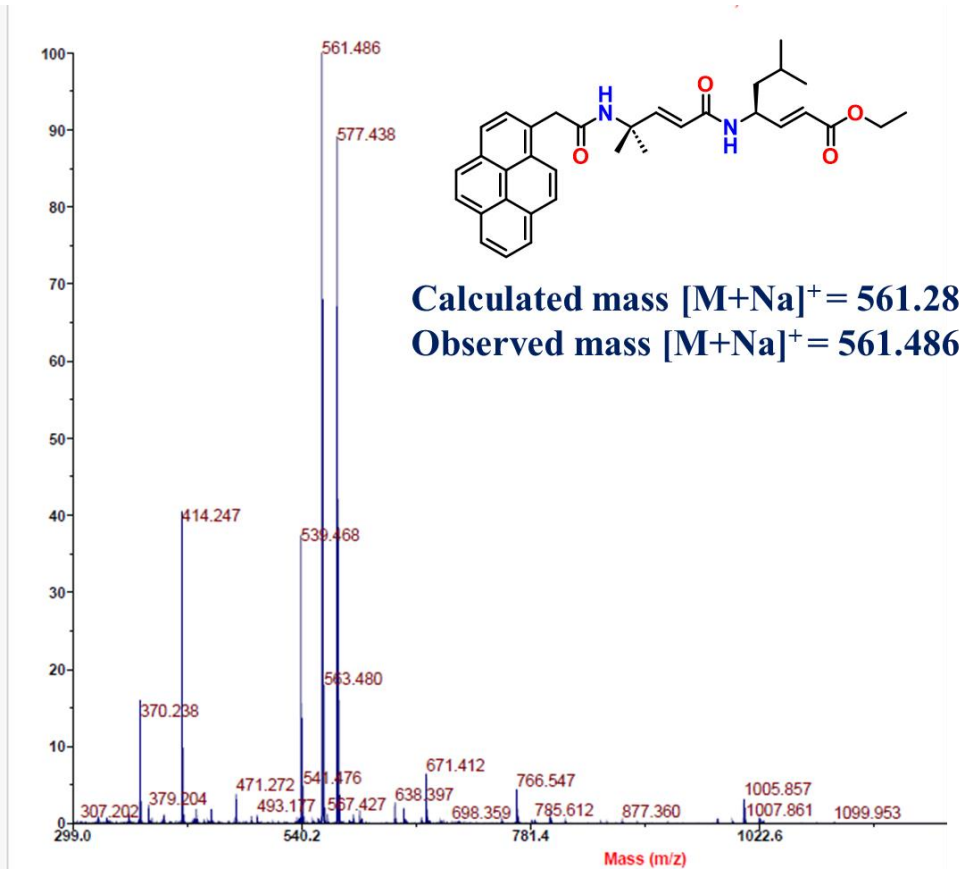




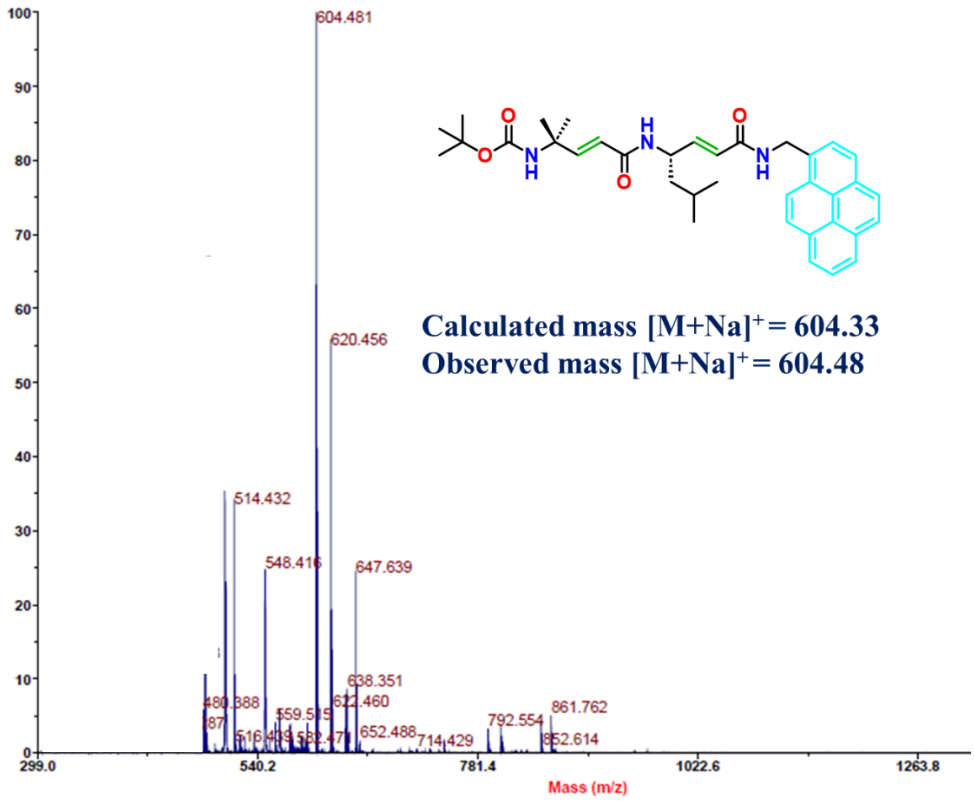

O
N
O
BocHN


8.62
8.62
8.60
8.60
8.23
8.23
8.21
8.20
7.78
7.76
7.76
7.74
7.27 CDCl3
7.27
4.98
4.70
4.39
4.37
4.36
3.57
3.55
3.54
3.52
1.33
1.29
0.00
1.94
1.94
2.00
0.75
2.05
2.03
9.27
f1 (ppm)

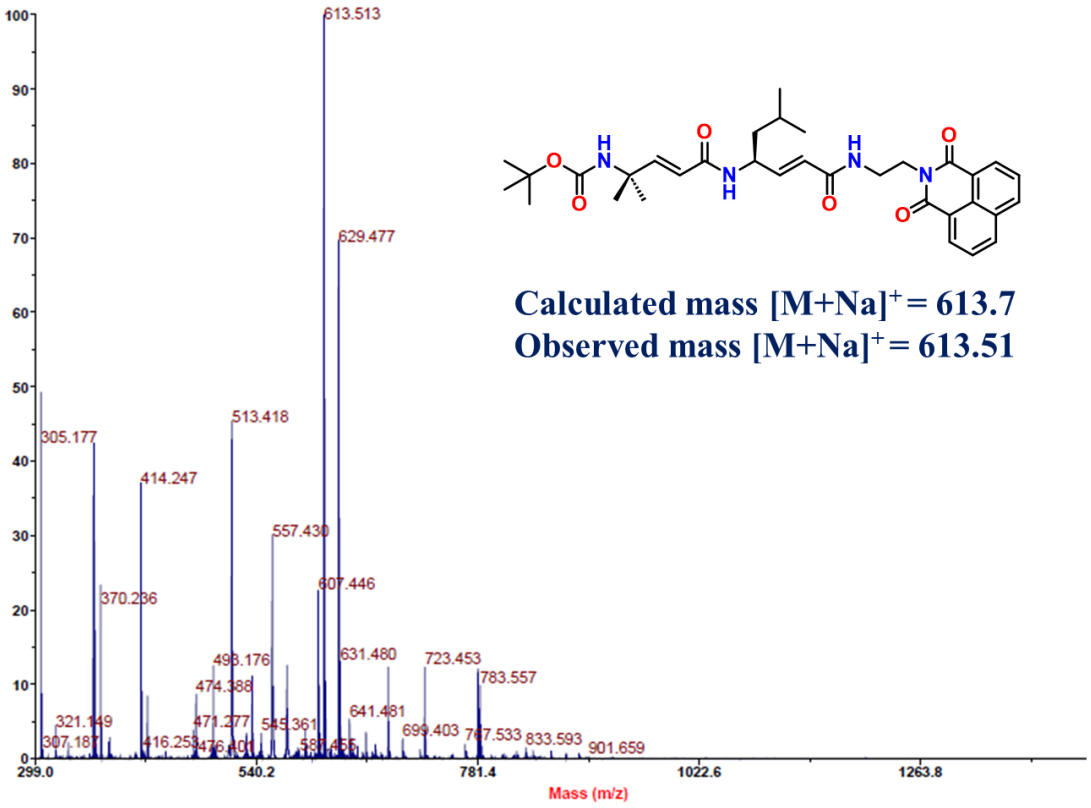

164.57
156.06
134.06
131.57
131.43
128.25
126.94
122.50
79.14
77.34 CDCl3
77.02 CDCl3
76.71 CDCl3
39.83
39.69
28.21
Chemical shift



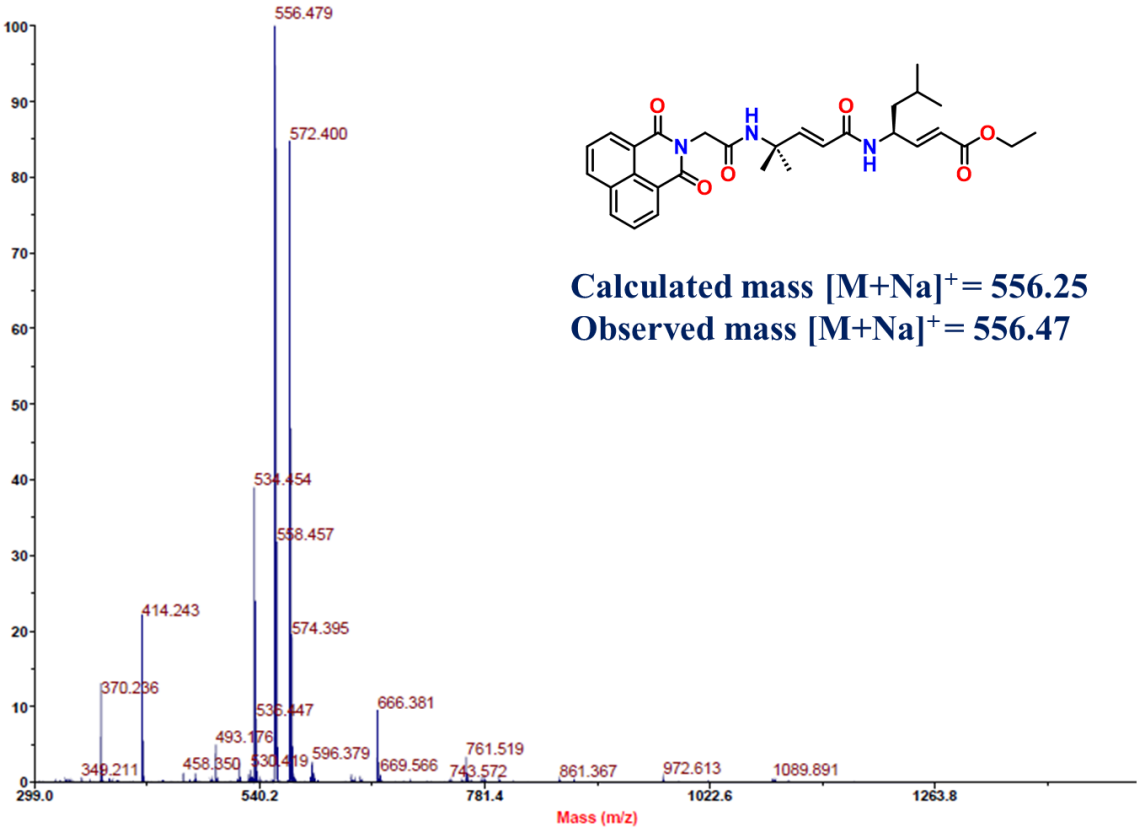
Calculated mass $[M+Na]^+ = 561.28$
Observed mass $[M+Na]^+ = 561.486$



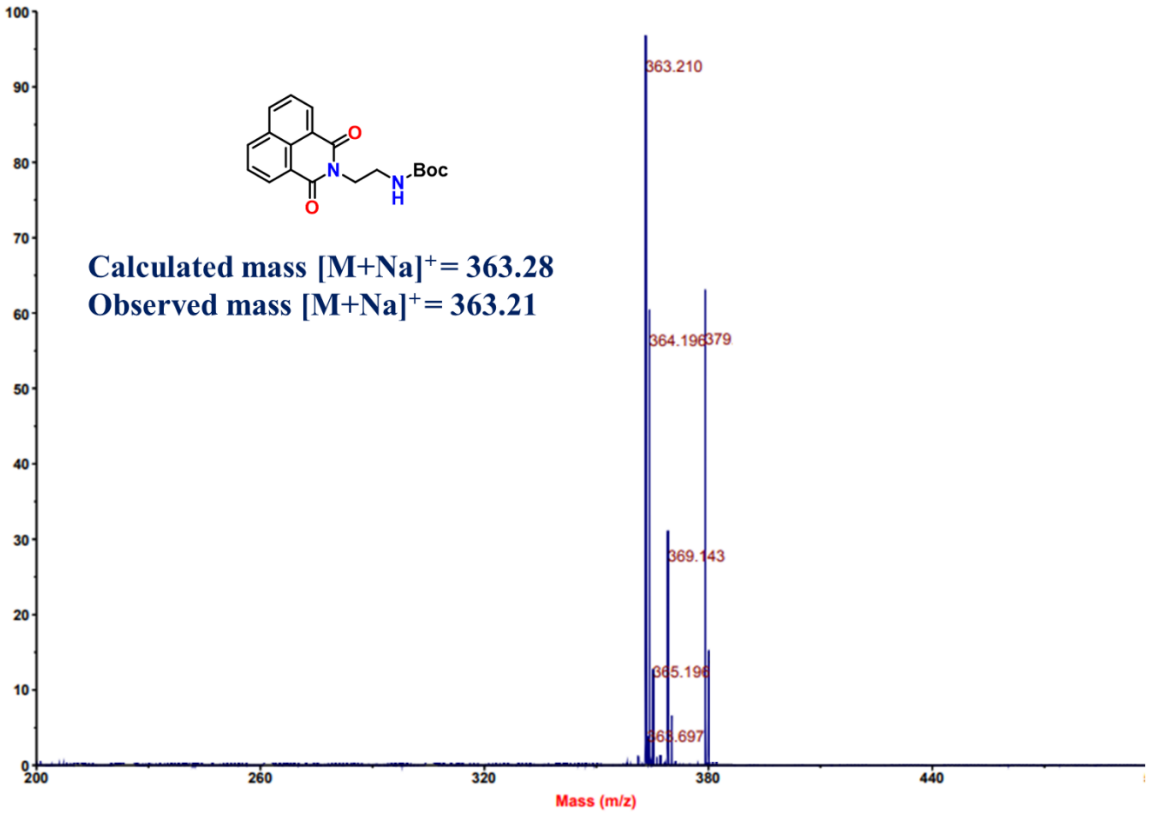
Calculated mass $[M+Na]^+ = 604.33$
Observed mass $[M+Na]^+ = 604.48$

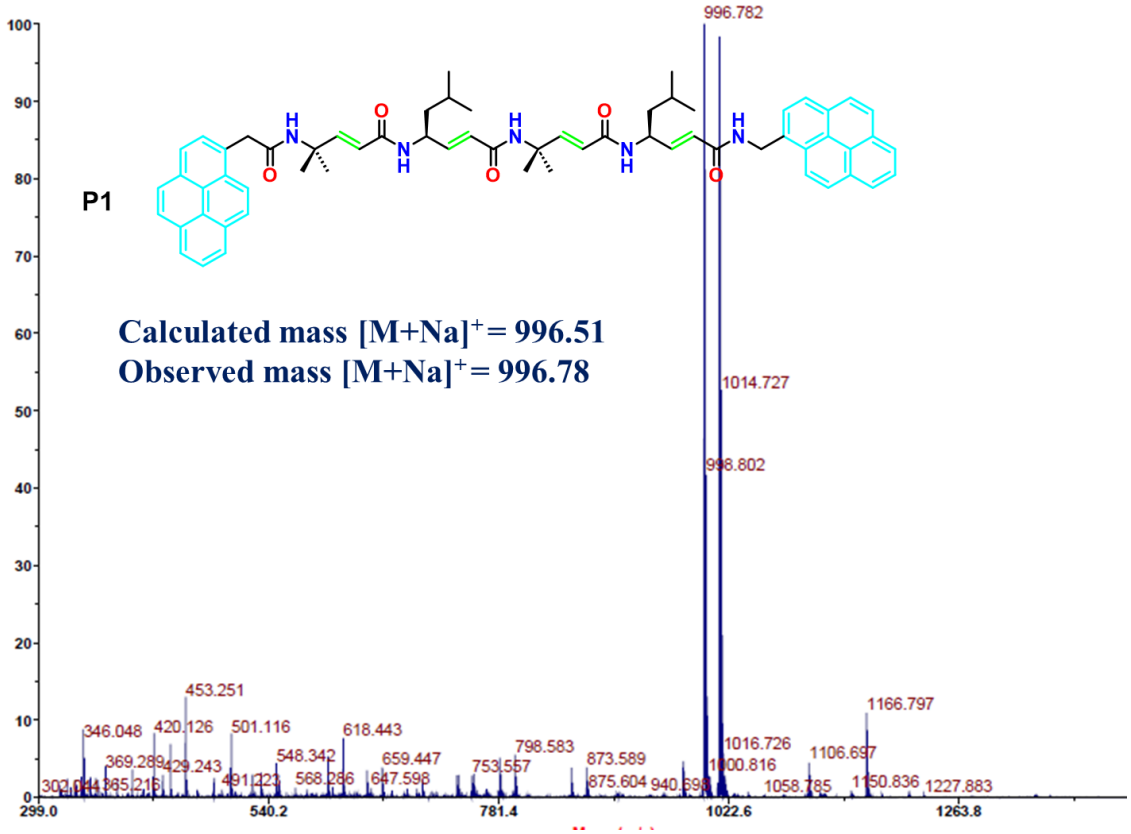


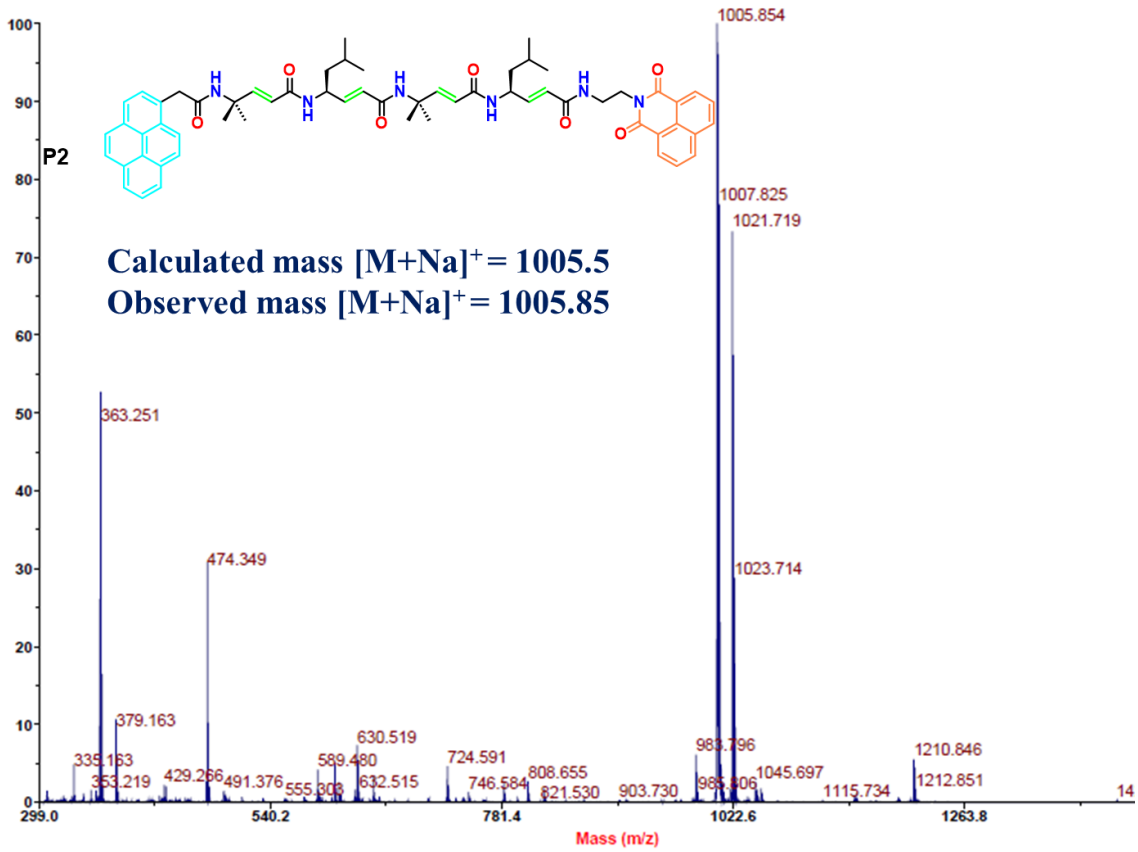
Calculated mass $[M+Na]^+ = 613.7$
Observed mass $[M+Na]^+ = 613.51$

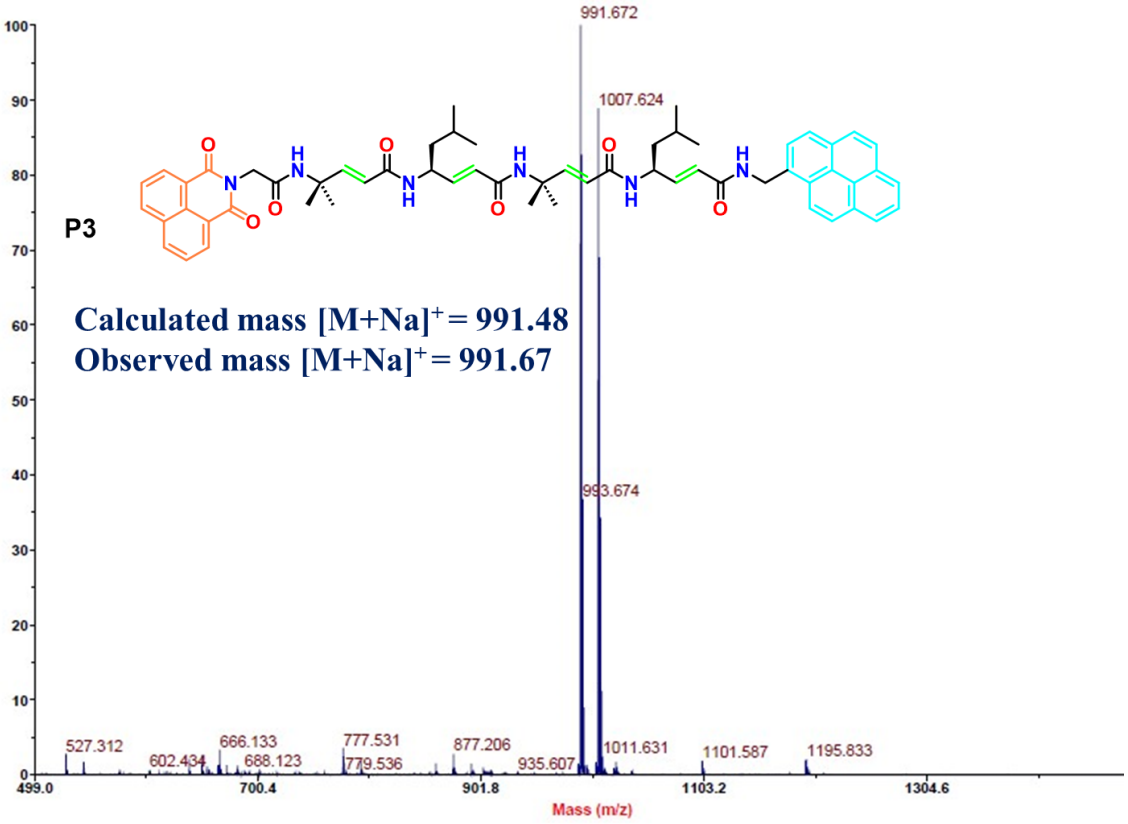


Calculated mass $[M+Na]^+ = 556.25$
Observed mass $[M+Na]^+ = 556.47$


Calculated mass [M+Na]+= 363.28
Observed mass [M+Na]+= 363.21
363.210
364.196379
369.143
365.196
368.697
Mass (m/z)


P1
Calculated mass [M+Na]+= 996.51
Observed mass [M+Na]+= 996.78
996.782
1014.727
998.802
453.251
346.048
420.126
501.116
618.443
548.342
659.447
798.583
753.557
873.589
1016.726
1166.797
1106.697
1058.785
1150.836
1227.883
Mass (m/z)


P2
Calculated mass [M+Na]+ = 1005.5
Observed mass [M+Na]+ = 1005.85
1005.854
1007.825
1021.719
1023.714
363.251
474.349
379.163
630.519
724.591
808.655
1210.846
1212.851
1045.697
1115.734
Mass (m/z)


P3
Calculated mass [M+Na]+ = 991.48
Observed mass [M+Na]+ = 991.67
991.672
1007.624
993.674
527.312
666.133
777.531
877.206
1011.631
1101.587
1195.833
Mass (m/z)

Permission for Reuse of Figures from Journals

Gmail

Saikat Pahan <pahansaikat@gmail.com>

Thank you for your order with RightsLink / John Wiley and Sons

1 message

no-reply@email.copyright.com <no-reply@email.copyright.com> Mon, Dec 4, 2023 at 7:35 PM
To: pahansaikat@gmail.com



Thank you for your order!

Dear Mr. SAIKAT PAHAN,

Thank you for placing your order through Copyright Clearance Center's RightsLink® service.

Order Summary

Licensee:	Mr. SAIKAT PAHAN
Order Date:	Dec 4, 2023
Order Number:	5681930107394
Publication:	Journal of Polymer Science Part A: Polymer Chemistry
Title:	Development of synthetic double helical polymers and oligomers
Type of Use:	Dissertation/Thesis
Order Ref:	https://doi.org/10.1002/pola.23596
Order Total:	0.00 USD

View or print complete details of your order and the publisher's terms and conditions.

Sincerely,

Copyright Clearance Center

customercare@copyright.com
https://myaccount.copyright.com

CCC RightsLink

Gmail

Saikat Pahan <pahansaikat@gmail.com>

Thank you for your order with RightsLink / John Wiley and Sons

1 message

no-reply@email.copyright.com <no-reply@email.copyright.com> Sat, Dec 9, 2023 at 7:22 AM
To: pahansaikat@gmail.com



Thank you for your order!

Dear Mr. SAIKAT PAHAN,

Thank you for placing your order through Copyright Clearance Center's RightsLink® service.

Order Summary

Licensee:	Mr. SAIKAT PAHAN
Order Date:	Dec 8, 2023
Order Number:	5684491038755
Publication:	Angewandte Chemie International Edition
Title:	Design of Chiral β-Double Helices from γ-Peptide Foldamers
Type of Use:	Dissertation/Thesis
Order Total:	0.00 USD

View or print complete details of your order and the publisher's terms and conditions.

Sincerely,

Copyright Clearance Center

customercare@copyright.com
https://myaccount.copyright.com

CCC RightsLink